AWARD NUMBER: W81XWH-18-1-0431

TITLE: Receptors in Endosomes Mediate Chronic Pain Associated with Trauma and Stress: Non-opioid Targets for Pain

PRINCIPAL INVESTIGATOR: Nigel Bunnett, PhD

CONTRACTING ORGANIZATION: New York University

REPORT DATE: SEPTEMBER 2020

TYPE OF REPORT: Annual Technical/Progress Report

PREPARED FOR: U.S. Army Medical Research and Materiel Command
Fort Detrick, Maryland 21702-5012

DISTRIBUTION STATEMENT: Approved for Public Release;
Distribution Unlimited

# REPORT DOCUMENTATION PAGE	*Form Approved* *OMB No. 0704-0188*

1. REPORT DATE SEPTEMBER 2020	**2. REPORT TYPE** Annual Technical/Progress Report	**3. DATES COVERED** 9/1/2019 - 8/31/2020

4. TITLE AND SUBTITLE

Receptors in Endosomes Mediate Chronic Pain Associated with Trauma and Stress: Non-Opioid Targets for Pain

5a. CONTRACT NUMBER W81XWH-18-10431

5b. GRANT NUMBER PR170507

5c. PROGRAM ELEMENT NUMBER

6. AUTHOR(S)

Nigel Bunnett, PhD

E-Mail: nwb2@nyu.edu

5d. PROJECT NUMBER 0011176521

5e. TASK NUMBER

5f. WORK UNIT NUMBER

7. PERFORMING ORGANIZATION NAME(S) AND ADDRESS(ES)

NEW YORK UNIVERSITY
70 Washington Square
New York, NY 10010

8. PERFORMING ORGANIZATION REPORT NUMBER

U.S. Army Medical Research and Development Command
Fort Detrick, Maryland 21702-5012

10. SPONSOR/MONITOR'S ACRONYM(S)

11. SPONSOR/MONITOR'S REPORT NUMBER(S)

12. DISTRIBUTION / AVAILABILITY STATEMENT

Approved for Public Release; Distribution Unlimited

13. SUPPLEMENTARY NOTES

14. ABSTRACT The grant seeks to determine whether G protein-coupled receptors (GPCRs) in endosomes, rather than at the plasma membrane, are mediators and therapeutic targets for chronic pain. Aim 1 examines whether GPCRs in endosomes control activity of ion channels and expression of genes that induce sustained neuronal excitation. Aim 2 determines whether endosomally-targeted antagonists inhibit channel activity, gene expression and hyperexcitability of neurons. Aim 3 evaluates the therapeutic potential of endosomally-targeted GPCR antagonists in trauma- and stress-induced pain relevant to military personnel. Progress has been made in all aims. Neuropeptides (substance P, calcitonin gene-related peptide) and proteases (trypsin) stimulated GPCR endocytosis and evoked sustained signals and hyperexcitability in pain-sensing neurons. Dynamin and clathrin inhibitors suppressed endocytosis, signaling and hyperexcitability. Therapies have been developed to block endosomal signaling and evaluated in preclinical models of trauma- and stress-induced pain. Therapies include: dynamin and clathrin inhibitors; lipid-conjugated antagonists that accumulate in endosomes; antagonists encapsulated into nanoparticles that disassemble in acidic endosomes. These antagonists effectively reversed nociception in preclinical models of visceral pain, migraine pain, and nerve injury pain. They were more effective than conventional antagonists of plasma membrane GPCRs. Thus, endosomal GPCRs have been identified as major mediators and therapeutic targets for chronic pain.

15. SUBJECT TERMS Chronic pain; neuropathic pain; head injury pain; migraine pain; irritable bowel syndrome pain; G proteincoupled receptors; endosomes; analgesics.

16. SECURITY CLASSIFICATION OF:			**17. LIMITATION OF ABSTRACT**	**18. NUMBER OF PAGES**	**19a. NAME OF RESPONSIBLE PERSON** USAMRMC
a. REPORT Unclassified	**b. ABSTRACT** Unclassified	**c. THIS PAGE** Unclassified	Unclassified	181	**19b. TELEPHONE NUMBER** *(include area code)*

TABLE OF CONTENTS

1. INTRODUCTION:

G protein-coupled receptors (GPCRs) are the largest class of transmembrane signaling proteins. They control most physiological and pathological processes, including pain, and are the target of over one third of FDA-approved drugs. GPCRs are traditionally considered to function at the plasma membrane, allowing cells to detect extracellular ligands. However, plasma membrane signaling is transient, and activated GPCRs usually undergo clathrin- and dynamin-mediated endocytosis. Endosomes were once considered merely conduits for GPCR trafficking to recycling or degradatory pathways. This grant investigates the novel concept that endosomes are a vital site for continued GPCR signaling in pain-sensing neurons that mediates sustained neuronal activity and pain. Thus, selective antagonists of endosomal GPCRs might provide superior relief from chronic pain than conventional drugs that are designed to target GPCRs at the plasma membrane. The inability of such drugs to effectively engage GPCRs in acidic endosomes might explain their lack of efficacy in clinical trials of chronic pain. The application focuses on receptors for neuropeptides (substance P [SP] neurokinin 1 receptor [NK_1R]; calcitonin gene-related peptide [CGRP] calcitonin like receptor [CLR]) and proteases (protease-activated receptor-2 [PAR_2]). These receptors have been implicated in nerve injury pain, migraine pain, and colonic pain of irritable bowel syndrome (IBS).

2. KEYWORDS:

Chronic pain; neuropathic pain; head injury pain; migraine pain; irritable bowel syndrome pain; G protein-coupled receptors; endosomes; analgesics

3. ACCOMPLISHMENTS:

Goals of Project. The table indicates approved Statement of Work tasks, date of completed tasks, and percentage of tasks accomplished by those dates.

Abbreviations: GPCR, G Protein-Coupled Receptor; DRG, Dorsal Root Ganglia; PAR_2, Protease-Activated Receptor-2; NK_1R, Neurokinin 1 Receptor; CLR, Calcitonin Receptor-like Receptor; TRP, Transient Receptor Potential (ion channel); muGFP, monomeric ultrastable Green Fluorescent Protein; IBS-D, Irritable Bowel Syndrome, Diarrhea-Predominant; HC, Healthy Control; ABP, Activity-Based Probe; PTH, Post Traumatic Headache; FRET, Förster Resonance Energy Transfer; BRET, Bioluminescence Resonance Energy Transfer; RNA-Seq, RNA Sequencing

Aim 1: To determine whether GPCRs in endosomes of pain-sensing neurons control the activity of ion channels and the transcription of genes that induce sustained neuronal excitation.	**Date**	**%**
Major Task 1: Determine whether endosomal PAR_2 in DRG neurons generates compartmentalized signals that regulate channel activity and sensitization		
Subtask 1: Establish breeding colonies of PAR_2-muGFP mice.	9/29/20	100
Subtask 2: Analyze endocytosis-dependent compartmentalized signaling in DRG neurons	9/29/20	100
Subtask 3: Assess PAR_2-mediated sensitization and TRP channel activation in DRG neurons	9/29/20	75
Major Task 2: Determine whether proteases in human colon biopsy specimens activate endosomal PAR_2 in DRG neurons to generate signals that regulate channel activity and sensitization		
Subtask 1: Collect and process human colon biopsies from IBS-D (N=50) and HC (N=50) patients	9/29/20	100
Subtask 2: Determine whether proteases in human IBS-D biopsies sensitize DRG neurons and activate TRP channel through endosomal PAR_2.	9/29/20	25
Subtask 3: Profile activated serine and cysteine proteases in supernatants of IBS-D and HC biopsies using ABPs	9/29/20	25
Major Task 3: Determine whether endosomal PAR_2, NK_1R and CLR signals regulate transcription in pain-sensing neurons		

Subtask 1: Determine whether endosomal PAR_2, NK_1R and CLR signaling regulates transcription in DRG and spinal neurons	9/29/20	10
Aim 2: To determine whether endosomally-targeted antagonists inhibit endosomal GPCR signaling, channel activation, gene transcription and sustained hyperexcitability of pain-sensing neurons.		
Subtask 1: Generate small molecule tripartite PAR_2, NK_1R and CLR antagonists; generate small molecule quadripartite NK_1R and CLR antagonists; generate fluorescent probes	9/29/20	100
Major Task 1: Determine whether tripartite and quadripartite antagonists disrupt endosomal PAR_2, NK_1R and CLR signaling in HEK293 cells		
Subtask 1: Determine whether lipidated antagonists disrupt ligand/receptor interactions in endosomes	9/29/20	50
Subtask 2: Determine whether lipidated antagonists inhibit endosomal signaling of PAR_2, NK_1R and CLR in HEK293 cells	9/29/20	100
Major Task 2: Determine whether tripartite and quadripartite antagonists target PAR_2 in endosomes of DRG neurons and NK_1R and CLR in endosomes of spinal neurons, and inhibit endosomal signaling		
Subtask 1: Determine whether tripartite and quadripartite antagonists colocalize with PAR_2, NK_1R and CLR on endosomes of pain-sensing neurons	9/29/20	100
Subtask 2: Determine whether tripartite and quadripartite antagonists inhibit endosomal signaling of PAR_2, NK_1R and CLR in pain-sensing neurons	9/29/20	100
Major Task 3: Determine whether tripartite and quadripartite antagonists disrupt PAR_2-induced sensitization and transcription in DRG neurons and NK_1R- and CLR-induced sensitization and transcription in spinal neurons		
Subtask 1: Determine whether tripartite and quadripartite antagonists inhibit sensitization and TRP activation in neurons	9/29/20	75
Subtask 2: Examine whether antagonists suppress gene expression	9/29/20	0
Aim 3: To investigate the therapeutic potential of endosomally-targeted GPCR antagonists in trauma- and stress-induced pain that is relevant to disorders of military personnel and veterans.		
Major Task 1: Conduct studies in preclinical model of migraine headache to determine feasibility of using tripartite CLR antagonists for migraine pain.		
Subtask 1: Generate tripartite antagonists of PAR_2, NK_1R and CLR; generate quadripartite probes for NK_1R and CLR antagonists, similar to Aim 2 above	9/29/20	100
Subtask 2: Develop a GTN-evoked model of migraine headache pain in C57BL/6 mice	9/29/20	100
Subtask 3: Determine efficacy of tripartite or non-lipidated CLR antagonists	9/29/20	100
Major Task 2: Conduct studies in preclinical model of nerve injury pain to determine feasibility of using quadripartite NK_1R/CLR antagonists for nerve injury pain.		
Subtask 1: Develop a spared nerve injury model of neuropathic pain in C57BL/6 mice	9/29/20	100
Subtask 2: Determine efficacy of quadripartite NK_1R/CLR antagonists and non-lipidated antagonists	9/29/20	100
Major Task 3: Conduct studies in preclinical model of IBS pain to determine feasibility of using tripartite PAR_2 antagonists for post-inflammatory IBS pain.		
Subtask 1: Generate an IBS mouse model in C57BL/6 mice	9/29/20	75
Subtask 2: Training of electrophysiologist in Dr. Schmidt's laboratory by Dr. Bunnett's team on visceromotor responses following graded colorectal distention	9/29/20	75
Subtask 3: Determine efficacy of tripartite PAR_2 antagonists and non-lipidated antagonists	9/29/20	75

Accomplishments

The general hypothesis of our DoD project is that activated G protein-coupled receptors (GPCRs) traffic to endosomes of nociceptors (*i.e.,* pain sensing neurons) and second order spinal neurons (*i.e.,* pain transmitting neurons) during injury and inflammation, including nerve-injury pain, irritable bowel syndrome (IBS) pain, and migraine/post-traumatic headache pain. GPCRs continue to signal from endosomes to control persistent hyperexcitability and chronic pain. Antagonists designed to target GPCRs in endosomes thus offer superior relief from pain.

a) Profiling proteases in diseased human tissues. We sought to identify proteases that are activated in painful diseases in patients and to determine the mechanisms by which they evoke pain. Through our collaboration with the Salisbury VA, we have collected biopsies of colonic mucosa from veterans: patients with the painful disorder IBS and healthy controls. We are now analyzing biopsy supernatants for protease activity using a panel of activity-based probes (ABPs) for serine and cysteine proteases.

We have published the development of two novel ABPs for neutrophil elastase and cathepsin (Cat) X, and have used these probes to profile activated proteases in tissues from mice and patients with inflammatory bowel disease (IBD). Cat-S has previously been implicated in IBD pain. Using broad-spectrum and specific ABPs, we investigated Cat-S activation in human and mouse colitis. We observed a significant increase in fecal Cat-S in patients with ulcerative colitis compared to healthy controls (**Fig. 1A, B**). Mice with experimental colitis exhibited a modest increase in mucosal activity of both Cat-S and Cat-X compared to naïve mice. Luminal secretion of Cat-S was increased upon colitis induction. Using confocal microscopy, we determined the source of Cat-S to be CD68$^+$ macrophages in the mucosa. To investigate the contribution of Cat-S and Cat-X to colitis, we induced colitis in cathepsin-deficient mice. Cat-X-deficient mice exhibited no clear differences in disease indicators compared to wild-type mice, while Cat-S-deficient mice exhibited less rectal bleeding, less splenomegaly and improved histological scores. To determine whether pharmacologic inhibition of Cat-S activity would likewise ameliorate symptoms of colitis, a reversible inhibitor LY3000328 was administered to mice with colitis. LY3000328 provoked a clear upregulation of Cat-S and L activity, likely through a compensatory mechanism or accumulation of undegraded cathepsins. This increase in protease activity was associated with exacerbated histological scores and splenomegaly. Collectively, these results suggest that Cat-S, but not Cat-X, may promote symptoms of experimental colitis. This work is under review in Am. J. Physiol.

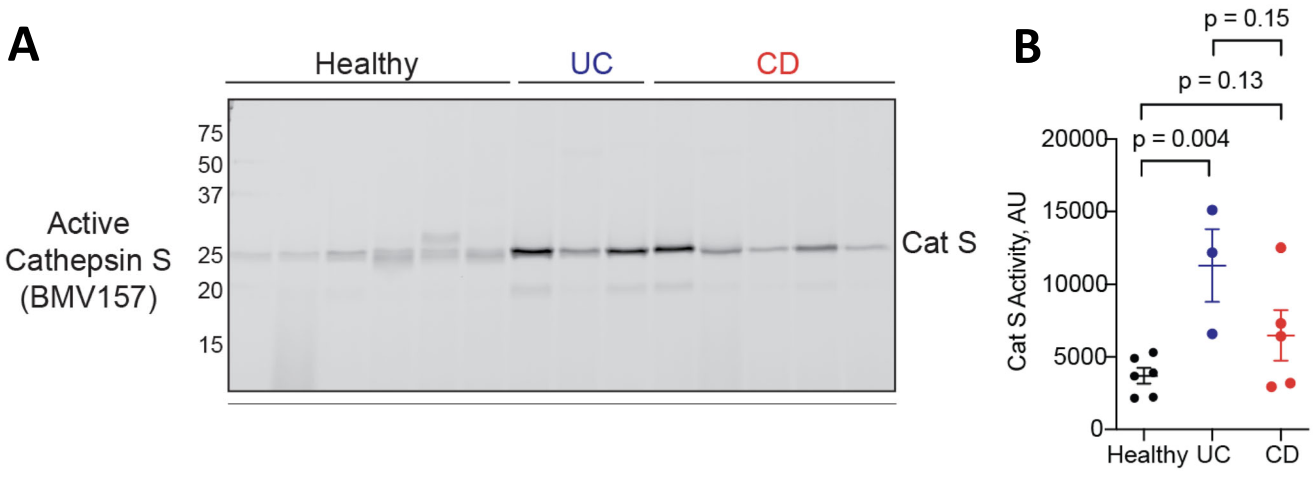

Figure 1. Protease profiling in human disease. Detection of activated Cat-S in fecal samples from patients with ulcerative colitis (UC) and Crohn's Disease (CD). A. Gel. B. Quantification of activity.

b) Generation and characterization of knockin mice expressing PAR$_2$ fused to muGFP. To specifically localize protease-activated receptor-2 (PAR$_2$) in tissues and to assess PAR$_2$ endocytosis during disease, we generated knock-in mice expressing PAR$_2$ fused to monomeric ultrastable GFP (muGFP). Breeding colonies have been established and mice have been fully characterized. Analysis of gastrointestinal tissues and DRG by Q-PCR, revealed similar levels of expression of PAR$_2$ and PAR$_2$-muGFP mRNA in wild type and knockin mice, respectively. Intraplanar administration of trypsin to wild type and knockin mice caused identical allodynia, confirming normal function of PAR_2-muGFP *in vivo*. We mapped the distribution of PAR_2 in the intestinal tract and in dorsal root ganglia (DRG) using antibodies to GFP, to amplify the signal, and RNAScope using probes to PAR_2 and GFP. PAR_2-muGFP was robustly expressed by enterocytes and colonocytes, determined by immunofluorescence and RNAScope. RNAScope analysis revealed expression of PAR_2 in a small subset of DRG neurons. In mice with colitis, PAR_2-muGFP was redistributed from the basolateral membranes of colonocytes to endosomes, consistent with the generation of proinflammatory proteases that activate PAR_2. Exposure of isolated segments of colon to trypsin and a PAR_2-selective agonist also evoked endocytosis of PAR_2 in colonocytes. Inhibitors of dynamin and clathrin blunted endocytosis, suggesting that endocytosis of PAR_2 proceeds by a dynamin and clathrin-mediated mechanism. To ascertain the importance of PAR_2 endocytosis and endosomal signaling to colonic pain, we administered a PAR_2 agonist into the colon and measured nociception by stimulating the abdomen with calibrated von Frey filaments. The PAR_2 agonist caused robust visceral nociception. We are currently determining whether intracolonic administration of dynamin and clathrin inhibitors attenuates PAR_2-evoked nociception. We expect to submit this work for publication by December 2020.

c) Endosomal signaling of proteases and PAR_2 in IBS pain. In the previous reporting period, we published a study supporting a major role for proteases and PAR_2 in IBS pain. We found that colonic mucosa from patients with IBS releases proteases that evoke endocytosis of PAR_2 in nociceptors from mice. PAR_2 signals from endosomes of nociceptors to induce hyperexcitability and colonic pain. We developed a lipidated antagonist of PAR_2 that attenuated endosomal signaling and prevented IBS protease-evoked sensitization of nociceptors. In the current reporting period we have extended these findings by studying the capacity of proteases released from colonic biopsies from veterans with IBS to excite nociceptors.

d) Proteases, PAR_2 and trigeminal pain. For the migraine and post-traumatic headache models, we measure the withdrawal response to stimulation of the facial (*i.e.,* trigeminal) region with calibrated von Frey fibers. Two protease activators of PAR_2 that have not been tested for their capacity to induce trigeminal nociception are legumain (Lgmn) and Cat-S. Lgmn is a cysteine protease that requires an acidic pH (for example, inflamed or injured tissue) for activation. Cat-S is a cysteine lysosomal protease that is secreted by macrophages, in the periphery, and microglia in the brain. Since submission of the previous progress report, we tested the role of Lgmn and Cat-S in trigeminal nociception. The role of PAR_2 in Lgmn- and Cat-S-mediated trigeminal nociception was tested using $Par_2Na_v1.8$ mice, which lack PAR_2 in $Na_v1.8$-positive neurons such as nociceptors. We measured withdrawal responses to mechanical stimulation of the left cheek with von Frey filaments. After measurement of baseline responses, Lgmn or Cat-S was injected subcutaneously to the left cheek. Nociception was then tested at various times after protease injection. Lgmn and Cat-S induced facial nociception in wild type but not $Par_2Na_v1.8$ mice (Figure 2, A-C). Our findings demonstrate that Lgmn and Cat-S produce nociception in the facial region through activation of PAR_2 on trigeminal afferent neurons, which are responsible for migraine and post-traumatic headache. Future studies will test whether the protease activators contribute to nociceptive behavior in the migraine and post-traumatic headache models.

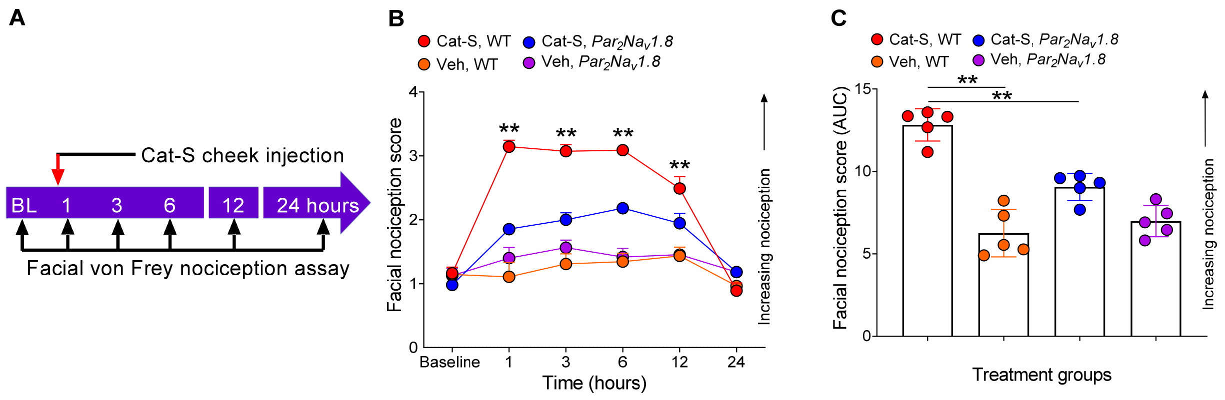

Figure 2. Cat-S induces trigeminal nociception through PAR_2. (A) Experimental timeline. (B) Cat-S increased the facial nociception score in WT, but not $Par_2Na_v1.8$ mice. **p<0.01 Cat-S, WT versus Veh, WT at indicated time point, two-way ANOVA multiple comparisons. (C) Area under the curve (AUC) for each mouse presented in (B). **p<0.01 Student's t-test.

e) Tripartite antagonists of endosomal GPCR signaling. GPCRs can continue to signal from endosomes to control important pathophysiological processes. We previously reported that sustained endosomal signaling of the substance P (SP) neurokinin 1 receptor (NK_1R) in spinal neurons mediates nociception. An NK_1R antagonist, Spantide I, conjugated to cholestanol (Span-Chol) accumulates in endosomes, inhibits endosomal NK_1R signaling, and causes prolonged antinociception in mice. We have now characterized in detail the mechanisms underlying the antinociceptive actions of Span-Chol. We used fluorescent correlation spectroscopy and biosensors targeted to subcellular compartments to determine the long-term location and activity of lipid-anchored probes. The cholestanol-anchor increased in the local concentration of probe at the plasma membrane. This localized enrichment corresponded with an increase in NK_1R binding affinity over time, and increased potency for inhibition of NK_1R calcium signaling. Span-Chol, but not Span, caused a persistent (>4 h) decrease in NK_1R recruitment of β-arrestin and receptor internalization to early endosomes. Using targeted biosensors, we mapped the relative inhibition of NK_1R signaling as the receptor moved into the cell. Span selectively inhibited cell surface signaling whereas Span-Chol selectively inhibited endosomal signaling. In a preclinical model of pain, Span-Chol caused prolonged antinociception (>9 h), which is attributable to increased local concentration at membranes, decreased NK_1R endocytosis, and inhibition of endosomal signaling. Identifying the mechanisms that contribute to the increased preclinical efficacy of lipid-anchored NK_1R antagonists is an important step toward understanding how we can effectively target intracellular GPCRs in disease. This manuscript is in revision for J. Biol. Chem.

f) Nanoparticle-encapsulated antagonists of endosomal GPCR signaling. We have developed nanoparticle-encapsulated antagonists of endosomal GPCRs for the treatment of pain. Nanoparticle encapsulation improves drug efficacy by enhancing the stability, tolerability, delivery and retention in diseased tissues. Nanoparticle-mediated drug delivery is especially useful for targets within endosomes because of the endosomal transport mechanisms of many nanomedicines within cells. We reported the design of a pH-responsive, soft polymeric nanoparticle for the targeting of acidified endosomes to precisely inhibit endosomal signalling events leading to chronic pain. In chronic pain, the SP NK_1R redistributes from the plasma membrane to acidified endosomes, where it signals to maintain pain. Therefore, the NK_1R in endosomes provides an important target for pain relief. The pH-responsive nanoparticles entered cells by clathrin- and dynamin-dependent endocytosis and accumulated in NK_1R-containing endosomes. Following intrathecal injection into rodents, the nanoparticles, containing the FDA-approved NK_1R antagonist aprepitant, inhibited SP-induced activation of spinal neurons and thus prevent pain transmission. Treatment with the nanoparticles led to complete and persistent relief from nociceptive, inflammatory and neuropathic nociception. This approach offers a much-needed nonopioid treatment option for chronic pain. We have expanded this work to examine the efficacy of nanoparticle-encapsulated and free aprepitant in neuropathic pain in mice. In the sural nerve spared model of neuropathic pain, nanoparticle-encapsulated aprepitant provided a more efficacious and sustained relief from mechanical hyperalgesia and cold allodynia than free aprepitant, at all doses tested (**Figure 3**). The intrathecal injection of inhibitors of endocytosis also inhibited nociception, reinforcing a role for endosomal signaling in neuropathic pain.

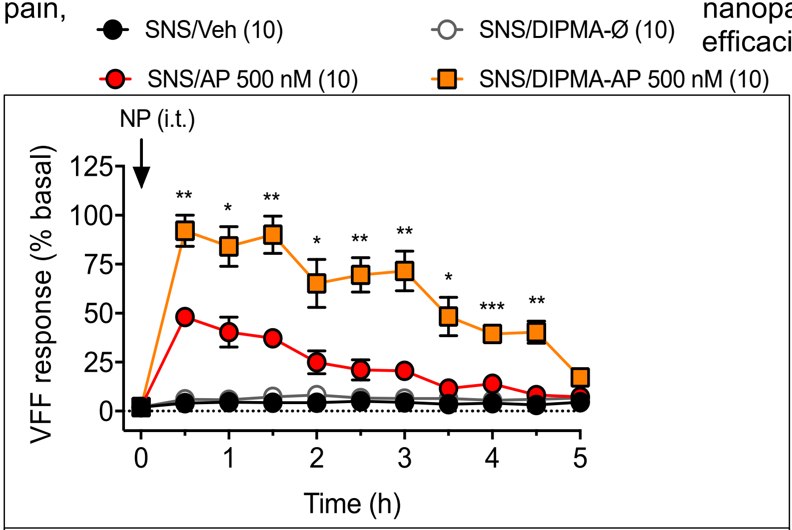

Figure 3. Nanoparticle-mediated relief from nerve injury pain. The sural nerve spared (SNS) model of neuropathic pain was studied in mice. After 10 days, free aprepitant (AP) or nanoparticle-encapsulated aprepitant (DIPMA-AP) was injected intrathecally (5 µl, 500 nM). DIPMA-AP provided more complete and sustained relief from pain.

We have further refined nanoparticle-mediated drug delivery by developing nanoparticles to target endosomes of pain sensing and transmitting neurons. We reported that opioids from the inflamed colon activate δ-opioid receptors (DOPr) in endosomes of nociceptors. Biopsies of inflamed colonic mucosa from patients and mice with colitis released opioids that activated DOPr on nociceptors to cause a sustained decrease in excitability. DOPr agonists inhibited mechanically-sensitive colonic nociceptors. DOPr endocytosis and endosomal signaling by protein kinase C (PKC) and extracellular signal regulated kinase (ERK) pathways mediated the sustained inhibitory actions of endogenous opioids and DOPr agonists. DOPr agonists stimulated recruitment of $G\alpha_{i/o}$ and β-arrestin1/2 to endosomes. Analysis of compartmentalized signaling revealed a requirement of DOPr endocytosis for activation of PKC at the plasma membrane and in the cytosol and ERK in the nucleus. We explored a nanoparticle delivery strategy to evaluate whether endosomal DOPr might be a therapeutic target for pain. The DOPr agonist DADLE was coupled to a liposome shell for targeting DOPr-positive nociceptors and incorporated into a mesoporous silica core for release in the acidic and reducing endosomal environment. Nanoparticles activated DOPr at the plasma membrane, were preferentially endocytosed by DOPr-expressing cells, and were delivered to DOPr-positive early endosomes. Nanoparticles caused a long-lasting activation of DOPr in endosomes, which provided sustained inhibition of nociceptor excitability and relief from inflammatory pain. Conversely, nanoparticles containing a DOPr antagonist abolished the sustained inhibitory effects of DADLE. Thus, DOPr in endosomes is an endogenous mechanism and a therapeutic target for relief from chronic inflammatory pain.

g) Endosomal signaling of CGRP/CLR in Schwann cells and migraine pain. We have reported a major role for Schwann cells in neuropathic pain. In the current reporting period, we have discovered a key role for Schwann cells and endosomal signaling in migraine pain. We observed that a human Schwann cell line and primary mouse Schwann cells express mRNA encoding calcitonin-like receptor (CLR) and receptor activity modifying protein 1 (RAMP1), the receptors for calcitonin-gene related peptide (CGRP). CGRP and CLR are therapeutic targets for chronic migraine in patients. In preclinical models of migraine pain in mice, selective deletion of CGRP receptors from Schwann cells abrogated supraorbital allodynia evoked by administration of CGRP and trinitroglycerin. The local injection of inhibitors of clathrin and dynamin also attenuated nociception. A small molecule CLR antagonist, MK-43207, incorporated into soft polymer nanoparticles, more effectively attenuated nociception than free MK-43207 (**Figure 4**). These results suggest that endosomal CGRP/CLR signaling in Schwann cells underlies migraine pain in mice. We studied the pathway by which endosomal CLR signals pain in isolated Schwann cells. CGRP evoked CLR endocytosis and activated adenylyl cyclase and protein kinase A, leading to generation of reactive oxygen species, which in turn activated the transient receptor potential ankyrin 1 (TRPA1) channel on nociceptors. Thus, CGRP/CLR signaling in endosomes of Schwann cells provides a peripheral mechanism for signaling migraine pain in mice. Endosomal CLR is a new target for the treatment of migraine pain. We are now preparing this work for submission to Cell.

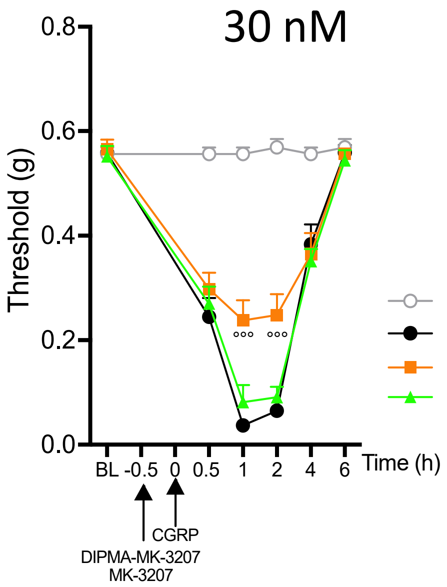

Figure 4. Nanoparticle-mediated relief from migraine pain. Free MK-43207 or MK-43207 encapsulated into nanoparticles (DIPMA-MK43207) (both 30 nM) was injected into the periorbital region of mice 30 min before injection of CGRP. Periorbital mechanical allodynia was measured for 6 h. DIPMA-MK43207 provide superior antinociception.

Training and Professional Development

The NYU Department of Molecular Pathobiology provides opportunities for mentorship, research training and professional development. Post-doctoral fellows have a faculty mentoring committee. Trainees learn laboratory skills from experienced investigators, and receive mentorship from the PI on literature reviews, experimental design, data analysis, scientific writing and presentation. They attend weekly laboratory meetings and journal clubs, and attend symposia and seminars at NYU. A team science training program of bimonthly seminars proves training in ethical conduct of research, rigor and reproducibility, experimental design, and career development.

Dissemination of Results

The Bunnett and Schmidt laboratories meet as a group each week to evaluate progress, provide feedback on technical issues and results, arrange transfer of mice and chemical resources, and trouble-shoot problems. Technical methods specific to the project are discussed. Member of the laboratory including students, postdoctoral fellows, scientists and principal investigators attend this joint laboratory meeting.

Dr. Bunnett has presented findings at the following meetings and seminar series:

2019

- National Center for Advancing Translational Science, Washington DC
- The Opioid Crisis and the Future of Addiction and Pain Therapeutics: Opportunities, Tools, and Technologies Symposium, NIH Washington DC
- US Army Medical Research and Materiel Command Congressionally Directed Medical Research Programs: Chronic Pain Management Research Program Stakeholders Meeting, Baltimore, MD
- 9th Congress of Federation of Asian and Oceanian Physiological Societies, Kobe, Japan
- Biogen, Boston, MA.

2020

- University of Arizona
- University of California, San Francisco
- New York University

Plans for Next Reporting Period

Priorities for the next reporting period include:

Analysis of the mechanisms by which GPCRs in endosomes regulate TRP channel activity at the plasma membrane and gene expression in the nucleus of neurons that sense and transmit pain.

Analysis of proteases in biopsies of human colonic mucosa using activity-based probes, including newly developed and existing probes for serine and cysteine proteases. Investigation of whether activate proteases cause hyperexcitability of nociceptors *via* endosomal PAR_2.

4. IMPACT:

Impact on principal discipline. This work has identified new targets for the treatment of chronic pain. We have discovered that painful stimuli cause the translocation of receptors from the cell surface to endosomes of neurons that sense and transmit pain. Receptors in endosomes are primarily responsible for signaling persistent pain. Drugs that target these receptors provide more effective relief from chronic pain than conventional drugs that target receptors at the surface of cells. The failure of conventional drugs in clinical trials of chronic pain may be due to their inability to inhibit receptors in endosomes.

Impact on other disciplines. GPCRs mediate many diseases beyond pain, including cardiovascular disease, inflammatory diseases and cancer. Antagonists and agonists of GPCRs represent the single largest class of drugs; more than one third of FDA-approved drugs target GPCRs. The concept that GPCRs in endosomes generate sustained signals that may underlie disease processes raises the prospect that GPCRs in endosomes might be the optimal target for the treatment of many chronic diseases.

Impact on technology transfer. The PI is a scientific founder of Endosome Therapeutics, a start-up company that seeks to develop and commercialize drugs that target endosomal GPCRs. The National Center for Advancing Translational Science (NCATS) has initiated a collaboration to develop nanoparticle-encapsulated antagonists of GPCRs for the treatment of chronic pain.

Impact on society. The development of non-opioid treatments for chronic pain has the potential to lessen the opioid crisis, which is a major cause of mortality and morbidity in the USA.

5. CHANGES/PROBLEMS:

Changes in approach and reasons for change. Nothing to report.

Actual or anticipated problems or delays and actions or plans to resolve them.

PI Dr. N.W. Bunnett accepted the Chair of the Department of Molecular Pathobiology at New York University, effective 10/1/2019. This relocation has facilitated collaborations with Dr. B.L. Schmidt, the partnering PI.

The COVID19 crisis closed NYU laboratories from March to July 2020, which affected productivity but provided opportunities for writing. Laboratories are now fully operational.

Changes that had a significant impact on expenditures. Nothing to report.

Significant changes in use or care of human subjects, vertebrate animals, biohazards, and/or select agents. Nothing to report.

Significant changes in use or care of human subjects. Nothing to report.

Significant changes in use or care of vertebrate animals. Nothing to report.

Significant changes in use of biohazards and/or select agents. Nothing to report.

6. PRODUCTS:

* Papers included in appendix

Journal publications

1. *Anderson, B.M., Poole, D.P., Aurelio, L., Ng, G.Z., Fleischmann, M., Kasperkiewicz, P., Morissette, C., Drag, M., van Driel, I.R., Schmidt, B.L., Vanner, S.J., Bunnett, N.W. & Edgington-Mitchell, L.E. Application of a chemical probe to detect neutrophil elastase activation during inflammatory bowel disease. *Sci Rep* **9**, 13295, 2019. PMC6746801. Federal support: Yes
2. *Mountford, S.J., Anderson, B.M., Xu, B., Tay, E.S.V., Szabo, M., Hoang, M.L., Diao, J., Aurelio, L., Campden, R.I., Lindstrom, E., Sloan, E.K., Yates, R.M., Bunnett, N.W., Thompson, P.E. & Edgington-Mitchell, L.E. Application of a Sulfoxonium Ylide Electrophile to Generate Cathepsin X-Selective Activity-Based Probes. *ACS Chem Biol* **15**, 718-727, 2020. Federal support: Yes
3. *Anderson, B.M., Campden, R.I., Wu, H., McQuade, R.M., Carbone, S.E., Poole, D.P., Lomax, A.E., Vanner, S.J., Yates, R.M., Bunnett, N.W., Edgington-Mitchell, L.E. Probing the contribution of cysteine cathepsins to inflammatory bowel diseases. *Am. J. Physiol,* Submitted, 2020. Federal support: Yes
4. *Mai, Q.N., Shenoy, P., Quach, T., Retamal-Santibanez, J., Yeatman, H.R., Aurelio, L., Conner, J.W., Poole, D.P., Canals, M., Graham, B., Briddon, S.J., Hill, S.J., Porter, C.J., Bunnett, N.W., Halls, M.L., Veldhuis, N.A. A three-pronged mechanism of action underlies the prolonged analgesia mediated by lipid-anchored antagonists of the neurokinin 1 receptor. *J. Biol. Chem*. In revision. Federal support: Yes
5. *Ramirez-Garcia, P.D., Retamal, J.S., Shenoy, P., Imlach, W., Sykes, M., Truong, N., Constandil, L., Pelissier, T., Nowell, C.J., Khor, S.Y., Layani, L.M., Lumb, C., Poole, D.P., Lieu, T., Stewart, G.D., Mai, Q.N., Jensen, D.D., Latorre, R., Scheff, N.N., Schmidt, B.L., Quinn, J.F., Whittaker, M.R., Veldhuis, N.A., Davis, T.P. & Bunnett, N.W. A pH-responsive nanoparticle targets the neurokinin 1 receptor in endosomes to prevent chronic pain. *Nat Nanotechnol* **14**, 1150-1159, 2019. Federal support: Yes
6. *Jimenez-Vargas, N.N., Gong, J., Wisdom, M.J., Jensen, D.D., Latorre, R., Hegron, A., Teng, S., DiCello, J.J., Rajasekhar, P., Veldhuis, N.A., Carbone, S.E., Yu, Y., Lopez-Lopez, C., Jaramillo-Polanco, J., Canals, M., Reed, D.E., Lomax, A.E., Schmidt, B.L., Leong, K.W., Vanner, S.J., Halls, M.L., Bunnett, N.W. & Poole, D.P. Endosomal signaling of delta opioid receptors is an endogenous mechanism and therapeutic target for relief from inflammatory pain. *Proc Natl Acad Sci U S A* **117**, 15281-15292, 2020. PMC7334524. Federal support: Yes
7. *De Logu, F., Li Puma, S., Landini, L., Portelli, F., Innocenti, A., de Araujo, D.S.M., Janal, M.N., Patacchini, R., Bunnett, N.W., Geppetti, P. & Nassini, R. Schwann cells expressing nociceptive channel TRPA1 orchestrate ethanol-evoked neuropathic pain in mice. *J Clin Invest* **129**, 5424-5441, 2019. PMC6877331. Federal support: Yes
8. Tewari, D., Cook, A.D., Lee, M.C., Christensen, A.D., Croxford, A., Becher, B., Poole, D., Rajasekhar, P., Bunnett, N., Smith, J.E., Hamilton, J.A. & McMahon, S.B. Granulocyte-Macrophage Colony Stimulating Factor As an Indirect Mediator of Nociceptor Activation and Pain. *J Neurosci* **40**, 2189-2199, 2020. PMC7083288. Federal support: Yes

9. *Castro, J., Harrington, A.M., Lieu, T., Garcia-Caraballo, S., Maddern, J., Schober, G., O'Donnell, T., Grundy, L., Lumsden, A.L., Miller, P., Ghetti, A., Steinhoff, M.S., Poole, D.P., Dong, X., Chang, L., Bunnett, N.W. & Brierley, S.M. Activation of pruritogenic TGR5, MrgprA3, and MrgprC11 on colon-innervating afferents induces visceral hypersensitivity. *JCI Insight* **4**2019. PMC6824308. Federal support: Yes
10. Israelyan, N., Del Colle, A., Li, Z., Park, Y., Xing, A., Jacobsen, J.P.R., Luna, R.A., Jensen, D.D., Madra, M., Saurman, V., Rahim, R., Latorre, R., Law, K., Carson, W., Bunnett, N.W., Caron, M.G. & Margolis, K.G. Effects of Serotonin and Slow-Release 5-Hydroxytryptophan on Gastrointestinal Motility in a Mouse Model of Depression. *Gastroenterology* **157**, 507-521 e504, 2019. PMC6650329. Federal support: Yes
11. *Zhao, P., Pattison, L.A., Jensen, D.D., Jimenez-Vargas, N.N., Latorre, R., Lieu, T., Jaramillo, J.O., Lopez-Lopez, C., Poole, D.P., Vanner, S.J., Schmidt, B.L. & Bunnett, N.W. Protein kinase D and Gbetagamma mediate sustained nociceptive signaling by biased agonists of protease-activated receptor-2. *J Biol Chem* **294**, 10649-10662, 2019. PMC6615677. Federal support: Yes

Books. Nothing to report.

Other. Nothing to report.

Websites. Bunnett Laboratory Website: https://dental.nyu.edu/faculty/molecular-pathobiology/bunnett-lab.html

Technologies and techniques. Nothing to report.

Inventions and patents. Nothing to report.

Other products. Nothing to report.

7. PARTICIPANTS AND OTHER COLLABORATING ORGANIZATIONS:

Individuals who have worked on project

NEW YORK UNIVERSITY

Name:	Nigel Bunnett, PhD
Project Role:	PI
Researcher Identifier (e.g. ORCID ID):	0000-0003-3367-0644
Nearest person month worked:	2.4 calendar
Contribution to Project:	Project conception; experimental design; interpreting results; writing manuscripts.
Funding Support:	5R01NS102722; 5R01DE026806; 5R01DK118971; 1R01DE029951-01

Name:	Alex Thomsen, PhD
Project Role:	Co-Investigator
Researcher Identifier (e.g. ORCID ID):	N/A
Nearest person month worked:	0.25 calendar
Contribution to Project:	Design of experiments to examine endosomal signaling pathways.
Funding Support:	Leo Foundation; 5R01NS102722;5R01DK118971;

Name:	Rocco Latorre, PhD
Project Role:	Assistant Research Scientist
Researcher Identifier (e.g. ORCID ID):	0000-0003-2737-8233
Nearest person month worked:	6 calendar
Contribution to Project:	Analysis of the role of endosomal signaling in preclinical models of pain.
Funding Support:	5R01NS102722; 5R01DK118971; 1R01DE029951-01

Name:	Alan Hegron, PhD
Project Role:	Postdoctoral Associate
Researcher Identifier (e.g. ORCID ID):	0000-0002-7588-9209
Nearest person month worked:	3 calendar
Contribution to Project:	Analysis of the pathways of endosomal signaling and gene transcription.
Funding Support:	5R01NS102722; 5R01DK118971; 1R01DE029951-01

Change in support since last reporting period

<u>Nigel Bunnett, PhD (PI)</u>

NEW SUPPORT

1R01DE029951-01 Bunnett/Schmidt (MPI) 9/15/2020-8/31/2024
Targeting Endosomal Receptors for Treatment of Chronic Pain

COMPLETED SUPPORT

Nothing to report

Other organizations. Nothing to report

8. SPECIAL REPORTING REQUIREMENTS:

This is a collaborative award between Dr. N.W. Bunnett (New York University) and B.L. Schmidt (New York University). Dr. Schmidt will submit his report for the 10/01/20 deadline.

9. APPENDICES:

PDF of most relevant published manuscripts and manuscripts under revision and re-review.

SCIENTIFIC REPORTS
natureresearch

OPEN

Application of a chemical probe to detect neutrophil elastase activation during inflammatory bowel disease

Received: 12 April 2019
Accepted: 31 August 2019

Bethany M. Anderson[1,2], Daniel P. Poole[2], Luigi Aurelio[3], Garrett Z. Ng[1], Markus Fleischmann[1,4], Paulina Kasperkiewicz[5], Celine Morissette[6], Marcin Drag[5], Ian R. van Driel[1], Brian L. Schmidt[7], Stephen J. Vanner[6], Nigel W. Bunnett[2,8,9] & Laura E. Edgington-Mitchell[1,2,7]

Neutrophil elastase is a serine protease that has been implicated in the pathogenesis of inflammatory bowel disease. Due to post-translational control of its activation and high expression of its inhibitors in the gut, measurements of total expression poorly reflect the pool of active, functional neutrophil elastase. Fluorogenic substrate probes have been used to measure neutrophil elastase activity, though these tools lack specificity and traceability. PK105 is a recently described fluorescent activity-based probe, which binds to neutrophil elastase in an activity-dependent manner. The irreversible nature of this probe allows for accurate identification of its targets in complex protein mixtures. We describe the reactivity profile of PK105b, a new analogue of PK105, against recombinant serine proteases and in tissue extracts from healthy mice and from models of inflammation induced by oral cancer and *Legionella pneumophila* infection. We apply PK105b to measure neutrophil elastase activation in an acute model of experimental colitis. Neutrophil elastase activity is detected in inflamed but not healthy, colons. We corroborate this finding in mucosal biopsies from patients with ulcerative colitis. Thus, PK105b facilitates detection of neutrophil elastase activity in tissue lysates, and we have applied it to demonstrate that this protease is unequivocally activated during colitis.

Neutrophil elastase (NE) is a serine protease found within azurophilic granules of neutrophils[1]. During infection, active NE contributes to killing of pathogens, and mice lacking NE are more susceptible to bacterial and fungal infections[1]. NE also mediates inflammation by processing cytokines, chemokines and growth factors[1]. Furthermore, NE cleaves the extracellular N termini of protease-activated receptors (PARs), a family of G protein-coupled receptors (GPCRs), to initiate cellular signaling events that lead to inflammation and pain[2–4].

NE has recently been implicated in the pathogenesis of inflammatory bowel diseases (IBD), which are characterized by chronic and relapsing inflammation in the gastrointestinal tract[5]. IBD comprises ulcerative colitis (UC) and Crohn's disease (CD), both of which are associated with diarrhea, rectal bleeding, increased urgency and pain. Mice lacking one copy of NE and a closely related neutrophil serine protease, proteinase 3 (PR3), exhibit improved symptoms in mouse models of colitis[6]. Enforced expression of elafin, an endogenous serine protease

[1]Department of Biochemistry and Molecular Biology, Bio21 Molecular Science and Biotechnology Institute, The University of Melbourne, Parkville, VIC, Australia. [2]Drug Discovery Biology, Monash Institute of Pharmaceutical Sciences, Monash University, Parkville, VIC, Australia. [3]Medicinal Chemistry, Monash Institute of Pharmaceutical Sciences, Monash University, Parkville, VIC, Australia. [4]Department of Cellular Immunology, Institute of Experimental Immunology, University Hospital Bonn, Bonn, Germany. [5]Department of Bioorganic Chemistry, Wroclaw University of Technology, Wroclaw, Poland. [6]Gastrointestinal Diseases Research Unit, Kingston General Hospital, Queen's University, Kingston, ON, Canada. [7]Department of Oral and Maxillofacial Surgery, New York University College of Dentistry, Bluestone Center for Clinical Research, New York, New York, USA. [8]Departments of Surgery and Pharmacology, Columbia University, New York, New York, USA. [9]Department of Pharmacology and Experimental Therapeutics, The University of Melbourne, Parkville, VIC, Australia. Correspondence and requests for materials should be addressed to L.E.E.-M. (email: laura.edgingtonmitchell@unimelb.edu.au)

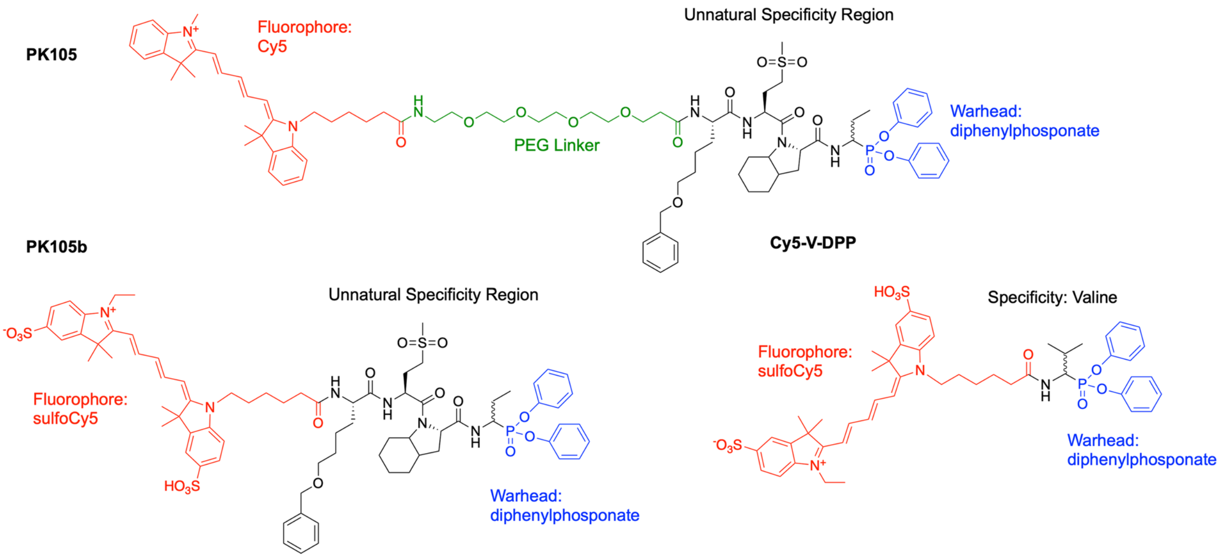

Figure 1. Structures of PK105[16], PK105b, and Cy5-V-DPP[13].

inhibitor, either by intracolonic administration of adenoviral vectors or introduction of elafin-expressing lactic acid bacteria, resulted in attenuation of symptoms in mouse models of colitis[6]. Treatment with a NE-selective inhibitor also reduced colitis symptoms[7].

Colonic mucosal biopsies from patients with IBD exhibit elevated NE expression compared to healthy controls at both mRNA and protein levels[8,9]. Because NE is expressed as an inactive zymogen and can be tightly controlled by endogenous inhibitors once activated, measures of mRNA or total protein expression rarely reflect the pool of active functional enzyme[10]. Thus, tools to measure the specific activity of NE are required.

Commercially available chromogenic and fluorogenic substrate probes, including AAPV-p-nitroanilide and BODIPY-FL-elastin, respectively, have indicated an increase in elastase-like activity in biopsies from UC and CD patients and in mouse models of IBD[6,7,11,12]. However, these probes lack specificity and can be cleaved by multiple proteases[5,10]. Because the probes do not bind directly to the proteases upon cleavage, it is difficult to estimate the proportion of cleavage that is dependent on NE. Thus, improved tools are required to specifically measure NE activation and to improve our understanding of its functions during IBD pathogenesis.

We previously applied a fluorescent activity-based probe (ABP) for NE, Cy5-V-DPP, to track NE activation during colitis[13]. This probe contained a sulfonated cyanine 5 (Cy5) fluorophore and a P1 valine residue coupled to a diphenylphosphonate electrophile (DPP; 'warhead') that reacts with the active site serine of active NE in a covalent, irreversible manner (Fig. 1). While Cy5-V-DPP efficiently labeled recombinant NE and NE in cells with high expression (*e.g.*, bone marrow), we had little success in detecting NE activity in colitis tissues, presumably due to a lack of sensitivity. Use of hybrid combinatorial substrate libraries allowed for optimization of the NE substrate recognition sequence, which was coupled to Cy5 and the DPP warhead to generate the ABP, PK105[14–17]. While PK105 has been extensively characterized in purified neutrophils, its efficacy and specificity for NE in more complex tissue lysates has not been explored until now.

Herein, we characterized the reactivity profile of PK105b, an analogue of PK105, and explored its efficacy in complex tissue lysates. We applied PK105b in a mouse model of acute colitis and in human mucosal biopsies from patients with IBD to clearly measure activation of NE in inflamed tissue.

Results

Selectivity and potency of PK105b against ed serine proteases. We synthesized an analogue of our previously published PK105 probe[16], referred to as PK105b, in which the polyethylene glycol (PEG) linker was omitted and sulfoCy5 was used in place of the unsulfonated version (Fig. 1). This change allowed for a more direct comparison to our Cy5-V-DPP probe[13], which included sulfoCy5 and no PEG. The only difference between the two probes compared in this study is the specificity region: Cy5-V-DPP contains a single P1 valine residue, while PK105b contains a tetrapeptide consisting of non-natural amino acids (Nle(OBzl)-Met(O)2-Oic-Abu) (Fig. 1).

We tested the reactivity of the PK105b against recombinant serine proteases, and compared its potency with Cy5-V-DPP. After incubation of proteases with increasing concentrations of probes for 30 minutes, the proteins were resolved by SDS-PAGE and binding was detected by in-gel fluorescence. Both probes clearly labeled NE and PR-3 in a concentration-dependent manner (Fig. 2A), though PK105b was more potent than Cy5-V-DPP. PK105b also clearly labeled trypsin, another serine protease, while trypsin binding by Cy5-V-DPP was negligible (Fig. 2A).

Using a commercially available fluorogenic substrate probe, AAPV-AMC, we compared the ability of the two probes to inhibit recombinant NE. Like Sivelestat, a commonly used NE inhibitor, PK105b immediately inhibited rNE activity at 0.1 µM while Cy5-V-DPP only partially inhibited rNE activity at 1 and 10 µM (Fig. 2B). These results indicate that PK105b binds to rNE more rapidly and more potently than Cy5-V-DPP. As Cy5-V-DPP and

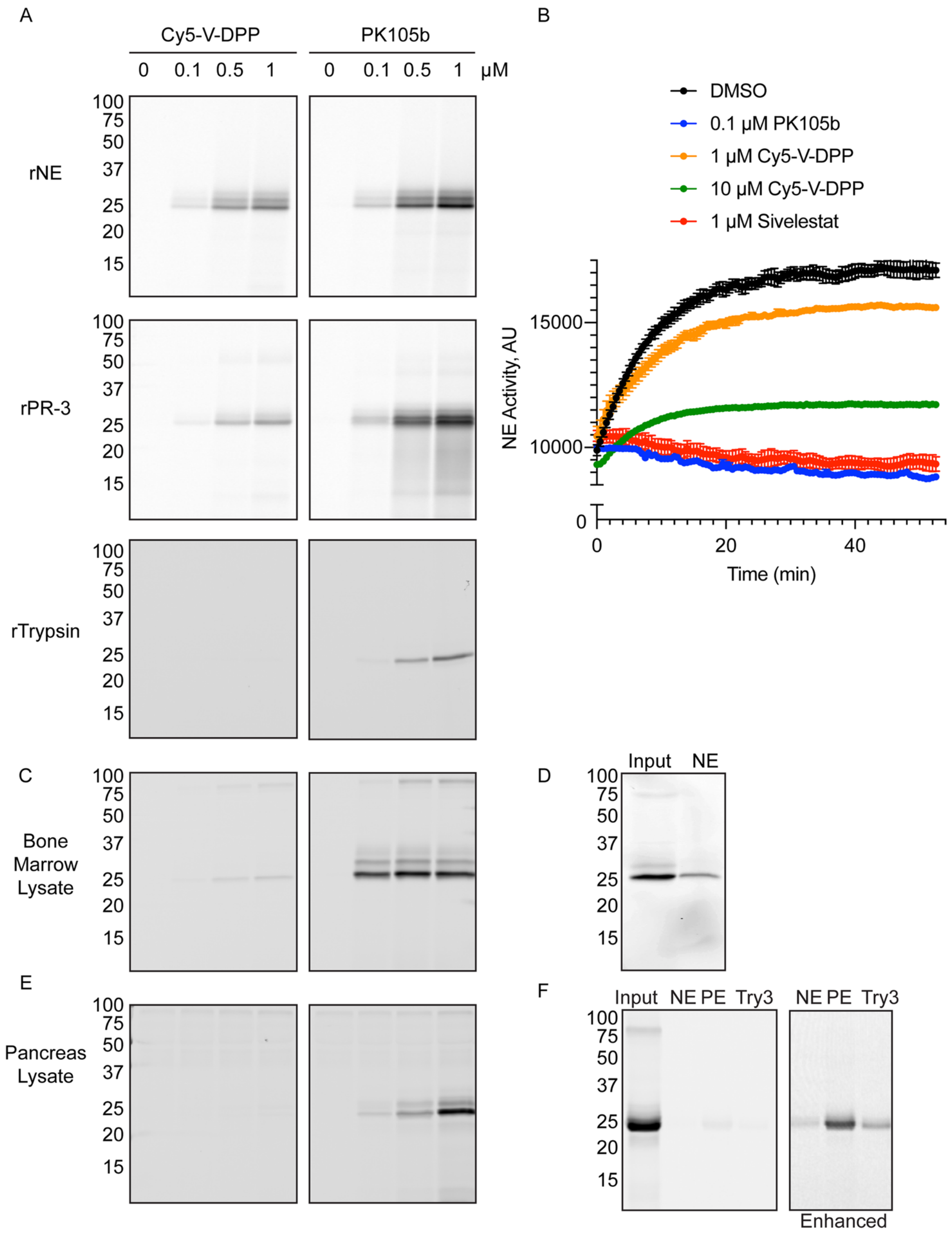

Figure 2. Comparison of selectivity profile for PK105b and Cy5-V-DPP. (**A**) Recombinant serine proteases (neutrophil elastase, proteinase 3, or trypsin) were incubated with increasing concentrations of Cy5-V-DPP or PK105b and binding was assessed by in-gel fluorescence. (**B**) Kinetic measurements of recombinant neutrophil elastase activity using the fluorogenic substrate probe, AAPV-AMC in the presence of DMSO (vehicle control) or the indicated concentration of PK105b, Cy5-V-DPP or Sivelestat. Error bars are shown as mean ± SEM. (**C**,**E**) Lysates from mouse bone marrow or pancreas were incubated with increasing concentrations of Cy5-V-DPP or PK105b and binding was assessed by in-gel fluorescence. (**D**,**F**) PK105b-labeled lysates were immunoprecipitated with antibodies for neutrophil elastase, pancreatic elastase (PE) or trypsin 3 (Try3), as indicated. In (**F**), gain settings for pulldowns were enhanced in order to observe faint bands (right panel). Note: Cy5-V-DPP and PK105b labeling are depicted at equal gain settings, set independently for each sample type.

PK105b have identical DPP warheads, linkers, and sulfoCy5 fluorophores, we can attribute the improved potency and kinetics of PK105b to its extended non-natural specificity region, which likely fits better within the NE active site than valine alone.

Selectivity and potency of PK105b in normal tissue lysates. We compared the ability of PK105b and Cy5-V-DPP to detect protease activity in lysates prepared from mouse bone marrow. Two proteases were labeled by PK105b (Fig. 2C), and the 25-kDa protein was confirmed to be NE by immunoprecipitation with an NE-specific antibody (Fig. 2D). NE was specifically labeled by Cy5-V-DPP, but with a much lower potency than PK105b. We also examined the reactivity of the probes in lysates prepared from mouse pancreas, a tissue rich in serine proteases. With PK105b, we observed strong labeling of 25-kDa proteins that was much more apparent than labeling by Cy5-V-DPP (Fig. 2E). Immunoprecipitation of PK105b-labeled lysates revealed that the target proteases consisted of a combination of NE, pancreatic elastase (PE), and trypsin 3 (Try3, also known as PRSS3 or mesotrypsin; Fig. 2F). Thus, PK105b exhibits a dramatic improvement in labeling efficiency in protein lysates over Cy5-V-DPP. In addition to the improved binding kinetics demonstrated above, the improved labeling profile of PK105b may also be due in part to enhanced stability of the compound afforded by the non-natural specificity region, which may be less prone to degradation than Cy5-V-DPP.

Validation of PK105b in inflamed tissues. To determine the effectiveness of PK105b to measure NE activation in inflamed tissues, we used a mouse model of *Legionella pneumophila* infection. *L. pneumophila* infection may result in Legionnaire's disease, a common cause of community or hospital-acquired pneumonia, and is associated with high neutrophil infiltration in the lung[18,19]. PK105b labeling was significantly increased in lysates prepared from infected lung tissues compared to uninfected lungs (Fig. 3A,C). The identity of the major 25-kDa species was confirmed to be NE by immunoblotting (Fig. 3B,D,E) and immunoprecipitation (Fig. 3F) with an NE-specific antibody. We also confirmed that PK105b binding was mediated by the DPP warhead and the specificity region, as the labelling could be competed by pre-treatment with PK101[14,15], a biotinylated (non-fluorescent) analogue of PK105 (Fig. 3G). As neutrophils are the predominant source of NE during *L. pneumophila* infection, we also examined PK105b labelling in neutrophils from infected-lungs, which were sorted by flow cytometry at >97% purity (Fig. S1). Within this population of cells, we observed specific labeling of NE by PK105b (Fig. 3H).

We next determined the utility of PK105b to detect NE activation in a cancer setting, which is also rich in neutrophils[20–22]. Specifically, we utilized a mouse orthotopic xenograft model of oral squamous cell carcinoma in which human cancer cells (HSC-3) were injected into the tongue[23]. In this context, we observed clear labeling of a 25-KDa species in tumor tissues, but not normal tongue tissues (Fig. 4A,C). This species coincided with the size of mature NE as determined by immunoblot (Fig. 4B,D,E) and immunoprecipitation (Fig. 4F) with an NE-specific antibody. Several other high-molecular weight species were abundantly labeled by PK105b in these lysates (Fig. 4A), but they have not yet been identified. Nonetheless, they are likely to be binding to PK105b through the DPP and specificity region, and not Cy5, as binding could largely be competed with PK101, the non-fluorescent PK105 analogue (Fig. 4G).

Application of PK105b to measure NE activation in experimental colitis. Having validated PK105b in inflamed mouse tissues, we next applied this probe to investigate NE activation during acute experimental colitis induced by trinitrobenzenesulfonate (TNBS). As expected, mice exhibited loose stools, delayed defecation, weight loss (Fig. S2A), and colon shortening (Fig. S2B). We also observed damage to the mucosa by histological evaluation, as well as edema and inflammatory infiltrate (Fig. S2C). We analyzed colon lysates for NE activation by PK105b labeling and measurement of in-gel fluorescence. In proximal colons from healthy and inflamed mice, we observed little PK105b labeling. By contrast, in the distal region of inflamed colons, which is most affected in the TNBS model, we observed clear labeling of a 25-kDa protein (Fig. 5A). This band was virtually absent in distal colons of healthy mice that received vehicle instead of TNBS (Fig. 5A). We confirmed the identity of the protease to be NE by immunoprecipitation with an NE-specific antibody (Fig. 5D). All of the PK105b bands could be competed by PK101, the non-fluorescent PK105 analogue (Fig. 5E).

We also transferred the fluorescent gels to nitrocellulose membranes in order to immunoblot the samples for total NE expression. In all proximal colons and in healthy distal colons, we observed bands at 37 and 25 kDa (Fig. 5B). In the TNBS-treated distal colons, a new band appeared just below the 25-kDa protein. Only the lower species was labeled by PK105b, as revealed by overlay of the Cy5 fluorescence (Fig. 5C) and immunoprecipitation (Fig. 5D). To verify that the appearance of this smaller NE species was not an artefact of probe labeling, we immunoblotted inflamed distal colon samples in the presence and absence of PK105b. The smaller species was detected regardless of the presence of PK105b (Fig. 5F). Taken together, these data suggest that NE is subject to trimming in inflamed regions of the colon that permits its activation and thus its reaction with the PK105b probe.

For comparison, we also tested our previous NE probe, Cy5-V-DPP, in distal colon lysates and labeling of the 25-kDa species was barely distinguishable from the background (Fig. 5G). Thus, PK105b is clearly superior to Cy5-V-DPP for its ability to detect NE activity in tissue lysates. Both probes exhibit binding to several species in the 50–75-kDa range (Fig. 5A), and future proteomics assays will be required to determine their identity. Furthermore, we investigated secreted proteases found in the lumen of the colon (either luminal flush or in fecal pellets) with PK105b (Fig. 6A). In both samples, we observed two labeled proteases at 25 kDa. Immunoprecipitation confirmed low levels of NE in these samples, with pancreatic elastase and trypsin 3 being the predominant species (Fig. 6C). Nonetheless, NE activity could be clearly delineated by PK105b in lysates from colon tissues.

Application of PK105b to measure NE activation in mucosal biopsies from IBD patients. To translate our findings in mouse colitis to human disease, we examined PK105b labeling in mucosal biopsies from patients (Table 1). As in mice, we observed a significant increase in labeling in samples from patients with active UC compared to healthy individuals brought in for routine colonoscopy screening (Fig. 7A,D). In contrast to mice, where we observed a single 25-kDa species at labeled by PK105b, three species were labeled in human mucosal lysates, with the smallest form having the most activity. The banding pattern resembled that which was observed with recombinant human NE (Fig. 2A and in refs[24,25]). We confirmed these bands to be NE by immunoprecipitation with an NE-specific antibody (Fig. 7G), and they could be competed with PK101 (Fig. 7H).

Furthermore, when the same samples were immunoblotted for total NE expression, we observed NE bands in the healthy tissue at 37 and 25 kDa (Fig. 7B). UC tissues, however, displayed an additional doublet that was smaller than the 25-kDa species. The most active species, as indicated by PK105b labeling, corresponded to these

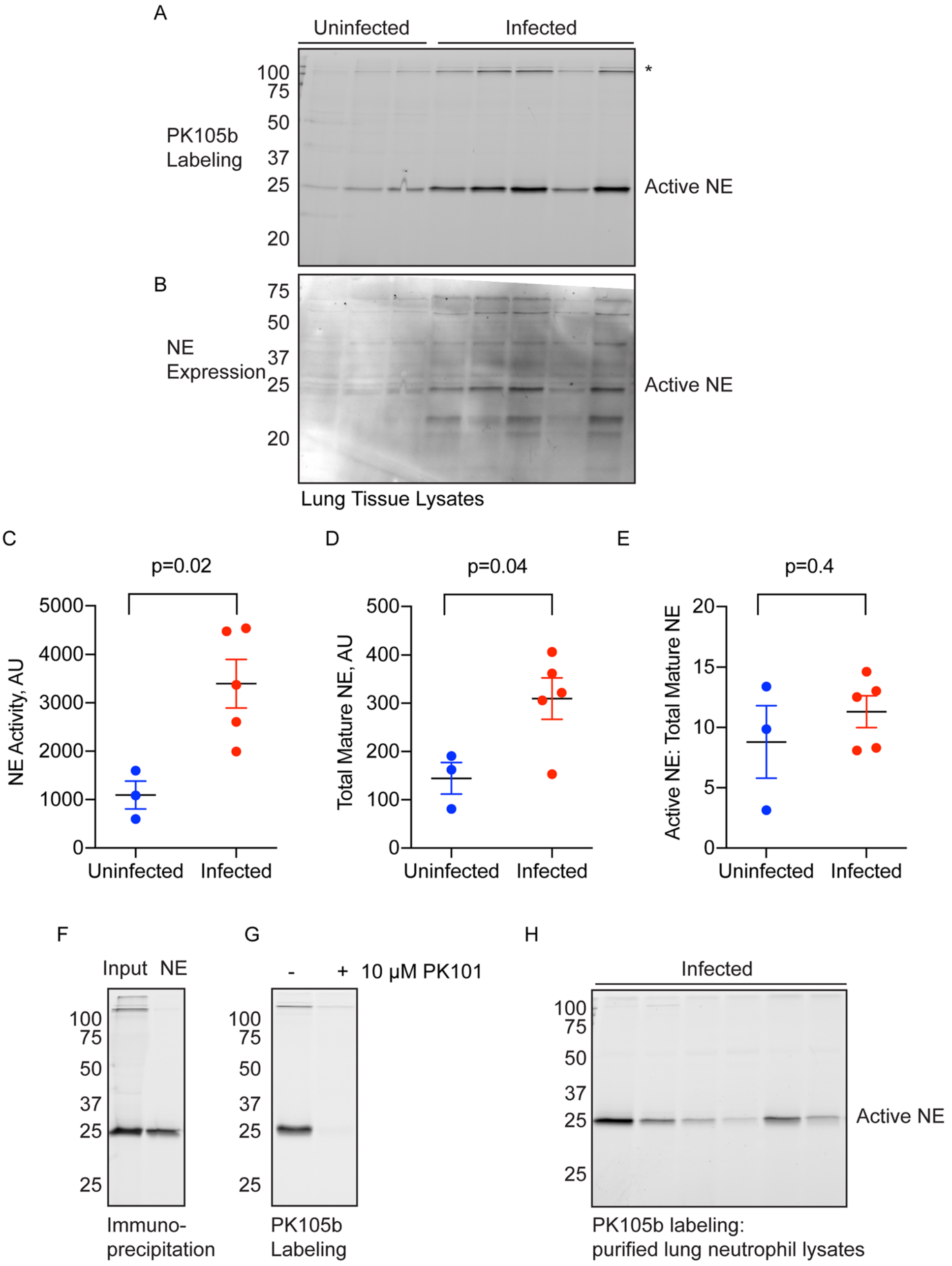

Figure 3. Detection of NE activity in *L. pneumophila*-infected lung tissue. (**A**) Lysates prepared from uninfected or *L. pneumophila*-infected lungs were labeled with 1 μM PK105b and analyzed by in-gel fluorescence (n = 3–5). *Indicates high-molecular weight species of unknown identity. (**B**) Total NE expression in the samples in (**A**) was measured by immunoblotting with an NE-specific antibody. (**C,D**) Densitometry analysis of active NE in (**A**) and total mature NE in (**B**), respectively. (**E**) Ratios of active to total mature NE in the samples. (**F**) Labeling of NE by PK105b in infected lung tissue was confirmed by immunoprecipitation with an NE-specific antibody. (**G**) Competetion of PK105b labeling in an infected lung lysate with PK101. (**H**) PK105b labeling in neutrophils isolated from infected lung tissue, as analyzed by in-gel fluorescence (refer to Fig. S1 for sorting strategy). Error bars are shown as mean ± SEM.

smaller species (Fig. 7C,G). Thus, as we observed in mouse colitis, NE undergoes trimming during human UC that permits its activation and binding to PK105b.

Patient #13 was originally diagnosed with UC and we initially considered this biopsy to be an outlier given the low levels of NE activation. Upon follow-up studies, however, this diagnosis was re-evaluated and the patient was found to have an ileal stricture. The biopsies analyzed in this study were taken from normal tissue regions. These data therefore highlight the potential utility of using NE activity as a diagnostic marker for ulcerative colitis.

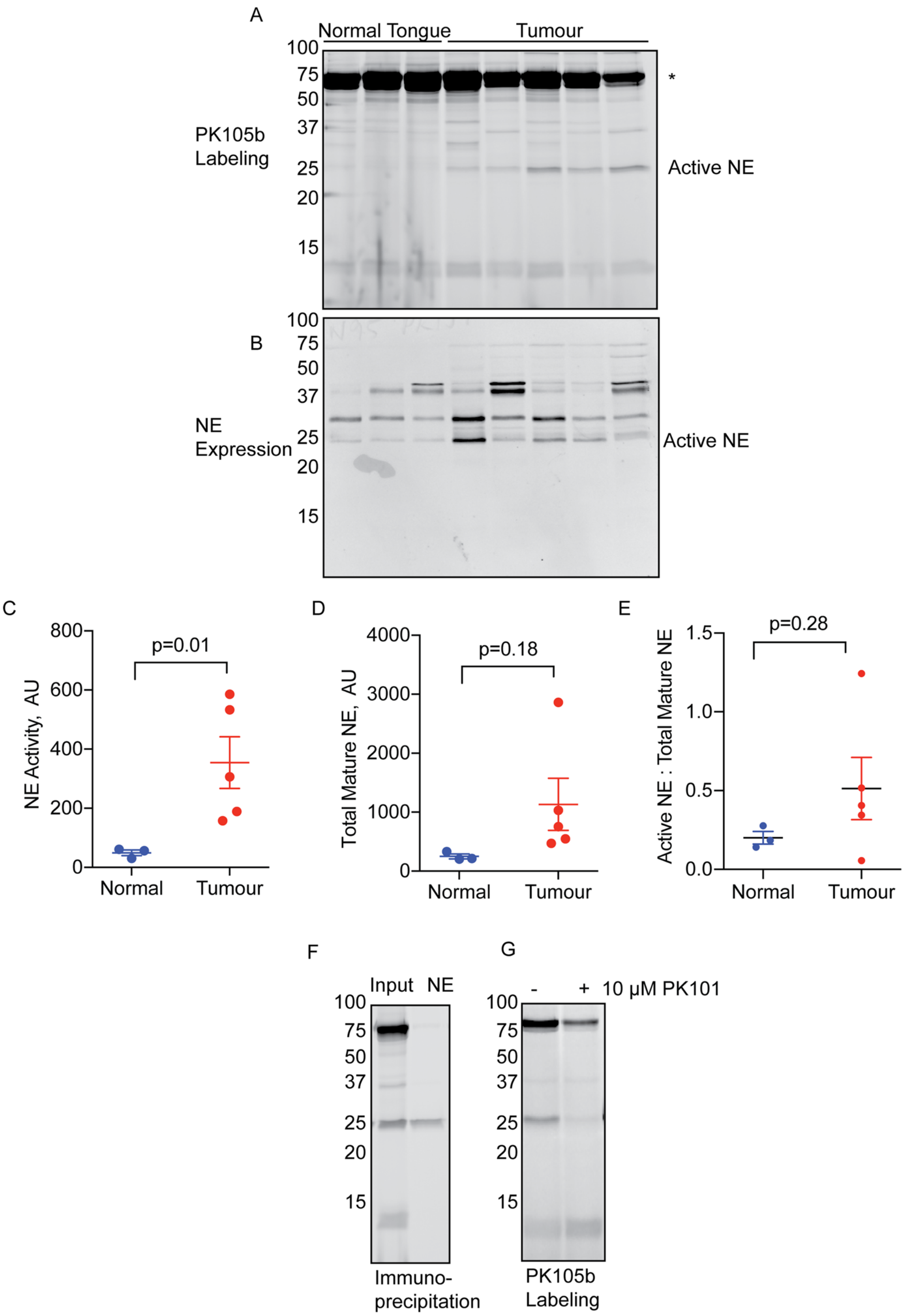

Figure 4. Detection of NE activity in oral cancer tissues. (**A**) Lysates prepared from normal mouse tongues or HSC-3 oral cancer tissues were labeled with 1 μM PK105b and analyzed by in-gel fluorescence (n = 3–5). *Indicates high-molecular weight species of unknown identity. (**B**) Total NE expression in the samples in (**A**) was measured by immunoblotting with an NE-specific antibody. (**C**,**D**) Densitometry analysis of active NE in (**A**) and total mature NE in (**B**), respectively. (**E**) Ratio of active to total mature NE in the samples. Error bars are shown as mean ± SEM. (**F**) NE labelling in cancer tissue was confirmed by immunoprecipitation with an NE-specific antibody. (**G**) Competition of PK105b labeling in oral cancer tissue lysate with PK101.

Discussion

While PK105 was selective for NE in purified neutrophils, its ability to label NE in tissue lysates, which contain many cell types and proteases, had not been established. We tested PK105b, a close analogue of PK105, in bone marrow, pancreas, inflamed lungs, oral cancer, and human and mouse colitis tissues and fecal samples. Due to the covalent nature of PK105b, we could verify that NE was clearly targeted by this probe. We also observed that PK105b exhibited cross-reactivity with other serine proteases such as pancreatic elastase, proteinase-3, trypsin 3

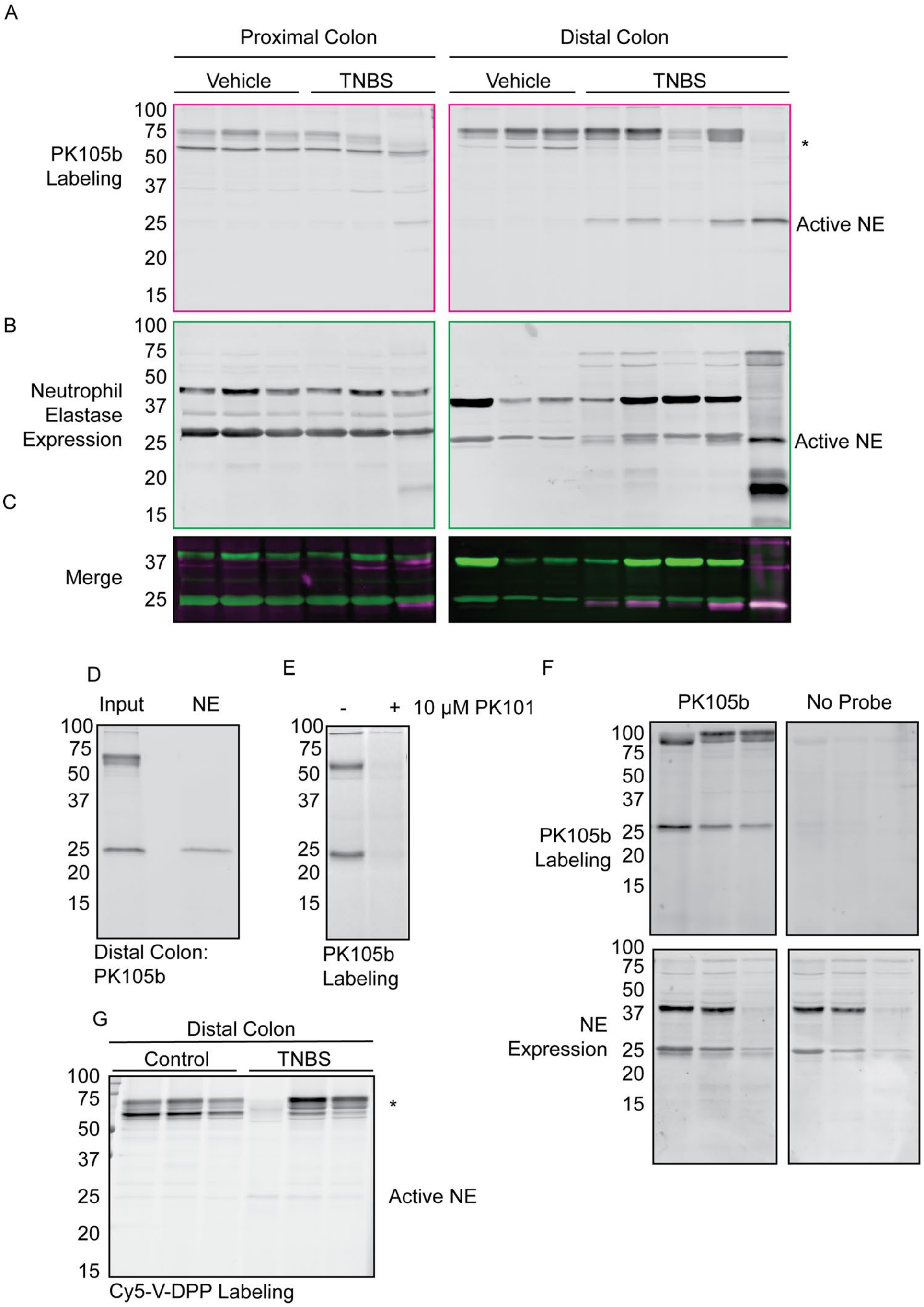

Figure 5. Application of PK105b to measure NE activation in acute experimental colitis. (**A**) Distal or proximal colons were excised from mice with acute colitis induced by TNBS and labeled *ex vivo* with 1 µM PK105b. Probe binding was detected by in-gel fluorescence (n = 3–5). *Indicates high-molecular weight species of unknown identity. (**B**) Immunoblotting of samples in (**A**) with an NE-specific antibody to reveal total NE expression. (**C**) Merged image of PK105b labeling (active NE; magenta) and immunoblot (total NE expression; green). (**D**) Immunoprecipitation of PK105b-labeled inflamed distal colon lysate with a NE-specific antibody. (**E**) Competition of PK105b labeling in inflamed distal colon lysates with PK101. (**F**) In-gel fluorescence and NE immunoblot of distal colon lysates with or without PK105b labeling. (**G**) Distal colon lysates from A labeled with Cy5-V-DPP.

and other unknown proteases. This cross-reactivity was dependent on the tissues examined, with greater selectivity observed in purified lung neutrophils, lung tissue, and human colon biopsies and more cross-reactivity in pancreas, fecal samples, and cancer tissue. We confirmed that all PK105b binding was mediated by the DPP warhead in combination with the specificity region, and not due to non-specific binding via the Cy5 fluorophore, as all labeling could be blocked by pre-treatment with PK101, a non-fluorescent analogue of PK105.

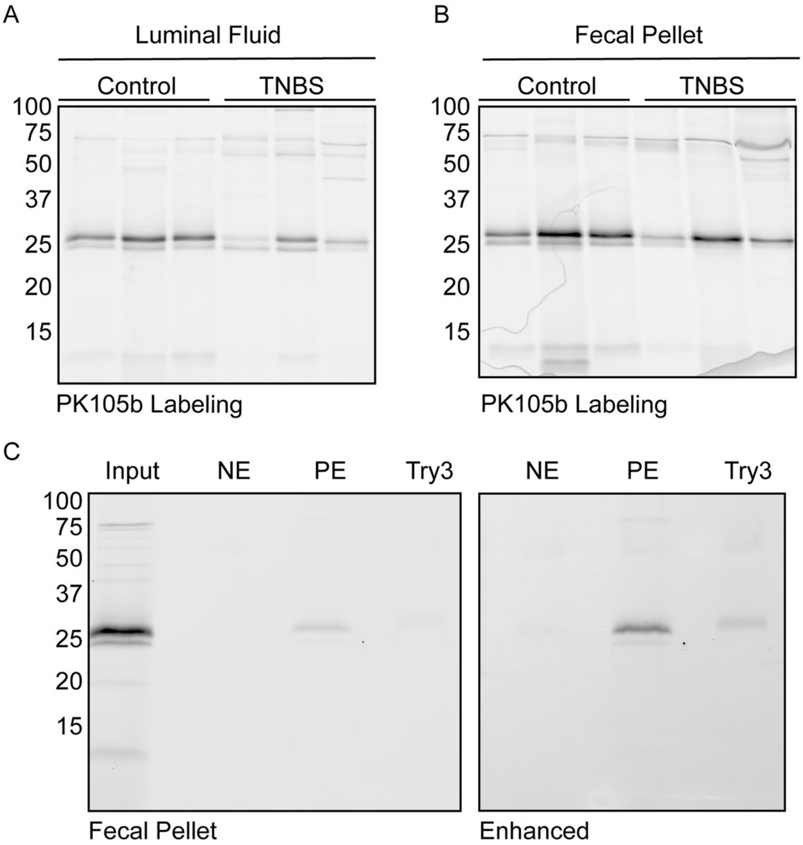

Figure 6. Luminal protease activity in acute experimental colitis. (**A**,**B**) Labeling of luminal fluids or fecal pellets from control or TNBS-treated mice with PK105b. (**C**) Immunoprecipitation of PK105b-labeled fecal samples with NE, PE, or trypsin 3-specific antibodies. Gain settings for the pulldowns were enhanced in order to observe faint bands (right panel).

While PK105b clearly has limitations, it is advantageous over traditional substrate probes such as AAPV-p-nitroanilide and BODIPY-FL-elastin, as these tools do not bind their targets covalently and the extent of their cross-reactivity in various contexts cannot readily be determined. Additionally, PK105b was advantageous over our previous diphenylphosphonate probe, Cy5-V-DPP[13]. In competition assays with the fluorogenic substrate, AAPV-AMC, PK105b reacted with rNE much more rapidly and potently than Cy5-V-DPP. This is most likely mediated by the improved non-natural specificity region in PK105b, which may bind more tightly within the NE active site. PK105b may also have enhanced sensitivity in tissue lysates due to increased stability, as its non-natural peptide sequence may be more resistant to degradation by other proteases than valine. PK105b is therefore one of the most effective tools available to study NE activation.

We applied PK105b to investigate NE activation during mouse colitis. In inflamed colons, we observed labeling of active NE, which was significantly increased compared to control tissue. Probe-labeled NE corresponded to the most mature species of NE detected by immunoblotting, which was not present in healthy tissue. We corroborated these findings in human colitis using mucosal biopsies from patients with UC, unequivocally demonstrating for the first time that NE is activated in IBD. Thus, PK105b is well suited for detection of both mouse and human NE during IBD and will be a valuable resource for future investigation of NE function. Furthermore, it may have utility as a diagnostic agent for IBD and for validating target engagement and efficacy of neutrophil elastase inhibitors in preclinical development as therapeutic agents.

Experimental Procedures

Probe synthesis and characterization. Refer to Supplemental Materials for information on the synthesis of PK105b. Cy5-V-DPP[13] and PK101[14] were synthesized in house as described previously.

Recombinant protease labeling. Recombinant proteases (500 ng) were diluted in 20 µl of phosphate-buffered saline (PBS): human neutrophil elastase (Elastin Products Company), porcine pancreatic trypsin type II-S (beta trypsin; Sigma), and human proteinase-3 (Sigma). PK105b or Cy5-V-DPP (0, 0.1, 0.5 or 1 µM) was added from a 100x DMSO stock, and reaction was carried out at 37 °C for 30 minutes. Proteins were solubilized in 4x sample buffer (40% glycerol, 200 mM Tris-Cl [pH 6.8], 8% SDS, 0.04% bromophenol blue, 5% beta-mercaptoethanol), boiled and resolved on a 15% SDS-PAGE gel under reducing conditions. Probe labeling was detected by scanning the gel for Cy5 fluorescence on a Typhoon 5 flatbed laser scanner (GE Healthcare). Detailed protocols for ABP application are available in ref.[26].

Pt #	Symptoms	Medication	Pathology	Endoscopy
1	none	none	normal tissue	none
2	none	none	normal tissue	none
3	none	none	normal tissue	none
4	none	none	normal tissue	none
5	flare-up, 15–20 bm/d	Steroids, biologic	chronic inflammation, severe activity	pancolitis, Mayo 3 distal, 2 proximal
6	flare-up, 10 bm/d	none	chronic inflammation, moderate to severe activity	pancolitis, Mayo 2
7	chronic active, 4 bm/d	none	chronic inflammation, mild activity	proctitis, Mayo 1
8	chronic active, 2–3 bm/d	5-ASA	chronic inflammation, marked activity	pancolitis, Mayo 3 distal, 2 proximal
9	new onset, 6–8 bm/d	none	chronic inflammation, moderate activity	pancolitis, Mayo 2
10	chronic active, 12 bm/d*	Steroid enema, 5-ASA	chronic inflammation, mild activity	proctitis, Mayo 2
11	flare-up, 6–8 bm/d	Imuran	acute, chronic inflammation, deep ulcers	ileocolitis, deep ulcers
12	flare-up, 4–5 bm/d	5-ASA	chronic inflammation, severe activity	colitis
13	flare-up, pain, +2 bm/d	5-ASA	normal tissue; chronic stricture with no active inflammation	ileal stricture, blind biopsies
14	flare-up, 2–5 bm/day	none	chronic inflammation, moderate activity	pancolitis, Mayo 1–2

Table 1. Profiles of patients from which mucosal biopsies were collected. 5-ASA = 5 aminosalicylic acid; *mucous, but infrequent stool; **suspected flare up initially but with further imaging dx. with chronic stricture with no active inflammation; bm = bowel movement, most were bloody.

Fluorogenic substrate assay. Recombinant neutrophil elastase (20 nM) was diluted in PBS, and MeOSuc-Ala-Ala-Pro-Val-AMC (AAPV-AMC; 20 µM; Bachem) was diluted in PBS containing PK105b (0.2 µM), Cy5-V-DPP (2 or 20 µM), sivelestat (2 µM; Sigma) or 2% DMSO (vehicle control). The two solutions were mixed 1:1 in an opaque 96-well plate (100 µl final volume), and probe-dependent fluorescence (355 nm excitation/460 nm emission) was immediately measured at 30 s intervals over the course of 1 h on a FLUOstar Omega plate reader (BMG Labtech).

Animal ethics. All animal experiments were conducted in accordance with the guidelines for the use of laboratory animals in research and approved protocols. Experiments involving healthy mice and colitis experiments were approved by the Monash University Animal Ethics Committee. Oral cancer experiments were approved by the Committee on Animal Research at New York University. Legionella experiments were approved by the University of Melbourne Animal Ethics Committee.

***Ex vivo* tissue labeling.** Bone marrow was obtained by flushing tibias and femurs from healthy C57BL/6J mice with PBS. Cells were washed and resuspended in PBS prior to sonication on ice. Tissues were lysed by sonication on ice in PBS (10 µl/mg tissue), and supernatants were cleared by centrifugation at 21,000 g for 10 min at 4 °C. Total protein (60 µg, as measured by BCA assay, Pierce) was aliquoted in a total volume of 20 µl PBS, and probe labeling and SDS-PAGE was carried out as above. Where indicated, PK101 (10 µM) was added for 10 minutes prior to the addition of PK105b.

Western blotting. Fluorescent gels were transferred to nitrocellulose membranes and blotted using the Turbo Blot system (BioRad). Membranes were blocked using Li-Cor Odyssey blocking buffer diluted by 50% with PBS containing 0.05% Tween 20. Sheep anti-mouse neutrophil elastase/ELA2 (1:1000; R&D AF4517) was incubated overnight at 4 °C. Secondary antibody (goat-IR800, 1:5000; LiCor) was incubated for one hour at room temperature. Binding was detected by scanning with the IRLong filter on the Typhoon 5.

Immunoprecipitation. PK105b-labeled lysates (boiled in sample buffer) were divided into input and immunoprecipitation (IP) samples (100 µg each). The IP samples were diluted in 500 µl IP buffer (PBS [pH 7.4], 1 mM EDTA, 0.5% NP-40) along with 10 µl antibody: Sheep anti-neutrophil elastase/ELA2 (R&D AF4517); rabbit anti-PRSS3 (Abcam ab105123); rabbit anti-pancreatic elastase (Abcam ab21593). Protein A/G beads (40 µl slurry; Santa Cruz) were washed with IP buffer and then added to the sample. Tubes were rocked overnight at 4 °C. Beads were washed four times with IP buffer and once with 0.9% sodium chloride. After the last wash, all buffer was removed and beads were boiled in 2x sample buffer (20 µl). Supernatants were then analyzed, alongside the input sample, by fluorescent SDS-PAGE as above.

***Legionella pneumophila* infection model.** C57BL/6 mice were infected by intranasal inoculation with 2.5×10^6 *L. pneumophila* 130b ΔflaA in 50 µL of PBS. Three days after infection, lungs were collected, minced and digested in 4 mL RPMI-1640 (Gibco) containing 3% FCS, 1 mg/mL DNaseI (Sigma-Aldrich) and 1 mg/mL Collagenase III (Worthington). Cells were collected by filtration through a 70-µM filter, centrifuged and red blood cells lysed by resuspension in buffer containing 150 mM ammonium chloride and 50 mM Tris-HCl (pH 7.5) for 5 min. After washing with PBS containing 0.1% BSA and 2 mM EDTA, cells were stained with anti-Ly6G-FITC (1A8, BD Pharmingen), anti-CD11c-PE (N418, eBioscience), anti-Siglec-F-BV421 (E50-2440, BD Horizon), anti-CD64-Alexa 647 (X54-5/7.1, BD Pharmingen) and anti-FcγII/III (2.4G2, WEHI monoclonal facility) for

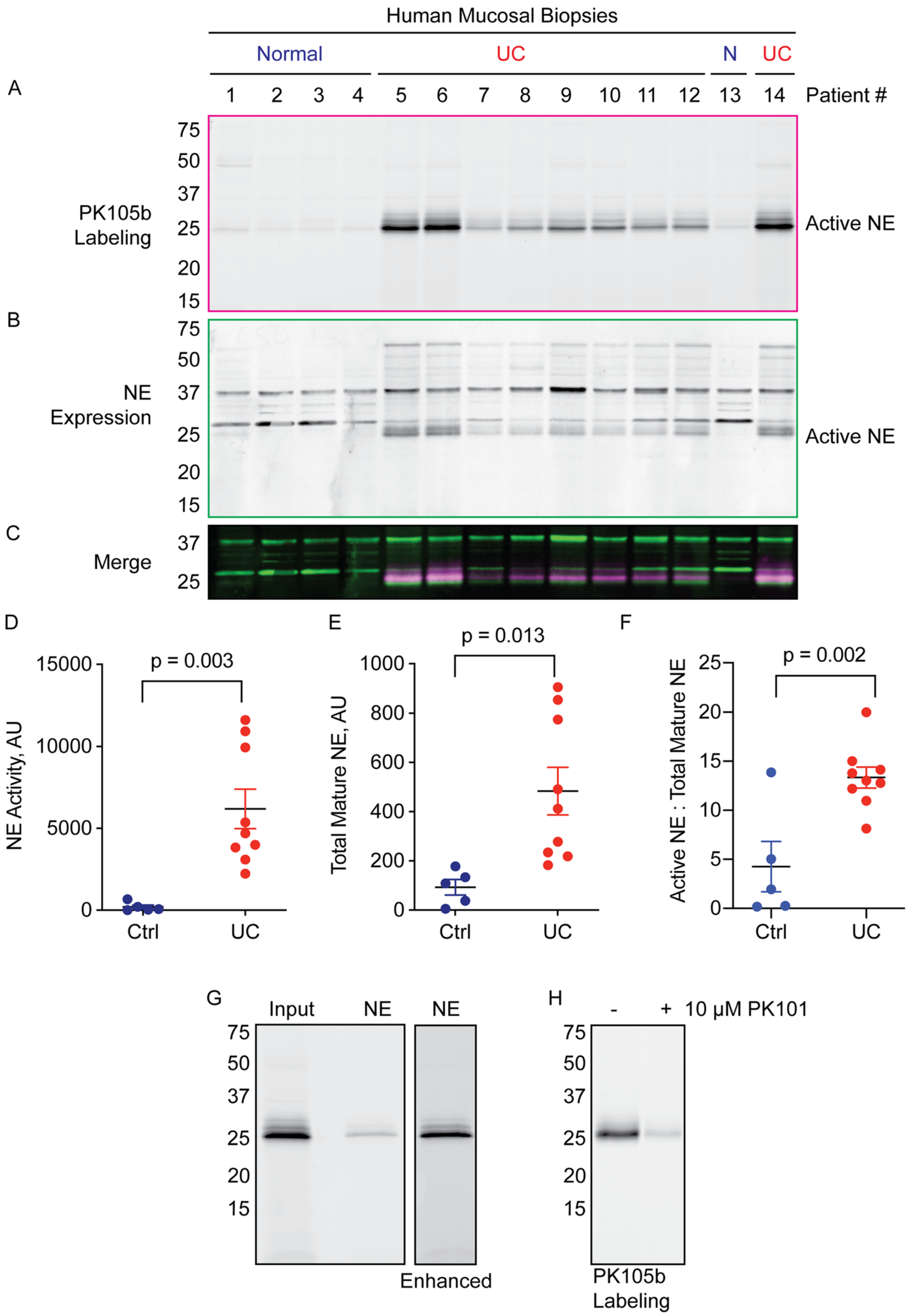

Figure 7. Application of PK105b to measure NE activation in mucosal biopsies from patients with IBD. (**A**) Mucosal biopsies from healthy controls (n = 5) or patients with active UC (n = 9) were labeled *ex vivo* with 1 μM PK105b. Probe binding was assessed by in-gel fluorescence. (**B**) Samples in (**A**) were immunoblotted for total NE expression. (**C**) Merged image of PK105b labeling (active NE; magenta) and immunoblot (total NE expression; green). (**D**,**E**) Densitometry of active NE in (**A**) and total mature NE in (**B**), respectively. (**F**) Ratio of active to total mature NE in the biopsy lysates. Error bars are shown as mean ± SEM. (**G**) Immunoprecipitation of PK105b-labeled UC biopsy lysates with an NE-specific antibody. Gain settings for pulldown were enhanced in order to view faint bands (right panel). (**H**) Competition of PK105b labeling in inflamed colon lysates with PK101.

30 min at 4 °C. Cells were washed and resuspended in FACS buffer with 0.25 μg/mL 7-AAD. Neutrophils were isolated using a Beckman Coulter MoFlo Astrios cell sorter into FCS and pellets of 10^6 cells snap frozen at −80 °C. Purities were assessed post-sorting using the same gating strategy. Purified neutrophils were lysed on ice in PBS with 0.1% Triton X-100, and supernatants were cleared by centrifugation. Alternatively, lung tissues from the same mice were snap frozen at the time of harvest and processed as above.

Oral cancer model. Female BALB/c nude mice (6–8 weeks old, Charles River Laboratories) were injected in the left lateral tongue under anesthesia (3×10^5 HSC-3 human oral squamous cell carcinoma cells suspended in 50 µl vehicle [1:2 mixture of DMEM and Matrigel; Becton Dickinson], or vehicle alone). After two weeks, the resulting xenografted tumors and vehicle-injected tongues were excised, snap frozen, and analyzed as above.

Colitis model. Mice were purchased from the Monash University in-house colony. Colitis was induced in 10-week old male C57BL/6J mice by intracolonic infusion of picrylsulfonic acid solution (2,4,6-Trinitrobenzenesulfonic acid solution, TNBS; Sigma; 2.5 mg dissolved in 50% ethanol). Body weight and symptoms were recorded daily, and mice were humanely killed after three days. Upon colon extraction, luminal fluids were collected by flushing colons with PBS. Solids were removed by centrifugation and supernatant was concentrated using a 3-kDa cut-off centrifugal filter (Amgen). Pieces of proximal and distal colon were frozen for protease analysis or fixed in 4% paraformaldehyde overnight, paraffin embedded, sectioned, and stained with haematoxylin and eosin.

Human mucosal biopsies. Human mucosal biopsies were obtained from individuals during colonoscopy procedures at Hotel Dieu Hospital in Kingston, Ontario, Canada. Informed written and verbal consent was obtained prior to enrolment and all protocols were approved by and carried out in accordance with the guidelines and regulations of the Queen's University Human Ethics Committee. Patients were well-characterized individuals with active UC or healthy individuals undergoing routine colonoscopy for cancer screening (Table 1). For UC patients, biopsies were obtained from sites of active inflammation. Fresh biopsies were washed in PBS and then snap frozen for protease analysis as above.

Statistical analysis. All experiments were performed with at least three biological replicates. Data are reported as means ± SEM. Statistical significance was determined by comparing two groups using a Student's t test, and p values of less than 0.05 were considered significant.

Data Availability

All data generated or analyzed during this study are included in this published article (and its Supplementary Information files).

References

1. Korkmaz, B., Horwitz, M. S., Jenne, D. E. & Gauthier, F. Neutrophil elastase, proteinase 3, and cathepsin G as therapeutic targets in human diseases. *Pharmacol. Rev.* **62**, 726–759 (2010).
2. Zhao, P. *et al*. Neutrophil Elastase Activates Protease-activated Receptor-2 (PAR2) and Transient Receptor Potential Vanilloid 4 (TRPV4) to Cause Inflammation and Pain. *J. Biol. Chem.* **290**, 13875–13887 (2015).
3. Lieu, T. *et al*. Antagonism of the proinflammatory and pronociceptive actions of canonical and biased agonists of protease-activated receptor-2. *Brit. J. Pharmacol.* **173**, 2752–2765 (2016).
4. Jimenez-Vargas, N. N. *et al*. Protease-activated receptor-2 in endosomes signals persistent pain of irritable bowel syndrome. *Proc. Nat. Acad. Sci.* **115**, E7438–E7447 (2018).
5. Edgington-Mitchell, L. E. Pathophysiological roles of proteases in gastrointestinal disease. *Am. J. Physiol. Gastrointest. Liver Physiol.* **310**, G234–239 (2015).
6. Motta, J. P. *et al*. Modifying the Protease, Antiprotease Pattern by Elafin Overexpression Protects Mice From Colitis. *Gastroenterol.* **140**, 1272–1282 (2011).
7. Morohoshi, Y. *et al*. Inhibition of neutrophil elastase prevents the development of murine dextran sulfate sodium-induced colitis. *J. Gastroenterol.* **41**, 318–324 (2006).
8. Uchiyama, K. *et al*. Serpin B1 protects colonic epithelial cell via blockage of neutrophil elastase activity and its expression is enhanced in patients with ulcerative colitis. *Am. J. Physiol. Gastrointest. Liver Physiol.* **302**, G1163–G1170 (2012).
9. Kuno, Y. *et al*. Possible involvement of neutrophil elastase in impaired mucosal repair in patients with ulcerative colitis. *J. Gastroenterol.* **37**, 22–32 (2002).
10. Edgington, L. E., Verdoes, M. & Bogyo, M. Functional imaging of proteases: recent advances in the design and application of substrate-based and activity-based probes. *Cur. Op. Chem. Biol.* **15**, 798–805 (2011).
11. Gecse, K. *et al*. Increased faecal serine protease activity in diarrhoeic IBS patients: a colonic lumenal factor impairing colonic permeability and sensitivity. *Gut* **57**, 591–599 (2008).
12. Motta, J. P. *et al*. Food-Grade Bacteria Expressing Elafin Protect Against Inflammation and Restore Colon Homeostasis. *Sci. Translat. Med*. **4**, 158ra144 (2012).
13. Edgington-Mitchell, L. E. *et al*. Fluorescent diphenylphosphonate-based probes for detection of serine protease activity during inflammation. *Bioorg. Med. Chem. Lett.* **27**, 254–260 (2017).
14. Kasperkiewicz, P. *et al*. Design of ultrasensitive probes for human neutrophil elastase through hybrid combinatorial substrate library profiling. *Proc. Nat. Acad. Sci.* **111**, 2518–2523 (2014).
15. Lechtenberg, B. C., Kasperkiewicz, P., Robinson, H., Drag, M. & Riedl, S. J. The Elastase-PK101 Structure: Mechanism of an Ultrasensitive Activity-based Probe Revealed. *ACS Chem. Biol.* **10**, 945–951 (2015).
16. Kasperkiewicz, P., Altman, Y., D'Angelo, M., Salvesen, G. S. & Drag, M. Toolbox of Fluorescent Probes for Parallel Imaging Reveals Uneven Location of Serine Proteases in Neutrophils. *J. Am. Chem. Soc.* **139**, 10115–10125 (2017).
17. Kasperkiewicz, P., Poreba, M., Groborz, K. & Drag, M. Emerging challenges in the design of selective protease substrates, inhibitors and activity-based probes for indistinguishable proteases. *FEBS J.* **284**, 1518–1539 (2017).
18. Brown, A. S. *et al*. Cooperation between Monocyte-Derived Cells and Lymphoid Cells in the Acute Response to a Bacterial Lung Pathogen. *PLoS Pathog.* **12**, e1005691–20 (2016).
19. Brown, A. S., Yang, C., Hartland, E. L. & van Driel, I. R. The regulation of acute immune responses to the bacterial lung pathogen Legionella pneumophila. *J. Leukocyte Biol.* **101**, 875–886 (2017).
20. Lerman, I. & Hammes, S. R. Neutrophil elastase in the tumor microenvironment. *Steroids* **133**, 96–101 (2018).
21. Kistowski, M. *et al*. A Strong Neutrophil Elastase Proteolytic Fingerprint Marks the Carcinoma Tumor Proteome. *Mol. Cell Proteomics* **16**, 213–227 (2017).
22. Scheff, N. N. *et al*. Tumor necrosis factor alpha secreted from oral squamous cell carcinoma contributes to cancer pain and associated inflammation. *Pain* **158**, 2396–2409 (2017).

23. Lam, D. K., Dang, D., Zhang, J., Dolan, J. C. & Schmidt, B. L. Novel Animal Models of Acute and Chronic Cancer Pain: A Pivotal Role for PAR2. *J. Neurosci.* **32**, 14178–14183 (2012).
24. Dau, T., Sarker, R. S. J., Yildirim, A. O., Eickelberg, O. & Jenne, D. E. Autoprocessing of neutrophil elastase near its active site reduces the efficiency of natural and synthetic elastase inhibitors. *Nat. Comm.* **6**, 1–8 (2015).
25. Schulz-Fincke, A.-C., Blaut, M., Braune, A. & Gütschow, M. A BODIPY-Tagged Phosphono Peptide as Activity-Based Probe for Human Leukocyte Elastase. *ACS Med. Chem. Lett.* **9**, 345–350 (2018).
26. Edgington, L. E. & Bogyo, M. *In vivo* imaging and biochemical characterization of protease function using fluorescent activity-based probes. *Curr. Protoc. Chem. Biol.* **5**, 25–44 (2013).

Acknowledgements

We thank Cameron Nowell for maintaining the imaging facilities at the Monash Institute of Pharmaceutical Sciences, the Melbourne Histology Platform, and The Peter Doherty Institute ImmunoID flow cytometry facility. L.E.M. was supported by an Early Career Fellowship from the National Health and Medical Research Council of Australia (NHMRC, GNT1091636), a Grimwade Fellowship from the Russell and Mab Grimwade Miegunyah Fund at The University of Melbourne, a DECRA Fellowship from the Australian Research Council (ARC, DE180100418) and seed grants from Monash University. N.W.B. was supported by grants from the National Institutes of Health (NS102722, DE026806, DK118971) and the United States Department of Defense (W81XWH1810431). I.R.vD., G.Z.N., and M.F. were supported by NHMRC grants (GNT1145244). M.F. was also supported by a fellowship by the German Research Council (DFG GRK 2168) and a Graduate Research Scholarship from The University of Melbourne. The content is solely the responsibility of the authors and does not necessarily represent the official views of the National Institutes of Health.

Author Contributions

L.E.M. conceived study, planned all experiments, analyzed data, contributed funding, coordinated all collaborators, and wrote the manuscript. P.K. and M.D. produced the PK105 probe and contributed intermediates towards the synthesis of PK105b, which was made by L.A. B.M.A. obtained the biological data. G.Z.N., M.F., and I.R.v.D. provided samples for the *L. pneumophila* experiments. B.L.S. provided the oral cancer tissues. D.P.P. and N.B. contributed funding and intellectual input. S.V. and C.M. provided the human mucosal biopsies.

Additional Information

Supplementary information accompanies this paper at https://doi.org/10.1038/s41598-019-49840-4.

Competing Interests: N.W.B. is a founding scientist of Endosome Therapeutics Inc. Research in N.W.B. and DP's laboratories is supported in part by Takeda Pharmaceuticals, Inc.

ACS chemical biology
pubs.acs.org/acschemicalbiology
Articles

Application of a Sulfoxonium Ylide Electrophile to Generate Cathepsin X-Selective Activity-Based Probes

Simon J. Mountford,◆ Bethany M. Anderson,◆ Bangyan Xu, Elean S. V. Tay, Monika Szabo, My-Linh Hoang, Jiayin Diao, Luigi Aurelio, Rhiannon I. Campden, Erik Lindström, Erica K. Sloan, Robin M. Yates, Nigel W. Bunnett, Philip E. Thompson, and Laura E. Edgington-Mitchell*

Cite This: *ACS Chem. Biol.* 2020, 15, 718−727

Read Online

ACCESS | Metrics & More | Article Recommendations | Supporting Information

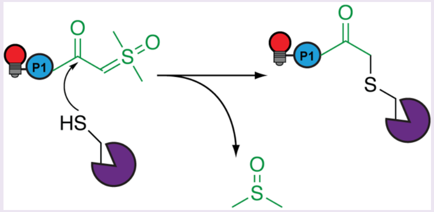

ABSTRACT: Cathepsin X/Z/P is cysteine cathepsin with unique carboxypeptidase activity. Its expression is associated with cancer and neurodegenerative diseases, although its roles during normal physiology are still poorly understood. Advances in our understanding of its function have been hindered by a lack of available tools that can specifically measure the proteolytic activity of cathepsin X. We present a series of activity-based probes that incorporate a sulfoxonium ylide warhead, which exhibit improved specificity for cathepsin X compared to previously reported probes. We apply these probes to detect cathepsin X activity in cell and tissue lysates, in live cells and in vivo, and to localize active cathepsin X in mouse tissues by microscopy. Finally, we utilize an improved method to generate chloromethylketones, necessary intermediates for synthesis of acyloxymethylketones probes, by way of sulfoxonium ylide intermediates. In conclusion, the probes presented in this study will be valuable for investigating cathepsin X pathophysiology.

■ INTRODUCTION

Cathepsin X (also referred to as cathepsin Z or P) is a cysteine cathepsin protease that is unique among its family members in that it exhibits strict carboxypeptidase activity. It is one of the most recently discovered cysteine cathepsins, and its functions during health and disease are still incompletely understood. Cathepsin X contributes to adhesion and maturation of macrophages and dendritic cells and suppresses clathrin-dependent phagocytosis through cleavage of profilin.[1,2] Cathepsin X regulates hormone signaling, where its cleavage of bradykinin, kallidin, or angiotensin leads to alterations in specificity toward their cognate receptors and divergent downstream signaling.[3] Cathepsin X is also expressed by neurons, where its cleavage of α-enolase regulates survival and the outgrowth of neurites.[4] Furthermore, cathepsin X expression is enriched in amyloid plaques, where it may have a protective effect against neurodegenerative disorders such as Alzheimer's disease,[5,6] and in the spinal cord during neuropathic pain.[7] Upregulation of cathepsin X mRNA has been reported in pathology-free regions of multiple sclerosis-affected brains,[8] and it has been implicated in the generation of IL-1β[9,10] and in mediating neuroinflammation.[9] It is also upregulated in the microenvironment of breast,[11] pancreatic,[12] prostate,[13] and gastric cancers,[14,15] where it likely promotes tumor invasion. Thus, cathepsin X holds promise as a clinical biomarker and therapeutic target in diverse diseases.

Like most cathepsins, cathepsin X is synthesized as a zymogen that becomes activated in the acidic environment of endolysosomes. Once activated, it may also be negatively regulated by endogenous inhibitors, though likely not cystatin C or stefin A.[16,17] In addition to its proteolytic functions, cathepsin X can also promote integrin-mediated signaling through an Arg-Gly-Asp (RGD) motif in its pro-domain.[12] As a result of these complex modes of post-translational regulation, traditional biochemical methods that survey total protein levels rarely reflect the pool of proteolytically active enzyme. The ability to specifically measure cathepsin X activity in its native environment is therefore required to define its precise proteolytic functions during health and disease.

To this end, efforts have been focused on developing fluorescent activity-based probes (ABPs) for cathepsin X. ABPs are small molecules that contain an electrophilic moiety (warhead), a recognition sequence that confers selectivity, and a fluorophore for detection.[18−20] When active, the protease initiates a nucleophilic attack on the warhead, resulting in the formation of a covalent, irreversible bond. Assessment of probe labeling can then be used to quantify protease activity by SDS-PAGE (in-gel fluorescence), fluorescent microscopy, flow cytometry, or optical imaging of whole tissues or organisms. Importantly, the covalent nature of probe binding allows for target confirmation by immunoprecipitation with specific antibodies or affinity purification followed by proteomic analysis.

Received: November 28, 2019
Accepted: February 5, 2020
Published: February 5, 2020

https://dx.doi.org/10.1021/acschembio.9b00961

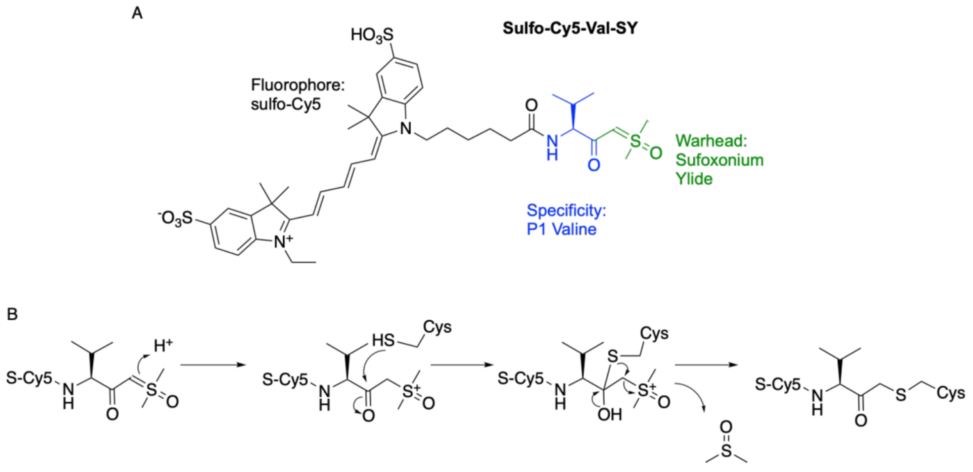

Figure 1. Design of a sulfoxonium ylide-based activity-based probe. (A) Structure of sCy5-Val-SY (**17**) probe. (B) The proposed mechanism by which sCy5-Val-SY binds to an activated cysteine protease.

Scheme 1. Synthesis of sCy5-AA-SY Probes[a]

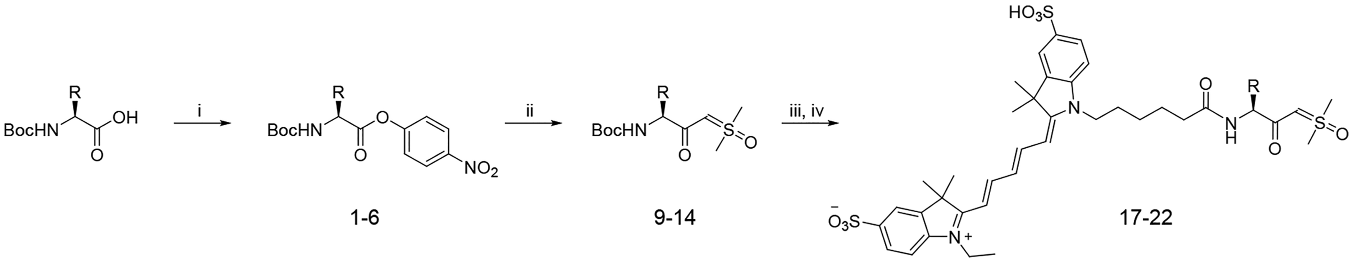

[a] (i) 4-Nitrophenylchloroformate, Et_3N, DMAP, CH_2Cl_2, 0°C, 6 h. (ii) $SOMe_3^+I^-$, KOtBu, THF, reflux, then cool to 0°C and add nitrophenyl ester. (iii) TFA/CH_2Cl_2 (1:1), (iv) sulfo-Cy5, PyClock, DIPEA, DMF, rt, 18 h. The synthetic routes for related compounds Cbz-Lys(sCy5)-SY (**7**, **15**, **23**) and sCy5-Phe-Val-SY (**8**, **16**, **24**) can be found in Scheme S1 and S2, respectively).

Probes with absolute specificity for cathepsin X have not been previously reported. BMV109, a fluorescently quenched ABP with a tetrafluorophenoxymethyl ketone warhead, is a pan-cathepsin probe that targets X, B, S, and L.[21] Because cathepsin X is a similar size as cathepsin B, one of the most abundant and ubiquitously expressed cathepsins, it can be difficult to clearly resolve these two proteases by SDS-PAGE, which precludes accurate quantification by in-gel fluorescence. MGP140 is an epoxide-based probe that exhibits greater specificity for cathepsin X than BMV109 but also potently reacts with cathepsin B.[22] If mice are pretreated with GB11-NH_2, an inhibitor of cathepsin B, S, and L, prior to MGP140 injection, specific labeling of cathepsin X can be achieved. However, this manipulation of the system results in hyper-activation of cathepsin X, possibly a compensatory response due to the loss of cathepsin B activity. Thus, it is crucial to develop probes with improved specificity for cathepsin X to allow for a more detailed investigation of its physiological activity.

Herein, we describe a series of ABPs containing a novel sulfoxonium ylide warhead that exhibit previously unseen selectivity for cathepsin X. We applied these probes to measure cathepsin X activity in lysates and live cells and in live mice. We also used the sulfoxonium ylide as a stepping stone to access chloromethylketones, which are intermediates in the synthesis of acyloxymethylketones (AOMK), warheads commonly used in probes for cathepsins and other cysteine proteases. This new method does not require generation of diazomethanes to access chloromethylketones and is thus a safer alternative to the previously used methods. By comparison to the sulfoxonium ylide probes, AOMK probes bearing identical recognition sequences exhibited unique specificity profiles and low reactivity with cathepsin X. Thus, sulfoxonium ylide probes represent a clear advancement in the tools that are available to study cathepsin X function.

■ RESULTS AND DISCUSSION

Design and Characterization of a Sulfoxonium Ylide Probe. To explore new potential warheads for cysteine cathepsins, we designed and synthesized an ABP containing a dimethyl sulfoxonium ylide electrophile. This design was initially inspired by a dimethyl sulfonium salt reported to inhibit cathepsin B in 1988 by Shaw.[23] To increase the electrophilicity of this warhead, and thus its reactivity with the catalytic cysteine residue, we modified the dimethyl sulfonium salt to a dimethyl sulfoxonium ylide. We also incorporated a valine residue as the P1 recognition sequence and a sulfo-Cyanine 5 (sCy5) fluorophore to yield our initial probe, sCy5-Val-SY (**17**; Figure 1), synthesized according to Scheme 1.

To determine its reactivity profile, we first incubated sCy5-Val-SY (**17**) with protein lysates prepared from RAW264.7 cells, an immortalized mouse macrophage line that contains high levels of active cysteine cathepsins.[21] Cells were lysed in citrate buffer (pH 5.5) to provide optimal conditions for preserving cathepsin activity, and the probe was added at 1 μM for 20 min. We then resolved the lysates by SDS-PAGE and scanned the gel for sCy5 fluorescence using a flatbed laser scanner. We observed exclusive, concentration- and time-

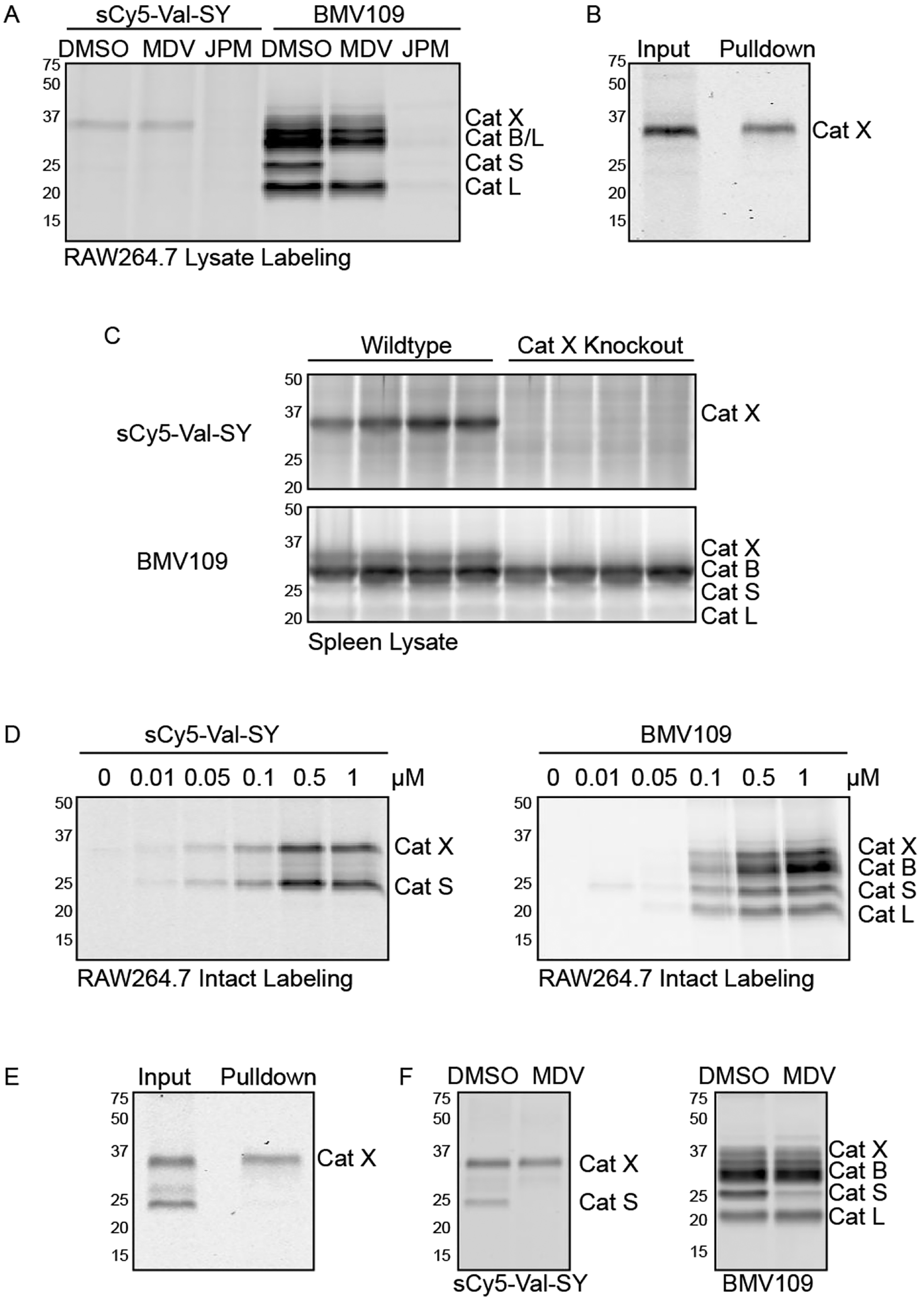

Figure 2. In vitro characterization of sCy5-Val-SY (17). (A) Labeling of RAW264.7 lysates with sCy5-Val-SY or BMV109 alone or after pretreatment with 10 μM MDV-590 (cathepsin S inhibitor) or JPM-OEt (pan cysteine cathepsin inhibitor). (B) Immunoprecipitation of sCy5-Val-SY-labeled samples in A with a cathepsin X-specific antibody. (C) Labeling of splenic lysates from wildtype or cathepsin X-deficient mice with sCy5-Val-SY or BMV109. (D) Labeling of living RAW264.7 cells with increasing doses of sCy5-Val-SY or BMV109 for 2 h. (E) Immunoprecipitation of sCy5-Val-SY-labeled samples in D with a cathepsin X-specific antibody. (F) Labeling of living RAW264.7 cells with and without overnight pretreatment with 10 μM MDV-590 with sCy5-Val-SY or BMV109 (1 μM, 2 h). Also refer to Figure S1.

dependent labeling of a ~35-kDa protease (Figures 2A and S1A,B). This labeling was prevented by pretreatment of the lysates with JPM-OEt, a pan-cysteine cathepsin inhibitor, confirming that this protease was a member of the cysteine cathepsin family (Figure 2A). In contrast, MDV-590, a specific inhibitor for cathepsin S,[24] did not compete for sCy5-Val-SY (**17**) binding. We compared the labeling profile to that of BMV109, the pan-cathepsin probe and found that the sCy5-Val-SY (**17**)-labeled protease was the same molecular weight as BMV109-labeled cathepsin X.[21] We confirmed that this protease was indeed cathepsin X by immunoprecipitating sCy5-Val-SY (**17**)-labeled lysates with a cathepsin X-specific antibody (Figure 2B).

Next, we tested the ability of sCy5-Val-SY (**17**) to label cathepsin X in mouse splenic lysates. As we observed in macrophage lysates, the probe exhibited exclusive reactivity with cathepsin X in splenic lysates from wildtype mice, and this labeling was absent in lysates prepared from spleens of cathepsin X-deficient mice (Figure 2C). By comparison, BMV109 strongly labeled cathepsin B and, to a lesser extent, cathepsin S and L.

Having observed unique specificity of sCy5-Val-SY (**17**) in cell and tissue lysates, we sought to assess the probe's permeability and specificity profile in living RAW264.7 cells. After incubating the probe with live cells for increasing lengths of time (at 1 μM) or with increasing probe concentrations (for 2 h), we analyzed lysates by in-gel fluorescence as above. Here, we observed time- and concentration-dependent labeling of two proteases (Figures 2D and S1C), which we identified as cathepsin X and S by immunoprecipitation (Figure 2E) and competition with MDV-590 (Figure 2F), respectively. We were surprised to see cathepsin S labeling in live cells, given its lack of binding to sCy5-Val-SY (**17**) in cell lysates, where we had confirmed high levels of cathepsin S activity with BMV109. This suggests that the reactivity of cathepsin S with the sulfoxonium ylide is dependent on the labeling conditions. We attempted to explore this by lysing the cells in various buffers that might mimic the endosomal environment of cathepsin S but we were not able to improve the labeling of cathepsin S in lysates (not shown).

Nonetheless, the sulfoxonium ylide probe exhibited clear labeling of cathepsin X in lysates and live cells with considerably improved selectivity compared to BMV109 (Figure 2D,F). To our knowledge, it is the first covalent ABP for cathepsin X that does not also bind to cathepsin B or L. As observed in Figure 2, it is difficult to distinguish cathepsin X labeling from cathepsin B with BMV109 due to the similarity in size of the two proteases. However, sCy5-Val-SY (**17**) allows for clear delineation of cathepsin X activity.

Sulfoxium Ylide Library with Variable P1 Residues. To improve the specificity and potency of the probe for cathepsin X, we generated a small library of sulfoxonium ylide probes by varying the amino acids in the P1 position (Scheme 1, Table 1). In RAW264.7 lysates, probes bearing Ile (**18**), Leu (**19**), Nle (**20**), and Phe (**21**) all showed similar specificity for cathepsin X as sCy5-Val-SY (**17**) with sCy5-Leu-SY (**19**) and sCy5-Nle-SY (**20**) exhibiting a clear improvement in potency (Figure 3A). Cbz-Lys(sCy5)-SY (**23**), in which the sCy5 was attached via the lysine side chain, exhibited a loss of specificity, favoring cathepsin S over X and B. sCy5-Phe-Val-SY (**24**), in which a P2 Phe residue was incorporated, also exhibited a loss of specificity (Figures 3A and S2). The labeling profile of this probe was similar to BMV109, though it showed improved potencies for cathepsin X and S compared to BMV109. A hydrophobic S2 pocket is a feature of virtually all cysteine cathepsins, which may explain the increased affinity of a dipeptide probe for other members of the family.[25]

Table 1. Amino Acids Used in Compounds 1−24 (Scheme 1)

Boc-AA-OH	Boc-AA-ONp	Boc-AA-SY	sCy5-AA-SY
Boc-Val-OH	1	9	17
Boc-Ile-OH	2	10	18
Boc-Leu-OH	3	11	19
Boc-Nle−OH	4	12	20
Boc-Phe-OH	5	13	21
Boc-Trp-OH	6	14	22

In murine kidney lysates, Leu and Nle conferred the most potency and specificity for cathepsin X with Cbz-Lys (**23**), Phe (**21**), and Phe-Val (**24**) yielding broader reactivity and Val (**17**) and Ile (**18**) exhibiting weaker labeling (Figures 3B and S2).

To examine the potency and permeability of the sulfoxinium ylide probe series in living cells, we applied them to RAW264.7 cells for 2 h. Probes bearing Trp (**22**), Val (**17**), Ile (**18**), Leu (**19**), Nle (**20**), and Phe (**21**) labeled cathepsin X and S to similar extents and with similar potency, whereas Cbz-Lys (**23**) exhibited a preference for cathepsin S, and Phe-Val (**24**) labeled B and L in addition to X and S (Figures 3C and S2A,C−G). We confirmed the 25-kDa protease labeled by sCy5-Nle-SY (**20**) to be cathepsin S by competition with two cathepsin S-specific inhibitors, MDV-590 and Z-FL-COCHO (Figure S2B).

We tested the specificity of these probes for cathepsin X in a human breast cancer line known to express very low levels of cathepsin S, MDA-MB-231^{HM}.[26] These cells also allowed us to test whether the probes could bind to human cathepsin X (in addition to mouse cathepsin X shown previously). When we incubated the probes with MDA-MB-231 cells for shorter time periods, we observed very little labeling of cathepsin X (not shown); however, clear labeling was observed after overnight incubation (Figure 3D). This likely reflects differences in the rates of endocytosis between macrophages and tumor cells and suggests that the probes may be taken up directly into the endolysosomal pathway rather than by diffusion through membranes. The sulfoxonium ylide probe series generally shows specific labeling of cathepsin X in these cells with minimal cross-reactivity occurring only at 5 μM. Cbz-Lys(sCy5)-SY (**23**) and especially sCy5-Phe-Val-SY (**24**) exhibited the most cross-reactivity with cathepsin B and L.

In Vivo Characterization of sCy5-Nle-SY. Taking into consideration all of the data from cell and tissue lysates and live mouse and human cells, sCy5-Nle-SY (**20**) emerged as the probe showing the highest potency and selectivity for cathepsin X. Thus, we elected to move forward with this probe for in vivo studies. We injected the probe into mice intravenously, and after 2 h of circulation tissues were harvested, lysed, and analyzed for probe labeling by fluorescent SDS-PAGE. We observed labeling of cathepsin X in liver, kidney, colon, stomach, and spleen (Figure 4A), and this was confirmed by immunoprecipitation with a cathepsin X antibody (Figure 4B). While some labeling of cathepsin S was also observed, the overall specificity profile was clearly improved compared to BMV109, which also strongly labels cathepsin B and L.

It is important to note that, in addition to cathepsin X and S, we also observed the labeling of additional species in vivo at 55 and 15 kDa with sCy5-Nle-SY (**20**). The 55-kDa species was weakly observed when kidney lysates were labeled but not the 15-kDa species. We synthesized a biotinylated Nle-SY probe in attempt to affinity purify these species; however, labeling with this probe was much weaker than the sCy5 probe suggesting that sCy5 contributes in part to selectivity (not shown). Efforts to develop new affinity probes are ongoing.

We then used confocal microscopy to image sCy5-Nle-SY (**20**) fluorescence in kidney cryosections after in vivo probe administration. We observed strong punctate sCy5 fluorescence reminiscent of endolysomal staining, and this signal largely overlapped with immunoreactive cathepsin X (Figure 5). Thus, we could use sCy5-Nle-SY (**20**) to distinguish active cathepsin X relative to total cathepsin X in tissues after in vivo administration.

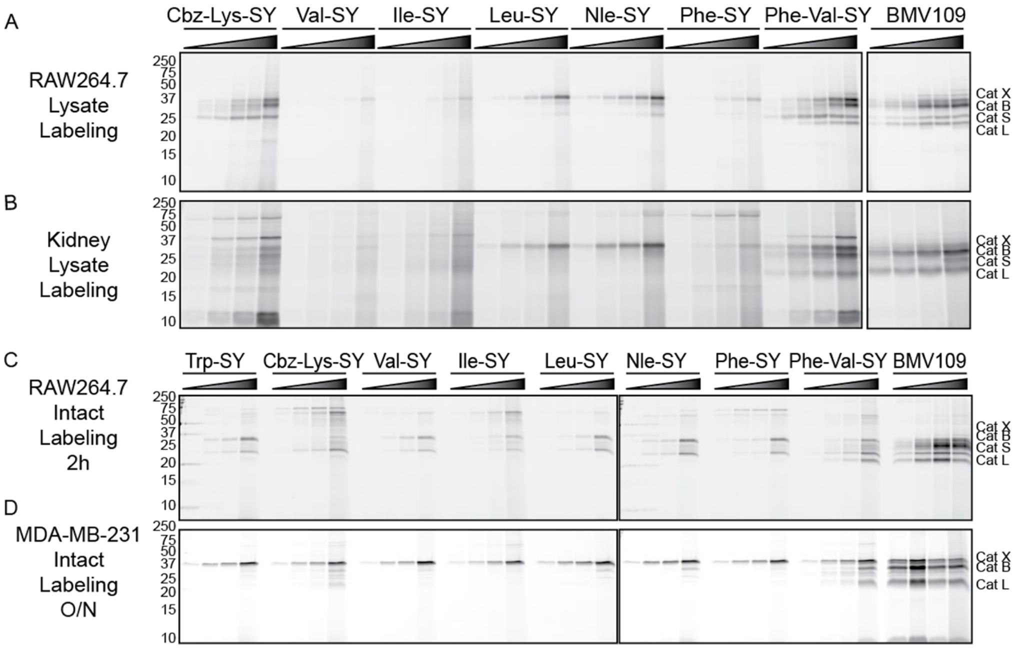

Figure 3. In vitro characterization of a sulfoxonium ylide library in lysates and live cells. Labeling of (A) RAW264.7 lysates (0.01, 0.05, 0.1, 0.5, 1, 5 μM), (B) kidney lysates (0.1, 0.5, 1, 5 μM), (C) live RAW264.7 cells (0.1, 0.5, 1, 5 μM), or (D) live MDA-MB-231^{HM} cells (0.1, 0.5, 1, 5 μM) with the indicated SY probe or BMV109, as analyzed by in-gel fluorescence. Also refer to Figure S2.

Sulfoxonium Ylides as a Route to Acyloxymethylketone Probes. Many of the reported activity-based probes for cysteine proteases incorporate AOMK or phenoxymethylketone (PMK) warheads.[21,27−31] Synthesis of these electrophiles requires generation of chloromethylketone intermediates, a process that has historically been achieved, among other methods, through generation of diazomethane, an extremely explosive yellow gas.[32] To avoid this potentially dangerous reaction, we utilized sulfoxonium ylides as key intermediates to make AOMK derivatives (Scheme 2, Table 2). Previous studies have shown that chiral integrity was maintained after both ylide formation and conversion to the chloromethylketone using these conditions.[33,34]

Using this method, we successfully generated three AOMK probes bearing Nle (**31**), Phe (**32**), and Cbz-Lys (**33**), suggesting that this method could be broadly applied to the synthesis of diverse ABPs. We compared the reactivity of the new AOMK probes with the corresponding sulfoxonium ylide probes in living RAW2647 cells. The AOMK probes were much less potent than the ylide probes, suggesting reduced reactivity. These probes labeled cathepsin B and S but not X (Figure 6A,B), We also compared the labeling profile of sCy5-Nle-SY (**20**) and sCy5-Nle-AOMK (**31**) in RAW264.7 lysates. Here, we could only observe clear labeling of cathepsin B with the AOMK probe at 50 μM, whereas with the SY probe we observed cathepsin X labeling at 0.1 μM (Figure S3A,B). We also treated living RAW264.7 cells overnight, and again 5 μM sCy5-Nle-AOMK labeled cathepsin B and S but minimal cathepsin X (Figure S3C,D).

We compared the serum stability of sCy5-Nle-SY and sCy5-Nle-AOMK probes by preincubating them with fetal calf serum. No loss of activity was observed, compared to untreated probes, suggesting that both probes are stable in serum (Figure S4A). In splenic lysates from wildtype mice, sCy5-Nle-SY (1 μM) clearly labeled cathepsin X and to a lesser extent cathepsin S, but no labeling of cathepsin X was observed in splenic lysates from cathepsin X-deficient mice. As in RAW264.7 lysates, 1 μM sCy5-Nle-AOMK exhibited only weak labeling of cathepsin B splenic lysates, which did not differ between wildtype and cathepsin X-deficient mice (Figure S4B). Finally, we tested sCy5-Nle-AOMK in vivo and analyzed its labeling in tissues. Only weak labeling of cathepsin B and S was observed in the colon but not in other tissues examined (Figure S4C).

■ CONCLUSIONS

We have designed a new dimethyl sulfoxonium ylide warhead that exhibits unique selectivity toward cysteine cathepsin proteases in cell lysates, live cells, and in mouse and human tissues. Our best probe, sCy5-Nle-SY (**20**), is the most selective probe for cathepsin X to date, showing specificity in cell lysates and cells that express low levels of cathepsin S. While this probe does cross-react with cathepsin S in live macrophages and in vivo, it does not appreciably label cathepsin B or L, which is a clear improvement over the only other covalent probes that target cathepsin X (BMV109, MGP140, DCG-04). The use of sCy5-Nle-SY (**20**) allows for clear measurement of the activity of the cathepsin X by SDS-PAGE, whereas this was difficult with previous probes due to confounding levels of cathepsin B labeling.

Furthermore, we established that the sulfoxonium ylide warhead is stable enough for in vivo detection of cathepsin X activity. While the probe is most reliable in gel-based analyses of tissue lysates, sCy5-Nle-SY (**20**) signal was bright enough to detect by confocal microscopy. In conjunction with cathepsin X-specific antibodies, this method can distinguish active from inactive cathepsin X by cellular imaging and in the future could be applied to advance our understanding of the function of cathepsin X in animal models of disease.

Little is known about the preferred cleavage sequence for cathepsin X and this may be partially due to the difficulties in profiling carboxypeptidases with fluorogenic substrate libraries

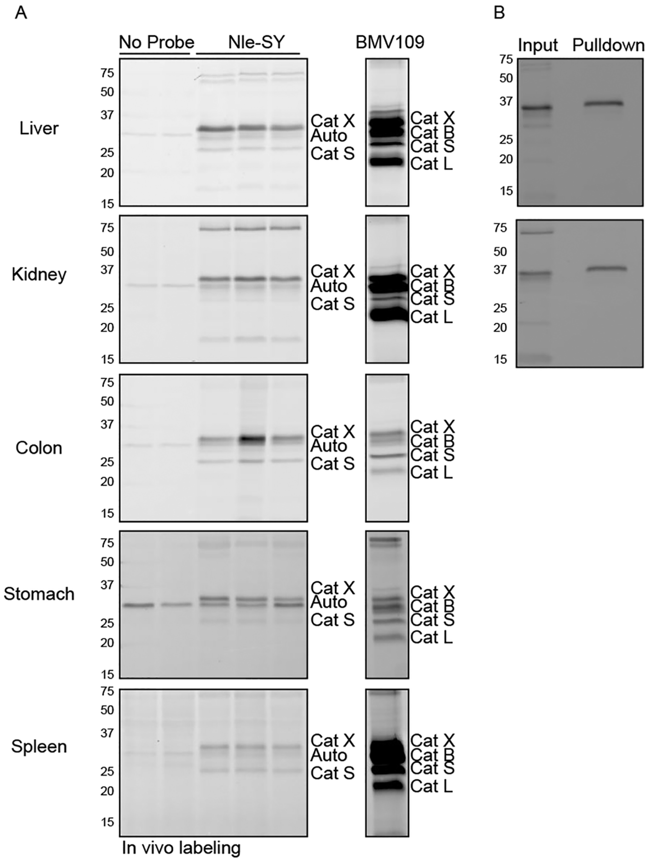

Figure 4. In vivo characterization of sCy5-Nle-SY (20). (A) SDS-PAGE and in-gel fluorescence of tissue lysates prepared from mice that received no probe (NP), sCy5-Nle-SY, or BMV109. BMV109-labeled samples were cut from the same gel and are presented at the same gain setting as the other samples in the corresponding tissue. Gains for each tissue were set individually to display optimal contrast for cathepsin X labeling. An autofluorescent band was observed in the no-probe control (labeled as Auto). (B) Immunoprecipitation of liver and kidney samples from A with a cathepsin X-specific antibody. Also refer to Figure S2.

(i.e., its preference for a free carboxylic acid limits the choice and placement of the fluorophore). A study by Devanathan and colleagues used a fluorogenic substrate library based on the aminobenzoic acid-Phe(4-NO_2) fluorophore-quencher pair to explore the preferred P1 and P2 residues of cathepsin X.[35] In the P1 position, weak reactivity was observed with Met, Phe, Tyr, Thr, Gln, Glu, Lys, and Arg; however, Val, Ile, Leu, and Trp (among others) were not tolerated at all. By contrast, these residues were among the most potent in the P1 position of our sulfoxonium ylide library. In a similar study by Puzer and colleagues, in which aminobenzoic acid and Lys-(dinitrophenol) were used as the fluorophore quencher pair, Leu was well tolerated in the P1 position.[36] In both screens, most residues were well tolerated in the P2 position with the exception of proline. In direct contrast to this, cathepsin X has been shown to cleave natural substrates such as CXCL-12 with proline at the P2 position.[37] Collectively, these studies demonstrate the dependence of probe structure on specificity and warrant the development of larger sulfoxonium ylide libraries with greater diversity of P1, P2, and P3 residues. Given the observed crossreactivity of the current probes with other as yet unknown proteases (e.g., in the kidney), we anticipate that expanding the sulfoxonium ylide library will open the door to selective ABPs for other proteases in addition to cathepsin X.

In conclusion, our new sulfoxonium ylide-based probes will be valuable for understanding the contribution of cathepsin X to normal physiology and disease and for establishing cathepsin X and a drug target and diagnostic marker for cancer and other inflammatory and neurodegenerative diseases.

■ EXPERIMENTAL SECTION

Synthetic Methods and Key Resources. Detailed synthetic methods and a table summarizing the source of all key reagents (antibodies, chemicals, biochemical assays, cell lines, and mouse strains) can be found within the Supporting Information.

Cell Culture. RAW264.7 or MDA-MB-231^{HM} cells were cultured in DMEM containing 10% fetal bovine serum (v/v) and 1% antibiotic/antimycotic (v/v). RAW264.7 cells were passaged by scraping with a rubber policeman, while MDA-MB-231^{HM} cells were lifted with 0.02% EDTA (w/v) in phosphate-buffered saline (PBS).

Animals. All experiments involving animals were approved by the Monash University Animal Ethics Committee. Male C57BL/6J mice were obtained from the Monash Animal Research Platform and used in accordance with the guidelines at 8−10 weeks of age. Snap-frozen spleens from wildtype and cathepsin X knockout mice, as described in ref 38 were obtained from the University of Calgary and used in accordance with the University of Calgary Animal Care and Use Committee.

Cell Lysate Labeling and SDS-PAGE Analysis. Cells were harvested by scraping, washed once with PBS, and resuspended in lysis buffer containing 50 mM citrate [pH 5.5], 0.5% CHAPS (w/v), 0.1% Triton X-100 (v/v), and 4 mM DTT. Cells were incubated on ice for at least 10 min with intermittent vortexing followed by centrifugation ($21\times g$ at 4 °C for 5 min). Cleared supernatants were then transferred to a fresh tube and protein concentration was determined by BCA. Total protein (50 μg) was aliquoted into tubes in a final volume of 20 μL lysis buffer. Where indicated, JPM-OEt or MD-590 was added from a 100× DMSO stock and incubated at 37 °C for 20 min prior to probe addition. The indicated concentration of the probe was added from a 100× DMSO stock. Labeling was carried out at 37 °C for 20 min, and the reactions were quenched by the addition of 5× sample buffer (200 mM Tris-Cl [pH 6.8], 8% SDS (w/v), 0.04% bromophenol blue (w/v), 5% β-mercaptoethanol (v/v), and 40% glycerol (v/v)). Samples were then boiled for 5 min and proteins were resolved on a 15% SDS-PAGE gel. The gels were scanned on a Typhoon 5 flatbed laser scanner at 633/670 nm excitation/emission to detect sCy5 fluorescence.

Live Cell Labeling. RAW cells or MDA-MB-231^{HM} cells were plated in 12-well plates. Where indicated, MDV-590, a closely related analogue to the cathepsin S-specific inhibitor MIV-247,[24] Z-FL-COCHO[39] or DMSO (vehicle) was added at 10 μM or 20 μM, respectively, from a 1000× DMSO stock for overnight incubation. When the cell density reached 80%, the indicated probes were added at the indicated concentrations from a 1000× DMSO stock and allowed to incubate for the indicated time. Media was then removed and replaced with PBS. The cells were then scraped and transferred to tubes, and lysis and SDS-PAGE analysis were carried out as above, except skipping the probe addition step.

Serum Stability Test. Probes (5 mM) were diluted 10-fold in fetal calf serum followed by 3 h incubation at 37 °C. Probe-containing serum was then diluted 10-fold in serum-free DMEM, followed by incubation with living RAW265.7 cells for 2 h (5 μM final probe concentration). Serum-free media containing 5 μM probe was used as a control. Cells were then harvested, lysed, and analyzed by in-gel fluorescence as above.

Tissue Analysis. Tissues or biopsies were harvested from healthy mice or patients, respectively, and snap frozen. At the time of analysis, lysis buffer was added at 10× (v/w), and tissues were sonicated on ice. Cleared lysates were labeled with the indicated probe and analyzed as above. For in vivo labeled tissues, mice were first injected

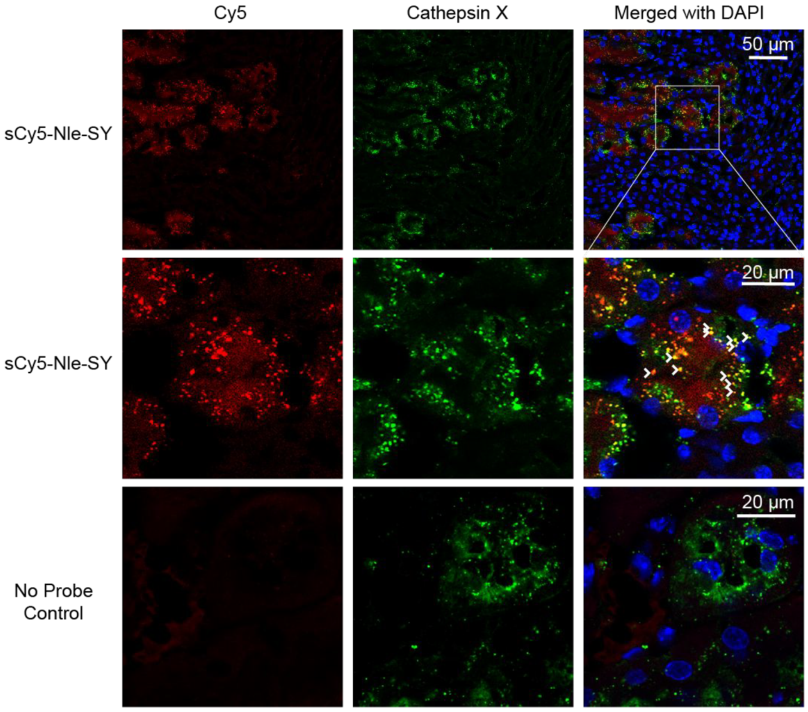

Figure 5. Confocal microscopy of cathepsin X labeling in kidney with sCy5-Nle-SY. Kidney sections from sCy5-Nle-SY-injected mice or no-probe control were analyzed for sCy5 fluorescence (red) or cathepsin X immunoreactivity (green) along with DAPI (blue) to visualize nuclei. The middle row is a zoomed-in image of the top row, as denoted by the white box. White arrowheads point to areas where the probe and immunoreactive cathepsin X are overlaid.

Scheme 2. Synthesis of sCy5-AA-AOMK Probes via a Sulfoxonium Ylide Intermediate[a]

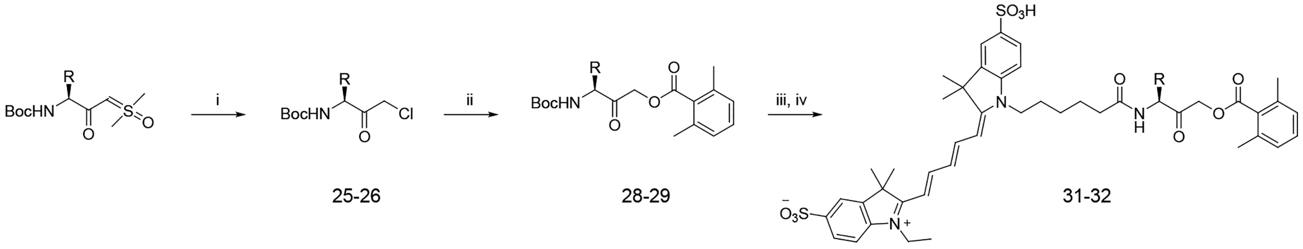

25-26

28-29

31-32

[a](i) 1.15 eq HCl in dioxane, THF, reflux, 4 h. (ii) 2,6-dimethylbenzoic acid, KF, DMF, rt, 18 h. (iii) TFA/CH_2Cl_2 (1:1), (iv) sulfo-Cy5, PyClock, DIPEA, DMF, rt, 18 h. The synthetic route for the related compound Cbz-Lys(sCy5)-AOMK (**27**, **30**, **33**) can be found in Scheme S1.

Table 2. Amino Acids Used in Compounds 25–33 (Scheme 2)

Boc-AA-SY	Boc-AA-CH_2Cl	Boc-AA-AOMK	sCy5-AA-AOMK
Boc-Nle-SY 12	25	28	31
Boc-Phe-SY 13	26	29	32

intravenously via the tail vein with sCy5-Nle-SY, BMV109, or sCy5-Nle-AOMK (50 nmol in 100 μL 10% DMSO/PBS (v/v) or vehicle control). Tissues were harvested after 2 h and analyzed as above except without further probe addition.

Immunoblotting. After detection of in-gel fluorescence, human cancer samples were transferred to a nitrocellulose membrane using the TransBlot system (Bio-Rad). Loading and transfer efficiency were assessed by Ponceau Stain (Sigma). The membrane was then incubated overnight at 4 °C with a goat anticathepsin X antibody (1:1000) in Odyssey Blocking Buffer (LiCor) diluted by 50% in PBS (v/v) containing 0.05% Tween-20 (v/v; PBS-T). After washing the membrane three times with PBS-T, it was incubated with donkey antigoat-IRDYE800 (1:10 000) at rt for 1 h. After washing, binding was detected by scanning the membrane on a Typhoon 5 (IR-long filter).

Immunoprecipitation Assay. Probe-labeled lysate from above (in sample buffer) was divided into input or pulldown (~50 μg total protein each). The input sample was stored at −20 °C. The pulldown sample was diluted in 500 μL IP buffer (PBS [pH 7.4], 0.5% NP-40 (*v*/*v*), 1 mM EDTA). Goat anticathepsin X antibody (10 μL) was added along with 40 μL slurry of prewashed Protein A/G agarose beads. Samples were rotated overnight at 4 °C. Beads were then washed four times with IP buffer followed by a final wash in 0.9% NaCl (w/v). Beads were then resuspended in 2× sample buffer and boiled. The pulldown supernatants, alongside the input samples, were analyzed by fluorescent SDS-PAGE as above.

Confocal Microscopy. Kidney tissues from mice that received sCy5-Nle-SY (or vehicle control) above were fixed overnight in 4% paraformaldehyde in PBS (w/v) followed by overnight cryoprotection in 30% sucrose (v/v). Tissues were embedded in OCT, frozen on dry ice, and sectioned at 10 μm. Immunostaining for cathepsin X was carried out according to standard protocols. In brief, sections were air-dried, fixed in cold acetone for 10 min, air-dried again, and then rehydrated in PBS. Sections were blocked in PBS containing 3% normal horse serum (v/v) with 0.1% Triton X-100 (v/v). Goat

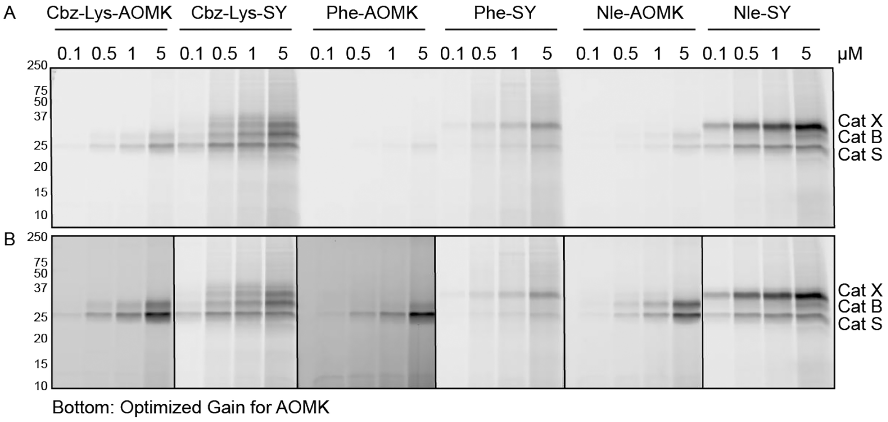

Figure 6. In vitro and in vivo characterization of AOMK and sulfoxonium ylide probes. (A) Labeling of living RAW264.7 cells with the indicated AOMK and SY probes (0.1, 0.5, 1, 5 μM), as analyzed by in-gel fluorescence. In the top panel, gain settings are equal for all samples. In the bottom panel (B), gain settings were individually set to show optimal contrast for the AOMK probes. Also refer to Figures S3 and S4.

anticathepsin X was added at 1:100 in blocking buffer overnight at 4 °C. Sections were then washed, and a secondary antibody, donkey antigoat-AlexaFluor594, was added at 1:500 for 1 h at rt. Sections were stained with DAPI for 5 min, washed, and mounted with ProLong Diamond. Staining was analyzed using a Leica SP8 inverted confocal microscope.

Statistical Analysis. All experiments were performed with at least three biological replicates. Data are reported as means ± SEM. Statistical significance was determined by comparing two groups using a Student's t test, and p values of less than 0.05 were considered significant.

■ ASSOCIATED CONTENT

Supporting Information

The Supporting Information is available free of charge at https://pubs.acs.org/doi/10.1021/acschembio.9b00961.

Detailed synthetic methods, molecular formula strings and a key resource table, as well as additional synthetic schemes (PDF)

Experimental data (XLS)

■ AUTHOR INFORMATION

Corresponding Author

Laura E. Edgington-Mitchell − *Department of Biochemistry and Molecular Biology, Bio21 Molecular Science and Biotechnology Institute, The University of Melbourne, Parkville, Victoria 3052, Australia; Drug Discovery Biology, Monash Institute of Pharmaceutical Sciences, Monash University, Parkville, Victoria 3052, Australia; Department of Oral and Maxillofacial Surgery, Bluestone Center for Clinical Research, New York University College of Dentistry, New York, New York 10010, United States;* orcid.org/0000-0002-6810-6149; Email: laura.edgingtonmitchell@unimelb.edu.au

Authors

Simon J. Mountford − *Medicinal Chemistry, Monash Institute of Pharmaceutical Sciences, Monash University, Parkville, Victoria 3052, Australia*

Bethany M. Anderson − *Department of Biochemistry and Molecular Biology, Bio21 Molecular Science and Biotechnology Institute, The University of Melbourne, Parkville, Victoria 3052, Australia; Drug Discovery Biology, Monash Institute of Pharmaceutical Sciences, Monash University, Parkville, Victoria 3052, Australia*

Bangyan Xu − *Department of Biochemistry and Molecular Biology, Bio21 Molecular Science and Biotechnology Institute, The University of Melbourne, Parkville, Victoria 3052, Australia*

Elean S. V. Tay − *Department of Biochemistry and Molecular Biology, Bio21 Molecular Science and Biotechnology Institute, The University of Melbourne, Parkville, Victoria 3052, Australia*

Monika Szabo − *Medicinal Chemistry, Monash Institute of Pharmaceutical Sciences, Monash University, Parkville, Victoria 3052, Australia*

My-Linh Hoang − *Medicinal Chemistry, Monash Institute of Pharmaceutical Sciences, Monash University, Parkville, Victoria 3052, Australia*

Jiayin Diao − *Drug Discovery Biology, Monash Institute of Pharmaceutical Sciences, Monash University, Parkville, Victoria 3052, Australia*

Luigi Aurelio − *Medicinal Chemistry, Monash Institute of Pharmaceutical Sciences, Monash University, Parkville, Victoria 3052, Australia*

Rhiannon I. Campden − *Snyder Institute for Chronic Disease and Department of Biochemistry and Molecular Biology, University of Calgary, Calgary, Alberta T2N 1N4, Canada*

Erik Lindström − *Medivir AB, Huddinge 141 22, Sweden*

Erica K. Sloan − *Drug Discovery Biology, Monash Institute of Pharmaceutical Sciences, Monash University, Parkville, Victoria 3052, Australia*

Robin M. Yates − *Snyder Institute for Chronic Disease and Department of Biochemistry and Molecular Biology, University of Calgary, Calgary, Alberta T2N 1N4, Canada*

Nigel W. Bunnett − *Drug Discovery Biology, Monash Institute of Pharmaceutical Sciences, Monash University, Parkville, Victoria 3052, Australia; Department of Craniofacial Biology, New York University College of Dentistry, New York, New York 10010, United States; Department of Pharmacology and Experimental Therapeutics, The University of Melbourne, Parkville, Victoria 3052, Australia*

Philip E. Thompson − *Medicinal Chemistry, Monash Institute of Pharmaceutical Sciences, Monash University, Parkville, Victoria 3052, Australia;* orcid.org/0000-0002-5910-7625

Complete contact information is available at: https://pubs.acs.org/10.1021/acschembio.9b00961

Author Contributions

◆S.J.M. and B.M.A. contributed equally to this work.

Author Contributions

LEM conceived study, planned all experiments, analyzed data, wrote manuscript, and contributed funding. SJM, MLH, MS, and LA synthesized the compounds included in the study. SJM completed the compound characterization and contributed to the writing of the manuscript. BMA, BX, ESVT, MLH, and JD executed the experiments and collected data. RIC and RMY contributed cathepsin X knockout tissues for the study. EKS provided MDA-MB-231^{HM} cells. EL provided cathepsin S inhibitor. PT contributed intellectually and supervised the compound synthesis. NB contributed funds for the work.

Notes

The authors declare the following competing financial interest(s): N.W.B. is a founding scientist of Endosome Therapeutics Inc. Research in N.W.B.'s laboratory is supported in part by Takeda Pharmaceuticals, Inc.

■ ACKNOWLEDGMENTS

We thank C. Nowell for maintaining the imaging facilities at the Monash Institute of Pharmaceutical Sciences. MDA-MB-231^{HM} cells were a kind gift from Z. Ou, Fudan University, Shanghai Cancer Center. L.E.M. was supported by an Early Career Fellowship from the National Health and Medical Research Council of Australia (NHMRC, GNT1091636), a Grimwade Fellowship funded by the Russell and Mab Grimwade Miegunyah Fund at the University of Melbourne, a DECRA Fellowship from the Australian Research Council (ARC, DE180100418), and by seed grants from Monash University. N.W.B. was supported by grants from the National Institutes of Health (NS102722, DE026806, DK118971) and the United States Department of Defense (W81XWH1810431).

■ ABBREVIATIONS

ABP, activity-based probe
SY, sulfoxonium ylide
AOMK, acyloxymethylketone
PMK, phenoxymethylketone

■ REFERENCES

(1) Obermajer, N., Švajger, U., Bogyo, M., Jeras, M., and Kos, J. (2008) Maturation of Dendritic Cells Depends on Proteolytic Cleavage by Cathepsin X. *J. Leukocyte Biol. 84*, 1306−1315.

(2) Pečar Fonović, U., and Kos, J. (2015) Cathepsin X Cleaves Profilin 1 C-Terminal Tyr139 and Influences Clathrin-Mediated Endocytosis. *PLoS One 10*, e0137217.

(3) Nägler, D. K., Kraus, S., Feierler, J., Mentele, R., Lottspeich, F., Jochum, M., and Faussner, A. (2010) A Cysteine-Type Carboxypeptidase, Cathepsin X, Generates Peptide Receptor Agonists. *Int. Immunopharmacol. 10*, 134−139.

(4) Obermajer, N., Doljak, B., Jamnik, P., Fonović, U. P., and Kos, J. (2009) Cathepsin X Cleaves the C-Terminal Dipeptide of Alpha- and Gamma-Enolase and Impairs Survival and Neuritogenesis of Neuronal Cells. *Int. J. Biochem. Cell Biol. 41*, 1685−1696.

(5) Wendt, W., Zhu, X.-R., Lübbert, H., and Stichel, C. C. (2007) Differential Expression of Cathepsin X in Aging and Pathological Central Nervous System of Mice. *Exp. Neurol. 204*, 525−540.

(6) Hafner, A., Glavan, G., Obermajer, N., Živin, M., Schliebs, R., and Kos, J. (2013) Neuroprotective Role of Γ-Enolase in Microglia in a Mouse Model of Alzheimer's Disease Is Regulated by Cathepsin X. *Aging Cell 12*, 604−614.

(7) Leichsenring, A., Bäcker, I., Wendt, W., Andriske, M., Schmitz, B., Stichel, C. C., and Lübbert, H. (2008) Differential Expression of Cathepsin S and X in the Spinal Cord of a Rat Neuropathic Pain Model. *BMC Neurosci. 9*, 80−13.

(8) Huynh, J. L., Garg, P., Thin, T. H., Yoo, S., Dutta, R., Trapp, B. D., Haroutunian, V., Zhu, J., Donovan, M. J., Sharp, A. J., and Casaccia, P. (2014) Epigenome-Wide Differences in Pathology-Free Regions of Multiple Sclerosis−Affected Brains. *Nat. Neurosci. 17*, 121−130.

(9) Allan, E. R. O., Campden, R. I., Ewanchuk, B. W., Tailor, P., Balce, D. R., McKenna, N. T., Greene, C. J., Warren, A. L., Reinheckel, T., and Yates, R. M. (2017) A Role for Cathepsin Z in Neuroinflammation Provides Mechanistic Support for an Epigenetic Risk Factor in Multiple Sclerosis. *J. Neuroinflammation 14*, 103.

(10) Orlowski, G. M., Colbert, J. D., Sharma, S., Bogyo, M., Robertson, S. A., and Rock, K. L. (2015) Multiple Cathepsins Promote Pro−IL-1β Synthesis and NLRP3-Mediated IL-1β Activation. *J. Immunol. 195*, 1685−1697.

(11) Edgington-Mitchell, L. E., Rautela, J., Duivenvoorden, H. M., Jayatilleke, K. M., van der Linden, W. A., Verdoes, M., Bogyo, M., and Parker, B. S. (2015) Cysteine Cathepsin Activity Suppresses Osteoclastogenesis of Myeloid-Derived Suppressor Cells in Breast Cancer. *Oncotarget 6*, 27008−27022.

(12) Akkari, L., Gocheva, V., Kester, J. C., Hunter, K. E., Quick, M. L., Sevenich, L., Wang, H.-W., Peters, C., Tang, L. H., Klimstra, D. S., Reinheckel, T., and Joyce, J. A. (2014) Distinct Functions of Macrophage-Derived and Cancer Cell-Derived Cathepsin Z Combine to Promote Tumor Malignancy via Interactions with the Extracellular Matrix. *Genes Dev. 28*, 2134−2150.

(13) Nägler, D. K., Krüger, S., Kellner, A., Ziomek, E., Ménard, R., Buhtz, P., Krams, M., Roessner, A., and Kellner, U. (2004) Up-Regulation of Cathepsin X in Prostate Cancer and Prostatic Intraepithelial Neoplasia. *Prostate 60*, 109−119.

(14) Bernhardt, A., Kuester, D., Roessner, A., Reinheckel, T., and Krueger, S. (2010) Cathepsin X-Deficient Gastric Epithelial Cells in Co-Culture with Macrophages: Characterization of cytokine response and migration capability after Helicobacter pylori infection. *J. Biol. Chem. 285*, 33691−33700.

(15) Krueger, S., Kalinski, T., Hundertmark, T., Wex, T., Küster, D., Peitz, U., Ebert, M., Nägler, D. K., Kellner, U., Malfertheiner, P., Naumann, M., Röcken, C., and Roessner, A. (2005) Up-Regulation of Cathepsin X inHelicobacter Pylori Gastritis and Gastric Cancer. *J. Pathol. 207*, 32−42.

(16) Nägler, D. K., Zhang, R., Tam, W., Sulea, T., Purisima, E. O., and Ménard, R. (1999) Human Cathepsin X: a Cysteine Protease with Unique Carboxypeptidase Activity. *Biochemistry 38*, 12648−12654.

(17) Duivenvoorden, H. M., Rautela, J., Edgington-Mitchell, L. E., Spurling, A., Greening, D. W., Nowell, C. J., Molloy, T. J., Robbins, E., Brockwell, N. K., Lee, C. S., Chen, M., Holliday, A., Selinger, C. I., Hu, M., Britt, K. L., Stroud, D. A., Bogyo, M., Möller, A., Polyak, K., Sloane, B. F., O'Toole, S. A., and Parker, B. S. (2017) Myoepithelial Cell-Specific Expression of Stefin a as a Suppressor of Early Breast Cancer Invasion. *J. Pathol. 243*, 496−509.

(18) Edgington, L. E., Verdoes, M., and Bogyo, M. (2011) Functional Imaging of Proteases: Recent Advances in the Design and Application of Substrate-Based and Activity-Based Probes. *Curr. Opin. Chem. Biol. 15*, 798−805.

(19) Edgington, L. E., and Bogyo, M. (2013) In Vivo Imaging and Biochemical Characterization of Protease Function Using Fluorescent Activity-Based Probes. *Curr. Protoc. Chem. Biol. 5*, 25−44.

(20) Sanman, L. E., and Bogyo, M. (2014) Activity-Based Profiling of Proteases. *Annu. Rev. Biochem. 83*, 249−273.

(21) Verdoes, M., Oresic Bender, K., Segal, E., van der Linden, W. A., Syed, S., Withana, N. P., Sanman, L. E., and Bogyo, M. (2013) Improved Quenched Fluorescent Probe for Imaging of Cysteine Cathepsin Activity. *J. Am. Chem. Soc. 135*, 14726−14730.

(22) Paulick, M. G., and Bogyo, M. (2011) Development of Activity-Based Probes for Cathepsin X. *ACS Chem. Biol. 6*, 563−572.

(23) Shaw, E. (1988) Peptidyl Sulfonium Salts. a New Class of Protease Inhibitors. *J. Biol. Chem. 263*, 2768−2772.

(24) Hewitt, E., Pitcher, T., Rizoska, B., Tunblad, K., Henderson, I., Sahlberg, B. L., Grabowska, U., Classon, B., Edenius, C., Malcangio, M., and Lindstrom, E. (2016) Selective Cathepsin S Inhibition with MIV-247 Attenuates Mechanical Allodynia and Enhances the Antiallodynic Effects of Gabapentin and Pregabalin in a Mouse Model of Neuropathic Pain. *J. Pharmacol. Exp. Ther. 358*, 387−396.

(25) Turk, V., Stoka, V., Vasiljeva, O., Renko, M., Sun, T., Turk, B., and Turk, D. (2012) Cysteine Cathepsins: From Structure, Function and Regulation to New Frontiers. *Biochim. Biophys. Acta, Proteins Proteomics 1824*, 68−88.

(26) Chang, X.-Z., Li, D.-Q., Hou, Y.-F., Wu, J., Lu, J.-S., Di, G.-H., Jin, W., Ou, Z.-L., Shen, Z.-Z., and Shao, Z.-M. (2008) Identification of the Functional Role of AF1Q in the Progression of Breast Cancer. *Breast Cancer Res. Treat. 111*, 65−78.

(27) Edgington, L. E., van Raam, B. J., Verdoes, M., Wierschem, C., Salvesen, G. S., and Bogyo, M. (2012) An Optimized Activity-Based Probe for the Study of Caspase-6 Activation. *Chem. Biol. 19*, 340−352.

(28) Edgington, L. E., Verdoes, M., Ortega, A., Withana, N. P., Lee, J., Syed, S., Bachmann, M. H., Blum, G., and Bogyo, M. (2013) Functional Imaging of Legumain in Cancer Using a New Quenched Activity-Based Probe. *J. Am. Chem. Soc. 135*, 174−182.

(29) Edgington, L. E., Berger, A. B., Blum, G., Albrow, V. E., Paulick, M. G., Lineberry, N., and Bogyo, M. (2009) Noninvasive Optical Imaging of Apoptosis by Caspase-Targeted Activity-Based Probes. *Nat. Med. 15*, 967−973.

(30) Verdoes, M., Edgington, L. E., Scheeren, F. A., Leyva, M., Blum, G., Weiskopf, K., Bachmann, M. H., Ellman, J. A., and Bogyo, M. (2012) A Nonpeptidic Cathepsin S Activity-Based Probe for Noninvasive Optical Imaging of Tumor-Associated Macrophages. *Chem. Biol. 19*, 619−628.

(31) Oresic Bender, K., Ofori, L., van der Linden, W. A., Mock, E. D., Datta, G. K., Chowdhury, S., Li, H., Segal, E., Sanchez Lopez, M., Ellman, J. A., Figdor, C. G., Bogyo, M., and Verdoes, M. (2015) Design of a Highly Selective Quenched Activity-Based Probe and Its Application in Dual Color Imaging Studies of Cathepsin S Activity Localization. *J. Am. Chem. Soc. 137*, 4771−4777.

(32) Pace, V., Castoldi, L., and Pregnolato, M. (2013) α-Amino-α'-Halomethylketones: Synthetic Methodologies and Pharmaceutical Applications as Serine and Cysteine Protease Inhibitors. *Mini-Rev. Med. Chem. 13*, 988−996.

(33) Wang, D., Schwinden, M. D., Radesca, L., Patel, B., Kronenthal, D., Huang, M.-H., and Nugent, W. A. (2004) One-Carbon Chain Extension of Esters to α-chloroketones: A Safer Route without Diazomethane. *J. Org. Chem. 69*, 1629−1633.

(34) Wang, D., and Nugent, W. A. (2007) Synthesis of anti-α-amino epoxide by one carbon homologation of an α-amino ester: (2S,3S)-1,2-epoxy-3-(Boc-amino)-4-phenylbutane. *Org. Syntheses 84*, 58−67.

(35) Devanathan, G., Turnbull, J. L., Ziomek, E., Purisima, E. O., Ménard, R., and Sulea, T. (2005) Carboxy-Monopeptidase Substrate Specificity of Human Cathepsin X. *Biochem. Biophys. Res. Commun. 329*, 445−452.

(36) Puzer, L., Cotrin, S. S., Cezari, M. H. S., Hirata, I. Y., Juliano, M. A., Stefe, I., Turk, D., Turk, B., Juliano, L., and Carmona, A. K. (2005) Recombinant Human Cathepsin X Is a Carboxymonopeptidase Only: a Comparison with Cathepsins B and L. *Biol. Chem. 386*, 2321−2325.

(37) Staudt, N. D., Aicher, W. K., Kalbacher, H., Stevanovic, S., Carmona, A. K., Bogyo, M., and Klein, G. (2010) Cathepsin X Is Secreted by Human Osteoblasts, Digests CXCL-12 and Impairs Adhesion of Hematopoietic Stem and Progenitor Cells to Osteoblasts. *Haematologica 95*, 1452−1460.

(38) Sevenich, L., Schurigt, U., Sachse, K., Gajda, M., Werner, F., Muller, S., Vasiljeva, O., Schwinde, A., Klemm, N., Deussing, J., Peters, C., and Reinheckel, T. (2010) Synergistic Antitumor Effects of Combined Cathepsin B and Cathepsin Z Deficiencies on Breast Cancer Progression and Metastasis in Mice. *Proc. Natl. Acad. Sci. U. S. A. 107*, 2497−2502.

(39) Walker, B., Lynas, J. F., Meighan, M. A., and Brömme, D. (2000) Evaluation of Dipeptide A-Keto-B-Aldehydes as New Inhibitors of Cathepsin S. *Biochem. Biophys. Res. Commun. 275*, 401−405.

Probing the contribution of cysteine cathepsins to inflammatory bowel diseases

Bethany M. Anderson[1,2], Rhiannon I. Campden[3], Hongyi Wu[1], Rachel M. McQuade[4], Simona E. Carbone[2], Daniel P. Poole[2], Alan E. Lomax[5], Stephen S. Vanner[5], Robin M. Yates[3], Nigel W. Bunnett[6], and Laura E. Edgington-Mitchell[1,2,7,#]

[1]Department of Biochemistry and Molecular Biology, Bio21 Molecular Science and Biotechnology Institute, The University of Melbourne, Parkville, Victoria, Australia.

[2]Drug Discovery Biology, Monash Institute of Pharmaceutical Sciences, Monash University, Parkville, Victoria, Australia.

[3]Snyder Institute for Chronic Disease and Department of Biochemistry and Molecular Biology, University of Calgary, Calgary, Alberta, Canada.

[4]RACHEL'S AFFILIATION

[5]Gastrointestinal Diseases Research Unit, Queen's University, Kingston, Ontario, Canada.

[6]Department of Molecular Pathobiology, New York University College of Dentistry, New York, New York, USA.

[7]Department of Oral and Maxillofacial Surgery, New York University College of Dentistry, Bluestone Center for Clinical Research, New York, New York, USA.

[#]Corresponding author: Laura E. Edgington-Mitchell
laura.edgingtonmitchell@unimelb.edu.au

Keywords: protease, cathepsin, activity-based probes, functional imaging, colitis, inflammatory bowel disease

Abstract

Cathepsin S is a cysteine protease that has previously been implicated in inflammatory bowel diseases (IBD) for its ability to promote visceral pain. Given its pro-inflammatory roles in diverse diseases, we hypothesized that cathepsin S would drive other symptoms associated with IBD. Using broad-spectrum and specific activity-based probes (ABPs), we investigated cathepsin S activation in human and mouse colitis. We observed a significant increase in fecal cathepsin S in patients with ulcerative colitis compared to healthy controls, while cathepsin S in mucosal biopsies was unaffected. Mice with experimental colitis exhibited a modest increase in mucosal activity of both cathepsin S and X compared to naïve mice. Luminal secretion of cathepsin S was dramatically increased upon colitis induction. Using confocal microscopy, we determined the source of cathepsin S to be CD68$^+$ macrophages in the mucosa. To investigate the contribution of cathepsin S and cathepsin X to colitis, we induced experimental colitis in cathepsin-deficient mice. Cathepsin X-deficient mice exhibited no clear differences in disease indicators compared to wild-type mice, while cathepsin S-deficient mice exhibited less rectal bleeding, less splenomegaly and improved histological scores. To determine whether pharmacologic inhibition of cathepsin S activity would likewise ameliorate symptoms of colitis, a reversible inhibitor LY3000328 was administered to mice with colitis. LY3000328 provoked a clear upregulation of cathepsin S and L activity, likely through a compensatory mechanism or accumulation of undegraded cathepsins. This increase in protease activity was associated with exacerbated histological scores and splenomegaly. Collectively, these results suggest that cathepsin S, but not cathepsin X, may promote symptoms of experimental colitis. While cathepsin S has potential to be a therapeutic target in colitis, improved strategies to sustain its inhibition are required in future.

Introduction

Inflammatory bowel diseases (IBD), including ulcerative colitis (UC) and Crohn’s disease (CD), are characterized by relapsing and remitting bouts of diarrhea, rectal bleeding, increased urgency and pain. The etiology of IBDs is not well understood. It has been hypothesized that damage to the intestinal epithelium leads to impaired barrier function, leakage of microbes into the mucosa and activation of pro-inflammatory neutrophils, macrophages, and mast cells. Macrophages are a rich source of cysteine cathepsin proteases, which contribute to inflammation associated with diverse pathologies.

Cathepsin S is a lysosomal cysteine protease with diverse substrates associated with inflammation. Among these are protease-activated receptor 2 (PAR_2), where cleavage activates the receptor in a biased manner (Zhao et al., 2014), and invariant chain, which is important for MHC II-mediated antigen presentation (Riese et al., 1996). Compared to other cysteine cathepsins, cathepsin S has a relatively broad pH optimum and is able to maintain its enzymatic activity extracellularly (Shi, Munger, Meara, Rich, & Chapman, 1992).

Using a model of piroxicam-induced colitis in IL-10-deficient mice, cathepsin S was previously demonstrated to be activated in the proximal colon, cecum, and luminal fluids (Cattaruzza et al., 2011). Cleavage of PAR_2 by cathepsin S results in hyperexcitability of enteric neurons.

Colonic infusion of cathepsin S increased the visceromotor response to colorectal distension in wild-type mice, and this was attenuated in mice lacking PAR_2. Cathepsin S-deficient mice with trinitrobenzosulfonate (TNBS)-induced colitis exhibited reduced visceromotor response to colorectal distension compared to wild-type mice. Collectively, these results indicate a role for cathepsin S in provoking inflammatory pain associated with colitis.

In addition to visceral pain, activation of PAR_2 is known to provoke other features of colitis, including increased motility and secretion, loss of barrier function, submucosal edema, cytokine production, and inflammatory infiltration (Cenac et al., 2007; Gecse et al., 2008; Hyun, Andrade-Gordon, Steinhoff, & Vergnolle, 2008; Lohman et al., 2012). Accordingly, antagonism of PAR_2 or inhibition of other PAR_2-activiting proteases has resulted in improved outcomes in mouse models of experimental colitis (Lohman et al., 2012; Tremaine et al., 2002). Whether cathepsin S contributes to the development of colitis and associated symptoms through its actions on PAR_2 or other targets has not been investigated in detail.

Steimle and colleagues demonstrated that negative regulation of cathepsin S activity by commensal bacteria such as *Bacteroides vulgatus* may be important for maintaining intestinal equilibrium (Steimle et al., 2016). In the presence of symbiotic bacteria, cathepsin S may be inhibited by cystatin C, its endogenous inhibitor. Reactive oxygen species induced by a pathobiotic bacteria such as *E. coli* provoke homodimerization of cystatin C, rendering it unable to bind to cathepsin S. Elevated cathepsin S activity in the presence of pathogenic bacteria may therefore contribute to intestinal host inflammatory responses. In $CD4^+$ T cell-mediated colitis in Rag1-deficient mice, administration of *B. vulgatus* or a cathepsin S inhibitor LY3000328 attenuated weight loss, improved histological scores, and reduced $CD3^+CD4^+$ T cells and MHC-$II^{hi}CD11c^+$ dendritic cells to a similar extent, providing additional support for this hypothesis.

To investigate the contribution of cysteine cathepsins to colitis in more detail, we applied activity-based probes to measure their proteolytic activity in mucosal biopsies and fecal samples from patients with IBD and in a model of experimental colitis induced by dextran sulfate sodium (DSS). We then investigated the effects of cathepsin deletion and inhibition on colitis development and associated symptoms.

Experimental Procedures

Human samples

Written and verbal consent were obtained prior to enrolment and all protocols were approved by and carried out in accordance with the Queen's University Human Ethics Committee or XXXX. Patients were well-characterized individuals with active UC or CD. Healthy individuals were volunteers experiencing no gastrointestinal abnormalities or abdominal pain. For UC and CD patients, biopsies were obtained from sites of active inflammation. Fresh biopsies were washed in PBS and then snap frozen for protease analysis. Fecal samples were homogenized in 0.7% NaCl (0.5g per 4 mL) and centrifuged to clear solids. Supernatants were frozen for protease analysis. For the secretion assay, full-thickness regions of normal colon were obtained during a cancer resection surgery and processed as below.

DSS-induced colitis

All animal studies were approved by and carried out in accordance with the guidelines of the Animal Ethics Committee at Monash University or the Animal Care and Use Committee at the University of Calgary. Wild-type C57Bl/6J mice were purchased from the Monash University in-house colony. Cathepsin S- and cathepsin X-deficient mice were bred at the University of Calgary. All mice were maintained with free access to food and water under temperature and light controlled conditions. Colitis was induced in 8-10-week old male mice by administering dextran sulfate sodium (MPBio; 3% unless otherwise indicated) in the drinking water for 6 days. Control mice received drinking water alone. Body weights and symptoms were monitored daily. Fecal pellets were scored using scales for consistency (0 – dry; 1 – moist but firm; 2 – soft but still formed; 3 – unformed but bulky; 4 – liquid) and blood (0- no blood; 1 – subtle blood or darkening of the stool; 2 – red streaks in stool; 4 – obvious rectal bleeding). Fecal samples were collected and frozen daily. Unless otherwise indicated, mice were humanely killed on day 6. Colons were harvested and flushed with phosphate buffered saline (PBS). Luminal fluid was collected, centrifuged to clear solids, and frozen. Proximal colon tissue was divided and frozen for gel analysis and myeloperoxidase (MPO) assay or fixed for microscopy or histology. Spleens were also harvested and frozen. For cathepsin S inhibitor trial, 2% DSS was used. LY3000328 (30 mg/kg in 200 µl 85% NaCl (0.9%), 10% DMSO and 5% Tween-20) was administered daily by intraperitoneal injection.

Ex vivo tissue imaging

On day 6, naïve or DSS-treated mice were injected with BMV109 or BMV157 intravenously by tail vein (20 nmol in 100 µl 20% DMSO/PBS). After six hours, colons were harvested, flushed with PBS, and imaged for Cy5 fluorescence using an IVIS Lumina XR III in vivo imaging system (Perkin Elmer). Proximal colons were cut along the mesenteric border and pinned onto Sylgard-lined 35 mm dishes (mucosa down) for fixation in 4% paraformaldehyde overnight at 4°C. Whole mount preparations were washed with PBS azide (0.1%) and blocked for 1 hour in 3% normal horse serum and 0.1% triton X-100 in PBS azide. Preparations were washed 3 times with PBS azide and then incubated overnight at 4°C with rabbit anti-CD68 (1:500; 137001; BioLegend) in blocking buffer. After a further 3 washes, donkey anti-rabbit-AlexFluor488 (1:500; A-21208; Life Technologies) in PBS azide was applied for 1 h. After 3 additional washes, whole mount preparations were mounted using ProLong Gold (Invitrogen) and imaged with a Leica SP8 confocal microscope.

Analysis of cathepsin probe labeling by SDS-PAGE

Human mucosal biopsies and mouse proximal colon tissues were lysed by sonication in PBS (for in vivo-labeled samples) or citrate buffer (for in vitro-labeled samples; 50 mM citrate, pH 5.5, 0.5% CHAPS, 0.1% Triton X-100, 4 mM DTT). Lysates were cleared by centrifugation at 14,000 x g for 5 min at 4°C. Cleared luminal fluids were concentrated using a 3-KDa cutoff column (Amicon). Fecal pellets were homogenized in PBS and centrifuged to clear solids. Total protein concentration was measured in colon lysate, luminal fluid and fecal supernatant using a BCA assay and diluted into PBS or citrate buffer (50 µg total protein in 20µl). For in vivo-labeled samples, 5x sample buffer was immediately added (50% glycerol, 250 mM Tris-Cl, pH 6.8, 10% SDS, 0.04% bromophenol blue, 6.25% beta-mercaptoethanol). For in vitro-labeled samples, BMV109 (0.5 µM) or BMV157 (1 µM) were added from a 100x DMSO stock and incubated at 37°C for 30 min. Where indicated LY3000328 (10 nM – 100 µM) or MDV590 (10 µM) were added 30 min prior to probe addition. Labeling reaction was quenched by addition of 5x sample buffer. Samples were boiled for 5 min and resolved on a homemade 15% SDS-PAGE gel. Gels were scanned for Cy5 fluorescence using a Typhoon 5 flatbed laser scanner (GE Healthcare). After transferring to nitrocellulose membranes, membranes were immunoblotted overnight with goat anti-cathepsin S (1:1000; AF1183; R&D) or goat-anti-cathepsin X (1:1000; AF1033; R&D) followed by detection with donkey anti-goat-IR800

(1:10,000; 9263-2214; Licor). Membranes were scanned using a Typhoon 5 or Odyssey Imaging System (LiCor).

Immunoprecipitation

Probe-labeled samples were divided into input and pulldown, each containing 50 µg total protein. Pulldown samples were diluted in 500 µl immunoprecipitation (IP) buffer (PBS, pH 7.4, 0.5% NP-40, 1 mM EDTA) followed by 10 µl of the indicated antibody (all from R&D): anti-cathepsin S (AF1183), anti-cathepsin X (AF1033), anti-cathepsin L (AF1515) or anti-cathepsin B (AF965). Protein A/G agarose beads (40 µl slurry; Santa Cruz Biotechnology) were washed in IP buffer and added. Pulldowns were rotated overnight at 4°C. Supernatants were collected and precipitated in acetone for 1 h at -20°C. Proteins were pelleted and dried prior to dissolving in 20 µl 1x sample buffer. Beads were washed 4 times in IP buffer and once in NaCl (0.9%) and resuspended in 20 µl 2x sample buffer. Input, pulldown and supernatants were boiled for 5 min and resolved by fluorescent SDS-PAGE as above.

Secretion assay

Proximal colon tissue from naïve and DSS-treated mice were weighed and incubated overnight at 37°C in 500 µl DMEM containing 10% fetal bovine serum. Supernatant was collected, filtered with a 50-kDa cutoff spin column to exclude large serum proteins and concentrated with a 3-kDa spin column (Amicon). Cathepsins were then labeled with BMV109 and analyzed as above. Regions of healthy human colon obtained from a cancer resection were dissected into muscle and mucosal layers and incubated for 5 h at 37°C in 50 µl PBS. Supernatants were collected and the tissues were sonicated. Both lysate and supernatant were labeled with BMV109 and analyzed as above.

Histology

Colon tissues were fixed overnight at 4°C in 4% paraformaldehyde in PBS, paraffin embedded, sectioned and stained with hematoxylin and eosin according to standard protocols. Slides were stained on a Mirax Digital Slide Scanner (Zeiss). Four random regions from each colon were blinded and scored for inflammatory infiltrate, crypt organization, and goblet cell numbers.

Myeloperoxidase activity assay

Tissues were sonicated in buffer containing 50 mM potassium phosphate, pH 6.0, 0.5% hexadecyl trimethylammonium bromide (50 mg tissue per mL) and supernatants were cleared by sonication. In a 96 well plate, 7 µl sample was diluted in 193 µl substrate solution containing 50 mM potassium phosphate, pH 6.0, O-dianisidine HCl (0.167 mg/mL) and 0.0005% H_2O_2. Absorbance at 460 nm was measured every 30 s for 15 min on a Flexstation 3 (Molecular Devices) and slopes were recorded.

Statistical analyses

All experiments were performed with at least 3 biological replicates. Data are reported as means ± SEM. Statistical significance was determined by comparing two groups using a Student's t test, and p values of less than 0.05 were considered significant.

Results

Cathepsin S secretion is increased in IBD patients

To determine whether cathepsin S is activated in the colons of patients with ulcerative colitis, we applied a fluorescently quenched activity-based probe, BMV157 (Oresic Bender et al., 2015). Cathepsin S binds to BMV157 in an activity-dependent manner, triggering the release of a QSY21 quenching group and subsequent emission of Cy5 fluorescence. Probe binding is irreversible and can be detected by scanning gel-resolved proteins for Cy5 fluorescence or imaging whole tissue or tissue sections (Edgington, Verdoes, & Bogyo, 2011). In lysates from mucosal biopsies prepared at pH 5.5 or 7.4, we did not observe any statistically significant differences in BMV157 labeling between healthy volunteers and patients with ulcerative colitis (**Fig S1**). By contrast, in homogenates prepared from stool samples, cathepsin S activity was significantly increased in patients with ulcerative colitis compared to healthy volunteers (**Fig 1A,C**). While more variable, samples from some patients with Crohn's disease also exhibited elevated fecal cathepsin S. We confirmed the identity of the BMV157-labeled protease by immunoblotting (**Fig 1B**) and immunoprecipitating (**Fig 1C**) the samples with a cathepsin S-specific antibody. These data suggest that luminal secretion of cathepsin S is increased in patients with active inflammatory bowel diseases.

Cathepsin S secretion is increased in experimental colitis

Next, we investigated cathepsin S activation in a model of experimental colitis induced by DSS. In addition to BMV157, we used BMV109, a pan-cathepsin probe that binds to cathepsin X, B, S, and L (Verdoes et al., 2013). After in vivo administration of BMV109 or BMV157, we imaged probe fluorescence in colon tissues ex vivo. With both probes, we observed a significant increase in fluorescence in the proximal region of colons from DSS-treated mice compared to those from naïve mice (**Fig 2A-B**). There was no difference in the distal region of the colons. In whole mount submucosal preparations, most of the cathepsin S-specific signal from BMV157 was confined to $CD68^+$ macrophages (**Fig 2C**).

We next analyzed in vivo probe binding in colon tissue, luminal fluids and fecal pellets by in-gel fluorescence (**Fig 3A-F**). In colon tissue, there was a subtle but significant increase in BMV157-labeled cathepsin S (1.6-fold), whereas in fecal pellets and luminal fluids, the increase was more dramatic (5- and 7.8-fold, respectively) (**Fig 3A-F**). Similarly, BMV109-labeled cathepsin S was increased in DSS-treated fecal pellets and luminal fluids by 3.2- and 10.3-fold, respectively, while it was not was not statistically different in proximal colon tissue (**Fig 3A-F**). Cathepsin X, B and L activities were similar in naïve and inflamed colon tissue, though they all trended towards an increase (**Fig 3A, S4B**). Immunoprecipitation was used to confirm the identity of all proteases labeled by BMV109 in colon tissue (**Fig 3H**).

To exclude the possibility that probe uptake was higher in inflamed colons due to increased blood flow, etc., we also labeled colon tissue lysates, fecal homogenates, and luminal fluids with BMV109 and BMV157 ex vivo. Cathepsin S activity was significantly increased in all sample types with both probes (**Fig S2A-F**). We confirmed the identity of ex vivo-labeled cathepsin S by immunoprecipitation (**Fig S2H**). We also demonstrated that cathepsin S labeling could be abolished by pre-treating the samples with MDV-590, a cathepsin-S specific inhibitor (**Fig S2I**) (Hewitt et al., 2016). Furthermore, fecal cathepsin S activity remained elevated after mice were permitted to drink normal water for two days after cessation of DSS treatment (**Fig S3**). By ex vivo labeling, the activities of cathepsins X, B, and L were also significantly increased in inflamed colons (1.7-, 1.3-, and 2.8-fold, respectively; **Fig S2A,G**). By immunoblot, we observed increased levels of pro-cathepsin X in inflamed colons (**Fig S4**).

To further investigate cathepsin S secretion, we incubated segments of proximal colon from naïve and DSS-treated mice in culture overnight and analyzed the conditioned media for cathepsin S activity. Both groups clearly secreted cathepsin S (**Fig S5A-B**). There was a trend towards increased secretion from inflamed colons compared to naïve, but this was not significant. Likewise, normal human colon tissues secrete cathepsin S, but only from the mucosal layer, and not muscle (**Fig S5C**). As another potential source of cathepsin S, we also examined mesenteric lymph nodes. While cathepsin S could clearly be detected in lymph node lysates, there was no difference in cathepsin S activity between naïve and inflamed nodes (**Fig 5SD**). We also examined cathepsin S activity throughout the length of the lower GI tract in naïve mice (**Fig 5SE**). Its activity is much higher in the small intestine and distal colon than the proximal colon. While we have not yet examined small intestine during DSS colitis, secretions from these regions may contribute to the elevated cathepsin S in luminal fluid and fecal pellets.

Collectively, these data demonstrate that cathepsin S is secreted from normal human and mouse colons, and this secretion is elevated during ulcerative colitis and acute experimental colitis. In mice, the activities cathepsin S, X, B, and L are also modestly elevated in proximal colon tissue during colitis.

Cathepsin S deletion, but not cathepsin X, improves symptoms of experimental colitis

Next we sought to investigate the contributions of cathepsin S and cathepsin X to DSS-induced colitis using cathepsin-deficient mice. As mice from a Canadian colony were used in these experiments, while Australian mice were used for all other experiments, we first analyzed cathepsin activation in colon tissue, fecal pellets and luminal fluids after DSS treatment. In colon tissues labeled ex vivo with BMV109, activities of cathepsin S, X, and L were significantly increased after DSS treatment in wild-type mice, while cathepsin B activity was unchanged (**Fig 4A, S6A-D**). In cathepsin S-deficient colons, we did not observe any compensatory changes to the other cathepsins. In the absence of cathepsin X, however, cathepsin L activity was significantly upregulated (**Fig 4A, S6C**).

Surprisingly, naïve wild-type mice from the Canadian colony exhibited much higher protease activity in luminal fluids and fecal pellets than the Australian mice, with a greater diversity of proteins labeled by BMV109 (**Fig 4B-C, S5E-F**). Secretion of cathepsin S did not increase in response to DSS treatment, contrary to what we reproducibly observed in the Australian colony. Moreover, mice deficient in cathepsin S or X had much less fecal cysteine protease activity than the wild-type mice (**Fig 4C**).

As the changes to protease activity in colon tissue were similar in both colonies, we decided to continue with a comparative analysis of colitis symptoms in wild-type and cathepsin-deficient mice from the Canadian colony. DSS-treated mice lost weight to the same extent, regardless of their genotype (**Fig 5A**). Fecal consistency was likewise similar in all mice, indicating that cathepsin deficiency did not prevent diarrhea (**Fig 5B**). Cathepsin S-deficient mice, however, exhibited far less rectal bleeding than wild-type mice or cathepsin X-deficient mice (**Fig 5C,E**). Colon shortening (**Fig 5D-E**) and myeloperoxidase (MPO) activity (**Fig 5F**) were not affected by cathepsin deficiency. Unlike wild-type and cathepsin X-deficient mice, spleens from Cathepsin S-deficient mice were not enlarged after DSS treatment (**Fig 5G**). Cathepsin S activity in spleens, however, was minimal and was not altered by DSS treatment (**Fig S6G**). Histological evaluation of colon sections revealed less immune infiltrate, goblet cells, and crypt disorganization in cathepsin S-deficient mice compared to wild-type or cathepsin X-deficient mice (**Fig 5H-L**).

Collectively, these data suggest that loss of cathepsin S results in improvement of some, but not all, symptoms of colitis, while loss of cathepsin X had no obvious effects.

Pharmacological inhibition of cathepsin S results in exacerbated colitis

Having observed that cathepsin S deficiency results in improved colitis symptoms, we hypothesized that pharmacologic inhibition of its proteolytic activity would have similar effects. We selected the reversible inhibitor LY3000328 as it has previously shown efficacy in a T cell-induced model of colitis, as well as a model of abdominal aortic aneurysm (Jadhav et al., 2014; Steimle et al., 2016). We used a milder model of colitis (2% DSS) in hopes of exacerbating differences in symptoms between treated and untreated mice. Mice were treated daily with vehicle or LY3000328 (30 mg/kg) and symptoms were monitored over time. LY3000328-treated mice lost significantly less weight than the vehicle-treated controls (**Fig 6A**). No significant differences were observed in fecal consistency (**Fig 6B**) or fecal blood (**Fig 7C**), although treated mice trended towards worse scores at end point. Colon length (**Fig 6D**) and colon MPO activity (**Fig 6E**) were unaffected by LY3000328. Spleens from treated mice exhibited greater splenomegaly than vehicle controls (**Fig 6F**). Histological evaluation indicated that treated mice had a higher degree of inflammatory infiltrates, goblet cells, and crypt disorganization than controls (**Fig 6G-K**).

Overall, LY3000328 treatment had a negative impact on colitis symptoms, which was contrary to our hypothesis based on the results in the cathepsin S-deficient mice. To ensure that LY3000328 had effectively inhibited cathepsin S activity, we analyzed colon tissue and fecal pellets from these mice using BMV109 ex vivo (**Fig 7A-E**). LY3000328-treated colon lysates contained increased cathepsin S and L activity compared to the vehicle controls (**Fig 7A,C,D**). This corresponded to an increase in total levels of cathepsin S and L as shown by immunoblot (**Fig 7F**). Fecal cathepsin S was unaffected by LY3000328 (**Fig 7B,E**). Thus, not only did LY3000328 fail to block cathepsin S activity, it stimulated increased activity of both cathepsin S and L. We confirmed that the inhibitor was capable of blocking cathepsin S activity in colon lysates in a concentration-dependent manner (**Fig S7**). While it was selective for cathepsin S, we also observed inhibition of cathepsin X, B, and L in response to in vitro LY3000328 treatment.

Collectively, these data demonstrate that LY3000328 increased cathepsin S and L activity in proximal colon tissue, and this corresponded to a worsening of colitis symptoms.

Discussion

In this study, we employed broad-spectrum and specific activity-based probes to profile cathepsin activity during human and mouse colitis. In fecal samples from patients with ulcerative colitis and Crohn's disease, cathepsin S was increased compared to those from healthy volunteers. These data suggest an increase in luminal cathepsin S secretion during colitis. Likewise, we observed an increase in cathepsin S activity in luminal fluids and fecal samples in DSS-induced mouse colitis. This corroborates the previous observation that cathepsin S secretion was increased in piroxicam-induced colitis (Cattaruzza et al., 2011). We demonstrated that cathepsin S can be directly secreted from mouse and human colon tissue, and that CD68$^+$ macrophages are the richest source of cathepsin S.

While enhanced cathepsin S secretion in DSS-treated mice was extremely reproducible in the Australian colony of mice, it was not observed in the Canadian mouse colony. Furthermore, the Canadian wild-type mice exhibited much broader diversity in BMV109-labeled fecal proteases at baseline compared to the Australian mice, while fecal samples from both cathepsin S- and cathepsin X-deficient Canadian mice had little protease labeling at any time point examined. These differences may be attributed to divergence in mouse strains over time or to differences in the gastrointestinal flora populated by the two groups of mice. While the BMV109-labeled proteases in the Canadian wild-type mice were not further characterized, it is possible that a subset of them could be microbially derived.

Two complementary approaches were employed to assess the contribution of cathepsin S to DSS-induced colitis. Genetic deletion of cathepsin S resulted in less rectal bleeding, less splenomegaly, and improved histological scores. Inhibition of cathepsin S activity ultimately resulted in exacerbated levels of cathepsin S and L, greater splenomegaly and worsened histological scores. While not statistically significant, there was also a trend towards greater colonic shortening, rectal bleeding and diarrhea in the inhibitor-treated mice. Collectively, these data suggest a role for cathepsin S in promoting colitis symptoms.

Splenomegaly was among the most striking changes upon cathepsin S loss or hyper-activation. This was also observed in a mouse model of periodontitis involving systemic exposure to lipopolysaccharide from *Porphyromonas gingivalis* (PgLPS). Like colitis, PgLPS exposure leads to splenomegaly in wild-type mice, and this was clearly suppressed in cathepsin S-deficient mice (Dekita et al., 2017). Cathepsin S deficiency was also marked by reduced CD11c$^+$ dendritic cells in the spleen, lower production of IL-6 and less differentiation of Th17 cells. PgLPS was demonstrated to provoke cathepsin S-dependent activation of PAR$_2$, which couples to the PI3K/Akt pathway to promote IL-6-dependent splenic Th17 cell differentiation. Another study demonstrated that in corneal epithelial cells, cathepsin S provoked PAR$_2$-dependent release of IL-6, IL-8, TNFα, IL-1β, and matrix metalloproteinase 9 (MMP-9) (Klinngam, Fu, Janga, Edman, & Hamm-Alvarez, 2018), all of which are important in IBD pathogenesis. In particular, IL-6 signaling is central to the development of intestinal inflammation and its neutralization has been under investigation as a therapeutic strategy for IBDs (Waldner & Neurath, 2014). IL-6 is also known synergize with IL-4 to stimulate secretion of cathepsin S from bone-marrow derived macrophages through STAT3/6-dependent mechanisms (Yan, Wang, Bowman, & Joyce, 2016). This may result in a positive feedback loop to augment cathepsin S secretion during colitis. Furthermore, cathepsin S was also recently shown to cleave and activate IL-36γ (Ainscough et al., 2017), another cytokine with known impacts on antimicrobial defense and barrier function (Ngo et al., 2018).

In phase I clinical trials, a single dose of LY3000328 exhibited a bi-phasic effect on plasma cathepsin S activity (Payne et al., 2014). After a decrease in activity over the first 12 hours, cathepsin S activity returned to baseline followed by an increase in activity that was sustained for at least 48 h. We observed a similar upregulation of cathepsin S activity in mouse colon tissue after daily doses of LY3000328 for five days (**Fig 7A**). Cathepsin L activity was also similarly increased by LY3000328. Both proteases were increased at the total protein level, so this effect is unlikely to be the result of modulation of endogenous cathepsins inhibitors. In vitro, we demonstrated that LY3000328 inhibited the activity of cathepsin S, X, B, and L, though it was most potent for cathepsin S. Increased protease levels may be a compensatory response to the loss of cathepsin activity, although transcriptional activity of cathepsin S and L was not assessed in this study or in the human trial. An alternate explanation is that inhibited proteases are more stable than the active enzymes and therefore do not degrade as readily. Inhibition of another lysosomal cysteine protease called legumain results in transcriptional upregulation of itself and other lysosomal hydrolases, likely through a STAT3-mediated mechanism (Martinez-Fabregas et al., 2018). We previously showed that legumain accumulates in vivo after administration of the small-molecule inhibitor, LI-1 (Edgington-Mitchell et al., 2016). As LI-1 is an irreversible inhibitor, however, legumain activity was completely blocked despite the increase in total legumain protein. These data suggest that an irreversible inhibitor might be more appropriate for ensuring sustained inhibition of cathepsin S in vivo and improved therapeutic outcomes.

We also investigated the contribution of cathepsin X (also known as cathepsin Z) to colitis. This had not previously been explored, and there is limited information on its role in other inflammatory diseases. In the GI tract of naïve mice, cathepsin X activity is highest in the stomach (Fig S5E) and its activity may contribute to chronic mucosal inflammation associated with *H. pylori*-induced gastritis and gastric cancer (Krueger et al., 2005). In multiple sclerosis, cathepsin X-deficient mice exhibited less neuroinflammation and secretion of inflammatory cytokines (Allan et al., 2017). In a mouse model of silicosis, loss of cathepsin X was associated with reduced inflammation and improved histopathology scores (Campden et al in review). Based on these studies and our observation that cathepsin X expression was upregulated during colitis, we hypothesized that cathepsin X deficiency would similarly ameliorate symptoms of colitis. On the contrary, cathepsin X knockout mice were statistically indistinguishable from wild-type mice for all symptoms examined. Thus, cathepsin X is unlikely to be a suitable therapeutic target for colitis.

Conclusions

Cathepsin S is secreted during human and murine colitis, and fecal cathepsin S may have value as a diagnostic marker. Loss of cathepsin S, but not cathepsin X, improved symptoms of colitis, while pharmacological inhibition of cathepsin S by LY3000328 ultimately led to increased cathepsin activity and exacerbated colitis symptoms. Together these data suggest a role for cathepsin S in driving inflammation, either through actions upon PAR_2 or other substrates. Improved inhibitors that can promote sustained and specific inhibition of cathepsin S may have value as a therapeutic for intestinal inflammation as well as visceral pain.

Acknowledgements

We thank C. Nowell for maintaining the imaging facilities at the Monash Institute of Pharmaceutical Sciences. We thank the L. Leone and T. Cardamone from the Melbourne Histology Platform and Australian Phenomics Network for histological services. We thank R. Kochappan, J. Di Cello, and P. Rajasekhar for technical assistance. LEM was supported by an Early Career Fellowship from the National Health and Medical Research Council of Australia (NHMRC, GNT1091636), a Grimwade Fellowship funded by the Russell and Mab Grimwade Miegunyah Fund at the University of Melbourne, a DECRA Fellowship from the Australian Research Council (ARC, DE180100418), and by seed grants from Monash University and University of Melbourne EMCRA. NWB was supported by grants from the National Institutes of Health (NS102722, DE026806, DK118971) and the United States Department of Defense (W81XWH1810431).

Declarations of Interest

NWB is a founding scientist of Endosome Therapeutics Inc. Research in NWB’s laboratory is supported in part by Takeda Pharmaceuticals, Inc.

Author Contributions

LEM conceived study, planned all experiments, analyzed data, wrote manuscript, and contributed funding. BMA, RIC, HW, and SEC executed the experiments and collected data. RM assisted with data analysis. AEM and SJV supplied human samples. RMY, DPP and NWB contributed funds for the work and contributed intellectually.

References

Ainscough, J. S., Macleod, T., McGonagle, D., Brakefield, R., Baron, J. M., Alase, A., . . . Stacey, M. (2017). Cathepsin S is the major activator of the psoriasis-associated proinflammatory cytokine IL-36gamma. *Proc Natl Acad Sci U S A, 114*(13), E2748-E2757. doi:10.1073/pnas.1620954114

Allan, E. R. O., Campden, R. I., Ewanchuk, B. W., Tailor, P., Balce, D. R., McKenna, N. T., . . . Yates, R. M. (2017). A role for cathepsin Z in neuroinflammation provides mechanistic support for an epigenetic risk factor in multiple sclerosis. *J Neuroinflammation, 14*(1), 103. doi:10.1186/s12974-017-0874-x

Cattaruzza, F., Lyo, V., Jones, E., Pham, D., Hawkins, J., Kirkwood, K., . . . Bunnett, N. W. (2011). Cathepsin S is activated during colitis and causes visceral hyperalgesia by a PAR2-dependent mechanism in mice. *Gastroenterology, 141*(5), 1864-1874 e1861-1863. doi:10.1053/j.gastro.2011.07.035

Cenac, N., Andrews, C. N., Holzhausen, M., Chapman, K., Cottrell, G., Andrade-Gordon, P., . . . Vergnolle, N. (2007). Role for protease activity in visceral pain in irritable bowel syndrome. *J Clin Invest, 117*(3), 636-647. doi:10.1172/JCI29255

Dekita, M., Wu, Z., Ni, J., Zhang, X., Liu, Y., Yan, X., . . . Takahashi, I. (2017). Cathepsin S Is Involved in Th17 Differentiation Through the Upregulation of IL-6 by Activating PAR-2 after Systemic Exposure to Lipopolysaccharide from Porphyromonas gingivalis. *Front Pharmacol, 8*, 470. doi:10.3389/fphar.2017.00470

Edgington, L. E., Verdoes, M., & Bogyo, M. (2011). Functional imaging of proteases: recent advances in the design and application of substrate-based and activity-based probes. *Curr Opin Chem Biol, 15*(6), 798-805. doi:10.1016/j.cbpa.2011.10.012

Edgington-Mitchell, L. E., Wartmann, T., Fleming, A. K., Gocheva, V., van der Linden, W. A., Withana, N. P., . . . Bunnett, N. W. (2016). Legumain is activated in macrophages during pancreatitis. *Am J Physiol Gastrointest Liver Physiol, 311*(3), G548-560. doi:10.1152/ajpgi.00047.2016

Gecse, K., Roka, R., Ferrier, L., Leveque, M., Eutamene, H., Cartier, C., . . . Bueno, L. (2008). Increased faecal serine protease activity in diarrhoeic IBS patients: a colonic lumenal factor impairing colonic permeability and sensitivity. *Gut, 57*(5), 591-599. doi:10.1136/gut.2007.140210

Hewitt, E., Pitcher, T., Rizoska, B., Tunblad, K., Henderson, I., Sahlberg, B. L., . . . Lindstrom, E. (2016). Selective Cathepsin S Inhibition with MIV-247 Attenuates Mechanical Allodynia and Enhances the Antiallodynic Effects of Gabapentin and Pregabalin in a Mouse Model of Neuropathic Pain. *J Pharmacol Exp Ther, 358*(3), 387-396. doi:10.1124/jpet.116.232926

Hyun, E., Andrade-Gordon, P., Steinhoff, M., & Vergnolle, N. (2008). Protease-activated receptor-2 activation: a major actor in intestinal inflammation. *Gut, 57*(9), 1222-1229. doi:10.1136/gut.2008.150722

Jadhav, P. K., Schiffler, M. A., Gavardinas, K., Kim, E. J., Matthews, D. P., Staszak, M. A., . . . Deng, G. G. (2014). Discovery of Cathepsin S Inhibitor LY3000328 for the Treatment of Abdominal Aortic Aneurysm. *ACS Med Chem Lett, 5*(10), 1138-1142. doi:10.1021/ml500283g

Klinngam, W., Fu, R., Janga, S. R., Edman, M. C., & Hamm-Alvarez, S. F. (2018). Cathepsin S Alters the Expression of Pro-Inflammatory Cytokines and MMP-9, Partially through Protease-Activated Receptor-2, in Human Corneal Epithelial Cells. *Int J Mol Sci, 19*(11). doi:10.3390/ijms19113530

Krueger, S., Kalinski, T., Hundertmark, T., Wex, T., Kuster, D., Peitz, U., . . . Roessner, A. (2005). Up-regulation of cathepsin X in Helicobacter pylori gastritis and gastric cancer. *J Pathol, 207*(1), 32-42. doi:10.1002/path.1820

Lohman, R. J., Cotterell, A. J., Suen, J., Liu, L., Do, A. T., Vesey, D. A., & Fairlie, D. P. (2012). Antagonism of protease-activated receptor 2 protects against experimental colitis. *J Pharmacol Exp Ther, 340*(2), 256-265. doi:10.1124/jpet.111.187062

Martinez-Fabregas, J., Prescott, A., van Kasteren, S., Pedrioli, D. L., McLean, I., Moles, A., . . . Watts, C. (2018). Lysosomal protease deficiency or substrate overload induces an oxidative-stress mediated STAT3-dependent pathway of lysosomal homeostasis. *Nat Commun, 9*(1), 5343. doi:10.1038/s41467-018-07741-6

Ngo, V. L., Abo, H., Maxim, E., Harusato, A., Geem, D., Medina-Contreras, O., . . . Denning, T. L. (2018). A cytokine network involving IL-36gamma, IL-23, and IL-22 promotes antimicrobial defense and recovery from intestinal barrier damage. *Proc Natl Acad Sci U S A, 115*(22), E5076-E5085. doi:10.1073/pnas.1718902115

Oresic Bender, K., Ofori, L., van der Linden, W. A., Mock, E. D., Datta, G. K., Chowdhury, S., . . . Verdoes, M. (2015). Design of a highly selective quenched activity-based probe and its application in dual color imaging studies of cathepsin S activity localization. *J Am Chem Soc, 137*(14), 4771-4777. doi:10.1021/jacs.5b00315

Payne, C. D., Deeg, M. A., Chan, M., Tan, L. H., LaBell, E. S., Shen, T., & DeBrota, D. J. (2014). Pharmacokinetics and pharmacodynamics of the cathepsin S inhibitor, LY3000328, in healthy subjects. *Br J Clin Pharmacol, 78*(6), 1334-1342. doi:10.1111/bcp.12470

Riese, R. J., Wolf, P. R., Bromme, D., Natkin, L. R., Villadangos, J. A., Ploegh, H. L., & Chapman, H. A. (1996). Essential Role for Cathepsin S in MHC Class II–Associated Invariant Chain Processing and Peptide Loading. *Immunity, 4*, 357-366. doi:10.1016/s1074-7613(00)80249-6

Shi, G. P., Munger, J. S., Meara, J. P., Rich, D. H., & Chapman, H. A. (1992). Molecular Cloning and Expression of Human Alveolar Macrophage Cathepsin S, an Elastinolytic Cysteine Protease. *J Biol Chem, 267*(11), 7258-7262.

Steimle, A., Gronbach, K., Beifuss, B., Schafer, A., Harmening, R., Bender, A., . . . Frick, J. S. (2016). Symbiotic gut commensal bacteria act as host cathepsin S activity regulators. *J Autoimmun, 75*, 82-95. doi:10.1016/j.jaut.2016.07.009

Tremaine, W. J., Brzezinski, A., Katz, J. A., Wolf, D. C., Fleming, T. J., Mordenti, J., . . . Group, A. U. C. S. (2002). Treatment of mildly to moderately active ulcerative colitis with a tryptase inhibitor (APC 2059): an open-label pilot study. *Aliment Pharmacol Ther, 16*(3), 407-413. doi:10.1046/j.1365-2036.2002.01194.x

Verdoes, M., Oresic Bender, K., Segal, E., van der Linden, W. A., Syed, S., Withana, N. P., . . . Bogyo, M. (2013). Improved quenched fluorescent probe for imaging of cysteine cathepsin activity. *J Am Chem Soc, 135*(39), 14726-14730. doi:10.1021/ja4056068

Waldner, M. J., & Neurath, M. F. (2014). Master regulator of intestinal disease: IL-6 in chronic inflammation and cancer development. *Semin Immunol, 26*(1), 75-79. doi:10.1016/j.smim.2013.12.003

Yan, D., Wang, H. W., Bowman, R. L., & Joyce, J. A. (2016). STAT3 and STAT6 Signaling Pathways Synergize to Promote Cathepsin Secretion from Macrophages via IRE1alpha Activation. *Cell Rep, 16*(11), 2914-2927. doi:10.1016/j.celrep.2016.08.035

Zhao, P., Lieu, T., Barlow, N., Metcalf, M., Veldhuis, N. A., Jensen, D. D., . . . Bunnett, N. W. (2014). Cathepsin S causes inflammatory pain via biased agonism of PAR2 and TRPV4. *J Biol Chem, 289*(39), 27215-27234. doi:10.1074/jbc.M114.599712

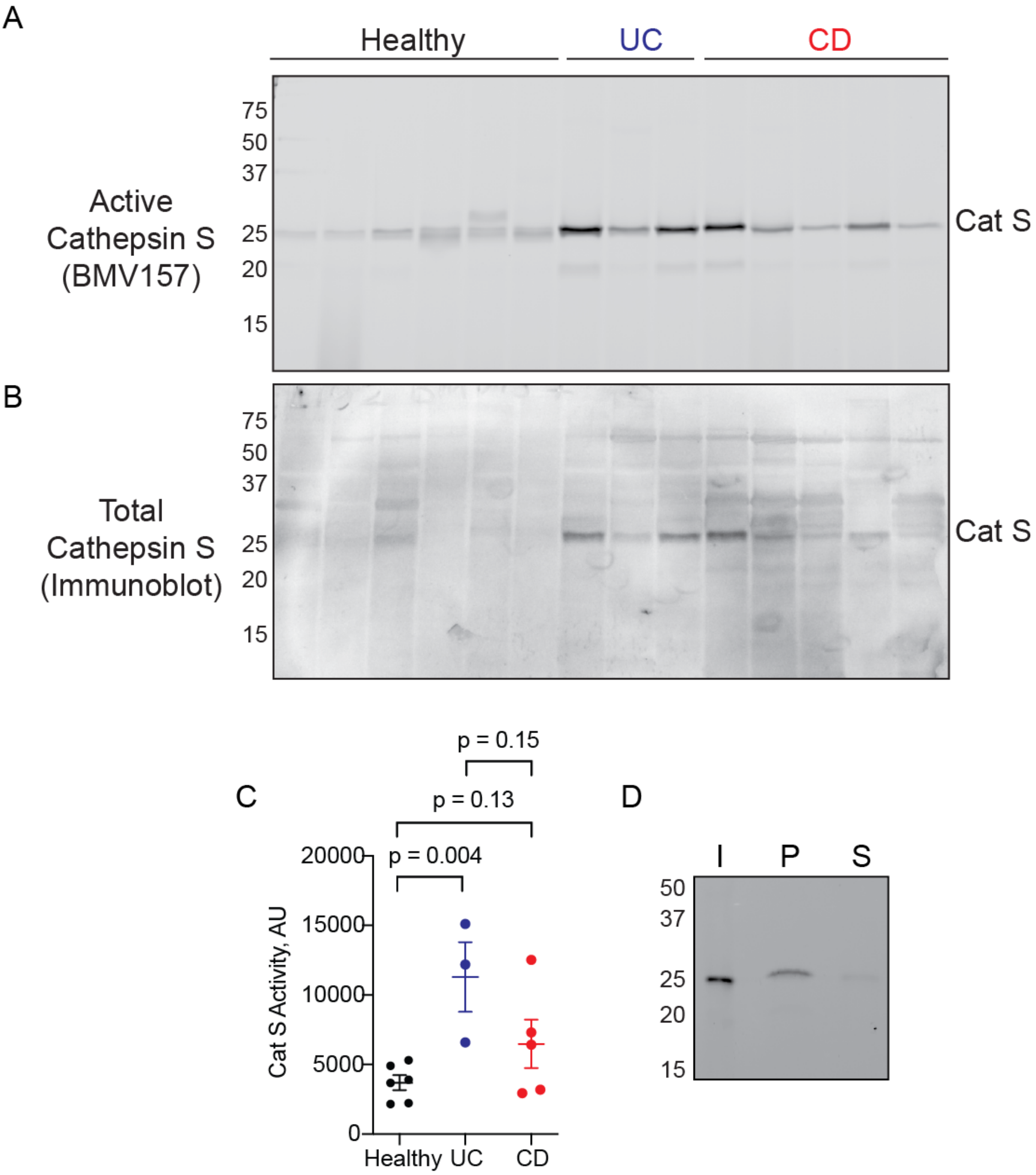

Figure 1. Cathepsin S is increased in fecal samples of patients with inflammatory bowel diseases. A) Homegenized fecal samples from healthy volunteers or patients with ulcerative colitis (UC) or Crohn's disease (CD) were labeled with BMV157 followed by analysis of in-gel fluorescence. **B)** Cathepsin S immunoblot of samples in (A). **C)** Densitometry analysis of cathepsin S activity in (A) Data are represented as means ± SEM (n = 3-6). **D)** Immunoprecipitation of CD sample with a cathepsin S-specific antibody. I = input, P = pulldown, S = supernatant.

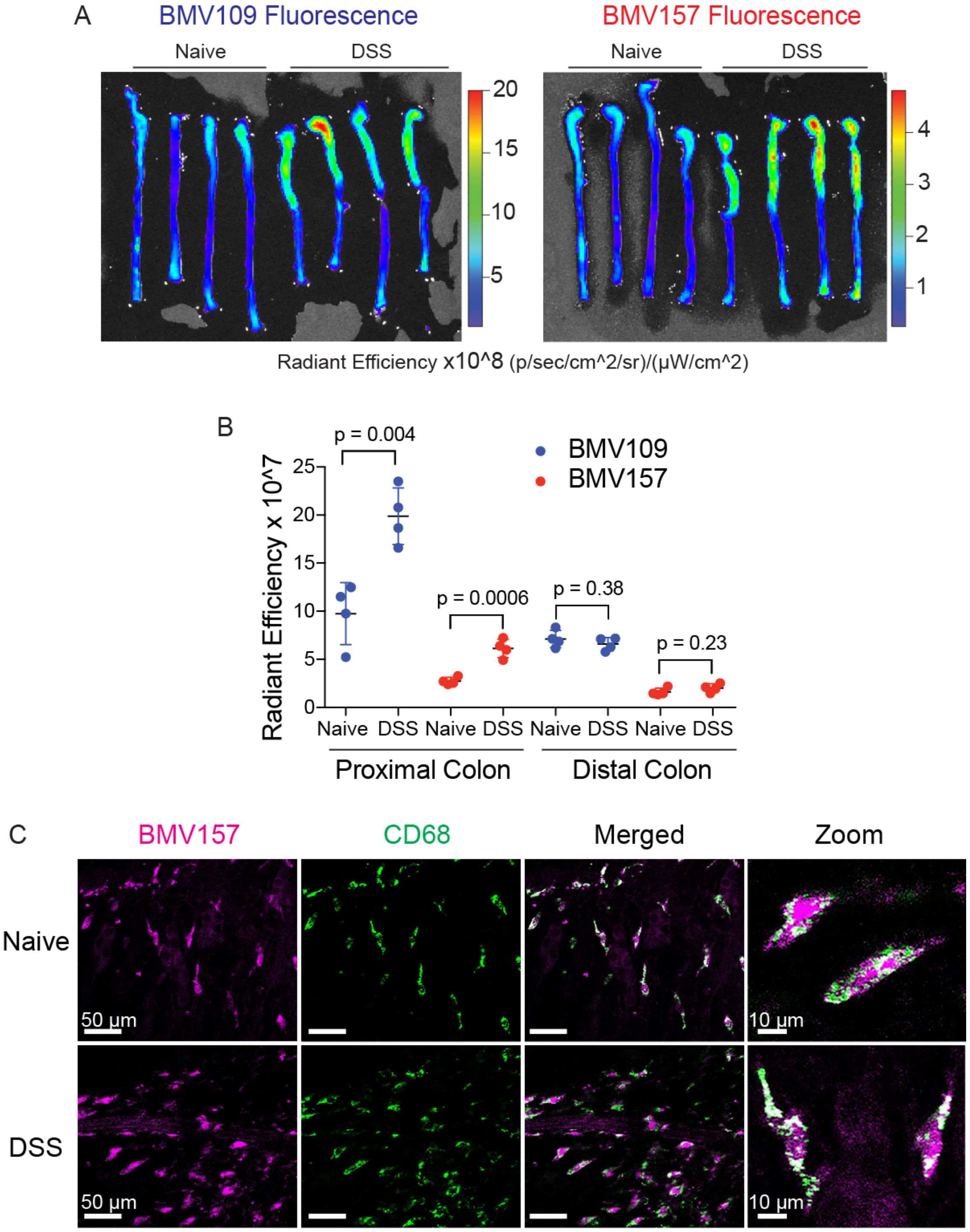

Figure 2. Cathepsin activity is increased in proximal colons during DSS-induced colitis. A) Naïve or DSS-treated mice were injected with BMV109 (pan-cysteine cathepsin probe) or BMV157 (cathepsin S-selective probe) on day 6. Colons were removed and imaged for Cy5 fluorescence. Gains were set for each probe independently. **B)** Quantification of fluorescent signal (radiant efficiency) in proximal and distal colons from (A). Data are represented as means ± SEM (n = 4). **C)** Representative whole mount submucosal preparation from naïve and DSS-treated mouse after in vivo labeling with BMV157 (cathepsin S activity – magenta) and immunostaining with anti-CD68 (green). Note: these samples were collected from Australian mice.

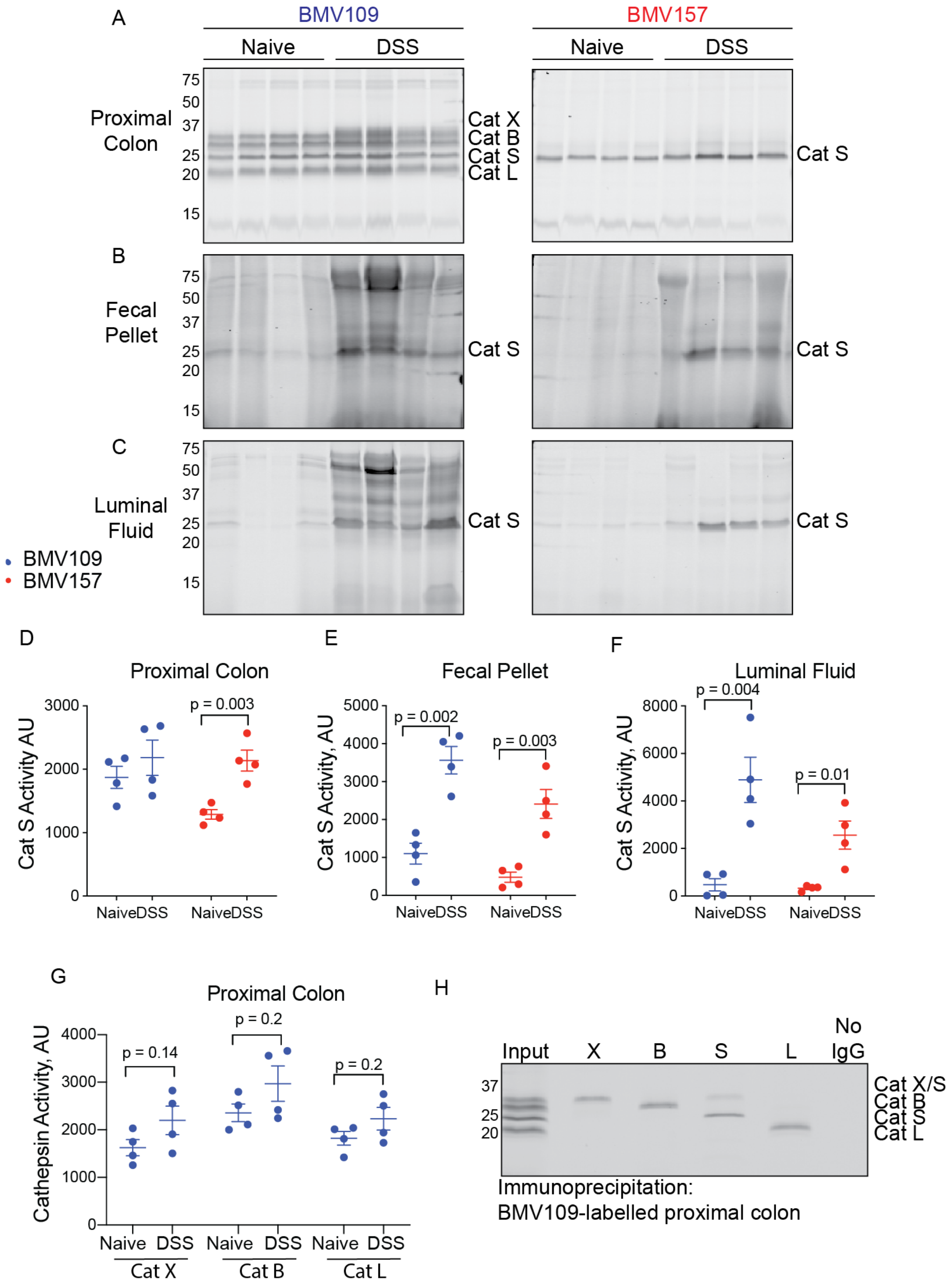

Figure 3. Cathepsin S secretion is increased during DSS-induced colitis. Proximal colons **(A)**, fecal pellets **(B)** and luminal fluids **(C)** from naïve and DSS-treated mice labeled in vivo with BMV109 (left) or BMV157 (right) were analyzed for in-gel fluorescence. Densitometry of cathepsin S labeling by BMV109 (blue) and BMV157 (red) in proximal colon **(D)**, fecal pellets **(E)**, and luminal fluid **(F)**. **G)** Densitometry of cathepsin X, cathepsin B, and cathepsin L labeling in colons by BMV109. Data are represented as means ± SEM (n = 4). **H)** Immunoprecipitation of BMV109-labeled proximal colon lysates with antibodies for cathepsin X, B, S, and L. No IgG indicates a negative control in which no antibody was added. Note: these samples were collected from Australian mice.

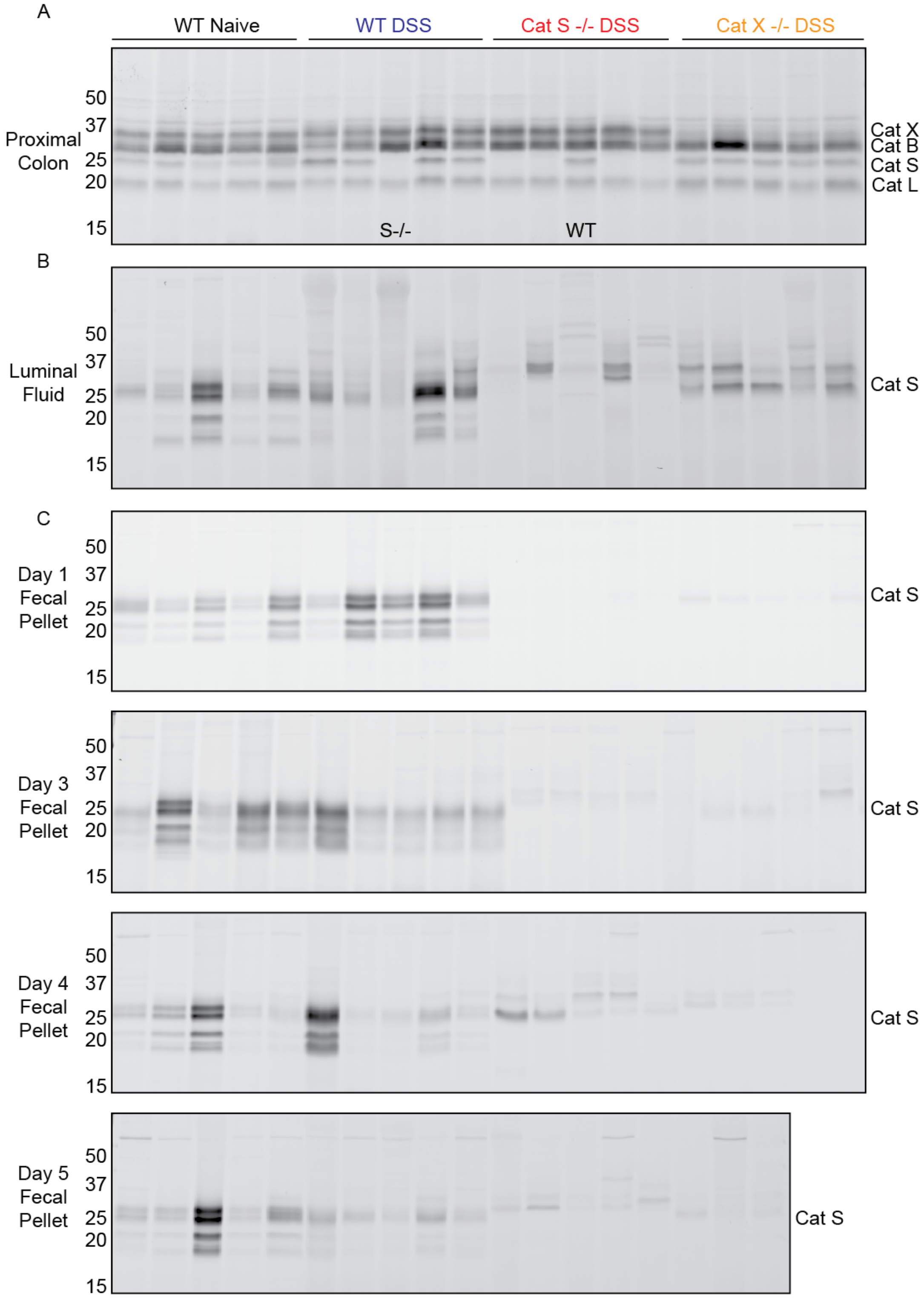

Figure 4. Cathepsin activation in wild-type and cathepsin S- or cathepsin X-deficient mice during experimental colitis. Proximal colons **(A)**, luminal fluids **(B)** or fecal pellets collected at day 1, 3, 4, or 5 **(C)** from wild-type or cathepsin S- or cathepsin X-deficient mice (naïve or DSS-treated) were labeled ex vivo with BMV109 followed by analysis of in-gel fluorescence. Gel quantification can be found in Figure S6 (n = 5). Note: these samples were collected from Canadian mice.

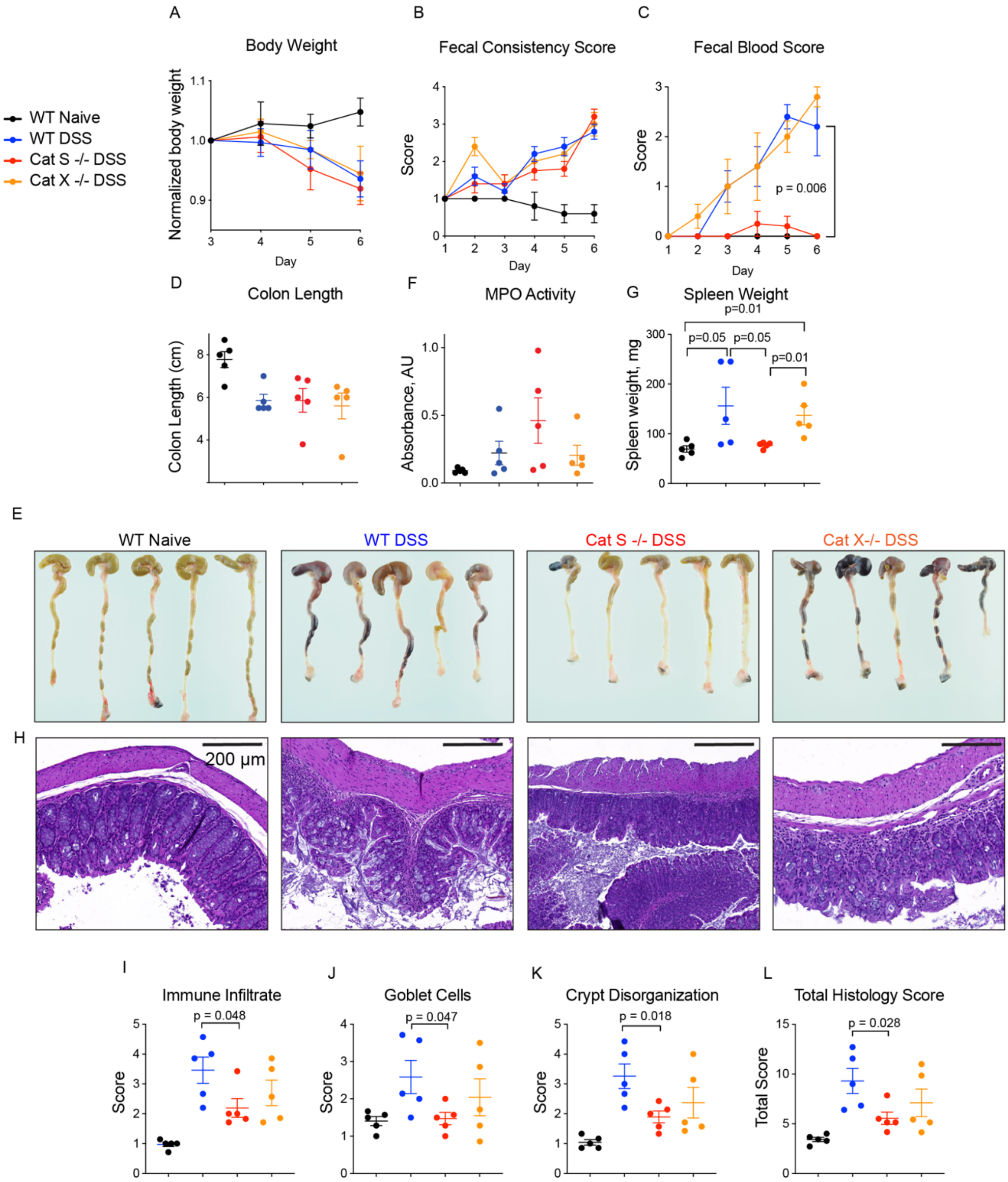

Figure 5. Cathepsin S-deficient mice have improved symptoms of colitis compared to wild-type mice. Naïve mice or mice treated with DSS (wild-type, cathepsin S- or cathepsin X-deficient) were monitored daily for symptoms of colitis, including weight loss **(A)**, fecal consistency **(B)** and fecal blood **(C)**. At end point, colons were excised, measured **(D)** photographed **(E)**, and assayed for myeloperoxidase (MPO) activity **(F)**. **G)** Spleens were weighed at endpoint. Data are represented as means ± SEM (n = 5). Note: these samples were collected from Canadian mice. **H)** Hematoxylin and eosin staining of colons from naïve or DSS-treated mice (wild-type or cathepsin S- or cathepsin X-deficient). Scoring the sections in **H)** for immune infiltrate **(I)**, goblet cells **(J)** or crypt disorganization **(K)** and their combination **(L)**. Data are represented as means ± SEM (n = 5). Note: these samples were collected from Canadian mice.

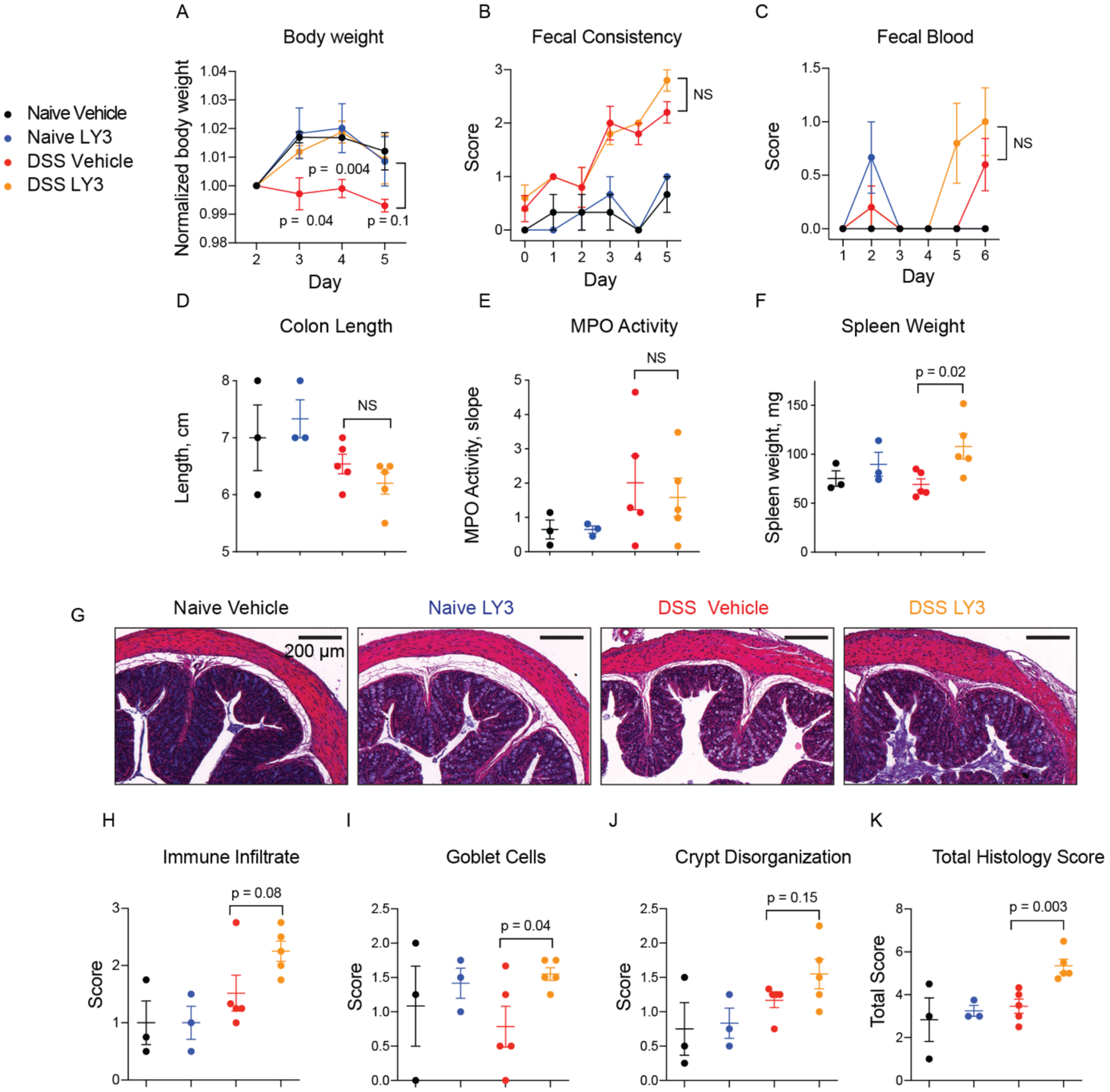

Figure 6. Pharmacological inhibition of cathepsin S exacerbates DSS-induced colitis. Naïve or DSS-treated mice were administered either vehicle or LY3000328 daily over the course of colitis induction. Mice were monitored daily for symptoms of colitis, including weight loss **(A)**, fecal consistency **(B)** and fecal blood **(C)**. At end point, colons were excised, measured **(D)** and assayed for myeloperoxidase (MPO) activity **(E)**. **F)** Spleens were weighed at endpoint. Data are represented as means ± SEM (n = 5). **G)** Hematoxylin and eosin staining of colons, which were scored for immune infiltrate **(H)**, goblet cells **(I)** crypt disorganization **(J)** or their combination **(K)**. Data are represented as means ± SEM (n = 5). Note: these samples were collected from Australian mice.

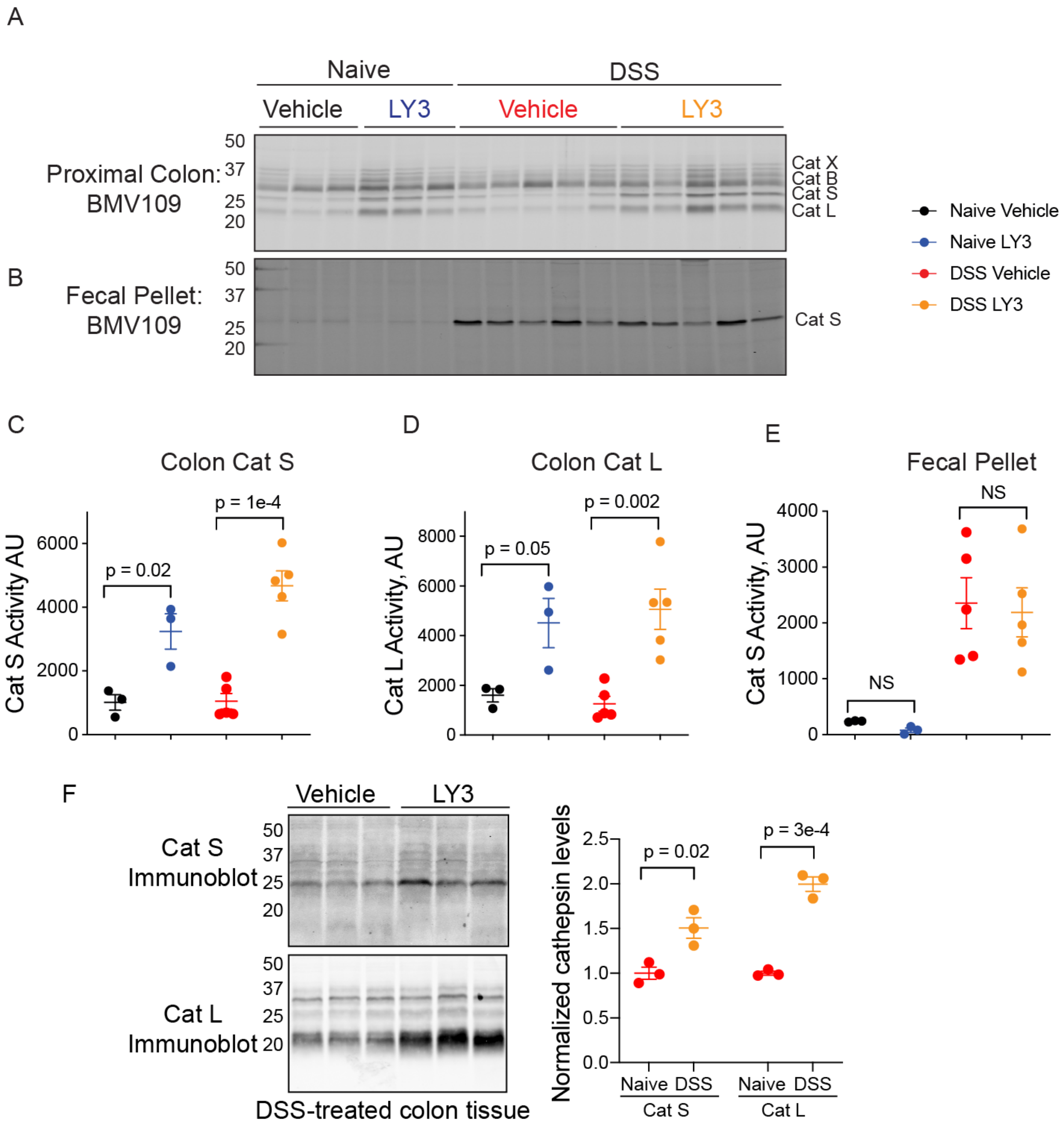

Figure 7. Pharmacological inhibition of cathepsin S exacerbates cathepsin S and L levels. Proximal colons (A) and fecal samples (B) from mice characterized in figure 7 were labeled with BMV109 ex vivo and analyzed by in-gel fluorescence. Densitometry of colon cathepsin S labeling (C), colon cathepsin L labeling (D) or fecal cathepsin S labeling (E). Data are represented as means ± SEM (n = 5). (F) DSS-treated colon tissue lysates from vehicle or LY3000328-treated mice were immunoblotted with antibodies for cathepsin S or cathepsin L and their levels were quantified by densitometry. Data are represented as means ± SEM (n = 3). Note: these samples were collected from Australian mice.

Pt #	Symptoms	Medications	Pathology	Endoscopy
2	none	none	normal tissue	none
3	none	none	normal tissue	none
4	none	none	normal tissue	none
5	flare-up, 15-20 bm/d	Steroids, biologic	chronic inflammation, severe activity	pancolitis, Mayo 3 distal, 2 proximal
6	flare-up, 10 bm/d	none	chronic inflammation, moderate to severe activity	pancolitis, Mayo 2
7	chronic active, 4 bm/d	none	chronic inflammation, mild activity	proctitis, Mayo 1
8	chronic active, 2-3 bm/d	5-ASA	chronic inflammation, marked activity	pancolitis, Mayo 3 distal, 2 proximal
9	new onset, 6-8 bm/d	none	chronic inflammation, moderate activity	pancolitis, Mayo 2
10	chronic active, 12bm/d*	Steroid enema, 5-ASA	chronic inflammation, mild activity	proctitis, Mayo 2
11	flare-up, 6-8 bm/d	Imuran	acute, chronic inflammation, deep ulcers	ileocolitis, deep ulcers
12	flare-up, 4-5bm/d	5-ASA	chronic inflammation, severe activity	colitis
13	flare-up, pain, +2bm/d	5-ASA	normal tissue; chronic stricture with no active inflammation	ileal stricture, blind biopsies
14	flare-up, 2-5bm/day	none	chronic inflammation, moderate activity	pancolitis, Mayo 1-2

5-ASA = 5 aminosalicylic acid; *= mucous, but infrequent stool; ** suspected flare up initially but with further imaging dx. with chronic stricture with no active inflammation; bm = bowel movement, most were bloody

Supplemental Table 1. Profiles of patients from which mucosal biopsies were collected.

Pt #	Symptoms	Medication	Pathology	Endoscopy
C1				
C5				
C6				
C2				
C3				
C4				
UC1				
UC3				
UC5				
CD1				
CD3				
CD5				
CD6				
CD7				

Supplemental Table 2. Profiles of patients from which mucosal biopsies were collected.

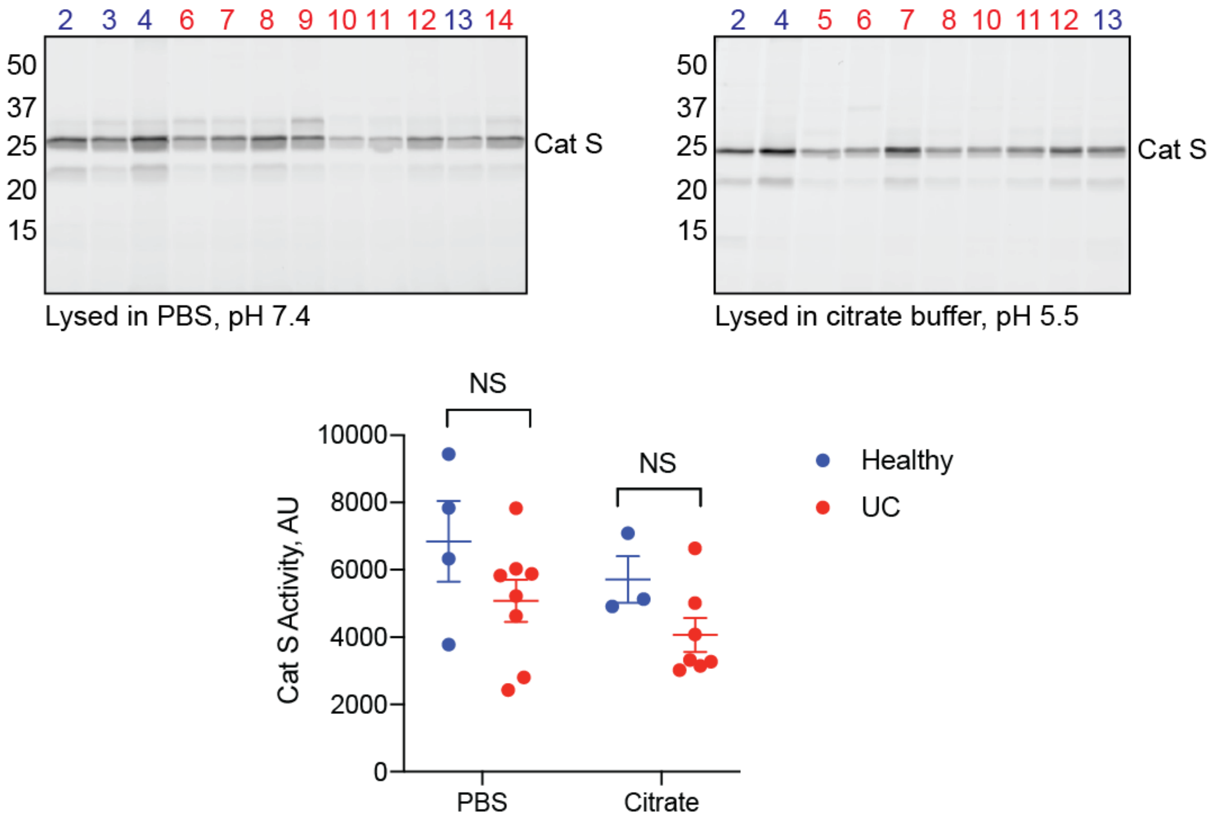

Figure S1. Cathepsin S activity in biopsies from healthy individuals and patients with ulcerative colitis is not significantly different. Mucosal biopsies were lysed in PBS, pH 7.4 (left) or citrate buffer, pH 5.5 (right), labeled with BMV157 and analyzed by in gel fluorescence. Cathepsin S labeling was quantified by densitometry. Data are represented as means ± SEM (n = 3-8).

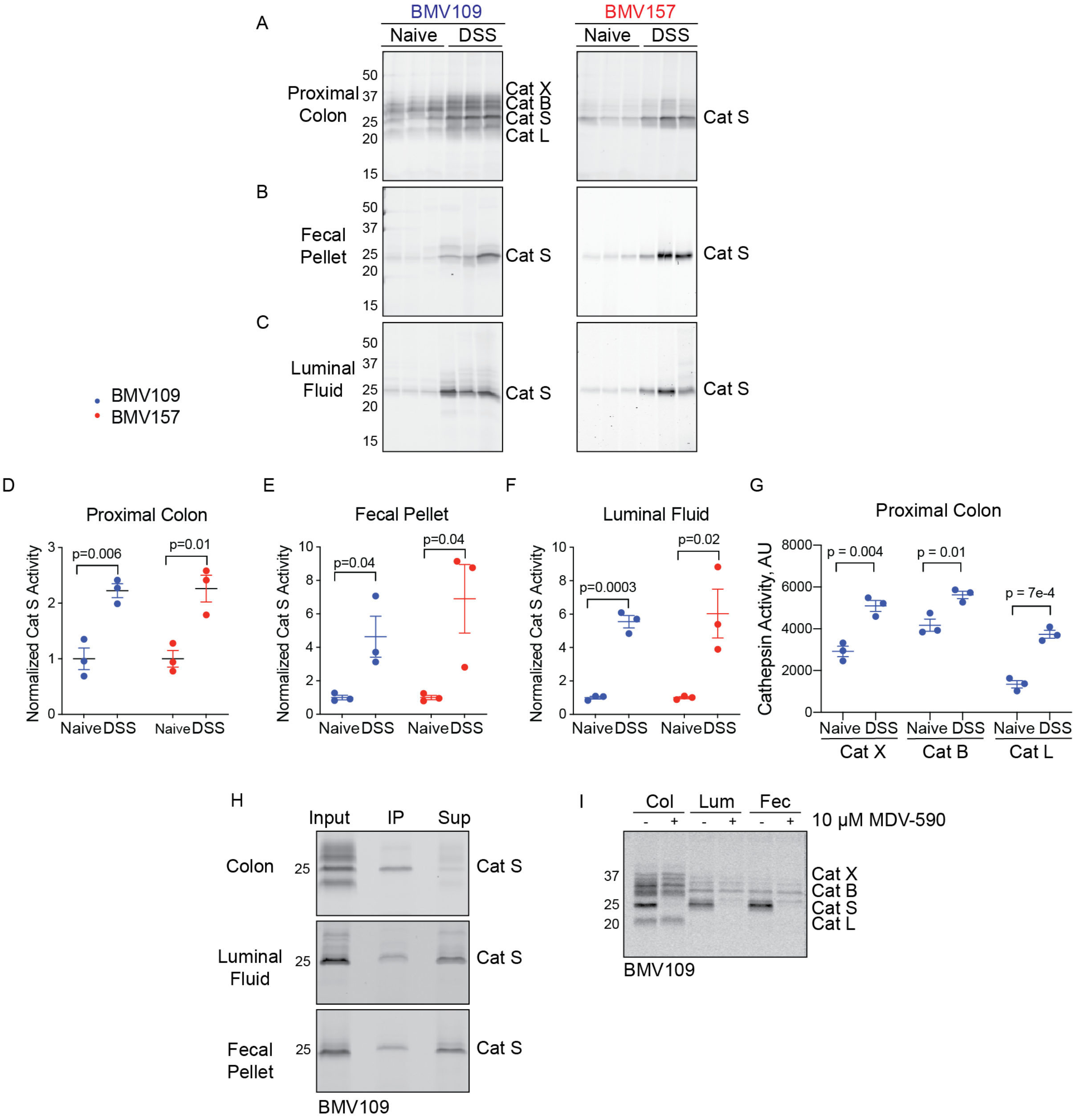

Figure S2. Cathepsin S secretion is increased during DSS-induced colitis. Lysates of proximal colons **(A)**, fecal pellets **(B)** and luminal fluids **(C)** from naïve and DSS-treated mice were labeled in vitro with BMV109 (left) or BMV157 (right) and analyzed for in-gel fluorescence. Densitometry of cathepsin S labeling by BMV109 (blue) and BMV157 (red) in proximal colon **(D)**, fecal pellets **(E)**, and luminal fluid **(F)**. **G)** Densitometry of cathepsin X, cathepsin B, and cathepsin L labeling in proximal colon lysates by BMV109. Data are represented as means ± SEM (n = 3). **H)** Immunoprecipitation of BMV109-labeled proximal colon lysates, luminal fluids and fecal supernatant with a cathepsin S-specific antibody. IP = immunoprecipitation, sup = supernatant. I) Colon lysate (col), luminal fluid (lum) or fecal supernatant (fec) were pre-treated with MDV-590 or vehicle followed by labeling with BMV109 to assess residual cathepsin activity by in-gel fluorescence. Note: these samples were collected from Australian mice.

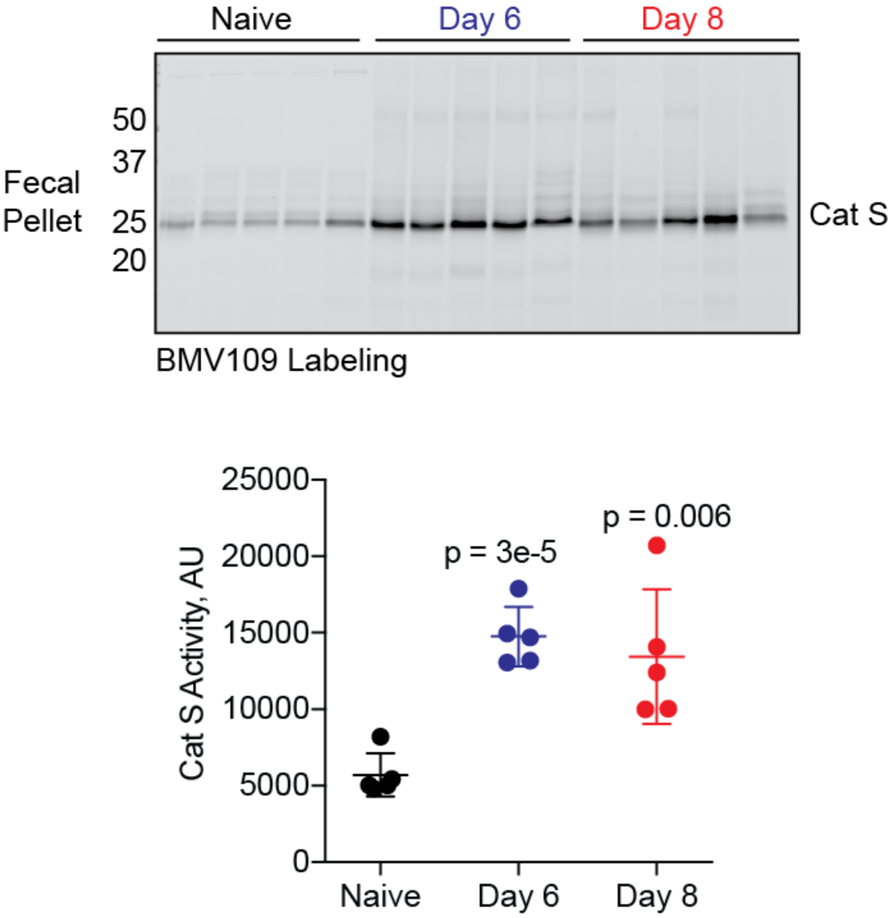

Figure S3. Fecal cathepsin S remains elevated after cessation of DSS. Mice were treated with DSS for 6 days and harvested immediately or after two additional days of normal drinking water. Fecal samples were labeled with BMV109 to measure cathepsin S activity by in-gel fluorescence and the labeling was quantified by densitometry. Data are represented as means ± SEM (n = 5). Note: these samples were collected from Australian mice.

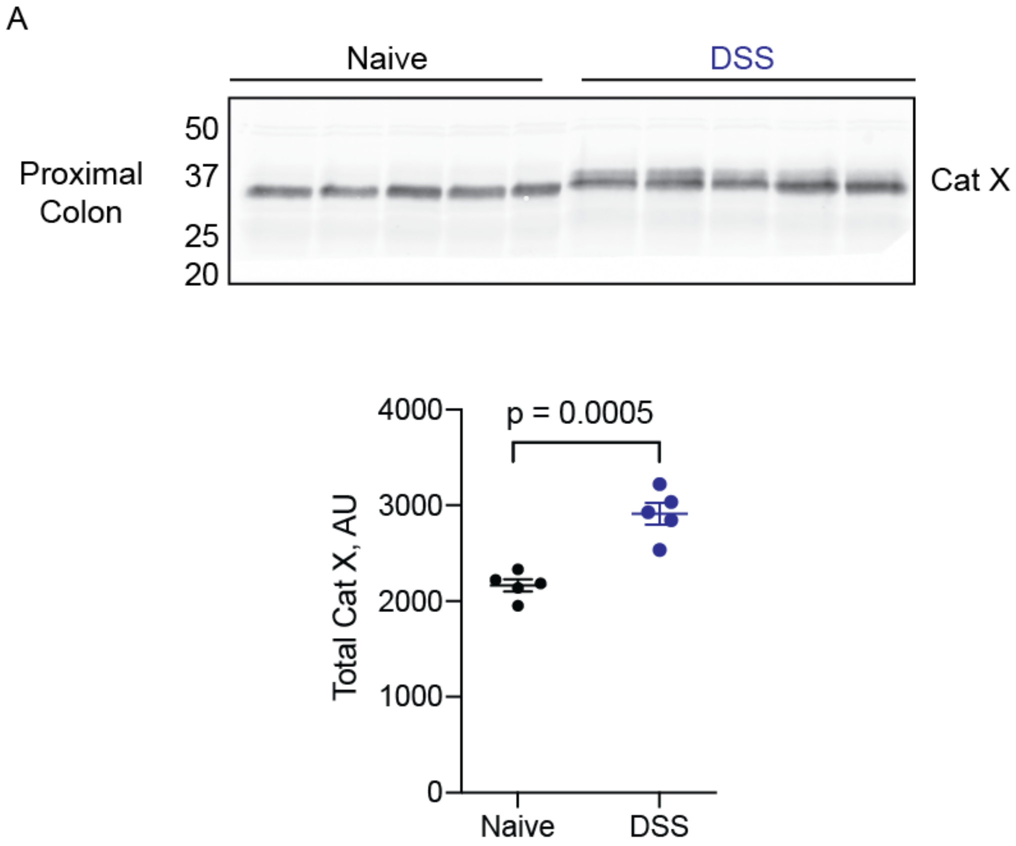

Figure S4. Cathepsin X expression is elevated after DSS treatment. Proximal colon tissues from naïve or DSS-treated mice were lysed and analyzed by immunblot with a cathepsin X-specific antibody. Bands were quantified by densitometry. Data are represented as means ± SEM (n = 5). Note: these samples were collected from Australian mice.

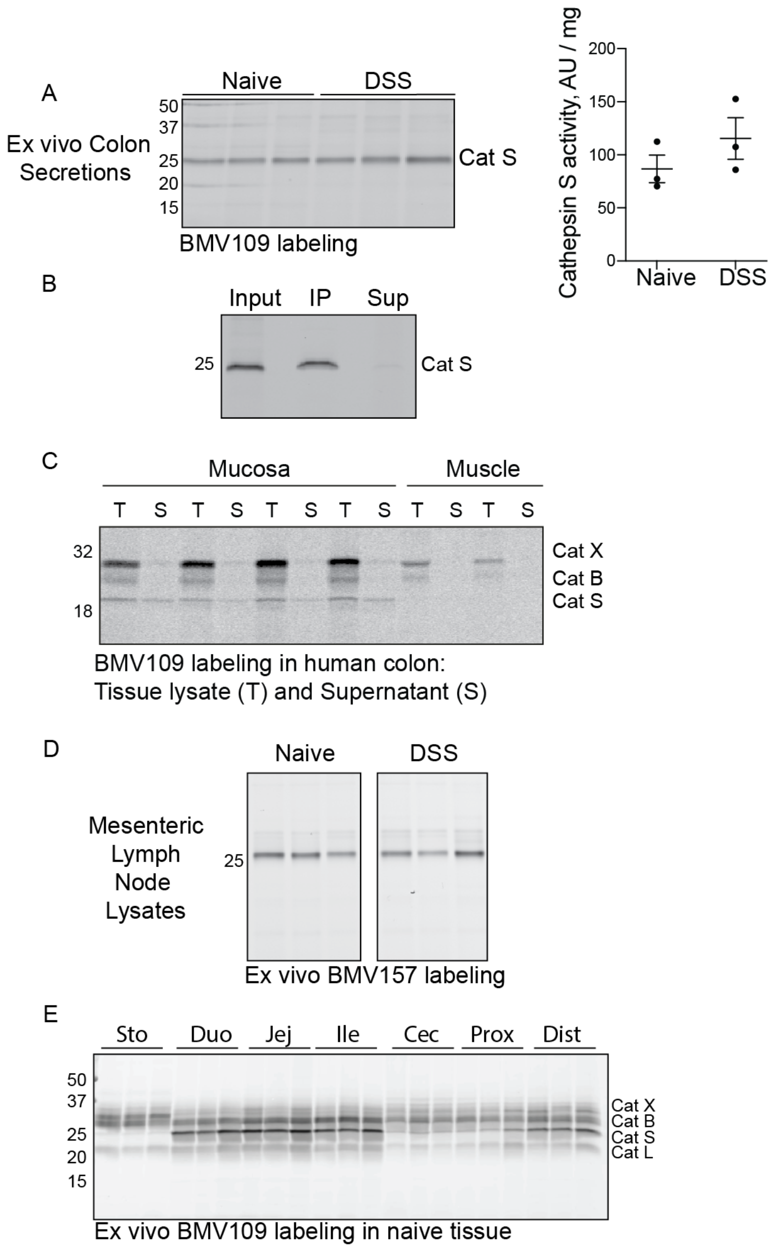

Figure S5. Cathepsin S is secreted from colon tissue. A) Proximal colon tissues from naïve or DSS-treated mice were incubated in media overnight. Supernatants were collected, labeled with BMV109 and analyzed by in-gel fluorescence. Labeling was quantified by densitometry and normalized to the weight of each tissue. Data are represented as means ± SEM (n = 3). **B)** Supernatants from A were subject to immunoprecipitation with a cathepsin S-specific antibody. IP = immunoprecipitation; Sup = supernatant. **C)** Resected human colon tissue was divided into mucosal and muscle layers and incubated in PBS for 5 h. Tissue (T) and supernatant (S) were collected, labeled with BMV109 and analyzed by in-gel fluorescence. 2-4 technical replicates are shown from one patient. **D)** Mesenteric lymph nodes from naïve or DSS-treated mice were lysed, labeled with BMV109 and analyzed by in-gel fluorescence (n=3). Note: these samples were collected from Australian mice. **E)** Tissues from the GI tract of naïve mice were labeled with BMV109 ex vivo and analyzed by in-gel fluorescence. Sto = stomach; Duo = duodenum; Jej = jejunum; Ile = ileum; cec = cecum; prox = proximal colon; dist = distal colon.

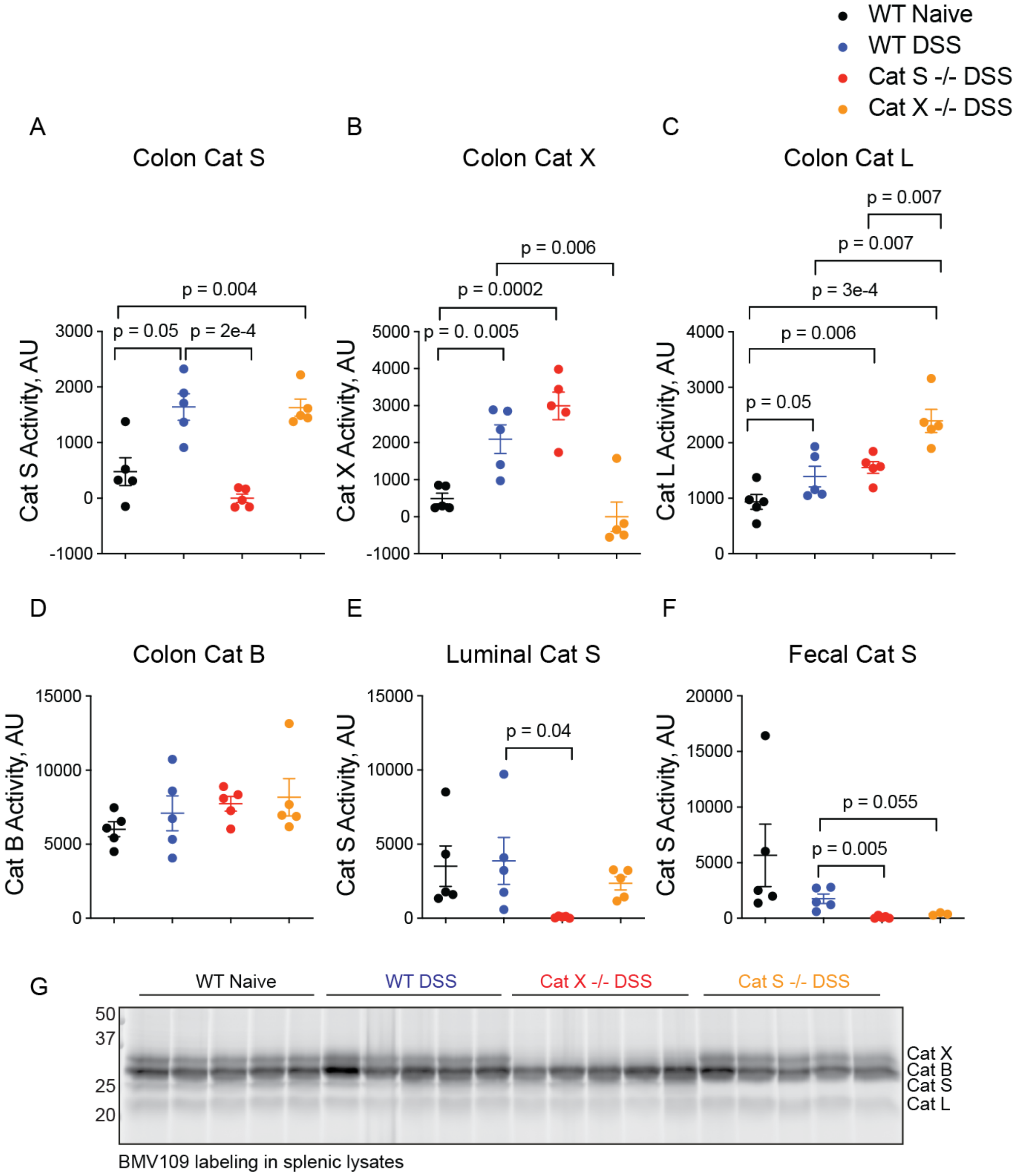

Figure S6. Quantification of cathepsin labeling in tissues from mice analyzed in Figure 5-6. Proximal colons, luminal fluids, and fecal pellets were collected from naïve or DSS-treated mice (wild-type or cathepsin S- or cathepsin X-deficient), labeled with BMV109 and analyzed by in-gel fluorescence. Labeling of cathepsin S, X, L, and B in colon tissue lysates was quantified by densitometry (A-D), as well as cathepsin S activity in luminal fluids (E) and fecal pellets (F). Data are represented as means ± SEM (n = 5). G) Spleens from the same mice were lysed, labeled ex vivo with BMV109, and analyzed by in-gel fluorescence. Note: these samples were collected from Canadian mice.

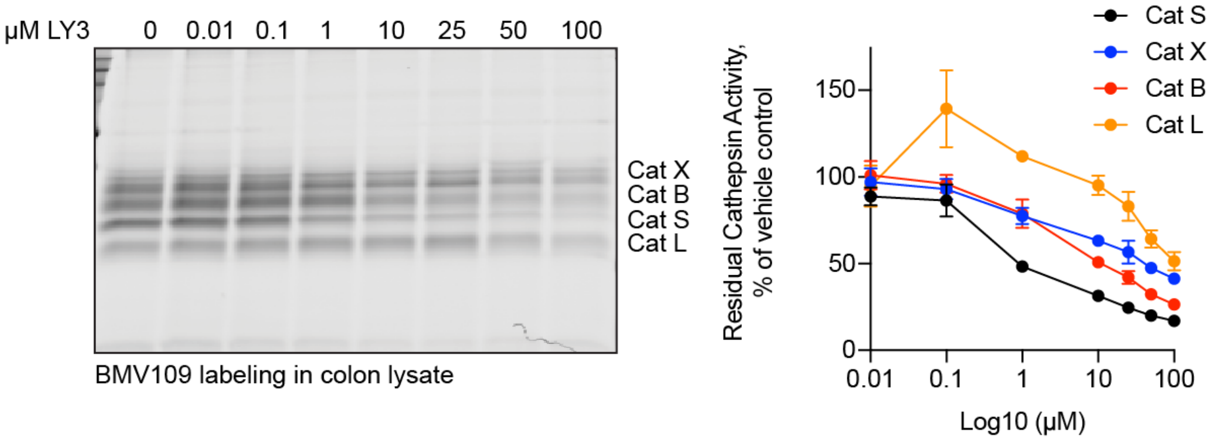

Figure S7. Inhibition of cysteine cathepsins by LY3000328. Colon lysates were pre-treated with the indicated concentration of LY3000328 for 30 minutes followed by 10 minute incubation with BMV109 to detect residual cathepsin activity. Labeling was detected by in-gel fluorescence and analyzed by densitometry. Data are represented as means ± SEM (n = 3).

A three-pronged mechanism of action underlies the prolonged analgesia mediated by lipid-anchored antagonists of the neurokinin 1 receptor

Quynh N. Mai[1,2, 3,4], Priyank Shenoy[1,3], Tim Quach[2], Jeffri Retamal-Santibanez[1,2,3], Holly R. Yeatman[1], Luigi Aurelio[1], Josh W. Conner[1, 3], Daniel P. Poole[1, 3], Meritxell Canals[4], Bimbil Graham[1], Stephen J. Briddon[4], Stephen J. Hill[4], Christopher J. Porter[2,3], Nigel W. Bunnett[1,3,4, 5], Michelle L. Halls[1,*], and Nicholas A. Veldhuis[1,3,*]

[1]Drug Discovery Biology Theme, [2]Drug Delivery, Disposition and Dynamics Theme and [3]Australian Research Council Centre of Excellence in Convergent Bio-Nano Science and Technology, Monash Institute of Pharmaceutical Sciences, Monash University, Parkville, VIC 3052, Australia;
[4]Division of Physiology, Pharmacology and Neuroscience, School of Life Sciences, The University of Nottingham Medical School, Nottingham, UK and Centre of Membrane Proteins and Receptors, Universities of Birmingham and Nottingham, the Midlands, U.K
[5]Department of Pharmacology and Therapeutics, University of Melbourne, Parkville, VIC 3010, Australia
[6]Department of Molecular Pathobiology, New York University College of Dentistry, New York, NY 10010, USA.
My affiliations are Monash, U Melb and NYU not Nottingham

Present addresses:
QNM: Cardiovascular Research Institute, Department of Biochemistry and Biophysics, University of California, San Francisco, CA 94158

*Corresponding authors: Nicholas A. Veldhuis (nicholas.veldhuis@monash.edu), Michelle L. Halls (michelle.halls@monash.edu), Nigel W. Bunnett (nwb2@nyu.edu)

Running title: Lipid conjugation for targeting endosomal GPCRs

Key words: Lipid-conjugation; drug delivery; tachykinin; endosome; endosomal signaling

---

ABSTRACT

G protein-coupled receptors (GPCRs) can continue to signal from endosomes to control important pathophysiological processes. Sustained endosomal signaling of the neurokinin 1 receptor (NK_1R) in spinal neurons mediates nociception. An NK_1R antagonist Spantide I conjugated to cholestanol (Span-Chol) accumulates in endosomes, inhibits endosomal NK_1R signaling, and causes prolonged anti-nocicpetion. Herein, we used fluorescent correlation spectroscopy and biosensors targeted to subcellular compartments to determine the long-term location and activity of lipid-anchored probes Not a drug!. The cholestanol-anchor increased in the local concentration of probe at the plasma membrane. This localized enrichment corresponded with an increase in NK_1R binding affinity over time, and increased potency for inhibition of NK_1R calcium signaling. Span-Chol, but not Span, caused a persistent (>4 h) decrease in NK_1R recruitment of β-arrestin and receptor internalization to early endosomes. Using targeted biosensors, we mapped the relative inhibition of NK_1R signaling as the receptor moved into the cell. Span selectively inhibited cell surface signaling whereas Span-Chol selectively inhibited endosomal signaling. In a preclinical model of pain, Span-Chol caused prolonged antinociception (>9h), which is attributable to increased local concentration at membranes, decreased NK_1R endocytosis, and inhibition of endosomal signaling. Identifying the mechanisms that contribute to the increased preclinical efficacy of lipid-anchored NK_1R antagonists is an important step toward understanding how we can effectively target intracellular GPCRs in disease.

G protein-coupled receptors (GPCRs) are tractable therapeutic targets because they have druggable sites on the cell surface and control most pathophysiological processes (1). However, many GPCRs can also signal from intracellular compartments, including endosomes, the Golgi, mitochondria and the nucleus (2-5). These intracellular signals dictate physiologically responses that are distinct from those that emanate from signaling at the plasma membrane (5-10). Drug discovery efforts typically target GPCRs at the cell surface, and as a consequence many drugs targeting GPCRs are not designed to cross the plasma membrane. This inability to effectively engage intracellular GPCRs might explain why some drugs with high efficacy in cell-based assays of plasma membrane signaling fail in clinical trials.

This could be the case for the GPCR for substance P (SP), the neurokinin 1 receptor (NK_1R), where multiple antagonists have failed in clinical trials of chronic neurological diseases, including pain (11-13). Activation of the NK_1R causes two spatially and temporally distinct rounds of signaling (Figure S1). At the cell surface, SP-bound NK_1R rapidly activates $G\alpha_q$ G proteins to increase Ca^{2+} mobilization, protein kinase C (PKC) activity and cAMP formation in the vicinity of the plasma membrane (5,14). The NK1R also transactivates the epidermal growth factor receptor (EGFR) to stimulate extracellular signal-regulated kinase (ERK) activity in the cytoplasm. These signals are all relatively short-lived (<15 min) (14). During this time, GPCR kinases rapidly phosphorylate the NK_1R leading to association with β-arrestins and receptor endocytosis to early endosomes (<2 min) (5). Within endosomes, the SP-NK_1R complex continues to signal via $G\alpha_q$- and β-arrestin-mediated mechanisms, causing increased PKC and cAMP in the cytosol and increased ERK within the nucleus (5,14). These signals from the endosomally localized receptor are longer-lived (>20 min). It is these sustained signals from the intracellular NK_1R that mediate persistent excitation of spinal neurons and central pain transmission (7,14,15).

Ligands can have spatially-specific, or ‘location biased’ pharmacological actions in cells (16). We have previously assessed the potential for drug delivery strategies to locally deliver NK_1R antagonists to endosomes. This includes pH-responsive nanoparticles that deliver and release the NK_1R antagonist aprepitant directly into endosomes (17), and lipid-anchored NK_1R antagonists that accumulate in endosomal membranes (5). Both of these approaches improved drug efficacy in preclinical models of pain (2-5-fold more effective analgesia, 2-4-fold longer duration of action compared to free drug) (5,17). The localized delivery of an NK_1R antagonist to endosomes using nanoparticles is a selective approach, that bypasses any effects on receptors at the cell surface. In contrast, lipid-anchored NK_1R antagonists first partition into the plasma membrane, before they are trafficked to endosomes. It is therefore possible that lipid-anchored antagonists also affect the signaling and trafficking of plasma membrane-localized NK_1R, in addition to their later antagonism of endosomal receptors. This dual antagonism – initial blockade of plasma membrane receptors during partitioning, and then prolonged blockade of the pathophysiologically relevant signal from endosomes – could enhance therapeutic efficacy.

In the current investigation, we used live cell imaging and biophysical approaches to assess NK_1R signaling and trafficking in subcellular compartments, in conjunction with behavioral assays of nociception to investigate the mechanisms by which lipid-anchored antagonists inhibit endosomal signaling. We observed that the lipid-anchor allows an initial enrichment of antagonist concentration at the plasma membrane, which correlates with an increased antagonist potency at proximal pathways (Ca^{2+} mobilization). The lipid-anchored antagonist also inhibits NK_1R-β-arrestin recruitment and NK_1R endocytosis. Over time, the lipid-anchored antagonist travels from the plasma membrane to early endosomes and late endosomes. This movement deeper into the endosomal network correlates with sustained inhibition of endosomal-selective NK_1R signaling pathways, including cytosolic cAMP and PKC activity (in addition to nuclear ERK). Consistent with this finding, the lipid-anchored antagonist has long-lasting anti-nociceptive actions in preclinical models of pain (>9 h). We find that lipid anchors increase the local membrane concentration of GPCR antagonists, cause inhibition of receptor trafficking from the plasma membrane, and prolonged inhibition of signaling from endosomes. This three-pronged mechanism allows lipid-anchored antagonists to very effectively target endosomal-derived signaling pathways of pathophysiological importance.

RESULTS

Lipid-anchors increase the available concentration of drug at the cell surface – Inspired by prior studies using lipid-drug conjugates (18,19), we previously synthesized a series of lipid-anchored probes comprising the sterol cholestanol as a lipid conjugate for anchoring a pharmacophore to membranes; a flexible polyethylene glycol linker (PEG4-PEG3-PEG4); and a cargo (5). For the cargo we used Cyanine 5 (Cy5) to generate a fluorescent reporter of lipid-anchor location (Cy5-Chol), or the NK_1R antagonist, Spantide I, to generate a lipid-anchored antagonist (Span-Chol) (Figure S2). We also generated control probes including a non-lipidated control fluorescent probe (ethyl-ester group, PEG linker, Cy5; Cy5-EE), and a lipid anchor control probe (cholestanol group, PEG linker, biotin; Chol).

Fluorescence correlation spectroscopy (FCS) enables measurement of the concentrations of fluorescent molecules within a defined volume (20). We used this approach to determine the concentration of Cy5 probes (Cy5-Chol or the control, Cy5-EE) in the extracellular fluid immediately above the plasma membrane and at increasing distances above the cell (30 μm - 200 μm). Consistent with our previous studies (5), brightfield and fluorescence confocal imaging confirmed that Cy5-Chol rapidly incorporated into the plasma membrane of HEK293 cells (Figure 1A), but Cy5-EE remained in extracellular fluid (Figure 1B). We then used FCS to quantify the concentration of Cy5 fluorescence at the membrane of cells incubated with a nominal concentration of probe (10 nM). The concentration of Cy5-Chol in the extracellular fluid at 5 μm above the plasma membrane was 23.8 ± 7.1 nM, which decreased more than 4-fold to 5.6 ± 1.4 nM at 30 μm (Figure 1C,E). In contrast, the measured concentration Cy5-EE was 6.5 ± 1.1 nM at 5 μm above the plasma membrane, which increased more than 3-fold to 21.8 ± 3.8 nM at 200 μm (Figure 1D,E). A comparison of probe concentrations at increasing distances (5 μm intervals) above the plasma membrane suggested that there was an enrichment of Cy5-Chol proximal to the plasma membrane, while the Cy5-EE reporter molecule could freely diffuse through the extracellular fluid (Figure 1E). Therefore, the addition of a lipid anchor results in an enhanced association of a probe with cell membranes. This creates a high local concentration of probe at the cell surface.

Lipid-anchoring increases the affinity and potency of an NK_1R antagonist - To determine whether the addition of a lipid anchor influences the affinity and potency of an NK_1R antagonist, we compared unconjugated ("free") Spantide I (Span) and Span-Chol. A high-content imaging competition binding assay was used to evaluate the capacity of these antagonists to disrupt binding of SP labelled with fluorescent tetramethylrhodamine (SP-TAMRA) to the NK_1R in HEK293 cells. Cells were analyzed using an established granularity algorithm to provide a measure of total cell binding (includes both cell surface and intracellular) (21,22). We assessed antagonist affinity at two times following probe addition: 30 min (where most Cy5-Chol is still at the plasma membrane) and 4 h (when Cy5-Chol has trafficked to early endosomes) (5).

To assess competition binding after 30 min, HEK-NK_1R cells were co-incubated with an EC_{50} concentration of SP-TAMRA (0.5 nM) and increasing concentrations of Span or Span-Chol for 30 min. The affinity of Span-Chol and Span for NK_1R were similar with pIC_{50} values of 6.28 ± 0.09 and 5.99 ± 0.13, respectively (Figure 2A-B). Therefore, peptide modification by attachment of a PEG_{12} linker and cholestanol anchor does not diminish the affinity of Spantide for the NK_1R.

To assess ligand binding after 4 h, HEK-NK_1R cells were pre-incubated with antagonist for 3.5 h, then with SP-TAMRA for a further 30 min (4 h total). The affinity of Span for the NK_1R was significantly reduced compared to that of Span-Chol (pIC_{50} 5.55 ± 0.17 vs 6.50 ± 0.12, p=0.0018, unpaired t-test) (Figure 2C). This suggests that the addition of a lipid anchor improves the kinetic properties of Spantide by sustaining its ability to compete SP-TAMRA at the NK_1R over a 4 h period. This could be due to access of the lipid anchored antagonist to the endosomal pool of NK_1R.

To determine if lipid conjugation influenced the potency of Spantide, we compared the ability of Span and Span-Chol to inhibit SP-stimulated Ca^{2+} signaling in HEK-NK_1R cells at different time points after addition. In initial experiments, HEK-NK_1R cells were pre-incubated with increasing concentrations of Span or Span-

Chol for 30 min, prior to challenge with an EC_{80} concentration of SP (1 nM). Ca^{2+} transients were measured for 90 s post-stimulation. Pre-incubation of cells with Span or Span-Chol caused a concentration-dependent inhibition of Ca^{2+} flux (Figure 2D). A comparison of pIC_{50} values for Span and Span-Chol (4.87 ± 0.33 and 6.25 ± 0.19, respectively) revealed a significant increase in the potency of the lipidated antagonist ($p=0.0112$). This is consistent with FCS experiments (Figure 1) and may be due to the lipid anchoring of the antagonist to the plasma membrane, thereby effectively increasing the local concentration of the antagonist near the receptor even at acute time periods (23,24).

While lipid anchored probes initially partition into the plasma membrane, they are then quickly trafficked into endosomal compartments (5). As such, the continuous removal of lipidated antagonists from the plasma membrane by constitutive endocytosis could affect the relative potency of Span-Chol compared to soluble Span over time. To assess this possibility, we compared continuous exposure to the antagonists for 4 h to a "pulsed" administration whereby the cells were pre-incubated with antagonist for 30 min, washed to remove any excess ligand, and then left at 37°C for 3.5 h (4 h total). In both protocols, cells were challenged with 1 nM SP 4 h after the initial antagonist addition. There was no change in the pIC_{50} of the antagonists when the cells were continuously incubated with Span or Span-Chol for 4 h (5.11 ± 0.76 and 6.36 ± 0.17, respectively) compared to the 30 min pre-incubation (Figure 2E-F). In contrast, after pulsed administration, only Span-Chol retained its ability to antagonize SP-stimulated Ca^{2+} signaling after 4 h (pIC_{50} 6.15 ± 0.11) (Figure 2F). This is likely due to the wash (after the initial 30 min incubation with antagonist) decreasing the available concentration of free Span in the extracellular fluid. In contrast, the potency of Span-Chol was not lost following the wash, confirming that lipidation causes an increased association of the antagonist with the cell membrane. Notably, the potency of Span-Chol was sustained over 4 h despite the increasing internalization of lipid-anchored probes over time (5). This could indicate a prolonged retention of the lipid anchored antagonist at the plasma membrane (in addition to internalization to the endosomal network). Overall, these data demonstrate that cholestanol conjugation can enhance the potency and affinity of antagonists by increasing their retention in the plasma membrane and therefore their effective local concentration.

A lipid-anchored antagonist decreases endocytosis of the activated NK_1R – Span-Chol has a high local concentration at the cell surface (Figure 1) and maintains antagonistic activity at cell surface receptors even after 4 h (Figure 2). It is therefore possible that lipidated antagonists continually act at the plasma membrane to inhibit SP-induced endocytosis of the NK_1R, which could contribute to their long-lasting therapeutic efficacy. To assess this possibility, we measured the proximity between NK_1R-RLuc8 and β-arrestin2-YFP, KRas-Venus (marker of the plasma membrane) or Rab5a-Venus (marker of early endosomes) in HEK293 cells using BRET. We compared the effectiveness of Span vs Span-Chol after short (30 min) or prolonged (4 h) incubation. In order to observe any differences between the antagonists that were due to the prolonged retention of Span-Chol at the cell surface, we used the "pulsed" incubation protocol: 30 min antagonist, wash, 3.5 h recovery (4 h total).

In control cells, SP induced an increase in NK_1R-RLuc8/β-arrestin2-YFP BRET, consistent with β-arrestin2 recruitment to NK_1R (Figure 3A-C). After 30 min pre-incubation, Span and Span-Chol (0.1, 1, or 10 μM) caused a concentration-dependent inhibition of SP-stimulated NK_1R-RLuc8/β-arrestin2-YFP BRET. After a pulsed 4 h pre-incubation with antagonists, Span had no effect on SP-stimulated NK_1R-RLuc8/β-arrestin2-YFP BRET at any tested concentration tested (Figure 3B,C). In contrast, Span-Chol inhibited SP-stimulated NK_1R-RLuc8/β-arrestin2-YFP BRET at the two highest concentrations of antagonist (1 and 10 μM).

Similar results were obtained when we measured the effect of Span or Span-Chol on the SP-stimulated change in BRET between NK_1R-RLuc8 and KRas-Venus (Figures 3D-F) or Rab5a-Venus (Figures 3G-I). In control cells, SP caused a decrease in BRET between NK_1R-RLuc8 and KRas-Venus (Figures 3D-F) which corresponded to an increase in BRET between NK_1R-RLuc8 and Rab5a-Venus (Figures 3G-I). This is consistent with receptor internalization from the plasma membrane (KRas) to early endosomes (Rab5a).

After a 30 min pre-incubation, both Span and Span-Chol inhibited the SP-stimulated change in BRET between NK_1R-RLuc8 and KRas-Venus (Figures 3D,F) or Rab5a-Venus (Figures 3G,I). However, after a pulsed 4 h pre-incubation, only Span-Chol inhibited the SP-stimulated change in BRET between NK_1R-RLuc8 and KRas-Venus (Figures 3E-F) or Rab5a-Venus (Figures 3H-I).

Since alterations in the composition of membrane lipids could artefactually affect BRET between transmembrane and associated proteins, we also studied the effects of a control cholestanol-PEG-biotin probe (Chol). There was no effect of any tested concentration of Chol (0.1, 1, 10 μM) on the SP-induced changes in BRET between NK_1R-RLuc8 and β-arrestin2-YFP, KRas-Venus or Rab5a-Venus (Figure S3).

Our results show that Span-Chol can antagonize the NK_1R at the plasma membrane to inhibit β-arrestin2 recruitment and receptor endocytosis. This effect is prolonged for up to 4 h, suggesting that some Span-Chol is retained at the plasma membrane despite significant movement of the lipid anchored antagonist into endosomes (5).

Lipid anchored probes traffic from the plasma membrane to endosomal compartments - We have previously demonstrated that the Cy5-Chol probe accumulates in early endosomes after continuous incubation with HEK293 cells for 4 h, as indicated by colocalization with Rab5a (5). However, we still observe effects of Span-Chol at the plasma membrane at this time point, and the distribution of lipid-anchored probes into other endosomal signaling compartments (i.e. late endosomes) has not been investigated. We therefore set out to map the intracellular distribution of Cy5-Chol over short and longer time scales (Figure 4).

HEK293 cells were infected with CellLight fluorescent fusion proteins resident to signaling endocytic compartments, including early endosomes (EE-RFP) and late endosomes (LE-GFP). The distribution of Cy5-Chol (1.5 μM) was examined in live cells by confocal microscopy. After a 30 min pre-incubation, Cy5-Chol fluorescence was readily observed at the plasma membrane, in early endosomes (EE-RFP) and late endosomes (LE-GFP) (Figure 4A). A much higher proportion of Cy5-Chol was observed at the plasma membrane, compared to intracellular compartments (Figure 4B). We then assessed distribution of Cy5-Chol after a pulsed incubation protocol (30 min incubation with Cy5-Chol, wash, 3.5 h recovery; 4 h total). We observed co-incident detection of Cy5-Chol with markers of early endosomes (EE-RFP) and late endosomes (LE-GFP) (Figure 4C). This correlated with a change in the overall distribution of Cy5-Chol in the cell, with similar fluorescence observed at the plasma membrane and within intracellular compartments (Figure 4D). To determine the long-term intracellular distribution of a lipidated probe, HEK293 cells were incubated with Cy5-Chol for 24 h (Figure 4E,F). After 24 h we still detected Cy5-Chol co-distribution with reporters for early endosomes (EE-RFP) and late endosomes (LE-GFP) (Figure 4E). However, the relative distribution of Cy5-Chol over the whole cell was enriched in intracellular compartments compared to the plasma membrane (Figure 4F).

Together, these data indicate that the internalized cholestanol-conjugated reporter resides within the endocytic pathway for sustained periods. Over time, the amount of Cy5-Chol at the plasma membrane decreases, which corresponds with a movement of Cy5-Chol further into the endosomal network. These findings support the use of sterol-based lipid anchors for targeting antagonists to populations of endosomal GPCRs.

Lipid-anchored antagonists cannot efficiently block plasma membrane NK_1R signaling – We then investigated in detail the capacity of Span versus Span-Chol to target NK_1R signaling in different cellular regions. Our previous analysis had focused only on ERK activity, showing selective inhibition of nuclear ERK by Span-Chol (versus Span) (5). This is because only endosomal NK_1R can increase nuclear ERK in response to SP (5). Here, we used an expanded toolbox of targeted FRET biosensors to follow the signaling of the NK_1R in live cells as the receptor moves from the plasma membrane to early endosomes.

At the cell surface, SP stimulation of NK_1R causes activation of short-lived $G\alpha_q$ signaling which is limited to the plasma membrane (5,14). NK_1R-$G\alpha_q$ stimulates phospholipase C (PLC)-dependent formation of inositol trisphosphate ($InsP_3$) and diacylglycerol (DAG). $InsP_3$ causes the release of Ca^{2+}, and then both DAG and Ca^{2+} activate protein kinase C (PKC). PKC can then activate adenylyl cyclase (AC) to increase cAMP (Figure S1).

We can measure changes in these transient signals from the NK_1R at the plasma membrane of live cells. In HEK293 cells transfected with HA-NK_1R and a PKC FRET biosensor (cytoCKAR), fast imaging shows a transient increase in PKC activity in response to SP, which declined to a steady state level by 30 sec following receptor stimulation (Figure 5A). In HEK293 cells transfected with HA-NK_1R and a plasma membrane cAMP FRET biosensor (pmEpac2), this transient PKC signal was followed by a slightly delayed but also transient increase in cAMP at the plasma membrane in response to SP. With a peak at ~5 min, the cAMP response declined towards baseline 15 min after receptor stimulation (Figure 5B). This high-resolution examination of localized signaling allowed us to assemble a timescale of events at the plasma membrane following NK_1R stimulation (Figure 5C). The activated receptor causes a fast peak of both Ca^{2+} and PKC in the first 30 sec, which overlaps the start of the transient cAMP and cytosolic ERK signals. The peak of cAMP and cytosolic ERK signaling coincides with a plateau in the recruitment of β-arrestins (2-5 min post receptor stimulation) (5). The cAMP and cytosolic ERK signals then decline back to baseline, which coincides with a plateau in the internalization of NK_1R to early endosomes (10-15 min post receptor activation) (5).

Using this time scale of events at the cell surface, we assessed the relative impact of Span versus Span-Chol on NK_1R signaling from the plasma membrane. We used a continuous incubation protocol for 4 h, so as not to wash away the free Span. This allows us to compare the spatial efficacy of both antagonists. A long pre-incubation of the cells with Span inhibited the fast peak of PKC activity in response to SP, but there was no effect of Span-Chol on this signal (Figures 5D-E, S4A-B). Similarly, a long pre-incubation of the cells with Span inhibited the SP-induced increase in cAMP at the plasma membrane, with no effect of pre-incubation with Span-Chol on this signal (Figures 5F-G, S4C-D).

These data suggest that Span-Chol is unable to affect the PKC and cAMP signals activated by the SP-stimulated NK_1R at the plasma membrane. In contrast, the free Span inhibits signaling of the plasma membrane-localized receptor.

Only a lipid-anchored antagonist can inhibit endosomal NK_1R signaling – Following NK_1R activation by SP, there is a rapid recruitment of β-arrestins and internalization of the receptor to early endosomes. Here, the NK_1R also co-localizes with $G\alpha_q$ and causes a sustained increase in PKC, cAMP and ERK (5) (Figure S1).

We can measure changes in these sustained signals from the NK_1R in endosomes of live cells. In HEK293 cells transfected with the HA-NK_1R and cytoCKAR, longer interval high content imaging showed a sustained increase in PKC activity by 1 min, which was maintained over a 20 min measurement period. (Figure 6A). Similarly, in HEK293 cells transfected with HA-NK_1R and a cytosolic cAMP FRET biosensor (cytoEpac2), we observed a prolonged increase in cAMP which peaks by 2 min and was sustained over the 20 min (Figure 6B). This high-resolution examination of localized signaling allowed us to assemble a timescale of events at early endosomes following NK_1R stimulation (Figure 6C). The activated NK1R rapidly traffics to early endosomes that also contain $G\alpha_q$ (as early as 1 min post receptor stimulation) (5). This allows a rapid and sustained increase in PKC and cAMP over very similar timescales. The sustained increase in nuclear ERK mediated by the endosomal NK_1R is slightly delayed (peaks ~10 min post receptor stimulation) (5).

Using this intracellular time scale of events, we assessed the relative impact of Span versus Span-Chol on NK_1R signaling from early endosomes. We used a continuous incubation protocol for 4 h, so as not to wash away the free Span. This allowed us to compare the spatial efficacy of both antagonists. A long pre-incubation of the cells with Span had no effect on the SP-induced increase in PKC or cAMP (Figures 6D-E, S4E-H). In contrast, pre-incubation with Span-Chol inhibited SP-induced PKC and cAMP signaling (Figures 6F-G, S4E-H).

Given the clear time distinction between the two PKC events stimulated by the plasma membrane versus endosomal NK_1R, we can visualize the changing spatial efficacies of the two antagonists (Figure 6H, S4I). Under control conditions, SP causes an initial peak in PKC activity from the plasma membrane NK_1R, and then a steady increase in PKC activity from endosomes. A long pre-incubation with Span inhibits the PKC signal from cell surface NK_1R but has no effect on the PKC signals activated by the endosomal NK_1R. In contrast, long pre-incubation with Span-Chol has no effect on the initial PKC signal from the activated cell surface NK_1R, but selectively inhibits signals from the endosomal NK_1R.

These data suggest that Span-Chol selectively inhibits the PKC and cAMP signals activated by the SP-stimulated NK_1R from endosomes. In contrast, free Span is unable to block the intracellular NK_1R.

The three-pronged mechanism of action of Span-Chol contributes to its long-lasting antinociceptive actions – We have previously demonstrated that blockade of endosomal (compared to plasma membrane) NK_1R causes much more effective analgesia (5,17). In pre-clinical models of pain, the analgesic effect of Span-Chol was maintained for up to 6 h (5). However, it is unknown for how long this analgesic effect is sustained. We recently examined the analgesic effect of directly delivering an NK_1R antagonist (aprepitant) to endosomes over a 24 h period, and found that analgesia was maintained for 6 h, before dropping back to baseline (17).

The three-pronged mechanism of Span-Chol identified in this study (higher local concentration at membranes, decreased receptor internalization, sustained inhibition of endosomal signaling) suggests that Span-Chol could lead to more prolonged pain relief. To evaluate this possibility, Span, Span-Chol or controls were administered by intrathecal injection to three different groups of mice (Figure 7A). Each group received an injection of capsaicin into the plantar surface of the left hindpaw at different times after intrathecal administration of the antagonists (i.e. capsaicin injected 3 h, 6 h or 12 h after antagonist administration). Mechanical nociception was evaluated by measurement of paw withdrawal responses to stimulation of the plantar surface with calibrated von Frey filaments every h for 4 h after administration of capsaicin. As mechanical nociception to capsaicin was measured over exactly the same time period for all groups (4 h), this allowed us to build a time scale of the analgesic effect of Span-Chol over a cumulative 16 h period (Figure 7).

In control mice receiving intrathecal vehicle, capsaicin caused a prolonged allodynia over 4 h (Figure 7B-D). Neither free Span nor the Chol control had any effect at any time tested. In contrast, Span-Chol had a marked anti-nociceptive action that was already present at 4 h post intrathecal injection and was fully maintained for 9 h after intrathecal injection. Thus, intrathecal delivery of Span-Chol resulted in a significant increase in the duration of anti-nociception.

DISCUSSION

The NK_1R is expressed throughout the nervous, immune, digestive, respiratory and urogenital systems, where it is regulates pain, inflammation, motility and secretion (25-30). In the context of pain, noxious stimuli evoke the release of SP from peripheral and central projections of primary afferent neurons. In the dorsal horn of the spinal cord, SP then activates the NK_1R on second order spinal neurons to mediate pain transmission (25). Despite this clear role in pain transmission, there has been limited clinical success for drug discovery programs targeting the NK_1R for chronic pain (25,31). Previously, we reported that pain transmission is dependent on sustained signaling from the NK_1R internalized to endosomes, and that we could improve analgesic effect and duration in a pre-clinical model of pain by specifically blocking endosomal (and not cell surface) NK_1R (5,17). Here, in addition to blockade of endosomal NK_1R, we have identified two further effects of a lipid-anchored NK_1R antagonist, that contribute to its increased efficacy. First, we find that the addition of a lipid anchor causes a 4-fold increase in the local concentration of a probe directly above the cell membrane. Second, although the probe quickly internalizes, X% of the lipid-anchored probe remains at the plasma membrane even 24 h after administration. This residual plasma membrane localization facilitates an inhibition of NK_1R trafficking to endosomes. Together, this three-pronged mechanism – increased local concentration, inhibition of NK_1R trafficking to endosomes, and sustained blockade of endosomal signaling – all contribute to the prolonged analgesic effects of lipidated antagonists in pre-clinical models of pain.

Cholestanol has a high affinity for sterol-rich microdomains of the outer leaflet of lipid bilayers. The binding of cholestanol to the sterol-rich microdomains then promotes internalization into endosomal compartments (32). The use of cholestanol to target a drug to endosomes was used for an inhibitor of the recycling endopeptidase, β-site amyloid precursor protein cleaving enzyme 1 (BACE-1), which localizes to early endosomes (33). A lipid conjugated, but not a free antagonist, inhibited the cleavage of amyloid precursor protein at the BACE-1 ectodomain, a rate limiting step in the production of the β-amyloid peptide. We subsequently used this approach to target an NK_1R antagonist to endosomes, and we observed selective and prolonged inhibition of endosomal NK_1R signaling, with no effect on signaling from the plasma membrane-localized receptor (5). However, we now find that the effects of a cholestanol-conjugated NK_1R antagonist are not limited to blockade of endosomal signaling. In addition to delivery to endosomes, we found that cholestanol-conjugation causes a prolonged increase in the partitioning of the cargo into the plasma membrane. Increasing the lipophilic properties of soluble drugs, such as GPCR antagonists, can increase their association with membranes and may therefore enhance their local potency (23,34). Here we found that the addition of cholestanol caused ~4-fold increase in the concentration of Cy5 directly above the plasma membrane when we measured Cy5-Chol compared to Cy5-EE concentrations using FCS. Interestingly, a previous study reported a 2-fold local enrichment of GPCR ligand concentration at the surface of cells transfected with the target GPCR, compared to non-transfected cells (35). This increase in local concentration was achieved without any change in the lipophilic properties of the ligand itself. As such, we would expect the local concentration of a lipid-anchored GPCR ligand to be *at least* 4-fold higher at the surface of target cells. Consistent this this, we observed a corresponding increase in the potency and affinity of Span-Chol as compared to Span. This suggests that the blockade of endosomal signaling of the NK_1R by Span-Chol is not only due to its spatial distribution but could also be influenced by a high local concentration of Span-Chol at endosomal membranes.

Given the inherent ability of cholestanol-conjugation to cause a prolonged increase in partitioning into membranes, it is important to map where the probes travel in cells. After initial incorporation into the plasma membrane, cholestanol probes translocate from the plasma membrane to endosomes. Within endosomes, cholestanol-conjugated antagonists inhibit the endosomal signaling of the NK_1R that underlies persistent excitation of spinal neurons and pain transmission (5). Consistent with our previous study, we find that Cy5-Chol is rapidly internalized into the endosomal network where it is co-distributed with early and late endosomes. Despite this large movement of the Cy5-Chol into the cell, after 24 h some of the probe remains at the plasma membrane. This persistent partitioning of Cy5-Chol into the plasma membrane led us to look for an effect of Span-Chol on NK_1R endocytosis. BRET receptor trafficking studies revealed that up to 4 h after a pulse administration of Span-Chol, the lipid-anchored antagonist could inhibit receptor trafficking by blocking the recruitment of β-arrestins, and therefore subsequent receptor internalization to early endosomes. This inhibition of receptor movement into endosomes will contribute to the overall decrease in endosomal signaling.

Despite plasma membrane Span-Chol decreasing NK_1R recruitment of β-arrestins and receptor internalization, signaling of the plasma membrane localized NK_1R appears largely unaffected. Using an expanded toolbox of targeted FRET biosensors we have mapped the signaling of the NK_1R as it traffics from the plasma membrane to endosomes. After 4 h continuous administration, we find Span only blocks signaling from the plasma membrane localized NK_1R. In contrast, Span-Chol only blocks signaling from the endosomal NK_1R. It is interesting that Span-Chol appears to block NK_1R internalization but not signaling from the plasma membrane. GPCRs are highly flexible proteins that fluctuate between many different conformational states (36,37). They may adopt different conformations at the plasma membrane versus in endosomes due large differences in the curvature of the two membranes, the composition of the associated membrane lipids, and allosteric effects of associations with receptor signaling complexes (37-43). This could effectively facilitate slightly different binding orientations for Span-Chol in the two locations. Alternatively, the enclosed and small volume of an endosome could effectively result in a much higher local concentration of the antagonist compared to the open and large volume of the extracellular space. The end result is that Span-Chol is apparently more effective at inhibiting receptor internalization than signaling. Signaling, in contrast to receptor internalization, is typically a highly amplified event. The recruitment of β-arrestins to a receptor and subsequent β-arrestin-mediated internalization, is generally considered a low amplification event (44). In contrast, a single GPCR can activate multiple G proteins, which in turn switch on (or off) kinases or enzymes. For example, it is estimated that a single photon of light hitting a GPCR can activate between 16-60 G proteins which activates phosphodiesterases to hydrolyze 2,000-72,000 molecules of cGMP (45). Small differences in the local concentration of Span-Chol or even its binding orientation could therefore have dramatic effects on receptor trafficking without seeming to affect receptor signaling at the plasma membrane.

The inhibition of endosomal NK_1R signaling by Span-Chol occurs via a three-pronged mechanism: increased local concentration of the antagonist at membranes, decreased NK_1R trafficking to endosomes, and inhibition of NK_1R signaling from endosomes. We previously showed that Span-Chol could inhibit sustained pain transmission for up to 6 h following administration in pre-clinical models (5). Here we extended this analysis to show that Span-Chol remains analgesic for >9 h following administration. This study demonstrates that lipidation is a viable approach, not only for enhancing membrane affinity of soluble GPCR antagonists, but also for selectively targeting compartmentalized NK_1R signaling pathways of pathophysiological importance. Furthermore, this novel approach improves the pharmacological properties of an otherwise low potency NK_1R antagonist for the selective inhibition of signaling events associated with central pain transmission.

One explanation for the failure of previous drug discovery programs targeting the NK_1R for chronic pain, is that they have only targeted plasma membrane localized NK_1R. Until very recently, GPCRs were only considered to be active at the cell surface, and therefore most drugs targeting GPCRs are not required to cross the plasma membrane. There is now clear evidence to show that activation of receptors in endosomes (compared to the cell surface) encodes for distinct physiological outcomes (5,8,46-49). It is therefore important to consider the subcellular location of a target GPCR, and whether they reside in or are delivered to a particular location. For example, the β_1-adrenoceptor is localized to two distinct pools in cells, one at the cell surface, and a second at the Golgi (16). Golgi-localized signaling of the β_1-adrenoceptor requires a pre-existing pool of receptors (i.e. they are not delivered to the Golgi following internalization from the cell surface). In this case, as these two receptor populations are distinct, a targeting strategy involving direct delivery would be better suited than one that also facilitates inhibition of cell surface receptor endocytosis. In contrast, the two NK_1R receptor pools at the cell surface and endosomes are linked by receptor internalization. As such, blockade of the endosomal pool is enhanced by preventing movement of the pool at the cell surface into the endosomal network. This could explain the prolonged analgesic activity of a lipidated-NK_1R antagonists versus an antagonist directly delivered to endosomes (5,17) (Figure 7).

Whether preventing NK_1R internalization (in addition to inhibition of endosomal NK_1R signaling) would be of benefit in situations of chronic pain is uncertain. In patients suffering from chronic visceral pain, the NK_1R is no longer available at the cell surface, but is instead found principally within intracellular compartments (31). In this case, as for the Golgi-localized β_1-adrenoceptor, there may be no added benefit of blocking receptor internalization from the cell surface. Future studies will need to directly compare different methods of endosomal drug delivery and their resulting efficacy in a variety of disease models. Identifying additional mechanisms that contribute to the increased preclinical efficacy of lipid-anchored NK_1R antagonists is an important step toward understanding how we can effectively target intracellular GPCRs in disease.

EXPERIMENTAL PROCEDURES

Probes – The tripartite probes Span-Chol, Cy5-Chol and Cy5-EE were synthesized as described previously (5). Tetramethylrhodamine (TAMRA)-labeled SP (TAMRA-SP) was synthesized by GL Biochem (Shangai, China).

cDNAs - Rat NK_1R-GFP, HA-NK_1R and NK_1R-RLuc8 have been described (14,50). SNAP-NK_1R was from Cisbio. CytoCKAR (Addgene plasmid

14870) was from A. Newton (51). CytoEpac2-camps was from M. Lohse (University of Wurzburg, Germany) (9) and pmEpac2-camps was from D. Cooper (University of Cambridge, UK) (52). KRas-Venus (53) and Rab5a-Venus (54) were from N. Lambert. β-arrestin 2-YFP was from M. Caron (University of North Carolina).

Cell culture and transfection – HEK293 cells (ATCC, negative for mycoplasma contamination) were maintained in Dulbecco's modified Eagle's medium (DMEM) supplemented with 5% (v/v) FBS. HEK293 cells were transfected using linear polyethyleneimine. HEK293-FlpIn cells stably expressing rat HA-NK_1R (HEK-NK_1R) and SNAP-NK_1R (HEK-SNAP-NK_1R) have been described (5,15). HEK-NK_1R and HEK-SNAP-NK_1R cells were maintained in DMEM supplemented with 10% (v/v) FBS and 100 μg/mL Hygromycin B. All assay dishes and plates were coated with poly-D-lysine (5 $\mu g/cm^2$).

Fluorescence Correlation Spectroscopy (FCS) - FCS measurements were made using a Zeiss LSM510Meta ConfoCor 3 microscope fitted with a c-Apochromat 40x NA 1.2 water immersion objective lens (55). Prior to each experiment, the system was calibrated for the 633 nm laser line. Cy5 NHS ester (GE healthcare, Buckingham, UK) was used to calibrate the 633 nm detection volume using a literature value for diffusion coefficient (D) of $3.16x10^{-10}$ m^2/s, as described (35,55).

HEK-NK_1R-SNAP were plated on Nunc Lab-Tek 8-well coverglass (SLS, Nottingham, UK). After 24 h, Cy5-Chol and Cy5-EE were prepared in HBSS and cells were incubated with a 10 nM solution of each ligand for 10 min at 37ºC in a final volume of 400 µL. A reference confocal image of each cell was captured, before positioning the FCS detection volume in x-y using a live confocal image. A fluorescence intensity scan in the z direction was used to determine the position of the plasma membrane and the focal point was positioned at defined distances above this point using the microscope's harmonic z-drive. FCS fluctuations were recorded at each point (ex λ: 633 nm HeNe, em λ: LP650 nm filter) for 20 sec, at a laser power of 60% with 10% AOTF dampening applied (~1 kW/cm^2).

Probe dwell times and particle numbers were obtained from subsequent autocorrelation analysis of the fluctuations, performed with a 1 component, 3D Brownian model fit incorporating a triplet state pre-exponential using Zeiss 2010 Black software (35). Probe concentration and diffusion coefficients were calculated from measurements of dwell time and particle number, respectively, using the dimensions of the detection volume calculated from the Cy5 calibration data.

High content fluorescent competition binding - HEK-NK_1R cells in black optically-clear 96 well plates were grown to 80% confluency. Cells were pre-treated at 37°C with increasing concentrations of Span or Span-Chol for the indicated times, followed by an EC_{50} concentration (0.5 nM) of SP-TAMRA. Total binding was determined by pre-incubation with a vehicle control (0.1% v/v DMSO). Cell nuclei were stained with Hoechst 33342 (1 µg/mL, 30 min, 37°C). Images were acquired using an ImageXpress Ultra confocal high-content plate reader (Molecular Devices, Sunnyvale, CA, USA) with Fluor 40x NA0.6 objective. Cells were imaged using the 405 and 561 laser excitations for Hoechst and TAMRA, respectively. The experiment was performed in triplicate with four fields of view imaged per well. Images were analyzed with MetaXpress 2.0 software (Molecular Devices), using an automated granularity module with the granule range set to 5-10 µm and intensity thresholds for granule classification set for each experiment based on the positive and negative controls (i.e. total and non-specific binding). A nuclear count from the Hoechst 33342 image was obtained and the granularity analysis calculated the average intensity per cell, as previously described (21,56). Data were fit with a competitive binding, one site, fit $logIC_{50}$ model.

Confocal imaging - To identify endosomal compartments, HEK293 cells were transduced with fluorescent fusion proteins using CellLight BacMam 2.0 virus (Life Technologies) for 16 h. CellLight fusion proteins used were as follows: early endosome-RFP, late endosome-GFP. Cells were equilibrated in Hanks' Balanced Salt Solution (HBSS) for 30 min prior to imaging.

Images were obtained using a Leica TCS SP8 Laser-scanning confocal microscope with HCX PL APO 40x (NA 1.30) and HCX PL APO 63x (NA 1.40) oil objectives in a humidified and temperature-controlled chamber at 37°C. For each cell, three baseline images were captured (4-6 optical sections) before addition of Cy5-Chol (1.5 µM). Cells were imaged at different time points following probe addition, as indicated.

Imaging was performed on at least 3 different days with separate drug preparations. Line scan intensity was processed using the FIJI distribution of Image J (57). The proportion of Cy5 fluorescence at the plasma membrane compared to the rest of the cell was calculated by XXX

Measurement of intracellular Ca^{2+} - HEK-NK_1R cells in 96-well plates were washed with calcium buffer (10 mM HEPES, 0.5% w/v BSA, 10 mM D-glucose, 2.2 mM $CaCl_2$ 1.18 mM $MgCl_2$, 2.6 mM KCl, 150 mM NaCl, 4 mM probenecid, 0.05% v/v pluronic acid F127; pH 7.4) then loaded with 1 µM Fura-2 AM ester (Life Technologies) in calcium buffer for 45 min at 37°C. For short antagonist pre-incubation, increasing concentrations of Span or Span-Chol were incubated with the cells for 30 min during Fura-2 AM loading. For long antagonist pre-incubation, cells were incubated with increasing concentrations of Span or Span-Chol for the indicated time periods prior to Fura-2 AM loading.

Calcium was measuring using a FlexStation 3 plate reader (Molecular Devices). Fluorescence (excitation: 340 nm and 380 nm; emission: 520 nm) was measured at 4 s intervals for a total of 45 s. After establishing baseline fluorescence, cells were stimulated with vehicle, 1 nM SP or 1 µM ionomycin (to obtain a maximal response). SoftMax Pro (v5.4.4) software was used to calculate the area under the curve from the kinetic data from at least 4 experiments performed in duplicate.

Receptor trafficking using BRET – HEK293 cells in 10 cm dishes were co-transfected with 1 µg of NK_1R-RLuc8 and 4 µg β-arrestin 2-YFP, KRas-Venus or Rab5a-Venus. After 24 h, cells were re-plated in 96-well white opaque CulturPlates (PerkinElmer). 48 h after transfection, cells were pre-treated with antagonists. For short pre-incubations, cells were incubated with increasing concentrations of Span, Span-Chol or Chol in HBSS for 30 min. For "pulsed" long pre-incubations, cells were incubated with increasing concentrations of Span, Span-Chol or Chol for 30 min, washed, media was replaced for 3 h, prior to equilibration for 30 min in HBSS (4 h total). Coelenterazine h (Promega) was added at a final concentration of 5 µM and the cells were incubated for a further 5 min.

The BRET baseline was measured every 1 min for 4 min, before addition of vehicle or 1 nM SP, with BRET measurements continued every 1 min for 25 min. BRET was measured using a PHERAstar Omega microplate reader (BMG Labtech) with sequential integration of the signals detected at 475 ± 30 nm and 535 ± 30 nm with filters with the appropriate band pass. Data are shown as the BRET ratio (calculated as the ratio of the YFP/Venus signal to the RLuc8 signal) expressed as the SP-induced change in BRET (corrected for vehicle) for time course graphs or as the 20 min area under the curve (AUC) relative to the control SP response ($BRET/BRET_{SP}$) for bar graphs.

Spatial PKC and cAMP using high content and confocal ratiometric FRET imaging – High-content ratiometric FRET imaging was performed as described previously (58). HEK293 cells in black, optically-clear 96-well plates were grown to 70% confluency before co-transfection with 55 ng/well HA-NK_1R and 40 ng/well cytoCKAR, pmEpac2 or cytoEpac2 for 48 h. Before the experiment, cells were partially serum-restricted overnight in 0.5% (v/v) FBS DMEM. On the day of the experiment, cells were pre-incubated with Span or Span-Chol (both 1 µM) for 4 h before the medium was replaced with HBSS and cells were equilibrated for 30 min at 37°C. High-content fluorescence imaging was performed using the INCell 2000 Analyzer with a Nikon Plan Fluor ELWD 40× (NA, 0.6) objective and FRET module (GE Healthcare) (14,58). Cells were sequentially excited using a CFP filter (430/24) with emission measured using YFP (535/30) and CFP (470/24) filters with a polychroic optimized for this filter pair (Quad 3). The FRET baseline was measured every 1 min for 4 min, before addition of vehicle control (X% v/v MilliQ H_2O) or 1 nM SP, with image capture continued for 20 min. At the end of each experiment, the same cells were stimulated with positive controls to maximally activate the biosensor: 200 nM phorbol 12,13-dibutyrate (PDBu) with phosphatase inhibitor cocktail (Merck) for CKAR, or 10 µM forskolin with 100 µM 3-isobutyl-1-methylxanthine for Epac2. After 10 min incubation, images were captured every 1 min for a final 4 min.

For fast confocal imaging experiments, HEK293 cells in 8-well Ibidi chamber slides were grown to 50% confluency before co-transfection with 55 ng/well HA-NK$_1$R and 40 ng/well cytoCKAR,. Before the experiment, cells were partially serum-restricted overnight in 0.5% (v/v) FBS DMEM. 48 h after transfection, cells were pre-incubated with Span or Span-Chol (both 1 μM) for 4 h before the medium was replaced with HBSS and cells were equilibrated for 30 min at 37°C. Fast capture imaging was performed using a Zeiss LSM710 confocal fluorescence microscope with a Zeiss 40x NA1.34, oil immersion objective, with pinhole set to 2 AU. Cells were excited at 458 nm (CFP), with dual emission measured at 481 nm (CFP) and 540 nm (YFP). The FRET baseline was measured every 3 sec for 30 sec, before addition of vehicle control (X% v/v MilliQ H_2O) or 1 nM SP, with image capture continued every 3 sec for 2 min. At the end of each experiment, the same cells were stimulated with a positive control, 200 nM PDBu, and imaged for a further 5 min.

For both high content and fast imaging experiments, only cells with >3% change in F/F_0 (FRET ratio relative to baseline for each cell) after stimulation with the positive controls were selected for analysis. The average F/F_0 was calculated for each experiment and combined. Data were analyzed using in-house scripts written for the Fiji distribution of Image J (57), as described previously (58).

Animal models of mechanical nociception - A total of 72 male C57Bl/6 mice (6-12 weeks old) were used in this study. Mice were maintained in a temperature and humidity-controlled room (23ºC ± 2º C) under a 12 h light/dark cycle with food and water *ad libitum*. The study was conducted in accordance with the ethical guidelines of the International Association for the Study of Pain (59) and was approved by the animal ethics committee of Monash Institute of Pharmaceutical Sciences, Monash University. Mice were randomly assigned to experimental groups.

Mice were acclimatized to the experimental conditions on two successive days for 1-2 h. On the day of the study, withdrawal thresholds were measured in duplicate to establish baseline readings for each mouse. Span, Span-Chol, Chol (all 50 μM) or vehicle (1% v/v DMSO/0.9% v/v saline) were injected intrathecally (5 μL, L3-L4) into conscious mice (n=6 per group). At 3, 6 and 12 h after drug administration, capsaicin (5 μg, vehicle: 20% v/v ethanol, 10% v/v Tween 80 in saline solution; 10 μL) was administered by intraplantar injection under isoflurane anesthesia (1-3% in oxygen) to the left hind paw. Nociception was assessed by measuring paw withdrawal thresholds with von Frey filaments of ascending force, applied to the plantar surface of the hind paws as previously described (5,60). Paw withdrawal thresholds were measured for both the ipsilateral and contralateral hind paws every hour for 4 h. The data were subsequently normalized to the baseline paw withdrawal threshold for each animal. Investigators were blinded to drug treatments and experimental groups.

Data analysis - Graphs were generated using GraphPad Prism 8 (San Diego, CA). Data are presented as mean ± S.E.M, unless otherwise stated.

DATA AVAILABILITY All data is contained within the manuscript.

ACKNOWLEDGEMENTS We thank Mr. Cameron Nowell (Manager of Imaging, Flow Cytometry and Analysis Facility at the Monash Institute of Pharmaceutical Sciences) for advice regarding imaging.

FUNDING AND ADDITIONAL INFORMATION This work was supported by grants from the National Institutes of Health (NS102722, DE026806, DK118971 to NWB), Department of Defence (W81XWH1810431 to NWB), National Health and Medical Research Council (63303, 1049682, 1031886 to NWB), ARC Centre of Excellence in Convergent Bio-Nano Science and Technology (NWB) and Medical Research Council (MR/N020081/1; SJB & SJH). MLH was a NHMRC RD Wright Fellow (1061687). QNM was part of the Joint Award Doctoral Training Centre in Molecular Pharmacology and Drug Discovery at Monash University (Australia) and the University of Nottingham (UK).

CONFLICT OF INTEREST NWB is a founding scientist of Endosome Therapeutics Inc. Research in the laboratories of NWB, NV and DPP is funded in part by Takeda Pharmaceuticals Inc.

REFERENCES

1. Hauser, A. S., Attwood, M. M., Rask-Andersen, M., Schioth, H. B., and Gloriam, D. E. (2017) Trends in GPCR drug discovery: new agents, targets and indications. *Nat Rev Drug Discov* **16**, 829-842
2. Luttrell, L. M., Ferguson, S. S., Daaka, Y., Miller, W. E., Maudsley, S., Della Rocca, G. J., Lin, F., Kawakatsu, H., Owada, K., Luttrell, D. K., Caron, M. G., and Lefkowitz, R. J. (1999) Beta-arrestin-dependent formation of beta2 adrenergic receptor-Src protein kinase complexes. *Science* **283**, 655-661
3. Slessareva, J. E., Routt, S. M., Temple, B., Bankaitis, V. A., and Dohlman, H. G. (2006) Activation of the phosphatidylinositol 3-kinase Vps34 by a G protein alpha subunit at the endosome. *Cell* **126**, 191-203
4. Sorkin, A., and von Zastrow, M. (2009) Endocytosis and signalling: intertwining molecular networks. *Nat Rev Mol Cell Biol* **10**, 609-622
5. Jensen, D. D., Lieu, T., Halls, M. L., Veldhuis, N. A., Imlach, W. L., Mai, Q. N., Poole, D. P., Quach, T., Aurelio, L., Conner, J., Herenbrink, C. K., Barlow, N., Simpson, J. S., Scanlon, M. J., Graham, B., McCluskey, A., Robinson, P. J., Escriou, V., Nassini, R., Materazzi, S., Geppetti, P., Hicks, G. A., Christie, M. J., Porter, C. J. H., Canals, M., and Bunnett, N. W. (2017) Neurokinin 1 receptor signaling in endosomes mediates sustained nociception and is a viable therapeutic target for prolonged pain relief. *Sci Transl Med* **9**
6. Irannejad, R., Tomshine, J. C., Tomshine, J. R., Chevalier, M., Mahoney, J. P., Steyaert, J., Rasmussen, S. G., Sunahara, R. K., El-Samad, H., Huang, B., and von Zastrow, M. (2013) Conformational biosensors reveal GPCR signalling from endosomes. *Nature* **495**, 534-538
7. Murphy, J. E., Padilla, B. E., Hasdemir, B., Cottrell, G. S., and Bunnett, N. W. (2009) Endosomes: a legitimate platform for the signaling train. *PNAS* **106**, 17615-17622
8. Yarwood, R. E., Imlach, W. L., Lieu, T., Veldhuis, N. A., Jensen, D. D., Klein Herenbrink, C., Aurelio, L., Cai, Z., Christie, M. J., Poole, D. P., Porter, C. J. H., McLean, P., Hicks, G. A., Geppetti, P., Halls, M. L., Canals, M., and Bunnett, N. W. (2017) Endosomal signaling of the receptor for calcitonin gene-related peptide mediates pain transmission. *PNAS* **114**, 12309-12314
9. Nikolaev, V. O., Bunemann, M., Hein, L., Hannawacker, A., and Lohse, M. J. (2004) Novel single chain cAMP sensors for receptor-induced signal propagation. *J Biol Chem* **279**, 37215-37218
10. Calebiro, D., Nikolaev, V. O., Gagliani, M. C., de Filippis, T., Dees, C., Tacchetti, C., Persani, L., and Lohse, M. J. (2009) Persistent cAMP-signals triggered by internalized G-protein-coupled receptors. *PLoS Biol* **7**, e1000172

11. Dionne, R. A., Max, M. B., Gordon, S. M., Parada, S., Sang, C., Gracely, R. H., Sethna, N. F., and MacLean, D. B. (1998) The substance P receptor antagonist CP-99,994 reduces acute postoperative pain. *Clin Pharmacol Ther* **64**, 562-568
12. Diener, H. C., and Group, R. P. R. S. (2003) RPR100893, a substance-P antagonist, is not effective in the treatment of migraine attacks. *Cephalalgia* **23**, 183-185
13. Goldstein, D. J., Wang, O., Saper, J. R., Stoltz, R., Silberstein, S. D., and Mathew, N. T. (1997) Ineffectiveness of neurokinin-1 antagonist in acute migraine: a crossover study. *Cephalalgia* **17**, 785-790
14. Jensen, D. D., Halls, M. L., Murphy, J. E., Canals, M., Cattaruzza, F., Poole, D. P., Lieu, T., Koon, H. W., Pothoulakis, C., and Bunnett, N. W. (2014) Endothelin-converting enzyme 1 and beta-arrestins exert spatiotemporal control of substance P-induced inflammatory signals. *J Biol Chem* **289**, 20283-20294
15. Cottrell, G. S., Padilla, B. E., Amadesi, S., Poole, D. P., Murphy, J. E., Hardt, M., Roosterman, D., Steinhoff, M., and Bunnett, N. W. (2009) Endosomal endothelin-converting enzyme-1: a regulator of beta-arrestin-dependent ERK signaling. *J Biol Chem* **284**, 22411-22425
16. Irannejad, R., Pessino, V., Mika, D., Huang, B., Wedegaertner, P. B., Conti, M., and von Zastrow, M. (2017) Functional selectivity of GPCR-directed drug action through location bias. *Nat Chem Biol* **13**, 799-806
17. Ramirez-Garcia, P. D., Retamal, J. S., Shenoy, P., Imlach, W., Sykes, M., Truong, N., Constandil, L., Pelissier, T., Nowell, C. J., Khor, S. Y., Layani, L. M., Lumb, C., Poole, D. P., Lieu, T., Stewart, G. D., Mai, Q. N., Jensen, D. D., Latorre, R., Scheff, N. N., Schmidt, B. L., Quinn, J. F., Whittaker, M. R., Veldhuis, N. A., Davis, T. P., and Bunnett, N. W. (2019) A pH-responsive nanoparticle targets the neurokinin 1 receptor in endosomes to prevent chronic pain. *Nat Nanotechnol* **14**, 1150-1159
18. Rajendran, L., Schneider, A., Schlechtingen, G., Weidlich, S., Ries, J., Braxmeier, T., Schwille, P., Schulz, J. B., Schroeder, C., Simons, M., Jennings, G., Knolker, H. J., and Simons, K. (2008) Efficient inhibition of the Alzheimer's disease beta-secretase by membrane targeting. *Science* **320**, 520-523
19. Linning, P., Haussmann, U., Beyer, I., Weidlich, S., Schieb, H., Wiltfang, J., Klafki, H. W., and Knolker, H. J. (2012) Optimisation of BACE1 inhibition of tripartite structures by modification of membrane anchors, spacers and pharmacophores - development of potential agents for the treatment of Alzheimer's disease. *Org Biomol Chem* **10**, 8216-8235
20. Briddon, S. J., and Hill, S. J. (2007) Pharmacology under the microscope: the use of fluorescence correlation spectroscopy to determine the properties of ligand-receptor complexes. *Trends Pharmacol Sci* **28**, 637-645
21. Stoddart, L. A., Vernall, A. J., Briddon, S. J., Kellam, B., and Hill, S. J. (2015) Direct visualisation of internalization of the adenosine A3 receptor and localization with arrestin3 using a fluorescent agonist. *Neuropharmacology* **98**, 68-77
22. Stoddart, L. A., Vernall, A. J., Denman, J. L., Briddon, S. J., Kellam, B., and Hill, S. J. (2012) Fragment screening at adenosine-A(3) receptors in living cells using a fluorescence-based binding assay. *Chem Biol* **19**, 1105-1115
23. Vauquelin, G., and Charlton, S. J. (2010) Long-lasting target binding and rebinding as mechanisms to prolong in vivo drug action. *Br J Pharmacol* **161**, 488-508
24. Sykes, D. A., Parry, C., Reilly, J., Wright, P., Fairhurst, R. A., and Charlton, S. J. (2014) Observed drug-receptor association rates are governed by membrane affinity: the importance of establishing "micro-pharmacokinetic/pharmacodynamic relationships" at the beta2-adrenoceptor. *Mol Pharmacol* **85**, 608-617
25. Steinhoff, M. S., von Mentzer, B., Geppetti, P., Pothoulakis, C., and Bunnett, N. W. (2014) Tachykinins and their receptors: contributions to physiological control and the mechanisms of disease. *Physiol Rev* **94**, 265-301

26. Caberlotto, L., Hurd, Y. L., Murdock, P., Wahlin, J. P., Melotto, S., Corsi, M., and Carletti, R. (2003) Neurokinin 1 receptor and relative abundance of the short and long isoforms in the human brain. *Eur J Neurosci* **17**, 1736-1746
27. Hargreaves, R. (2002) Imaging substance P receptors (NK1) in the living human brain using positron emission tomography. *J Clin Psychiatry* **63 Suppl 11**, 18-24
28. Renzi, D., Pellegrini, B., Tonelli, F., Surrenti, C., and Calabro, A. (2000) Substance P (neurokinin-1) and neurokinin A (neurokinin-2) receptor gene and protein expression in the healthy and inflamed human intestine. *Am J Pathol* **157**, 1511-1522
29. Pinto, F. M., Almeida, T. A., Hernandez, M., Devillier, P., Advenier, C., and Candenas, M. L. (2004) mRNA expression of tachykinins and tachykinin receptors in different human tissues. *Eur J Pharmacol* **494**, 233-239
30. Greeno, E. W., Mantyh, P., Vercellotti, G. M., and Moldow, C. F. (1993) Functional neurokinin 1 receptors for substance P are expressed by human vascular endothelium. *J Exp Med* **177**, 1269-1276
31. Jarcho, J. M., Feier, N. A., Bert, A., Labus, J. A., Lee, M., Stains, J., Ebrat, B., Groman, S. M., Tillisch, K., Brody, A. L., London, E. D., Mandelkern, M. A., and Mayer, E. A. (2013) Diminished neurokinin-1 receptor availability in patients with two forms of chronic visceral pain. *Pain* **154**, 987-996
32. Levental, I., Grzybek, M., and Simons, K. (2010) Greasing their way: lipid modifications determine protein association with membrane rafts. *Biochemistry* **49**, 6305-6316
33. Rajendran, L., and Annaert, W. (2012) Membrane trafficking pathways in Alzheimer's disease. *Traffic* **13**, 759-770
34. Rose, R. H., Briddon, S. J., and Hill, S. J. (2012) A novel fluorescent histamine H(1) receptor antagonist demonstrates the advantage of using fluorescence correlation spectroscopy to study the binding of lipophilic ligands. *Br J Pharmacol* **165**, 1789-1800
35. Gherbi, K., Briddon, S. J., and Charlton, S. J. (2018) Micro-pharmacokinetics: Quantifying local drug concentration at live cell membranes. *Sci Rep* **8**, 3479
36. Kobilka, B. K., and Deupi, X. (2007) Conformational complexity of G-protein-coupled receptors. *Trends Pharmacol Sci* **28**, 397-406
37. Latorraca, N. R., Venkatakrishnan, A. J., and Dror, R. O. (2017) GPCR Dynamics: Structures in Motion. *Chem Rev* **117**, 139-155
38. Jarsch, I. K., Daste, F., and Gallop, J. L. (2016) Membrane curvature in cell biology: An integration of molecular mechanisms. *J Cell Biol* **214**, 375-387
39. McMahon, H. T., and Boucrot, E. (2015) Membrane curvature at a glance. *J Cell Sci* **128**, 1065-1070
40. Civciristov, S., Ellisdon, A. M., Suderman, R., Pon, C. K., Evans, B. A., Kleifeld, O., Charlton, S. J., Hlavacek, W. S., Canals, M., and Halls, M. L. (2018) Preassembled GPCR signaling complexes mediate distinct cellular responses to ultralow ligand concentrations. *Sci Signal* **11**
41. Huang, W., Masureel, M., Qu, Q., Janetzko, J., Inoue, A., Kato, H. E., Robertson, M. J., Nguyen, K. C., Glenn, J. S., Skiniotis, G., and Kobilka, B. K. (2020) Structure of the neurotensin receptor 1 in complex with beta-arrestin 1. *Nature* **579**, 303-308
42. Wu, F. J., Williams, L. M., Abdul-Ridha, A., Gunatilaka, A., Vaid, T. M., Kocan, M., Whitehead, A. R., Griffin, M. D. W., Bathgate, R. A. D., Scott, D. J., and Gooley, P. R. (2020) Probing the correlation between ligand efficacy and conformational diversity at the alpha1A-adrenoreceptor reveals allosteric coupling of its microswitches. *J Biol Chem* **295**, 7404-7417
43. Liang, Y. L., Belousoff, M. J., Fletcher, M. M., Zhang, X., Khoshouei, M., Deganutti, G., Koole, C., Furness, S. G. B., Miller, L. J., Hay, D. L., Christopoulos, A., Reynolds, C. A., Danev, R., Wootten, D., and Sexton, P. M. (2020) Structure and Dynamics of Adrenomedullin Receptors AM1 and AM2 Reveal Key Mechanisms in the Control of Receptor Phenotype by Receptor Activity-Modifying Proteins. *ACS Pharmacol Transl Sci* **3**, 263-284

44. Eichel, K., Jullie, D., Barsi-Rhyne, B., Latorraca, N. R., Masureel, M., Sibarita, J. B., Dror, R. O., and von Zastrow, M. (2018) Catalytic activation of beta-arrestin by GPCRs. *Nature* **557**, 381-386
45. Arshavsky, V. Y., and Burns, M. E. (2014) Current understanding of signal amplification in phototransduction. *Cell Logist* **4**, e29390
46. Tsvetanova, N. G., and von Zastrow, M. (2014) Spatial encoding of cyclic AMP signaling specificity by GPCR endocytosis. *Nat Chem Biol* **10**, 1061-1065
47. Johannessen, L., Remsberg, J., Gaponenko, V., Adams, K. M., Barchi, J. J., Jr., Tarasov, S. G., Jiang, S., and Tarasova, N. I. (2011) Peptide structure stabilization by membrane anchoring and its general applicability to the development of potent cell-permeable inhibitors. *Chembiochem* **12**, 914-921
48. Merriam, L. A., Baran, C. N., Girard, B. M., Hardwick, J. C., May, V., and Parsons, R. L. (2013) Pituitary adenylate cyclase 1 receptor internalization and endosomal signaling mediate the pituitary adenylate cyclase activating polypeptide-induced increase in guinea pig cardiac neuron excitability. *J Neurosci* **33**, 4614-4622
49. Jimenez-Vargas, N. N., Gong, J., Wisdom, M., Jensen, D. D., Latorre, R., Hegron, A., Teng, S., DiCello, J. J., Rajasekhar, P., Veldhuis, N. A., Carbone, S. E., Yu, Y., Lopez-Lopez, C., Jaramillo-Polance, J., Canals, M., Reed, D. E., Lomax, A. E., Schmidt, B. L., Leong, K., Vanner, S. J., Halls, M. L., Bunnett, N. W., and Poole, D. P. (2020) Endosomal signaling of delta opioid receptors is an endogenous mechanism and therapeutic target for relief from inflammatory pain. *PNAS* **in press**
50. Cattaruzza, F., Cottrell, G. S., Vaksman, N., and Bunnett, N. W. (2009) Endothelin-converting enzyme 1 promotes re-sensitization of neurokinin 1 receptor-dependent neurogenic inflammation. *Br J Pharmacol* **156**, 730-739
51. Violin, J. D., Zhang, J., Tsien, R. Y., and Newton, A. C. (2003) A genetically encoded fluorescent reporter reveals oscillatory phosphorylation by protein kinase C. *J Cell Biol* **161**, 899-909
52. Wachten, S., Masada, N., Ayling, L. J., Ciruela, A., Nikolaev, V. O., Lohse, M. J., and Cooper, D. M. (2010) Distinct pools of cAMP centre on different isoforms of adenylyl cyclase in pituitary-derived GH3B6 cells. *J Cell Sci* **123**, 95-106
53. Lan, T. H., Liu, Q., Li, C., Wu, G., and Lambert, N. A. (2012) Sensitive and high resolution localization and tracking of membrane proteins in live cells with BRET. *Traffic* **13**, 1450-1456
54. Jensen, D. D., Godfrey, C. B., Niklas, C., Canals, M., Kocan, M., Poole, D. P., Murphy, J. E., Alemi, F., Cottrell, G. S., Korbmacher, C., Lambert, N. A., Bunnett, N. W., and Corvera, C. U. (2013) The bile acid receptor TGR5 does not interact with beta-arrestins or traffic to endosomes but transmits sustained signals from plasma membrane rafts. *J Biol Chem* **288**, 22942-22960
55. Ayling, L. J., Briddon, S. J., Halls, M. L., Hammond, G. R., Vaca, L., Pacheco, J., Hill, S. J., and Cooper, D. M. (2012) Adenylyl cyclase AC8 directly controls its micro-environment by recruiting the actin cytoskeleton in a cholesterol-rich milieu. *J Cell Sci* **125**, 869-886
56. Kilpatrick, L. E., Briddon, S. J., Hill, S. J., and Holliday, N. D. (2010) Quantitative analysis of neuropeptide Y receptor association with beta-arrestin2 measured by bimolecular fluorescence complementation. *Br J Pharmacol* **160**, 892-906
57. Schindelin, J., Arganda-Carreras, I., Frise, E., Kaynig, V., Longair, M., Pietzsch, T., Preibisch, S., Rueden, C., Saalfeld, S., Schmid, B., Tinevez, J. Y., White, D. J., Hartenstein, V., Eliceiri, K., Tomancak, P., and Cardona, A. (2012) Fiji: an open-source platform for biological-image analysis. *Nat Methods* **9**, 676-682
58. Halls, M. L., Poole, D. P., Ellisdon, A. M., Nowell, C. J., and Canals, M. (2015) Detection and Quantification of Intracellular Signaling Using FRET-Based Biosensors and High Content Imaging. *Methods Mol Biol* **1335**, 131-161
59. Zimmermann, M. (1983) Ethical guidelines for investigations of experimental pain in conscious animals. *Pain* **16**, 109-110
60. Alemi, F., Kwon, E., Poole, D. P., Lieu, T., Lyo, V., Cattaruzza, F., Cevikbas, F., Steinhoff, M., Nassini, R., Materazzi, S., Guerrero-Alba, R., Valdez-Morales, E., Cottrell, G. S., Schoonjans, K.,

Geppetti, P., Vanner, S. J., Bunnett, N. W., and Corvera, C. U. (2013) The TGR5 receptor mediates bile acid-induced itch and analgesia. *J Clin Invest* **123**, 1513-1530

ABBREVIATIONS

AC, adenylyl cyclase
BACE-1, β-site amyloid precursor protein cleaving enzyme 1
BRET, bioluminescence resonance energy transfer
Chol, biotin conjugated to cholestanol via a PEG linker
CFP, cyan fluorescent protein
Cy5, cyanine 5
Cy5-Chol, cyanine 5 with cholestanol linked via PEG
Cy5-EE, cyanine 5 with an ethyl ester linked via PEG
cytoCKAR, cytosolic C kinase activity reporter FRET biosensor
cytoEpac2, cytosolic Epac2-camps FRET biosensor
DAG, diacylgycerol
DMEM, Dulbecco's modified Eagle's medium
EE, ethyl ester
EGFR, epidermal growth factor receptor
ERK, extracellular signal regulated kinase (mitogen activated protein kinase)
FBS, fetal bovine serum
FCS, fluorescent correlation spectroscopy
GPCR, G protein-coupled receptor
InsP$_3$, inositol trisphosphate
NK$_1$R, neurokinin 1 receptor
PKA, protein kinase A
PKC, protein kinase C
pmEpac2, plasma membrane localized Epac2-camps FRET biosensor
RLuc8, renilla luciferase
SP, substance P
Span, Spantide
Span-Chol, spantide conjugated to cholestanol via PEG linker
TAMRA, tetramethylrhodamine
YFP, yellow fluorescent protein

FIGURES AND FIGURE LEGENDS

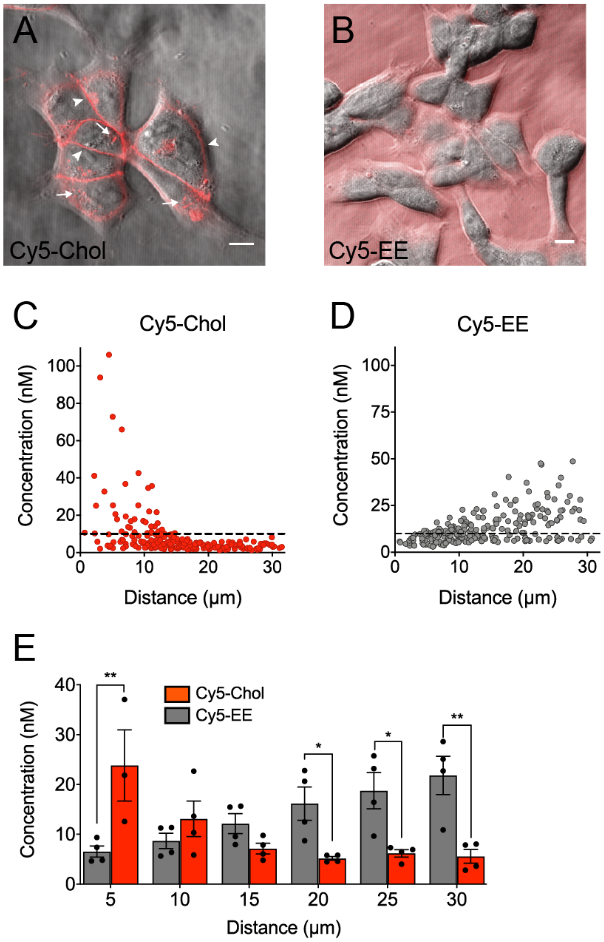

Figure 1. A cholestanol lipid-anchor increases the concentration of Cy5 immediately above the plasma membrane. A-B. Confocal images of HEK293 cells after incubation with 1 µM Cy5-Chol (A) or Cy5-EE (B). Arrows indicate intracellular Cy5 fluorescence, and arrow heads indicate Cy5 fluorescence at the plasma membrane. Scale bar, 10 µm. **C-D.** The concentration of 10 nM solution of Cy5-Chol (C) or Cy5-EE (D) at increasing distances above the plasma membrane of HEK293 cells was calculated using FCS. Data points show the concentrations measured at 6 distance intervals averaged from 3-4 independent experiments. The concentration of the added solution (10 nM) is shown by a dashed line. **E.** The concentration of Cy5-Chol and Cy5-EE binned at increasing 5 µm intervals above the plasma membrane. Bars show the mean, error bars show the S.E.M., and data points show the average concentrations obtained from each individual experiment (n=4). * $p<0.05$, ** $p<0.01$ Cy5-EE vs Cy5-Chol; two-way ANOVA with Sidak's multiple comparison test.

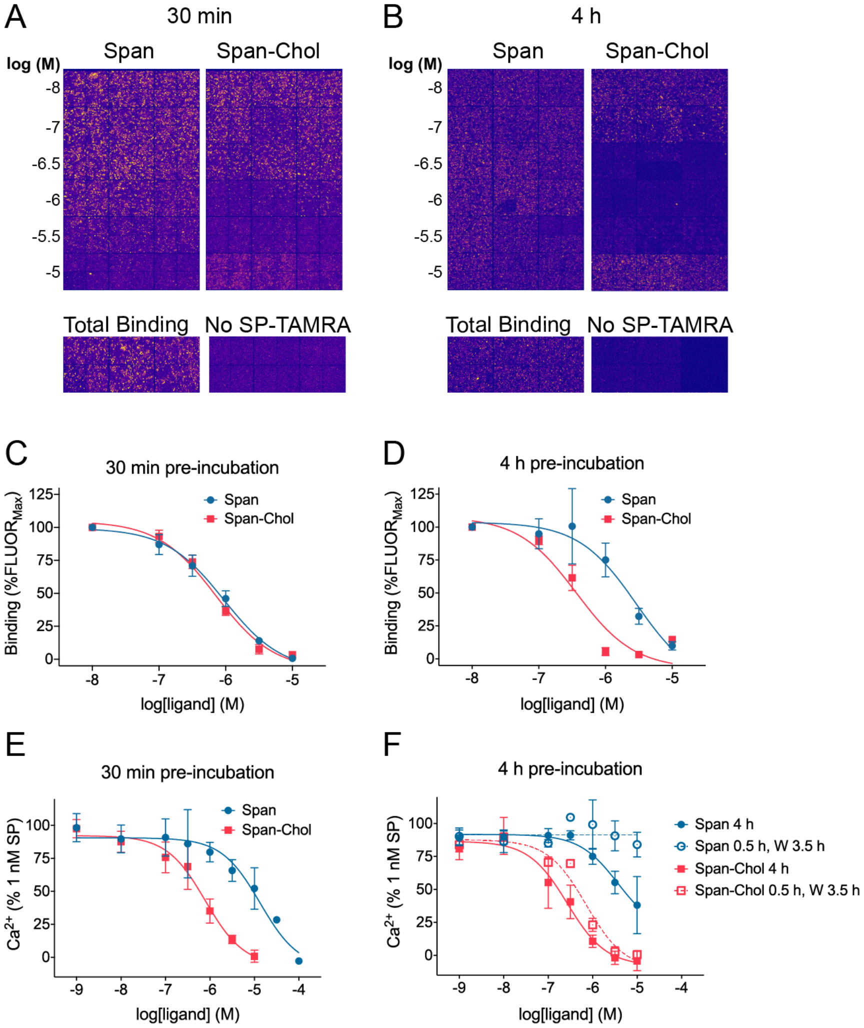

Figure 2. A cholestanol lipid-anchor increases the relative affinity and potency of an NK$_1$R antagonist. A-D. The affinity of Span compared to Span-Chol was assessed by competition with fluorescent TAMRA-SP in HEK-NK$_1$R cells by high content imaging (n=5). HEK-NK$_1$R cells were pre-incubated with vehicle (0.1% v/v DMSO; total binding) or increasing concentrations of Span or Span-Chol prior to addition of 0.5 nM TAMRA-SP for a total of 30 min (A,C) or 4 h (B,D) at 37°C. **A-B**, representative pseudocolored images of TAMRA-SP binding after 30 min (A) or 4 h (B). **C-D,** combined competition binding curves after 30 min (C) or 4 h (D). Data are expressed as a percentage of the fluorescent intensity measured in the presence of 10 nM Span or Span-Chol (%FLUOR$_{Max}$). Symbols show means, and error bars S.E.M. of 5 independent experiments performed in triplicate. **E-F.** Calcium transients were measured in HEK-NK$_1$R cells in response to 1 nM SP following short (30 min; E) or long (4 h; F) pre-incubation with increasing concentrations of Span or Span-Chol (n=3). 4 h pre-incubation experiments compared continuous exposure to antagonist (4 h) vs a "pulsed" exposure (0.5h exposure, wash [W], 3.5 h rest). Symbols show means, and error bars S.E.M. of 3 independent experiments performed in triplicate.

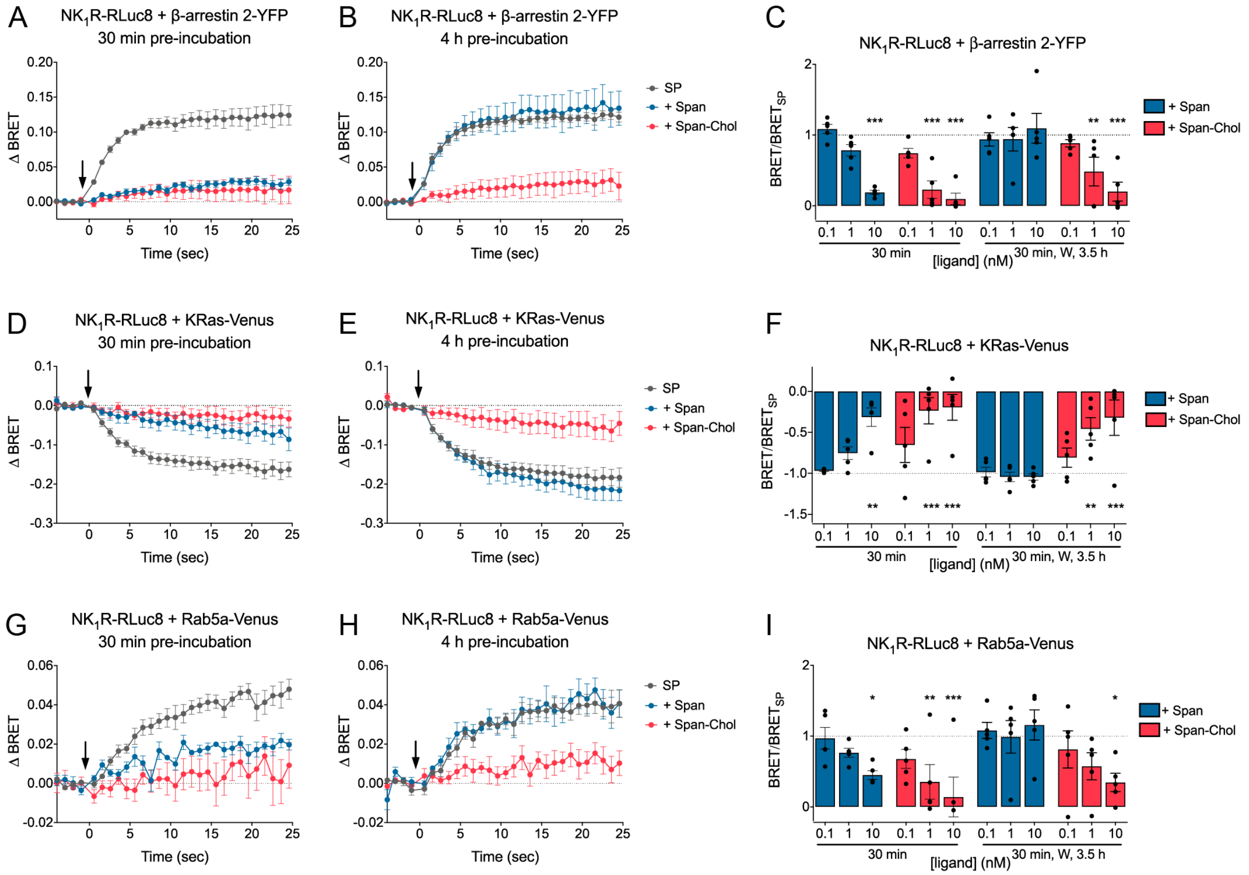

Figure 3. Span-Chol causes sustained inhibition of NK$_1$R-induced recruitment of β-arrestin and receptor internalization to early endosomes. The effect of short (30 min) versus long (4 h) pre-incubation with Span or Span-Chol on the NK$_1$R-induced recruitment of β-arrestin and receptor internalization to early endosomes was determined using BRET in HEK cells (n=5). **A-C.** 1 nM SP-induced change in BRET between NK$_1$R-Rluc8 and β-arrestin 2-YFP after pre-incubation with 10 µM Span or Span-Chol for 30 min (A) or 4 h (B). C, the area under the curve (AUC) calculated from BRET time courses (as per A and B) after pre-incubation with 0.1 µM, 1 µM or 10 µM antagonist, expressed relative to SP alone. **D-F.** 1 nM SP-induced change in BRET between NK$_1$R-Rluc8 and KRas-Venus after pre-incubation with 10 µM Span or Span-Chol for 30 min (D) or 4 h (E). F, the area under the curve (AUC) calculated from BRET time courses (as per D and E) after pre-incubation with 0.1 µM, 1 µM or 10 µM antagonist, expressed relative to SP alone. **G-I.** 1 nM SP-induced change in BRET between NK$_1$R-Rluc8 and Rab5a-Venus after pre-incubation with 10 µM Span or Span-Chol for 30 min (G) or 4 h (H). I, the area under the curve (AUC) calculated from BRET time courses (as per G and H) after pre-incubation with 0.1 µM, 1 µM or 10 µM antagonist, expressed relative to SP alone. For time courses, symbols show means and error bars S.E.M; for bar graphs, columns show means, error bars show S.E.M. and symbols show the mean of each individual experiment performed in duplicate. * $p<0.05$, ** $p<0.01$ and *** $p<0.001$ versus SP alone, two-way ANOVA with Dunnett's multiple comparisons test.

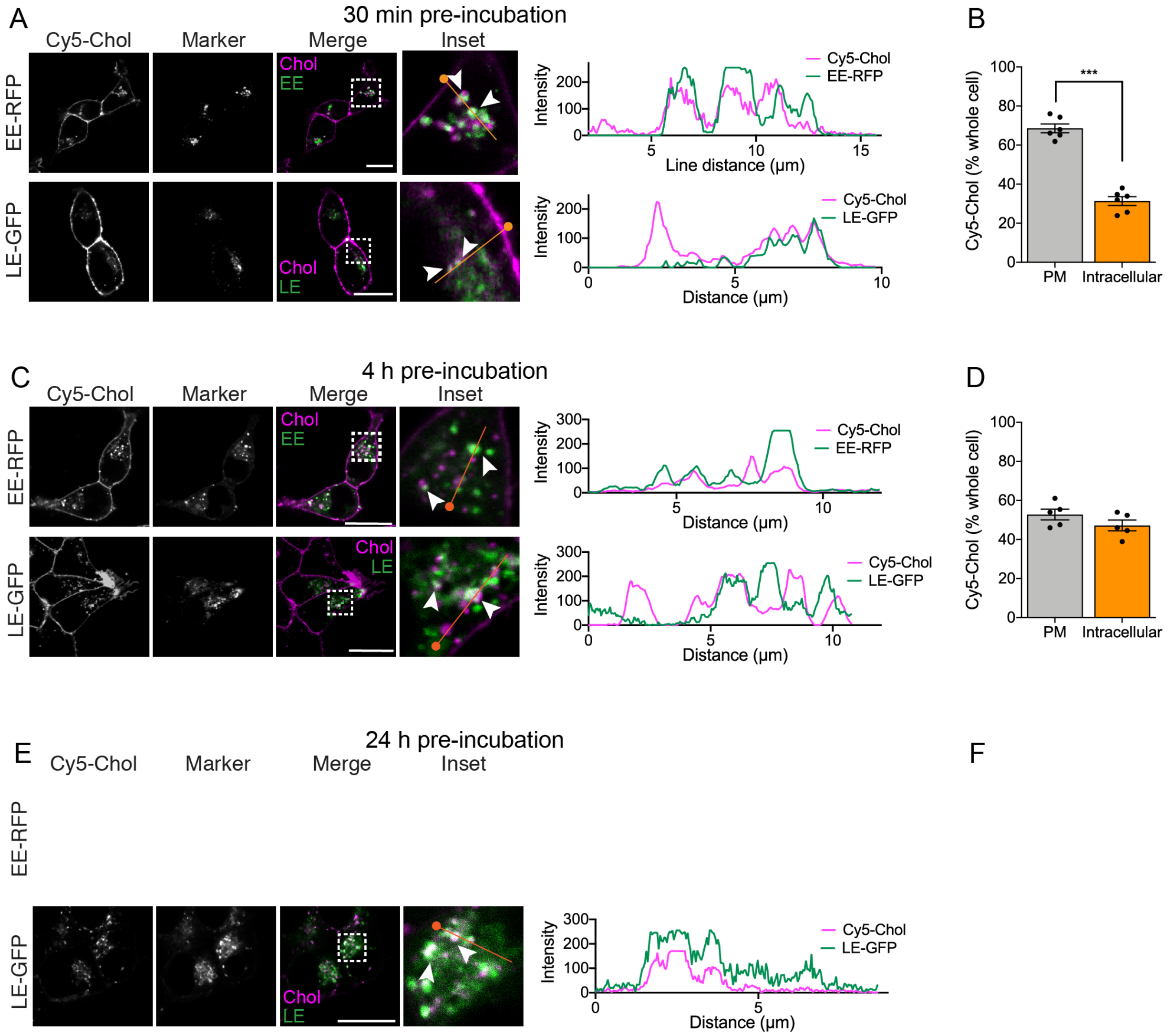

Figure 4. The cholestanol lipid-anchor causes Cy5 movement from the plasma membrane deeper into endosomal pathways over 24 h. The location of the Cy5-Chol probe (1.5 µM) was determined after 30 min (A,B), 4 h (C, D) or 24 h (E,F) by confocal microscopy in HEK cells labelled with location markers of the endosomal network (CellLights: early endosome(EE)-RFP or late endosome(LE)-GFP) (n=6). **A,C,D**. Representative, merged and zoomed images of HEK cells with location markers pseudocoloured green, after 30 min incubation with Cy5-Chol (pseudocoloured magenta). Dotted box indicates zoomed region for inset image. Arrow heads indicate co-incidence of the Cy5-Chol with the location marker. Orange line indicates region highlighted in line scan intensity graph (right panel), with the start of the line indicated by a circle. Scale bar 20 µm. **B,D,F**. The proportion of Cy5-Chol fluorescence at the plasma membrane compared to the rest of the cell (defined as intracellular Cy5). Bars show the grouped mean, and error bars S.E.M. of grouped cells from 6 independent experiments (symbols). *** p<0.001, unpaired t-test.

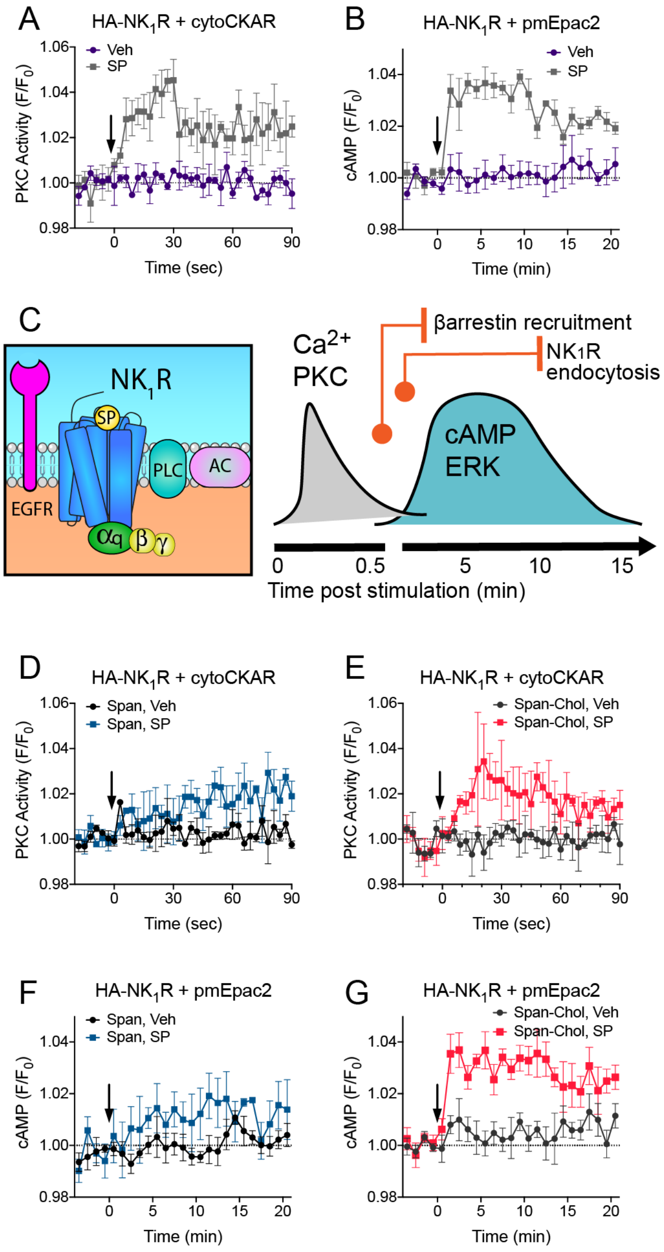

Figure 5. Only Span, and not Span-Chol, inhibits NK$_1$R signaling from the plasma membrane. After a 4 h pre-incubation Span, but not Span-Chol, blocks SP-stimulated transient increases in PKC and cAMP (n=3). **A-B.** HEK cells transfected with HA-NK$_1$R and cytoCKAR (A) or pmEpac2 (B) were stimulated with vehicle (XX% MilliQ H2O) or 1 nM SP and signaling was measured over time. **C.** Cartoon of the sequence of events following NK$_1$R stimulation at the plasma membrane. Orange circles indicate the time at which a regulatory event starts, and vertical orange lines indicate when it reaches a plateau. Signaling is represented by black lines. **D-G.** HEK cells transfected with HA-NK$_1$R and cytoCKAR (D-E) or pmEpac2 (F-G) were pre-treated with 1 μM Span (D,F) or Span-Chol (E,G) for 4 h prior to addition of vehicle (XX% MilliQ H2O) or 1 nM SP. Data are expressed as the FRET relative to the baseline FRET (F/F_0). Arrows indicate time of vehicle/SP addition. Symbols show the mean, and error bars S.E.M. of grouped cells from 3 independent experiments.

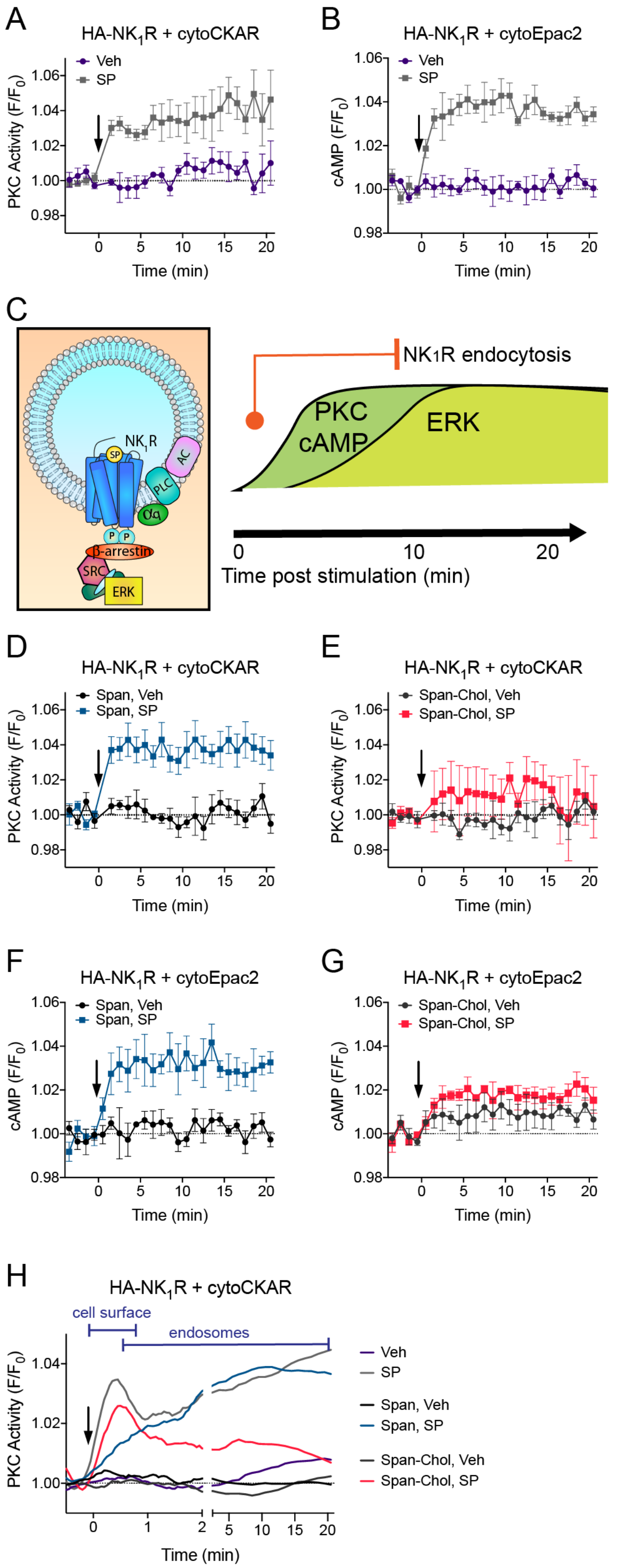

Figure 6. Only Span-Chol, and not Span, inhibits NK$_1$R signaling from endosomes. After a 4 h pre-incubation Span-Chol, but not Span, blocks SP-stimulated sustained increases in PKC and cAMP (n=3). **A-**

B. HEK cells transfected with HA-NK$_1$R and cytoCKAR (A) or cytoEpac2 (B) were stimulated with vehicle (XX% MilliQ H2O) or 1 nM SP and signaling was measured over 20 min. **C.** Cartoon of the sequence of events in endosomes following NK$_1$R stimulation. The orange circle indicates the time at which internalization starts, and the vertical orange line indicates when it reaches a plateau. Signaling is represented by black lines. **D-H.** HEK cells transfected with HA-NK$_1$R and cytoCKAR (D-E) or cytoEpac2 (F-G) were pre-treated with 1 μM Span (D,F) or Span-Chol (E,G) for 4 h prior to addition of vehicle (XX% MilliQ H2O) or 1 nM SP. Symbols show the mean, and error bars S.E.M. of grouped cells from 3 independent experiments. **H.** Smoothed time course traces showing the change in effectiveness of Span vs Span-Chol at blocking SP-stimulated PKC signaling as the NK$_1$R transitions from the plasma membrane (data taken from Figure 5A) to endosomes (data from Figure 6A). Data are expressed as the FRET relative to the baseline FRET (F/F$_0$). Arrows indicate time of vehicle/SP addition.

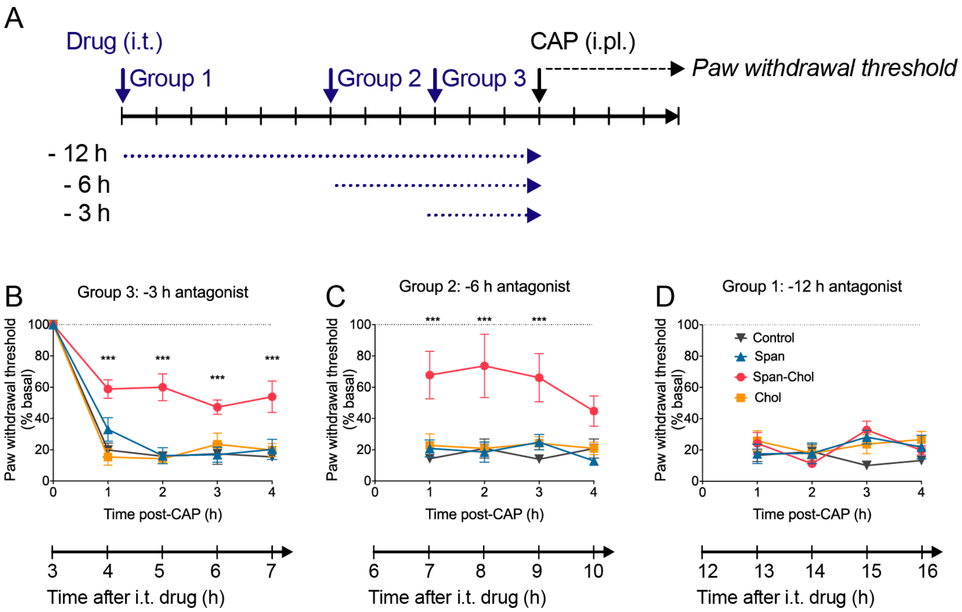

Figure 7. Span-Chol causes a prolonged anti-nociception in mice up to 9 h post administration. The analgesic effects of Span-Chol were assessed over 16 h in a mouse model of mechanical nociception (n=6). **A.** Illustration of the experimental protocol: Span (50 μM), Span-Chol (50 μM), Chol (50 μM) or vehicle (1% v/v DMSO/saline) was administered by intrathecal (i.t.) injection to three different groups of mice. The mice were left for 12 h (group 1), 6 h (group 2) or 3 h (group 3) before intraplantar (i.pl.) injection of capsaicin (CAP, 5 μg, 5 μl). Paw withdrawal responses to stimulation with von Frey filaments were measured hourly for 4 h. **B-D.** Paw withdrawal responses measured in the different groups of mice at 3 h (B), 6 h (C) or 12 h (D) after i.t. drug administration. Data are expressed relative to the baseline paw withdrawal threshold established for each mouse at the start of the experiment. Symbols show the mean, and error bars S.E.M. from 6 mice. *** p<0.001 compared to mice that received i.t. vehicle, two-way ANOVA with Bonferroni post-test.

nature.com/nnano

December 2019 Vol. 14 No. 12

nature nanotechnology

A non-opioid treatment option for chronic pain

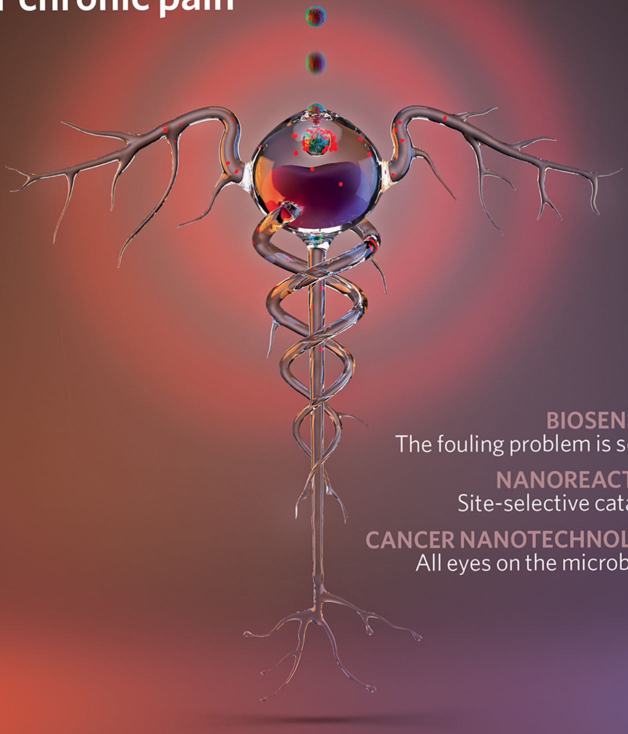

BIOSENSING
The fouling problem is solved

NANOREACTORS
Site-selective catalysis

CANCER NANOTECHNOLOGY
All eyes on the microbiome

nature nanotechnology

ARTICLES

https://doi.org/10.1038/s41565-019-0568-x

A pH-responsive nanoparticle targets the neurokinin 1 receptor in endosomes to prevent chronic pain

Paulina D. Ramírez-García[1,2], Jeffri S. Retamal[1,2], Priyank Shenoy[1,2], Wendy Imlach[3], Matthew Sykes[3], Nghia Truong[1,2], Luis Constandil[4], Teresa Pelissier[4], Cameron J. Nowell[1], Song Y. Khor[1,2], Louis M. Layani[1,2], Chris Lumb[1,2], Daniel P. Poole[1,2], TinaMarie Lieu[1,2], Gregory D. Stewart[1], Quynh N. Mai[1,2], Dane D. Jensen[5], Rocco Latorre[5], Nicole N. Scheff[6], Brian L. Schmidt[6], John F. Quinn[1,2], Michael R. Whittaker[1,2], Nicholas A. Veldhuis[1,2]*, Thomas P. Davis[1,2,7]* and Nigel W. Bunnett[1,2,5,8]*

Nanoparticle-mediated drug delivery is especially useful for targets within endosomes because of the endosomal transport mechanisms of many nanomedicines within cells. Here, we report the design of a pH-responsive, soft polymeric nanoparticle for the targeting of acidified endosomes to precisely inhibit endosomal signalling events leading to chronic pain. In chronic pain, the substance P (SP) neurokinin 1 receptor (NK_1R) redistributes from the plasma membrane to acidified endosomes, where it signals to maintain pain. Therefore, the NK_1R in endosomes provides an important target for pain relief. The pH-responsive nanoparticles enter cells by clathrin- and dynamin-dependent endocytosis and accumulate in NK_1R-containing endosomes. Following intrathecal injection into rodents, the nanoparticles, containing the FDA-approved NK_1R antagonist aprepitant, inhibit SP-induced activation of spinal neurons and thus prevent pain transmission. Treatment with the nanoparticles leads to complete and persistent relief from nociceptive, inflammatory and neuropathic nociception and offers a much-needed non-opioid treatment option for chronic pain.

Nanoparticle encapsulation improves drug efficacy by enhancing the stability, tolerability, delivery and retention in diseased tissues[1–3]. Interest in using nanoparticles to deliver anticancer drugs is perpetuated by the prospect of targeted delivery to tumour cells, and by the leaky vasculature and poor lymphatic drainage of tumours, which promote nanoparticle accumulation and uptake[4]. Stimulus-responsive nanoparticles can enhance targeted delivery and avoid undesirable exposure, further improving efficacy[5]. Triggers for nanoparticle disassembly and drug release include acidity, protease activity and redox imbalance within tumours. Inflammation and infection also acidify extracellular microenvironments[6–9]. However, few nanoparticle-based chemotherapeutics have been tested in patients, and the rationale has been questioned[10].

Acidification of intracellular compartments, including endosomes and lysosomes, can be exploited for intracellular drug delivery[11]. For applications that require therapeutics to reach cytoplasmic or nuclear targets, the necessity and challenges of endosomal escape limit the usefulness of nanoparticle-mediated endosomal delivery[12]. The identification of drug targets within endosomes provides opportunities for harnessing pH-sensitive materials to chaperone drugs to intracellular targets. The realization that G protein-coupled receptors (GPCRs) can signal from endosomes has created opportunities to improve drug efficacy and repurpose medicines[13].

GPCRs are a large (>800) family of seven transmembrane proteins that control most physiological and pathological processes, and such GPCRs are the target of more than 30% of therapeutic drugs[14]. GPCR signalling is not confined to the plasma membrane, but also occurs within endosomes[15,16]. Location-biased compounds favour interactions with GPCRs in subcellular locations, leading to distinct signals[17,18]. Endosomal signalling of the substance P (SP) neurokinin 1 receptor (NK_1R), calcitonin receptor-like receptor and protease-activated receptor-2 in primary sensory and spinal neurons mediates nociception[19–21]. Inhibitors of endocytosis and lipid-conjugated antagonists that target these receptors in endosomes provide effective anti-nociception[19–21]. Because these compounds are unlikely to be drug candidates, there remains the need to explore endosomal delivery of existing medicines. Endosomal delivery of GPCR ligands could enhance the treatment of many disorders[13].

Herein, we demonstrate that soft polymeric pH-responsive nanoparticles alter the distribution and efficacy of an FDA-approved NK_1R antagonist, aprepitant, which is used to treat emesis but has

---

[1]Monash Institute of Pharmaceutical Sciences, Monash University, Parkville, Victoria, Australia. [2]Australian Research Council Centre of Excellence in Convergent Bio-Nano Science and Technology, Monash University, Parkville, Victoria, Australia. [3]Monash Biomedicine Discovery Institute, Monash University, Melbourne, Victoria, Australia. [4]Laboratory of Neurobiology, Center for the Development of Nanoscience and Nanotechnology (CEDENNA), University of Santiago de Chile, Santiago, Chile. [5]Departments of Surgery and Pharmacology, Columbia University Vagelos College of Physicians and Surgeons, Columbia University in the City of New York, New York , NY, USA. [6]Bluestone Centre for Clinical Research, New York University College of Dentistry, New York, NY, USA. [7]Australian Institute for Bioengineering and Nanotechnology, University of Queensland, Brisbane, Queensland, Australia. [8]Department of Pharmacology and Therapeutics, University of Melbourne, Parkville, Victoria, Australia. *e-mail: nicholas.veldhuis@monash.edu; thomas.p.davis@monash.edu; nwb2@nyu.edu

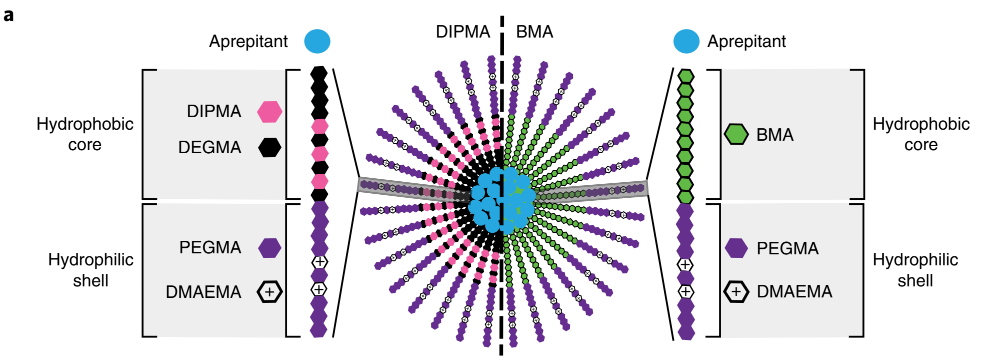

b

Nanoparticle	Diameter (nm)	ζ potential (mV)	Aprepitant loading (%)	CMC (μg ml^{-1})	pH of disassembly
DIPMA-AP	40.4 ± 5.1 (30)	−0.2 ± 1.6 (18)	57.8 ± 11.1 (27)	2.4 ± 0.5 (3)	6.08 ± 0.064 (3)
DIPMA-Ø	37.0 ± 4.2 (18)	−0.5 ± 2.0 (11)	NA	1.9 ± 1.1 (3)	6.08 ± 0.064 (3)
BMA-AP	28.0 ± 2.5 (27)	−1.1 ± 2.8 (16)	61.5 ± 12.5 (10)	1.5 ± 0.8 (3)	NA
BMA-Ø	30.0 ± 4.4 (13)	−0.3 ± 0.3 (11)	NA	1.5 ± 1.1 (3)	NA

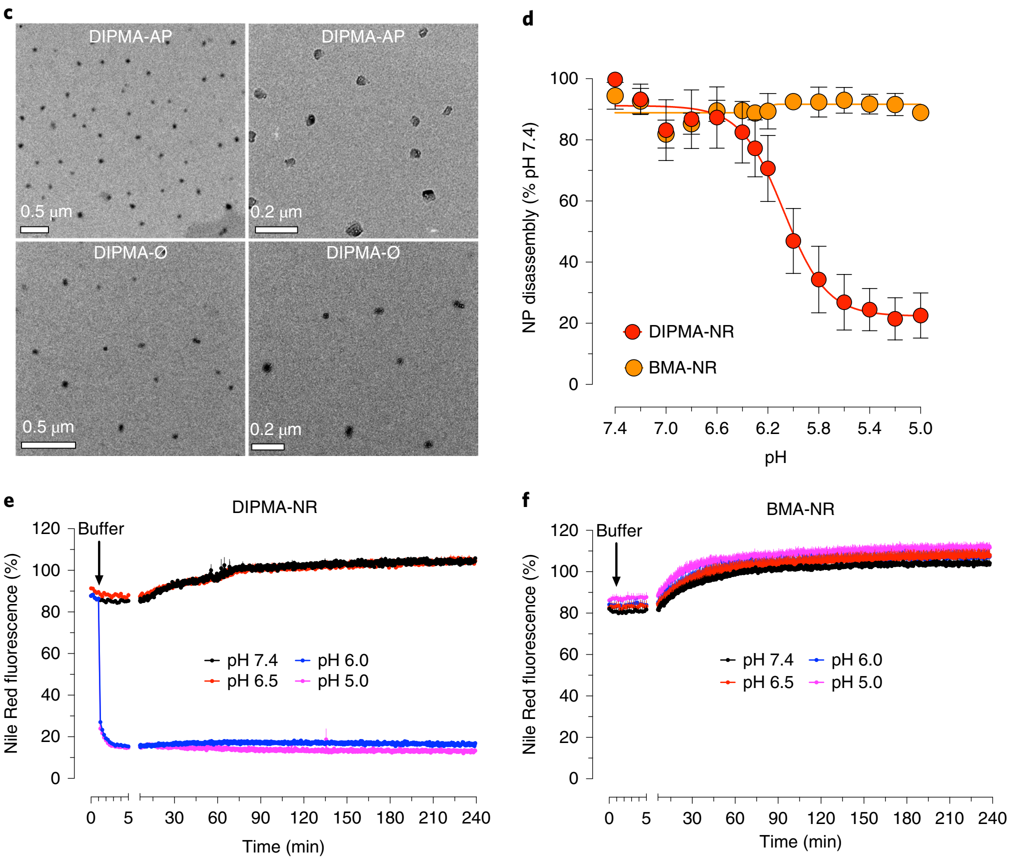

Fig. 1 | Characterization of DIPMA and BMA nanoparticles. **a**, Structure of pH-responsive (DIPMA) and pH-non-responsive (BMA) nanoparticles. Nanoparticles share the same hydrophilic shell of P(PEGMA-co-DMAEMA) but have different hydrophobic cores: P(DIPMA-co-DEGMA) or BMA. **b**, Properties of DIPMA-Ø, BMA-Ø, DIPMA-AP and BMA-AP (100 nM aprepitant) nanoparticles. Ø, empty; AP, aprepitant. Data are presented as mean ± s.d. Values in parenthesis indicate the number (*n*) of independent experimental replicates. Aprepitant incorporation for nanoparticles containing lower aprepitant concentrations (% initial aprepitant (mean ± s.d.)): DIPMA-AP, 50 nM, 58.4 ± 7.7, *n* = 9 experiments; 25 nM, 62.6 ± 16.3, *n* = 9; BMA-AP, 50 nM, 62.4 ± 11.7, *n* = 9; 25 nM, 65.2 ± 16.2, *n* = 9. CMC, critical micellar concentration. NA, not applicable. **c**, Transmission electron microscopy images of DIPMA-AP (100 nM aprepitant) and DIPMA-Ø nanoparticles. Representative images of *n* = 2 independent experiments are shown. **d**, pH-dependent Nile Red (NR) quenching of DIPMA-NR and BMA-NR nanoparticles in vitro, indicative of nanoparticle disassembly. Data are presented as mean ± s.e.m., *n* = 3 independent experiments, triplicate observations. **e**,**f**, Time course of NR quenching of DIPMA-NR (**e**) and BMA-NR (**f**) nanoparticles in vitro and pH levels of 7.4, 6.5, 6.0 and 5.0. Data are presented as mean ± s.e.m., *n* = 3 independent experiments, triplicate observations.

failed in trials for other indications[22–24]. Nanoparticles delivered aprepitant to endosomes containing activated NK$_1$R, and induced a more complete and sustained anti-nociception in preclinical models than conventional therapies, including opioids. Nanoparticle delivery minimized the dose of aprepitant required for anti-nociception, which might avoid off-target effects. Thus, nanoparticles have potential beyond bulk drug delivery for cancer therapy and in fields where, to date, their applicability has been unrecognized. The use of nanoparticles to direct drugs to subcellular compartments from which GPCRs generate disease-relevant signals has broad applicability. The discovery that nanoparticle encapsulation enhances and prolongs analgesia provides opportunities for developing much-needed non-opioid therapies for pain.

Results

Synthesis and pH-dependent disassembly of nanoparticles. Diblock copolymers were synthesized with the same hydrophilic shell of P(PEGMA-co-DMAEMA), but with different hydrophobic cores of P(DIPMA-co-DEGMA) to form pH-responsive nanoparticles or P(BMA) to form non-pH-responsive nanoparticles (DIPMA or BMA nanoparticles, respectively; Fig. 1a and Supplementary Fig. 1a,b). Gel permeation chromatography and ^{1}H-NMR confirmed the molecular weight and composition of the nanoparticles (Supplementary Fig. 1c,d).

Nanoparticles were self-assembled with aprepitant (MK-869[22]), a hydrophobic NK$_1$R antagonist, forming DIPMA-aprepitant (DIPMA-AP) and BMA-aprepitant (BMA-AP) (Fig. 1b). To generate nanoparticles for delivery of graded concentrations of aprepitant (25, 50 or 100 nM) but a constant concentration of polymer, nanoparticles were self-assembled with graded amounts of aprepitant and a fixed amount of polymer. For most studies, nanoparticles containing 100 nM aprepitant were used, with similar incorporation efficiency (Fig. 1b).

Nanoparticles are dynamic structures that remain assembled when the concentration of polymer exceeds the critical micelle concentration (Supplementary Fig. 2). The critical micellar concentrations of DIPMA-empty (DIPMA-Ø), BMA-Ø, DIPMA-AP and BMA-AP were comparable (Fig. 1b). Nanoparticles were uniformly spherical, with similar diameters and ζ potentials (Fig. 1b).

To examine pH-dependent disassembly, nanoparticles were loaded with Nile Red (NR), which fluoresces only in the hydrophobic core. Fluorescence quenching in aqueous solutions of graded pH was used to evaluate nanoparticle disassembly. DIPMA-NR fluorescence declined with increasing acidity (50% decrease, pH 6.08 ± 0.06; Fig. 1d), consistent with the protonation of the DIPMA tertiary amine ($pK_a = 6.1$), charge repulsion and disassembly (Supplementary Fig. 2). BMA-NR fluorescence was unaffected by acidification (Fig. 1d). DIPMA-NR fluorescence declined to minimum levels within 4 min at pH 6.0 or 5.0 (Fig. 1e) whereas BMA-NR did not decline in acidic buffers (Fig. 1f). There was a small unexplainable increase in DIPMA-NR fluorescence at pH 6.5 or 7.4 and in BMA-NR fluorescence at pH 7.4, 6.5, 6.0 or 5.0.

Uptake and disassembly of nanoparticles in cells. Cellular uptake and trafficking of DIPMA nanoparticles labelled with cyanine 5 (DIPMA-Cy5) were examined by confocal microscopy in HEK-293 cells. NK$_1$R endosomal trafficking and signalling are similar in HEK-293 cells and spinal neurons[19]. After incubation for 30 or 60 min, DIPMA-Cy5 nanoparticles were localized to early and late endosomes (Fig. 2a, Supplementary Fig. 3a and Supplementary Videos 1 and 2). HEK-293 cells expressing rat (r)NK$_1$R-GFP were treated with SP to evoke NK$_1$R endocytosis. At 30 and 60 min after SP, DIPMA-Cy5 nanoparticles co-localized with rNK$_1$R-GFP in endosomes (Fig. 2b, Supplementary Fig. 3b and Supplementary Video 3). Determination of the Manders overlap coefficient[25] confirmed DIPMA-Cy5 co-localization with rNK$_1$R-GFP, Rab5a-GFP and Rab7a-GFP (Fig. 2c).

The uptake and disassembly of DIPMA nanoparticles loaded with Coumarin 153 (DIPMA-CO), which fluoresces in an aqueous environment but not in the hydrophobic core, were examined by confocal microscopy and high content imaging. When DIPMA-CO nanoparticles were incubated with HEK-293 cells, there was an increase in intracellular fluorescence from 1 to 10 min that continued for 30 min (Fig. 2e,f). Inhibitors of clathrin (PitStop2)[26], dynamin (Dyngo4a)[27] and endosomal acidification (Bafilomycin A1, which inhibits the vacuolar H$^+$ATPase; NH$_4$Cl, a lysosomotropic weak base) attenuated cellular fluorescence (Fig. 2c–f). These results are consistent with clathrin- and dynamin-dependent endocytosis, and pH-dependent disassembly of DIPMA nanoparticles in acidified endosomes. When non-pH-disassembling BMA-Cy5 nanoparticles were incubated with HEK-293 cells, there was a smaller increase in fluorescence from 1 to 10 min (Fig. 2d,e). Although PitStop2 and Dyngo4a suppressed the fluorescence, Bafilomycin A1 and NH$_4$Cl had no effect (Fig. 2d–f). BMA nanoparticles also enter cells by clathrin- and dynamin-dependent endocytosis, and release cargo by mechanisms that do not require endosomal acidification.

Biodistribution and delivery of nanoparticle cargo. To examine nanoparticle distribution in vivo, DIPMA-Cy5 or BMA-Cy5 nanoparticles were injected intrathecally (L4/L5), which delivers NK$_1$R antagonists to spinal neurons[19]. Non-invasive imaging revealed that Cy5 fluorescence, which might be incorporated within nanoparticles or disassembled fluorophore, remained within the injection site for up to 24 h (Fig. 3a,b). Confocal imaging showed that DIPMA-Cy5 and BMA-Cy5 nanoparticles accumulated in a perinuclear region in cells throughout laminae I, II and III of the dorsal horn (Fig. 3c and Supplementary Videos 4 and 5). DIPMA-Cy5 nanoparticles were present in neurons, identified by co-localization with the neuronal marker PGP9.5, although detailed analysis of the cellular distribution was not possible due to loss of nanoparticle fluorescence during immunostaining.

To evaluate the usefulness of nanoparticles for drug delivery, free aprepitant, DIPMA-AP or BMA-AP was injected intrathecally to mice, then liquid chromatography–mass spectrometry (LC-MS) was used to quantify aprepitant in the spinal cord. At 1 h after injection, the spinal aprepitant concentration was approximately twofold higher for DIPMA-AP than for BMA-AP and approximately fourfold higher than for free aprepitant (Fig. 3d). At 4 h, spinal aprepitant was similar for DIPMA-AP and BMA-AP, and almost undetectable for free aprepitant. Thus, nanoparticle encapsulation causes retention of aprepitant within the spinal cord.

Effects of nanoparticles on nociception. To examine the hypothesis that incorporation into nanoparticles enhances the anti-nociceptive actions of aprepitant due to delivery to spinal neurons, the efficacy of free or nanoparticle-encapsulated aprepitant was evaluated in preclinical models of nociceptive, inflammatory and neuropathic pain (Fig. 4d). Nanoparticles, free aprepitant or vehicle was injected intrathecally before or after intraplanar injection of algogens or nerve injury. Mechanical nociception was studied in mice by measuring withdrawal responses to stimulation of the plantar surface of the hindpaw with calibrated von Frey filaments (VFFs) and in rats by measuring the pressure that induced withdrawal of the hindpaw (Randall–Selitto test).

Assessment of nociception requires normal motor coordination, which allows paw withdrawal from painful stimuli. The latency to fall from a rotarod was the same in mice after intrathecal injection of vehicle, DIPMA-AP, BMA-AP or DIPMA-Ø (Supplementary Fig. 4). Nanoparticles do not interfere with motor coordination.

Capsaicin. Intraplantar capsaicin activates transient receptor potential-1 on primary sensory neurons to release SP in the dorsal horn, which evokes NK$_1$R endocytosis in spinal neurons and allodynia[19,28]. In mice pretreated with intrathecal vehicle or DIPMA-Ø, capsaicin decreased the VFF threshold from 0.5 to 4 h, which returned to baseline after 24 h (Fig. 4b,c). Free aprepitant (100 nM) and DIPMA-Ø mixed with free aprepitant (100 nM) caused a modest anti-nociception after 1 h (16 ± 4 and 15 ± 3% inhibition, respectively). BMA-AP

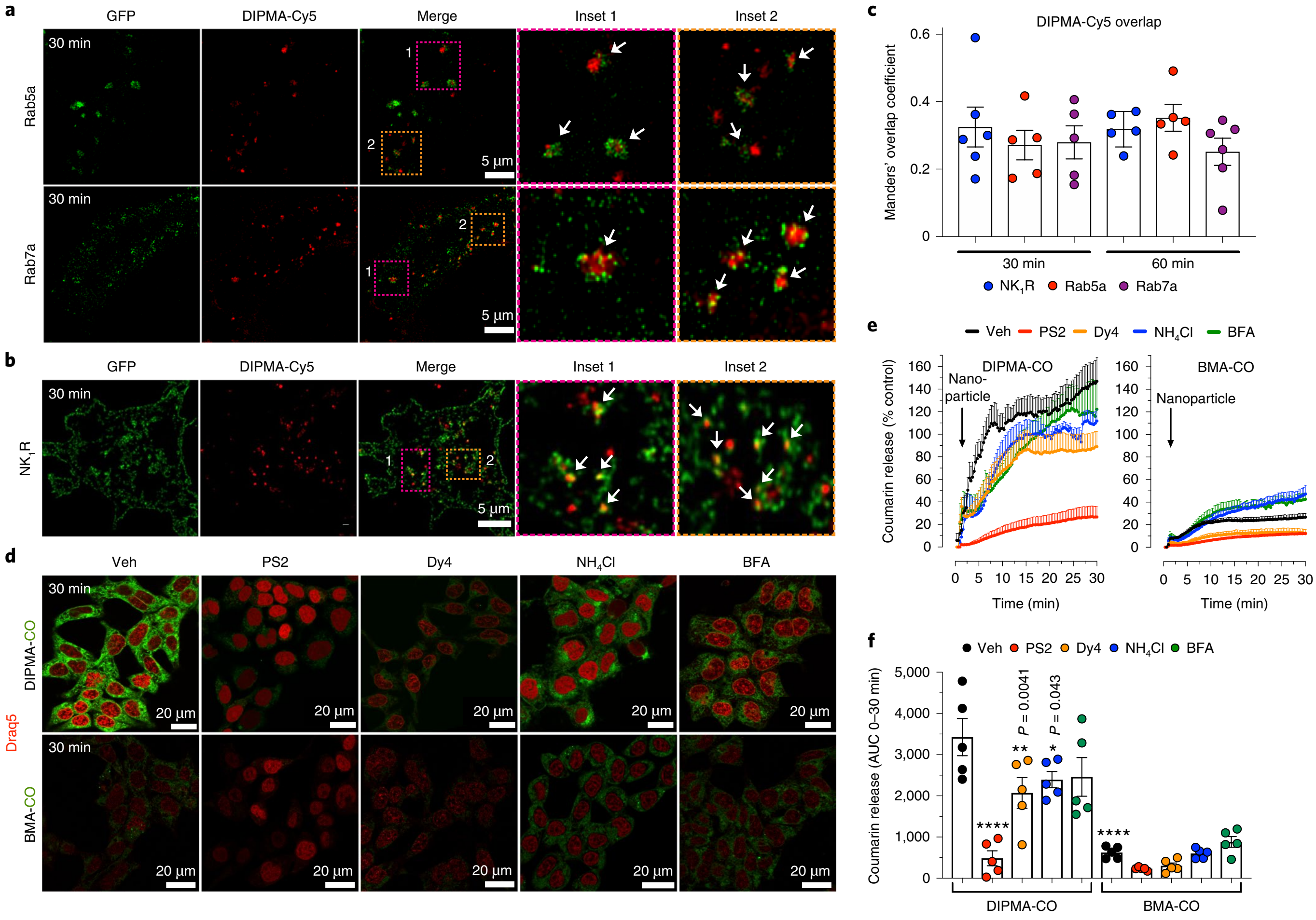

Fig. 2 | Uptake and disassembly of DIPMA and BMA nanoparticles in HEK-293 cells. a, To examine trafficking to endosomes, DIPMA-Cy5 nanoparticles were incubated with HEK-293 cells expressing Rab5a-GFP, which identifies early endosomes, or Rab7a-GFP, which marks late endosomes. Images show localization of DIPMA-Cy5 nanoparticles in Rab5a-GFP-positive early endosomes and Rab7a-GFP-positive late endosomes after incubation with HEK-293 cells for 30 min. Representative images of $n = 5$ independent experiments are shown. **b**, To determine whether nanoparticles traffic to endosomes containing the NK_1R, DIPMA-Cy5 nanoparticles were incubated with HEK-293 cells transfected with rNK_1R-GFP; after 30 min, cells were challenged with 10 nM SP to promote internalization of rNK_1R-GFP. The images show co-localization of DIPMA-Cy5 nanoparticles and NK_1R-GFP in HEK-rNK_1R cells at 30 min after stimulation with SP to induce NK_1R endocytosis. Representative images of $n = 5$ independent experiments are shown. **c**, Manders overlap coefficient to assess the degree of co-localization of DIPMA-Cy5 with NK_1R-GFP, Rab5a-GFP and Rab5a-GFP at 30 min and 60 min. Data are presented as mean ± s.e.m., $n = 5$ independent experiments. **d–f**, Uptake of DIPMA-CO and BMA-CO nanoparticles into HEK-293 cells. **d**, Representative images of $n = 5$ independent experiments at 30 min after addition of DIPMA-CO or BMA-CO nanoparticles; Coumarin 153 is green, Draq5 nuclear stain is red. **e**,**f**, Kinetic analysis and quantification of uptake and disassembly of DIPMA-CO and MBA-CO nanoparticles assessed by Coumarin 153 fluorescence. In cells treated with DIPMA-CO, Coumarin 153 rapidly accumulated in the cytosol, indicative of rapid nanoparticle disassembly. PitStop2 (PS2), Dyngo4a (Dy4), Bafilomycin A1 (BFA) and NH_4Cl inhibited the appearance of Coumarin 153 and nanoparticle disassembly. In cells treated with BMA-CO, Coumarin 153 slowly accumulated in the cytosol, indicative of minimal nanoparticle disassembly. PitStop2 and Dyngo4a, but not Bafilomycin A1 and NH_4Cl, inhibited appearance of Coumarin 153 and nanoparticle disassembly. Data are presented as mean ± s.e.m., $n = 5$ (**e**,**f**) independent experiments. $^*P < 0.05$, $^{**}P < 0.01$, $^{****}P < 0.0001$ compared to DIPMA-CO treated with vehicle. Two-way analysis of variance (ANOVA), Dunnett's post-hoc test.

(100 nM aprepitant) had a similar effect after 0.5–1 h, although the effect was sustained for 2 h. DIPMA-AP (100 nM aprepitant) caused marked anti-nociception at 0.5–1 h (1 h, 34 ± 3% inhibition) that was sustained for 4 h (35 ± 2% inhibition).

Complete Freund's adjuvant. Intraplantar complete Freund's adjuvant (CFA) causes sustained mechanical allodynia and NK_1R endocytosis in spinal neurons[19,29], which allowed examination of the capacity of nanoparticle-encapsulated aprepitant to reverse inflammatory nociception. By 48 h after CFA injection, there was a marked decrease in VFF threshold (Fig. 4d–f). Intrathecal vehicle did not affect mechanical hyperalgesia, which persisted for 24 h. Aprepitant (100 and 300 nM) dose-dependently reversed hyperalgesia for 2–3 h (1.5 h, % inhibition: 100 nM, 30 ± 6; 300 nM, 47 ± 3%). BMA-AP (100 nM aprepitant) was as effective as free aprepitant (300 nM). DIPMA-AP (100 nM aprepitant) produced a larger inhibition of allodynia than the same dose of free aprepitant (1.5 h, % inhibition: 54 ± 4%), and the inhibition was maintained for 6 h, when other treatments were ineffective. Although systemic morphine (3 mg kg^{-1}, intraperitoneal) fully reversed the mechanical allodynia after 0.5 h, the effect waned after 3 h.

Nerve injury. The sural nerve spared (SNS) model produces a mechanical hyperalgesia in rats for >50 days[30,31], which permitted examination of the efficacy of nanoparticle-encapsulated aprepitant to relieve chronic neuropathic nociception in another species.

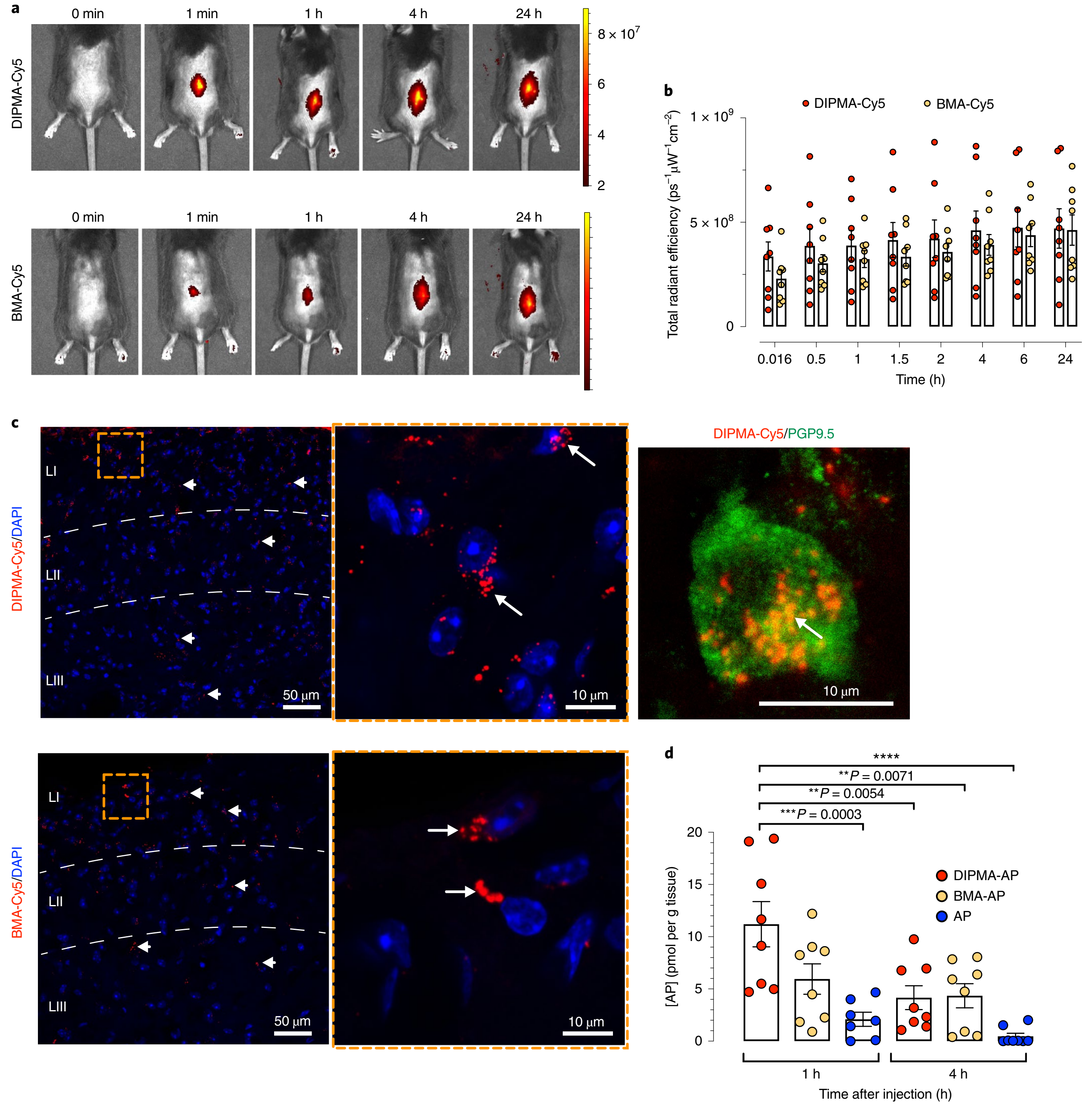

Fig. 3 | Biodistribution and cellular uptake of nanoparticles and aprepitant delivery. a, Distribution of DIPMA-Cy5 and BMA-Cy5 nanoparticles at various times after intrathecal injection of mice. Representative images of experiments on $n = 8$ mice are shown. Scale bar, Cy5 fluorescence intensity measured as radiant efficiency with units $\mathrm{ps^{-1}\mu W^{-1}cm^{-2}}$. p, photons. s, seconds. W, watts. **b**, Quantification of the distribution of DIPMA-Cy5 and BMA-Cy5-nanoparticles at various times after intrathecal injection of mice assessed as the radiant efficiency of the images. Data are presented as mean ± s.e.m., $n = 8$ mice. **c**, Localization of DIPMA-Cy5 and BMA-Cy5 nanoparticles in the dorsal horn (laminae, LI–III) 1 h after intrathecal injection. The inset to the right shows accumulation of DIPMA-Cy5 nanoparticles in a perinuclear region of a spinal neuron, as confirmed by labelling with anti-PGP9.5. Representative images from $n = 5$ mice. **d**, Aprepitant concentrations in the spinal cord measured 1 h and 4 h after intrathecal injection of DIPMA-AP, BMA-AP or free aprepitant (100 nM). Data are presented as mean ± s.e.m.; $n = 7$ mice for aprepitant at 1 h and $n = 8$ mice for aprepitant at 4 h (and DIPMA-AP and BMA-AP at 1 h and 4 h). $^{**}P < 0.01$, $^{***}P < 0.001$, $^{****}P < 0.0001$. Two-way ANOVA, Tukey's post-hoc test.

To confirm activation of the SP/NK$_1$R system, we localized NK$_1$R immunoreactivity (IR) in spinal neurons at 10 days after sham or SNS surgery by immunofluorescence. In sham rats, NK$_1$R-IR was confined to the plasma membrane of the soma and neurites of lamina I neurons (Supplementary Fig. 5a and Supplementary Video 6). In SNS rats, NK$_1$R-IR was detected in endosomes of ipsilateral lamina I neurons but was localized to the plasma membrane of contralateral lamina I neurons (Supplementary Fig. 5a and Supplementary

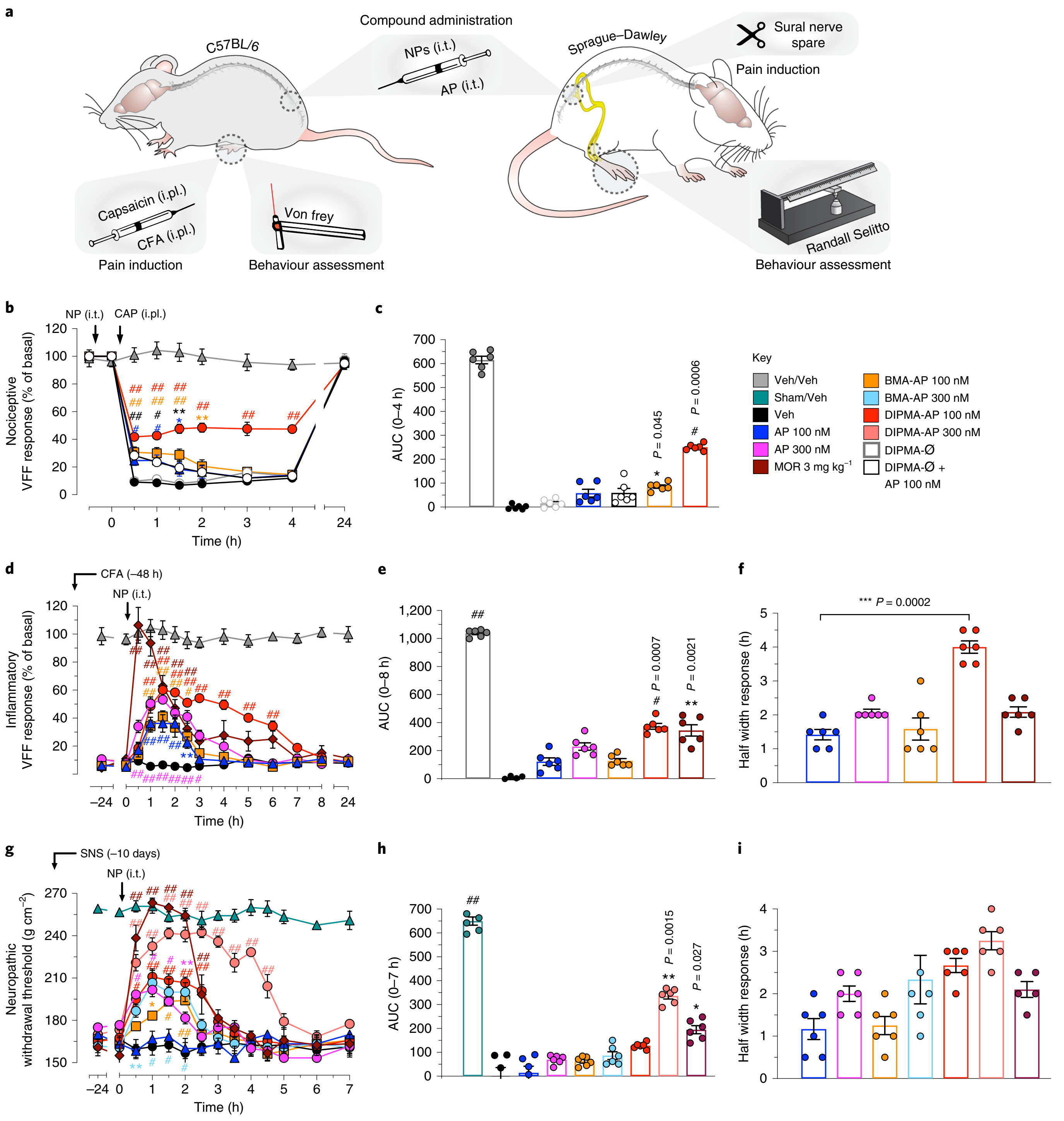

Fig. 4 | Effects of nanoparticles on nociceptive, inflammatory and neuropathic nociception. **a**, Preclinical models of nociceptive, inflammatory and neuropathic pain. In the capsaicin-evoked model of acute nociceptive pain in mice, AP, nanoparticles (NPs) or vehicle (Veh) (5 µl) was injected intrathecally (i.t.) 30 min before intraplantar (i.pl.) injection of capsaicin (CAP) or Veh. Withdrawal responses were measured to stimulation of the plantar surface of the injected hindpaw with VFF. In the complete Freund's adjuvant (CFA)-evoked model of sustained inflammatory nociceptifon in mice, CFA or Veh was administered by i.pl. injection; after 48 h, AP, NP or Veh was administered by i.t. injection (5 µl). Withdrawal responses were measured to VFF stimulation of the plantar surface of the injected hindpaw. In the sural nerve spared (SNS) model, rats underwent SNS or sham surgery; after 10 days, AP, NP or Veh (10 µl) was injected i.t. Withdrawal responses were assessed using the Randall–Selitto test. **b**,**c**, Capsaicin-induced mechanical allodynia in mice: kinetic VFF response (**b**) and integrated response as area under the curve (AUC) (**c**). **d**–**f**, CFA-evoked mechanical hyperalgesia in mice: VFF response (**d**), AUC (**e**) and half width response (**f**). **g**–**i**, SNS-evoked mechanical hyperalgesia in rats: neuropathic withdrawal threshold response (**g**), AUC (**h**) and half width response (**i**). Data are presented as mean ± s.e.m., *n* = 6 animals for all experiments. $^{*}P < 0.05$, $^{**}P < 0.005$, $^{***,\#}P < 0.001$, $^{\#\#}P < 0.0001$ compared to vehicle. Two-way ANOVA, Dunnett's post-hoc test (**b**,**d**,**g**); one-way ANOVA, Dunn's post-hoc test (**c**,**e**,**f**,**h**,**i**).

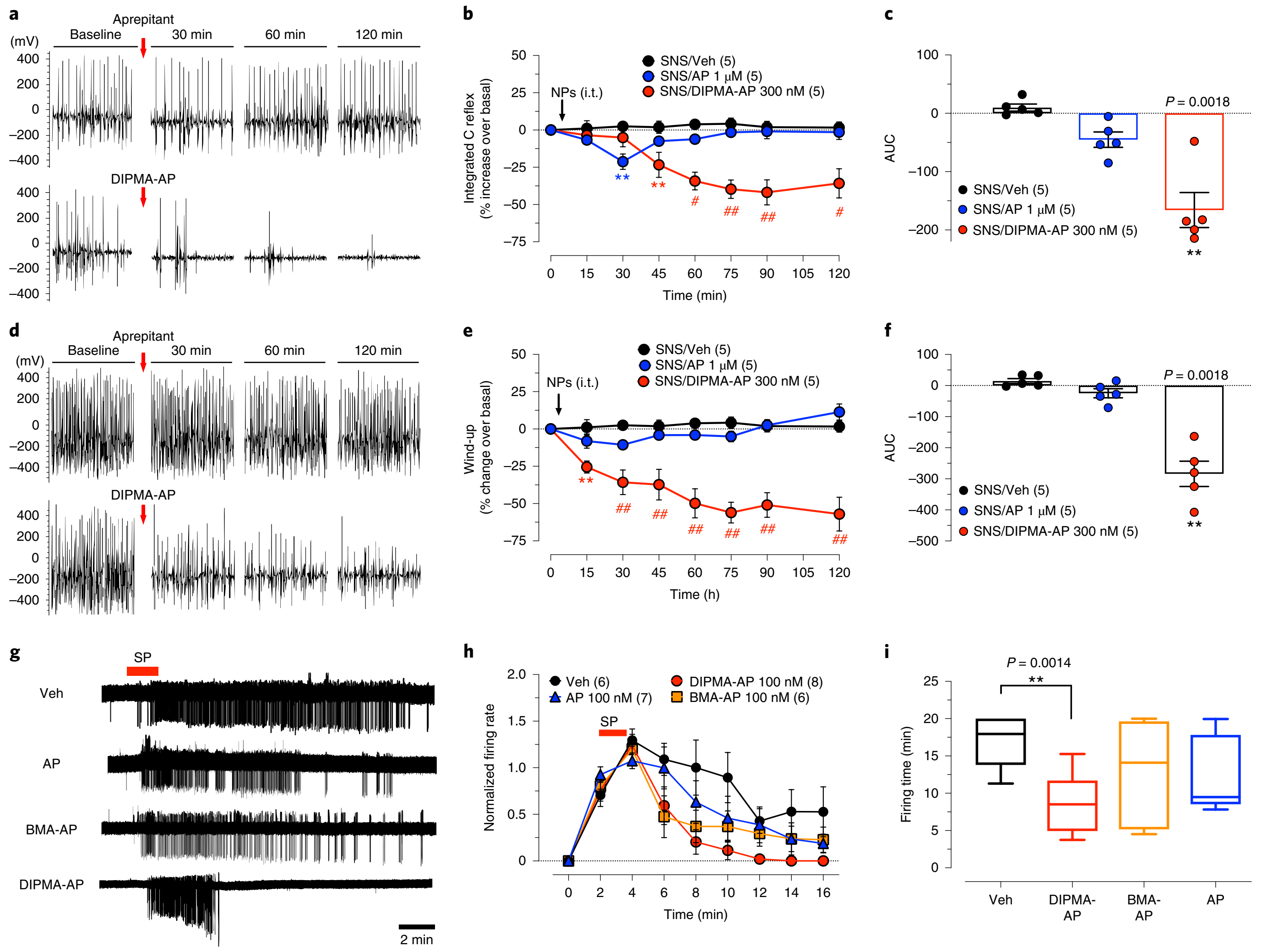

Fig. 5 | Sensitization and activation of nociceptive transmission. **a**–**f**, C-fibre reflex and wind-up in SNS rats. C-fibre reflexes (**a**–**c**) and wind-up (**d**–**f**) were measured at 10 days after SNS. AP, DIPMA-AP NP or Veh was administered by i.t. injection (10 μl). **a**,**d**, Representative recordings comparing AP and DIPMA-AP. **b**,**e**, Time course of effects. Data are presented as mean ± s.e.m., $n = 5$ rats per group (in parentheses). $^{**}P < 0.005$, $^{\#}P < 0.001$, $^{\#\#}P < 0.0001$ compared to vehicle. Two-way ANOVA, Dunn's post-hoc test. **c**,**f**, Integrated responses (AUC, $n = 5$ rats). $^{**}P < 0.005$, vehicle compared to DIPMA-AP, one-way ANOVA, Dunn's post-hoc test. **g**–**i**, Cell-attached patch-clamp recordings of SP-induced excitation of lamina I neurons in slices of rat spinal cord. Tissues were preincubated with AP, NP or Veh, and then superfused with SP (1 μM, 2 min). Action potential firing was measured: representative traces (**g**); normalized firing rate (**h**); firing time (**i**). Data are presented as mean ± s.e.m., $n = 6$ for rats for Veh, $n = 7$ rats for AP, $n = 8$ rats for DIPMA-AP and $n = 6$ rats for BMA-AP. $^{**}P = 0.005$, vehicle compared to DIPMA-AP. Unpaired *t*-test (two-sided).

Video 7). Quantification confirmed NK$_1$R endocytosis. These results suggest activation of the SP/NK$_1$R system, and are consistent with NK$_1$R upregulation in the dorsal horn during neuropathic pain[32].

At 10 days, SNS reduced the pressure that induced withdrawal of the hindpaw when compared to sham-operated rats, indicating mechanical hyperalgesia (Fig. 4g–i). Intrathecal vehicle did not affect mechanical hyperalgesia, which persisted for 7 h. Although low doses of aprepitant (100 nM) did not modify the withdrawal threshold, higher doses (300 nM) inhibited withdrawal thresholds after 0.5 h to a maximum of 40 ± 2% inhibition after 1 h, with return to baseline after 2.5 h. Aprepitant (1 μM) almost fully reversed hyperalgesia after 1 h (75 ± 4% inhibition), although hyperalgesia returned to baseline after 3 h (Supplementary Fig. 4). BMA-AP (100 and 300 nM aprepitant) inhibited hyperalgesia to a similar degree as free aprepitant (300 nM). DIPMA-AP (100 and 300 nM aprepitant) strongly reversed hyperalgesia, with almost complete inhibition after 1.5 h (300 nM, 80 ± 4% inhibition) and maintenance for 4.5 h, when none of the other treatments were effective. DIPMA-AP (500 nM) provided complete relief from hyperalgesia for 4.5 h (Supplementary Fig. 6). Although morphine fully reversed hyperalgesia for 2 h, the effect was absent after 2.5 h.

The enhanced effects of DIPMA-AP could be related to delivery and retention of aprepitant in endosomes of spinal neurons containing activated NK$_1$R, and the continued release of aprepitant as nanoparticles encounter increasingly acidified endosomal compartments. The anti-nociceptive actions of BMA-AP might be due to non-pH-responsive aprepitant release by unknown mechanisms.

Effects of nanoparticles on neuronal activity. Nociceptor C-fibres transmit painful stimuli centrally by releasing SP, calcitonin gene related peptide and glutamate in the dorsal horn[33]. Central sensitization (that is, amplified nociceptive transmission, decreased nociceptive threshold) is a hallmark of chronic pain. To examine sensitization, we measured the threshold current required to activate C-fibre reflexes, and assessed wind-up, a frequency-dependent increase in the excitability of spinal cord neurons induced by electrical stimulation of C-fibres[31]. The threshold current required for activation of the C-fibre-mediated reflexes in the ipsilateral biceps femoris muscle was reduced in SNS rats compared to sham controls (SNS, 3.2 ± 2.8 mA; sham, 10.3 ± 1.2 mA, $P < 0.05$), consistent with sensitization. Repeated 0.1 Hz electrical stimuli caused a constant and stable C-reflex activity over time, while repeated 1.0 Hz stimuli evoked a progressive increase in C-reflex frequency or wind-up (Fig. 5a–f). In SNS rats, intrathecal aprepitant (1 μM) decreased the C-reflex only at 30 min, but did not affect wind-up. In contrast, DIPMA-AP (300 nM aprepitant) decreased C-reflex within 45 min and wind-up activity within 15 min, and inhibited responses for the duration of observations (120 min).

The effectiveness of DIPMA-AP to suppress nociception could be due to antagonism of sustained SP-induced excitation of spinal neurons, which requires NK_1R signalling from endosomes[19]. To examine this possibility, we made cell-attached patch-clamp recordings from lamina I neurons in slices of rat spinal cord. In vehicle-treated slices, SP (1 μM, 2 min) caused a rapid onset in action potential firing that persisted for 16 min after washout (Fig. 5g–i). Aprepitant (100 nM) or BMA-AP (100 nM aprepitant) had minimal effect on the onset, rate or duration of SP-induced firing. DIPMA-AP (100 nM) did not affect the initial onset of SP-evoked firing, but inhibited the rate of discharge after washout and the duration of excitation. When delivered in pH-responsive nanoparticles, aprepitant antagonizes endosomal NK_1R signals that drive sustained excitation of spinal neurons.

Effects of nanoparticles on endosomal signalling. Endosomal NK_1R signalling in HEK-293 cells activates nuclear extracellular signal-regulated kinase (ERK), which mediates SP-induced excitation of spinal neurons[19]. Painful stimuli (capsaicin) evoke phosphorylation of ERK (pERK) in spinal neurons, which requires NK_1R endocytosis[19]. We examined whether nanoparticle-encapsulated aprepitant prevents capsaicin-evoked ERK activation in spinal neurons in vivo. Capsaicin induced a 3.9-fold increase in the number of pERK-IR expressing neurons in laminae I, II and III of the ipsilateral but not contralateral dorsal horn (Fig. 6a,b). Free aprepitant caused a 43% reduction, BMA-AP a 63% reduction and DIPMA-AP an 81% reduction in pERK-IR neurons. The more complete inhibitory action of DIPMA-AP on ERK signalling concurs with its enhanced anti-nociceptive actions.

ERK signalling in vitro was studied in primary cultures of mouse striatal neurons. SP increased $[Ca^{2+}]_i$ in striatal neurons; pretreatment with aprepitant abolished responses, which are NK_1R-dependent (Supplementary Fig. 7a,b). After neurons were incubated with DIPMA-Cy5 nanoparticles and SP (100 nM) for 30 min, nanoparticles were detected in close proximity to endosomes containing NK_1R-IR (Fig. 6c). SP (100 nM) and phorbol 12,13-dibutyrate (positive control, 10 μM) stimulated nuclear pERK in striatal neurons (Fig. 6d and Supplementary Fig. 7c). DIPMA-AP reduced responses to basal levels, whereas free aprepitant was ineffective.

Förster resonance energy transfer (FRET) biosensors allow analysis of signalling in living cells with high spatiotemporal fidelity[34]. To examine activation of nuclear ERK, HEK-293 cells expressing human (h) NK_1R were transfected with NucEKAR (nuclear ERK biosensor). SP (100 pM–1 μM) activated nuclear ERK (half-maximal effective concentration, EC_{50}, of 5.9 nM) (Supplementary Fig. 8a,b). Aprepitant inhibited the response to 5 nM SP (~EC_{50}), but only at high concentrations (0.1, 1 and 10 μM; half-maximal inhibitory concentration, IC_{50}, of 45 nM) (Supplementary Fig. 8c,d). To determine the requirement for NK_1R endosomal signalling, we transfected HEK-hNK_1R cells with wild-type dynamin or dominant negative dynamin K44E, which inhibits NK_1R endocytosis[19]. Compared to cells expressing wild-type dynamin, dynamin K44E attenuated ERK responses to all concentrations of SP, abolished the response to 10 nM SP, and reduced the potency of SP by approximately twofold and the efficacy by ~30% (Supplementary Fig. 8e–g).

DIPMA-Ø or BMA-Ø nanoparticles (10, 20 and 30 μg ml^{-1}, 30 min) did not activate nuclear ERK in HEK-293 cells (Supplementary Fig. 8h). DIPMA-Ø nanoparticles had no effect on SP (5 nM) stimulated activation of nuclear ERK in HEK-hNK_1R cells, although 30 μg ml^{-1} BMA had a small inhibitory effect (Supplementary Fig. 8i). DIPMA-Ø or BMA-Ø nanoparticles (1–100 μg ml^{-1}, 24 or 48 h) did not affect the viability of HEK-293 cells (Supplementary Fig. 8j).

To compare the capacity of free aprepitant and nanoparticle-encapsulated aprepitant to antagonize the NK_1R in endosomes, we measured SP-induced activation of nuclear ERK in HEK-hNK_1R cells. Cells were preincubated with vehicle, free aprepitant or DIPMA-AP (25, 50 and 100 nM aprepitant) for 30 min, and were challenged with SP (5 nM). In vehicle-treated cells, SP stimulated a rapid and sustained activation of nuclear ERK (Fig. 6e,g). At all concentrations, DIPMA-AP more completely inhibited this response than free aprepitant. To compare sustained antagonism of endosomal NK_1R, cells were preincubated with vehicle, aprepitant or DIPMA-AP (100 nM) for 30 min, washed, recovered in medium without antagonist for 30 or 120 min, and then challenged with SP. Free aprepitant was now inactive, whereas DIPMA-AP (100 nM) abolished SP-induced activation of nuclear ERK (Fig. 6f–h). Although BMA-AP was less efficacious than DIPMA-AP in assays of nociception and ERK activity in spi-

Fig. 6 | Antagonism of NK_1R signalling in endosomes. a,**b**, Localization of pERK in the spinal cord: representative images (a) and the number of pERK-IR neurons per section (**b**). AP, BMA-AP, DIPMA-AP or Veh was injected i.t. into mice. After 30 min, CAP or Veh was administered by i.pl. injection. After 4 h, the spinal cord was collected for localization of pERK-IR or NeuN-IR (pan-neuronal marker). Data are presented as mean ± s.e.m., $n = 5$ mice for Veh/Veh, Veh/CAP, AP/CAP, DIPMA-AP/CAP groups or $n = 6$ mice for BMA-AP/CAP groups. $^{****}P < 0.0001$ compared to Veh/CAP; $^{\#\#\#\#}P < 0.0001$ compared to AP/CAP; $^{\dagger\dagger\dagger}P < 0.001$ compared to BMA-AP/CAP. One-way ANOVA, Bonferroni post-hoc test. **c**, Uptake of DIPMA-Cy5 nanoparticles in proximity to NK_1R-IR endosomes in cultured striatal neurons stimulated with 100 nM SP for 30 min. Representative images from $n = 4$ independent experiments are shown. **d**, Nuclear ERK signalling in primary cultures of mouse striatal neurons. Neurons were preincubated with Veh, free AP or DIPMA-AP (100 nM, 30 min), washed and recovered for 30 min. Neurons were challenged with SP (100 nM) or phorbol 12,13-dibutyrate (positive control, 10 μM) for 30 min. Nuclear pERK-IR and total ERK-IR were detected by immunofluorescence and confocal imaging, and expressed as the ratio of phospho-ERK1/2 (Thr202/Tyr204) to total ERK. Data are presented as mean ± s.e.m., $n = 41$ neurons for Veh/Veh, 68 neurons for SP/Veh, 46 neurons for SP/AP, 43 neurons for SP/DIPMA-AP, 52 neurons for SP/BMA-AP and 51 neurons for phorbol 12, 13-dibutyrate (PBDU, positive control), from four experiments (Veh, SP/AP, SP/DIPMA, SP/BMA) or six experiments (SP/Veh, PBDU) tested with independent nanoparticle preparations. $^{***}P < 0.001$. One-way ANOVA, Tukey's post-hoc test. **e**–**h**, Effects of free AP, DIPMA-AP and BMA-AP on SP-induced activation of nuclear ERK in HEK-hNK_1R cells. Cells were preincubated with Veh, AP or DIPMA-AP for 30 min; they were either challenged with SP (no recovery, **e**), or were washed, recovered in antagonist-free medium for 30 or 120 min and then challenged with SP (30 min recovery, **f**). **g**,**h**, AUC of ERK assays. Results are expressed as normalized values by the maximum nuclear ERK response to 1 μM phorbol 12,13-dibutyrate. Data are presented as mean ± s.e.m., $n = 7$ independent experiments for SP (no recovery and 30 min recovery) and AP (100 nM, no recovery), $n = 5$ independent experiments for 120 min recovery and $n = 6$ independent experiments for all other data points; observations are in triplicate. $^{**}P < 0.005$, $^{***}P < 0.001$, $^{\#\#}P < 0.0001$ compared to vehicle. One-way ANOVA, Tukey's post-hoc test.

nal neurons in vivo, BMA-AP inhibited SP-induced activation of nuclear ERK in HEK-hNK$_1$R cells to a similar degree as DIPMA-AP (Fig. 6e–h). Intracellular disassembly of BMA-AP nanoparticles by unknown mechanisms might release sufficient quantities of aprepitant to effectively antagonize the NK$_1$R in endosomes. Non-selective effects of BMA on SP-stimulated nuclear ERK (Supplementary Fig. 8i) could also contribute.

Discussion

The rationale for the current study is that painful stimuli evoke NK$_1$R endocytosis in spinal neurons[24,28], where NK$_1$R endosomal signals mediate excitation and nociception[19]. Clathrin and dynamin inhibitors and lipid-conjugated antagonists that target the NK$_1$R in endosomes inhibit nociception[19]. Considerable effort will be required to advance these compounds to the clinic. Dynamin

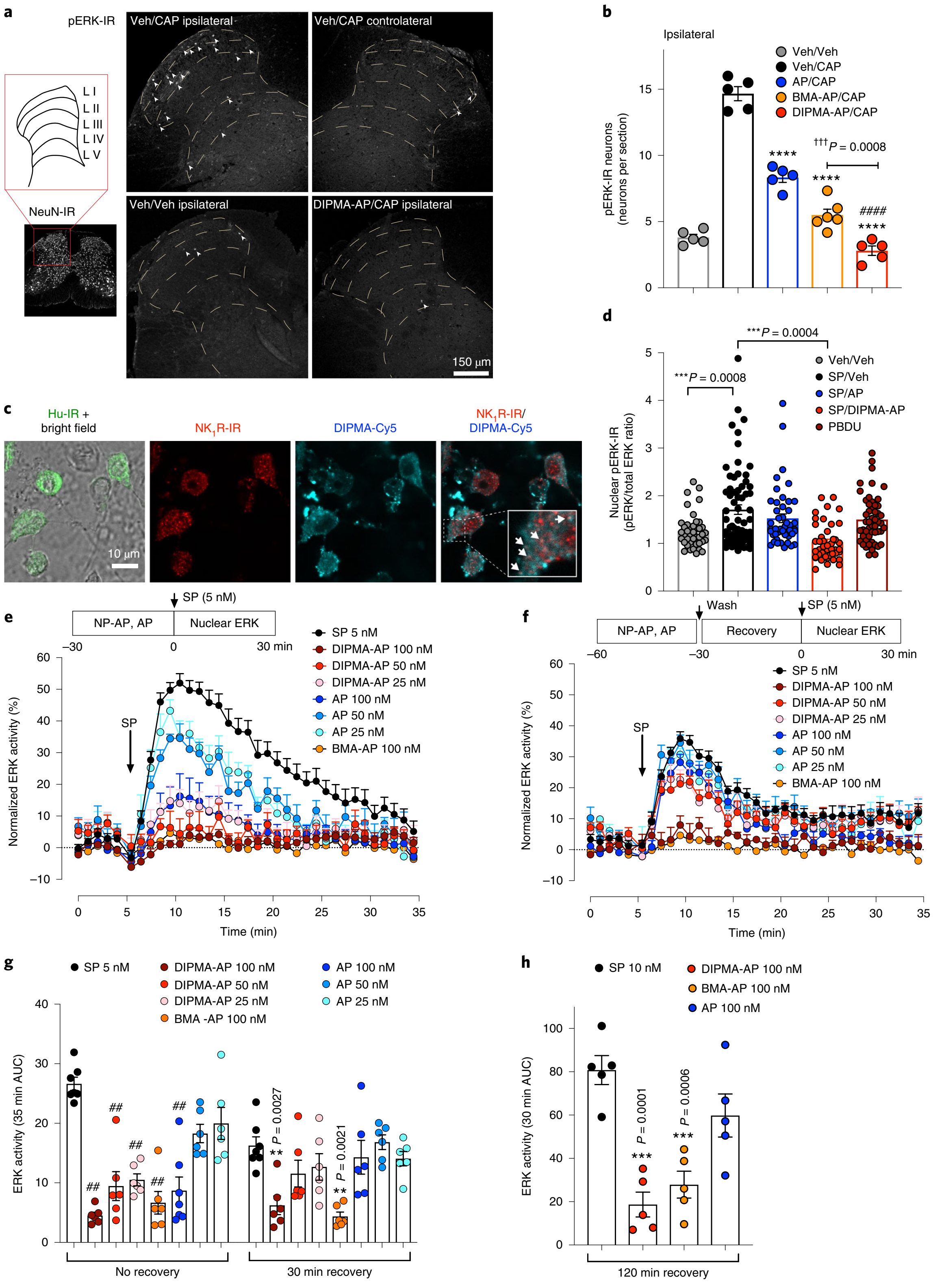

and clathrin inhibitors disrupt trafficking of many receptors and channels that control nociception. Lipid-conjugated antagonists can lose potency. Because lipidated antagonists incorporate into plasma and endosomal membranes, they cannot exclusively target endosomal signalling. pH-responsive nanoparticles deliver aprepitant to endosomes, without loss of potency. Nanoparticle encapsulation enhanced the anti-nociceptive actions of aprepitant in preclinical models of pain. These findings are consistent with the improved capacity of nanoparticle-encapsulated aprepitant to inhibit SP-induced excitation of spinal neurons and to cause a sustained inhibition of endosomal signalling. Nanoparticle uptake and sustained release of aprepitant in acidic endosomes containing the activated NK_1R could account for these enhanced and persistent anti-nociceptive effects.

Further studies are necessary before nanoparticle-encapsulated analgesics can be advanced to clinical trials. They include toxicology, pharmacokinetic and pharmacodynamic studies in disease-relevant preclinical models. Therapeutic efficacy could be improved by combining into the same nanoparticles antagonists of different GPCRs that co-mediate pain transmission (for example, NK_1R, calcitonin receptor-like receptor)[19,21]. By incorporating targeting groups into the nanoparticle shell, it might be possible to deliver drugs selectively to pain-transmitting neurons. Limitations of our study include the following: analysis of nociception rather than the perception of pain, which requires human studies; study of evoked rather than spontaneous nociception; examination of nanoparticle actions in cell lines or primary striatal neurons, rather than the spinal neurons that are the target of nanoparticle-encapsulated aprepitant.

Nanoparticle encapsulation could improve the therapeutic efficacy of antagonists and agonists of many GPCRs that signal from endosomes[13,15,35]. Although GPCRs are the target of most clinically approved drugs, many drugs fail during development for unknown reasons. Nanoparticle encapsulation could advance the development of drugs to treat multiple diseases by altering their intracellular distribution to fine-tune signalling processes of pathophysiological importance.

Online content

Any methods, additional references, Nature Research reporting summaries, source data, extended data, supplementary information, acknowledgements, peer review information; details of author contributions and competing interests; and statements of data and code availability are available at https://doi.org/10.1038/s41565-019-0568-x.

Received: 22 October 2018; Accepted: 2 October 2019;

References

1. De Jong, W. H. & Borm, P. Drug delivery and nanoparticles: applications and hazards. *Int. J. Nanomed.* **3**, 133–149 (2008).
2. Farokhzad, O. C. & Langer, R. Impact of nanotechnology on drug delivery. *ACS Nano* **3**, 16–20 (2009).
3. Uhrich, K. E., Cannizzaro, S. M., Langer, R. S. & Shakesheff, K. M. Polymeric systems for controlled drug release. *Chem. Rev.* **99**, 3181–3198 (1999).
4. Maeda, H. et al. Tumor vascular permeability and the EPR effect in macromolecular therapeutics: a review. *J. Control Rel.* **65**, 271–284 (2000).
5. Such, G. K., Yan, Y., Johnston, A. P. R., Gunawan, S. T. & Caruso, F. Interfacing materials science and biology for drug carrier design. *Adv. Mater.* **27**, 2278–2297 (2015).
6. Chan, J. M., Farokhzad, O. C. & Gao, W. pH-responsive nanoparticles for drug delivery. *Mol. Pharm.* **7**, 1913–1920 (2010).
7. Lynn, D. M., Amiji, M. M. & Langer, R. pH-responsive polymer microspheres: rapid release of encapsulated material within the range of intracellular pH. *Angew. Chem. Int. Ed.* **40**, 1707–1710 (2001).
8. Mura, S., Nicolas, J. & Couvreur, P. Stimuli-responsive nanocarriers for drug delivery. *Nat. Mater.* **12**, 991–1003 (2013).
9. Schmaljohann, D. Thermo- and pH-responsive polymers in drug delivery. *Adv. Drug Deliv. Rev.* **58**, 1655–1670 (2006).
10. Wilhelm, S. et al. Analysis of nanoparticle delivery to tumours. *Nat. Rev. Mater.* **1**, 16014 (2016).
11. Zhou, K. et al. Tunable, ultrasensitive pH-responsive nanoparticles targeting specific endocytic organelles in living cells. *Angew. Chem. Int. Ed.* **50**, 6109–6114 (2011).
12. Nelson, C. E. et al. Balancing cationic and hydrophobic content of PEGylated siRNA polyplexes enhances endosome escape, stability, blood circulation time and bioactivity in vivo. *ACS Nano* **7**, 8870–8880 (2013).
13. Thomsen, A. R. B., Jensen, D. D., Hicks, G. A. & Bunnett, N. W. Therapeutic targeting of endosomal G protein-coupled receptors. *Trends Pharmacol. Sci.* **39**, 879–891 (2018).
14. Hauser, A. S., Attwood, M. M., Rask-Andersen, M., Schiöth, H. B. & Gloriam, D. E. Trends in GPCR drug discovery: new agents, targets and indications. *Nat. Rev. Drug Discov.* **16**, 829–842 (2017).
15. Murphy, J. E., Padilla, B. E., Hasdemir, B., Cottrell, G. S. & Bunnett, N. W. Endosomes: a legitimate platform for the signaling train. *Proc. Natl Acad. Sci. USA* **106**, 17615–17622 (2009).
16. Vilardaga, J. P., Jean-Alphonse, F. G. & Gardella, T. J. Endosomal generation of cAMP in GPCR signaling. *Nat. Chem. Biol.* **10**, 700–706 (2014).
17. Irannejad, R. et al. Functional selectivity of GPCR-directed drug action through location bias. *Nat. Chem. Biol.* **13**, 799–806 (2017).
18. Stoeber, M. et al. A genetically encoded biosensor reveals location bias of opioid drug action. *Neuron* **98**, 963–976 (2018).
19. Jensen, D. D. et al. Neurokinin 1 receptor signaling in endosomes mediates sustained nociception and is a viable therapeutic target for prolonged pain relief. *Sci. Transl. Med.* **9**, eaal3447 (2017).
20. Jimenez-Vargas, N. N. et al. Protease-activated receptor-2 in endosomes signals persistent pain of irritable bowel syndrome. *Proc. Natl Acad. Sci. USA* **115**, E7438–E7447 (2018).
21. Yarwood, R. E. et al. Endosomal signaling of the receptor for calcitonin gene-related peptide mediates pain transmission. *Proc. Natl Acad. Sci. USA* **114**, 12309–12314 (2017).
22. Kramer, M. S. et al. Distinct mechanism for antidepressant activity by blockade of central substance P receptors. *Science* **281**, 1640–1645 (1998).
23. Quartara, L., Altamura, M., Evangelista, S. & Maggi, C. A. Tachykinin receptor antagonists in clinical trials. *Expert Opin. Investig. Drugs* **18**, 1843–1864 (2009).
24. Steinhoff, M. S., Von Mentzer, B., Geppetti, P., Pothoulakis, C. & Bunnett, N. W. Tachykinins and their receptors: contributions to physiological control and the mechanisms of disease. *Physiol. Rev.* **94**, 265–301 (2014).
25. Manders, E. M. M., Verbeek, F. J. & Aten, J. A. Measurement of co-localization of objects in dual-colour confocal images. *J. Microsc.* **169**, 375–382 (1993).
26. Robertson, M. J. et al. Synthesis of the PitStop family of clathrin inhibitors. *Nat. Protoc.* **9**, 1592–1606 (2014).
27. Robertson, M. J., Deane, F. M., Robinson, P. J. & McCluskey, A. Synthesis of Dynole 34-2, Dynole 2-24 and Dyngo 4a for investigating dynamin GTPase. *Nat. Protoc.* **9**, 851–870 (2014).
28. Mantyh, P. W. et al. Receptor endocytosis and dendrite reshaping in spinal neurons after somatosensory stimulation. *Science* **268**, 1629–1632 (1995).
29. Stein, C., Millan, M. J. & Herz, A. Unilateral inflammation of the hindpaw in rats as a model of prolonged noxious stimulation: alterations in behavior and nociceptive thresholds. *Pharmacol. Biochem. Behav.* **31**, 445–451 (1988).
30. Decosterd, I. & Woolf, C. J. Spared nerve injury: an animal model of persistent peripheral neuropathic pain. *Pain* **87**, 149–158 (2000).
31. Bravo, D. et al. Pannexin 1: a novel participant in neuropathic pain signaling in the rat spinal cord. *Pain* **155**, 2108–2115 (2014).
32. Abbadie, C., Brown, J. L., Mantyh, P. W. & Basbaum, A. I. Spinal cord substance P receptor immunoreactivity increases in both inflammatory and nerve injury models of persistent pain. *Neuroscience* **70**, 201–209 (1996).
33. Geppetti, P., Veldhuis, N. A., Lieu, T. & Bunnett, N. W. G protein-coupled receptors: dynamic machines for signaling pain and itch. *Neuron* **88**, 635–649 (2015).
34. Halls, M. L. & Canals, M. Genetically encoded FRET biosensors to illuminate compartmentalised GPCR signalling. *Trends Pharmacol. Sci.* **39**, 148–157 (2018).
35. Irannejad, R. & von Zastrow, M. GPCR signaling along the endocytic pathway. *Curr. Opin. Cell Biol.* **27**, 109–116 (2014).

Methods

Materials. Reagents were purchased from Sigma-Aldrich unless otherwise specified.

Diblock copolymers and nanoparticles. Polymer synthesis and characterization and nanoparticle assembly, pH-dependent disassembly in vitro and characterization are described in the Supplementary Methods.

Cell lines. The human (h) NK$_1$R long isoform open reading frame with a CD8 signal sequence and N-terminal FLAG-tag was cloned into pcDNA5 FRT/TO between KpnI and NotI restriction sites using Gibson assembly (NEB). A stable cell line expressing hNK$_1$R (HEK-hNK$_1$R) was produced by co-transfecting Flpn HEK-293 cells with hNK$_1$R vector and pOG44 (0.5 μg and 4 μg, respectively), using polyethylenimine (PEI, Polysciences) at a 1:6 DNA:PEI ratio. Cells (~0.7×10^6) were seeded into T-25 tissue culture flasks (Perkin Elmer) in Dulbecco's modified Eagle medium (DMEM) supplemented with penicillin (50 U ml^{-1}) and streptomycin (50 U ml^{-1}) (DMEM/pen/strep) and incubated for 24 h (37 °C, 5% CO$_2$). Culture medium was changed to fresh DMEM/pen/strep prior to transfection and incubated for 24 h (37 °C, 5% CO$_2$). The medium was changed to DMEM supplemented with 10% (vol/vol) fetal bovine serum (FBS) and hygromycin B (200 μg ml^{-1}, Thermo Fisher Scientific) for stable cell line selection. Cell lines were tested and confirmed free of mycoplasma.

Nanoparticle trafficking in HEK-293 cells. HEK-293 cells were plated on poly-d-lysine coated chambers (ibidi, Germany) in DMEM supplemented with 10% (vol/vol) FBS (DMEM/FBS). After 24 h, cells were transfected with 300 ng of rat (r) NK$_1$R-GFP per chamber and cultured for 48 h. To identify endosomal compartments, HEK-293 cells were infected with Rab5a-GFP (resident in early endosomes) or Rab7a-GFP (late endosomes) CellLight BacMam2.0 (Thermo Fisher Scientific) for 16 h. To examine localization of nanoparticles, cells were incubated in Leibovitz´s L-15 medium with DIPMA-Cy5 nanoparticles (20 μg ml^{-1}, 30 min, 37 °C) or vehicle, followed by addition of SP (10 nM). Cells were imaged at 30 and 60 min post-SP addition using a Leica SP8 confocal microscope equipped with HCX PL APO ×40 (NA 1.30) and HCX PL APO ×63 (NA 1.40) oil objectives. Images were analysed using Fiji[36] and deconvolved with Huygens Professional version 18.04 (Scientific Volume Imaging, http://svi.nl), using the CMLE algorithm with a signal-to-noise ratio of 10 and 100 iterations. Co-localization was evaluated by determination of the Manders overlap coefficient[25].

Uptake and disassembly of nanoparticles in HEK-293 cells. Nanoparticles were self-assembled with 0.5 mg of Coumarin 153 per mg of DIPMA or BMA polymer (DIPMA-CO, BMA-CO). HEK-293 cells were preincubated for 30 min with vehicle (Hank's balanced salt solution, HBSS), dynamin inhibitor (Dyngo4a, 30 μM)[27], clathrin inhibitor (PitStop2, 30 μM)[26], vacuolar H$^+$ATPase inhibitor (Bafilomycin A1, 1 μM) or NH$_4$Cl (20 mM), which acts as a lysosomotropic weak base. Nuclei were stained using Draq5. Images were obtained with a Leica SP8 confocal microscope using an HCX PL APO ×63 (NA 2.0) oil objective. Images were taken every 10 s for 30 min, where the first five readings correspond to baseline images before the addition of DIPMA-CO nanoparticles (20 μg ml^{-1}). All images were analysed using Fiji[36]. Kinetic data were normalized to the fluorescence of free Coumarin 153 (5 μg ml^{-1}) at 30 min.

Animals. Male C57BL/6 mice (6–10 weeks) and pregnant Asmu:Swiss mice were sourced from the Monash Animal Research Platform. Male Sprague–Dawley rats (225–250 g) were obtained from the Faculty of Medicine of the University of Chile. Animals were housed in groups of four, maintained at a temperature of 22 ± 4 °C in a humidity-controlled environment with a 12 h light/dark cycle. Food and water were available ad libitum. For behavioural tests, investigators were blinded to the treatment groups and animals were randomly assigned to treatments and studied during the light cycle. Animals were euthanized by anaesthetic overdose and thoracotomy. Studies on animals were performed in accordance with the Guide for the Care and Use of Laboratory Animals of the National Institutes of Health and adhered to the ethical guidelines of the International Association for the Study of Pain[37]. Studies were approved by the Animal Ethics Committee of Monash Institute of Pharmaceutical Sciences, Monash University and the Bioethics Committee of the University of Santiago of Chile.

Drug administration. *Mice.* The following drugs were administered by intrathecal injection (5 μl) into the intervertebral space (L4/L5) of conscious mice: aprepitant (100 and 300 nM), nanoparticles delivering an equivalent dose of aprepitant (DIPMA-AP, BMA-AP, 10 μg ml^{-1} 100 nM aprepitant, 30 μg ml^{-1} 300 nM aprepitant), controls (10 μg ml^{-1} of DIPMA-Ø and a mixture of 10 μg ml^{-1} of DIPMA-Ø and aprepitant 100 nM) or vehicle (artificial cerebrospinal fluid, aCSF). Treatments were administered 30 min before rotarod experiments and the induction of acute nociceptive pain or 48 h after the establishment of inflammatory nociception. For biodistribution studies, nanoparticles (50 μg ml^{-1}) were administered intrathecally immediately after obtaining control images. For localization of nanoparticles in the spinal cord, nanoparticles (50 μg ml^{-1}) were administered intrathecally 30 min after the induction of acute nociception with capsaicin (see below). Morphine (3 mg kg^{-1} intraperitoneal) was administered 48 h after induction of inflammatory nociception.

Rats. Drugs were administered by intrathecal injection (10 μl) into the intervertebral space (L4/L5) of conscious rats: aprepitant (100 nM, 300 nM, 1 μM), nanoparticles loaded with aprepitant (DIPMA-AP, BMA-AP, 10 μg ml^{-1} 100 nM aprepitant, 30 μg ml^{-1} 300 nM aprepitant, 50 μg ml^{-1} 500 nM aprepitant), DIPMA-Ø nanoparticles (10, 30 and 50 μg ml^{-1}) or vehicle (aCSF). Treatments were administered 10 days after sural nerve transection or sham surgery. For electrophysiological studies, drugs were administered by intrathecal injection under anaesthesia (isoflurane 1.2–1.5%): aprepitant (1 μM) or nanoparticles (30 μg ml^{-1} 300 nM aprepitant). Morphine (3 mg kg^{-1}, intraperitoneal) was administered 10 days after sural nerve transection.

Biodistribution of nanoparticles in the spinal cord. Mice were sedated (2% isoflurane) and placed in an in vivo imaging system (IVIS spectrum Lumina II, Perkin Elmer). Posterior images were obtained using the Perkin Elmer Living Image software v4.3.1. After collection of a baseline image, nanoparticles (50 μg ml^{-1}) were administered intrathecally (5 μl). Images were collected at 0.5, 1, 1.5, 2, 4, 8 and 24 h post DIPMA-Cy5 or BMA-Cy5 administration.

Uptake of nanoparticles in the spinal cord. Cy5-labelled nanoparticles were administered to mice (intrathecal). After 30 min, capsaicin (5 μg) was administered by subcutaneous intraplantar injection (10 μl) into the left hindpaw under sedation (2% isoflurane). This approach was used to mimic the therapeutic situation where nanoparticle-encapsulated drugs might be used to treat pain. At 1 h after nanoparticle administration, mice were transcardially perfused with 50 ml of PBS followed by 50 ml of ice-cold 4% paraformaldehyde (PFA). The spinal cord was removed, immersion fixed in 4% PFA (2 h, 4 °C) and cryoprotected in PBS containing 30% sucrose (24 h, 4 °C). The spinal cord (L3–L6) was embedded in tissue freezing medium (TFM, General Data), and 30 μm serial coronal sections were cut and mounted on Colorfrost Plus microscope slides (Fisher Scientific). Sections were washed twice in PBS, counter-stained with DAPI (5 μg ml^{-1}, 5 min) and cover-slipped with ProLong Glass mounting medium (Thermo Fisher Scientific). Some sections were processed to detect neurons. Sections were blocked in PBS containing 0.2% Triton X-100 and 10% normal horse serum (NHS; 30 min, room temperature). Sections were incubated with rabbit anti-PGP9.5 (1:500, Abcam ab27053) in PBS containing 0.2% Triton X-100 and 3% NHS (60 min, room temperature). Sections were washed four times in PBS and incubated with donkey anti-rabbit Alexa488 (1:1,000, Thermo Fisher Scientific; 30 min, room temperature). Sections were imaged on a Leica SP8 confocal microscope with HC PLAPO ×40 or ×63 oil objectives.

Determination of aprepitant concentration in the spinal cord. Aprepitant (100 nM) or nanoparticles delivering an equivalent dose of aprepitant (10 μg ml^{-1} 100 nM aprepitant) was administered by intrathecal injection to conscious mice. Mice were killed 1 h and 4 h post-treatment. The spinal cord (L2–L6) was removed for determination of the tissue concentration of aprepitant by LC-MS, as described in the Supplementary Methods.

Acute and inflammatory nociception in mice. *Nociceptive pain.* Capsaicin (5 μg) or vehicle (0.9% NaCl) was administered by intraplantar injection (10 μl) into the left hindpaw of sedated mice (2% isoflurane) 30 min after intrathecal injection of drugs[19].

Inflammatory pain. CFA (0.5 mg ml^{-1}) or vehicle (0.9% NaCl) was administered by intraplantar injection (10 μl) into the left hindpaw of sedated mice (2% isoflurane)[19,29]. Drugs were administered by intrathecal injection 48 h after CFA.

Mechanical allodynia. Mechanical nociception was assessed by measuring withdrawal thresholds to stimulation of the plantar surfaces of the ipsilateral and contralateral hindpaws with calibrated VFFs[19]. Before experiments, mice were acclimatized to the experimental apparatus and environment for 2 h on two successive days. VFF withdrawal thresholds were measured in triplicate to establish a baseline for each mouse. For the capsaicin model, VFF withdrawal thresholds were measured at 30 min intervals for the first 2 h after drug administration, then at 60 min intervals for the next 2 h, and finally after 24 h. For the CFA model, VFF withdrawal thresholds were measured every 30 min for the first 3 h after drug administration, then at 60 min intervals for the next 5 h, and finally after 24 h. Results were normalized to the baseline withdrawal thresholds of each mouse. Results are expressed as a percentage of baseline, as AUC and as the half width response (the duration of the effect of each treatment calculated as the time to attain 50% of the maximal analgesic response).

pERK localization in mouse spinal cord. Vehicle (control), free aprepitant and nanoparticles (all 100 nM aprepitant) were administered by intrathecal injection to mice as described above. After 30 min, mice were sedated (2% isoflurane) and vehicle (0.9% NaCl) or capsaicin (5 μg) was administered by intraplantar injection (10 μl) into the left hindpaw. After 4 h, sections of spinal cord (L3–L6) were prepared as described above. Fixation, staining and imaging of sections are described in detail in the Supplementary Methods.

Rotarod test. Motor coordination was assessed in mice by a rotarod test as described in the Supplementary Methods.

Neuropathic nociception in rats. *Neuropathic pain.* Neuropathic nociception was induced in rats using a variation of the SNS injury model, which induces rapid onset and sustained mechanical and thermal hyperalgesia[30]. Under anaesthesia (2% isoflurane), the three terminal distal branches of the sciatic nerve (tibial, common peroneal and sural nerves) were identified and the sural nerve was transected[31]. For controls (sham), rats underwent a similar surgery but without transection of the sural nerve. After surgery, ketoprofen (3 mg kg^{-1}) and enrofloxacin (5 mg kg^{-1}) were administered subcutaneously for 2 days.

Mechanical hyperalgesia. Mechanical hyperalgesia was assessed in rats by measuring hindpaw withdrawal pressure thresholds using an algesimeter (Ugo Basile) with a cutoff value of 570 g to prevent injury[38,39]. Mechanical hyperalgesia was evaluated before (basal) and 5, 9 and 10 days after surgery. After evaluation at day 10, drugs were administered by intrathecal injection, and withdrawal thresholds were recorded every 30 min for 7 h. Results are expressed as the paw withdrawal pressure threshold (g cm^{-2}), AUC and half-width response.

Electrophysiological assessment of nociception in rats. Nociceptive synaptic transmission was evaluated by measurement of electromyographic activity associated with the hind limb-flexion nociceptive reflex evoked by electrical activation of C-fibres of the sural nerve (C-reflex) as described previously[40] and in detail in the Supplementary Methods.

Cell-attached patch-clamp recordings of rat spinal neurons. Parasagittal slices (340 µm) were prepared from rat lumbar spinal cord as described in refs. [19,41]. Slices were transferred to a recording chamber and superfused with aCSF (2 ml min^{-1}, 36 °C). Dodt-contrast optics were used to identify large (capacitance ≥20 pF), putative NK$_1$R-positive neurons in lamina I based on their position, size and fusiform shape with dendrites that were restricted to lamina I. Spontaneous currents were recorded from NK$_1$R-positive lamina I neurons in a cell-attached configuration in voltage clamp. Slices were preincubated in DIPMA-AP (10 µg ml^{-1} 100 nM aprepitant), BMA-AP (10 µg ml^{-1} 100 nM aprepitant) or aprepitant (100 nM) for 120 min, washed and incubated in antagonist-free aCSF for a further 30–60 min before recording. Slices were challenged with SP (1 µM, 2 min) and the firing rate for each cell was normalized to the response between the 2 and 4 min time points, which was not significantly different between groups. The firing time was determined as the duration of the response to the last action potential.

NK$_1$R localization in rat spinal cord. At 10 days after sham or SNS surgery, rats were anaesthetized and transcardially perfused with 250 ml PBS followed by 250 ml 4% PFA. The spinal cord was removed, immersion fixed in 4% PFA (2 h, 4 °C) and cryoprotected in 30% sucrose in 0.1 M PBS (24 h, 4 °C). The spinal cord (L3–L6) was embedded in TFM (General Data) and 30 µm serial coronal sections were cut into 48-well plates containing PBS. Fixation, immunostaining, imaging and image analysis of spinal cord sections are described in the Supplementary Methods.

Nanoparticle uptake and SP signalling in striatal neurons. *Neuronal isolation and culture.* Primary striatal neurons were dissociated from E15-16 Asmu:Swiss mouse embryos as described in ref. [42]. Neurons (200,000 per well) were plated on poly-d-lysine-coated eight-well chamber slides (ibidi) in Neurobasal medium supplemented with B-27, 2 mM l-glutamine and penicillin/streptomycin.

Nanoparticle uptake and NK$_1$R localization. At 5 days after isolation, neurons were equilibrated in HEPES-buffered saline (10 mM HEPES, 0.5% BSA, 10 mM d-glucose, 2.2 mM $CaCl_2.H_2O$, $MgCl_2.6H_2O$, 2.6 mM KCl, 150 mM NaCl, pH 7.4) for 30 min and then incubated with 50 µg ml^{-1} DIPMA-Cy5 and 100 nM SP for 30 min. Neurons were fixed in 2% PFA and 1% sucrose in PBS (room temperature, 20 min) and blocked in PBS containing 0.3% Triton X-100 and 5% NHS for 24 h at 4 °C. Neurons were stained as described above for rat spinal cord slices, using rabbit anti-NK$_1$R and mouse anti-Hu (HuC/HuD Monoclonal Antibody 16A11, Thermo Fisher Scientific; 24 h, 4 °C), washed in 4× PBS, and incubated with donkey anti-rabbit Alexa594 and donkey anti-mouse Alexa488 (1:500, Thermo Fisher Scientific; 24 h, 4 °C). Neurons were counter-stained with DAPI. Images were obtained on a Leica SP8 confocal microscope with HCX PL APO ×63 (NA 1.40) oil objective.

Ca^{2+} imaging. At 5 days after isolation, neurons were incubated with Fura-2 AM ester (2 µM, 45 min, 37 °C, Thermo Fisher Scientific) in HEPES-buffered saline containing 4 mM probenecid and 0.05% pluronic F127. Neurons were recovered in fresh HEPES-buffered saline for 30 min before imaging on a Leica DMI-6000B microscope with HC PLAN APO 0.4 NA ×10 objective at 37 °C. Images were collected at 1.5 s intervals (excitation, 340 nm/380 nm; emission, 530 nm). To assess the functional expression of NK$_1$R, neurons were preincubated with 300 nM aprepitant or vehicle (DMSO), and challenged with 100 nM SP and followed by 5 mM KCl.

ERK activity. At 8 days after isolation, neurons were equilibrated for 30 min in HEPES-buffered saline and then preincubated with DIPMA-AP (10 µg ml^{-1} 100 nM aprepitant), aprepitant (100 nM) or vehicle (PBS) for 30 min. Neurons were washed, recovered for 30 min and challenged with SP (100 nM) or the positive control, phorbol 12,13-dibutyrate (10 µM), for 30 min. Neurons were fixed in 4% PFA (20 min at 4 °C) and blocked (0.3% Triton X-100 and 5% NHS; 24 h at 4 °C). Neurons were incubated with rabbit anti-phospho-p44/42 MAPK (ERK1/2 phospho-Thr202/Tyr204, 1:100, #4370, Cell Signalling Technology) and mouse anti-p44/42 MAPK (1:100, #4696, Cell Signalling Technology) (24 h at 4 °C). Neurons were washed four times in PBS and incubated with donkey anti-rabbit Alexa488 and donkey anti-mouse Alexa647 (1:500, Thermo Fisher Scientific; 2 h at room temperature). The nucleus was counter-stained with DAPI. Neurons were imaged using a Leica SP8 confocal microscope with an HCX PL APO ×63 (NA 1.40) oil objective. Nuclei of neurons were selected as regions of interest and the ratio of phospho-ERK to total ERK was calculated using mean fluorescence intensity values. The mean ERK ratio for all neurons within a single well was determined and the means of four experiments were compared for statistical analyses.

FRET assays of endosomal NK$_1$R signalling in HEK-293 cells. HEK-hNK$_1$R cells (~2×10^6) were seeded into a 90 mm Petri dish (Corning) in DMEM/FBS/Hygro and incubated for 24 h (37 °C, 5% CO_2). Before transfection, the medium was changed to fresh DMEM/FBS/Hygro and the nuclear ERK (nucEKAR) plasmid was transfected (2.5 µg DNA per dish) using PEI at a 1:6 ratio[19]. After 24 h, cells were plated in a poly-l -lysine-coated black 96-well CulturPlate (Perkin Elmer) and incubated for a further 24 h (37 °C, 5% CO_2). On the day of the assay, cells were serum-starved for 6–8 h and then equilibrated in HBSS, supplemented with HEPES at 37 °C in a CO_2-free incubator. FRET was assessed using a PHERAstar FS (BMG LABTECH) with optic module FI 430 530 480 and measurements were made every 1 min. Baseline was measured for 5 min followed by stimulation with SP, vehicle (HBSS) or phorbol 12,13-dibutyrate (1 µM), and further measurements for 30 min. For the SP concentration response curve, half logarithmic dilutions of SP were added (1 µM to 100 pM) and EC_{50} was determined using the AUC after SP addition (30 min reading). For the aprepitant concentration response curve, logarithmic dilutions of aprepitant (10 µM to 1 pM) were added 30 min before baseline measurements, followed by the addition of 5 nM of SP. The IC_{50} was determined for aprepitant as described. To assess the effect of nanoparticles on nuclear ERK signalling, DIPMA-Ø, DIPMA-AP, BMA-Ø or BMA-AP (30, 20 and 10 µg ml^{-1}) was added 30 min before baseline measurements, followed by the addition of SP 5 nM or vehicle. Data were expressed as vehicle corrected values, normalized by the maximum response to the positive control.

Cell viability assays. Studies of the effects of nanoparticles on the viability of HEK-293 cells are described in the Supplementary Methods.

Statistical analysis. Data were analysed using GraphPad Prism 8 (GraphPad Software). Data are presented as mean ± s.e.m., unless noted otherwise. A two-tailed Student's *t*-test was used for two comparisons and exact *P* values are shown in the figures. For multiple comparisons, results were compared using one- or two-way ANOVA followed by post-hoc multiple comparison tests, as described in the figure legends. Exact adjusted *P* values are shown for bar graphs in figures when $P \geq 0.0001$. $P < 0.05$ was considered significant.

Reporting Summary. Further information on research design is available in the Nature Research Reporting Summary linked to this article.

Data availability

All data generated or analysed during this study are available in this Article and its Supplementary Information or from the corresponding authors upon request.

References

36. Schindelin, J. et al. Fiji: an open-source platform for biological-image analysis. *Nat. Methods* **9**, 676–682 (2012).
37. Zimmermann, M. Ethical guidelines for investigations of experimental pain in conscious animals. *Pain* **16**, 109–110 (1983).
38. Randall, L. O. & Selitto, J. J. A method for measurement of analgesic activity on inflamed tissue. *Arch. Int. Pharmacodyn. Ther.* **111**, 409–419 (1957).
39. Santos-Nogueira, E., Redondo Castro, E., Mancuso, R. & Navarro, X. Randall–Selitto test: a new approach for the detection of neuropathic pain after spinal cord injury. *J. Neurotrauma* **29**, 898–904 (2012).
40. Retamal, J. et al. Burst-like subcutaneous electrical stimulation induces BDNF-mediated, cyclotraxin B-sensitive central sensitization in rat spinal cord. *Front. Pharmacol.* **9**, 1143 (2018).
41. Imlach, W. L., Bhola, R. F., May, L. T., Christopoulos, A. & Macdonald, J. C. A positive allosteric modulator of the adenosine α1 receptor selectively inhibits primary afferent synaptic transmission in a neuropathic pain model. *Mol. Pharmacol.* **88**, 460–468 (2015).
42. Di Porzio, U., Daguet, M. C., Glowinski, J. & Prochiantz, A. Effect of striatal cells on in vitro maturation of mesencephalic dopaminergic neurones grown in serum-free conditions. *Nature* **288**, 370–373 (1980).

Acknowledgements

This work was supported by the National Institutes of Health (NS102722, DE026806, DK118971), the Department of Defense (PR170507), the National Health and Medical Research Council (63303, 1049682, 1031886; N.W.B.), the Australian Research Council Centre of Excellence in Convergent Bio-Nano Science and Technology (N.W.B. and T.P.D.), the Center for the Development of Nanoscience and Nanotechnology (CEDENNA, Fondecyt no. 1181622, L.C.) and Takeda Pharmaceuticals Inc. (N.W.B., N.A.V and D.P.P.). We thank F. Chiu for mass spectrometry analysis of aprepitant loading and P. Zhao for advice about signalling assays.

Author contributions

P.D.R.-G. prepared and characterized nanoparticles, examined nanoparticle uptake and disassembly, studied SP signalling in model cells and wrote the manuscript. J.S.R. studied the biodistribution and anti-nociceptive and in vivo electrophysiological actions of nanoparticles. P.S. studied the biodistribution and anti-nociceptive actions of nanoparticles. W.I. conceived and designed electrophysiological studies on spinal neurons. M.S. studied the excitation of spinal neurons, and N.T. prepared and characterized nanoparticles. L.C. conceived and designed neuropathic nociception and in vivo electrophysiological studies. T.P. conceived and designed neuropathic nociception. C.J.N. provided expertise in the analysis of confocal images and S.Y.K. obtained transmission electron microscopy images. L.M.L. characterized the critical micellar concentration and pH-disassembly of nanoparticles. C.L. studied SP signalling in model cells and D.P.P. studied nanoparticle uptake. T.M.L. studied anti-nociceptive actions of nanoparticles, G.D.S. prepared striatal neurons, and Q.N.M. prepared and characterized nanoparticles. D.D.J. examined NK1R endocytosis, nanoparticle uptake into spinal neurons, and SP signalling in model cells and striatal neurons. R.L. examined NK_1R endocytosis and nanoparticle uptake into spinal neurons. N.S.N. studied NK_1R endocytosis in rats. B.L.S. designed experiments to examine NK_1R endocytosis in rats. J.F.Q. designed nanoparticles and wrote the manuscript. M.R.W. designed nanoparticles. N.A.V. conceived experiments, studied SP signalling in neurons, interpreted the results and wrote the manuscript. T.P.D. conceived the experiments and designed the nanoparticles. N.W.B. conceived and designed the experiments, interpreted the results and wrote the manuscript.

Competing interests

Research in N.A.V.'s, D.P.P.'s and N.W.B.'s laboratories is funded, in part, by Takeda Pharmaceuticals. N.W.B. is a founding scientist of Endosome Therapeutics.

Additional information

Supplementary information is available for this paper at https://doi.org/10.1038/s41565-019-0568-x.

Correspondence and requests for materials should be addressed to N.A.V., T.P.D. or N.W.B.

Peer review information *Nature Nanotechnology* thanks Jean-Pierre Vilardaga and the other, anonymous, reviewer(s) for their contribution to the peer review of this work.

Reprints and permissions information is available at www.nature.com/reprints.

nature research

Corresponding author(s): Nigel W Bunnett

Last updated by author(s): Sep 27, 2019

Reporting Summary

Nature Research wishes to improve the reproducibility of the work that we publish. This form provides structure for consistency and transparency in reporting. For further information on Nature Research policies, see Authors & Referees and the Editorial Policy Checklist.

Statistics

For all statistical analyses, confirm that the following items are present in the figure legend, table legend, main text, or Methods section.

n/a	Confirmed	
☐	☒	The exact sample size (*n*) for each experimental group/condition, given as a discrete number and unit of measurement
☐	☒	A statement on whether measurements were taken from distinct samples or whether the same sample was measured repeatedly
☐	☒	The statistical test(s) used AND whether they are one- or two-sided *Only common tests should be described solely by name; describe more complex techniques in the Methods section.*
☐	☒	A description of all covariates tested
☐	☒	A description of any assumptions or corrections, such as tests of normality and adjustment for multiple comparisons
☐	☒	A full description of the statistical parameters including central tendency (e.g. means) or other basic estimates (e.g. regression coefficient) AND variation (e.g. standard deviation) or associated estimates of uncertainty (e.g. confidence intervals)
☐	☒	For null hypothesis testing, the test statistic (e.g. *F*, *t*, *r*) with confidence intervals, effect sizes, degrees of freedom and *P* value noted *Give P values as exact values whenever suitable.*
☒	☐	For Bayesian analysis, information on the choice of priors and Markov chain Monte Carlo settings
☒	☐	For hierarchical and complex designs, identification of the appropriate level for tests and full reporting of outcomes
☒	☐	Estimates of effect sizes (e.g. Cohen's *d*, Pearson's *r*), indicating how they were calculated

Our web collection on statistics for biologists contains articles on many of the points above.

Software and code

Policy information about availability of computer code

Data collection	All nanoparticle imaging (Cy5-labelled or loaded with Coumarin) was acquired using Leica LAX software on a SP8 confocal system. Subsequent processing was performed using FIJI (ImageJ) version 1.0. For Cy5 particles live cell imaging, images were processed by deconvolution using Huygens Professional version 18.04 (Scientific Volume Imaging, The Netherlands, http://svi.nl). Animal imaging to assess Cy5-particle distribution following intrathecal injection were acquired on the Perkin Elmer IVIS Lumina II system using Living Image software, v4.3.1. FRET biosensor ERK signalling was collected on a Pherastar FS (BMG LABTECH).
Data analysis	For statistics, data were analysed using Graph Prism 8 (GraphPad Software, Inc., USA). For microscopy, images were analysed using Fiji. Colocalization was evaluated by determination of the Manders overlap coefficient.

For manuscripts utilizing custom algorithms or software that are central to the research but not yet described in published literature, software must be made available to editors/reviewers. We strongly encourage code deposition in a community repository (e.g. GitHub). See the Nature Research guidelines for submitting code & software for further information.

Data

Policy information about availability of data

All manuscripts must include a data availability statement. This statement should provide the following information, where applicable:

- Accession codes, unique identifiers, or web links for publicly available datasets
- A list of figures that have associated raw data
- A description of any restrictions on data availability

All data generated or analysed during this study are available in this published article and its supplementary information files or from the corresponding author upon request.

Field-specific reporting

Please select the one below that is the best fit for your research. If you are not sure, read the appropriate sections before making your selection.

☒ Life sciences ☐ Behavioural & social sciences ☐ Ecological, evolutionary & environmental sciences

For a reference copy of the document with all sections, see nature.com/documents/nr-reporting-summary-flat.pdf

Life sciences study design

All studies must disclose on these points even when the disclosure is negative.

Sample size	No statistical method was used to determine sample size. The sample sizes for experiments on cells and animals were determined from our previously published investigations (Jensen et a, Science Trans Med, 2017, 9, eaal3447) and was sufficient to yield statistical significance.
Data exclusions	No data were excluded from the analyses.
Replication	For studies of cell lines and isolated cells, individual experiments (n) were replicated on different days with triplicate measurements for each individual experiment. For behavioral studies of nociception, experiments (n) were replicated on different individual animals.
Randomization	Cells from independent experiments were randomly selected for imaging and analysis. Animals were assigned at random to experimental treatments.
Blinding	For behavioural tests, investigators were blinded to the treatment groups.

Reporting for specific materials, systems and methods

We require information from authors about some types of materials, experimental systems and methods used in many studies. Here, indicate whether each material, system or method listed is relevant to your study. If you are not sure if a list item applies to your research, read the appropriate section before selecting a response.

Materials & experimental systems

n/a	Involved in the study	
☐	☒	Antibodies
☐	☒	Eukaryotic cell lines
☒	☐	Palaeontology
☐	☒	Animals and other organisms
☒	☐	Human research participants
☒	☐	Clinical data

Methods

n/a	Involved in the study	
☒	☐	ChIP-seq
☒	☐	Flow cytometry
☒	☐	MRI-based neuroimaging

Antibodies

Antibodies used	Primary antibodies: Rabbit NK1R antibody. Rabbit anti-PGP9.5 (1Abcam ab27053). Mouse anti-Hu (HuC/HuD Monoclonal Antibody 16A11, Thermo Fisher Scientific. Rabbit anti-phospho-p44/42 MAPK (ERK1/2 phospho-Thr202/Tyr204, #4370, Cell Signalling Technology). Mouse anti-p44/42 MAPK (#4696, Cell Signalling Technology). Secondary antibodies: Donkey anti-rabbit Alexa594 and donkey anti-mouse Alexa488 or 647 (Thermo Fisher Scientific).
Validation	NK1R antibody is characterized in: Grady, E.F., Baluk, P., Bohm, S., Gamp, P.D., Wong, H., Payan, D.G., Ansel, J., Portbury, A.L., Furness, J.B., McDonald, D.M. & Bunnett, N.W. Characterization of antisera specific to NK1, NK2, and NK3 neurokinin receptors and their utilization to localize receptors in the rat gastrointestinal tract. J Neurosci 16, 6975-6986 (1996). Other primary and secondary antibodies are widely used and were characterized by the manufacturer and by controls (including omission of primary or secondary antibodies). Where possible, antibodies are validated as described in: Bron, R. & Bunnett, N.W. Antibodies: friend or foe? Am J Physiol Gastrointest Liver Physiol 309, G717-718 (2015).

Eukaryotic cell lines

Policy information about cell lines

Cell line source(s)	HEK-293 cells were from ATTC.
Authentication	HEK-293 cells were authenticated by genomic sequencing.
Mycoplasma contamination	HEK-293 cell lines were tested and confirmed free of mycoplasma.

Commonly misidentified lines (See ICLAC register)	None.

Animals and other organisms

Policy information about studies involving animals; ARRIVE guidelines recommended for reporting animal research

Laboratory animals	Male C57BL/6 mice (6-10 weeks) and pregnant Asmu:Swiss mice were from the Monash Animal Research Platform. Male Sprague-Dawley rats (225–250 g) were from the facilities of the Faculty of Medicine of the University of Chile.
Wild animals	The study did not involve wild animals.
Field-collected samples	The study did not involve animals collected in the field.
Ethics oversight	Studies on animals were in accordance with the Guide for the Care and Use of Laboratory Animals of the National Institutes of Health and adhered to the ethical guidelines of the International Association for the Study of Pain. Studies were approved by the animal ethics committee of Monash Institute of Pharmaceutical Sciences, Monash University and the Bioethics Committee of the University of Santiago of Chile.

Note that full information on the approval of the study protocol must also be provided in the manuscript.

nature nanotechnology

SUPPLEMENTARY INFORMATION

https://doi.org/10.1038/s41565-019-0568-x

In the format provided by the authors and unedited.

A pH-responsive nanoparticle targets the neurokinin 1 receptor in endosomes to prevent chronic pain

Paulina D. Ramírez-García[1,2], Jeffri S. Retamal[1,2], Priyank Shenoy[1,2], Wendy Imlach[3], Matthew Sykes[3], Nghia Truong[1,2], Luis Constandil[4], Teresa Pelissier[4], Cameron J. Nowell[1], Song Y. Khor[1,2], Louis M. Layani[1,2], Chris Lumb[1,2], Daniel P. Poole[1,2], TinaMarie Lieu[1,2], Gregory D. Stewart[1], Quynh N. Mai[1,2], Dane D. Jensen[5], Rocco Latorre[5], Nicole N. Scheff[6], Brian L. Schmidt[6], John F. Quinn[1,2], Michael R. Whittaker[1,2], Nicholas A. Veldhuis[1,2]*, Thomas P. Davis[1,2,7]* and Nigel W. Bunnett[1,2,5,8]*

---

[1]Monash Institute of Pharmaceutical Sciences, Monash University, Parkville, Victoria, Australia. [2]Australian Research Council Centre of Excellence in Convergent Bio-Nano Science and Technology, Monash University, Parkville, Victoria, Australia. [3]Monash Biomedicine Discovery Institute, Monash University, Melbourne, Victoria, Australia. [4]Laboratory of Neurobiology, Center for the Development of Nanoscience and Nanotechnology (CEDENNA), University of Santiago de Chile, Santiago, Chile. [5]Departments of Surgery and Pharmacology, Columbia University Vagelos College of Physicians and Surgeons, Columbia University in the City of New York, New York , NY, USA. [6]Bluestone Centre for Clinical Research, New York University College of Dentistry, New York, NY, USA. [7]Australian Institute for Bioengineering and Nanotechnology, University of Queensland, Brisbane, Queensland, Australia. [8]Department of Pharmacology and Therapeutics, University of Melbourne, Parkville, Victoria, Australia. *e-mail: nicholas.veldhuis@monash.edu; thomas.p.davis@monash.edu; nwb2@nyu.edu

Supplementary Information

A pH-Responsive Nanoparticle Targets the Neurokinin 1 Receptor in Endosomes to Prevent Chronic Pain

Paulina D. Ramírez-García Jeffri S. Retamal, Priyank Shenoy, Wendy Imlach, Matthew Sykes, Nghia Truong, Luis Constandil, Teresa Pelissier, Cameron J. Nowell, Song Y. Khor, Louis M. Layani, Chris Lumb, Daniel P. Poole, TinaMarie Lieu, Gregory D. Stewart, Quynh N. Mai, Dane D. Jensen, Rocco Latorre, Nicole N. Scheff, Brian L. Schmidt, John F. Quinn, Michael R. Whittaker, Nicholas A. Veldhuis, Thomas P. Davis, Nigel W. Bunnett

Table of Contents

1. Supplementary Methods

1.1. Synthesis of diblock copolymers. Prior each synthesis, monomers were deinhibited using basic aluminium oxide. All polymers were synthesized via reversible addition fragmentation chain (RAFT) polymerization[1]. All reactions were carried out in toluene at 70°C and 400 RPM unless stated otherwise. Resulting polymers were purified by dialysis (molecular weight cut off, MWCO 3500, Membrane Filtration Products, USA) against acetone for 96 h. Residual solvent was evaporated and the final products were dried for 24 h in a vacuum oven at 37°C and 1000 mbar.

P(PEGMA-co-DMAEMA) hydrophilic block copolymer. The macromolecular chain transfer agent (macro-CTA), P(PEGMA-co-DMAEMA), was synthesized using 2-cyanoprop-2-yl dithiobenzoate (CPBD, 0.0736 g, $3.34\cdot10^{-4}$ mol) as a RAFT agent and azobisisobutyronitrile (AIBN, 0.0054 g, $3.34\cdot10^{-5}$ mol) as the initiator in a ratio of 1:0.1. The monomers poly(ethylene glycol) monomethyl ether methacrylate (PEGMA, 6 g, 0.02 mol) and 2-[*N,N*-(dimethylamino)ethyl] methacrylate (DMAEMA, 0.314 g, 0.001 mol) were added at a ratio of 10:1 and the mixture was left to react for 21 h.

P(PEGMA-co-DMAEMA)-b-P(DIPMA-co-DEGMA) diblock copolymer. The chain extension reaction was initiated by AIBN (0.0017 g, $1.033\cdot10^{-5}$ mol), using P(PEGMA-co-DMAEMA, 0.89 g, $6.89\cdot10^{-5}$ mol) and the monomers 2-[*N,N*-(diisopropylamino)ethyl] methacrylate (DIPMA, 1.47 g, $6.892\cdot10^{-3}$ mol) and di(ethylene glycol) methyl ether methacrylate (DEGMA, 0.1427 g, $7.58\cdot10^{-4}$) at a ratio of 0.15:1:100:11. The mixture was left to react for 17.5 h.

P(PEGMA-co-DMAEMA)-b-P(BMA) diblock copolymer. Butyl methacrylate (BMA, 0.582 g, 0.0041 mol) was polymerized from the hydrophilic P(PEGMA-co-DMAEMA) block by a chain extension reaction in the presence of AIBN (0.0008 g, $5.124\cdot10^{-6}$ mol) at a ratio of 120:1:0.2. The solution was left to react for 15 h.

P(PEGMA-co-DMAEMA)-b-P(DIPMA-co-DEGMA-co-Cy5) and P(PEGMA-co-DMAEMA)-b-P(BMA-co-Cy5) diblock copolymer. The chain extension of P(PEGMA-co-DMAEMA, 0.5 g, *$3.85\cdot10^{-5}$ mol*) was done by adding DIPMA (*0.82 g, $4.6\cdot10^{-3}$ mol)* and 4,4-dimethyl-2-vinyl-2-oxazolin-5-one (VDM, 0.027 g, *$1.92\cdot10^{-4}$ mol)* in the presence of AIBN (*0.95 mg, $5.77\cdot10^{-6}$ mol)* at a ratio of *1:100:11:5:0.15.* The mixture was left to react for *18 h.* For the BMA diblock copolymer only *BMA (0.66 g, 3.87·10-3 mol) was added* and the ratios of macro-CTA:BMA:VDM:AIBN were *1:120:5:0.15 and t*he mixture was left to react for *19* h. Cy5 coupling was achieved by mixing 250 µL of the reaction with Cyanine 5 amine (Cy5, 0.008 g, $1.20\cdot10^{-5}$ moles) and reacting at room temperature, 400 RPM for 72 h under dark conditions.

1.2. Analysis of diblock copolymers

Gel permeation chromatography. The molecular weights of polymers were determined by gel permeation chromatography using a Shimadzu (Kyoto, Japan) liquid chromatography system (Shimadzu, Japan) equipped with a (RID-10A) differential refractive index detector and SPD-20A ultraviolet-visible detector (λ = 633 nm). Samples were fractionated using 5.0 µm bead-size guard column (50 × 7.8 mm) and three Shodex KF-805L columns (300 × 8 mm, 10 µm bead-size, 5000 Å pore size) in series at 40°C. The eluent used was *N,N*-dimethylacetamide (DMAC, HPLC grade, with 0.03% w/v LiBr) with a flow rate of 1 mL/min. A molecular weight calibration curve was produced using polystyrene standards with narrow molecular weights distribution ranging from

500 to 2 × 10^6 Da.

Proton-nuclear magnetic resonance (^{1}H-NMR). The conversion of polymers was assessed by ^{1}H-NMR analysis using a Bruker Avance III 400 Ultrashield Plus spectrometer (USA) at 400 mHz running Topspin, version 1.3, using deuterated chloroform (chloroform-d) as solvent. Conversions (Conv%) and repeating monomer units (n) were calculated by ^{1}H-NMR using peak integrals (I) where the subscript number indicates the location of the peak in ppm (I_x). The Conv% and n for P(PEGMA-co-DMAEMA) were calculated using the ^{1}H-NMR spectra (Supplementary Fig. 1D.i) with $Conv\% = 100 \times \frac{(I_{4-4.6} - I_{5.7})}{I_{4-4.6}}, n_{PEGMA} = \frac{I_{4.25} - I_{2.5}}{I_{7.8-7.9}}$ and $n\ _{DMAEMA} = \frac{I_{2.5}}{I_{7.8-7.9}}$. Conv% and n for P(PEGMA-co-DMAEMA)-b-(DIPMA-co-DEGMA) were calculated using the ^{1}H-NMR spectra (Supplementary Fig. 1D.ii) with $Conv\% = 100 \times \frac{(PEGMA\ n + DEGMA\ n)}{(PEGMA\ n_{theoretical} + DEGMA\ n_{theoretical})}$, $n_{DIPMA} = \frac{I_3 + I_{2.6}}{2 \times I_{4-4.}} \times (n_{PEGMA} + n_{DMAEMA})$ and $n_{DEGMA} = \frac{I_{3.396}}{I_{3.378}} \times n_{PEGMA}$. Conv% and n for P(PEGMA-co-DMAEMA)-b-(BMA) were calculated using the ^{1}H-NMR spectra (Supplementary Fig. 1D.iii) with $Conv\% = 100 \times \frac{BMA\ n}{BMA\ n_{theoretical}}$ and $BMA\ n = \frac{I_{3.93}}{I_{4-4.2}} \times (PEGMA\ n + DEGMA\ n)$. Conv% and n for P(PEGMA-co-DMAEMA)-b-(DIPMA-co-DEGMA-co-VDM) and *P(PEGMA-co-DMAEMA)-b-(BMA-co-VDM)* were calculated as described for P(PEGMA-co-DMAEMA)-b-(DIPMA-co-DEGMA) *and P(PEGMA-co-DMAEMA)-b-(BMA)* (^{1}H-NMR spectra not shown).

1.3. Self-assembly of nanoparticles. P(PEGMA-co-DMAEMA)-b-P(DIPMA-co-DEGMA) was used as the diblock copolymer to self-assemble pH-responsive nanoparticles. P(PEGMA-co-DMAEMA)-b-P(BMA) was used to self-assemble control nanoparticles without pH responsive properties. For the self-assembly of nanoparticles loaded with aprepitant, a mixture of 5 mg of diblock copolymer and 53.5, 26.75 or 13.375 µg of aprepitant was dissolved in 0.5 mL of tetrahydrofuran (THF). Empty (Ø) nanoparticles were self-assembled without adding aprepitant. The mixture was then added into 4.5 mL of phosphate-buffered saline (PBS) under vigorous stirring at a flow rate of 1.2 mL/h, using a Harvard Apparatus syringe pump (USA) at room temperature. pH-responsive nanoparticles loaded with aprepitant (DIPMA-AP) and non-pH responsive nanoparticles loaded with aprepitant (BMA-AP) were dialyzed against PBS under nitrogen flow for 24 h (MWCO 3500). Assemblies without aprepitant (DIPMA-Ø and BMA-Ø) were dialyzed using Slide-A-Lyzer mini dialysis devices MWCO 3.5K (Thermo Fisher Scientific, USA) for 24 h. The assembly of nanoparticles for live cell imaging and biodistribution studies was done as described for nanoparticles without aprepitant using P(PEGMA-co-DMAEMA)-b-P(DIPMA-co-DEGMA-co-Cy5) *and P(PEGMA-co-DMAEMA)-b-(BMA-co-Cy5)*, which include Cy5 on the hydrophobic portion, resulting in nanoparticles with Cy5 localized in the core (DIPMA-Cy5 and BMA-Cy5).

1.4. Characterisation of nanoparticles

Dynamic light scattering (DLS). The size distribution of nanoparticles was determined by DLS using a Zetasizer Nano ZS ZEN3600 particle size analyser (Malvern, UK). DIPMA-AP, DIPMA-Ø and BMA-AP (1 mg/mL) were added to polystyrene cuvettes. Light scattering was measured at 25°C and 173° backscatter angle.

Ultra-performance liquid chromatography mass spectrometry (LC-MS). Aprepitant loading was assessed by LC-MS using a Waters Micromass Quattro Premier triple quadrupole mass spectrometer coupled to a Waters Acquity UPLC (USA). Freeze-dried DIPMA-AP and BMA-AP (1 mg/mL) were dissolved in a 5:2 mixture of DMSO:0.1% formic acid in water. Samples were prepared for analysis by mixing an aliquot with internal standard solution (diazepam, 5 µg/mL) in a 5:2 ratio and making up to 500 µL with the dilution solvent (1:1 mixture of 50% acetonitrile and 0.1% formic acid). Samples were fractionated on a Supelco Ascentis Express RP Amide column

(50 mm by 2.1 mm, 2.7 µm particle size) equipped with a Phenomenex SecurityGuard precolumn fitted with a Synergi Polar cartridge. Aprepitant loading was quantified against aprepitant standards (0.016 to 20 µM). The mobile phase consisted of 0.05% formic acid in water and acetonitrile and compounds were eluted under gradient conditions. Mass spectrometry was conducted in positive electrospray ionization conditions and elution of compounds monitored with multiple-reaction monitoring.

Determination of critical micelle concentration. The critical micellar concentration was determined by the pyrene I_1/I_3 ratio[2]. A pyrene stock solution (50 µM) was prepared in THF and 5 µL of pyrene stock were added to 995 µL of graded concentrations of nanoparticles (400 to 0.5 µg/mL), obtained by diluting nanoparticle stock solutions in PBS. The mixture was stirred for 3 h at room temperature and the fluorescence spectrum of pyrene was recorded from 360 to 410 nm using an excitation wavelength of 336 nm in a RF5301PC Espectrofluorophotometer (Shimadzu, Japan). The emission intensities measured at 373 nm (I_1) and 384 nm (I_3) were used to calculate the pyrene I_1/I_3 ratio.

Transmission electron microscopy. The morphology of nanoparticles was determined by transmission electron microscopy imaging using a Tecnai F20 transmission electron microscope at an accelerating voltage of 200 kV at ambient temperature. An aliquot (5 µL) of 0.1 wt% nanoparticle solution (diluted with Milli-Q water) was deposited on a Formvar coated copper grid (GSCu100F-50, Proscitech, Australia) and was allowed to dry overnight in air and at room temperature.

1.5. Nanoparticle disassembly. Nile Red (NR) is a solvatochromic dye that fluoresces only in non-polar solvents, allowing determination of the pH of disassembly for the nanoparticles. Specifically, the pH of disassembly is identified by observing the loss of fluorescence of NR due to release of NR from the core of nanoparticles. Nanoparticles were self-assembled using 0.1 mg of NR per mg of polymer and dialyzed as previously described. pH-responsive nanoparticles loaded with Nile red (DIPMA-NR) and non-pH responsive nanoparticles loaded with NR (BMA-NR) were prepared at a concentration of 200 µg/mL. For pH-dependent disassembly studies, nanoparticles were suspended in a mixture of 0.1 M citric acid and 0.2 M Na_2HPO_4 buffer solutions with a pH range from 7.6 to 5.0. pH-dependent disassembly was assessed by measuring NR fluorescence (excitation/emission 552/636nm) using a FlexStation 3 (Molecular Devices, USA). The time course of nanoparticle disassembly was examined by measuring NR fluorescence at pH 7.4, 6.5, 6.0 and 5.0 over a 12 h period using a CLARIOstar (BMG LABTECH, Germany).

1.6. pERK localization in mouse spinal cord. Spinal cord sections were preincubated in 10% normal donkey serum (NDS) in 0.1 M PBS (1 h, room temperature), followed by rabbit anti-phospho-p44/42 MAPK (ERK1/2) (Thr202/Tyr204) (1:200; #4370; Cell Signalling Technology, Danvers, MA) and guinea-pig anti-NeuN (1:1000, Millipore, #abN90) in PBS containing 0.3% Triton X-100 and 5% NDS (overnight, 4˚C). Sections were washed 4x in 0.1 M PBS containing 0.3% Triton X-100 and incubated with donkey anti-rabbit Alexa 488 and donkey anti-guinea-pig Alexa 568 (1:1000, Thermo Fisher Scientific) (45 min, room temperature). Sections were washed 5x in PBS, counter-stained with DAPI (10 µg/ml, 5 min) and cover-slipped with ProLong Glass mounting medium (Thermo Fisher Scientific). Sections were imaged on Leica SP8 confocal microscope with HC PLAPO 40X for counting pERK-immunoreactive (IR) neurons or a 20X objective to collect representative images. For each experimental group, 6 sections of ipsilateral and contralateral dorsal horn were imaged. Only pERK-positive neurons co-labelled with NeuN were counted. To avoid re-counting the same neurons, the analysed sections were 100 µm apart. The total number of neurons was averaged for each group.

1.7. Rotarod test. A rotarod test was used to assess whether the intrathecal injection of nanoparticles would affect normal motor function and thereby impede studies of nociception that require examination of paw withdrawal from a painful stimulus. Prior to experiments, mice were acclimatized and trained on the rotarod apparatus for three consecutive runs on two successive days. On the day of the experiment, three baseline readings were recorded and a cut-off threshold of 120 second was pre-set. Nanoparticles (DIPMA-AP, BMA-AP, DIPMA-Ø, 10 µg/mL) or vehicle (aCSF) was injected intrathecally as described above. Subsequently, the latency of mice to fall (seconds) were recorded at 30, 60, 90, 120, 180 and 240 min post-injection[3].

1.8. Electrophysiological assessment of nociception in rats. Rats were maintained under anaesthesia (1.2-1.5% isoflurane in oxygen using a diaphragm rodent facemask) and placed on a regulated thermal pad (37 ± 0.5°C). EMG activity was measured using a pair of platinum stimulation electrodes inserted subcutaneously into the lateral part of the third and fourth toes, and recording electrodes inserted through the skin into the ipsilateral biceps femoris muscle[4]. The C-reflex corresponds to the integration of the reflex response into a 150-450 ms time window post-stimulus. Wind-up is a potentiation of the C-reflex response when the stimulating frequency is increased to 1 Hz. The wind-up score corresponds to the slope of the first seven consecutive C-reflex recordings obtained at 1 Hz stimulation. After recording to obtain a stable C-reflex response (~30 min), the threshold for C-reflex was estimated and the rats remained stimulated at 2X the threshold intensity for the duration of the experiment. The C-reflex was evaluated by the mean of 15 consecutive stimuli at 0.1 Hz while the next 7 stimuli at 1 Hz were used to evaluate wind-up. Recordings were made 10 days after surgery before (basal) and 30, 60, 90 and 120 min after intrathecal drug administration. The integrated C-reflex responses were expressed as a percentage of basal response.

1.9. NK_1R localization in rat spinal cord. Free floating sections were blocked in PBS containing 0.3% Triton x-100 and 10% NDS (1 h, room temperature). Sections were incubated with rabbit anti-NK_1R (1:1000, #94168) and guinea-pig anti-NeuN (1:1000, Millipore, abn90) in PBS containing 0.3% Triton X-100 and 3% NDS (overnight, 4°C). Sections were washed 4x in PBS and incubated with donkey anti-rabbit Alexa488 and donkey anti-guinea-pig Alexa568 (1:1000, Thermo Fisher Scientific) (2 h, room temperature). Sections were washed 5x in PBS, counter stained with DAPI (10 µg/ml, 5 min), and mounted onto ColorFrost Plus slides (VWR) with ProLong Glass mounting medium (Thermo Fisher Scientific). Sections were imaged on Leica SP8 confocal microscope with a HC PL APO 63x oil objective (NA 1.4). Z stacks of NK_1R-positive neurons in lamina I of the dorsal horn were collected with a digital zoom of 5. To quantify NK_1R endocytosis in lamina I neurons, the border of the cytoplasm of the soma was delineated by NeuN fluorescence. NK_1R immunoreactivity within 5 pixels (0.5 µm) of the border was defined as plasma membrane receptor. The ratio of plasma membrane to cytosolic NK_1R-IR fluorescence was determined in >6 lamina I neurons per condition.

1.10. Cell viability assays. HEK-hNK_1R cells were incubated with empty nanoparticles (1-100 µg/mL) for 24 and 48 h. Medium was replaced by phenol red-free DMEM, followed by incubation for 2 h (37°C, 5% CO_2) with 10% (v/v) alamarBlue reagent (Thermo Fisher Scientific, USA). Fluorescence of the reduced active compound, resofurin, was measured (510/610nm exc/em) using a ClarioStar (BMG LABTECH, Germany).

Supplementary Figures

A

Polymer	Conversion (%)	GPC Mn (g/mol)	GPC PDI	^{1}H-NMR Mn (g/mol)	Composition PEGMA	DMAEMA	DIPMA	DEGMA	BMA
P(PEGMA-co-DMAEMA)	54	12,377	1.20	17,600	56	6	-	-	-
P(PEGMA-co-DMAEMA)-b-(DIPMA-co-DEGMA)	92	17,581	1.36	39,444	56	6	91	12	-
P(PEGMA-co-DMAEMA)-b-P-(BMA)	82	18,225	1.37	31,654	56	6	-	-	98
P(PEGMA-co-DMAEMA)-b-(DIPMA-co-DEGMA-co-VDM)	95	19,380	1.22	39,881	56	6	95	11	-
P(PEGMA-co-DMAEMA)-b-P-(BMA-co-VDM)	62	18,576	1.29	28,220	56	6	-	-	74

B Raft polymerization of diblock copolymers

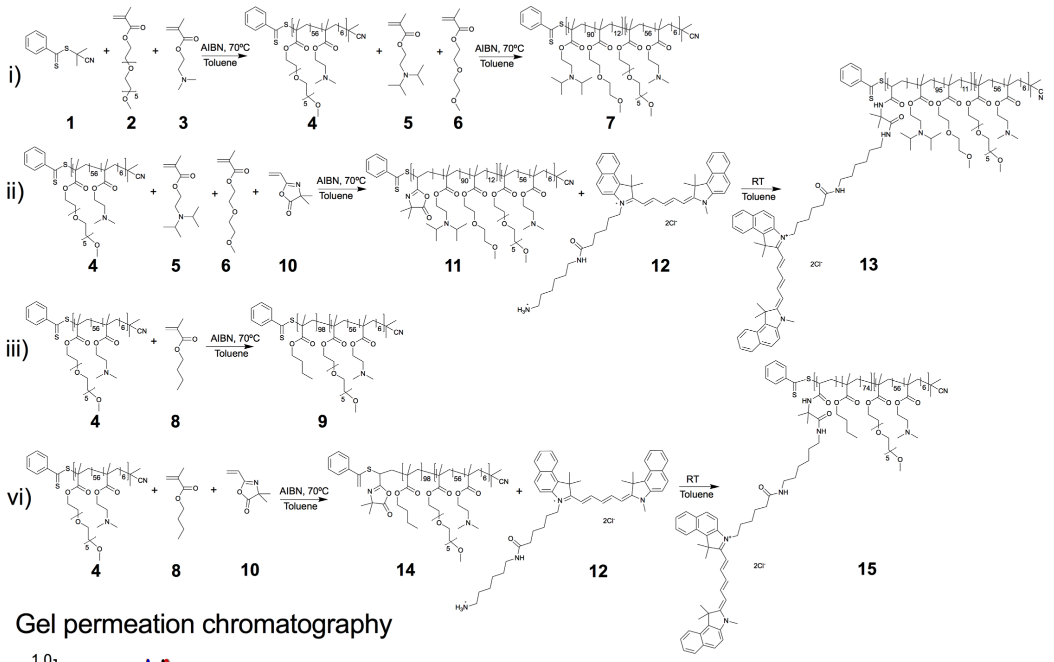

C Gel permeation chromatography

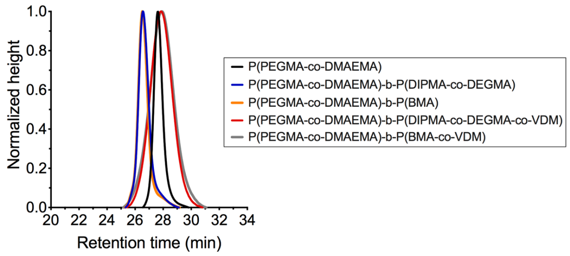

D Proton nuclear magnetic resonance

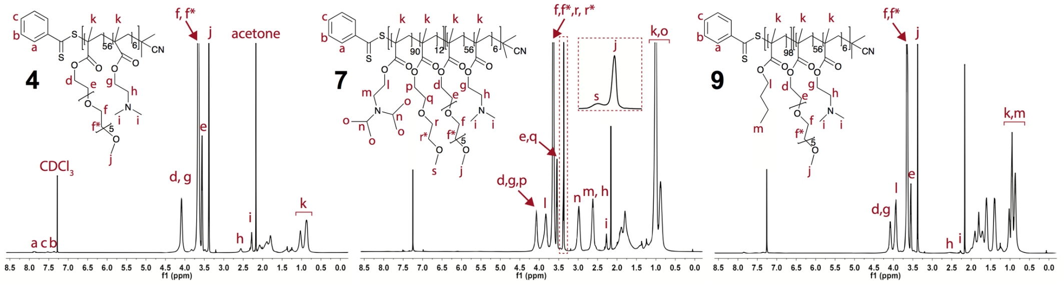

Figure S1. Synthesis and characterization of P(PEGMA-co-DMAEMA)-b-P(DIPMA-co-

DEGMA) and P(PEGMA-co-DMAEMA)-b-P(BMA-co-DEGMA) diblock copolymers. A. Characterization of the hydrophilic block copolymers and the diblock copolymers. **B. i)** Sequential RAFT polymerization indicating synthesis of the hydrophilic block using (**1**) CPDB, (**2**) PEGMA and (**3**) DMAEMA to form (**4**) p(PEGMA-c-DMAEMA); synthesis of P(PEGMA-co-DMAEMA)-b-P(DIPMA-co-DEGMA) by chain extension reaction, where addition of the pH-responsive monomer (**5**) DIPMA and the charge screening monomer (**6**) DEGMA to (**4**) the hydrophilic block forms (**7**) the diblock P(PEGMA-co-DMAEMA)-b-P(DIPMA-co-DEGMA); **ii)** Addition of (**5**) DIPMA, (**6**) DEGMA and (**10**) VDM to (**4**) the hydrophilic block to form the intermediate (**11**), followed by the addition of (**12**) Cy5 to form the final Cy5 conjugated polymer (**13**) P(PEGMA-co-DMAEMA)-b-P(DIPMA-co-DEGMA-co-Cy5). **iii)** Addition of (**8**) BMA to (**4**) the hydrophilic block forms (**9**) P(PEGMA-co-DMAEMA)-b-P(BMA). **iv)** Addition of (**8**) BMA and (**10**) VDM to (**4**) the hydrophilic block to form the intermediate (**14**), followed by the addition of (**12**) Cy5 to form the final Cy5 conjugated polymer (**15**) P(PEGMA-co-DMAEMA)-b-P(BMA-co-Cy5). **C.** Gel permeation chromatography traces showing a shift from P(PEGMA-co-DMAEMA) to higher molecular weight (*i.e.*, shorter retention time) after chain extension to form P(PEGMA-co-DMAEMA)-b-P(DIPMA-co-DEGMA) and P(PEGMA-co-DMAEMA)-b-P(BMA-co-DEGMA). **D.** ^{1}H-NMR spectra of the resulting polymers indicating the successful incorporation of the monomers. ^{1}H-NMR was used to estimate molecular weight since gel permeation chromatography was calibrated using polystyrene standards. **C** and **D** are from a single independent experiment because the polymer was made once and used throughout the project.

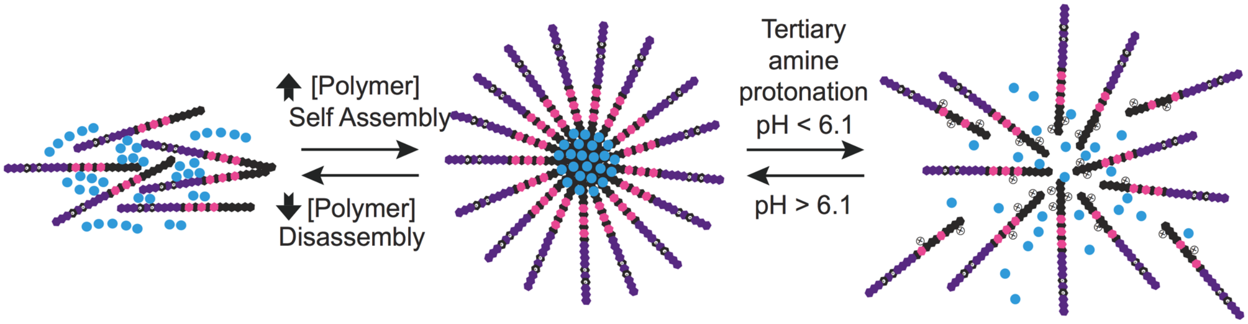

Figure S2. Mechanism of concentration-dependent self-assembly and pH-dependent disassembly of DIPMA nanoparticles. Increasing concentrations of polymer result in nanoparticle self-assembly in an aqueous solution. DIPMA nanoparticles possess a tertiary amine on the DIPMA units located in the core. At pH<6.1, protonation results in a change from neutral to positive charge on DIPMA that induce like-like charge repulsion, which destabilizes the nanoparticle core with the subsequent disassembly and release of cargo.

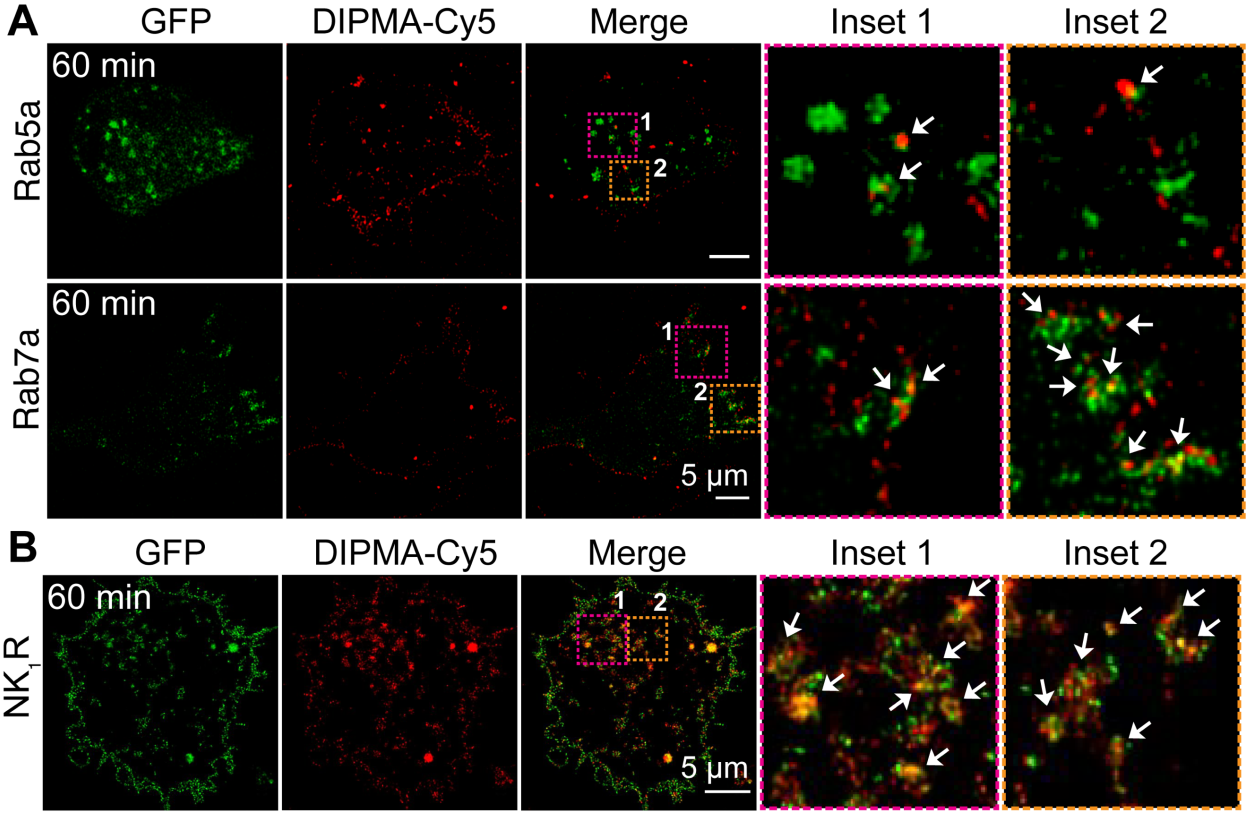

Figure S3. Uptake of DIPMA-Cy5 nanoparticles in HEK-293 cells. A. Localization of DIPMA-Cy5 nanoparticles in Rab5a-GFP early endosomes and Rab7a-GFP late endosomes after incubation with HEK-293 cells for 60 min. Representative results, *n* = 5 independent experiments. **B.** Colocalization of DIPMA-Cy5 nanoparticles and NK_1R-GFP in HEK-rNK_1R cells at 60 min after stimulation with SP to induce NK_1R endocytosis. Representative results, *n* = 5 independent experiments.

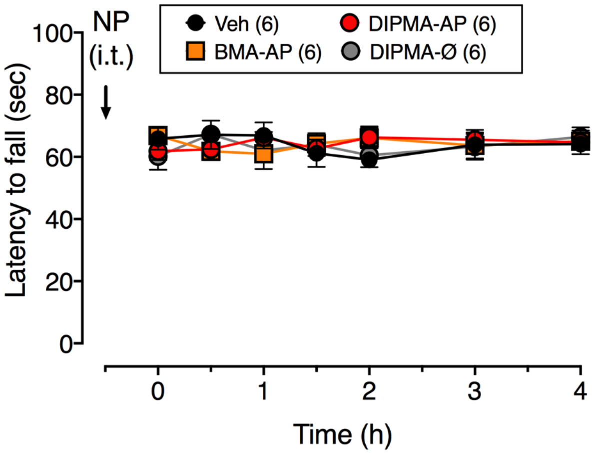

Figure S4. Effects of nanoparticles on rotarod latency. Effects of intrathecal (i.t.) injection of vehicle (Veh), DIPMA-Ø, BMA-AP or DIPMA-AP nanoparticles (NP) on latency to fall in mice, assessed using rotarod. Data are presented as mean ± SEM from *n* = 6 mice (numbers in parentheses) for each treatment group.

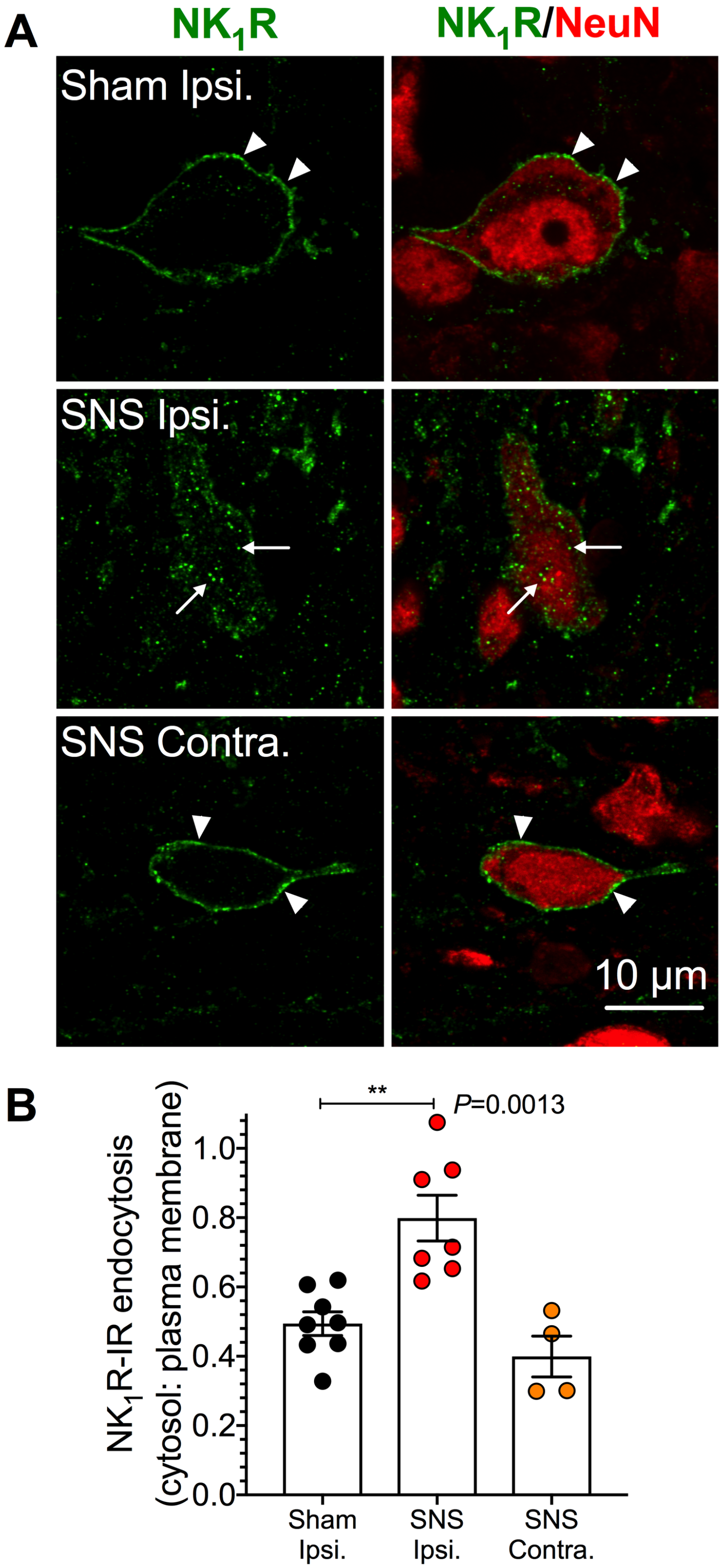

Figure S5. NK_1R endocytosis in chronic neuropathic nociception. To confirm activation of the SP/NK_1R system during chronic neuropathic nociception, the NK_1R was localized in the dorsal horn of rats 10 days after sural nerve spared (SNS) or sham surgery by immunofluorescence. **A.** Localization of NK_1R-IR and NeuN-IR to the ipsilateral (Ipsi.) or contralateral (Contra.) lamina I dorsal horn of sham or SNS rats. Arrow heads denote plasma membrane. Arrows denote endosomes. **B.** Quantification of NK_1R endocytosis, assessed as the cytosol:plasma membrane pixel intensity for NK_1R-IR neurons. Data are presented as mean ± SEM from sham ipsilateral ($n = 8$ rats), SNS ipsilateral ($n = 7$ rats) and SNS contralateral ($n = 4$ rats) groups. 1-way ANOVA, non-parametric Tukey post-hoc test. $^{**}P<0.01$.

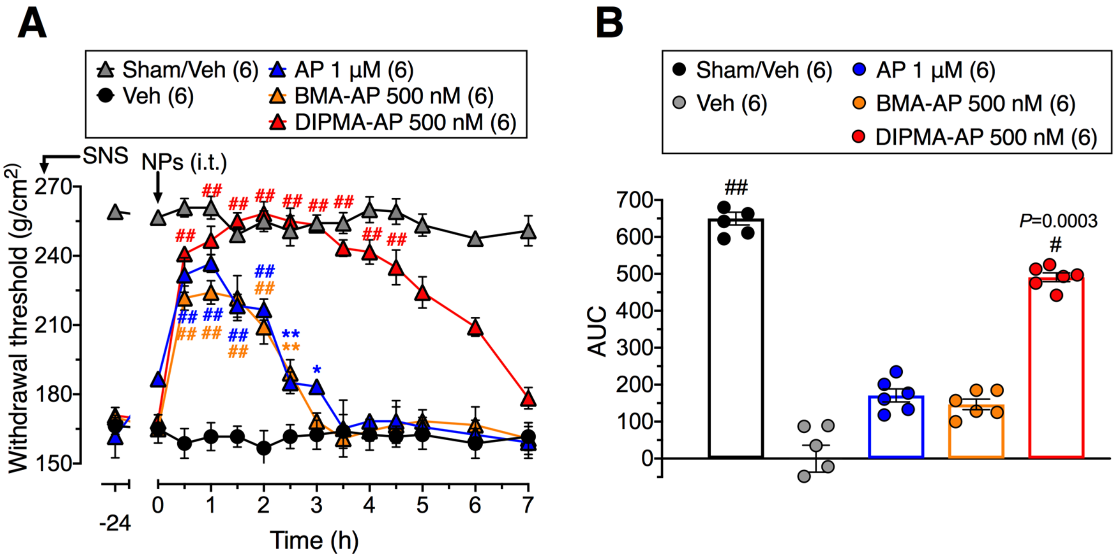

Figure S6. Effects of nanoparticles on neuropathic nociception. The sural nerve spared (SNS) model of chronic neuropathic pain was studied in rats. Vehicle (Veh), aprepitant (AP) or nanoparticle (NP) was administered by intrathecal injection 10 days after SNS or sham surgery. Paw withdrawal responses were assessed using the Randall-Selitto test. **A.** Time course of response. **B.** Area under curve (AUC) from 0-7 h. Data are presented as mean ± SEM from $n = 6$ rats (numbers in parentheses) for each treatment group. *$P<0.05$, **$P<0.005$, $^{\#}P<0.001$, $^{\#\#}P<0.0001$ compared to SNS vehicle. 1-way ANOVA, nonparametric Dunn's post-hoc test.

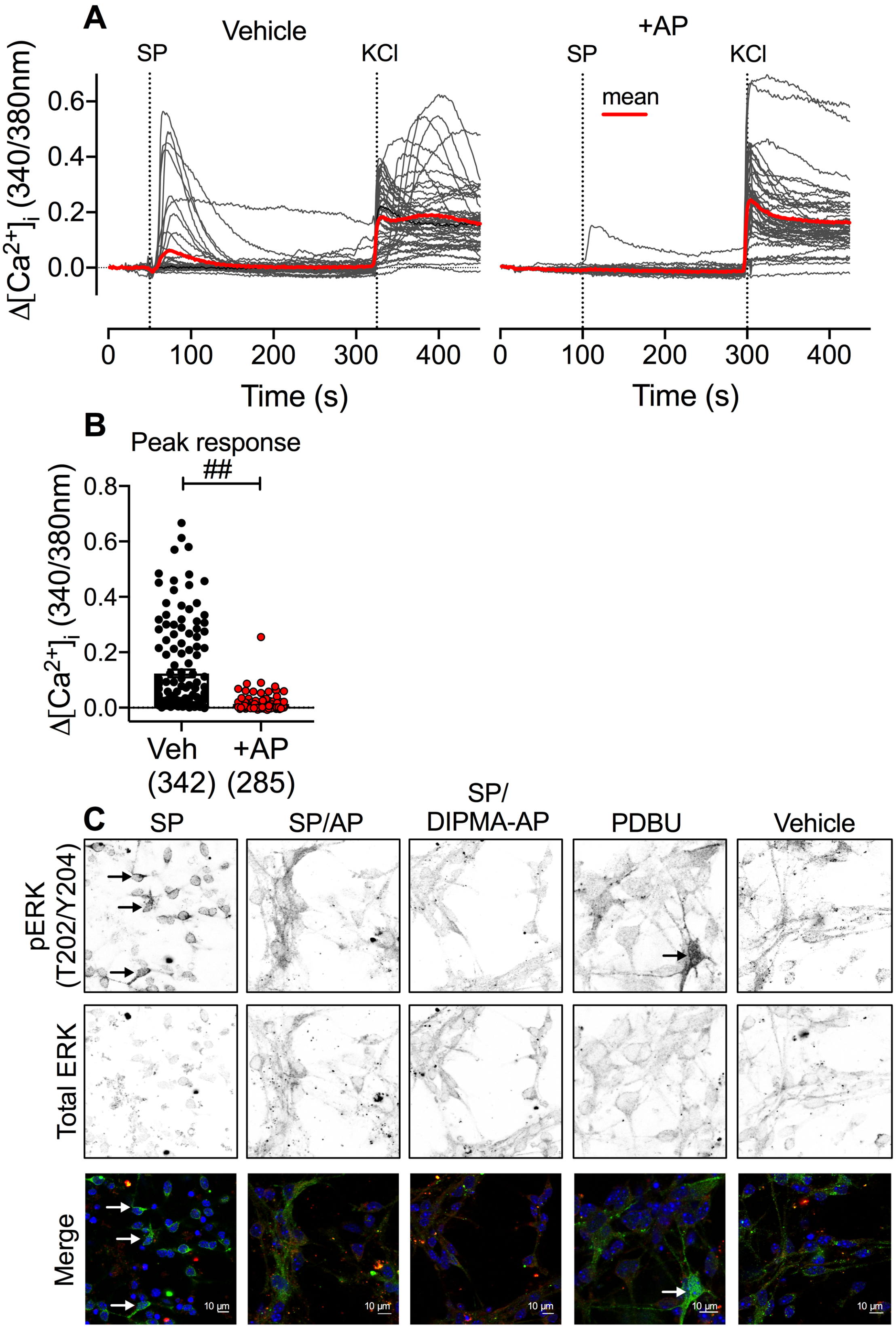

Fig. S7. SP signaling in mouse striatal neurons. SP (100 nM)-induced Ca^{2+} signaling in striatal neurons pretreated with vehicle (Veh) or aprepitant (AP). **A.** Representative traces of [Ca^2+]$_i$. Grey lines show responses of individual neurons. Red lines show mean responses. **B.** Peak [Ca^2+]$_i$ responses. Data are expressed as mean ± SEM from *n* = 342 neurons for SP plus vehicle or *n* = 285 neurons for SP plus aprepitant (numbers in parentheses) from *n* = 3 independent experiments for both treatment groups. ##*P*<0.0001, unpaired *t*-test (2-tailed). **C.** Representative images of phospho-ERK and total ERK immunostaining in cultured striatal neurons from *n* = 3 independent experiments. Neurons were treated with SP, SP plus aprepitant (AP), SP plus DIPMA-AP, phorbol 12,13-dibutyrate (PDBU) or vehicle.

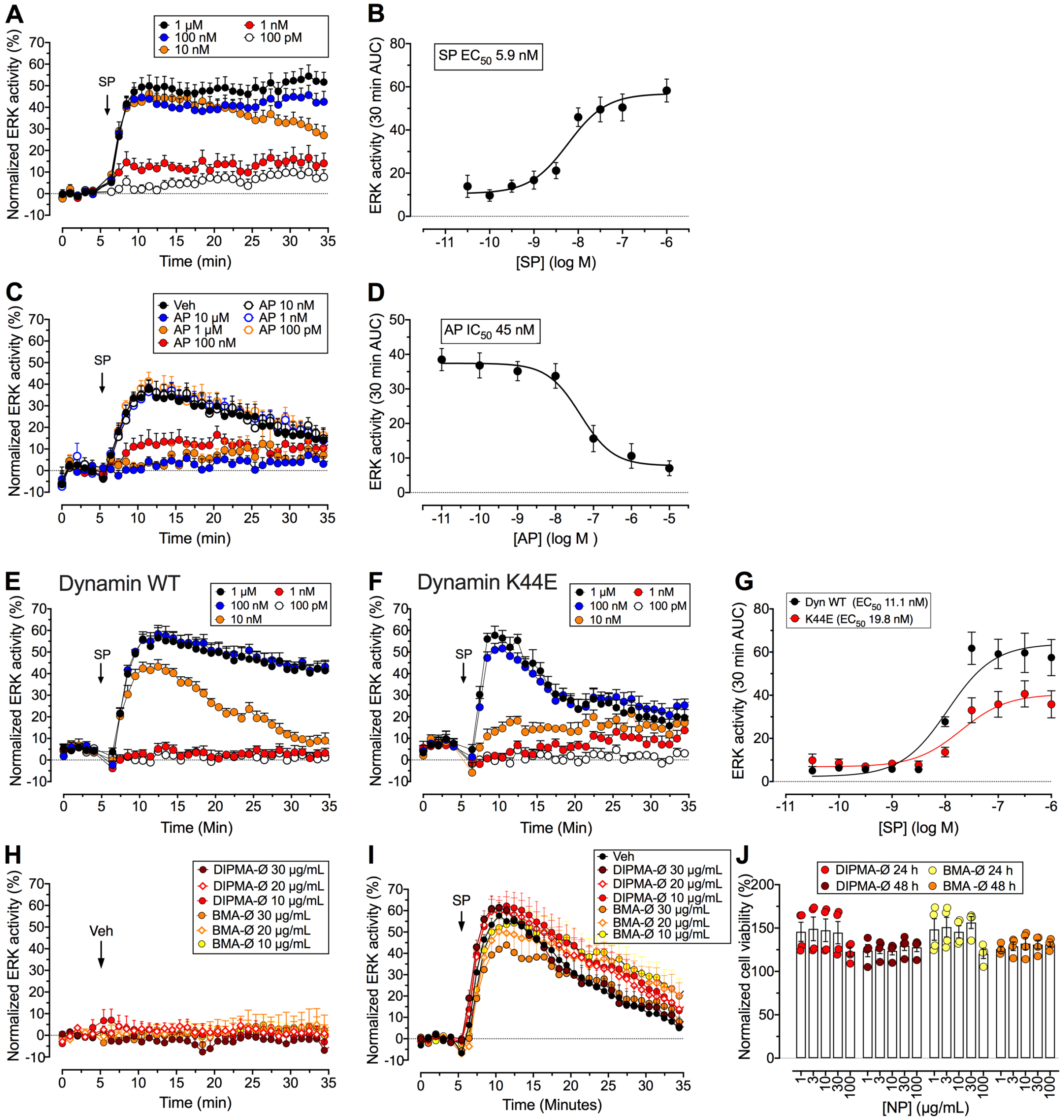

Figure S8. Nuclear ERK signalling and toxicity assays in HEK-293 cells. A-I. SP activation of nuclear ERK in HEK-hNK$_1$R cells. To examine activation of nuclear ERK, HEK-293 cells expressing hNK$_1$R were transfected with NucEKAR (FRET biosensor for nuclear ERK). Data are expressed as mean ± SEM, with triplicate observations made in each experiment. **A.** Effects of graded concentrations of SP on nuclear ERK activity; *n* = 8 independent experiments. **B.** SP concentration-response curves; *n* = 8 independent experiments. **C.** Effects of graded concentrations of aprepitant (AP) on nuclear ERK response to SP (5 nM); *n* = 7 independent experiments. **D.** Aprepitant concentration-response curves; *n* = 7 independent experiments. **E-G.** SP-induced activation of nuclear ERK in HEK-hNK$_1$R cells expressing dynamin wildtype (Dyn WT, **E**) or dynamin K44E (Dyn K44E, **F**); *n* = 6 independent experiments. **G.** SP concentration-response curves; *n* = 6 independent experiments. **H, I.** Effects of DIPMA-Ø and BMA-Ø on basal nuclear ERK activity in HEK-293 cells (**H**) and on SP-stimulated nuclear ERK activity in HEK-

hNK_1R cells (**I**) over 30 min; *n* = 7 independent experiments. **J.** Effects DIPMA-Ø and BMA-Ø on viability of HEK-293 cells over 24 h and 48 h. Viability was examined using alamarBlue, which assess the capability of viable cells to reduce rezasurin to resofurin; triplicate observations, *n* = 4 independent experiments.

Supplementary Videos

Video S1. Localization of DIPMA-Cy5 nanoparticles and Rab5a-GFP in HEK-293 cells. The video shows trafficking of DIPMA-Cy5 nanoparticles (red) to Rab5a-GFP early endosomes (green). Cells were incubated with DIPMA-Cy5 nanoparticles for 30 min.

Video S2. Localization of DIPMA-Cy5 nanoparticles and Rab7a-GFP in HEK-293 cells. The video shows trafficking of DIPMA-Cy5 nanoparticles (red) to Rab7a-GFP late endosomes (green). Cells were incubated with DIPMA-Cy5 nanoparticles for 30 min.

Video S3. Localization of DIPMA-Cy5 nanoparticles and NK_1R-GFP in HEK-293 cells. The video shows trafficking of DIPMA-Cy5 nanoparticles (red) and NK_1R-GFP (green). Cells were incubated with DIPMA-Cy5 nanoparticles for 90 min and with SP for 60 min to induce NK_1R endocytosis.

Video S4. Localization of DIPMA-Cy5 nanoparticles in the mouse dorsal horn. The video is a 3D projection of DIPMA-Cy5 nanoparticles in the perinuclear region of lamina I cells in the dorsal horn of the mouse spinal cord. The image was taken at 1 h after intrathecal injection of nanoparticles. Nuclei are stained with DAPI.

Video S5. Localization of BMA-Cy5 nanoparticles in the mouse dorsal horn. The video is a 3D projection of BMA-Cy5 nanoparticles in the perinuclear region of lamina I cells in the dorsal horn of the mouse spinal cord. The image was taken at 1 h after intrathecal injection of nanoparticles. Nuclei are stained with DAPI.

Video S6. Localization of NK_1R-IR in the rat dorsal horn after sham surgery. The video is a 3D projection showing the subcellular localization of NK_1R-IR (green) of lamina I spinal neuron (NeuN, red). The image was taken at 10 days after sham surgery.

Video S7. Localization of NK_1R-IR in the rat dorsal horn after SNS surgery. The video is a 3D projection showing the subcellular localization of NK_1R-IR (green) of lamina I spinal neuron (NeuN, red). The images were taken at 10 days after SNS surgery.

Supplementary References

1. Chiefari, J.*, et al.* Living free-radical polymerization by reversible addition−fragmentation chain transfer: The raft process. *Macromolecules* **31,** 5559-5562 (1998)

2. Aguiar, J., Carpena, P., Molina-Bolívar, J. A. & Carnero Ruiz, C. On the determination of the critical micelle concentration by the pyrene 1:3 ratio method. *J. Coll. Inter. Sci.* **258,** 116-122 (2003)

3. Jensen, D. D.*, et al.* Neurokinin 1 receptor signaling in endosomes mediates sustained nociception and is a viable therapeutic target for prolonged pain relief. *Sci. Trans. Med.* **9,** eaal3447 (2017)

4. Bravo, D.*, et al.* Pannexin 1: A novel participant in neuropathic pain signaling in the rat spinal cord. *Pain* **155,** 2108-2115 (2014)

Endosomal signaling of delta opioid receptors is an endogenous mechanism and therapeutic target for relief from inflammatory pain

Nestor N. Jimenez-Vargas[a], Jing Gong[b], Matthew J. Wisdom[c], Dane D. Jensen[c,d], Rocco Latorre[c], Alan Hegron[c], Shavonne Teng[c], Jesse J. DiCello[e], Pradeep Rajasekhar[e], Nicholas A. Veldhuis[e,f], Simona E. Carbone[e], Yang Yu[a], Cintya Lopez-Lopez[a], Josue Jaramillo-Polanco[a], Meritxell Canals[g], David E. Reed[a], Alan E. Lomax[a], Brian L. Schmidt[d], Kam W. Leong[b], Stephen J. Vanner[a], Michelle L. Halls[e,1], Nigel W. Bunnett[c,1], and Daniel P. Poole[e,f,1]

[a]Gastrointestinal Diseases Research Unit, Division of Gastroenterology, Queen's University, Kingston, ON, Canada K7L 2V7; [b]Department of Biomedical Engineering, Fu Foundation School of Engineering and Applied Science, Columbia University, New York, NY 10032; [c]Department of Molecular Pathobiology, New York University College of Dentistry, New York, NY 10010; [d]Bluestone Center for Clinical Research, New York University College of Dentistry, New York, NY 10010; [e]Drug Discovery Biology, Monash Institute of Pharmaceutical Sciences, Monash University, Parkville, VIC 3052, Australia; [f]Australian Research Council Centre of Excellence in Convergent Bio-Nano Science and Technology, Monash University, Parkville, VIC 3052, Australia; and [g]Centre for Membrane Proteins and Receptors and Division of Physiology, Pharmacology, and Neuroscience, School of Life Sciences, Queen's Medical Centre, University of Nottingham, NG7 2RD Nottingham, United Kingdom

Edited by Robert J. Lefkowitz, Howard Hughes Medical Institute and Duke University Medical Center, Durham, NC, and approved May 18, 2020 (received for review January 9, 2020)

Whether G protein-coupled receptors signal from endosomes to control important pathophysiological processes and are therapeutic targets is uncertain. We report that opioids from the inflamed colon activate δ-opioid receptors (DOPr) in endosomes of nociceptors. Biopsy samples of inflamed colonic mucosa from patients and mice with colitis released opioids that activated DOPr on nociceptors to cause a sustained decrease in excitability. DOPr agonists inhibited mechanically sensitive colonic nociceptors. DOPr endocytosis and endosomal signaling by protein kinase C (PKC) and extracellular signal-regulated kinase (ERK) pathways mediated the sustained inhibitory actions of endogenous opioids and DOPr agonists. DOPr agonists stimulated the recruitment of $G\alpha_{i/o}$ and β-arrestin1/2 to endosomes. Analysis of compartmentalized signaling revealed a requirement of DOPr endocytosis for activation of PKC at the plasma membrane and in the cytosol and ERK in the nucleus. We explored a nanoparticle delivery strategy to evaluate whether endosomal DOPr might be a therapeutic target for pain. The DOPr agonist DADLE was coupled to a liposome shell for targeting DOPr-positive nociceptors and incorporated into a mesoporous silica core for release in the acidic and reducing endosomal environment. Nanoparticles activated DOPr at the plasma membrane, were preferentially endocytosed by DOPr-expressing cells, and were delivered to DOPr-positive early endosomes. Nanoparticles caused a long-lasting activation of DOPr in endosomes, which provided sustained inhibition of nociceptor excitability and relief from inflammatory pain. Conversely, nanoparticles containing a DOPr antagonist abolished the sustained inhibitory effects of DADLE. Thus, DOPr in endosomes is an endogenous mechanism and a therapeutic target for relief from chronic inflammatory pain.

pain | inflammation | G protein-coupled receptors | signaling | nanomedicine

G protein-coupled receptors (GPCRs) control essential pathophysiological processes. One-third of Food and Drug Administration-approved drugs target GPCRs (1). GPCRs at the plasma membrane detect extracellular ligands and couple to heterotrimeric G proteins. Plasma membrane signaling is rapidly terminated. GPCR kinases phosphorylate activated GPCRs, which increases the affinity for β-arrestins (βARRs) (2). βARRs uncouple GPCRs from G proteins and desensitize signaling, and also couple GPCRs to the clathrin endocytic machinery (3). βARRs also recruit GPCRs, G proteins, and mitogen-activated protein kinases to endosomes (4, 5). Endosomes are an important site of continued GPCR signaling (6–8).

GPCRs control multiple steps of pain transmission (9). Endosomal signaling of protease-activated receptor-2 in primary sensory neurons and of neurokinin 1 receptor (NK_1R) and calcitonin-like receptor (CLR) in second-order neurons mediates neuronal excitation and pain transmission (10–13). The δ-, μ- and κ-opioid receptors (DOPr, MOPr, and KOPr) inhibit excitation of primary sensory, spinal, and supraspinal neurons and thereby induce analgesia (14). In patients with inflammatory bowel disease (IBD), infiltrating lymphocytes release opioids that activate opioid receptors on nociceptors to suppress excitability, providing an endogenous system of pain control (15–19). It is not known whether opioid receptors at the plasma

Significance

G protein-coupled receptors are considered to function principally at the cell surface. We present evidence that the δ-opioid receptor (DOPr) signals from endosomes to cause a sustained inhibition of pain. Opioids from the inflamed human and mouse colon, along with selective agonists that evoked DOPr internalization, inhibited the excitability of nociceptors by a mechanism requiring DOPr endocytosis. DOPr in endosomes generated a subset of signals in subcellular compartments that inhibited neuronal excitability. A DOPr agonist that was encapsulated into nanoparticles designed to selectively activate DOPr in endosomes of nociceptors caused a long-lasting inhibition of neuronal excitability and pain. Our results support the hypothesis that endosomal signaling of DOPr is an endogenous mechanism and therapeutic target for relief from inflammatory pain.

Author contributions: N.N.J.-V., J.G., D.D.J., R.L., A.H., J.J.D., P.R., N.A.V., S.E.C., Y.Y., C.L.-L., J.J.-P., M.C., D.E.R., A.E.L., B.L.S., K.W.L., S.J.V., M.L.H., N.W.B., and D.P.P. designed research; N.N.J.-V., J.G., M.J.W., D.D.J., R.L., A.H., S.T., J.J.D., P.R., N.A.V., S.E.C., Y.Y., C.L.-L., J.J.-P., D.E.R., and A.E.L. performed research; N.N.J.-V., J.G., M.J.W., D.D.J., R.L., A.H., J.J.D., P.R., N.A.V., S.E.C., Y.Y., C.L.-L., J.J.-P., M.C., D.E.R., A.E.L., B.L.S., K.W.L., S.J.V., M.L.H., N.W.B., and D.P.P. analyzed data; and N.N.J.-V., A.H., B.L.S., K.W.L., S.J.V., M.L.H., N.W.B., and D.P.P. wrote the paper.

Competing interest statement: N.W.B. is a founding scientist of Endosome Therapeutics Inc. Research in the laboratories of N.A.V., N.W.B., and D.P.P. is funded in part by Takeda Pharmaceuticals International.

This article is a PNAS Direct Submission.

[1]To whom correspondence may be addressed. Email: michelle.halls@monash.edu, nwb2@nyu.edu, or daniel.poole@monash.edu.

This article contains supporting information online at https://www.pnas.org/lookup/suppl/doi:10.1073/pnas.2000500117/-/DCSupplemental.

First published June 16, 2020.

membrane or in endosomes mediate this endogenous analgesic pathway and are the optimal target for treatment of inflammatory pain.

Here we investigated the hypothesis that opioids from the inflamed colon activate DOPr in endosomes of nociceptors to evoke signals that cause long-lasting inhibition of excitability and analgesia, and that DOPr in endosomes is a superior therapeutic target for inflammatory pain.

Results

DOPr Inhibits Inflammatory Pain. We investigated whether opioids from the inflamed colon activate opioid receptors on nociceptors and decrease excitability. Segments of colon from healthy control (HC) mice and from mice with colitis induced by chronic administration of dextran sulfate sodium (cDSS) were incubated in culture medium for 24 h to allow opioid release into the supernatant (16–18). Mouse dorsal root ganglia (DRG) neurons were exposed to HC or cDSS supernatant for 60 min and then washed (Fig. 1*A*).

To assess sustained changes in excitability, the rheobase (minimum input current required to fire an action potential) of small-diameter neurons was measured by patch-clamp recordings at 30 min after washing (T = 30 min) (11). The rheobase of neurons exposed to cDSS supernatant was 29 ± 6% higher than that of neurons exposed to HC supernatant ($P < 0.05$), consistent with decreased excitability (Fig. 1 *A* and *B*). To examine whether these findings translate to IBD, supernatants were obtained from colonic biopsy specimens from HC patients and patients with chronic ulcerative colitis (cUC). The rheobase of neurons exposed to cUC supernatant was 62 ± 16% higher than that of neurons exposed to HC supernatant ($P < 0.01$) (Fig. 1 *C* and *D*). Preincubation of neurons with the DOPr antagonist SDM25N (100 nM, 60 min) abolished the sustained effects of cDSS supernatant on rheobase, whereas the MOPr antagonist CTOP (100 nM, 60 min) had no effect (Fig. 1 *E* and *F*). Neither SDM25N nor CTOP affected the rheobase of neurons exposed to mouse HC supernatant (Fig. 1*F*). Thus, opioids from the inflamed colon cause a DOPr-mediated inhibition of nociceptors.

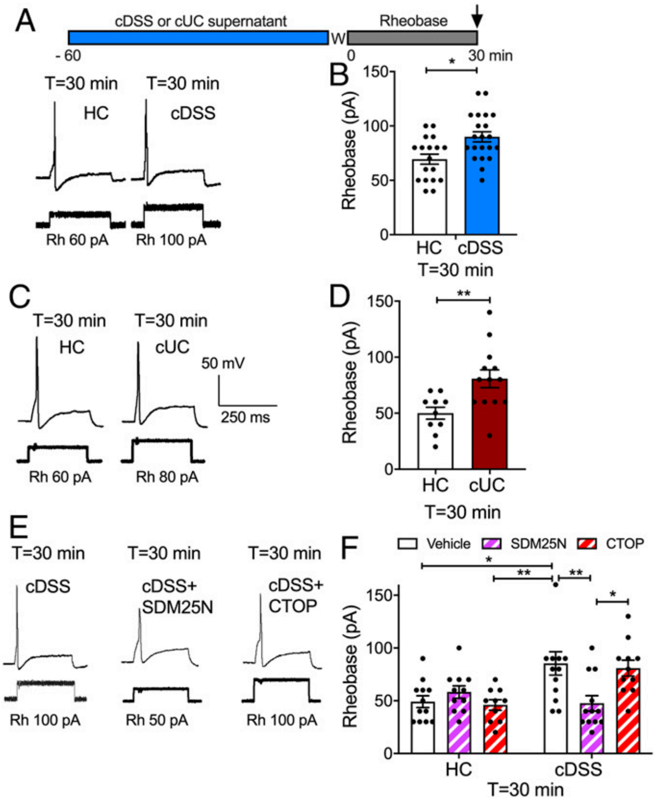

Fig. 1. Endogenous opioids and nociceptor excitability. Mouse DRG neurons were preincubated with supernatant from biopsies of HC, cDSS, or cUC colon and washed (W), and rheobase (Rh) was measured at 30 min after washing. Representative traces (*A*, *C*, and *E*) and pooled results (*B*, *D*, and *F*) of effects of supernatants from mouse (*A*, *B*, *E*, and *F*) and human (*C* and *D*) colonic biopsies. (*E* and *F*) Effects of antagonists of DOPr (SDM25N) or MOPr (CTOP) on responses to HC or cDSS supernatants. Data points indicate the number of studied neurons from $n = 12$ to 16 mice in *B*, 6 mice in *D*, and 8 mice in *F* for each treatment (mean ± SEM). *$P < 0.05$, **$P < 0.001$, two-way ANOVA with Tukey's post hoc test.

Endosomal DOPr Inhibits Nociceptor Excitability. To determine whether DOPr undergoes clathrin- and dynamin-mediated endocytosis in nociceptors, we isolated DRG neurons from knockin mice expressing DOPr fused to enhanced green fluorescent protein (DOPr-eGFP) (20). In vehicle-treated neurons, DOPr-eGFP was detected at the plasma membrane and in vesicles of the soma and neurites (Fig. 2*A*). The DOPr agonist DADLE (1 μM, 30 min) induced depletion of DOPr-eGFP from the plasma membrane and redistribution to endosomes. Dyngo4a (Dy4; 30 μM), which inhibits dynamin (21), and PitStop2 (PS2; 15 μM), which inhibits clathrin-mediated endocytosis (22), prevented DADLE-evoked endocytosis of DOPr-eGFP, as confirmed by quantification of plasma membrane and cytosolic DOPr-eGFP (Fig. 2*B*).

To examine the contribution of DOPr endocytosis to the inhibitory effects of endogenous opioids, we pretreated neurons with Dy4 or PS2 and then challenged them with cDSS, cUC, or HC supernatant. Neurons were washed, and rheobase was measured after 30 min. Dy4 and PS2 prevented the sustained increase in rheobase of neurons exposed to cDSS and cUC supernatants (Fig. 2 *C* and *D*). Inactive forms of Dy4 and PS2 do not affect the rheobase of nociceptors (11).

We similarly examined the contribution of endocytosis to the effects of DOPr- and MOPr-selective agonists on neuronal excitability. We exposed nociceptors to DOPr-selective agonists, including DADLE and SNC80 (10 nM, 15 min), which evoke βARR recruitment and DOPr endocytosis, and a 10-fold higher concentration of ARM390 (100 nM, 15 min), a weakly internalizing agonist (23) (Fig. 2*E*). Neurons were washed, and rheobase was measured immediately (T = 0 min) or 30 min (T = 30 min) after washing. DADLE and SNC80 caused both immediate (T = 0 min) and sustained (T = 30 min) increases in rheobase (Fig. 2 *E* and *F*). ARM390 increased rheobase at T = 0 min but not at T = 30 min (Fig. 2*G*). PS2 abolished the effects of DADLE and SNC80, but not of ARM390. The MOPr agonist DAMGO caused an immediate increase in rheobase that was not sustained and was inhibited by PS2 (Fig. 2*H*).

GPCRs in endosomes can activate protein kinase C (PKC) and extracellular signal-regulated kinases (ERKs), which control nociceptor excitability (11). To examine the role of these kinases in the sustained inhibitory actions of DOPr, we preincubated neurons with GF109203X (1 μM, 30 min), which inhibits PKC (24), or with PD98059 (50 μM, 30 min), which inhibits MEK1 (25). GF109203X and PD98059 abolished the sustained increase in rheobase (T = 30 min) to DADLE (Fig. 2 *I* and *J*).

To compare the chronic actions of DOPr agonists, neurons were incubated overnight with DADLE (100 nM) or ARM390 (300 nM). Neurons were washed, and rheobase was measured (Fig. 2*K*). DADLE caused both immediate (T = 0 min) and sustained (T = 30 min) increases in rheobase. PS2 blocked both phases (Fig. 2*K*). ARM390 caused an immediate increase (T = 0 min), but not a sustained (T = 30 min) increase, in rheobase, which was unaffected by PS2 (Fig. 2*L*). Thus, opioids from the inflamed colon and agonists that evoke DOPr endocytosis cause a sustained decrease in excitability of nociceptors that requires PKC and ERK signaling.

Endosomal DOPr Inhibits Colonic Afferent Activity. To assess whether endosomal DOPr signaling in the peripheral projections of colonic nociceptors mediates the inhibitory actions of opioids, we made extracellular recordings from lumbar splanchnic nerves innervating isolated segments of mouse distal colon (11). Nociceptors were identified by probing the colon or mesentery with von Frey filaments (VFF). Basal responses (1 g VFF, 100%) of each unit to repeated

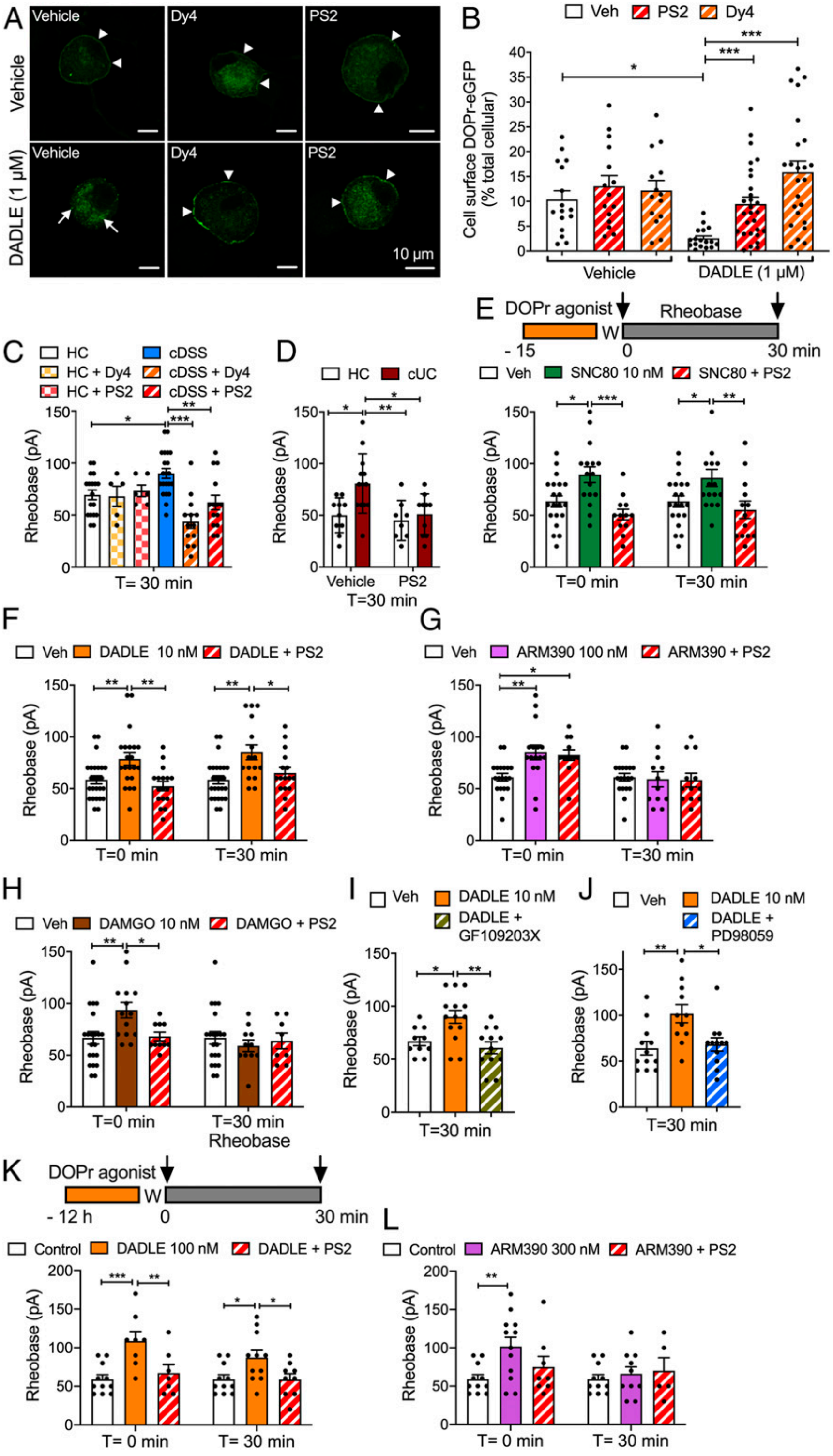

Fig. 2. Endosomal DOPr signaling and nociceptor excitability. (*A* and *B*) Endocytosis of DOPr-eGFP in DRG neurons from DOPr-eGFP mice. Neurons were incubated with vehicle (Veh) or DADLE (1 μM, 30 min), and DOPr-eGFP was localized by immunofluorescence. Neurons were preincubated with vehicle, Dy4, or PS2. (*A*) Representative images from four independent experiments. Arrowheads denote plasma membrane; arrows, endosomal DOPr-eGFP. (*B*) Quantification of the proportion of total cellular DOPr-eGFP at the plasma membrane. Data points indicate the number of studied neurons (N). $*P < 0.05$, $***P < 0.001$, two-way ANOVA with Tukey's post hoc test. (*C–L*) Rheobase of mouse DRG neurons at 0 or 30 min after exposure to supernatant or DOPr agonists and washing. (*C* and *D*) Supernatant from cDSS, cUC, or HC biopsy specimens. (*E–J*) Neurons were incubated with the following agonists for 15 min and washed (W), and rheobase was measured at 0 or 30 min after washing: DOPr agonists SNC80 (*E*, 10 nM, internalizing), DADLE (*F*, 10 nM, internalizing) or ARM390 (*G*, 100 nM, weakly internalizing), and MOPr agonist DAMGO (*H*, 10 nM). In *C–H*, neurons were preincubated with Dy4, PS2, or vehicle. In *I* and *J*, neurons were preincubated with PKC inhibitor GF10923X or MEK1 inhibitor PD98059 before DADLE. (*K* and *L*) Neurons were incubated with the following agonists overnight and washed, and rheobase was measured at 0 or 30 min after washing: DADLE (*K*, 100 nM, internalizing) or ARM390 (*L*, 300 nM, weakly internalizing). Data points indicate the number of studied neurons from 12 to 16 mice in *C*, 6 mice in *D*, 10 to 15 mice in *E–J*, and 6 mice in *K* and *L* for each treatment (mean ± SEM). $*P < 0.05$, $**P < 0.01$, $***P < 0.001$, one-way or two-way ANOVA with Tukey's post hoc test.

stimulation (three times for 3 s) were recorded (Fig. 3*A*). Agonists of DOPr (SNC80 and ARM390) or MOPr (DAMGO) (all 100 nM) were superfused into the organ bath for 15 min. Tissues were washed, and responses to VFF probing were reassessed every 15 min for 1 h. Compared with basal responses, DAMGO and ARM390 transiently inhibited the activity of colonic nociceptors, whereas SNC80 had a persistent inhibitory effect (Fig. 3 *B* and *C*). DAMGO maximally inhibited activity after 15 min of perfusion (i.e., 0 min, 53 ± 10% inhibition). ARM390 (weakly internalizing) inhibited activity only at 0 min (29 ± 4% inhibition). SNC80 (strongly internalizing) maximally inhibited activity at 30 min (33 ± 9% inhibition), which persisted for 60 min. PS2 (50 μM, 15 min) prevented the sustained inhibitory action of SNC80 (Fig. 3*D*). Thus, DOPr endosomal signaling within the peripheral projections of colonic nociceptors may induce a sustained inhibition of mechanical sensitivity.

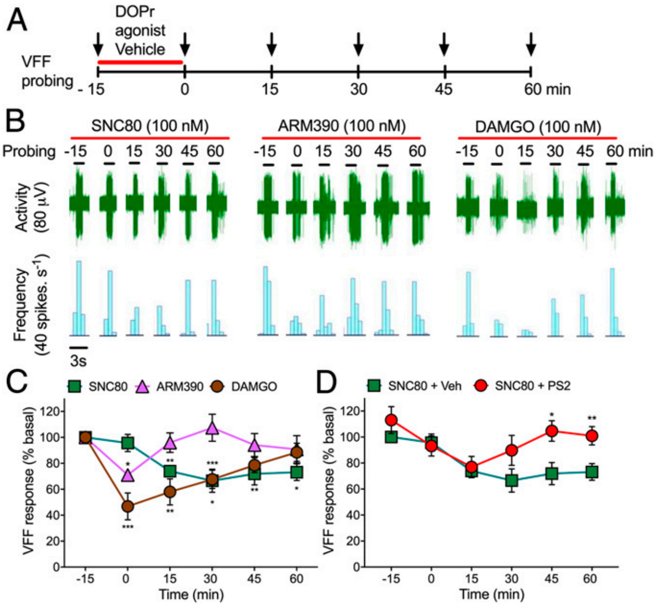

Fig. 3. MOPr and DOPr inhibition of colonic nociceptors. (*A*) Experimental protocol to examine MOPr and DOPr regulation of responses of colonic nociceptors to VFF probing. (*B*) Representative responses to agonists of DOPr (SNC80 and ARM390, 100 nM) and MOPr (DAMGO, 100 nM). (*C* and *D*) Time course of responses. In *D*, tissue was preincubated with PS2 or vehicle (Veh) before SNC80. $n = 5$ mice for each treatment. Data are mean ± SEM. $^{*}P < 0.05$, $^{**}P < 0.01$, $^{***}P < 0.001$, two-way ANOVA with Tukey's post hoc test.

DOPr Agonist Differentially Activate G Proteins, Recruit βARRs, and Stimulate Endocytosis. We characterized the differential effects of DOPr agonists on receptor signaling and trafficking using bioluminescence resonance energy transfer (BRET) (26). HEK293 cells were transiently transfected with Gα-Rluc8 subtypes plus Gγ2-Venus, Gβ1, and DOPr. Gα-Rluc8/Gγ2-Venus BRET was measured to assess G protein dissociation (activation). SNC80, DADLE, and ARM390 (100 nM) decreased $G\alpha_{i1}$-Rluc8/Gγ2-Venus and $G\alpha_{o}$-Rluc8/Gγ2-Venus BRET, indicative of $G\alpha_{i/o}$ and Gβγ activation (*SI Appendix*, Fig. S1 *A* and *B*). SNC80, DADLE, and ARM390 had no effect on $G\alpha_{s}$-Rluc8/Gγ2-Venus BRET or $G\alpha_{q}$-Rluc8/Gα-Rluc8 BRET (*SI Appendix*, Fig. S1 *C* and *D*). SNC80, DADLE, and ARM390 decreased $G\alpha_{i1,2,3,o}$-Rluc8/Gγ2-Venus BRET with similar efficacy and an order of potency of DADLE > SNC80 > ARM390 (*SI Appendix*, Fig. S1 *E*–*G*).

To investigate βARR recruitment, HEK293 cells were transfected with DOPr-Rluc and βARR1/2-YFP. SNC80 and DADLE, but not ARM390 (all 100 nM), increased DOPr-Rluc/βARR1/2-YFP BRET (*SI Appendix*, Fig. S1 *H* and *I*). ARM390 increased BRET only at high concentrations (>1 µM). The order of potency for βARR recruitment was DADLE > SNC80 > ARM390 (*SI Appendix*, Fig. S1 *J* and *K*).

Thus, SNC80, DADLE, and ARM390 induce DOPr coupling to $G\alpha_{i/o}$, and SNC80 and DADLE, but not ARM390, stimulate DOPr coupling to βARR1/2. These results are consistent with the capacity of SNC80, but not of ARM390, to promote DOPr-eGFP phosphorylation, which is required for βARR recruitment (27).

To assess DOPr trafficking, we measured bystander BRET between DOPr-Rluc and Venus-tagged proteins resident of the plasma membrane (HRas-Venus, lipid rich; KRas-Venus, non–lipid-rich) and endosomes (Rab5a, early; Rab7a, late; Rab11a, recycling) (26). SNC80 and DADLE (100 nM) decreased BRET between DOPr-Rluc, HRas-Venus, and KRas-Venus (*SI Appendix*, Fig. S1 *L* and *M*). These changes were mirrored by an increase in BRET between DOPr-Rluc and Rab5a-Venus (*SI Appendix*, Fig. S1*N*). SNC80 stimulated BRET between DOPr-Rluc and Rab7a-Venus (*SI Appendix*, Fig. S1*O*). ARM390 (100 nM) did not affect BRET between DOPr and plasma membrane or endosomal proteins. SNC80, DADLE, or ARM390 did not affect BRET between DOPr-Rluc and Rab11a-Venus (*SI Appendix*, Fig. S1*P*). Thus, SNC80 and DADLE cause DOPr internalization to early endosomes, whereas ARM390 does not. Internalized DOPr traffics to degradatory pathways in neurons (28).

DOPr Agonists Differentially Activate G Proteins and βARRs at the Plasma Membrane and in Endosomes. To assess activation of G proteins at the plasma membrane and in endosomes of HEK293 cells, we measured enhanced bystander (eb) BRET between mini-G proteins (Rluc8-$mG\alpha_{si/o/s/sq}$) (29, 30) and *Renilla* (R) GFP-CAAX (prenylation CAAX box of KRas) (31) for plasma membrane activation or tandem (td) RGFP-Rab5a for early endosome activation. Whereas Gα proteins associate with Gβγ subunits and GPCRs in the plasma membrane, mini-Gα proteins are N-terminally truncated and freely diffuse throughout the cytoplasm. Mini-Gα proteins can translocate to active GPCRs at the plasma membrane or in organelles. Mini-$G\alpha_{si}$ and $G\alpha_{sq}$ proteins were developed by mutating $mG\alpha_{s}$ residues to equivalent $G\alpha_{q}$ and $G\alpha_{i}$ residues. Recruitment of βARRs was assessed by measuring ebBRET between Rluc8-βARR1 (32) or Rluc2-βARR2 (31) and RGFP-CAAX or tdRGFP-Rab5a. Rab5a was localized to endosomes (*SI Appendix*, Fig. S2*A*). SNC80, DADLE, and ARM390 (100 nM) increased Rluc8-$mG\alpha_{si/o}$/RGFP-CAAX ebBRET (*SI Appendix*, Fig. S2 *B*–*E*) but did not affect Rluc8-$mG\alpha_{s/sq}$/RGFP-CAAX ebBRET (*SI Appendix*, Fig. S2 *F* and *G*). SNC80 and DADLE, but not ARM390, increased Rluc8-βARR1 or Rluc2-βARR2/RGFP-CAAX ebBRET (*SI Appendix*, Fig. S2 *H*–*K*). SNC80 and DADLE, but not ARM390, increased Rluc8-$mG\alpha_{si/o}$/tdRGFP-Rab5a ebBRET (*SI Appendix*, Fig. S2 *L*–*O*). These agonists did not affect Rluc8-$mG\alpha_{s/sq}$/tdRGFP-Rab5a ebBRET (*SI Appendix*, Fig. S2 *P* and *Q*). SNC80 and DADLE, but not ARM390, increased Rluc8-βARR1 or Rluc2-βARR2/tdRGFP-Rab5a ebBRET (*SI Appendix*, Fig. S2 *R*–*U*). Pertussis toxin blunted βARR recruitment to the plasma membrane (*SI Appendix*, Fig. S2 *H*–*K*) and endosomes (*SI Appendix*, Fig. S2 *R*–*U*), indicating involvement of $G\alpha_{i/o}$ signaling.

The foregoing results suggest that SNC80, DADLE, and ARM390 activate $G\alpha_{i/o}$ at the plasma membrane. Only agonists that strongly internalize DOPr (SNC80 and DADLE) activate $G\alpha_{i/o}$ in endosomes and recruit βARR1/2 to the plasma membrane and endosomes.

Endosomal DOPr Activates a Subset of Compartmentalized Signals. To examine DOPr signaling in subcellular compartments, we expressed DOPr and Förster resonance energy transfer (FRET) biosensors targeted to the plasma membrane, cytosol, or nucleus in HEK293 cells (10, 33). FRET biosensors included pmCKAR (plasma membrane PKC), cytoCKAR (cytosolic PKC), cytoEKAR (cytosolic ERK), and nucEKAR (nuclear ERK) (Fig. 4). To probe the link between endocytosis and compartmentalized signaling, we compared the effects of strongly internalizing (SNC80 and DADLE) and weakly internalizing (ARM390) DOPr agonists and used inhibitors of clathrin and dynamin.

SNC80 and DADLE (100 nM) stimulated a sustained increase in plasma membrane and cytosolic PKC activity (Fig. 4 *A*–*C*). ARM390 (100 nM) did not affect plasma membrane or cytosolic PKC activity. All three agonists stimulated a sustained increase in cytosolic ERK activity (Fig. 4 *D* and *F*). SNC80 and DADLE, but not ARM390, caused sustained activation of nuclear ERK (Fig. 4 *E* and *F*). These results suggest that DOPr signals from endosomes to activate plasma membrane and cytosolic PKC and nuclear ERK.

To assess the importance of endocytosis for compartmentalized signaling, we expressed wild-type (WT) dynamin or K44E dominant negative mutant dynamin (K44E dynamin) (34), or treated cells with PS2 or the inactive analog PS2 inactive. In control experiments with WT dynamin and PS2 inactive, SNC80 and DADLE induced rapid and sustained increases in PKC activity at the plasma membrane and in the cytosol (Fig. 5 *A*–*F*). Dynamin K44E and PS2 abolished SNC80 and DADLE stimulation of PKC at the plasma membrane and in the cytosol (Fig. 5 *A*–*F* and *SI Appendix*, Fig. S3 *A* and *B*). SNC80 and DADLE induced a gradual and sustained increase in

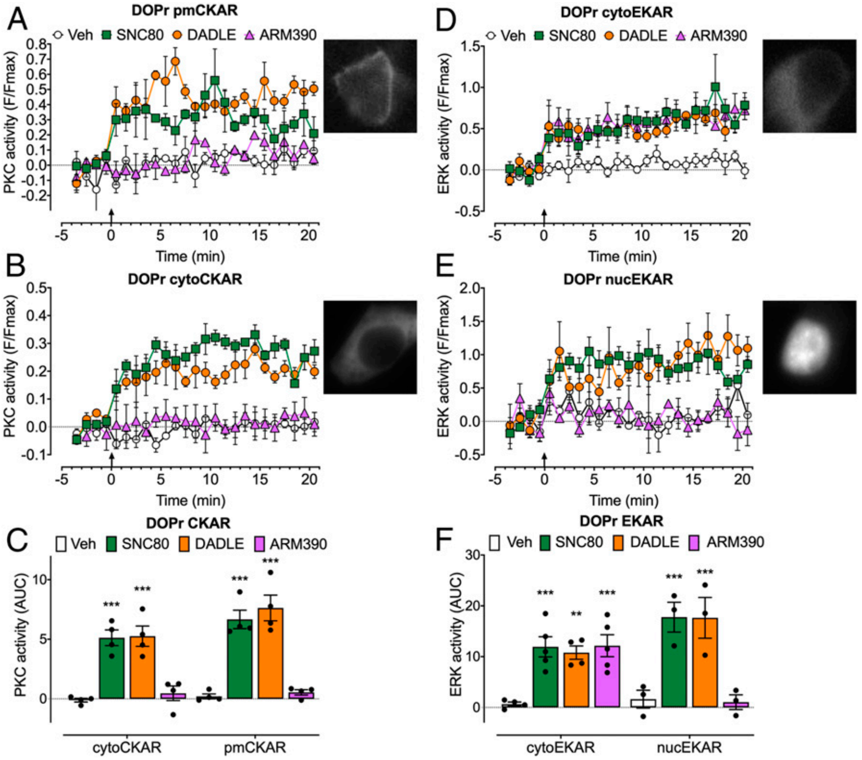

Fig. 4. DOPr-mediated PKC and ERK signaling in subcellular compartments of HEK293 cells. FRET biosensors for pmCKAR and cytoCKAR or cytoEKAR and nucEKAR were coexpressed with DOPr. *Insets* show cellular localization of FRET biosensors. Agonists (all 100 nM) or vehicle (Veh) were administered at the arrows. (*A* and *B*) Time course of plasma membrane (*A*) and cytosolic (*B*) PKC. (*C*) Integrated responses of plasma membrane and cytosolic PKC over 20 min (area under the curve [AUC]). (*D* and *E*) Time course of activation of cytosolic (*D*) and nuclear (*E*) ERK. (*F*) Integrated responses of cytosolic and nuclear ERK over 20 min (AUC). Data points show results of individual experiments. $n = 4$ (*A*–*C*), $n = 5$ cytoEKAR, $n = 3$ nucEKAR (*D*–*F*) independent experiments. Data are mean ± SEM. $^{**}P < 0.01$, $^{***}P < 0.001$ ligand to vehicle, one-way ANOVA with Tukey's post hoc test.

ERK activity in the cytosol and nucleus (Fig. 5 *G*–*L*). Dynamin K44E and PS2 did not affect SNC80- and DADLE-induced cytosolic ERK activity but abolished SNC80- and DADLE-induced nuclear ERK activity (Fig. 5 *G*–*L* and *SI Appendix*, Fig. S3 *C* and *D*). The contribution of βARR1/2 to signaling was examined by siRNA knockdown (10, 26). βARR1/2 siRNA, but not scrambled siRNA (control), inhibited SNC80-induced activation of nuclear, but not cytosolic, ERK (Fig. 5 *M*–*O*).

To evaluate DOPr compartmentalized signaling in nociceptors, we expressed FRET biosensors in DRG neurons from DOPr-eGFP mice. SNC80 and DADLE stimulated sustained activation of PKC at the plasma membrane and in the cytosol (Fig. 6 *A*–*C*) and of ERK in the cytosol and nucleus (Fig. 6 *D*–*F*). ARM390 stimulated a sustained activation of cytosolic ERK but did not affect plasma membrane PKC or nuclear ERK activity. Dy4 abolished SNC80-stimulated activation of nuclear ERK, whereas cytosolic ERK activity was unaffected (Fig. 6 *G*–*J*). These results suggest that DOPr endocytosis in HEK293 cells and primary nociceptors mediates activation of plasma membrane and cytosolic PKC and nuclear ERK, but not of cytosolic ERK.

Nanoparticle-Encapsulated Agonists Target Endosomal DOPr. The realization that endosomal DOPr signaling mediates the inhibitory actions of opioids on nociceptor excitability suggests that agonists that activate DOPr in endosomes might provide effective relief from inflammatory pain. Nanoparticles can be used to deliver an NK_1R antagonist into endosomes of spinal neurons, where acidification triggers nanoparticle disassembly and antagonist release, leading to sustained antinociception (12). We incorporated DADLE into mesoporous silica nanoparticles (MSNs) designed to dissolve and release cargo in the acidic and reducing endosomal environment (35, 36) (Fig. 7*A*). For selective targeting of DOPr-expressing neurons, we cloaked MSNs with PEGylated liposome covalently linked to DADLE.

Empty nanoparticles (LipoMSN), DADLE-coated nanoparticles (DADLE-LipoMSN), and nanoparticles with a DADLE coat and core (DADLE-LipoMSN-DADLE) were spherical with a hydrodynamic diameter of 140 to 210 nM, a surface charge of +28 to 36 mV, and a polydispersity index of 0.24 to 0.27 (Fig. 7 *B* and *C*). The loading efficiency of DADLE into the MSN core was 57 ± 6%. To examine MSN disassembly and cargo release, MSNs loaded with DADLE-Alexa647 (MSN-DADLE-Alexa647) were incubated in buffers at pH 7.2 or 5.2 or with or without 10 mM glutathione to mimic the acidic and reducing conditions of endosomes. The release of DADLE-Alexa647 into buffer was faster and more complete at pH 5.2 and in the presence of glutathione, and it continued for 24 h (Fig. 7 *D* and *E*).

To determine whether a DADLE-Lipo shell could facilitate selective uptake by DOPr-expressing cells, MSNs loaded with Alexa Fluor 647 and coated with DADLE-Lipo were incubated with untransfected HEK293 cells or HEK-DOPr cells for 2 h. The number of cells containing Alexa647 was determined by flow cytometry. DADLE-LipoMSN-Alexa647 was internalized into 66 ± 7% of HEK-DOPr cells, compared with 22 ± 1% of untransfected HEK293 cells ($P < 0.05$, t test), indicating preferential delivery to cells expressing DOPr (Fig. 7*F*). Dy4 and PS2, but not inactive analogs, inhibited DADLE-LipoMSN-Alexa647 uptake by HEK-DOPr cells, consistent with clathrin- and dynamin-mediated endocytosis (Fig. 7*G*).

To determine whether nanoparticles target DOPr in endosomes, HEK-HA-DOPr cells expressing Rab5a-GFP were incubated with HA antibodies to label surface DOPr. Cells were incubated with DADLE-LipoMSN-Alexa647 (20 μM DADLE, 200 μg/mL LipoMSN) and imaged by confocal microscopy. DADLE-LipoMSN-Alexa647 accumulated at the plasma membrane, stimulated endocytosis of HA-DOPr, and colocalized with HA-DOPr in early endosomes at 30 min (Fig. 7*H* and

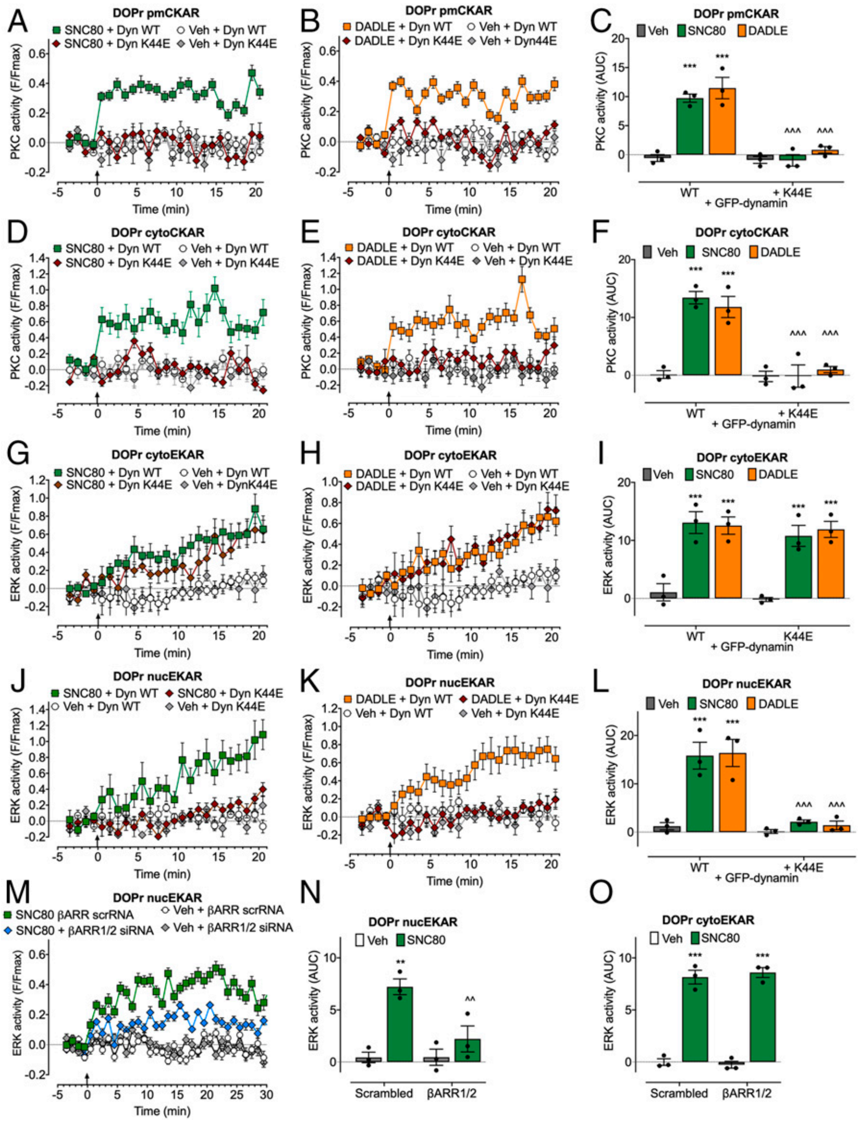

Fig. 5. Endosomal DOPr-mediated PKC and ERK signaling in subcellular compartments of HEK293 cells. FRET biosensors for pmCKAR and cytoCKAR or cytoEKAR and nucEKAR were coexpressed with DOPr and either dynamin WT (Dyn WT) or dominant negative dynamin K44E (Dyn K44E) (*A–L*) or with βARR1+2 siRNA or scrambled (scr) siRNA (control) (*M–O*). Agonists (all 100 nM) or vehicle (Veh) were administered at the arrows. (*A–C*) Plasma membrane PKC activity. (*D–F*) Cytosolic PKC activity. (*G–I* and *O*) Cytosolic ERK activity. (*J–N*) Nuclear ERK activity. (*A*, *B*, *D*, *E*, *G*, *H*, *J*, *K*, and *M*) Time course of responses. (*C*, *F*, *I*, *L*, *N*, and *O*) Integrated responses over 20 or 30 min (AUC). Data points show results of individual experiments. $n = 3$ independent experiments. Data are mean ± SEM. $^{**}P < 0.01$, $^{***}P < 0.001$ ligand to vehicle; ^^$P < 0.01$, ^^^$P < 0.001$ inhibitors to control; two-way ANOVA with Tukey's post hoc test.

SI Appendix, Fig. S4*A*). Live cell imaging, which avoided the loss of nanoparticle fluorescence during immunostaining, revealed DADLE-LipoMSN-Alexa647 binding to the plasma membrane and uptake into Rab5a-GFP endosomes within 30 min (Movie S1). Control LipoMSN-Alexa647, lacking the DADLE targeting group, showed diminished uptake (Movie S2).

We examined whether DADLE nanoparticles activate DOPr signaling at the plasma membrane (inhibition of cAMP, βARR1 recruitment) and in endosomes (nuclear ERK). Compared with Lipo-MSN or vehicle, DADLE (100 nM), DADLE-LipoMSN (20 μM DADLE), and DADLE-LipoMSN-DADLE (20 μM DADLE) inhibited forskolin (10 μM)-stimulated formation of cAMP in HEK-DOPr cells but not in untransfected HEK293 cells (Fig. 7*I* and *SI Appendix*, Fig. S4 *B* and *C*). DADLE and DADLE-LipoMSN-DADLE increased DOPr-Rluc8/βARR1-YFP BRET (Fig. 7*J* and *SI Appendix*, Fig. S4*D*). DADLE, DADLE-LipoMSN, and DADLE-LipoMSN-DADLE activated nuclear ERK, which was particularly sustained for DADLE-LipoMSN and DADLE-LipoMSN-DADLE (Fig. 7*K* and *SI Appendix*, Fig. S4*E*). These results suggest that DADLE coupled to the liposome shell can activate DOPr at the plasma membrane and stimulate DOPr endocytosis. DADLE released from the MSN core in endosomes might activate DOPr to stimulate nuclear ERK activity.

Primary cultures of DRG neurons from DOPr-eGFP knockin mice were studied to assess nanoparticle targeting and uptake into neurons. Neurons were incubated with DADLE, LipoMSN-Alexa647 (control), or DADLE-LipoMSN-Alexa647 (1 μM, 60 min, 37 °C) and fixed. GFP and the neuronal marker Hu were localized by immunofluorescence. DADLE evoked endocytosis of DOPr-eGFP in neurons (*SI Appendix*, Fig. S5*A*). LipoMSN-Alexa647 was detected at the surface of some neurons but did not promote DOPr-eGFP endocytosis (Fig. 8*A*). DADLE-LipoMSN-Alexa647 evoked DOPr-eGFP internalization and colocalized in endosomes with DOPr-eGFP.

A Nanoparticle-Encapsulated DOPr Agonist Provides Long-Lasting Antinociception. To assess antinociception, DRG neurons were incubated with DADLE, DADLE-LipoMSN, or DADLE-LipoMSN-DADLE (100 nM DADLE) for 30 min and washed, and then rheobase was

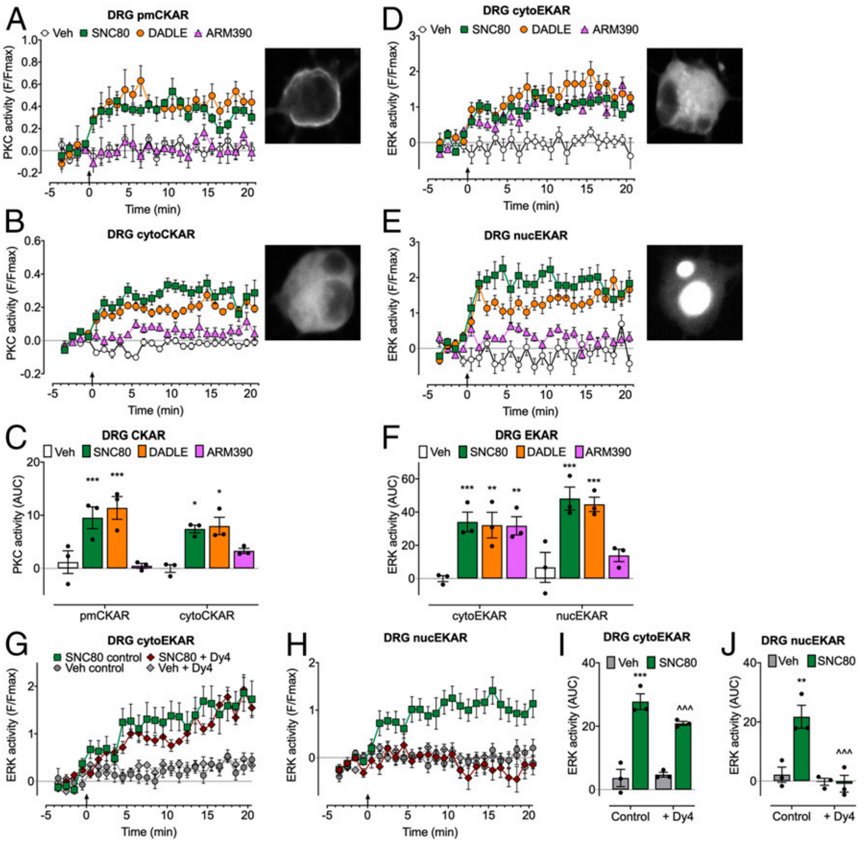

Fig. 6. Endosomal DOPr-mediated PKC and ERK signaling in subcellular compartments of DRG neurons. FRET biosensors for pmCKAR and cytoCKAR or cytoEKAR and nucEKAR were expressed in DRG neurons from DOPr-eGFP mice. *Insets* show localization of FRET biosensors. Agonists (all 100 nM) or vehicle (Veh) were administered at arrow. (*A* and *B*) Time course of plasma membrane (*A*) and cytosolic (*B*) PKC. (*C*) Effects of agonist treatments on PKC over 20 min (AUC). (*D* and *E*) Time course of cytosolic ERK (*D*) and nuclear ERK (*E*). (*F*) Effects of agonists on ERK activity over 20 min (AUC). (*G* and *H*) Time course of effects of dynamin inhibitor (Dy4) on cytosolic (*G*) and nuclear (*H*) ERK activity. (*I* and *J*) Effects of Dy4 treatments on ERK over 20 min (AUC). Data points show results of individual experiments. $n = 3$ independent experiments. Data are mean ± SEM. $^{*}P < 0.05$, $^{**}P < 0.01$, $^{***}P < 0.001$ ligand to vehicle; $^{\wedge\wedge\wedge}P < 0.001$ inhibitor to control; one-way ANOVA with Tukey's post hoc test.

measured at 0, 90, 120, or 180 min after washing. DADLE and DADLE-LipoMSN increased rheobase only at 0 min (Fig. 8 *B* and *C*). DADLE-LipoMSN-DADLE increased rheobase at 0, 90, and 120 min (26 ± 6% at 120 min). PS2 prevented the sustained inhibitory actions of DADLE-LipoMSN-DADLE (Fig. 8 *B* and *C*).

To assess the activity of peripheral colonic nociceptors, extracellular recordings were made from colonic afferents. DADLE-LipoMSN-DADLE (100 nM DADLE) was superfused into the organ bath for 30 min. Responses to VFF probing were assessed at 60 min and 120 min after washing. DADLE-LipoMSN-DADLE inhibited the activity of colonic nociceptors for at least 120 min (54 ± 13% inhibition) (Fig. 8*D*). PS2 prevented the sustained inhibitory action of DADLE-LipoMSN-DADLE.

To assess inflammatory nociception, complete Freund's adjuvant (CFA) was administered to mice by intraplantar injection, and withdrawal responses to stimulation of the plantar surface of the ipsilateral paw with VFFs were measured after 48 h. When administered by intrathecal injection to target DOPr on the central projections of nociceptors and on spinal neurons, DADLE (100 nM, 5 μL) had a moderate and transient antinociceptive action, whereas DADLE-LipoMSN-DADLE (100 nM DADLE, 5 μL) had a strong antinociceptive action that was sustained for 6 h (Fig. 8*E*). LipoMSN (1 μg/mL, 5 μL) had no effect. Nanoparticles did not affect withdrawal responses of the contralateral paw (*SI Appendix*, Fig. S5*B*). Thus, neuronal-targeted stimulus-responsive nanoparticles provide long-lasting antinociception.

A Nanoparticle-Encapsulated DOPr Antagonist Prevents the Sustained Antinociceptive Actions of DOPr. To provide evidence that DOPr endosomal signaling underlies sustained inhibition of neuronal excitability, we encapsulated the DOPr antagonist SDM25N into nanoparticles with a liposome shell (LipoMSN-SDM25N). LipoMSN-SDM25N had a hydrodynamic diameter of 176.5 ± 0.6 nm, a surface charge of +32 ± 3 mV, and a polydispersity index of 0.15 ± 0.02. SDM25N loading efficiency was 73.5 ± 0.8%. To assess the uptake of nanoparticles lacking the DADLE targeting group, LipoMSN-Alexa647 nanoparticles were incubated with HEK293 cells (0 to 4 h, 37 °C). After 120 min, LipoMSN-Alexa647 was detected in Rab5a-positive early endosomes (Fig. 8*F*). LipoMSN-Alexa647 was internalized in 67.7 ± 1.3% of HEK293 cells after 120 min, as assessed by flow cytometry (Fig. 8*G*). To determine whether an endosomally targeted DOPr antagonist can block nociception, DRG neurons were incubated with LipoMSN-SDM25N (100 nM SDM25N, 100 μg/mL LipoMSN) or LipoMSN (100 μg/mL, control) (120 min, 37 °C) (Fig. 8*H*), then washed, incubated with DADLE (10 nM, 15 min) and washed again. Rheobase was measured at 0 and 30 min after washing. In LipoMSN-treated neurons, DADLE increased rheobase at 0 min (53.44 ± 17.1%) and 30 min (55.56 ± 10.07%) compared with control. LipoMSN-SDM25N had no effect on the rheobase at 0 min (52.18 ± 13.78%) but abolished the inhibitory effect of DADLE at 30 min. These results support the hypothesis that DOPr signals from endosomes to cause persistent antinociception.

Discussion

Our results support the hypothesis that DOPr in endosomes is as a key component of an endogenous mechanism of pain control, and that endosomal DOPr is a viable therapeutic target for chronic inflammatory pain.

Antinociceptive Signaling of Endosomal DOPr. Several observations suggest that DOPr signaling in endosomes mediates the sustained antinociceptive actions of endogenous opioids and certain DOPr-selective agonists (*SI Appendix*, Fig. S6). Biopsy specimens of inflamed human and mouse colon released opioids that caused a sustained inhibition of the excitability of nociceptors, as revealed by increased rheobase. These effects are attributable to DOPr, because a selective antagonist prevented inhibition. Colitis evokes endocytosis of DOPr-eGFP in myenteric neurons, consistent with opioid release and DOPr activation (37). Our findings support reports of an opioid-mediated mechanism of antinociception in inflamed colon (15–19). DOPr agonists that stimulated robust receptor endocytosis (DADLE and SNC80) caused a persistent inhibition of nociceptor excitability, whereas a weakly internalizing DOPr agonist (ARM390) had only a transient inhibitory action. Inhibitors of clathrin and dynamin prevented agonist-evoked endocytosis of DOPr-eGFP in nociceptors and blocked the sustained inhibitory actions of endogenous opioids and internalizing DOPr agonists.

These results support a role for endosomal signaling of DOPr in regulating sustained excitability of the soma, which was examined by patch clamp recordings. Similar mechanisms may control the excitability of nerve endings in the colon, since SNC80 caused a long-lasting inhibition of mechanically sensitive nociceptors, whereas weakly internalizing ARM390 did not. A clathrin inhibitor blocked the effects of SNC80, which require endosomal signaling. DOPr endocytosis has also been linked to analgesic tolerance (23, 27, 38, 39). A DOPr antagonist (SDM25N) incorporated into nanoparticles designed to deliver and release cargo in endosomes prevented the sustained inhibitory actions of DADLE on nociceptor excitability. These findings suggest that DADLE continues to activate DOPr in endosomes to inhibit nociception.

Our results do not exclude a role for plasma membrane signaling of DOPr in antinociception. Inhibitors of endocytosis and nanoparticle-encapsulated SDM25N did not affect the short-term inhibitory effects of DOPr agonists on excitability. Thus, DOPr signaling at the plasma membrane and in endosomes mediates antinociception, but with different time courses.

Our results reveal spatial and temporal differences in the way in which DOPr and MOPr regulate the excitability of nociceptors. A MOPr antagonist did not prevent the inhibitory actions of colonic supernatants on neuronal excitability, suggesting that MOPr does not contribute antinociception during colitis. Although the MOPr agonist DAMGO transiently decreased the excitability of DRG neurons and colonic afferents, these effects were not sustained. A clathrin inhibitor prevented the transient inhibitory actions of DAMGO, which likely require endosomal signaling of MOPr. These results are in agreement with studies in which a conformationally selective nanobody was used to detect activated MOPr in subcellular compartments (40).

Biophysical approaches were used to examine DOPr trafficking and signaling in HEK-DOPr cells and nociceptors, with consistent results. All DOPr agonists (DADLE, SNC80, and ARM390) activated G$\alpha_{i/o}$ with similar efficacy. Only strongly internalizing agonists (DADLE and SNC80) potently recruited βARR1/2 and stimulated DOPr depletion from the plasma membrane and accumulation and retention in early endosomes. The results confirm reported differences in the ability of DADLE, SNC80, and ARM390 to promote DOPr internalization (23). These differences are attributable to GRK-induced DOPr phosphorylation; SNC80 induces DOPr phosphorylation at Ser^{363}, whereas ARM390 does not (27).

The use of FRET biosensors targeted to the plasma membrane, cytosol, or nucleus revealed that DOPr endocytosis is necessary for a subset of signals in subcellular compartments. Our results suggest that DOPr signaling from the plasma membrane activates ERK in the cytosol, whereas DOPr signaling in endosomes activates PKC at the plasma membrane and in the cytosol and activates ERK in the nucleus but not in the cytosol. Support for these conclusions derives from the observation that internalizing agonists alone activated plasma membrane and cytosolic PKC and nuclear ERK. Inhibitors of clathrin- and dynamin-mediated endocytosis, dominant negative dynamin, and βARR1/2 knockdown selectively suppressed these signals. Other GPCRs also signal from endosomes to regulate subsets of compartmentalized signals (10, 11, 13). Inhibitors of PKC and MEK1 prevented the sustained inhibitory actions of DADLE on neuronal excitability, providing a link between endosomal DOPr signaling and antinociception. PKC is a critical regulator of DOPr-mediated signaling and antinociception (41). DOPr endocytosis is also required for ERK activation and trafficking to perinuclear and nuclear locations (42).

G$\alpha_{i/o}$ and βARRs may mediate endosomal DOPr signaling, since internalizing, but not weakly internalizing, DOPr agonists stimulated the recruitment of mini-G$\alpha_{i/o}$ and βARR1/2 to early endosomes, as determined by BRET. βARR1/2 knockdown inhibited SNC80-stimulated nuclear ERK activation, possibly due to inhibition of DOPr endocytosis and endosomal signaling. Further studies are needed to determine the contribution of βARRs and G$\alpha_{i/o}$ to endosomal DOPr signaling.

Therapeutic Targeting of Endosomal DOPr. The realization that GPCRs can signal from endosomes to mediate pain has revealed endosomal GPCRs as a viable therapeutic target (8). Conjugation to transmembrane lipids or encapsulation into pH-tunable nanoparticles delivers antagonists of pronociceptive GPCRs to endosomes (10–13). Endosomally targeted antagonists preferentially inhibit endosomal signaling and provide enhanced antinociception compared with conventional antagonists. The present study shows that endosomally targeted agonists of antinociceptive GPCRs also provide long-lasting pain relief. DADLE-LipoMSN-DADLE inhibited nociceptor excitability for at least 3 h after washout, in contrast to the transient inhibitory action of free DADLE. DADLE-LipoMSN-DADLE caused a long-lasting inhibition of mechanically evoked activation of colonic nociceptors and effectively reversed inflammatory nociception. One component of the enhanced antinociceptive properties of nanoparticles might relate to the selective delivery of primary sensory neurons to endosomes. Targeted delivery to DOPr-expressing neurons was accomplished by cloaking MSNs with PEGylated liposomes covalently linked to DADLE. DADLE-LipoMSNs retained the ability to activate DOPr in HEK-DOPr cells, as assessed by inhibition of cAMP, recruitment of βARR1, stimulation of DOPr endocytosis, and activation of nuclear ERK (*SI Appendix*, Fig. S6). Uptake of DADLE-LipoMSNs by HEK-DOPr cells was threefold greater than that by untransfected HEK cells, suggesting preferential targeting. DADLE-LipoMSNs entered cells by clathrin-mediated endocytosis and were delivered to DOPr-positive early endosomes. Another component of enhanced antinociception could be the sustained activation of DOPr in endosomes, which was attained by incorporating DADLE into the MSN core. DADLE release was accelerated in the acidic and reducing endosomal environment and continued for 24 h. The finding that a clathrin inhibitor abrogated the antinociceptive actions of DADLE-LipoMSN-DADLE indicates a requirement for nanoparticle endocytosis.

More direct evidence for a role of endosomal DOPr in antinociception was provided by incorporating the DOPr antagonist SDM25N into nanoparticles. When preincubated with neurons to allow for endosomal accumulation, followed by extensive washing to remove extracellular antagonist, LipoMSN-SDM25N prevented the sustained inhibitory actions of DADLE on nociceptor excitability, supporting endosomal signaling. The immediate inhibitory actions of DADLE were unaffected and likely arose from plasma membrane DOPr.

Incorporation into nanoparticles can enhance the stability and delivery of drugs, thereby improving efficacy (43–45). Stimulus-responsive nanoparticles deliver combinations of chemotherapeutics to tumors, where increased vascular permeability and extracellular acidification promote delivery and cargo release (46, 47). Although nanoparticles are often endocytosed, endosomal disruption is necessary for drug delivery to cytosolic and nuclear targets, which can compromise efficacy (48). The discovery of GPCRs in endosomes as therapeutic targets provides an opportunity to use nanoparticles to deliver treatments for pain (8). Our results

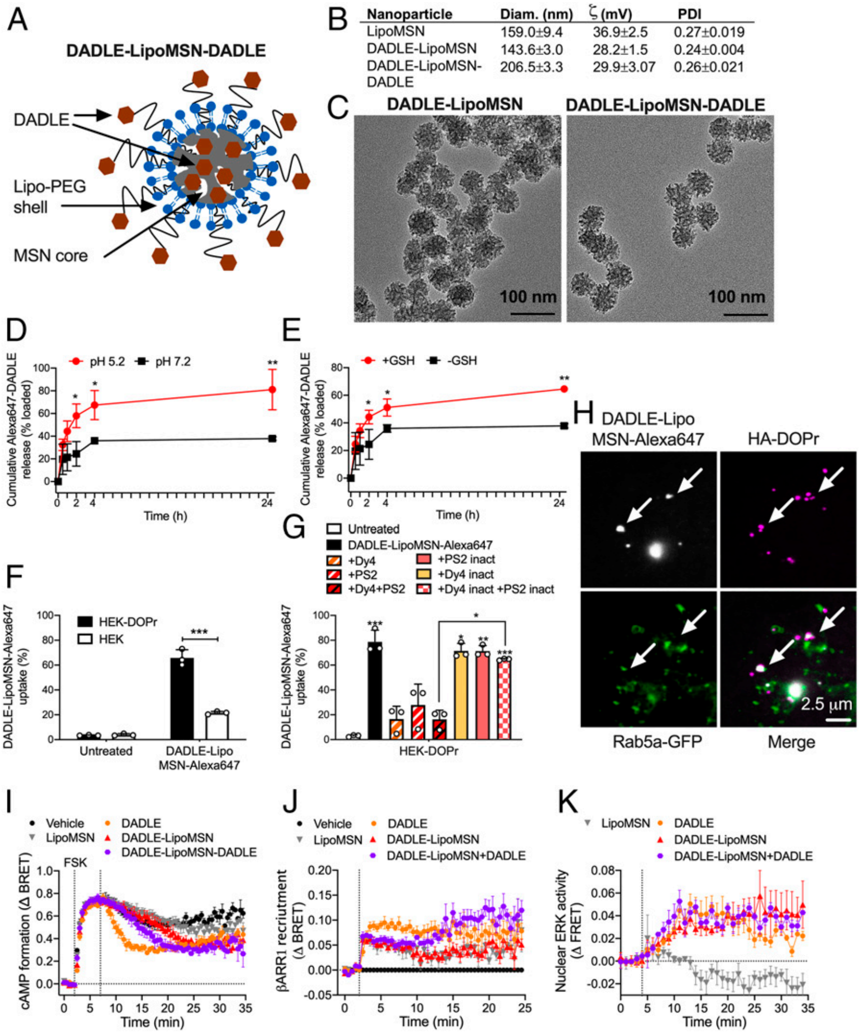

Nanoparticle	Diam. (nm)	ζ (mV)	PDI
LipoMSN	159.0±9.4	36.9±2.5	0.27±0.019
DADLE-LipoMSN	143.6±3.0	28.2±1.5	0.24±0.004
DADLE-LipoMSN-DADLE	206.5±3.3	29.9±3.07	0.26±0.021

Fig. 7. Characterization of nanoparticles. (*A*) Structure of DADLE-LipoMSN-DADLE. (*B*) Physical properties of nanoparticles. $n = 4$ experiments. (*C*) Transmission electron micrographs of DADLE-LipoMSN and DADLE-LipoMSN-DADLE. Representative images, $n = 3$ independent experiments. (*D* and *E*) Time course of in vitro release of DADLE-Alexa647 from MSN-DADLE-Alexa647 at graded pH (*D*) and glutathione concentrations (*E*). $n = 3$ independent experiments. $^*P < 0.05$, $^{**}P < 0.01$, *t* test with Holm–Sidak correction. (*F* and *G*) Uptake of DADLE-LipoMSN-DADLE-Alexa647 into HEK293 control and HEK-DOPr cells determined by flow cytometry. (*F*) Uptake into HEK293 control and HEK-DOPr cells after 2 h. $^{***}P < 0.001$, *t* test with Holm–Sidak correction. (*G*) Effects of inhibitors of clathrin and dynamin and inactive analogs on uptake into HEK-DOPr cells after 2 h. $n = 3$ independent experiments. $^*P < 0.05$, $^{**}P < 0.01$, $^{***}P < 0.001$ compared with untreated cells, one-way ANOVA with Tukey's post hoc test. (*H*) Uptake of DADLE-LipoMSN-DADLE-Alexa647 into HEK-HA-DOPr cells after 30 min. Arrows show colocalization of DADLE-LipoMSN-DADLE-Alexa647 with DOPr in Rab5a-positive early endosomes. Representative images from four independent experiments. (*I*–*K*) Effects of DADLE (100 nM), DADLE-LipoMSN (20 µM), and DADLE-LipoMSN-DADLE (20 µM) on forskolin (FSK; 10 µM)-stimulated cAMP formation (*I*), βARR1 recruitment (*J*), and activation of nuclear ERK (*K*). $n = 5$ independent experiments. All results are mean ± SEM.

demonstrate the feasibility of using nanoparticles to target nociceptors with consequent reductions in dose. Nanoparticles might allow the simultaneous delivery to endosomes of agonists or antagonists of several endosomal GPCRs involved in pain. Since multiple GPCRs control pain transmission (9), the ability to target multiple receptors in pain-transmitting neurons for prolonged periods might provide effective and long-lasting antinociception.

Nanoparticle-encapsulated GPCR ligands may have utility beyond the treatment of pain. GPCRs control many pathophysiological processes and are the targets of more than one-third of Food and Drug Administration-approved drugs (1). Many GPCRs internalize when activated and likely continue to signal from endosomes. The use of stimulus-responsive nanoparticles for delivery of drugs to endosomes of targeted cells might enhance efficacy with reduced doses and fewer side effects.

Limitations. This study has several limitations. We cannot exclude a possible role for plasma membrane signaling even in the sustained inhibitory actions of opioids. The relative contributions of plasma membrane and endosomal signaling likely depend on the nature and concentration of the ligand and the time at which nociception is assessed. The differential effects of DOPr agonists that strongly (SNC80 and DADLE) or weakly (ARM390) promote endocytosis support a role for endosomal DOPr signaling for sustained antinociception. ARM390 is a partial agonist for βARR recruitment, which may explain its inability to cause long-lasting antinociception. We were unable to determine whether DOPr endosomal signaling involves G proteins and βARRs, which mediate endosomal signaling of other GPCRs (4, 5, 10, 11, 49, 50). Although dynamin and clathrin inhibitors blocked a subset of DOPr signals and inhibited sustained antinociception, these inhibitors also have nonspecific actions (51). Dominant negative dynamin and βARR knockdown replicated some effects of endocytosis inhibitors but could affect other functions as well. We cannot exclude the possibility that DOPr signals from intracellular compartments other than endosomes, since MOPr can signal from different compartments depending on the membrane

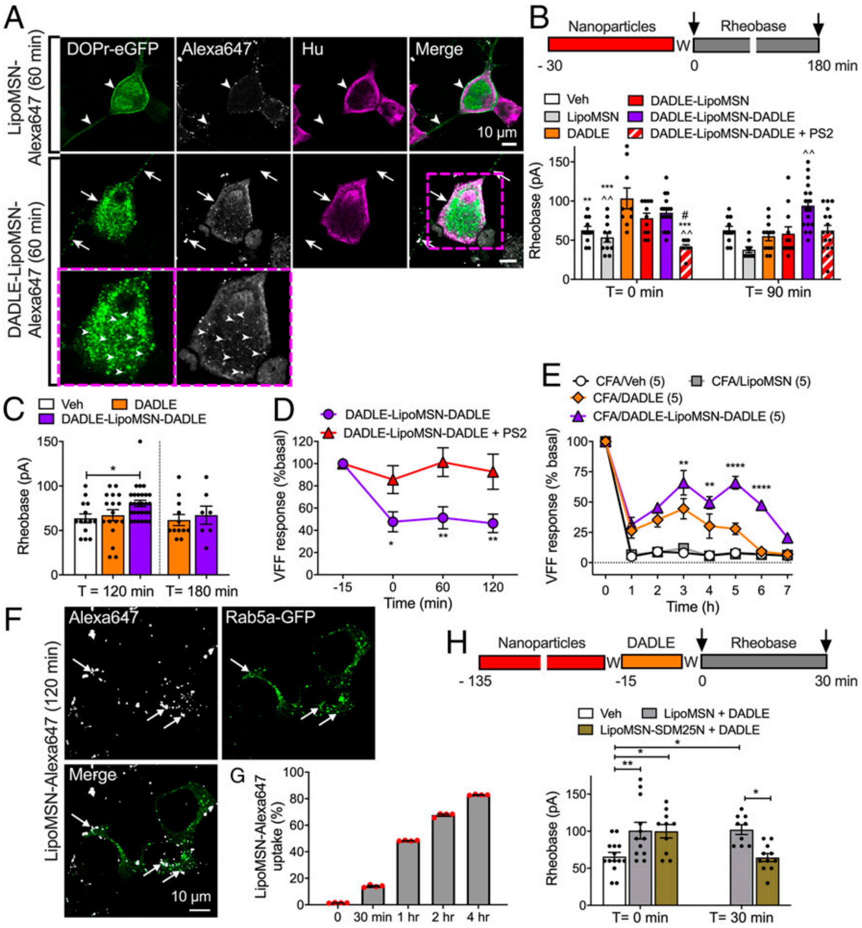

Fig. 8. Effects of nanoparticle-encapsulated DOPr ligands on nociceptors. (*A*) Uptake of LipoMSN-Alexa647 (control) or DADLE-LipoMSN-Alexa647 into primary cultures of DRG neurons from DOPr-eGFP mice. Neurons were incubated with nanoparticles for 60 min. Representative images from two experiments, from four mice. (*B* and *C*) Rheobase of mouse DRG neurons at 0, 90, 120, or 180 min after exposure to DADLE, DADLE-LipoMSN-DADLE, DADLE-LipoMSN (all 100 nM), LipoMSN (control), or vehicle (control) and washing. Some neurons were exposed to PS2 and DADLE-LipoMSN-DADLE. Data points indicate the number of studied neurons from $n = 6$ to 12 mice in *B* and *C* for each treatment. Compared with *DADLE, ^DADLE-LipoMSN-DADLE, and #DADLE-LipoMSN; $^{*\#}P < 0.05$, $^{**\wedge\wedge}P < 0.01$, $^{***}P < 0.001$, one-way (*B*) or two-way (*C*) ANOVA with Tukey's post hoc test. (*D*) Colonic afferent activity at 0, 60, or 120 min after exposure of tissues to DADLE-LipoMSN-DADLE (100 nM). Some preparations were exposed to PS2 and DADLE-LipoMSN-DADLE. $n = 5$ mice per group. $^{*}P < 0.05$, $^{**}P < 0.01$, two-way (*) ANOVA with Sidak's post hoc test. (*E*) Ipsilateral paw withdrawal responses in mice. DADLE, DADLE-LipoMSN-DADLE (both 100 nM DADLE), LipoMSN, or vehicle (Veh) was injected intrathecally at 48 h after intraplantar CFA. $n = 5$ mice per group. $^{**}P < 0.01$, $^{****}P < 0.0001$ DADLE compared with DADLE-LipoMSN-DADLE, two-way ANOVA with Tukey's multiple comparison post hoc test. (*F*) Uptake of LipoMSN-Alexa647 into endosomes of HEK293 cells expressing Rab5a-GFP after 120 min. (*G*) Time course of uptake of LipoMSN-Alexa647 into HEK293 cells. $n = 3$ independent experiments. (*H*) Rheobase of mouse DRG neurons. Neurons were incubated with LipoMSN-SDM25N (100 nM) or LipoMSN (control) for 120 min, washed (W), incubated with DADLE (10 nM, 15 min), and washed again. Rheobase was measured at 0 or 30 min after washing. Data points indicate the number of studied neurons from four mice for each treatment. $^{*}P < 0.05$, $^{**}P < 0.01$, two-way ANOVA with Tukey's post hoc test. All results are mean ± SEM.

permeability of the agonist (40). Although our results show that PKC and ERK mediate the inhibitory actions of endosomal DOPr on nociceptor excitability, the targets of these kinases and how they inhibit nociception remain to be defined. Toxicologic analysis of nanoparticle constituents, pharmacokinetic studies of nanoparticle cargo, and pharmacodynamic studies in preclinical models of pain will be necessary before this approach can be advanced to patients.

Materials and Methods

Animal Subjects. Institutional Ethics Committees approved the mouse studies.

Human Subjects. The Queen's University Human Ethics Committee approved the human studies. Patients undergoing colonoscopy for routine clinical care gave informed consent for biopsy specimens of the mucosa to be obtained from the descending colon during colonoscopy and for their data to be recorded for research purposes. Biopsy specimens of mucosa were collected from the descending colon of three patients with active cUC and three healthy control patients. Disease severity was evaluated using the endoscopy component of the Mayo Clinic score for ulcerative colitis (*SI Appendix*, Table S1).

Colon Supernatants. Mice were treated for three cycles with 2% DSS in drinking water to induce chronic colitis or with water (control). Segments of whole colon were incubated in medium (24 h) to obtain supernatants (16–18). Biopsy specimens of colonic mucosa from cUC patients and controls (*SI Appendix*, Table S1) were incubated in medium to obtain supernatants (11, 52).

Patch Clamp Recording. Patch clamp recordings were made from mouse DRG neurons (11, 16, 18, 52). Neurons were preincubated for 60 min with supernatants and then washed. Neurons were stimulated for 15 min with DADLE (10 nM), SNC80 (10 nM), ARM390 (100 nM), DAMGO (10 nM), or vehicle (control) and then washed. Neurons were also incubated overnight (12 to 16 h) with DADLE (100 nM) or ARM390 (300 nM) and then washed. In some experiments, neurons were preincubated for 30 min with SDM25N (100 nM), CTOP (100 nM), Dy4 (30 μM), PS2 (15 μM), GF109203X (1 μM), PD98059 (50 μM), or vehicle. Rheobase was measured after agonist treatment and washing.

Extracellular Recording. Extracellular recordings were made from the lumbar splanchnic nerve innervating isolated mouse distal colon (11, 53, 54). SNC80, ARM390, or DAMGO (all 100 nM) was superfused into the organ bath for 15 min. In some studies, colon was preincubated for 15 min with PS2 (50 μM) before SNC80.

cDNAs, Cell Culture, and Transfection. Details are provided in *SI Appendix, Materials and Methods*.

Dissociation of DRG Neurons. DRG neurons were dispersed from DOPr-eGFP mice (55).

BRET Assays. BRET was measured in HEK293 cells (10, 26).

FRET Assays. FRET was measured in HEK293 cells and DRG neurons from DOPr-eGFP mice (10, 55). After FRET imaging, DOPr-eGFP was localized by immunofluorescence. FRET was measured in neurons expressing DOPr-eGFP.

DOPr-eGFP Trafficking. DRG neurons from DOPr-eGFP mice were exposed to vehicle, DADLE (1 μM), DADLE-LipoMSN-Alexa647 (1 μM DADLE), or LipoMSN-Alexa647 (10 μg/mL LipoMSN) (30 or 60 min, 37 °C). In some experiments, neurons were preincubated with Dy4 (30 μM) or PS2 (15 μM) (30 min). DOPr-eGFP in neurons was localized by immunofluorescence.

Preparation and Physicochemical Characterization of Nanoparticles. Details are provided in *SI Appendix, Materials and Methods*.

Cellular Targeting of LipoMSNs. HEK293-HA-DOPr or untransfected cells were incubated with DADLE-LipoMSN-Alexa647 or LipoMSN-Alexa647 (40 μg/mL). Uptake of nanoparticles was quantified by flow cytometry. In some experiments, cells were preincubated with Dy4, PS2, or inactive analogs (10 μg/mL, 30 min). For imaging studies, cells were transduced with Rab5a-GFP. After 24 h, cells were preincubated with rat anti-HA. Cells were washed and incubated with DADLE-LipoMSN-Alexa647 or LipoMSN-Alexa647 (20 μM DADLE, 200 μg/mL LipoMSN). HA-DOPr was localized by immunofluorescence. In some experiments, LipoMSN-Alexa647 uptake was examined by live cell imaging.

LipoMSNs and DOPr Signaling. Details are provided in *SI Appendix, Materials and Methods*.

LipoMSNs and Electrophysiology. Rheobase was measured at 0 to 180 min after exposure to DADLE or SDM25N nanoparticles and washing. Colonic afferent responses were assessed at 0 to 120 min after exposure to nanoparticles and washing.

LipoMSNs and Inflammatory Pain. The investigator was blinded to the treatments. Mice were assigned at random to treatments and acclimatized. CFA (0.5 mg/mL) was administered by intraplantar injection (10 μL) into the left hindpaw. DADLE (100 nM), DADLE-LipoMSN-DADLE (100 nM DADLE, 0.8 μg/mL LipoMSN), LipoMSN (1 μg/mL LipoMSN, control), or vehicle (control) was injected intrathecally (5 μL) at 48 h after CFA. Paw withdrawal to VFF was determined (10, 12).

Statistics. Results were analyzed and graphs prepared using Prism 8. Results are expressed as mean ± SEM. Statistical significance was assessed using *t* tests or one-way or two-way ANOVA with Tukey's or Sidak's post hoc test (*SI Appendix*, Table S2).

Data Availability. All of the data and protocols are provided in the main text or the *SI Appendix*.

ACKNOWLEDGMENTS. We thank Lih En Tiah for technical support and Dr. Malvin Janal for statistical support. The tdRGFP-Rab5a plasmid was designed and validated by Christian LeGouill and Lucas Tabajara Parreiras e Silva from the laboratory of Dr. Michel Bouvier. RGFP-CAAX and β-arrestin2-Rluc2 were provided by the Bouvier laboratory. This work was supported by grants from the NIH (NS102722, DE026806, and DK118971 to B.L.S. and N.W.B.), Department of Defense (W81XWH1810431, to B.L.S. and N.W.B.), Crohn's Colitis Canada (D.E.R., A.E.L., and S.J.V.), National Health and Medical Research Council (63303, 1049682, 1031886, 1049730, 1121029, and 1083480 to M.C., M.L.H., N.W.B., and D.P.P.), and Australian Research Council Centre of Excellence in Convergent Bio-Nano Science and Technology (N.W.B.).

1. A. S. Hauser, M. M. Attwood, M. Rask-Andersen, H. B. Schiöth, D. E. Gloriam, Trends in GPCR drug discovery: New agents, targets and indications. *Nat. Rev. Drug Discov.* **16**, 829–842 (2017).
2. K. E. Komolov, J. L. Benovic, G protein-coupled receptor kinases: Past, present and future. *Cell. Signal.* **41**, 17–24 (2018).
3. Y. K. Peterson, L. M. Luttrell, The diverse roles of arrestin scaffolds in G protein-coupled receptor signaling. *Pharmacol. Rev.* **69**, 256–297 (2017).
4. K. A. DeFea *et al*., The proliferative and antiapoptotic effects of substance P are facilitated by formation of a beta-arrestin-dependent scaffolding complex. *Proc. Natl. Acad. Sci. U.S.A.* **97**, 11086–11091 (2000).
5. K. A. DeFea *et al*., Beta-arrestin-dependent endocytosis of proteinase-activated receptor 2 is required for intracellular targeting of activated ERK1/2. *J. Cell Biol.* **148**, 1267–1281 (2000).
6. R. Irannejad, M. von Zastrow, GPCR signaling along the endocytic pathway. *Curr. Opin. Cell Biol.* **27**, 109–116 (2014).
7. J. E. Murphy, B. E. Padilla, B. Hasdemir, G. S. Cottrell, N. W. Bunnett, Endosomes: A legitimate platform for the signaling train. *Proc. Natl. Acad. Sci. U.S.A.* **106**, 17615–17622 (2009).
8. A. R. B. Thomsen, D. D. Jensen, G. A. Hicks, N. W. Bunnett, Therapeutic targeting of endosomal G protein-coupled receptors. *Trends Pharmacol. Sci.* **39**, 879–891 (2018).
9. P. Geppetti, N. A. Veldhuis, T. Lieu, N. W. Bunnett, G. Protein-Coupled Receptors, G protein-coupled receptors: Dynamic machines for signaling pain and itch. *Neuron* **88**, 635–649 (2015).
10. D. D. Jensen *et al*., Neurokinin 1 receptor signaling in endosomes mediates sustained nociception and is a viable therapeutic target for prolonged pain relief. *Sci. Transl. Med.* **9**, eaal3447 (2017).
11. N. N. Jimenez-Vargas *et al*., Protease-activated receptor-2 in endosomes signals persistent pain of irritable bowel syndrome. *Proc. Natl. Acad. Sci. U.S.A.* **115**, E7438–E7447 (2018).
12. P. D. Ramírez-García *et al*., A pH-responsive nanoparticle targets the neurokinin 1 receptor in endosomes to prevent chronic pain. *Nat. Nanotechnol.* **14**, 1150–1159 (2019).
13. R. E. Yarwood *et al*., Endosomal signaling of the receptor for calcitonin gene-related peptide mediates pain transmission. *Proc. Natl. Acad. Sci. U.S.A.* **114**, 12309–12314 (2017).
14. G. Corder, D. C. Castro, M. R. Bruchas, G. Scherrer, Endogenous and exogenous opioids in pain. *Annu. Rev. Neurosci.* **41**, 453–473 (2018).
15. J. Boué *et al*., Endogenous regulation of visceral pain via production of opioids by colitogenic CD4(+) T cells in mice. *Gastroenterology* **146**, 166–175 (2014).
16. R. Guerrero-Alba *et al*., Co-expression of μ and δ opioid receptors by mouse colonic nociceptors. *Br. J. Pharmacol.* **175**, 2622–2634 (2018).
17. R. Guerrero-Alba *et al*., Stress activates pronociceptive endogenous opioid signalling in DRG neurons during chronic colitis. *Gut* **66**, 2121–2131 (2017).
18. E. Valdez-Morales *et al*., Release of endogenous opioids during a chronic IBD model suppresses the excitability of colonic DRG neurons. *Neurogastroenterol. Motil.* **25**, 39–46.e4 (2013).
19. M. Verma-Gandhu *et al*., CD4$^+$ T-cell modulation of visceral nociception in mice. *Gastroenterology* **130**, 1721–1728 (2006).
20. G. Scherrer *et al*., Knockin mice expressing fluorescent delta-opioid receptors uncover G protein-coupled receptor dynamics in vivo. *Proc. Natl. Acad. Sci. U.S.A.* **103**, 9691–9696 (2006).
21. M. J. Robertson, F. M. Deane, P. J. Robinson, A. McCluskey, Synthesis of dynole 34-2, dynole 2-24 and dyngo 4a for investigating dynamin GTPase. *Nat. Protoc.* **9**, 851–870 (2014).
22. M. J. Robertson *et al*., Synthesis of the Pitstop family of clathrin inhibitors. *Nat. Protoc.* **9**, 1592–1606 (2014).
23. A. A. Pradhan *et al*., Agonist-specific recruitment of arrestin isoforms differentially modify delta opioid receptor function. *J. Neurosci.* **36**, 3541–3551 (2016).
24. D. Toullec *et al*., The bisindolylmaleimide GF 109203X is a potent and selective inhibitor of protein kinase C. *J. Biol. Chem.* **266**, 15771–15781 (1991).
25. D. T. Dudley, L. Pang, S. J. Decker, A. J. Bridges, A. R. Saltiel, A synthetic inhibitor of the mitogen-activated protein kinase cascade. *Proc. Natl. Acad. Sci. U.S.A.* **92**, 7686–7689 (1995).
26. D. D. Jensen *et al*., Endothelin-converting enzyme 1 and β-arrestins exert spatiotemporal control of substance P-induced inflammatory signals. *J. Biol. Chem.* **289**, 20283–20294 (2014).
27. A. A. Pradhan *et al*., In vivo delta opioid receptor internalization controls behavioral effects of agonists. *PLoS One* **4**, e5425 (2009).

28. D. P. Poole *et al*., Localization and regulation of fluorescently labeled delta opioid receptor, expressed in enteric neurons of mice. *Gastroenterology* **141**, 982–991.e18 (2011).
29. Q. Wan *et al*., Mini G protein probes for active G protein-coupled receptors (GPCRs) in live cells. *J. Biol. Chem.* **293**, 7466–7473 (2018).
30. R. Nehmé *et al*., Mini-G proteins: Novel tools for studying GPCRs in their active conformation. *PLoS One* **12**, e0175642 (2017).
31. Y. Namkung *et al*., Monitoring G protein-coupled receptor and β-arrestin trafficking in live cells using enhanced bystander BRET. *Nat. Commun.* **7**, 12178 (2016).
32. P. Donthamsetti, J. R. Quejada, J. A. Javitch, V. V. Gurevich, N. A. Lambert, Using bioluminescence resonance energy transfer (BRET) to characterize agonist-induced arrestin recruitment to modified and unmodified G protein-coupled receptors. *Curr. Protoc. Pharmacol.* **70**, 2 14 11–12 14 14 (2015).
33. M. L. Halls, M. Canals, Genetically encoded FRET biosensors to illuminate compartmentalised GPCR signalling. *Trends Pharmacol. Sci.* **39**, 148–157 (2018).
34. J. S. Herskovits, C. C. Burgess, R. A. Obar, R. B. Vallee, Effects of mutant rat dynamin on endocytosis. *J. Cell Biol.* **122**, 565–578 (1993).
35. C. Pinese *et al*., Sustained delivery of siRNA/mesoporous silica nanoparticle complexes from nanofiber scaffolds for long-term gene silencing. *Acta Biomater.* **76**, 164–177 (2018).
36. D. Shao *et al*., Bioinspired diselenide-bridged mesoporous silica nanoparticles for dual-responsive protein delivery. *Adv. Mater.*, e1801198 (2018).
37. J. J. DiCello *et al*., Inflammation-associated changes in DOR expression and function in the mouse colon. *Am. J. Physiol. Gastrointest. Liver Physiol.* **315**, G544–G559 (2018).
38. C. M. Cahill, S. V. Holdridge, A. Morinville, Trafficking of delta-opioid receptors and other G-protein-coupled receptors: Implications for pain and analgesia. *Trends Pharmacol. Sci.* **28**, 23–31 (2007).
39. A. A. Pradhan *et al*., Ligand-directed trafficking of the δ-opioid receptor in vivo: Two paths toward analgesic tolerance. *J. Neurosci.* **30**, 16459–16468 (2010).
40. M. Stoeber *et al*., A genetically encoded biosensor reveals location bias of opioid drug action. *Neuron* **98**, 963–976.e5 (2018).
41. M. Narita, H. Mizoguchi, J. P. Kampine, L. F. Tseng, Role of protein kinase C in desensitization of spinal delta-opioid-mediated antinociception in the mouse. *Br. J. Pharmacol.* **118**, 1829–1835 (1996).
42. E. G. Ignatova, M. M. Belcheva, L. M. Bohn, M. C. Neuman, C. J. Coscia, Requirement of receptor internalization for opioid stimulation of mitogen-activated protein kinase: Biochemical and immunofluorescence confocal microscopic evidence. *J. Neurosci.* **19**, 56–63 (1999).
43. W. H. De Jong, P. J. Borm, Drug delivery and nanoparticles: Applications and hazards. *Int. J. Nanomedicine* **3**, 133–149 (2008).
44. O. C. Farokhzad, R. Langer, Impact of nanotechnology on drug delivery. *ACS Nano* **3**, 16–20 (2009).
45. K. E. Uhrich, S. M. Cannizzaro, R. S. Langer, K. M. Shakesheff, Polymeric systems for controlled drug release. *Chem. Rev.* **99**, 3181–3198 (1999).
46. H. Maeda, J. Wu, T. Sawa, Y. Matsumura, K. Hori, Tumor vascular permeability and the EPR effect in macromolecular therapeutics: A review. *J. Control. Release* **65**, 271–284 (2000).
47. G. K. Such, Y. Yan, A. P. Johnston, S. T. Gunawan, F. Caruso, Interfacing materials science and biology for drug carrier design. *Adv. Mater.* **27**, 2278–2297 (2015).
48. C. E. Nelson *et al*., Balancing cationic and hydrophobic content of PEGylated siRNA polyplexes enhances endosome escape, stability, blood circulation time, and bioactivity in vivo. *ACS Nano* **7**, 8870–8880 (2013).
49. D. Calebiro *et al*., Persistent cAMP-signals triggered by internalized G-protein-coupled receptors. *PLoS Biol.* **7**, e1000172 (2009).
50. R. Irannejad *et al*., Conformational biosensors reveal GPCR signalling from endosomes. *Nature* **495**, 534–538 (2013).
51. R. J. Park *et al*., Dynamin triple knockout cells reveal off target effects of commonly used dynamin inhibitors. *J. Cell Sci.* **126**, 5305–5312 (2013).
52. E. E. Valdez-Morales *et al*., Sensitization of peripheral sensory nerves by mediators from colonic biopsies of diarrhea-predominant irritable bowel syndrome patients: A role for PAR2. *Am. J. Gastroenterol.* **108**, 1634–1643 (2013).
53. S. M. Brierley, R. C. Jones, 3rd, G. F. Gebhart, L. A. Blackshaw, Splanchnic and pelvic mechanosensory afferents signal different qualities of colonic stimuli in mice. *Gastroenterology* **127**, 166–178 (2004).
54. P. A. Hughes *et al*., Post-inflammatory colonic afferent sensitisation: Different subtypes, different pathways and different time courses. *Gut* **58**, 1333–1341 (2009).
55. M. L. Halls, D. P. Poole, A. M. Ellisdon, C. J. Nowell, M. Canals, Detection and quantification of intracellular signaling using FRET-based biosensors and high content imaging. *Methods Mol. Biol.* **1335**, 131–161 (2015).

JCI insight

Activation of pruritogenic TGR5, MrgprA3, and MrgprC11 on colon-innervating afferents induces visceral hypersensitivity

Joel Castro, … , Nigel W. Bunnett, Stuart M. Brierley

JCI Insight. 2019;4(20):e131712. https://doi.org/10.1172/jci.insight.131712.

Research Article Gastroenterology Neuroscience

Graphical abstract

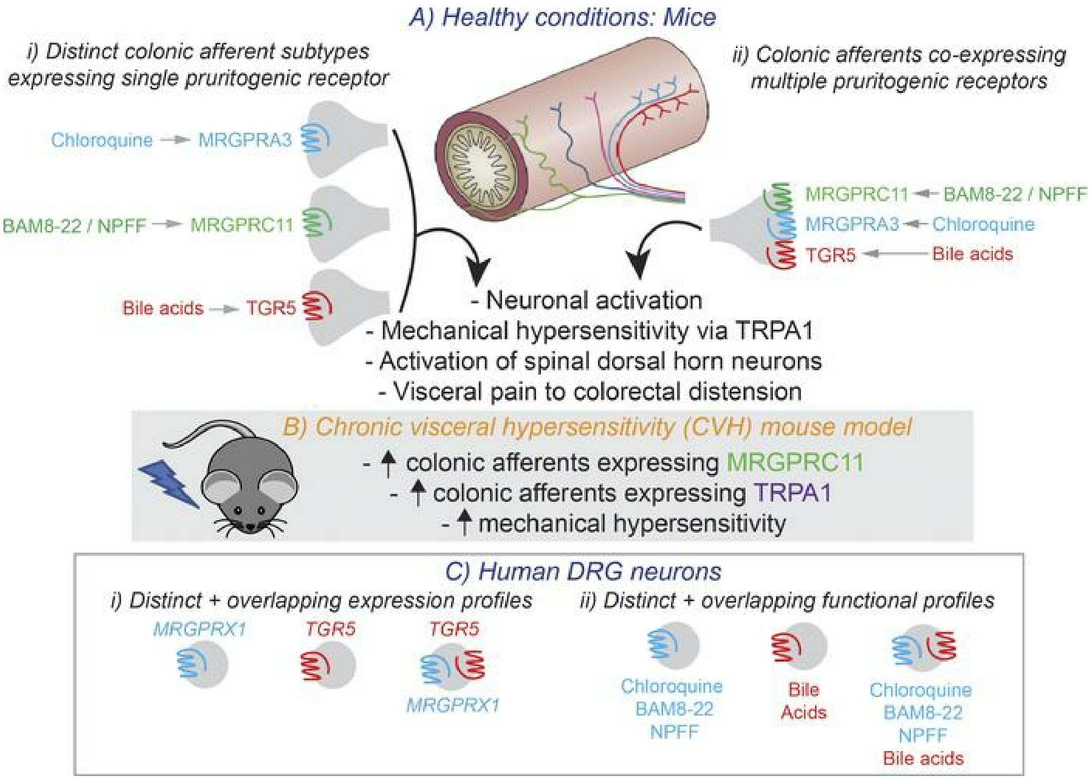

JCI insight

Activation of pruritogenic TGR5, MRGPRA3, and MRGPRC11 on colon-innervating afferents induces visceral hypersensitivity

Joel Castro,[1,2,3] Andrea M. Harrington,[1,2,3] TinaMarie Lieu,[4] Sonia Garcia-Caraballo,[1,2,3] Jessica Maddern,[1,2,3] Gudrun Schober,[1,2,3] Tracey O'Donnell,[1,2,3] Luke Grundy,[1,2,3] Amanda L. Lumsden,[1,2,3] Paul Miller,[5] Andre Ghetti,[5] Martin S. Steinhoff,[6,7,8] Daniel P. Poole,[4,9,10] Xinzhong Dong,[11] Lin Chang,[12] Nigel W. Bunnett,[13,14,15] Stuart M. Brierley[1,2,3]

[1]Visceral Pain Research Group, College of Medicine and Public Health, Flinders University, Bedford Park, South Australia, Australia. [2]Hopwood Centre for Neurobiology, Lifelong Health Theme, South Australian Health and Medical Research Institute (SAHMRI), North Terrace, Adelaide, South Australia, Australia. [3]Centre for Nutrition and Gastrointestinal Diseases, Discipline of Medicine, University of Adelaide, Adelaide, South Australia, Australia. [4]Monash Institute of Pharmaceutical Sciences, Monash University, Parkville, Victoria, Australia. [5]AnaBios Corporation, San Diego, California, USA. [6]Department of Dermatology and Dermatology Immunology Institute, Hamad Medical Corporation, Doha, Qatar. [7]Department of Dermatology, Weill Cornell Medicine-Qatar and Weill Cornell University, New York, New York, USA. [8]School of Medicine Qatar University, Doha, Qatar. [9]Australian Research Council Centre of Excellence in Convergent Bio-Nano Science and Technology, Monash University, Parkville, Victoria, Australia. [10]Department of Anatomy and Neuroscience, University of Melbourne, Parkville, Victoria, Australia. [11]The Solomon H. Snyder Department of Neuroscience, Center for Sensory Biology, School of Medicine, Howard Hughes Medical Institute, Johns Hopkins University, Baltimore, Maryland, USA. [12]G. Oppenheimer Centre for Neurobiology of Stress and Resilience, David Geffen School of Medicine at UCLA, UCLA, Los Angeles, California, USA. [13]Department of Pharmacology and Therapeutics, University of Melbourne, Parkville, Victoria, Australia. [14]Department of Surgery and [15]Department of Pharmacology, Columbia University, New York, New York, USA.

Itch induces scratching that removes irritants from the skin, whereas pain initiates withdrawal or avoidance of tissue damage. While pain arises from both the skin and viscera, we investigated whether pruritogenic irritant mechanisms also function within visceral pathways. We show that subsets of colon-innervating sensory neurons in mice express, either individually or in combination, the pruritogenic receptors *Tgr5* and the Mas-gene–related GPCRs *Mrgpra3* and *Mrgprc11*. Agonists of these receptors activated subsets of colonic sensory neurons and evoked colonic afferent mechanical hypersensitivity via a TRPA1-dependent mechanism. In vivo intracolonic administration of individual TGR5, MRGPRA3, or MRGPRC11 agonists induced pronounced visceral hypersensitivity to colorectal distension. Coadministration of these agonists as an "itch cocktail" augmented hypersensitivity to colorectal distension and changed mouse behavior. These irritant mechanisms were maintained and enhanced in a model of chronic visceral hypersensitivity relevant to irritable bowel syndrome. Neurons from human dorsal root ganglia also expressed *TGR5*, as well as the human ortholog *MRGPRX1*, and showed increased responsiveness to pruritogenic agonists in pathological states. These data support the existence of an irritant-sensing system in the colon that is a visceral representation of the itch pathways found in skin, thereby contributing to sensory disturbances accompanying common intestinal disorders.

Conflict of interest: NWB is a founding scientist of Endosome Therapeutics Inc. Research in NWB's laboratory is supported, in part, by Takeda Pharmaceuticals International.

Submitted: July 15, 2019
Accepted: September 11, 2019
Published: October 17, 2019.

Reference information: *JCI Insight*. 2019;4(20):e131712. https://doi.org/10.1172/jci.insight.131712.

Introduction

Itch, like pain, is a protective mechanism necessary for survival (1). Itch induces protective scratching that removes harmful irritants from the skin, while pain initiates withdrawal from and avoidance of noxious stimulants. Itch and pain are detected by primary sensory dorsal root ganglion (DRG) neurons that project from peripheral tissues into the dorsal horn (DH) of the spinal cord, where they release transmitters that excite spinal neurons (2). In the skin, histamine-dependent mechanisms contribute to itch; however, several distinct histamine-independent itch mechanisms have also been described. One involves the Mas-gene–related GPCR family, which includes MRGPRA3 and MRGPRC11 (2–5). Another mechanism involves the bile acid receptor TGR5, also known as GPR130 or GpBAR1 (6).

MRGPRA3 and MRGPRC11 are expressed by subsets of sensory DRG neurons innervating the skin (7, 8). Activation of MRGPRA3 by the antimalarial drug chloroquine (CQ) (8), or MRGPRC11 activation by the endogenous pruritogen, bovine adrenal medulla 8-22 peptide (BAM8-22), induces itch (3, 9). Mice lacking a cluster of *Mrgpr* genes (*Mrgpr-cluster*$^{-/-}$) display significant deficits in itch induced by either CQ or BAM8-22, but — crucially — not itch induced by histamine (8). TGR5 is also expressed by a subpopulation of peptidergic DRG neurons and activation of TGR5 by bile acids, such as deoxycholic acid (DCA) or oleanolic acid (OA), induces neuronal excitability and also induces itch in mice (6, 10). These effects are lost in *Tgr5*$^{-/-}$ mice and are exacerbated in mice overexpressing TGR5 (*Tgr5-Tg*), potentially explaining why pruritus is observed in patients with cholestatic liver disease, where circulating bile acids are increased by 20-fold (6). However, it remains unclear if both TGR5 and MRGPR mechanisms coexist within the same DRG neuronal populations or whether they exist in, and therefore recruit, distinct populations of DRG neurons.

In the colon, afferent sensitization occurs via a variety of processes (11), including histamine-dependent mechanisms (12); however, other pathways are also likely involved. For example, increased fecal levels of bile acids have been implicated as the cause of diarrhea in a subset of patients with irritable bowel syndrome (IBS) (13), while abdominal pain and cramping are known side-effects of CQ treatment (14). Therefore, as pain arises from both the skin and viscera, we wondered whether pruritogenic irritant mechanisms identified within the skin have analogous pathways within the viscera. This is important, as chronic abdominal pain or discomfort associated with altered bowel habits are key symptoms of IBS, a prevalent functional gastrointestinal disorder affecting ~11% of the global population (15). These symptoms significantly affect patient quality of life and are notoriously difficult to treat. Although the pathophysiology of IBS is not completely understood, hallmarks of IBS include hypersensitivity to mechanical events within the intestine in the absence of overt pathology to the intestinal mucosa, resulting in allodynia and hyperalgesia (15). While sensitization and neuroplasticity of colonic afferent pathways has been implicated in the development and maintenance of chronic abdominal pain in IBS (15–17), the underlying mechanisms contributing to afferent sensitization remain incompletely understood (18). We hypothesized that MRGPRA3-, MRGPRC11- and TGR5-dependent mechanisms could be important mechanisms in this process.

The aim of this study was to determine if colonic afferents express TGR5, MRGPRC11, and MRGPRA3, and if so, whether they are present in distinct or overlapping subsets of colon-innervating DRG neurons. We also aimed to determine if agonists for TGR5, MRGPRC11, and MRGPRA3 induce changes in colonic sensory signaling in vitro and ex vivo and whether this translated to altered visceral sensitivity and behavior in vivo. We determined if such mechanisms were present, or indeed augmented, in a model of chronic visceral hypersensitivity (CVH) relevant to IBS. Crucially, we aimed to translate these findings to humans by using colonic biopsies and DRG sensory neurons from human donors to confirm expression profiles and functional mechanisms.

We demonstrate that *Tgr5*, *MrgprA3*, and *MrgprC11* are all expressed by colon-innervating DRG neurons, in both distinct and overlapping subsets of sensory DRG neurons, and their activation causes fundamental signaling changes within colonic afferent pathways in healthy and disease states. In human DRG neurons, TGR5 and MRGPRX1 also display both distinct and overlapping molecular and functional expression profiles, with increased responsiveness to pruritogens in sensitized states.

Results

Agonists for TGR5, MRGPRA3, and MRGPRC11 evoke mechanical hypersensitivity in colonic afferents. In order to determine if pruritogenic receptors have a functional role in colonic sensory function, we made ex vivo recordings of colonic afferents from mice. Application of the TGR5 agonists DCA, OA, and 3-(2-chlorophenyl)-N-(4-chlorophenyl)-N,5-dimethyl-4-isoxazolecarboxamide (CCDC) evoked mechanical hypersensitivity in colonic afferent endings from healthy mice (Figure 1, A–C). Closer examination of individual afferent responses showed that some afferents were unaffected by TGR5 activation, whereas others displayed pronounced mechanical hypersensitivity (Figure 1, A–C), suggesting that TGR5 is expressed by specific subpopulations of colonic afferents. Notably, the effects of CCDC were exacerbated in colonic afferents from mice overexpressing TGR5 (*Tgr5-Tg*, Figure 1D) and lost in afferents from *Tgr5*-null mutant (*Tgr5*$^{-/-}$) mice (Figure 1E). As TGR5 activates transient

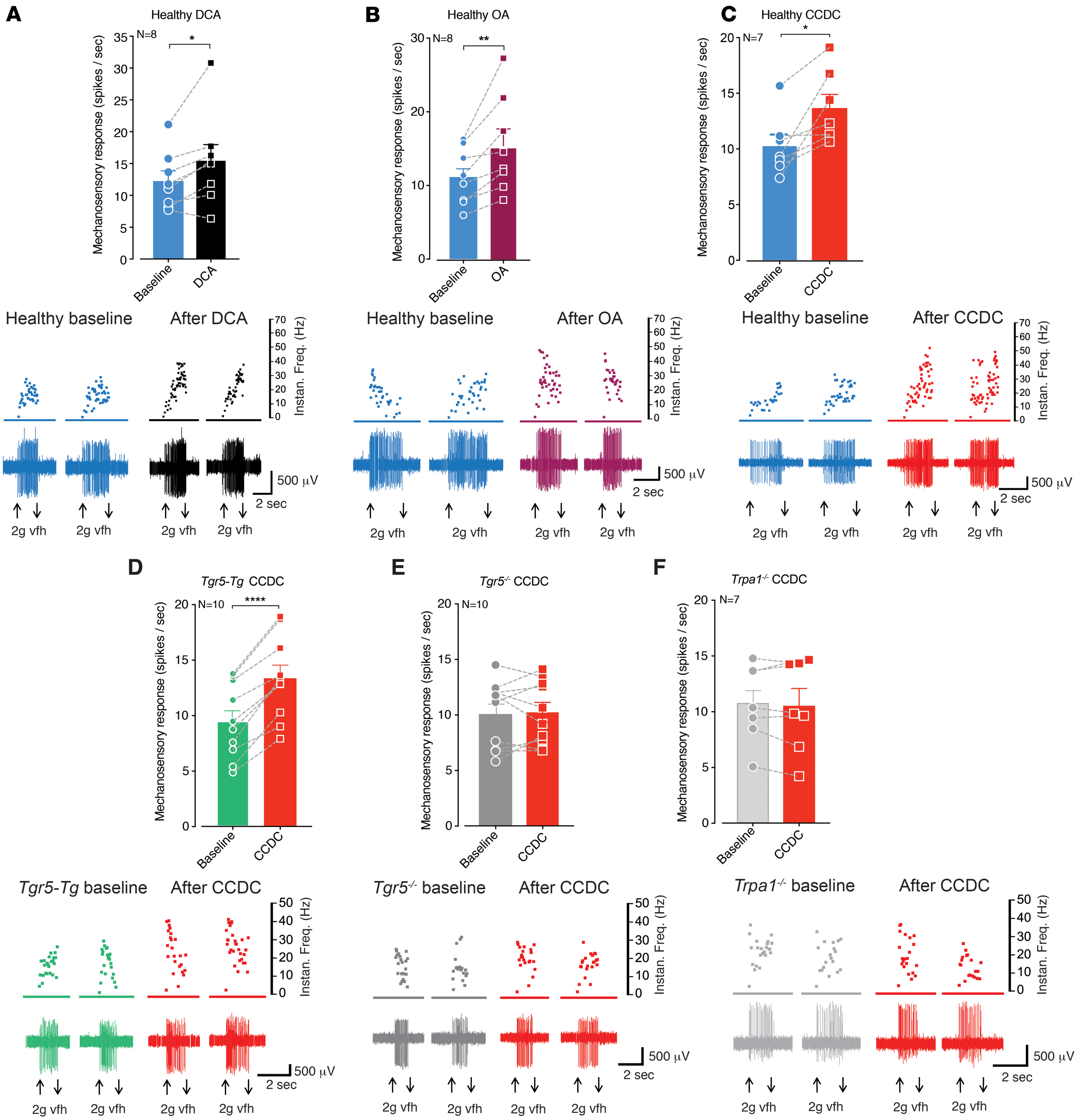

Figure 1. Agonists for TGR5 evoke mechanical hypersensitivity in colonic afferents. (**A**) Application of the TGR5 agonist deoxycholic acid (DCA; 100 µM) to the colonic mucosa for 5 minutes resulted in subsequent mechanical hypersensitivity of colonic nociceptors from healthy mice (*$P < 0.05$, $N = 8$). Dots represent values from individual afferents before and after DCA application. Lower panel shows representative recordings from a single colonic afferent nerve fiber responding to a 2 g von Frey hair (vfh) before and after incubation with DCA. (**B**) Application of the TGR5 agonist oleanolic acid (OA; 100 µM for 5 minutes) also caused mechanical hypersensitivity in nociceptors from healthy mice (**$P < 0.01$, $N = 8$). (**C**) The potent synthetic TGR5 agonist CCDC (100 µM for 5 minutes) also evoked mechanical hypersensitivity of colonic nociceptors from healthy mice (*$P < 0.05$, $N = 7$). (**D**) CCDC-induced (100 µM) mechanical hypersensitivity was enhanced in colonic nociceptors from mice overexpressing TGR5 (*Tgr5-Tg*, ****$P < 0.0001$, $N = 10$), but (**E**) was not observed in colonic nociceptors from *Tgr5*$^{-/-}$ mice ($P > 0.05$, $N = 10$). (**F**) Furthermore, CCDC-induced (100 µM) mechanical hypersensitivity was not observed in colonic nociceptors from *Trpa1*$^{-/-}$ mice ($P > 0.05$, $N = 7$), suggesting a key interaction between TGR5 and TRPA1 in the mechanical hypersensitivity evoked by TGR5 activation. Data represent mean ± SEM. *P* values determined by paired *t* tests.

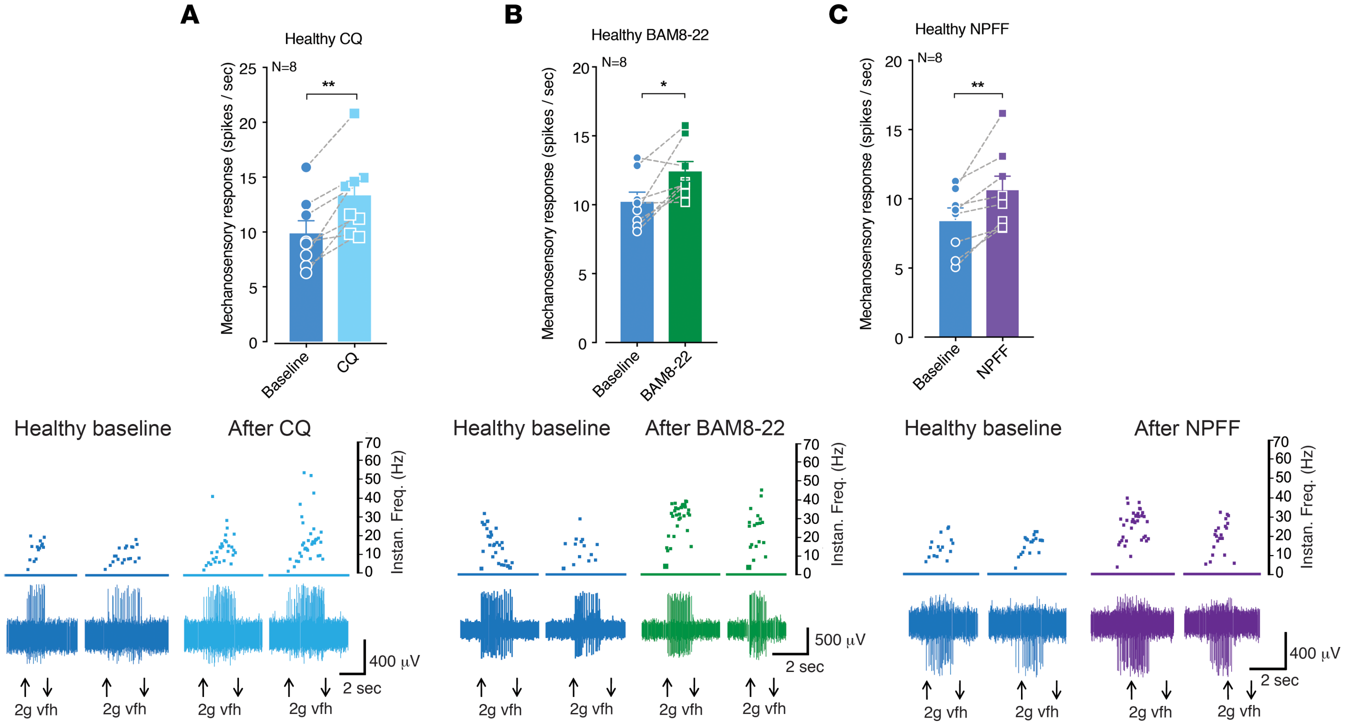

Figure 2. Agonists for MRGPRA3 and MRGPRC11 evoke mechanical hypersensitivity in colonic afferents. (**A**) Application of the MRGPRA3 agonist chloroquine (CQ; 10 µM for 5 minutes) resulted in subsequent mechanical hypersensitivity of colonic nociceptors from healthy mice (**$P < 0.01$, $N = 8$). (**B**) The MRGPRC11 agonist BAM8-22 (20 µM for 5 minutes) also caused mechanical hypersensitivity in nociceptors from healthy mice (*$P < 0.05$, $N = 8$). (**C**) Application of the combined MRGPRC11/MRGPRA4 agonist neuropeptide FF (NPFF; 5 µM for 5 minutes) also evoked mechanical hypersensitivity of colonic nociceptors from healthy mice (**$P < 0.01$, $N = 8$). Data represent mean ± SEM. *P* values determined by paired *t* tests.

receptor potential ankyrin 1 (TRPA1) to induce itch (10), TRPA1 mediates nociceptive responses (19, 20), and we have previously shown that TRPA1 is a key integrator for the induction of mechanical hypersensitivity in colonic afferents by a variety of mediators (21–23), we applied CCDC to colonic afferents from *Trpa1*$^{-/-}$ mice. Correspondingly, we found that CCDC failed to induce mechanical hypersensitivity in afferents from *Trpa1*$^{-/-}$ mice (Figure 1F), suggesting that a key integration between TGR5 and TRPA1 exists in colonic afferents. In terms of MRGPR signaling, CQ — an agonist of MRGPRA3 — also evoked mechanical hypersensitivity in colonic afferents from healthy mice (Figure 2A). Similarly, the MRGPRC11 agonist BAM8-22 (Figure 2B) and the combined MRGPRC11/MRGPRA4 agonist neuropeptide FF (NPFF) (Figure 2C) also evoked colonic afferent mechanical hypersensitivity. As observed with DCA, OA, and CCDC, closer examination of individual afferent responses showed that some afferents were unaffected by CQ, BAM8-22, or NPFF, whereas others displayed pronounced mechanical hypersensitivity (Figure 2, A–C), suggesting MRGPRA3 and MRGPRC11 expression on specific subpopulations of colon-innervating afferents.

To determine the mechanisms by which TGR5 and Mrgpr agonists induce colonic afferent hypersensitivity, we confirmed expression of *Tgr5*, *Mrgpra3*, and *Mrgprc11* mRNA using quantitative PCR (qPCR) and single-cell reverse transcription PCR (RT-PCR) studies of colonic DRG neurons. Analysis of colonic mucosa from healthy mice by qPCR revealed that *Tgr5*, *Mrgpra3*, and *Mrgprc11* mRNA were all expressed in low abundance, particularly when compared with a known epithelial target such a guanylate cyclase-C (*Gucy2c*; Figure 3A). To determine if *Tgr5*, *MrgprA3*, and *MrgprC11* were expressed by colonic afferent DRG neurons, we performed single-cell RT-PCR from retrogradely traced colon-innervating DRG neurons. We also compared expression profiles with *Trpv1* and *Trpa1*, key channels involved in colonic afferent function (11, 22, 24). Of 97 individual neurons, 19% expressed *Tgr5*, 27% expressed MrgprA3, and 40% expressed MrgprC11 (Figure 3B). In comparison, *Trpv1* and *Trpa1* were expressed by 72% and 56% of colon-innervating DRG neurons, respectively (Figure 3B). These findings indicate that these pruritogenic receptors are expressed on sensory neurons innervating the colon, correlating well with our observation that subpopulations of afferents display mechanical hypersensitivity following application of the respective

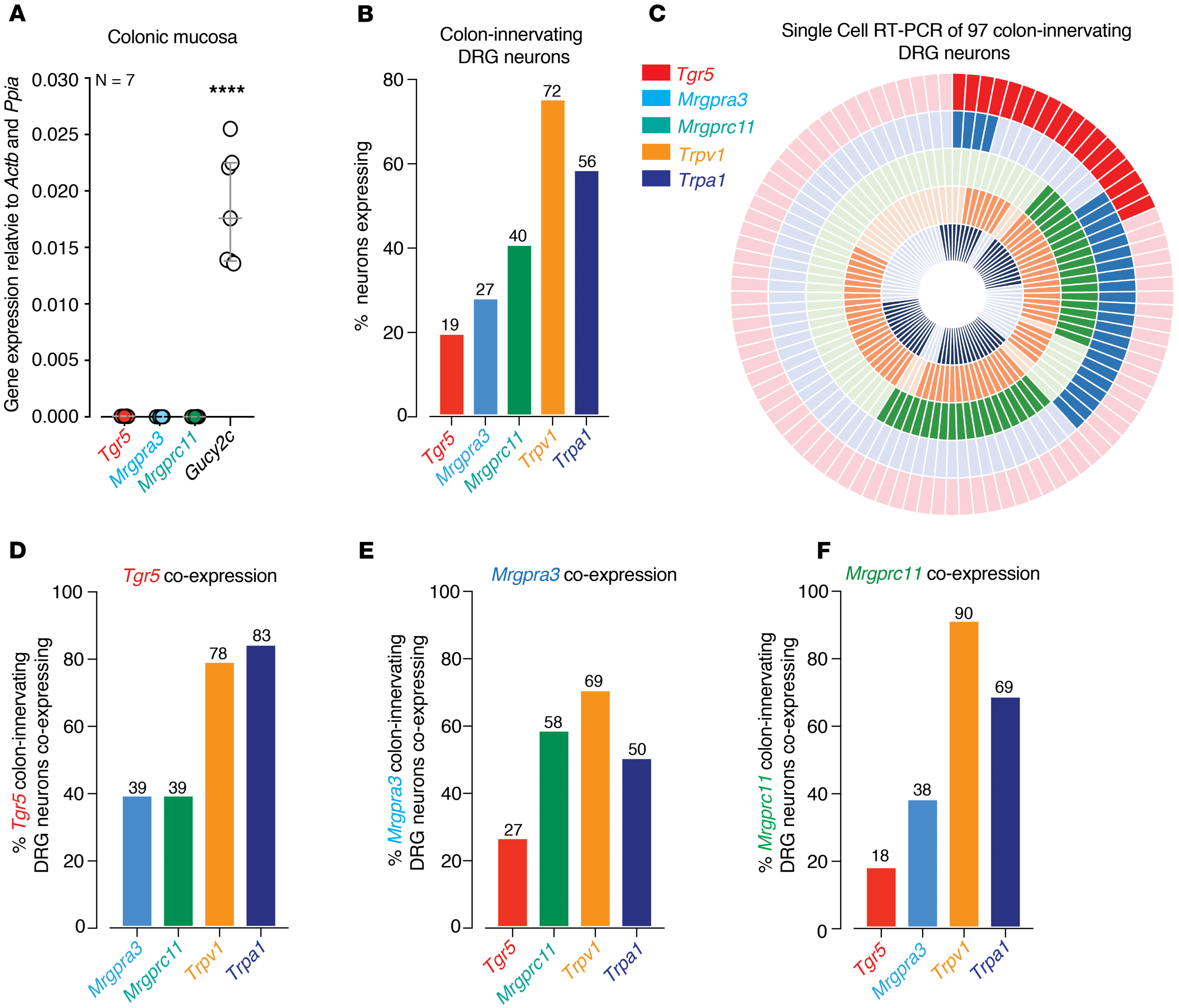

Figure 3. *Tgr5*, *Mrgprc11*, and *Mrgpra3* are expressed in both distinct and overlapping subpopulations of colon-innervating DRG neurons. (**A**) qPCR analysis showing low mRNA abundance for *Tgr5*, *Mrgpra3*, and *Mrgprc11* in the colonic mucosa compared with a known epithelial target *gucy2c* (guanylate cyclase-C, *****P* < 0.0001, *N* = 7; each dot represents data from an individual mouse). (**B**) Single-cell RT-PCR of 97 retrogradely traced colon-innervating DRG neurons (from *N* = 5 mice) reveals that subpopulations express transcripts encoding *Tgr5* (19%), *Mrgpra3* (27%), *Mrgprc11* (40%), *Trpv1* (72%), and *Trpa1* (56%). (**C**) Donut plot showing expression and coexpression of genes encoding *Tgr5*, *Mrgpra3*, *Mrgprc11*, *Trpv1*, and *Trpa1* in 97 individual retrogradely traced colon-innervating DRG neurons. Each color represents an individual gene with expression marked by bold shading. *Tgr5* is represented in the outer ring, with *Trpa1* in the inner ring. Individual neurons are arranged radially, such that coexpression of genes in a single neuron can be easily identified running from outside to inside. Some neurons express all targets, while other neurons express combinations of targets. (**D–F**) Group data showing that (**D**) *Tgr5*, (**E**) *Mrgpra3*, and (**F**) *Mrgprc11* are expressed individually within subpopulations of colon-innervating DRG neurons and also coexpress together in other subpopulations. For example, of the *Tgr5*-expressing colon-innervating DRG neurons from healthy mice, 39% coexpress *MrgprA3* and 39% coexpress *MrgprC11*. Furthermore, *Tgr5*, *Mrgpra3*, and *Mrgprc11* also coexpress with *Trpv1* (69%–90%) and *Trpa1* (50%–83%). Data in **A** represent mean ± SEM, with *P* values determined by 1-way ANOVA with Tukey's multiple comparison tests.

TGR5 and MRGPR agonists. Interestingly, we found that *Tgr5*, *Mrgpra3*, and *MrgprC11* were expressed either within the same colon-innervating DRG neuron or within separate subtypes of neurons (Figure 3C). For example, of the *Tgr5*-expressing population of colonic DRG neurons, 39% also expressed *Mrgpra3* and 39% *Mrgprc11* (Figure 3D). Of the *Mrgpra3* expressing population, 27% coexpressed *Tgr5*, while 58% coexpressed *Mrgprc11* (Figure 3E). Moreover, of the *Mrgprc11*-expressing neurons, 18% coexpressed *Tgr5*, with 38% coexpressing *Mrgpra3* (Figure 3F). Overall, *Tgr5*, *Mrgpra3*, and *Mrgprc11* were heavily coexpressed with both *Trpv1* (69%–90%) and *Trpa1* (50%–83%; Figure 3, C–F). Therefore, *Tgr5*, *Mrgpra3*, and *Mrgprc11*

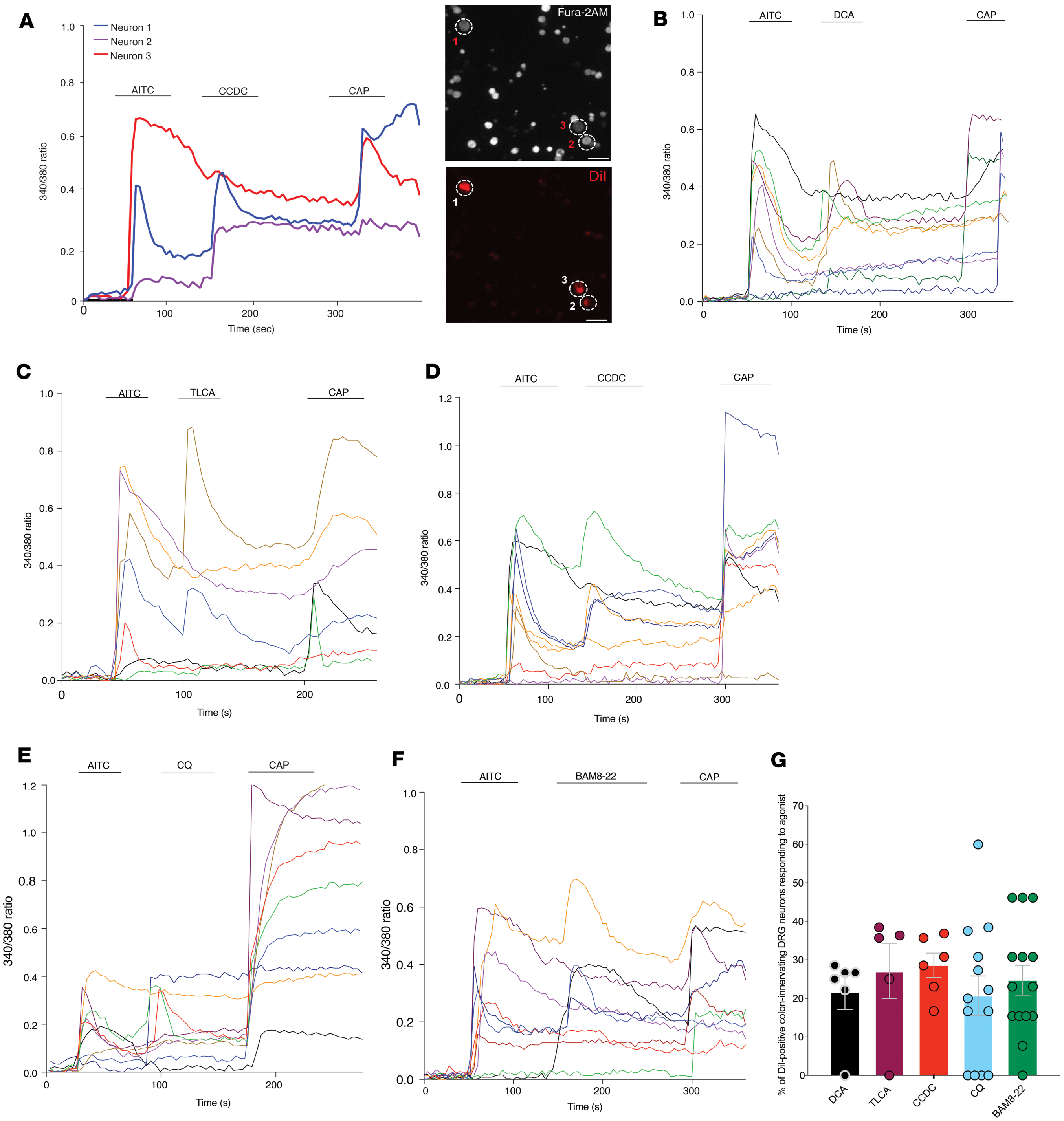

Figure 4. Colon-innervating DRG neurons respond to pruritogenic agonists for TGR5, MRGPRA3, and MRGPRC11. (**A**) Representative Ca^{2+} responses to the application of the TRPA1 agonist allyl isothiocyanate (AITC; 100 μM), the TGR5 agonist CCDC (100 μM), and the TRPV1 agonist capsaicin (CAP; 1 μM) in 3 DiI-labeled DRG neurons retrogradely labeled from the mouse colon. Right panels show Fura-2 AM image of all cells within the field of view and the 3 DiI-labeled colon-innervating DRG neurons recorded from the left panel. Scale bar: 20μm. (**B–F**) Representative traces of Ca^{2+} responses in DiI-labeled colon-innervating DRG neurons to sequential application of AITC (100 μM), the TGR5 agonists (**B**) deoxycholic acid (DCA; 100 μM), (**C**) taurolithocholic acid (TLCA; 100 μM), and (**D**) CCDC (100 μM), or the (**E**) MRGPRA3 agonist chloroquine (CQ; 10 μM) and the (**F**) MRGPRC11 agonist BAM8-22 (2 μM), followed by capsaicin (1 μM) and KCl (50 mM; not shown). DCA, TLCA, CCDC, CQ, and BAM8-22 all activated subpopulations of colon-innervating DRG neurons with varying functional coexpression with TRPA1 (AITC) and/or TRPV1 (capsaicin). (**G**) Group data showing the percentage of colon-innervating DRG neurons responding to DCA (61 neurons tested), TLCA (93 neurons tested), CCDC (93 neurons tested), CQ (94 neurons tested), and BAM8-22 (110 neurons tested). Each dot represents data from individual coverslips from a total of 6 mice. Data presented are mean ± SEM.

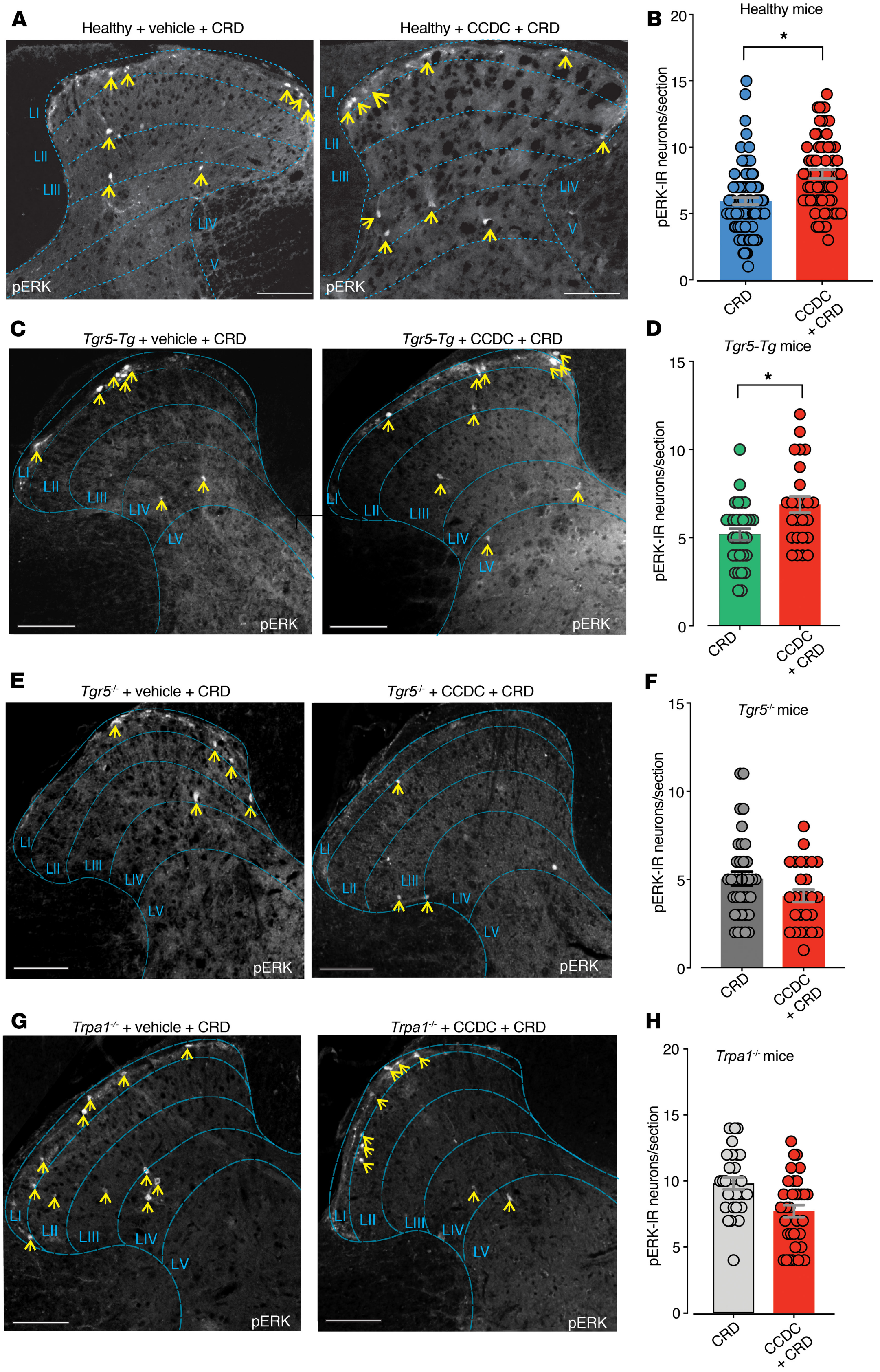
A
Healthy + vehicle + CRD
Healthy + CCDC + CRD
LI
LII
LIII
LIV
V
pERK
B
Healthy mice
*
pERK-IR neurons/section
0
5
10
15
20
CRD
CCDC + CRD
C
Tgr5-Tg + vehicle + CRD
Tgr5-Tg + CCDC + CRD
LI
LII
LIII
LIV
LV
pERK
D
Tgr5-Tg mice
*
pERK-IR neurons/section
0
5
10
15
CRD
CCDC + CRD
E
Tgr5-/- + vehicle + CRD
Tgr5-/- + CCDC + CRD
LI
LII
LIII
LIV
LV
pERK
F
Tgr5-/- mice
pERK-IR neurons/section
0
5
10
15
CRD
CCDC + CRD
G
Trpa1-/- + vehicle + CRD
Trpa1-/- + CCDC + CRD
LI
LII
LIII
LIV
LV
pERK
H
Trpa1-/- mice
pERK-IR neurons/section
0
5
10
15
20
CRD
CCDC + CRD

Figure 5. In vivo intracolonic administration of the TGR5 agonist CCDC enhances colorectal distension–induced signaling within the dorsal horn of the spinal cord. (**A**) Colorectal distension (CRD) at a pressure of 40 mmHg in healthy mice results in activation of dorsal horn (DH) neurons within the thoracolumbar (T10-L1) spinal cord, as indicated by phospho–MAP-kinase-ERK-1/2 immunoreactivity (pERK-IR, yellow arrows). pERK-IR neurons within the thoracolumbar DH, activated in response to 40 mmHg CRD, were predominantly located in laminae I–IV. (**B**) Group data showing that mice pretreated with intracolonic CCDC (100 μM) displayed significantly more pERK-IR DH neurons within the thoracolumbar spinal cord following 40 mmHg CRD compared with 40 mmHg CRD alone (*$P < 0.05$; dots indicate individual counts in spinal cord sections from CRD mice [$N = 7$] vs. CCDC + CRD mice [$N = 7$]). (**C** and **D**) Similarly, intracolonic pretreatment with CCDC in mice overexpressing TGR5 (*Tgr5-Tg*) increased the number of pERK-IR–activated neurons following 40 mmHg CRD, compared with 40 mmHg CRD alone (*$P < 0.05$; *Tgr5-Tg* CRD mice [$N = 4$] vs. *Tgr5-Tg* CCDC + CRD mice [$N = 4$]). (**E** and **F**) In contrast, intracolonic pretreatment with CCDC in $Tgr5^{-/-}$ mice did not result in an increase in pERK-IR–activated neurons following 40 mmHg CRD, compared with 40 mmHg CRD alone ($P > 0.05$, $Tgr5^{-/-}$ CRD mice [$N = 4$] vs. $Tgr5^{-/-}$ CCDC + CRD mice [$N = 4$]). (**G** and **H**) $Trpa1^{-/-}$ mice administered an intracolonic pretreatment with CCDC did not display increased numbers of pERK-IR neurons following 40 mmHg CRD, compared with 40 mmHg CRD alone ($P > 0.05$, CRD mice [$N = 4$] vs. CCDC + CRD mice [$N = 4$]). Data presented are mean ± SEM. *P* values determined by unpaired *t* tests (**B**, **D**, **F**, and **H**). Dots represent data from individual sections of spinal cord from $N = 4$–7 mice. Scale bars: 100μm (**A**, **C**, **E**, and **G**).

are expressed by both distinct and overlapping subsets of colon-innervating DRG neurons, the majority of which coexpress *Trpa1*, *Trpv1*, or both channels (Figure 3, C–F).

Agonists for TGR5, MRGPRA3, and MRGPRC11 activate multiple populations of isolated colon-innervating sensory neurons. In order to confirm the results of our single-cell RT-PCR at a functional level, and to investigate the roles of pruritogenic irritants in activating colon-innervating DRG neurons, we measured intracellular calcium ($[Ca^{2+}]_i$) using Fura-2 AM in response to application of TGR5 and MRGPR agonists (Figure 4, A–G). In previous studies, we have shown that DCA-evoked Ca^{2+} transients in DRG neurons are generated by a TGR5-dependent process (6, 10). Here, we show in colon-innervating DRG neurons from healthy mice, the TGR5 agonists DCA (Figure 4B), taurolithocholic acid (TLCA; Figure 4C), and CCDC (Figure 4D) all caused a robust increase in $[Ca^{2+}]_i$ in subpopulations of colon-innervating DRG neurons. Overall, 21.5% ± 4.4% of colonic DRG neurons responded to DCA, 27.1% ± 7.2% responded to TLCA, and 28.6% ± 3.1% responded to CCDC (Figure 4, B–D, and G). Furthermore, the MRGPRA3 agonist CQ activated 20.7% ± 5.1% of colon-innervating DRG neurons (Figure 4, E and G), with the MRGPRC11 agonist BAM8-22 activating 24.7% ± 3.8% of neurons (Figure 4, F and G).

To further characterize these subpopulations, we quantified the proportion of colon-innervating DRG neurons that responded to TGR5 (CCDC, DCA, TLCA), MRGPRA3 (CQ), or MRGPRC11 (BAM8-22), along with TRPA1 (allyl isothiocyanate; AITC) and TRPV1 (capsaicin) agonists (Figure 4, A–F). Overall, 6%–11% of colonic DRG neurons responded to the TGR5 agonists (either DCA, TLCA, or CCDC), AITC, and capsaicin, suggesting functional coexpression of TGR5, TRPA1, and TRPV1 (Supplemental Figure 1; supplemental material available online with this article; https://doi.org/10.1172/jci.insight.131712DS1). Furthermore, 7%–8% of colon-innervating DRG neurons responded to the TGR5 agonists and AITC, but not capsaicin (suggesting coexpression of TGR5 and TRPA1), with only about 2%–6% of neurons responding to the TGR5 agonists and capsaicin alone (coexpression of TGR5 and TRPV1; Supplemental Figure 1). Similarly, ~9% of colon-innervating DRG neurons responded to CQ, AITC, and capsaicin (MRGPRA3, TRPA1, TRPV1 coexpression), with 4% responding to CQ and AITC but not capsaicin, and 7% responding to CQ and capsaicin but not AITC (Supplemental Figure 1). Finally, ~10% of colon-innervating DRG neurons responded to BAM8-22, AITC, and capsaicin (MRGPRC11, TRPA1, TRPV1 coexpression), with 8% responding to BAM8-22 and AITC but not capsaicin, and 6% responding to BAM8-22 and capsaicin but not AITC (Supplemental Figure 1). These results support a functional role for TGR5, MRGPRA3, and MRGPRC11 in overlapping and distinct populations of TRPA1- and/or TRPV1-expressing colon-innervating DRG neurons.

In vivo intracolonic administration of pruritogenic agonists increases signaling within the DH of the spinal cord. To determine how activation and sensitization of colonic afferents by TGR5 and MRGPR agonists results in altered signaling within colonic pathways in vivo, we identified activated DH neurons by phosphorylated MAP-kinase-ERK-1/2 immunoreactivity (pERK-IR) in response to colorectal distension (CRD) (25–32). In healthy vehicle-treated mice, CRD at a pressure of 40 mmHg resulted in activation of DH neurons within the thoracolumbar (T10-L1) regions of the spinal cord (Figure 5, A and B). Pretreatment of healthy mice with the TGR5 agonist CCDC enhanced CRD-evoked activation of DH neurons (Figure 5, A and B). However, intracolonic administration of CCDC alone in healthy mice did not cause activation of DH neurons within the spinal cord (Supplemental Figure 2). Overall, these findings indicate that intracolonic CCDC induced colonic afferent mechanical hypersensitivity in vivo, which translated to increased neuronal activation within the spinal cord. Consistent with this action of TGR5, intracolonic pretreatment with CCDC in mice overexpressing

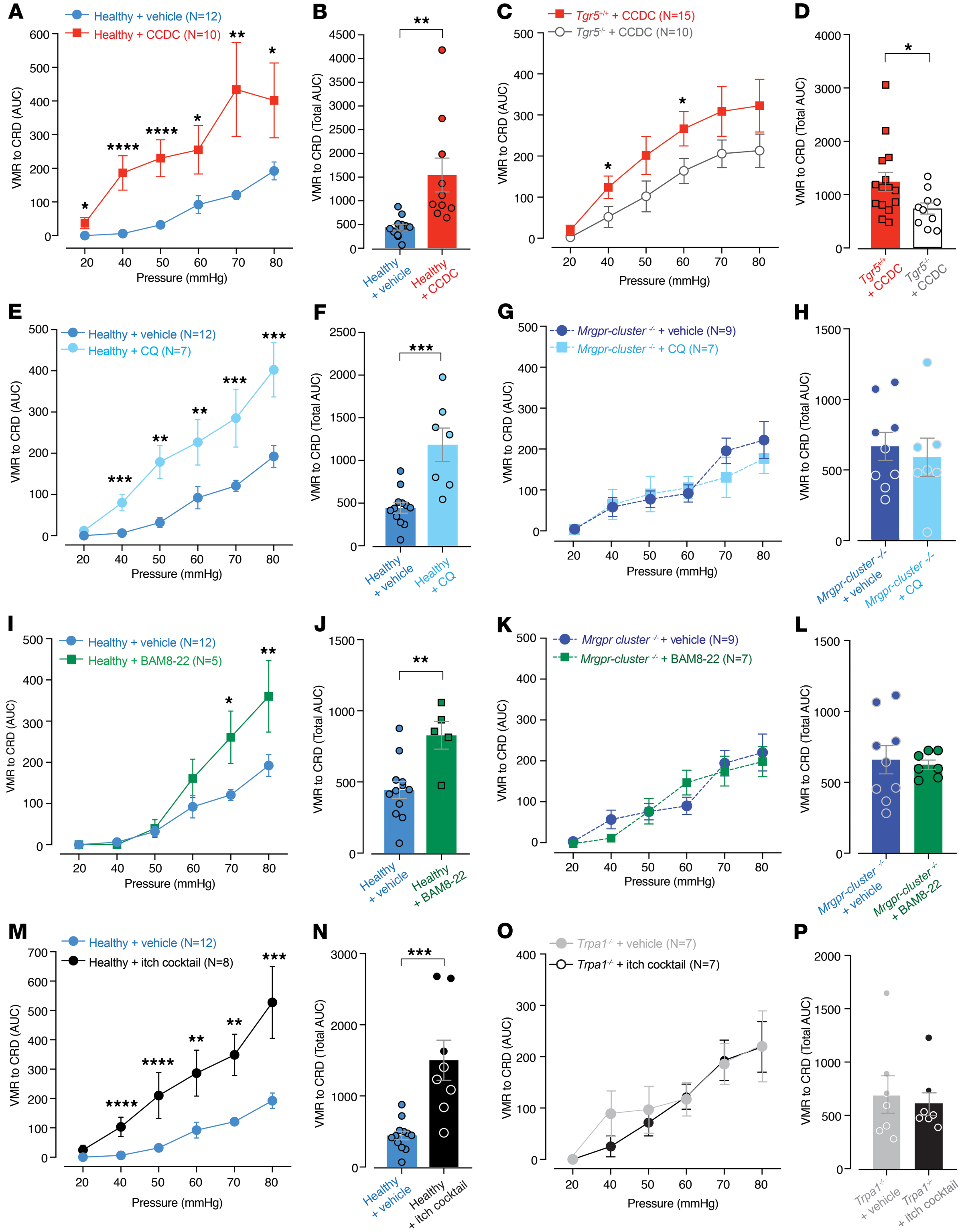

Figure 6. In vivo intracolonic administration of TGR5, MRGPRA3, and MRGPRC11 agonists, alone or in combination, induces visceral hypersensitivity to colorectal distension. (**A**) Intracolonic administration of CCDC (100μM) resulted in significantly enhanced visceromotor responses (VMRs) to colorectal distension (CRD) in healthy mice, with significant increases observed across all distension pressures. (**B**) Group data expressed as the total AUC of the VMR to CRD shows significantly elevated responses following intracolonic CCDC. Each dot represents the total AUC from an individual animal. (**C**) *Tgr5*$^{-/-}$ mice administered intracolonic CCDC (100 μM) showed significantly reduced VMRs compared with *Tgr5*$^{+/+}$ littermates administered intracolonic CCDC. (**D**) Significantly reduced total VMRs in *Tgr5*$^{-/-}$ mice administered CCDC compared with *Tgr5*$^{+/+}$. (**E**) Healthy mice administered intracolonic chloroquine (CQ; 10 μM) have significantly elevated VMRs, particularly at 40–80 mmHg distension. (**F**) Intracolonic CQ significantly enhanced total VMRs compared with vehicle. (**G**) *Mrgpr-cluster*$^{-/-}$ mice intracolonically administered 10 μM CQ did not show altered VMRs nor altered (**H**) total VMR relative to *Mrgpr-cluster*$^{-/-}$ mice administered vehicle ($P > 0.05$). (**I**) Mice administered intracolonic BAM8-22 (20 μM) have significantly elevated VMRs, particularly at noxious

distension pressures of 70–80 mmHg. (**J**) Intracolonic BAM8-22 significantly enhanced total VMRs compared with vehicle. (**K**) *Mrgpr-cluster*$^{-/-}$ mice intracolonically administered 20 μM BAM8-22 had unaltered VMRs and unaltered (**L**) total VMRs to CRD relative to *Mrgpr-cluster*$^{-/-}$ mice administered vehicle ($P > 0.05$). (**M**) An intracolonic itch cocktail consisting of a combination of CCDC (100 μM), BAM8-22 (20 μM), and CQ (10 μM) significantly enhanced VMRs in healthy mice. This hypersensitivity was evident at 40–50 mmHg, 60–70 mmHg, and 80 mmHg. (**N**) The itch cocktail also significantly enhanced the total VMR compared with vehicle. (**O**) *Trpa1*$^{-/-}$ mice intracolonically administered the itch cocktail did not show altered VMRs relative to vehicle-administered *Trpa1*$^{-/-}$ mice ($P > 0.05$). (**P**) Total VMR was unchanged in *Trpa1*$^{-/-}$ mice administered the itch cocktail compared with vehicle ($P > 0.05$). Data represent mean ± SEM. *P* values determined by generalized estimating equations, followed by least significant difference post hoc tests (**A**, **C**, **E**, **G**, **I**, **K**, **M**, **O**) or by unpaired *t* tests (**B**, **D**, **F**, **H**, **J**, **L**, **N**, **P**). $^{*}P < 0.05$, $^{**}P < 0.01$, $^{***}P < 0.001$, $^{****}P < 0.0001$.

TGR5 (*Tgr5-Tg*) significantly increased the number of pERK-IR neurons following CRD, compared with CRD plus vehicle in *Tgr5-Tg* mice (Figure 5, C and D). In contrast, intracolonic pretreatment with CCDC in *Tgr5*$^{-/-}$ mice did not alter the number of pERK-IR neurons following CRD compared with vehicle plus CRD *Tgr5*$^{-/-}$ mice (Figure 5, E and F), suggesting that TGR5 does indeed mediate the effects of CCDC. Finally, *Trpa1*$^{-/-}$ mice pretreated with intracolonic CCDC followed by CRD displayed no increase in the number of pERK-IR neurons compared with *Trpa1*$^{-/-}$ mice with vehicle plus CRD, confirming that TRPA1 is crucial for TGR5-mediated mechanical hypersensitivity (Figure 5, G and H). We also observed that intracolonic administration of CQ resulted in pronounced activation of neurons within the DH of the spinal cord, consistent with in vivo activation of MRGPRA3 in colonic sensory afferent pathways (Supplemental Figure 3).

In vivo intracolonic administration of pruritogenic agonists increases mechanically evoked responses to CRD and alters animal behavior. We next assessed whether TGR5- and MRGPR-induced activation of colonic afferents resulted in alterations in visceral sensitivity evoked by CRD in vivo. We measured the visceromotor response (VMR) to increasing CRD pressures by recording electromyographic (EMG) activity from electrodes surgically implanted into the abdominal muscles (30, 33–35). In healthy mice, intracolonic administration of CCDC significantly enhanced VMRs to CRD at all distension pressures, indicating visceral hypersensitivity (Figure 6, A and B, and Supplemental Figure 4). In comparison, intracolonic CCDC in *Tgr5*$^{-/-}$ mice failed to induce the elevated VMR to CRD observed in *Tgr5*$^{+/+}$ mice administered intracolonic CCDC (Figure 6, C and D, and Supplemental Figure 4). Intracolonic administration of the MRGPRA3 agonist CQ significantly enhanced the VMR to CRD in healthy mice, particularly at pressures ≥ 40 mmHg (Figure 6, E and F, and Supplemental Figure 4). However, CQ did not alter the VMR to CRD in *Mrgpr-cluster*$^{-/-}$ mice (Figure 6, G and H, and Supplemental Figure 4), confirming the role of MRGPRs in the actions of CQ in colonic pathways. Intracolonic administration of the MRGPRC11 agonist BAM8-22 in healthy mice also significantly enhanced the VMR to CRD, although this increase was most apparent at higher, noxious distension pressures of ≥ 60 mmHg (Figure 6, I and J, and Supplemental Figure 4). In contrast, BAM8-22 did not alter the VMR to CRD in *Mrgpr-cluster*$^{-/-}$ mice (Figure 6, K and L, and Supplemental Figure 4). Notably, these CCDC-, CQ-, and BAM8-22–induced changes in VMR to CRD were not due to changes in colonic compliance (Supplemental Figure 5, A–F), suggesting that the actions observed occurred via activation of receptors on afferent endings. Overall, these data show that application of the individual agonists for TGR5, MRGPRA3, and MRGPRC11 can each induce visceral hypersensitivity to CRD in healthy mice.

Since TGR5, MRGPRA3, and MRGPRC11 are expressed in distinct and overlapping populations of colon-innervating DRG neurons, we determined if coadministration of these agonists, as an “itch cocktail,” also exacerbated visceral hypersensitivity. Concurrent intracolonic administration of CCDC, CQ, and BAM8-22 evoked pronounced increases in the VMR to CRD at all distension pressures and significantly increased the total VMR (Figure 6, M and N, and Supplemental Figure 4). In contrast, *Trpa1*$^{-/-}$ mice intracolonically administered the itch cocktail did not show altered VMRs to CRD relative to vehicle-administered *Trpa1*$^{-/-}$ mice (Figure 6, O and P, Supplemental Figure 4), confirming that TRPA1 contributes to TGR5-, MRGPRA3-, and MRGPRC11-induced mechanical hypersensitivity in colonic afferent pathways.

To determine if concurrent activation of TGR5, MRGPRA3, and MRGPRC11 has effects beyond mechanically evoked visceral sensitization, we also recorded animal behavior in response to intracolonic administration of the itch cocktail. Healthy mice coadministered CCDC, CQ, and BAM8-22 covered significantly less distance in their enclosure (Figure 7, A–C), had a slower average velocity of travel (Figure 7D), displayed reduced locomotor activity (Figure 7E), and displayed more grooming behavior (Figure 7F) compared with vehicle-administered mice. These behavioral changes were not observed when TGR5, MRGPRA3, or MRGPRC11 agonists were applied individually (Supplemental Figure 6), suggesting full recruitment of these irritant pathways is required to induce profound behavioral changes in these mice. Notably, mice intracolonically administered CCDC, CQ, or BAM8-22, either individually or in combination, did not

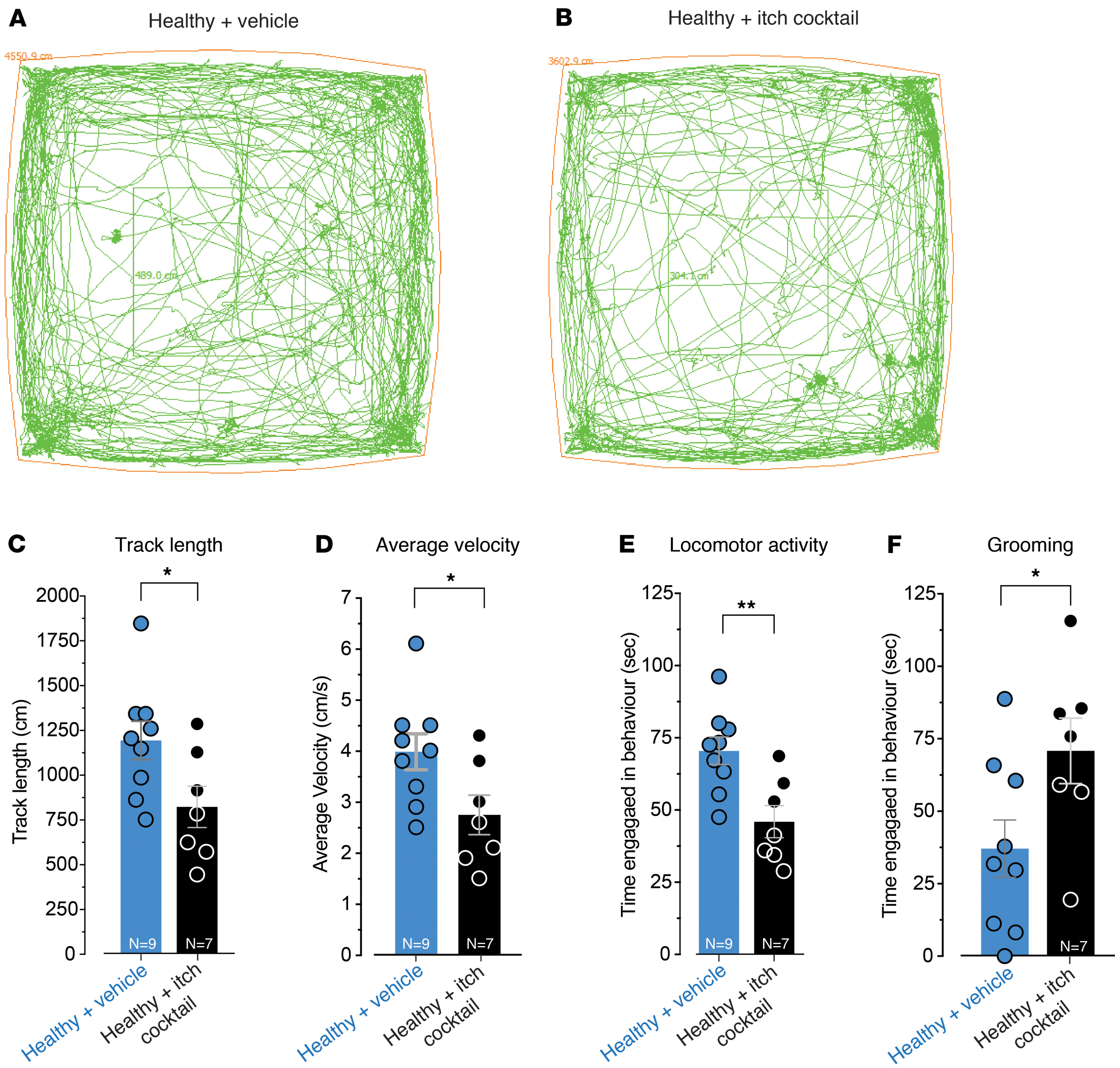

Figure 7. In vivo intracolonic administration of an itch cocktail consisting of TGR5, MRGPRA3, and MRGPRC11 agonists alters animal behavior. Representative track paths are shown for a (**A**) healthy mouse intracolonically administered vehicle (saline) and for a (**B**) healthy mouse intracolonically administered an itch cocktail consisting of a combination of CCDC (100 μM), BAM8-22 (20 μM), and CQ (10 μM). Intracolonic administration of the itch cocktail significantly reduced (**C**) the total track length covered (*$P < 0.05$; vehicle, $N = 9$; itch cocktail, $N = 7$), (**D**) the average velocity of travel (*$P < 0.05$; vehicle, $N = 9$; itch cocktail, $N = 7$), and (**E**) locomotor activity time compared with vehicle treatment (**$P < 0.01$; vehicle, $N = 9$; itch cocktail, $N = 7$). (**F**) Intracolonic administration of the itch cocktail also significantly increased grooming behavior compared with vehicle (*$P < 0.05$; vehicle, $N = 9$; itch cocktail, $N = 7$). Data represent mean ± SEM. Dots represent values from individual mice. P values were by unpaired t tests (**C**, **D**, **E**, **F**).

display increased scratching behavior (Supplemental Figure 7), suggesting that the agonists were localized to the colon and did not reach the systemic circulation. Overall, our results demonstrate crucial individual and combined roles for TGR5, MRGPRA3, and MRGPRC11 in the sensitization of colonic afferent pathways and the resultant changes in spinal cord processing, responsiveness to CRD, and animal behavior.

TGR5, MRGPRA3, and MRGPRC11 also contribute to the sensitization of colonic afferent pathways during CVH. In order to determine if the roles of TGR5, MRGPRA3, and MRGPRC11 in evoking visceral hypersensitivity extends into disease states, we used a CVH mouse model of IBS. CVH was induced by administration of intracolonic trinitrobenzenesulphonic acid (TNBS), which has been shown to induce colitis (36, 37). While colonic inflammation spontaneously heals over a 7-day period, these mice subsequently develop chronic mechanical hypersensitivity of colonic afferents in the postinflammatory state (25–27, 30, 34, 36, 38), display neuroplasticity within spinal cord pathways (16, 30, 31) and exhibit visceral hypersensitivity to CRD (30, 34).

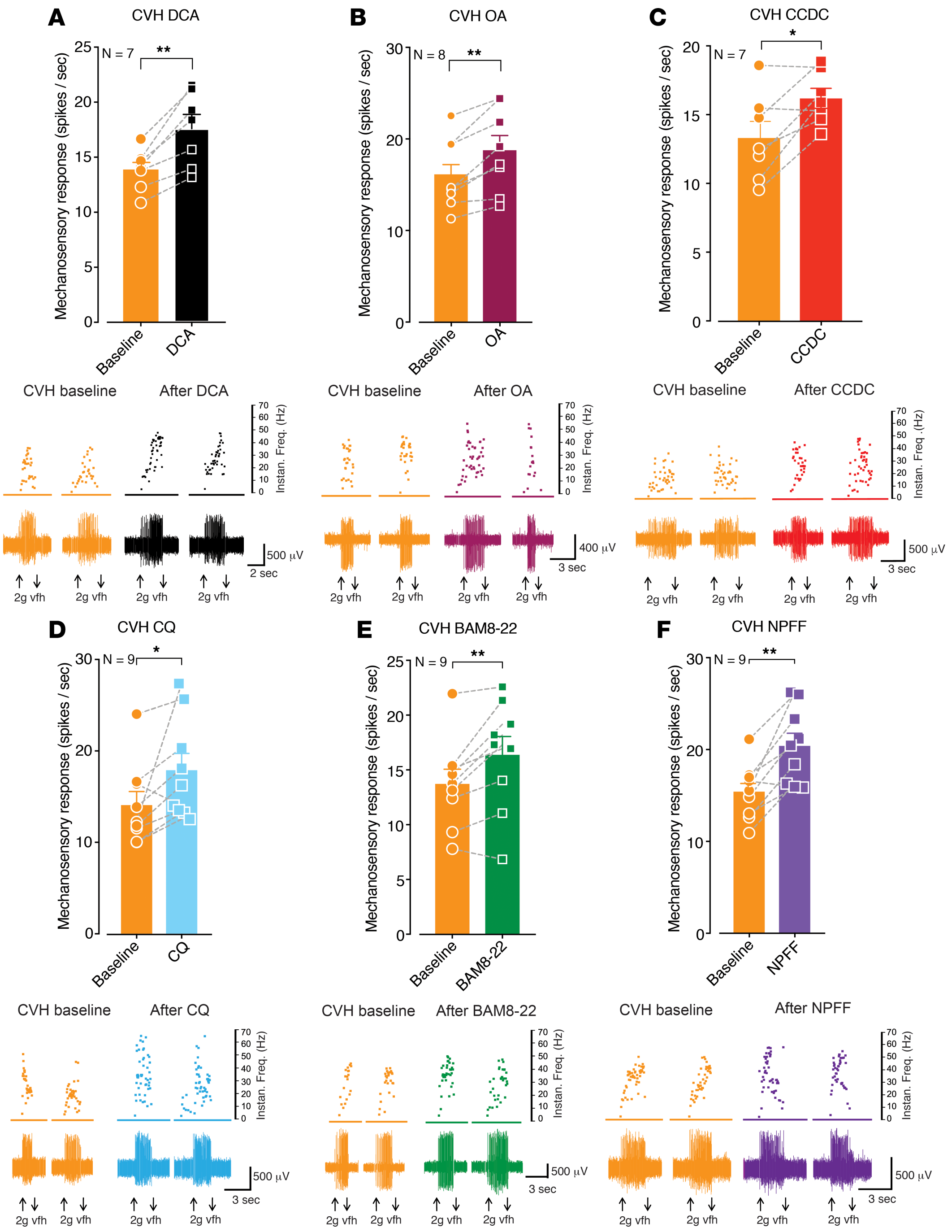

Figure 8. TGR5, MRGPRA3, and MRGPRC11 agonists evoke mechanical hypersensitivity in colonic afferents from mice with chronic visceral hypersensitivity (CVH). (**A**) Application of the TGR5 agonist deoxycholic acid (DCA; 100 µM) to the colonic mucosa of CVH mice induces mechanical hypersensitivity of colonic nociceptors (***P* < 0.01, *N* = 7). Dots represent values from individual CVH afferents before and after DCA application. Lower panels show representative recordings from a single colonic afferent nerve fiber from a CVH mouse responding to a 2 g vfh before and after incubation with DCA. (**B**) Application of the TGR5 agonist oleanolic acid (OA; 100 µM for 5 minutes) also caused mechanical hypersensitivity in nociceptors from CVH mice (***P* < 0.01, *N* = 8). (**C**) The TGR5 agonist CCDC (100 µM for 5 minutes) also evoked mechanical hypersensitivity of colonic nociceptors from CVH mice (**P* < 0.05, *N* = 7). (**D**) Colonic nociceptors from CVH mice also displayed mechanical hypersensitivity to the application of the MRGPRA3 agonist chloroquine (CQ, 10 µM for 5 minutes, **P* < 0.05, *N* = 9), (**E**) MRGPRC11 agonist BAM8-22 (20 µM for 5 minutes, ***P* < 0.01, *N* = 9), and (**F**) the combined MRGPRC11/MRGPRA4 agonist neuropeptide FF (NPFF; 5 µM for 5 minutes, ***P* < 0.01, *N* = 9 mice). Data represent Mean ± SEM. *P* values determined by paired *t* tests (**A–F**).

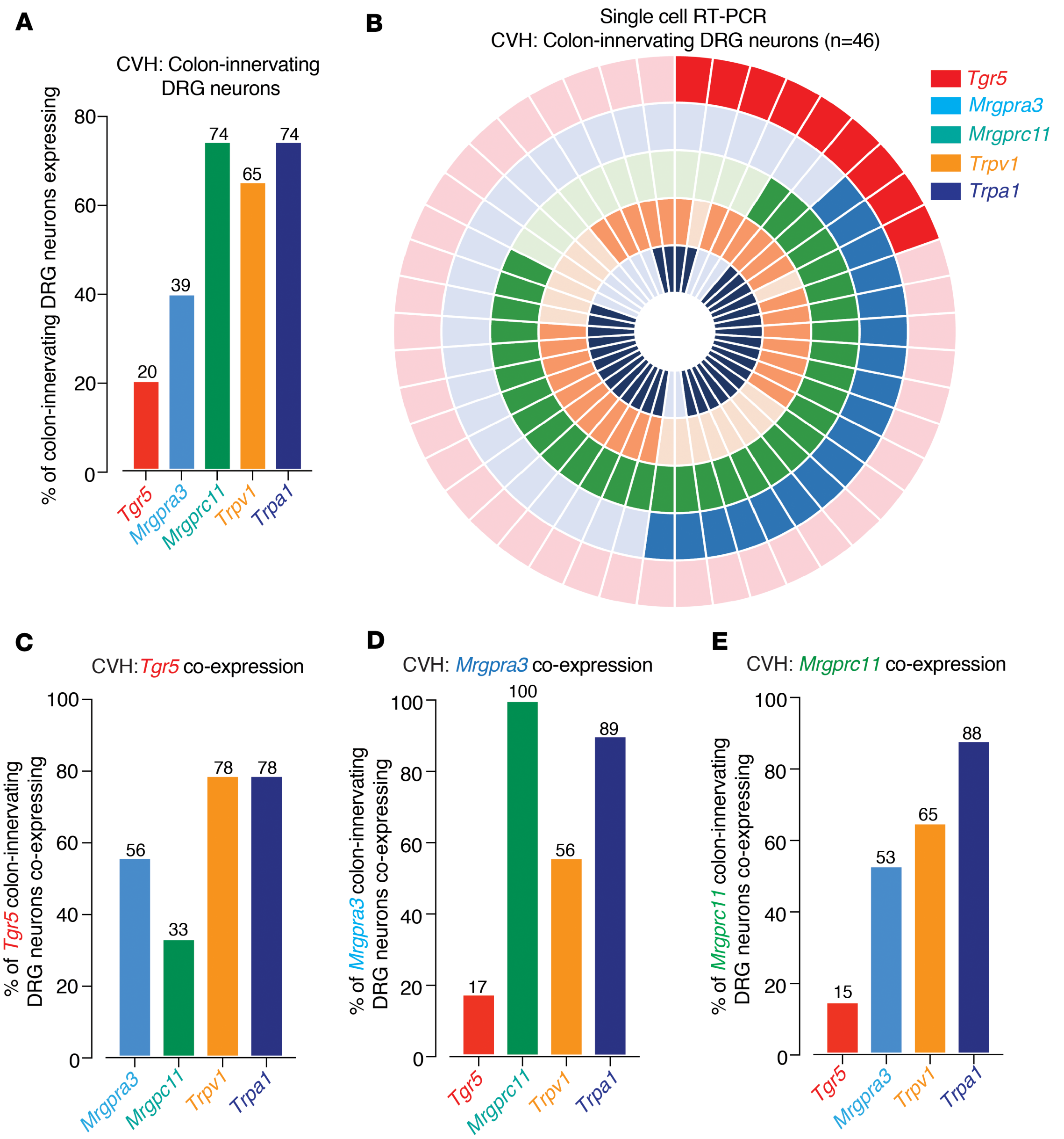

Figure 9. Distinct and overlapping expression patterns for *Tgr5*, *Mrgpra3*, and *Mrgprc11* in colon-innervating DRG neurons from CVH mice. (**A**) Single-cell RT-PCR of 46 retrogradely traced colon-innervating DRG neurons from 4 CVH mice reveals that subpopulations express *Tgr5* (20%), *Mrgpra3* (39%), *Mrgprc11* (74%), *Trpv1* (65%), and *Trpa1* (74%). (**B**) Donut plot showing expression and coexpression of genes encoding *Tgr5*, *Mrgpra3*, *Mrgprc11*, *Trpv1*, and *Trpa1* in 46 individual retrogradely traced colon-innervating DRG neurons from CVH mice. Each color represents an individual gene, with expression marked by bold shading (*Tgr5,* outer ring; *Trpa1*, inner ring). Some CVH DRG neurons express all targets, while other neurons express combinations of targets. (**C–E**) Group data showing (**C**) *Tgr5*, (**D**) *Mrgpra3*, and (**E**) *Mrgprc11* are expressed individually within subpopulations of colon-innervating DRG neurons and also coexpressed together in other subpopulations. For example, of the *Tgr5* expressing colon-innervating DRG neurons from CVH mice, 56% coexpress *Mrgpra3*, and 33% coexpress *Mrgprc11*. *Tgr5*, *Mrgpra3*, and *Mrgprc11* also heavily coexpress with *Trpv1* and, in particular, *Trpa1* in CVH states.

Colonic afferents from CVH mice displayed mechanical hypersensitivity relative to afferents from healthy mice (Supplemental Figure 8), as described previously (25–27, 30, 34, 36, 38). Interestingly, application of the TGR5 agonists DCA, OA, or CCDC further amplified mechanical hypersensitivity in CVH colonic afferents, above their already-elevated baseline levels (Figure 8, A–C). We also observed that a subpopulation of CVH afferents displayed action potential firing to application of the TGR5 agonists in the absence of mechanical stimuli, which rarely occurred in healthy colonic afferents (Supplemental Figure 9). Individual application of the MRGPRA3 agonist CQ, the MRGPRC11 agonist BAM8-22, or the MRGPRC11/MRGPRA4 agonist NPFF also further amplified mechanical hypersensitivity in CVH colonic afferents (Figure 8, D–F). This was also associated with action potential firing to application of the individual Mrgpr agonists,

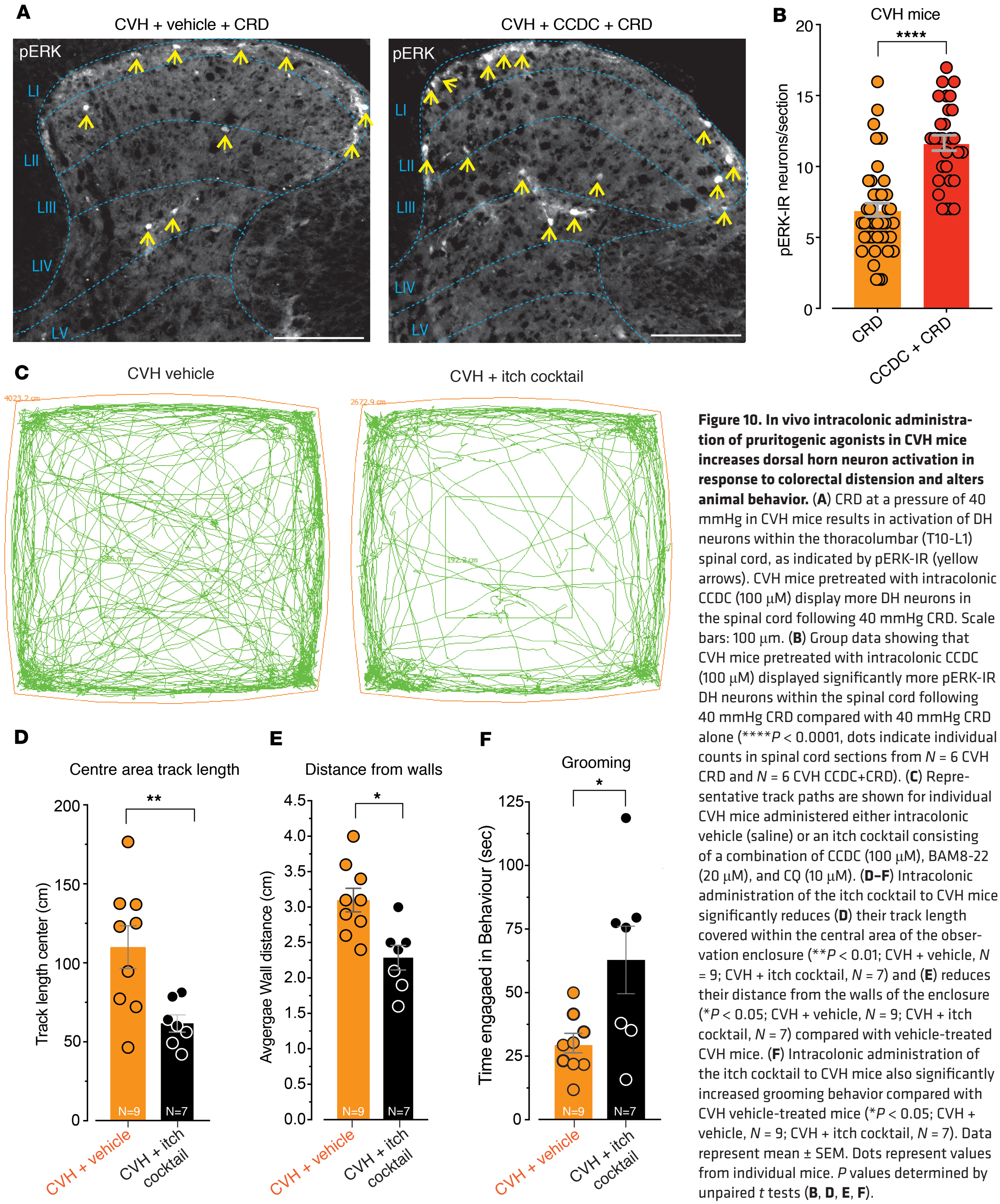

Figure 10. In vivo intracolonic administration of pruritogenic agonists in CVH mice increases dorsal horn neuron activation in response to colorectal distension and alters animal behavior. (**A**) CRD at a pressure of 40 mmHg in CVH mice results in activation of DH neurons within the thoracolumbar (T10-L1) spinal cord, as indicated by pERK-IR (yellow arrows). CVH mice pretreated with intracolonic CCDC (100 μM) display more DH neurons in the spinal cord following 40 mmHg CRD. Scale bars: 100 μm. (**B**) Group data showing that CVH mice pretreated with intracolonic CCDC (100 μM) displayed significantly more pERK-IR DH neurons within the spinal cord following 40 mmHg CRD compared with 40 mmHg CRD alone (****$P < 0.0001$, dots indicate individual counts in spinal cord sections from $N = 6$ CVH CRD and $N = 6$ CVH CCDC+CRD). (**C**) Representative track paths are shown for individual CVH mice administered either intracolonic vehicle (saline) or an itch cocktail consisting of a combination of CCDC (100 μM), BAM8-22 (20 μM), and CQ (10 μM). (**D–F**) Intracolonic administration of the itch cocktail to CVH mice significantly reduces (**D**) their track length covered within the central area of the observation enclosure (**$P < 0.01$; CVH + vehicle, $N = 9$; CVH + itch cocktail, $N = 7$) and (**E**) reduces their distance from the walls of the enclosure (*$P < 0.05$; CVH + vehicle, $N = 9$; CVH + itch cocktail, $N = 7$) compared with vehicle-treated CVH mice. (**F**) Intracolonic administration of the itch cocktail to CVH mice also significantly increased grooming behavior compared with CVH vehicle-treated mice (*$P < 0.05$; CVH + vehicle, $N = 9$; CVH + itch cocktail, $N = 7$). Data represent mean ± SEM. Dots represent values from individual mice. *P* values determined by unpaired *t* tests (**B**, **D**, **E**, **F**).

which rarely occurred in healthy colonic afferents (Supplemental Figure 9). Single-cell RT-PCR from CVH mice showed that 20% of colon-innervating DRG neurons expressed *Tgr5*, while 39% expressed *Mrgpra3* and 74% expressed *Mrgprc11*, with 65% expressing *Trpv1* and 74% *Trpa1* (Figure 9, A and B). Compared with healthy colon-innervating DRG neurons, this represented a significant increase in the proportion of

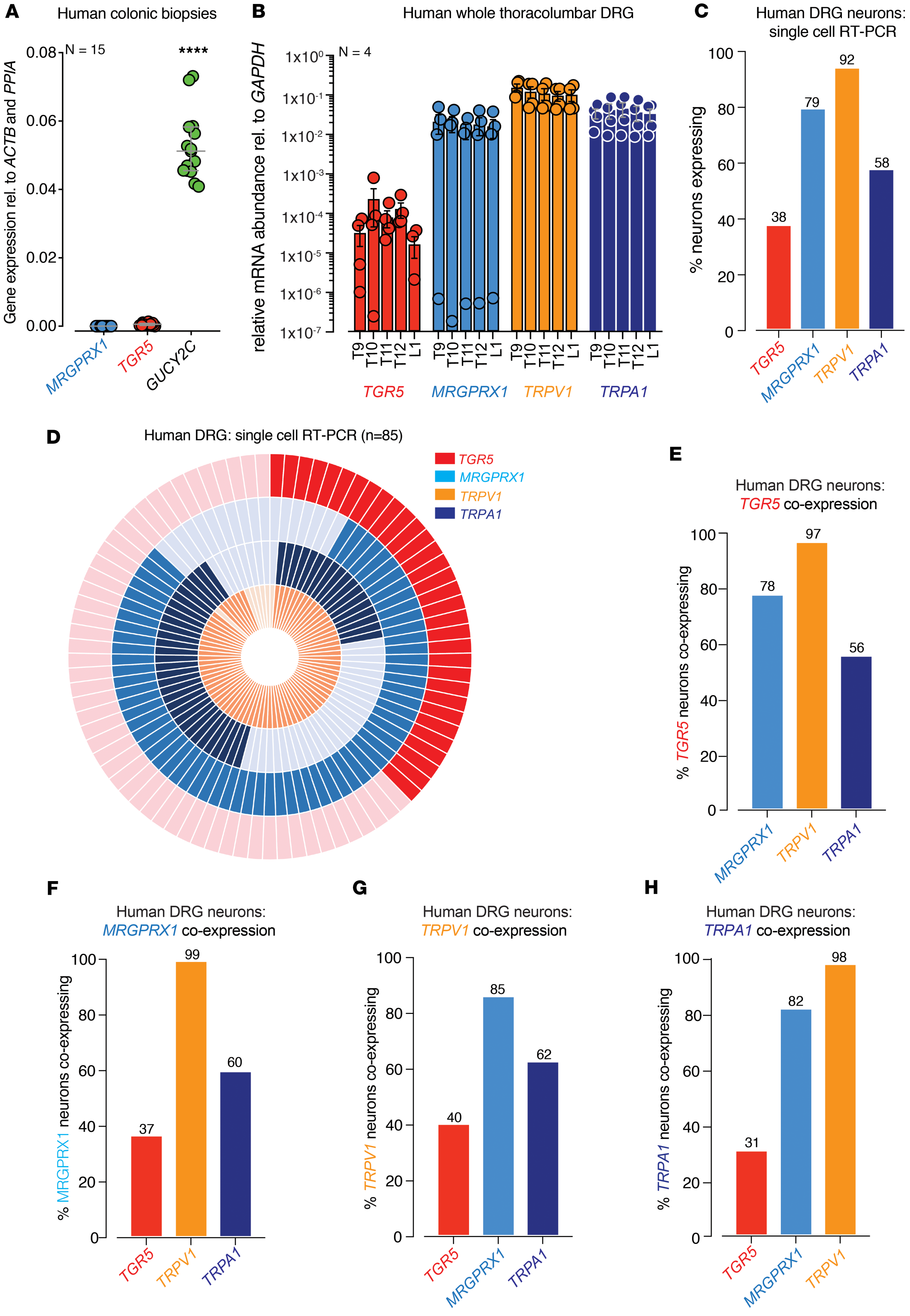
A
Human colonic biopsies
Gene expression rel. to ACTB and PPIA
N = 15
****
0.08
0.06
0.04
0.02
0.00
MRGPRX1
TGR5
GUCY2C
B
Human whole thoracolumbar DRG
relative mRNA abundance rel. to GAPDH
N = 4
1x10⁰
1x10⁻¹
1x10⁻²
1x10⁻³
1x10⁻⁴
1x10⁻⁵
1x10⁻⁶
1x10⁻⁷
T9
T10
T11
T12
L1
TGR5
MRGPRX1
TRPV1
TRPA1
C
Human DRG neurons: single cell RT-PCR
% neurons expressing
100
80
60
40
20
0
38
79
92
58
TGR5
MRGPRX1
TRPV1
TRPA1
D
Human DRG: single cell RT-PCR (n=85)
TGR5
MRGPRX1
TRPV1
TRPA1
E
Human DRG neurons: TGR5 co-expression
% TGR5 neurons co-expressing
100
80
60
40
20
0
78
97
56
MRGPRX1
TRPV1
TRPA1
F
Human DRG neurons: MRGPRX1 co-expression
% MRGPRX1 neurons co-expressing
100
80
60
40
20
0
37
99
60
TGR5
TRPV1
TRPA1
G
Human DRG neurons: TRPV1 co-expression
% TRPV1 neurons co-expressing
100
80
60
40
20
0
40
85
62
TGR5
MRGPRX1
TRPA1
H
Human DRG neurons: TRPA1 co-expression
% TRPA1 neurons co-expressing
100
80
60
40
20
0
31
82
98
TGR5
MRGPRX1
TRPV1

Figure 11. Human DRG neurons coexpress *TRG5*, *MRGPRX1*, *TRPV1*, and *TRPA1*. (**A**) qPCR analysis from colonic biopsies from healthy human subjects show low levels of mRNA expression for *TGR5* and absent *MRGPRX1* (human ortholog of the mouse *Mrgpra3* and *Mrgprc11*) compared with a known epithelial target *GUCY2C* (GC-C, ****$P < 0.0001$, $N = 15$ subjects. Dots represent averaged values from each patient sample). (**B**) qPCR expression analysis of whole human thoracolumbar (TL; T9-L1) DRG from 4 human donors. Analysis reveals abundant expression of *MRGPRX1*, *TRPV1*, and *TRPA1*, plus expression of the bile acid receptor *TGR5*. Dots represent averaged values from each donor at each DRG level. (**C**) Single-cell RT-PCR analysis showing the percentage of individual human DRG neurons expressing the *TGR5*, *MRGPRX1*, *TRPV1*, and *TRPA1*. Data show that, of the 85 individual human thoracolumbar DRG neurons examined, 38% express *TGR5*, 79% express *MRGPRX1*, 92% expressed *TRPV1*, with 58% expressing *TRPA1*. (**D**) Donut plot analysis showing coexpression profiles of 85 individual human TL DRG neurons using single-cell RT-PCR for *TGR5*, *MRGPRX1*, *TRPV1*, and *TRPA1*. (**E**) Of the 38% of human TL DRG neurons expressing *TGR5*, 78% coexpress *MRGPRX1*, 97% coexpress *TRPV1*, with 56% coexpressing *TRPA1*. (**F**) Of the 79% of human DRG neurons expressing *MRGPRX1*, 37% coexpress *TGR5*, 99% coexpress *TRPV1*, with 60% coexpressing *TRPA1*. (**G**) *TRPV1*-expressing human DRG neurons also express *TGR5* (40%), *MRGPRX1* (85%), and *TRPA1* (62%). (**H**) *TRPA1*-expressing human DRG neurons also express *TGR5* (31%), *MRGPRX1* (82%), and *TRPV1* (98%). Data in **A** and **B** represent mean ± SEM. *P* values determined by 1-way ANOVA with Tukey's multiple comparison tests (**A**).

DRG neurons expressing *Mrgprc11* or *Trpa1* in CVH states (Supplemental Figure 10). There were also significant changes in the coexpression profiles of CVH colon-innervating DRG neurons (Figure 9, C–E), with significantly more *Mrgpra3* expressing CVH DRG neurons coexpressing *Mrgprc11* and *Trpa1* (Supplemental Figure 10) and significantly fewer *Mrgprc11* neurons coexpressing *Trpv1* (Supplemental Figure 10).

We also found that intracolonic administration of CCDC alone in CVH mice resulted in pERK-IR within DH neurons of the spinal cord (Supplemental Figure 2). Furthermore, CVH mice pretreated with CCDC displayed significantly more pERK-IR DH neurons within the spinal cord following 40 mmHg CRD compared with CVH mice with vehicle plus CRD (Figure 10, A and B). These findings indicate that in vivo intracolonic CCDC activates colonic afferents and also induces mechanical hypersensitivity in CVH mice. In terms of behavioral responses, CVH mice intracolonically administered the itch cocktail of concurrent CCDC, CQ, and BAM8-22 displayed significantly reduced movement in terms of the distance travelled within the central observational area of the enclosure (Figure 10, C and D), a significantly decreased distance from the walls of the enclosure (Figure 10E), and a significantly increased time spent grooming (Figure 10F). However, these CVH mice did not display increased scratching behavior in response to the intracolonic itch cocktail (Supplemental Figure 7). Overall, our results demonstrate that TGR5, MRGPRA3, and MRGPRC11 each contribute to the sensitization of colonic afferent pathways in CVH states. There is an increase in MRGPRC11- and TRPA1-dependent mechanisms in CVH and that agonists for TGR5, MRGPRA3, and MRGPRC11 profoundly alter the behavior of CVH mice.

Human DRG neurons express TGR5 and MRGPRX1 and respond to pruritogenic agonists. To further investigate the translatability of our findings, we determined the mRNA expression profiles of *TGR5* and *MRGPRX1* (the human ortholog of murine *Mrgpra3* and *Mrgprc11*) in human tissue and also tested the responsiveness of human DRG neurons to TGR5, MRGPRX1, TRPV1, and TRPA1 agonists. Firstly, using colonic biopsies from 15 human healthy subjects, we found that *TGR5* had low expression compared with a known epithelial target *GUCY2C,* while *MRGPRX1* was absent (Figure 11A), which is consistent with our findings in mouse colonic mucosa (Figure 3A). qPCR of T9-L1 whole thoracolumbar DRG from 4 human donors showed expression of *TGR5*, with greater abundance of *MRGPRX1* and, in particular, *TRPA1* and *TRPV1* (Figure 11B). Single-cell RT-PCR from 85 individual human DRG neurons, of predominately smaller diameter, demonstrated that 38% expressed *TGR5*, 79% expressed *MRGPRX1*, 92% expressed *TRPV1*, and 58% expressed *TRPA1* (Figure 11, C and D). Consistent with our observations from mouse DRG, we found that *TGR5* and *MRGPRX1* were expressed in both distinct and overlapping populations of human DRG neurons, which heavily coexpressed *TRPV1* or *TRPA1* (Figure 11D). Specifically, of the *TGR5*-expressing human DRG neurons, 78% coexpressed *MRGPRX1*, 97% coexpressed *TRPV1*, and 56% coexpressed *TRPA1* (Figure 11E). Of the *MRGPRX1*-expressing population, 37% coexpressed *TGR5*, 99% coexpressed *TRPV1*, and 60% coexpressed *TRPA1* (Figure 11F). Of the *TRPV1*-expressing population, 40% coexpressed *TGR5*, 85% coexpressed *MRGPRX1,* and 62% coexpressed *TRPA1* (Figure 11G), while — of the *TRPA1*-expressing population — 31% coexpressed *TGR5*, 82% coexpressed *MRGPRX1*, and 98% coexpressed *TRPV1* (Figure 11H).

Using Ca^{2+} imaging of dissociated and cultured human DRG neurons, we found that subpopulations of neurons were activated by the application of CCDC (14%; Figure 12, A, G, and H), BAM8-22 (34%; Figure 12, B, G, and H), CQ (10%; Figure 12, C, G, and H), and NPFF (5%; Figure 12, D, G, and H), as indicated by robust increases in $[Ca^{2+}]_i$ (Figure 12, A–D). Many of these neurons also responded to capsaicin (62%; Figure 12, E, G, and H) or AITC (27%; Figure 12, F, G, and H). In order to simulate a pathological state, we transiently incubated neurons in culture with inflammatory mediators (histamine, PGE II, serotonin, bradykinin)

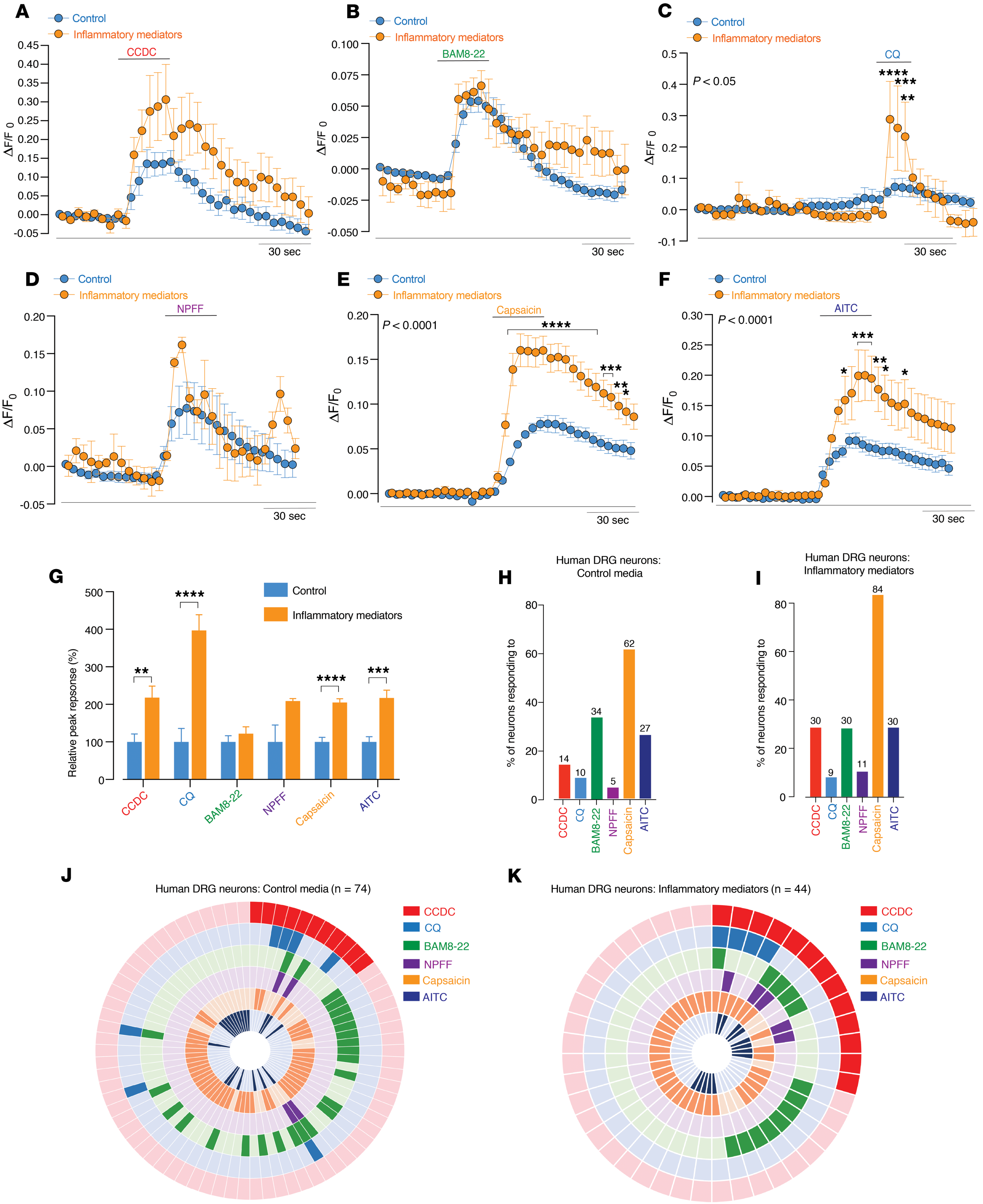

Figure 12. Human DRG neurons respond to pruritogenic agonists for TGR5, in addition to the MRGPRX1 agonists chloroquine and BAM8–22. (**A–F**) Human DRG neurons were cultured in control media, and in order to simulate a pathological state, a subset of cultures incubated with inflammatory mediators. This consisted of histamine (10 μM), PGE II (10 μM), serotonin (10 μM), and bradykinin (10 μM) being incubated with the neurons for 2 hours before Ca^{2+} imaging experiments commenced. Human DRG neurons from this cohort are referred to as inflammatory mediators. Grouped data of Ca^{2+} responses in control (*n* = 74) and inflammatory mediator (*n* = 44) cultured human DRG neurons to application of the (**A**) TGR5 agonist CCDC (100 μM),

MRGPRX1 agonists (**B**) BAM8-22 (2 μM), (**C**) CQ (1 μM), (**D**) NPFF (2 μM), (**E**) TRPV1 agonist capsaicin (100 nM), and (**F**) TRPA1 agonist AITC (50 M). Two-way ANOVA indicate responses to CQ ($*P < 0.05$), capsaicin ($***P < 0.001$), and AITC ($**P < 0.01$) are all significantly increased in neurons that had been exposed to inflammatory mediators. (**G**) Peak response of neurons to CCDC ($**P < 0.01$), CQ ($****P < 0.0001$), capsaicin ($****P < 0.0001$), and AITC ($***P < 0.001$) were all significantly increased in human DRG neurons incubated with inflammatory mediators. (**H and I**) Human DRG neurons from (**H**) control and (**I**) inflammatory mediator cultures responding to CCDC, CQ, BAM8-22, NPFF, capsaicin, and AITC. (**J and K**) Donut plot analysis showing the functional coexpression profiles as determined by Ca^{2+} imaging of (**J**) 74 individual human DRG neurons from control cultures and (**K**) 32 individual human DRG neurons from inflammatory mediator cultures in response to CCDC, CQ, BAM8-22, NPFF, capsaicin, and AITC. Data presented are mean ± SEM. *P* values determined by 2-way ANOVA and Bonferroni post hoc tests (significance indicated within panels) (**A–F**) or unpaired *t* tests (**G**).

for 2 hours prior to the Ca^{2+} imaging experiments. Human DRG neurons from these cultures displayed greater amplitudes of response to the application of CCDC (Figure 12, A and G), CQ (Figure 12, C and G), capsaicin (Figure 12, E and G), and AITC (Figure 12, F and G). Overall, 30% of neurons from the inflammatory mediator cultures responded to CCDC, 9% to CQ, 30% to BAM8-22, and 11% to NPFF, with 84% responding to capsaicin and 30% to AITC (Figure 12I). Overall, significantly more neurons from the inflammatory mediator cultures responded to capsaicin than in the normal untreated cultures (Figure 12, H–K, and Supplemental Figure 11). Overall, these findings in human DRG neurons largely resemble our findings in mouse colon-innervating DRG neurons and suggest that TGR5 and MRGPRX1 play important roles in pruritogenic signaling from human DRG neurons in a variety of conditions.

Discussion

IBS affects ~11% of the global population, and therapeutic treatments are currently lacking (15). Persistent hypersensitivity of sensory pathways innervating the colon is linked to the initiation, development, and maintenance of chronic discomfort and abdominal pain in IBS patients (15, 16, 39). Therefore, determining the mechanisms contributing to these processes is crucial. In the current study, we show that activation of TGR5, MRGPRA3, or MRGPRC11, commonly considered as itch receptors, either individually or collectively cause fundamental signaling changes within colonic afferent pathways in healthy states. Crucially, we also show that these mechanisms persist and, in the case of MRGPRC11, are augmented in CVH states. Therefore, this study provides insights on how the activation of pruritogenic receptors initiates colonic hypersensitivity and, importantly, how these receptors contribute to chronic hypersensitivity. Accordingly, this information may afford novel therapeutic strategies by directly targeting these receptors for the treatment of chronic discomfort and abdominal pain in IBS.

In the current study, we found that mRNA for the pruritogenic receptors *Tgr5*, *Mrgpra3*, and *Mrgprc11* were all expressed in a remarkably large population (19%, 27%, and 40%, respectively) of mouse colon-innervating DRG neurons in healthy states. Correspondingly, agonists for MRGPRA3 (CQ), MRGPRC11 (BAM8-22), and TGR5 (DCA, TLCA, CCDC) activated ~20%–35% of isolated colon-innervating DRG neurons from healthy mice. Moreover, the individual agonists for MRGPRA3, MRGPRC11, or TGR5 each induced mechanical hypersensitivity in subpopulations of colonic afferents from healthy mice. The ex vivo and in vivo sensitizing effects of CCDC were exacerbated in *Tgr5-Tg*–overexpressing mice and lost in $Tgr5^{-/-}$ mice, thereby confirming the role of TGR5 in these processes. Furthermore, mechanical hypersensitivity induced by either CQ or BAM8-22 was lost in *Mrgpr-cluster*$^{-/-}$ mice, confirming the roles of MRGPRs in this process. In vivo activation of either TGR5, MRGPRA3, or MRGPRC11 caused pronounced visceral hypersensitivity to CRD. These findings demonstrate clear and crucial individual roles for MRGPRA3, MRGPRC11, and TGR5 in activating colonic afferent neurons and inducing mechanical hypersensitivity.

The sensitizing effects of TGR5, MRGPRA3, or MRGPRC11 agonists on colonic afferents likely occurs via neuronal mechanisms. This is because MRGPRA3 and MRGPRC11 (40) are absent from colonic tissues but are expressed on mouse and human DRG neurons. While TGR5 is expressed on colonic afferents, it is also expressed on colonic epithelial cells and on enteric neurons (41, 42). However, we did not observe any changes in muscle compliance in our studies, suggesting the actions we observed were via direct actions on afferents rather than via secondary mechanisms. Indeed, very recent findings show that bile acid sensitize afferents in the proximal colon via 5-HT_3–dependent mechanisms, while these actions are 5-HT_3 independent more distally (43). Although not specifically investigated in the current study, TGR5 activation stimulates release of gastrin-releasing peptide (GRP) within the spinal cord (6), while MRGPR activation results in the release of both GRP (44) and natriuretic polypeptide B (4) within the spinal cord to induce scratching (45). These mechanisms may also contribute to the transmission of visceral irritant signaling from the periphery to the spinal cord and is subject to further investigation.

Importantly, we show for the first time to our knowledge that MRGPRs and TGR5 are expressed in both distinct and overlapping populations of neurons. Our single-cell RT-PCR analysis reveals that 62% of colon-innervating DRG neurons from healthy mice express at least 1 of the *Tgr5*, *Mrgprc11* or *Mrgpra3* receptors. This is an important finding, as these different molecular and functional expression profiles would therefore allow individual, overlapping, and additive signals to occur in response to a variety of pruritogenic irritants. To test this in vivo, we administered CCDC, CQ, or BAM8-22 individually to activate either TGR5, MRGPRA3, or MRGPRC11 on colonic afferents, respectively. In each scenario, mechanical hypersensitivity was evident in response to CRD, with CQ and CCDC evoking visceral hypersensitivity across a wide range of distension pressures. In the case of BAM8-22, visceral hypersensitivity to CRD was observed at more noxious distension pressures. This is consistent with very recent findings showing that BAM8-22 evoked elevated pain responses to CRD in healthy mice (40). While intracolonic administration of the individual agonists for TGR5, MRGPRA3, and MRGPRC11 evoked hypersensitivity to CRD, they did not fundamentally affect spontaneous animal behavior. When we administered an itch cocktail, consisting of a combination of CCDC, CQ, and BAM8-22, to concurrently activate TGR5, MRGPRA3, and MRGPRC11 on colonic afferents, this resulted in pronounced mechanical hypersensitivity to CRD across a wide range of distension pressures. Moreover, by recruiting the full complement of afferents within these irritant pathways, we also observed profound changes in spontaneous animal behavior evoked by visceral hypersensitivity, evident by a reduction in locomotor activity and increased grooming.

We found that the itch cocktail–induced mechanical hypersensitivity to CRD in vivo was not evoked in *Trpa1*$^{-/-}$ mice. Also, we did not observe afferent hypersensitivity, nor increased numbers of pERK-IR in the DH of the spinal cord in response to CCDC and CRD in *Trpa1*$^{-/-}$ mice. These results are consistent with the coupling mechanisms described in the skin, whereby TRPA1 has been identified as the downstream target of TGR5 (10), and both MRGPRA3 and MRGPRC11 (9). These previous studies demonstrated that neither TGR5 (10), MRGPRA3, nor MRGPRC11 (9) agonists directly activate TRPA1. However, *Trpa1*$^{-/-}$ mice display little to no scratching in response to CQ and BAM8-22 (9). Interestingly, the functional coupling between MRGPRA3 and TRPA1 is attenuated by disrupting Gβγ intracellular signaling, while coupling between MRGPRC11 and TRPA1 requires phospholipase-C (PLC) signaling (9). Similarly, TGR5 also activates TRPA1 to induce itch in mice, with TGR5 activating and sensitizing TRPA1 via a Gβγ- and protein kinase C–mediated (PKC-mediated) mechanisms (10). Although previous studies identify high coexpression of TRPV1 with MRGPRA3 and MRGPRC11 (9), as also shown in the current study, there appears to be little to no interaction between these targets. CQ- and BAM8-22–evoked Ca^{2+} signaling and neuronal sensitization is profoundly diminished in neurons from *Trpa1*$^{-/-}$ but not *Trpv1*$^{-/-}$ mice (9). Although *Trpv1* coexpresses with *Tgr5*, deletion or antagonism of TRPV1 has no effect on TGR5-induced itch (10). Comparably, in the current study, although we observed *Trpv1* coexpression in *Tgr5*- (78%), *Mrgpra3*- (69%), or *Mrgprc11*-expressing (90%) colon-innervating DRG neurons, mechanical hypersensitivity was completely lost in studies using *Trpa1*$^{-/-}$ mice. Accordingly, colonic afferents, like cutaneous afferents, appear to utilize coupling between TGR5, MRGPRA3, or MRGPRC11 via TRPA1 in order to mediate their sensitizing actions. These findings further highlight TRPA1 as a crucial integrator of sensory signals in colonic afferents by inducing mechanical hypersensitivity in response to bradykinin (22), TNF-α (23), and proteases (46) and now to bile acids, CQ, and BAM8-22. Conversely, histamine-dependent mechanisms in the colon contribute to afferent sensitization via TRPV1-dependent (12) and TRPV4-dependent (47) mechanisms, potentially suggesting divergent mechanisms between histamine-dependent and histamine-independent afferent sensitization.

Our observations raise the question of why functional itch receptors are found in colonic sensory pathways. There are several possible roles for such irritant-sensing pathways in the colon. Firstly, bile acids are normally present in the colonic lumen; they are secreted into the intestinal lumen during feeding, are absorbed in the ileum, and are modified by the colonic microbiome (48). Also, TGR5 in enteric neurons of the colon contributes to bile acid–dependent stimulation of peristalsis (41). Secondly, BAM8-22 is a proteolytically cleaved product of proenkephalin A, an endogenous ligand found throughout peripheral tissues, including the gastrointestinal tract (49, 50). Thirdly, while a well-recognized side-effect of the use of CQ in the treatment of malaria is itch, less-recognized symptoms of CQ treatment include abdominal cramping and pain (14). Therefore, while itch induces protective scratching that removes harmful irritants from the skin, identification of TGR5, *MRGRPA3*, and *MRGRPC11* in colonic afferents may represent an analogous system in the viscera. This would provide protective mechanisms for detecting harmful irritants within the colon and ultimately expel them from the body via activation of sensory afferents and recruitment of defecatory mechanisms (41). Accordingly, increased levels of bile acids are implicated in diarrhea-predominant IBS (51). Based on our current findings, bile acids also contribute to visceral hypersensitivity and the development of abdominal discomfort and pain via activation of TGR5 expressed on colonic afferents. In keeping with such a role, in vivo intracolonic administration of CCDC evoked mechanical hypersensitivity and increased the number of activated neurons within the DH of the spinal cord following CRD. Similarly, in vivo intracolonic CQ administration resulted in the subsequent activation of DH neurons within the spinal cord and evoked mechanical hypersensitivity to CRD.

We also demonstrate that TGR5-, MRGPRA3-, and MRGPRC11-dependent mechanisms extend beyond sensitization of colonic pathways in healthy states. Crucially, by using a CVH model, we show that colonic afferents from CVH mice display mechanical hypersensitivity compared with afferents from healthy mice. Application of CCDC, CQ, or BAM8-22 further enhanced CVH afferent responses to mechanical stimuli, significantly increasing responses above their already-elevated levels. Thus, activation of TGR5, MRGPRA3, or MRGPRC11 in CVH states can further exacerbate visceral hypersensitivity, leading to hyperalgesia. Correspondingly, we also show that afferents from CVH mice were more likely to fire action potentials in response to pruritogens and displayed increased numbers of pERK-IR DH neurons in response to intracolonic CCDC application in the absence of CRD. Notably, significantly more colon-innervating DRG neurons from CVH mice express *Mrgprc11* and *Trpa1*, with a significant increase in the proportion of *Mrgpra3*-expressing neurons now also coexpressing *Mrgprc11* and *Trpa1*. Our single-cell RT-PCR analysis reveals that 83% of colon-innervating DRG neurons from CVH mice express at least 1 of the *Tgr5*, *Mrgprc11*, or *Mrgpra3* receptors, compared with only in 62% in healthy states. This suggests alterations in the molecular and functional phenotypes of these neuronal subpopulations in CVH mice, allowing more afferents to be activated by pruritogens compared with healthy states. Correspondingly, we found that using an intracolonic itch cocktail of CCDC, CQ, and BAM8-22 to concurrently activate TGR5, MRGPRA3, and MRGPRC11 on colonic afferents in CVH mice caused decreases in locomotion and increased grooming and thigmotaxis, indicative of anxiety-like behavior. Interestingly, in addition to altered intestinal motility and chronic pain, IBS patients also suffer from psychiatric conditions, including depression and anxiety (15).

Finally, we show that these TGR5 and MRGPR mechanisms are also present in human DRG neurons. While MRGPRs have been previously detected in human DRG (7, 49), their coexpression profiles with TGR5, TRPA1 and TRPV1 are unclear. Although we could not specifically identify colon-innervating DRG neurons in humans, we could investigate DRG at spinal levels known to innervate the colon (T9-L1), in order to test the concept — both molecularly and functionally — that TGR5-, MRGPRX1-, TRPV1-, and TRPA1-coexpressing neurons exist in human DRG. This is important, as CQ induces itch in humans (52), while BAM8-22 produces itch and nociceptive sensations in humans independently of histamine release (53) and TGR5 is linked to cholestatic pruritus in humans (54). As per our findings in mouse DRG, we found that, with single-cell RT-PCR and calcium imaging studies, *TGR5* and *MRGPRX1* were expressed in both distinct and overlapping populations of human DRG neurons, which largely coexpressed *TRPV1* and/or *TRPA1*. While there are some discrepancies in absolute percentages between Ca^{2+} imaging and single-cell RT-PCR studies, this could be attributed to translational efficiency of mRNA to protein and surface expression of the receptors at the time of recording. By simulating a pathological state by incubating neurons with inflammatory mediators, significantly increased $[Ca^{2+}]_i$ responses were observed in human DRG neurons to CCDC, CQ, capsaicin, and AITC compared with normal culture conditions. This suggests, as in our mouse studies, that these neuronal responses to pruritogenic irritants can be readily "tuned" to induce hypersensitive responses in pathological conditions.

Overall, our findings shed new light on the mechanisms contributing to colonic afferent hypersensitivity in healthy and disease-relevant states. We identify mechanisms by which MRGPRA3, MRGPRC11, and the bile acid receptor TGR5 contribute to the induction of visceral hypersensitivity and altered behavior in response to known pruritogens. Our findings add to the recent discovery of an endogenous mediator, 5-Oxo-eicosatetraenoic acid (5-oxoETE), which activates afferents via a related MRGPR, MRGPRD, to evoke visceral hypersensitivity (55). Our findings demonstrate that the roles of TGR5, MRGPRA3, and MRGPRC11 extend beyond itch sensation in the skin, adding to recent work demonstrating that MRGPRC11 expressed on vagal sensory neurons contributes to bronchoconstriction and airway hyperresponsiveness (56). Our findings also demonstrate translatability of these TGR5 and MRGPR mechanisms and their coexpression with TRPV1 and TRPA1 to human DRG neurons. Accordingly, targeting the TGR5- and MRGPR-dependent mechanisms may prove useful in treating visceral hypersensitivity associated with common intestinal disorders.

Methods

For extensive descriptions of the methodology, please see the Supplemental Material.

Animals. Male C57BL/6J mice aged 13–17 weeks were used for studies and acquired from an in-house C57BL/6J breeding programme (strain no. 000664; originally purchased from The Jackson Laboratory, MP14) within SAHMRI's specific and opportunistic pathogen-free animal care facility. Some experiments also utilized male *Tgr5*$^{-/-}$ (6), *Trpa1*$^{-/-}$ (22), and *Mrgpr-cluster*$^{-/-}$ mice (8) or mice over expressing *Tgr5 (Tgr5-Tg)* (6) from in-house breeding colonies at SAHMRI. *Tgr5*$^{-/-}$ and *Tgr5-Tg* mice were gifts originally provided by Johan Auwerx and Kristina Schoonjans, Ecole Polytechnique de Lausanne (Lausanne, Switzerland). *Mrgpr-cluster*$^{-/-}$ mice were gifts from Xinzhong Dong (Johns Hopkins University). *Trpa1*$^{-/-}$ mice were gifts originally from David Corey (Harvard University, Cambridge, Massachusetts, USA).

Mouse model of CVH. Mice were administered intracolonic TNBS and developed colitis (25–27, 36, 38), which healed over 7 days. These mice subsequently developed chronic colonic afferent hypersensitivity (25–27, 36, 38).

Ex vivo single fiber colonic nociceptor recordings. Recordings were made from healthy, CVH, or *Tgr5*$^{-/-}$,*Tgr5-Tg*, or *Trpa1*$^{-/-}$ mice using standard protocols (25–27, 34, 38). Mechanosensitivity was determined before and after a 5-minute application of OA (100 μM), DCA (100 μM), CCDC (100 μM), BAM8-22 (20 μM), CQ (10 M), or NPFF (5 μM).

qPCR for pruritogenic receptors in mouse colonic epithelial cells. The epithelial layer was removed from the colon, and RNA was extracted. qPCR was performed using commercially available hydrolysis TaqMan probes for *Tgr5, Mrgpra3, Mrgprc11,* and *Gucy2c* (GC-C; Supplemental Table 1). Relative abundance was calculated using the ΔCq method (25).

Retrograde tracing to label the cell bodies of colon-innervating afferents. Dicarbocyanine dye,1,1-dioctadecyl-3,3,3,3-tetramethlindocarbocyanine methanesulfonate (DiI, 2% in ethanol; Invitrogen) or cholera toxin subunit B conjugated to AlexaFluor-555 (CTB-555; Invitrogen) was injected at 3 sites subserosally within the distal colon. Animals were left to recover for 7–10 days or 4 days, respectively, to identify cell bodies within the DRG (25, 31, 34).

Single-cell RT-PCR of colon-innervating DRG neurons from healthy and CVH mice. Individual retrogradely traced colon-innervating DRG neurons (97 from 7 healthy mice and 46 from 4 CVH mice) were picked, RNA was isolated, and mRNA expression was determined in each neuron for *tgr5, MrgprA3, MrgprC11, trpv1,* and *trpa1* using probes indicated within the Supplemental Methods (25).

$[Ca^{2+}]_i$ assays of colon-innervating DRG neurons from healthy mice. Neurons were enzymatically dissociated, plated onto coverslips, and cultured overnight. Neurons were loaded with Fura-2 AM (2 μM), and fluorescence was measured at 340 nm and 380 nm excitation and 530 nm emission (10). Neurons were tested with DCA (100 μM), CCDC (100 μM), TLCA (100 μM), CQ (10 μM), or BAM8-22 (20 μM) and then AITC (100 μM), capsaicin (1 μM), and KCl (50 mM).

Visualization of pERK neurons within the DH of the spinal cord following CRD. C57BL/6J healthy (32), CVH (25–27, 30), *Trpa1*$^{-/-}$ (21, 22), *Tgr5*$^{-/-}$ (6, 41), or *Tgr5-Tg* (6, 41) mice were briefly anesthetized with isoflurane anesthetic and a 100-μl enema of either CCDC (100 μM), CQ (10 μM), or saline (vehicle) administered intracolonically via a catheter. Subsequently, a 4-cm balloon catheter was inserted into the perianal canal, and 40 mmHg CRD was performed (10 seconds on, 5 second deflation, repeated 5 times). In separate experiments, an enema of CQ (10 μM) was applied for 5 minutes. After anesthetic overdose, mice were fixed by transcardial perfusion of 4% paraformaldehyde. The spinal cord was then removed and cryoprotected. Frozen sections were cut and incubated with monoclonal-rabbit anti-pERK (4370, Cell Signaling Technology; AB_2315112) and visualized with AlexaFluor-488 (A-21441, Molecular Probes, ThermoFisher Scientific) (25–27, 30–32).

In vivo VMR to CRD. Visceral sensitivity to CRD (20, 40, 50, 60, 70, and 80 mmHg, each 20-second durations, applied at 4-minute intervals) was assessed using abdominal electromyography (EMG) in fully awake healthy (30, 33, 34), *Tgr5*$^{-/-}$, *Mrgpr-cluster*$^{-/-}$, or *Trpa1*$^{-/-}$ mice, following intracolonic administration (100 μl) of either CCDC (100 μM), CQ (10 μM), BAM8-22 (20 μM), or an intracolonic itch cocktail consisting of a combination of CCDC (100 μM), BAM8-22 (20 μM), and CQ (10 μM). Colonic compliance was assessed by applying graded volumes (40–200 μl, 20-second duration) (33, 34).

In vivo assessment of animal behavior. Behavioral testing was evaluated using a behavioral spectrometer (Behavior Sequencer, Behavioral Instruments and BiObserve) (57). Healthy or CVH mice were briefly anesthetized with isoflurane, and a 100-μl enema of an itch cocktail, consisting of CCDC (100 μM), BAM8-22 (20 μM), and CQ (10 μM), was administered intracolonically via a lubricated catheter. A 100-μl saline enema was used as control. Mice were individually placed in the center of the behavioral spectrometer, and their behavior was filmed, tracked and evaluated, and analyzed by a computerized video tracking system (Viewer^3, BiObserve) for a total of 20 minutes.

Human tissue. Human DRG were acquired from 5 organ donors with whole ganglia processed for downstream qPCR or dissociated for single-cell RT-PCR analysis or Ca^{2+} imaging (25, 30). Human colonic biopsies from 15 healthy subjects were acquired from UCLA, recruited primarily by community advertisement.

mRNA analysis of pruritogenic targets from human tissue. RNA was extracted from colonic biopsies from 15 subjects and whole bilateral DRG from 4 donors. qPCR was performed using EXPRESS One-Step Superscript qPCR Kit reagents (Invitrogen) with commercially available TaqMan probes for *TGR5*, *MRGPRX1*, *GUCY2C*, *TRPA1*, and *TRPV1* (Supplemental Table 1). Relative abundance was estimated using ΔCq method (25).

Single-cell RT-PCR of human DRG neurons. A total of 53 human DRG neurons from 4 adult organ donors were individually picked. Ambion Single Cell-to-CT Kit (Invitrogen) was used on an Applied Biosystems 7500 Real-Time PCR System, with the TaqMan primers (Supplemental Table 1) to determine mRNA expression in each neuron for *TGR5*, *MRGPRX1* (human ortholog of mouse *Mrgpra3* and *Mrgprc11*), *TRPV1*, and *TRPA1*.

$[Ca^{2+}]_i$ assays of human DRG neurons in response to pruritogens. Human DRG were dissociated, and neurons were plated on coverslips and cultured. Some coverslips were cultured in normal media, while others — in order to mimic a pathological state — were preincubated with an "inflammatory soup" containing 10 μM each of histamine (MilliporeSigma), PGE II (Tocris), serotonin (Tocris), and bradykinin (MilliporeSigma) 2 hour prior to the experiments at 37°C. For the Ca^{2+} imaging experiments, neurons were loaded with 3 μM Fluo-8 AM, and responses to CCDC (100 μM), CQ (1 μM), BAM8-22 (2 μM), NPFF (2 μM), capsaicin (100 nM), and AITC (50 μM) were determined.

Statistics. Data are expressed as mean ± SEM or the percentage of neurons/afferents. Figures were prepared in GraphPad Prism 8 Software. N equals the number of animals, while n equals the number of neurons/afferents. A P value less than 0.05 was considered significant. Differences were indicated significant at levels of $^*P < 0.05$,$^{**}P < 0.01$,$^{***}P < 0.001$,$^{****}P < 0.0001$. VMR to CRD data were statistically analyzed by generalized estimating equations followed by LSD post hoc test using SPSS 23.0 (IMB). All other data were analyzed using GraphPad Prism 8 and analyzed if the data were normally distributed using Kolmogorov-Smirnov or Shapiro-Wilk tests. These data were then analyzed using either (a) 1-way ANOVA, with post hoc analysis conducted by making all possible comparisons among the treatment groups with the Tukey's tests; (b) 2-way ANOVA, with Bonferroni post hoc analysis conducted by making all possible comparisons among the treatment groups; (c) paired or (d) unpaired 2-tailed t tests; or (e) χ^2 analysis. The specific tests used to analyze each data set is indicated within the individual figure legends.

Study approval. All animal experiments were approved and conformed to regulatory standards and the ARRIVE guidelines. The Animal Ethics Committees of the SAHMRI, Flinders University, The University of Adelaide, and Monash University approved all experiments involving animals. All animal experiments conformed to the relevant regulatory standards and the ARRIVE guidelines. All human tissues used for the study were obtained by legal consent from organ donors in the United States. For DRG studies, the DRG were acquired from 5 organ donors with ethical consent. AnaBios Corporation's procurement network includes only US-based organ procurement organizations and hospitals. Policies for donor screening and consent are the ones established by the United Network for Organ Sharing (UNOS). Organizations supplying human tissues to AnaBios follow the standards and procedures established by the US Centres for Disease Control (CDC) and are inspected biannually by the Department of Health and Human Services (DHHS). Tissue distribution is governed by IRB procedures and compliance with HIPAA regulations regarding patient privacy. All transfers of donor organs to AnaBios are fully traceable and periodically reviewed by US federal authorities. For human colonic biopsies, study approval was obtained from UCLA IRBs (IRB 12-001731), and all subjects signed a written informed consent form prior to starting the study.

Author contributions

JC, LG, and SMB designed, performed, and analyzed the colonic afferent recordings. AMH, JM, TO, and SMB designed, performed, and analyzed the pERK DH studies. JC, JM, GS, and SMB designed, performed, and analyzed the VMR to CRD studies. GS and SMB designed and performed the behavioral studies. TML, SGC, NWB, and SMB designed, performed, and analyzed the mouse single-cell RT-PCR experiments. TML, DPP, NWB, and SMB designed, performed, and analyzed the mouse Ca^{2+} imaging experiments. SGC and SMB designed, performed, and analyzed the human DRG neuron single-cell PCR and whole human DRG qPCR expression studies. LC collected and provided human colonic biopsies. XD provided *Mrgpr-cluster*$^{-/-}$ mice. MSS and XD provided intellectual input on interpretation of the data. ALL and SMB designed, performed, and analyzed the mouse colonic mucosal and the human biopsy qPCR expression studies. PM, AG, and SMB designed, performed, and analyzed the human DRG Ca^{2+} imaging studies. All authors contributed to the discussion and interpretation of the results. SMB wrote the manuscript, with contributions and suggestions from all authors.

Acknowledgments

Work was supported by a National Health and Medical Research Council of Australia (NHMRC) Project Grant (1083480 to SMB and DPP), an NHMRC R.D. Wright Biomedical Research Fellow (APP1126378 to SMB), and an Australian Research Council (ARC) Discovery Early Career Research Award (DE130100223 to AMH). NWB was supported by grants from the NIH (NS102722; DE026806; DK118971) and the US Department of Defence (W81XWH1810431).

Address correspondence to: Stuart Brierley, Visceral Pain Research Group, Level 7, SAHMRI, North Terrace, Adelaide, SA 5000, Australia. Phone: 61.8.8128.4848; Email: stuart.brierley@flinders.edu.au.

---

1. Steinhoff M, Schmelz M, Szabó IL, Oaklander AL. Clinical presentation, management, and pathophysiology of neuropathic itch. *Lancet Neurol*. 2018;17(8):709–720.
2. McNeil B, Dong X. Mrgprs as Itch Receptors. In: Carstens E, Akiyama T, eds. *Itch: Mechanisms and Treatment*. Boca Raton, FL: CRC Press/Taylor & Francis; 2014.
3. Liu Q, et al. The distinct roles of two GPCRs, MrgprC11 and PAR2, in itch and hyperalgesia. *Sci Signal*. 2011;4(181):ra45.
4. Mishra SK, Hoon MA. The cells and circuitry for itch responses in mice. *Science*. 2013;340(6135):968–971.
5. LaMotte RH, Dong X, Ringkamp M. Sensory neurons and circuits mediating itch. *Nat Rev Neurosci*. 2014;15(1):19–31.
6. Alemi F, et al. The TGR5 receptor mediates bile acid-induced itch and analgesia. *J Clin Invest*. 2013;123(4):1513–1530.
7. Dong X, Han S, Zylka MJ, Simon MI, Anderson DJ. A diverse family of GPCRs expressed in specific subsets of nociceptive sensory neurons. *Cell*. 2001;106(5):619–632.
8. Liu Q, et al. Sensory neuron-specific GPCR Mrgprs are itch receptors mediating chloroquine-induced pruritus. *Cell*. 2009;139(7):1353–1365.
9. Wilson SR, et al. TRPA1 is required for histamine-independent, Mas-related G protein-coupled receptor-mediated itch. *Nat Neurosci*. 2011;14(5):595–602.
10. Lieu T, et al. The bile acid receptor TGR5 activates the TRPA1 channel to induce itch in mice. *Gastroenterology*. 2014;147(6):1417–1428.
11. Sadeghi M, et al. Contribution of membrane receptor signalling to chronic visceral pain. *Int J Biochem Cell Biol*. 2018;98:10–23.
12. Wouters MM, et al. Histamine Receptor H1-Mediated Sensitization of TRPV1 Mediates Visceral Hypersensitivity and Symptoms in Patients With Irritable Bowel Syndrome. *Gastroenterology*. 2016;150(4):875–87.e9.
13. Camilleri M. Bile Acid diarrhea: prevalence, pathogenesis, and therapy. *Gut Liver*. 2015;9(3):332–339.
14. NIH USNLoMMP. *Chloroquine*. https://medlineplus.gov/druginfo/meds/a682318.html. 2017;https://www.accessdata.fda.gov/drugsatfda_docs/label/2017/006002s044lbl.pdf Last Revised - 06/15/2017. Accessed: 03/02/2019.
15. Enck P, et al. Irritable bowel syndrome. *Nat Rev Dis Primers*. 2016;2:16014.
16. Brierley SM, Linden DR. Neuroplasticity and dysfunction after gastrointestinal inflammation. *Nat Rev Gastroenterol Hepatol*. 2014;11(10):611–627.
17. Chey WD, Kurlander J, Eswaran S. Irritable bowel syndrome: a clinical review. *JAMA*. 2015;313(9):949–958.
18. Spiegel B, Strickland A, Naliboff BD, Mayer EA, Chang L. Predictors of patient-assessed illness severity in irritable bowel syndrome. *Am J Gastroenterol*. 2008;103(10):2536–2543.
19. Bautista DM, et al. TRPA1 mediates the inflammatory actions of environmental irritants and proalgesic agents. *Cell*. 2006;124(6):1269–1282.
20. Malsch P, et al. Deletion of interleukin-6 signal transducer gp130 in small sensory neurons attenuates mechanonociception and down-regulates TRPA1 expression. *J Neurosci*. 2014;34(30):9845–9856.
21. Brierley SM, et al. TRPA1 contributes to specific mechanically activated currents and sensory neuron mechanical hypersensitivity. *J Physiol (Lond)*. 2011;589(Pt 14):3575–3593.
22. Brierley SM, et al. The ion channel TRPA1 is required for normal mechanosensation and is modulated by algesic stimuli. *Gastroenterology*. 2009;137(6):2084–2095.e3.

23. Hughes PA, et al. Sensory neuro-immune interactions differ between irritable bowel syndrome subtypes. *Gut*. 2013;62(10):1456–1465.
24. Brierley SM, et al. Differential chemosensory function and receptor expression of splanchnic and pelvic colonic afferents in mice. *J Physiol (Lond)*. 2005;567(Pt 1):267–281.
25. Castro J, et al. α-Conotoxin Vc1.1 inhibits human dorsal root ganglion neuroexcitability and mouse colonic nociception via GABA$_B$ receptors. *Gut*. 2017;66(6):1083–1094.
26. Castro J, et al. Linaclotide inhibits colonic nociceptors and relieves abdominal pain via guanylate cyclase-C and extracellular cyclic guanosine 3’,5’-monophosphate. *Gastroenterology*. 2013;145(6):1334–46.e1.
27. de Araujo AD, et al. Selenoether oxytocin analogues have analgesic properties in a mouse model of chronic abdominal pain. *Nat Commun*. 2014;5:3165.
28. Grundy L, et al. Tetrodotoxin-sensitive voltage-gated sodium channels regulate bladder afferent responses to distension. *Pain*. 2018;159(12):2573–2584.
29. Grundy L, et al. Translating peripheral bladder afferent mechanosensitivity to neuronal activation within the lumbosacral spinal cord of mice. *Pain*. 2019;160(4):793–804.
30. Grundy L, et al. Chronic linaclotide treatment reduces colitis-induced neuroplasticity and reverses persistent bladder dysfunction. *JCI Insight*. 2018;3(19):121841.
31. Harrington AM, Brierley SM, Isaacs N, Hughes PA, Castro J, Blackshaw LA. Sprouting of colonic afferent central terminals and increased spinal mitogen-activated protein kinase expression in a mouse model of chronic visceral hypersensitivity. *J Comp Neurol*. 2012;520(10):2241–2255.
32. Harrington AM, Caraballo SG, Maddern JE, Grundy L, Castro J, Brierley SM. Colonic afferent input and dorsal horn neuron activation differs between the thoracolumbar and lumbosacral spinal cord. *Am J Physiol Gastrointest Liver Physiol*. 2019;317(3):G285–G303.
33. Carstens BB, et al. Structure-Activity Studies of Cysteine-Rich α-Conotoxins that Inhibit High-Voltage-Activated Calcium Channels via GABA(B) Receptor Activation Reveal a Minimal Functional Motif. *Angew Chem Int Ed Engl*. 2016;55(15):4692–4696.
34. Castro J, et al. Cyclic analogues of α-conotoxin Vc1.1 inhibit colonic nociceptors and provide analgesia in a mouse model of chronic abdominal pain. *Br J Pharmacol*. 2018;175(12):2384–2398.
35. Salvatierra J, et al. NaV1.1 inhibition can reduce visceral hypersensitivity. *JCI Insight*. 2018;3(11):121000.
36. Hughes PA, Brierley SM, Blackshaw LA. Post-inflammatory modification of colonic afferent mechanosensitivity. *Clin Exp Pharmacol Physiol*. 2009;36(10):1034–1040.
37. Hughes PA, Brierley SM, Martin CM, Brookes SJ, Linden DR, Blackshaw LA. Post-inflammatory colonic afferent sensitisation: different subtypes, different pathways and different time courses. *Gut*. 2009;58(10):1333–1341.
38. Osteen JD, et al. Selective spider toxins reveal a role for the Nav1.1 channel in mechanical pain. *Nature*. 2016;534(7608):494–499.
39. Grundy L, Erickson A, Brierley SM. Visceral Pain. *Annu Rev Physiol*. 2019;81:261–284.
40. Van Remoortel S, et al. Mas-related G protein-coupled receptor C11 (Mrgprc11) induces visceral hypersensitivity in the mouse colon: A novel target in gut nociception? *Neurogastroenterol Motil*. 2019;31(8):1–12.
41. Alemi F, et al. The receptor TGR5 mediates the prokinetic actions of intestinal bile acids and is required for normal defecation in mice. *Gastroenterology*. 2013;144(1):145–154.
42. Cipriani S, et al. The bile acid receptor GPBAR-1 (TGR5) modulates integrity of intestinal barrier and immune response to experimental colitis. *PLoS ONE*. 2011;6(10):e25637.
43. Yu Y, et al. Deoxycholic acid activates colonic afferent nerves via 5-HT$_3$ receptor-dependent and -independent mechanisms. *Am J Physiol Gastrointest Liver Physiol*. 2019;317(3):G275–G284.
44. Sun YG, Chen ZF. A gastrin-releasing peptide receptor mediates the itch sensation in the spinal cord. *Nature*. 2007;448(7154):700–703.
45. Mu D, et al. A central neural circuit for itch sensation. *Science*. 2017;357(6352):695–699.
46. Cattaruzza F, Spreadbury I, Miranda-Morales M, Grady EF, Vanner S, Bunnett NW. Transient receptor potential ankyrin-1 has a major role in mediating visceral pain in mice. *Am J Physiol Gastrointest Liver Physiol*. 2010;298(1):G81–G91.
47. Cenac N, et al. Potentiation of TRPV4 signalling by histamine and serotonin: an important mechanism for visceral hypersensitivity. *Gut*. 2010;59(4):481–488.
48. Angelin B, Björkhem I. Postprandial serum bile acids in healthy man. Evidence for differences in absorptive pattern between individual bile acids. *Gut*. 1977;18(8):606–609.
49. Lembo PM, et al. Proenkephalin A gene products activate a new family of sensory neuron--specific GPCRs. *Nat Neurosci*. 2002;5(3):201–209.
50. Denning GM, et al. Proenkephalin expression and enkephalin release are widely observed in non-neuronal tissues. *Peptides*. 2008;29(1):83–92.
51. Camilleri M, Gores GJ. Therapeutic targeting of bile acids. *Am J Physiol Gastrointest Liver Physiol*. 2015;309(4):G209–G215.
52. Sowunmi A, Walker O, Salako LA. Pruritus and antimalarial drugs in Africans. *Lancet*. 1989;2(8656):213.
53. Sikand P, Dong X, LaMotte RH. BAM8-22 peptide produces itch and nociceptive sensations in humans independent of histamine release. *J Neurosci*. 2011;31(20):7563–7567.
54. Bergasa NV. The itch of liver disease. *Semin Cutan Med Surg*. 2011;30(2):93–98.
55. Bautzova T, et al. 5-oxoETE triggers nociception in constipation-predominant irritable bowel syndrome through MAS-related G protein-coupled receptor D. *Sci Signal*. 2018;11(561):eaal2171.
56. Han L, et al. Mrgprs on vagal sensory neurons contribute to bronchoconstriction and airway hyper-responsiveness. *Nat Neurosci*. 2018;21(3):324–328.
57. Inserra MC, et al. Multiple sodium channel isoforms mediate the pathological effects of Pacific ciguatoxin-1. *Sci Rep*. 2017;7:42810.

JBC ARTICLE

Protein kinase D and G$\beta\gamma$ mediate sustained nociceptive signaling by biased agonists of protease-activated receptor-2

Received for publication, November 30, 2018, and in revised form, May 23, 2019 Published, Papers in Press, May 29, 2019, DOI 10.1074/jbc.RA118.006935

Peishen Zhao[‡], Luke A. Pattison[‡], Dane D. Jensen[§], Nestor N. Jimenez-Vargas[¶], Rocco Latorre[§], TinaMarie Lieu[‡], Josue O. Jaramillo[¶], Cintya Lopez-Lopez[¶], Daniel P. Poole[‡], Stephen J. Vanner[¶], Brian L. Schmidt[‖], and Nigel W. Bunnett[§1]

From the [‡]Monash Institute of Pharmaceutical Sciences and Australian Research Council Centre of Excellence in Convergent Bio-Nano Science and Technology, Monash University, Parkville, Victoria 3052, Australia, the [§]Departments of Surgery and Pharmacology, Columbia University Vagelos College of Physicians and Surgeons, Columbia University, New York, New York 10032, the [¶]Gastrointestinal Diseases Research Unit, Division of Gastroenterology, Queen's University, Kingston, Ontario K7L 3N6, Canada, and the [‖]Bluestone Center for Clinical Research, New York University College of Dentistry, New York, New York 10010

Edited by Henrik G. Dohlman

Proteases sustain hyperexcitability and pain by cleaving protease-activated receptor-2 (PAR_2) on nociceptors through distinct mechanisms. Whereas trypsin induces PAR_2 coupling to $G\alpha_q$, $G\alpha_s$, and β-arrestins, cathepsin-S (CS) and neutrophil elastase (NE) cleave PAR_2 at distinct sites and activate it by biased mechanisms that induce coupling to $G\alpha_s$, but not to $G\alpha_q$ or β-arrestins. Because proteases activate PAR_2 by irreversible cleavage, and activated PAR_2 is degraded in lysosomes, sustained extracellular protease-mediated signaling requires mobilization of intact PAR_2 from the Golgi apparatus or *de novo* synthesis of new receptors by incompletely understood mechanisms. We found here that trypsin, CS, and NE stimulate PAR_2-dependent activation of protein kinase D (PKD) in the Golgi of HEK293 cells, in which PKD regulates protein trafficking. The proteases stimulated translocation of the PKD activator G$\beta\gamma$ to the Golgi, coinciding with PAR_2 mobilization from the Golgi. Proteases also induced translocation of a photoconverted PAR_2-Kaede fusion protein from the Golgi to the plasma membrane of KNRK cells. After incubation of HEK293 cells and dorsal root ganglia neurons with CS, NE, or trypsin, PAR_2 responsiveness initially declined, consistent with PAR_2 cleavage and desensitization, and then gradually recovered. Inhibitors of PKD, G$\beta\gamma$, and protein translation inhibited recovery of PAR_2 responsiveness. PKD and G$\beta\gamma$ inhibitors also attenuated protease-evoked mechanical allodynia in mice. We conclude that proteases that activate PAR_2 by canonical and biased mechanisms stimulate PKD in the Golgi; PAR_2 mobilization and *de novo* synthesis repopulate the cell surface with intact receptors and sustain nociceptive signaling by extracellular proteases.

Sustained signaling by membrane-impermeant agonists in the extracellular environment requires the presence of functional receptors at the surface of cells. The level of functional receptors at the plasma membrane is a dynamic balance between processes that inactivate or remove receptors and those that reactivate or replenish receptors (1). Desensitization and endocytosis inactivate and remove functional receptors from the plasma membrane and thereby diminish cellular responsiveness. Recovery of responsiveness requires repopulation of the plasma membrane with functional receptors by mechanisms that include resensitization of receptors or membrane insertion of fresh receptors. However, in contrast to the mechanisms of receptor desensitization and endocytosis, which have been extensively studied (2), the mechanisms that repopulate the plasma membrane with functional receptors are not fully understood (1).

G protein–coupled receptors (GPCRs)[2] comprise the largest family of transmembrane receptors and are the target of one-third of therapeutic drugs (3). The mechanisms that attenuate plasma membrane signaling of GPCRs have been extensively studied. G protein–coupled receptor kinases and second messenger kinases can phosphorylate activated receptors, which then associate with β-arrestins. By uncoupling GPCRs from G proteins and coupling GPCRs to clathrin and adaptor protein 2, β-arrestins mediate receptor desensitization and endocytosis, which together attenuate plasma membrane signaling (4). Some endocytosed receptors, including the substance P neurokinin 1 receptor (5) and the μ-opioid receptor (6), recycle back to the plasma membrane, which restores their function at the cell surface. Other receptors, exemplified by chemokine receptor type 4 (CXCR4), traffic to lysosomes (7). For these receptors, *de novo* protein synthesis or translocation of intact receptor from a preexisting pool is required for replenishment of the plasma membrane with functioning receptors.

This work was supported by National Institutes of Health Grants NS102722, DE026806, and DK118971; Department of Defense Grant W81XWH1810431 (to N. W. B. and B. L. S.); and National Health and Medical Research Council Grants 63303, 1049682, and 1031886) (to N. W. B.). Nigel Bunnett is a founding scientist of Endosome Therapeutics Inc. Research in Nigel Bunnett's laboratory was funded in part by Takeda Pharmaceuticals Inc. The content is solely the responsibility of the authors and does not necessarily represent the official views of the National Institutes of Health.

[1] To whom correspondence should be addressed: Columbia University Vagelos College of Physicians and Surgeons, 21 Audubon Av., Rm. 209, New York City, NY 10032. Tel.: 212-305-4480; E-mail: nb2733@cumc.columbia.edu.

[2] The abbreviations used are: GPCR, G protein–coupled receptor; PAR, protease-activated receptor; NE, neutrophil elastase; CS, cathepsin-S; PKC, protein kinase C; PKA, protein kinase A; PKD, protein kinase D; PAR, protease-activated receptor; hPAR, human PAR; BRET, bioluminescence resonance energy transfer; DRG, dorsal root ganglia; VFF, von Frey filament(s); HBSS, Hanks' balanced salt solution; AUC, area under the curve; HA, hemagglutinin; ANOVA, analysis of variance.

PARs are a small family of GPCRs that are activated by proteolytic cleavage within the extracellular N-terminal region (8). Several serine and cysteine proteases can cleave and activate PAR_2, including trypsins (9, 10), mast cell tryptase (11), kallikreins (12), NE (13, 14) and CS, a cysteine protease from antigen-presenting cells (15). Trypsin, tryptase, and kallikreins activate PAR_2 by a canonical mechanism. Trypsin cleaves PAR_2 at $R^{36} \downarrow S^{37}$, which reveals the tethered ligand domain (S^{37}LIGKV for human PAR_2). This cleavage results in PAR_2 coupling to $G\alpha_q$, $G\alpha_s$, and β-arrestins, leading to mobilization of Ca^{2+}, generation of cAMP, and activation of protein kinase C (PKC) and A (PKA) and of extracellular signal-regulated kinases (16, 17). β-Arrestins mediate desensitization and endocytosis of PAR_2, which then traffics to lysosomes and is degraded (17). Given the irreversible mechanism of proteolytic activation, cleaved PAR_2 cannot be reactivated by proteolysis (16). Recovery of cell surface PAR_2 signaling involves mobilization of intact receptors from a preexisting Golgi pool as well as synthesis of fresh receptors (16). NE and CS are activated and released from inflammatory cells at sites of injury and inflammation, retain activity in extracellular fluid, and can cause PAR_2-dependent inflammation and pain (14, 15, 18). However, CS and NE activate biased pathways of PAR_2 signaling and trafficking. CS cleaves human PAR_2 at $E^{56} \downarrow T^{57}$ to expose the tethered ligand (T^{57}VFSVDEFSA), which promotes PAR_2 coupling to $G\alpha_s$ (15). NE cleaves at $A^{66} \downarrow S^{67}$ and $S^{67} \downarrow V^{68}$, adjacent to the first transmembrane domain, which activates PAR_2 by a nontethered ligand mechanism and induces coupling to $G\alpha_s$ and $G\alpha_{12/13}$ (13, 14). CS- and NE-activated PAR_2 fails to couple to $G\alpha_q$ and neither recruits β-arrestins nor internalizes. We recently reported that trypsin cleavage of PAR_2 at the plasma membrane induces translocation of Gβγ to the Golgi apparatus, where Gβγ activates PKD (19). PKD mediates the mobilization of PAR_2 stores from the Golgi apparatus, which replenishes the plasma membrane with fresh receptors that are necessary for sustained trypsin signaling (19). In the present study, we investigated the mechanisms that underlie sustained signaling of proteases that activate PAR_2 by biased mechanisms.

Results

Proteases that activate PAR_2 by canonical and biased mechanisms induce PAR_2-dependent PKD activation

By using immunoblotting and immunofluorescence, we have previously reported that trypsin activation of PAR_2 leads to PKD phosphorylation (activation) in the Golgi apparatus (19). To quantitatively assess PKD activation in live cells with high spatial and temporal fidelity, we expressed in human embryonic kidney (HEK293) cells genetically encoded FRET biosensors for PKD that are targeted to the cytosol (Cyto-DKAR) or Golgi apparatus (Golgi-DKAR) (20). We examined whether proteases that activate PAR_2 by canonical or biased mechanisms can stimulate PKD activity in the cytosol or plasma membrane of HEK293 cells transiently expressing human PAR_2 ($hPAR_2$). To confirm that alterations in FRET were attributable to PKD activation, we expressed a T/A mutated PKD sensor (DKAR-T/A) in which the PKD phosphorylation site in the substrate domain is mutated.

We first confirmed the expected subcellular localization of PKD FRET biosensors expressed in HEK293 cells by confocal microscopy. Cyto-DKAR was uniformly distributed throughout the cytosol, whereas Golgi-DKAR colocalized exclusively with immunoreactive TGN58K, a marker of the Golgi apparatus (Fig. 1*A*).

Trypsin (10 nM), CS (100 nM), NE (100 nM), and the PAR_2-selective agonist 2-furoyl-LIGRLO-NH_2, an analogue of the tethered ligand (10 μM), increased PKD activity in the cytosol and Golgi apparatus within 2 min, which was sustained for at least 20 min (Fig. 1, *B–E*). The PAR_2 antagonist I-343 (18) (10 μM) inhibited trypsin-, CS-, and NE-induced PKD activation (Fig. 1, *F–H*). I-343 did not inhibit activation of PKD in the Golgi apparatus in response to phorbol 12,13-dibutyrate (200 nM) or thrombin (30 units/ml), a PAR_1 agonist, and I-343 alone had no effect on PKD activity (Fig. 1*I*). These results show that proteases that activate PAR_2 by canonical and biased mechanisms activate PKD in the cytosol and Golgi apparatus of HEK293 cells. These effects are mediated by PAR_2. There was no effect of trypsin or 2-furoyl-LIGRLO-NH_2 on DKAR-T/A FRET (Fig. 1, *B* and *E*), although CS and NE caused a minor increase in DKAR-T/A FRET (Fig. 1, *C* and *D*). One possibility is that kinases other than PKD might phosphorylate DKAR-T/A, such as PKA, which is robustly activated by NE (13, 14) and CS (15). Further studies are necessary to address this question.

Proteases that activate PAR_2 by canonical and biased mechanisms induce Gβγ translocation to Golgi

Gβγ subunits can activate PKD in the Golgi apparatus (21). Trypsin activation of PAR_2 at the cell surface induces translocation of Gβγ subunits to the Golgi apparatus, where Gβγ activates PKD (19). We used bioluminescence resonance energy transfer (BRET) to examine whether CS and NE, which activate PAR_2 by biased mechanisms, also promote Gβγ trafficking to the Golgi apparatus. We transiently expressed in HEK293 cells Gγ2-Venus and Giantin-RLuc8, a Golgi-resident protein (22), which permitted measurement of the proximity between Gγ2-Venus and Giantin-RLuc8 using bystander BRET. We also expressed $hPAR_2$, Gβ1, and either $G\alpha_q$ or $G\alpha_s$, which allowed assessment of the requirement of different Gα subunits.

We confirmed the expected subcellular localization of BRET biosensors expressed in HEK293 cells by confocal microscopy. In unstimulated cells, Gγ2-Venus was uniformly cytosolic, whereas Giantin-Venus colocalized exclusively with immunoreactive TGN58K in the Golgi apparatus (Fig. 2*A*). We were unable to localize Giantin-RLuc8 because of the lack of a suitable epitope tag or antibody, but we expect that it would have the identical localization as Giantin-Venus.

Trypsin increased Gγ2-Venus/Giantin-RLuc8 BRET in the presence of either $G\alpha_q$ or $G\alpha_s$ (Fig. 2, *B–D*). However, trypsin increased Gγ2-Venus/Giantin-RLuc8 BRET with higher potency in cells expressing $G\alpha_q$ (pEC_{50} (negative logarithm of the EC_{50}) - 12.74 ± 0.36) compared with $G\alpha_s$ ($pEC_{50} = 9.75 \pm 0.65$). CS also increased Gγ2-Venus/Giantin-RLuc8 BRET in the presence of either $G\alpha_q$ or $G\alpha_s$ (Fig. 2, *E–G*). In contrast to trypsin, CS increased BRET with higher potency in cells expressing $G\alpha_s$ ($pEC_{50} = 11.90 \pm 0.35$) than $G\alpha_q$ (pEC_{50} =

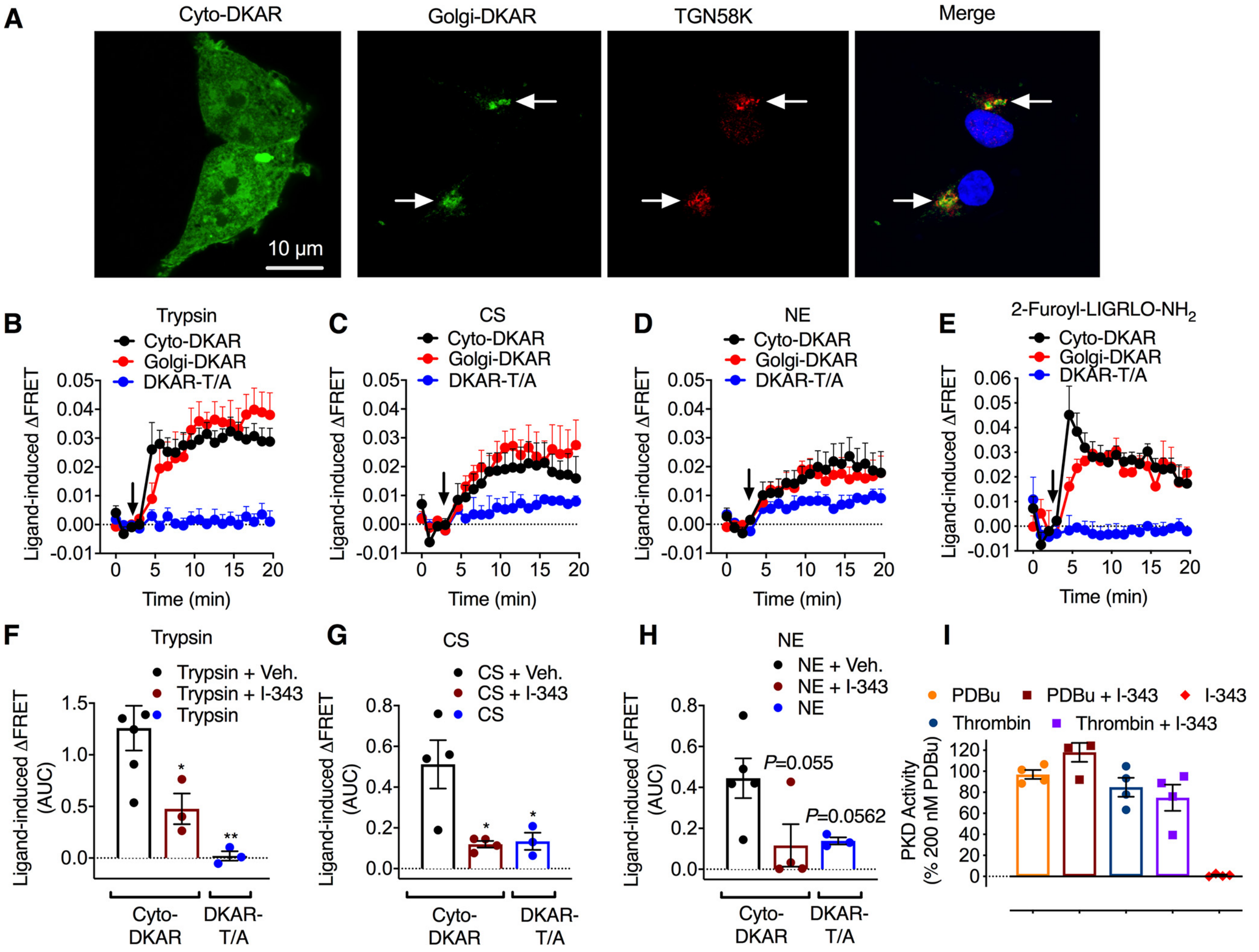

Figure 1. Protease-induced activation of PKD. *A*, localization of FRET PKD biosensors Cyto-DKAR and Golgi-DKAR with TGN58K in HEK293 cells. *B–E*, time course of trypsin-induced (*B*, 10 nM), CS-induced (*C*, 100 nM), NE-induced (*D*, 100 nM), and 2-furoyl-LIGRLO-NH$_2$–induced (*E*, 10 μM) PKD activity in HEK293 cells expressing FRET biosensors for PKD in the cytosol (*Cyto-DKAR*) and Golgi apparatus (*Golgi-DKAR*). DKAR-T/A is a PKD control sensor. Agonists were added at the *arrow*. *F–H*, AUC for Cyto-DKAR and DKAR-T/A in HEK293 cells treated with trypsin (*F*), CS (*G*), or NE (*H*) and either vehicle or PAR$_2$ antagonist (I-343). *I*, effects of I-343 on PKD activity in the Golgi apparatus stimulated by phorbol 12,13-dibutyrate (*PDBu*) or thrombin. $n = 3–5$ experimental replicates, triplicate observations. *, $p < 0.05$; **, $p < 0.01$ to vehicle (one-way ANOVA, Bonferroni multiple comparisons). *Error bars*, S.E.

10.35 ± 0.81). NE increased Gγ2-Venus/Giantin-RLuc8 BRET only in the presence of Gα_s (pEC$_{50}$ = 11.84 ± 0.45), not Gα_q (Fig. 2, *H–J*). Thus, proteases that activate PAR$_2$ at the cell surface by canonical and biased mechanisms may evoke the rapid translocation of Gβγ to the Golgi apparatus. Although Gβγ subunits could originate from the plasma membrane, it is also possible that PAR$_2$ activation evokes translocation of Gβγ from the cytosol to the Golgi apparatus or may reveal Gβγ subunits already present in the Golgi apparatus. The effects of overexpression of Gα subunits on Gγ2-Venus/Giantin-RLuc8 BRET are consistent with the capacity of trypsin-activated PAR$_2$ to couple to Gα_q or Gα_s and for CS- and NE-activated PAR$_2$ to couple preferentially to Gα_s (13–15). Studies with selective Gα inhibitors or with Gα-deficient HEK293 cells will be required to determine the absolute requirement of particular Gα subunits for protease-stimulated Gγ2-Venus/Giantin-RLuc8 BRET.

Proteases that activate PAR$_2$ by canonical and biased mechanisms mobilize PAR$_2$ from the Golgi apparatus

To quantitatively examine whether PAR$_2$ activation at the cell surface mobilizes receptors from the Golgi apparatus, we examined the proximity between PAR$_2$-RLuc8 and TGN38-Venus, a Golgi-resident protein (23). PAR$_2$-RLuc8 was prominently localized to the plasma membrane, and TGN38-Venus was confined to the Golgi apparatus, as confirmed by colocalization with immunoreactive TGN58K (Fig. 3*A*). Thus, BRET sensors have the expected subcellular localization.

Trypsin (10 and 100 nM), CS (100 nM), and NE (100 nM) all induced a rapid decrease in PAR$_2$-RLuc8/TGN38-Venus BRET within 2 min that was sustained for 20 min (Fig. 3, *B–D*). Gallein, which inhibits Gβγ activity (24), suppressed the decrease in PAR$_2$-RLuc8/TGN38-Venus BRET in cells exposed to trypsin, CS, and NE (Fig. 3, *E–J*). To confirm involvement of Gβγ, we treated cells with a peptide corresponding to the C terminus of GPCR kinase 2 (GRK2i), which inhibits Gβγ activity (25). GRK2i (100 μM) attenuated the decrease in PAR$_2$-RLuc8/TGN38-Venus BRET in cells exposed to trypsin, CS, and NE to a similar degree as gallein (Fig. 3, *H–J*).

We then evaluated the role of kinases in mobilization of PAR$_2$ from the Golgi apparatus. Surprisingly, in view of the known role of PKD in protein sorting within the Golgi apparatus (19, 21, 26, 27), the PKD inhibitor CRT0066101 (100 nM)

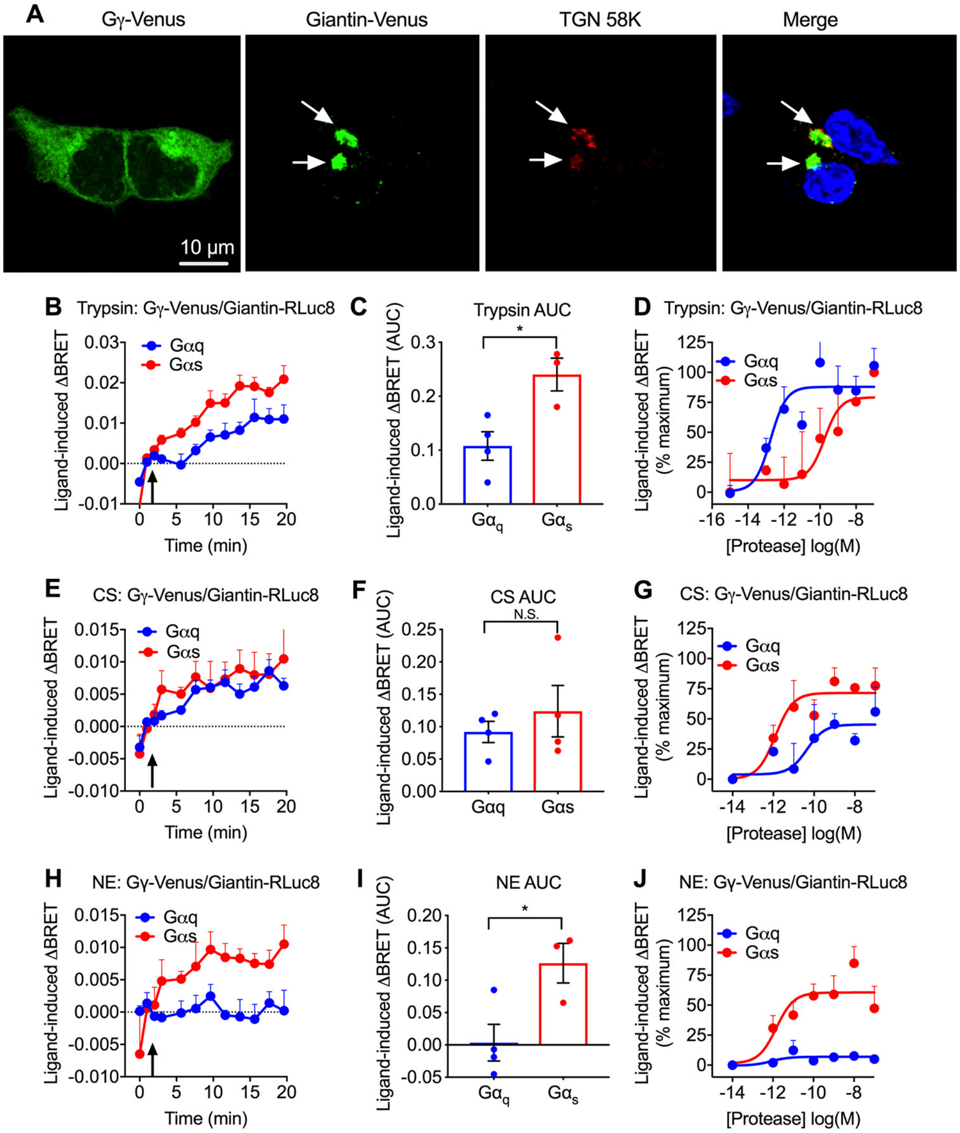

Figure 2. Protease-induced translocation of Gγ to Golgi apparatus. *A*, localization of BRET biosensors Gγ-Venus and Giantin-Venus with TGN 58K in HEK293 cells. *B–J*, protease-evoked BRET. Effects of trypsin (*B–D*), CS (*E–G*), and NE (*H–J*) on Gγ-Venus/Giantin-RLuc8 BRET in HEK293 cells. *B*, *E*, and *H*, time course of trypsin-induced (10 nM), CS-induced (100 nM), and NE-induced (100 nM) BRET. Agonists were added at the *arrow*. *C*, *F*, and *I*, AUC of BRET response. *D*, *G*, *J*, concentration–response analysis. Gβ was coexpressed with either $G\alpha_q$ or $G\alpha_s$. $n = 3–6$ experimental replicates, triplicate observations. *, $p < 0.05$ (Student's *t* test). *Error bars*, S.E.

(28) did not affect the decrease in PAR_2-RLuc8/TGN38-Venus BRET (Fig. 3, *E–J*). A $G\alpha_q/Ca^{2+}$/PKC pathway has been reported to control Golgi organization and secretion (29). Gö6983 (1 μM), a nonselective PKC inhibitor (30), did not significantly inhibit trypsin-, CS-, or NE-evoked mobilization of PAR_2 from the Golgi apparatus (Fig. 3, *E–J*). PKA has been shown to be required in the formation of vesicles from the Golgi (31). Given the capacity of CS- and NE-activated PAR_2 to couple to $G\alpha_s$, adenylyl cyclase, cAMP, and PKA, we also evaluated the contribution of PKA to PAR_2 mobilization from the Golgi apparatus. H-89 (1 μM), which inhibits PKA and other kinases (32, 33), had no effect on trypsin-, CS-, or NE-induced mobilization of PAR_2 (Fig. 3, *H–J*).

We confirmed that the PKD and PKC inhibitors blocked kinase activity in HEK293 cells by expressing FRET biosensors for cytosolic PKD (Cyto-DKAR) and PKC (Cyto-CKAR). CRT0066101 (100 nM) abolished trypsin (10 nM)-evoked activation of PKD (Fig. 4, *A* and *B*), and Gö6983 (1 μM) abolished trypsin-evoked activation of PKC (Fig. 4, *C* and *D*). We have previously shown that H-89 inhibits CS-mediated PAR_2 signaling events (15).

These results indicate a major role for Gβγ subunits in mediating the capacity of trypsin, CS, and NE to mobilize PAR_2 from the Golgi apparatus of HEK293 cells. Further studies are necessary to understand the unexpected finding that PKD inhibitors did not affect protease-evoked liberation of PAR_2 from the Golgi apparatus as determined by measurements of PAR_2-RLuc8/TGN38-Venus BRET. However, because TGN38 can shuttle between the Golgi apparatus and plasma membrane, it is possible that proximity between TGN38 and PAR_2 in the exocytic and endocytic pathways may confound the results (23).

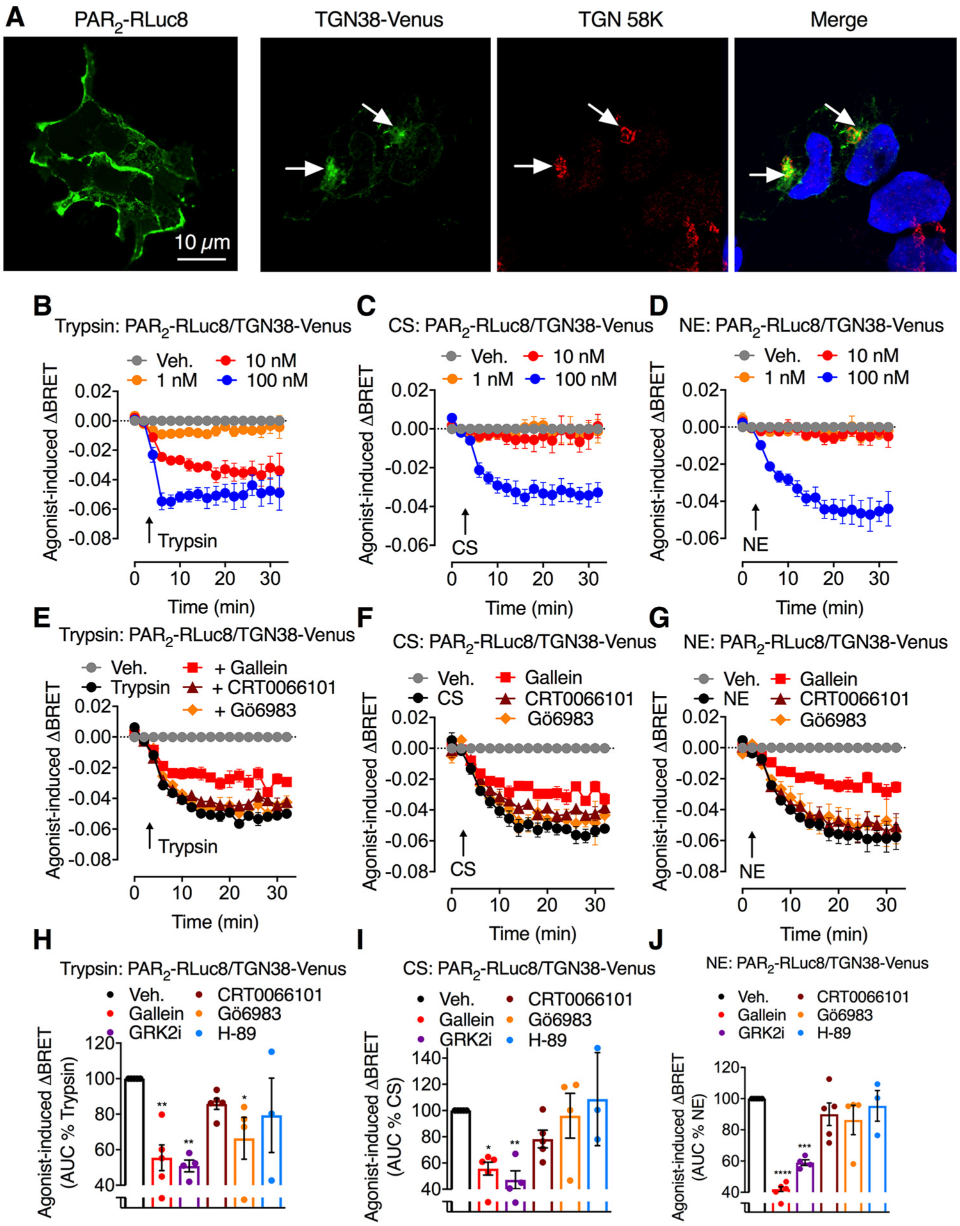

Figure 3. Protease-induced translocation of PAR_2 from the Golgi apparatus. *A*, localization of BRET biosensors PAR_2-RLuc8 and TGN38-Venus with TGN 58K in HEK293 cells. *B–J*, protease-evoked BRET. *B–D*, time course of trypsin-, CS-, and NE-induced BRET between PAR_2-RLuc8 and TGN38-Venus in HEK293 cells. *E–J*, effects of inhibitors of Gβγ (gallein), PKD (CRT0066101), PKC (Gö6983), and PKA (H-89) on trypsin-induced (10 nM), CS-induced (100 nM), and NE-induced (100 nM) BRET between PAR_2-RLuc8 and TGN38-Venus. *E–G*, time course. *H–J*, AUC. $n = 3$ (*A–C*) or 3–5 (*D–J*) experimental replicates, triplicate observations. *, $p < 0.05$; **, $p < 0.01$; ****, $p < 0.0001$ (one-way ANOVA, Bonferroni multiple comparisons). *Error bars*, S.E.

Proteases that activate PAR_2 by canonical and biased mechanisms induce Gβγ and PKD-dependent translocation of PAR_2 to the plasma membrane

In light of the paradoxical inhibition of PAR_2 mobilization from the Golgi apparatus by Gβγ inhibitors but not by PKD inhibitors, as determined by PAR_2-RLuc8/TGN38-Venus BRET, we sought an alternative approach to study depletion of PAR_2 from the Golgi apparatus. To localize the redistribution of PAR_2 from the Golgi apparatus to the plasma membrane, we expressed in rat kidney epithelial (KNRK) cells PAR_2 fused at the C terminus to Kaede, a photoconvertible protein. We have previously shown that PAR_2-Kaede is functional and suitable for analysis of intracellular trafficking of PAR_2 (19). We selected KNRK cells for these studies rather than HEK293 cells because the Golgi pool of PAR_2 is particularly distinct in KNRK cells compared with HEK293 cells, where it is diffuse and more challenging to localize (16). Trypsin induces β-arrestin–mediated endocytosis and endosomal signaling of PAR_2 of PAR_2 in KNRK cells (17, 34). The prominent Golgi store of PAR_2-Kaede was photoconverted from green to red using a confocal microscope laser. Cells were then exposed to proteases and monitored to assess depletion of PAR_2-Kaede from the Golgi apparatus and insertion of mobilized PAR_2-Kaede into the plasma membrane. Before photoconversion, PAR_2-Kaede (green) was detected at the plasma membrane and in the Golgi apparatus (Fig. 5, *A* and *B*). Confocal illumination of the Golgi resulted in rapid green to red photoconversion of PAR_2-Kaede in the Golgi apparatus but not the plasma membrane. NE (100 nM, 30 min)

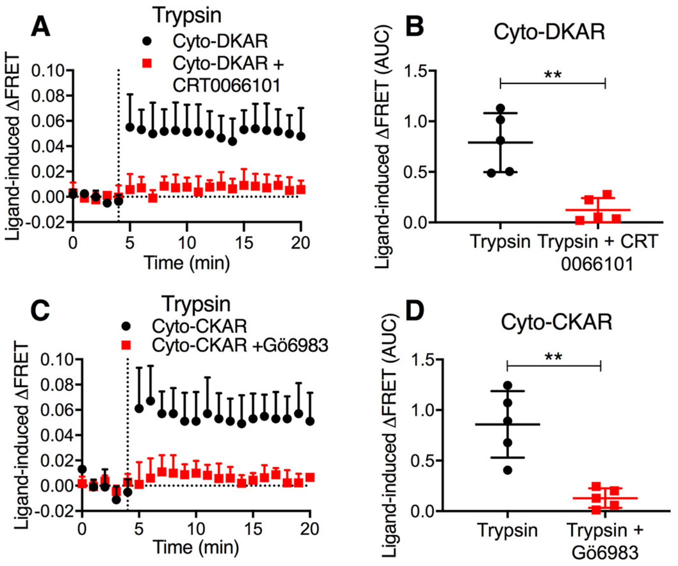

Figure 4. Antagonism of PKD and PKC. Time course (*A* and *C*) and AUC (*B* and *D*) of trypsin-stimulated activation of cytosolic PKD (*A* and *B*) and cytosolic PKC (*C* and *D*). The effects of inhibitors of PKD (CRT0066101) and PKC (Gö6983) are shown. $n = 5$ experimental replicates, triplicate observations. **, $p < 0.01$ (Student's *t* test). *Error bars*, S.E.

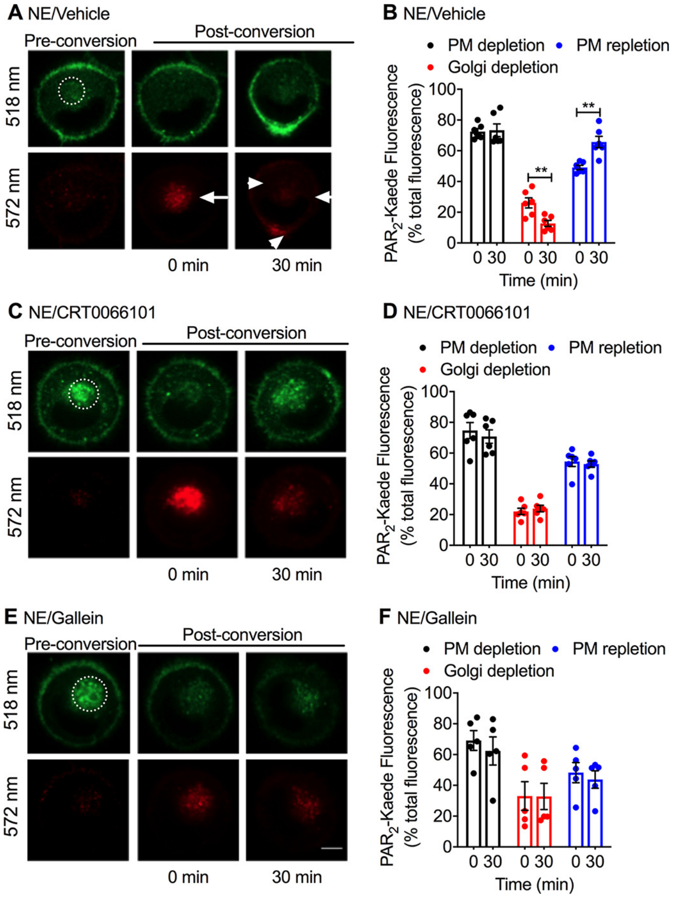

Figure 5. NE-induced trafficking of PAR$_2$-Kaede from the Golgi apparatus to the plasma membrane. PAR$_2$-Kaede located in the region of the perinuclear Golgi apparatus of KNRK-PAR$_2$-Kaede cells was green/red photoconverted using a confocal laser (*dashed circle*, illuminated region). Cells were then incubated with NE (100 nM) for 0 or 30 min. PAR$_2$-Kaede fluorescence was measured at 518 and 572 nm at the cell surface or Golgi. Cells were pre-incubated with vehicle (*A* and *B*), PKD inhibitor (CRT0066101, 100 nM) (*C* and *D*), or Gβγ inhibitor (gallein, 10 μM) (*E* and *F*). *A*, *C*, and *E*, representative images before and after photoconversion and at 0 or 30 min after protease challenge. *B*, *D*, and *F*, quantification of PAR2-Kaede (518 nm, *green*) at the plasma membrane and of photoconverted PAR$_2$-Kaede (572 nm, *red*) in the Golgi region and at the plasma membrane. $n = 5$–6 experiments, >30 cells analyzed per condition. **, $p < 0.01$ (Student's *t* test). *Scale bar*, 10 μm. *Error bars*, S.E.

induced a significant depletion of PAR$_2$-Kaede red from the Golgi apparatus and a corresponding increase in PAR$_2$-Kaede red at the plasma membrane (Fig. 5*A*). CRT0066101 (Fig. 5, *C* and *D*) and gallein (Fig. 5, *E* and *F*) both prevented the depletion of PAR$_2$-Kaede red from the Golgi apparatus and insertion into the plasma membrane. Similarly, CS (100 nM, 30 min) induced a significant depletion of PAR$_2$-Kaede red from the Golgi apparatus and a nonsignificant increase in PAR$_2$-Kaede red at the plasma membrane (Fig. 6*A*). CRT0066101 (Fig. 6*B*) and gallein (Fig. 6*C*) both prevented the depletion of PAR$_2$-Kaede red from the Golgi apparatus. These results suggest that NE and CS activate PAR$_2$ at the plasma membrane to induce Gβγ- and PKD-mediated recruitment of intact PAR$_2$ from the Golgi apparatus to the plasma membrane.

PKD and Gβγ mediate recovery of plasma membrane PAR$_2$ signaling

CS and NE cleave PAR$_2$ distal to the trypsin cleavage site and the trypsin-exposed tethered ligand (14, 15). By removing these domains, CS and NE prevent the capacity of trypsin to activate PAR$_2$. Recovery of responsiveness to trypsin thus requires repopulation of the plasma membrane with intact PAR$_2$. We made use of this paradigm to determine whether Gβγ- and PKD-induced mobilization of intact PAR$_2$ from the Golgi apparatus mediates the recovery of trypsin-responsiveness in HEK293 cells.

HEK293 cells were first exposed to trypsin (10 nM), CS (100 nM), NE (100 nM), or vehicle (control) for 10 min (Fig. 7*A*). Cells were then washed, recovered for 110 min at 37 °C, and challenged with trypsin (10 nM) at 120 min after the first challenge with proteases. $[Ca^{2+}]_i$ was monitored to assess PAR$_2$ activation. We have previously reported that exposure to CS and NE (100 nM, 10 min) prevents the capacity of trypsin to mobilize Ca^{2+}, which indicates that CS and NE can initially cleave and disarm the receptor under these conditions (14, 15). In some experiments, cells were pre-incubated with CTR0066101, gallein, or vehicle to assess the mechanism of recovery. The first challenge with trypsin caused a prompt increase in $[Ca^{2+}]_i$, and this response was unaffected by CRT0066101 or gallein (Figs. 7, *B*–*D* and 8*A*). In contrast, CS and NE did not affect $[Ca^{2+}]_i$, which is in accordance with the inability of CS- and NE-activated PAR$_2$ to couple to Gα_q and mobilize intracellular Ca^{2+} ions (14, 15). When cells were challenged with trypsin at 120 min after the first exposure to trypsin, CS, or NE, the secondary responses to trypsin were almost fully recovered relative to those of cells challenged initially with vehicle (Figs. 7, *C* and *D* and 8). These results are consistent with replenishment of the plasma membrane with intact PAR$_2$. CRT0066101 or gallein inhibited recovery of trypsin responsiveness in cells first challenged with trypsin, CS, or NE (Figs. 7, *C* and *D* and 8, *B*–*J*). The combination of both CTR0066101 and gallein had a further inhibitory effect, which might suggest parallel PKD and Gβγ pathways (Figs. 7, *C* and *D* and 8, *D*, *G*, and *J*). These data

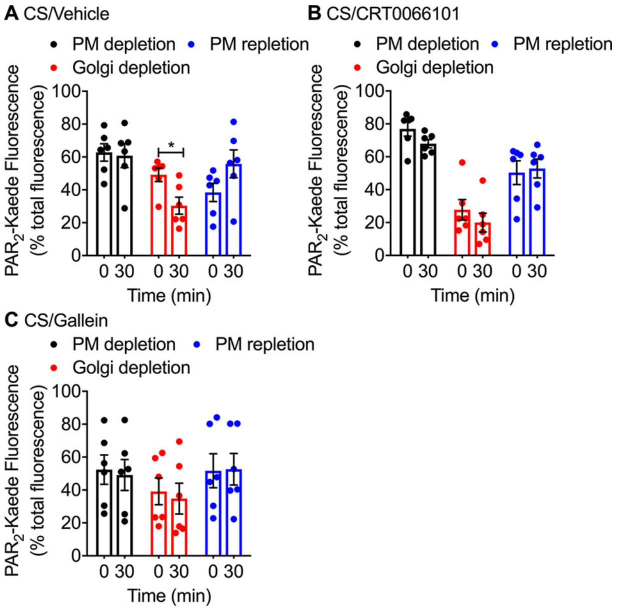

Figure 6. CS-induced trafficking of PAR$_2$-Kaede from the Golgi apparatus to the plasma membrane. PAR$_2$-Kaede located in the region of the perinuclear Golgi apparatus of KNRK-PAR$_2$-Kaede cells was green/red photoconverted. Cells were then incubated with CS (100 nM) for 0 or 30 min. PAR$_2$-Kaede fluorescence was measured at the cell surface or Golgi. Cells were pre-incubated with vehicle (*A*), PKD inhibitor (CRT0066101, 100 nM) (*B*), or Gβγ inhibitor (gallein, 10 μM) (*C*). Quantification of PAR$_2$-Kaede (518 nm, *green*) at the plasma membrane and of photoconverted PAR$_2$-Kaede (572 nm, *red*) in the Golgi region and at the plasma membrane is shown. $n = 6$ experiments, >30 cells analyzed per condition. *, $p < 0.05$ (Student's *t* test). *Error bars*, S.E.

suggest that Gβγ- and PKD-mediated recruitment of intact PAR$_2$ from the Golgi apparatus to the plasma membrane is required for recovery of trypsin responses in HEK293 cells.

NE-induced activation of PKD in the Golgi apparatus of nociceptors mediates sustained hyperexcitability

We have recently reported that trypsin, CS, and NE induce sustained nociception in mice by activating PAR$_2$ expressed by a subpopulation of primary sensory neurons (18). Trypsin, CS, and NE also cause a PAR$_2$-dependent hyperexcitability of nociceptors, which is a hallmark of chronic pain (18). PKD activity is necessary for maintaining trypsin-evoked hyperexcitability of nociceptors, consistent with PAR$_2$ mobilization from Golgi stores (19). We examined whether PKD and Gβγ contribute to the maintenance of protease-evoked hyperexcitability. The excitability of nociceptors of mouse dorsal root ganglia (DRG) was determined by measurement of the rheobase (minimum current required to fire a single action potential) using patch-clamp recordings. Neurons were exposed to NE (7.8 nM, 0.2 units/ml, 20 min) or vehicle (control) and washed, and rheobase was measured at 0, 30, or 150 min after washing (Fig. 9*A*). Immediately after washing (0 min), there was a 32% decrease in rheobase of NE-treated neurons, when compared with vehicle ($p < 0.001$), consistent with hyperexcitability (Fig. 8*B*). Hyperexcitability was maintained at 30 min after washing (25% decrease in rheobase compared with vehicle, $p < 0.05$), but after 150 min, hyperexcitability had declined to control levels (Fig. 9*B*). To determine whether neurons had recovered their capacity to respond to PAR$_2$ agonists at 150 min after exposure to NE and washing, they were challenged with trypsin (50 nM, 10 min) and washed, and rheobase was immediately measured. In NE-exposed neurons, trypsin induced a 35% decrease in rheobase when compared with vehicle-treated controls ($p < 0.01$) (Fig. 9*B*). These results show that NE causes an initial hyperexcitability of nociceptors, which is sustained for 30 min and declines after 150 min. At this time, neurons have regained their capacity to respond to trypsin, which may require mobilization of intact PAR$_2$.

To determine whether PKD, Gβγ, or new protein synthesis mediates this recovery of hyperexcitability, neurons were preincubated with CRT0066101 (10 nM, PKD inhibitor), gallein (10 μM, Gβγ inhibitor), cycloheximide (10 μg/ml, protein synthesis inhibitor), or vehicle 30 min before NE exposure; inhibitors were present throughout the experiment. NE- and trypsin-evoked hyperexcitability was determined. CRT0066101 and gallein had no effect on the capacity of NE to cause an immediate hyperexcitability (0 min after NE) (Fig. 9*C*). However, both the PKD and Gβγ inhibitors prevented trypsin-induced hyperexcitability at 150 min after NE exposure (Fig. 9*D*). Similarly, cycloheximide did not affect an initial response to trypsin (0 min), but abolished the recovery of trypsin-induced hyperexcitability at 150 min after NE (Fig. 9*D*). Thus, after exposure to NE, PKD, Gβγ, and new protein synthesis are necessary for the restoration of protease-evoked hyperexcitability. This result is consistent with the role of PKD and Gβγ in mobilization of newly synthesized PAR$_2$ from the Golgi apparatus and replenishment of the plasma membrane with fresh receptors that are required for recovery of protease signaling.

PKD and Gβγ are required for sustained nociception to proteases that activate PAR$_2$ by canonical and biased mechanisms

The local (intraplantar) injection of trypsin, CS, and NE causes persistent mechanical allodynia in mice by activating PAR$_2$ on nociceptors (18). Whereas PAR$_2$ signaling from endosomes mediates trypsin-induced allodynia, PAR$_2$ signaling from the plasma membrane mediates CS- and NE-induced allodynia. Because cleaved PAR$_2$ cannot be reactivated by proteases and is eventually degraded, the mobilization of fresh PAR$_2$ may be necessary for the continuation of protease-evoked pain. To examine this possibility, we administered to mice inhibitors of PKD and Gβγ. The PKD inhibitor CRT0066101 (80 mg/kg, orally), the Gβγ inhibitor gallein (100 mg/kg, intraperitoneally), or vehicle (control) was administered to mice. After 2 h (CRT0066101) or 30 min (gallein), mice received an intraplantar injection of trypsin (140 nM, 0.04 units/μl), CS (2.5 μM, 0.06 units/μl), or NE (1.18 μM, 0.03 units/μl) (10 μl). Paw withdrawal responses to stimulation of the plantar surface with calibrated von Frey filaments (VFF) were measured every hour for 4 h after protease injection. In vehicle-treated mice, trypsin, CS, and NE caused mechanical allodynia of the ipsilateral (protease-injected) paw after 1 h that was sustained for 4 h (Fig. 10). CRT0066101 significantly blunted responses to trypsin, CS, and NE from 1 to 2 h (Fig. 10, *A–C*). Gallein also inhibited trypsin-, CS-, and NE-induced allodynia (Fig. 9, *E–G*). CRT0066101 and gallein did not affect withdrawal responses of the contralateral (noninjected) paw (Fig. 10, *D* and *H*). These

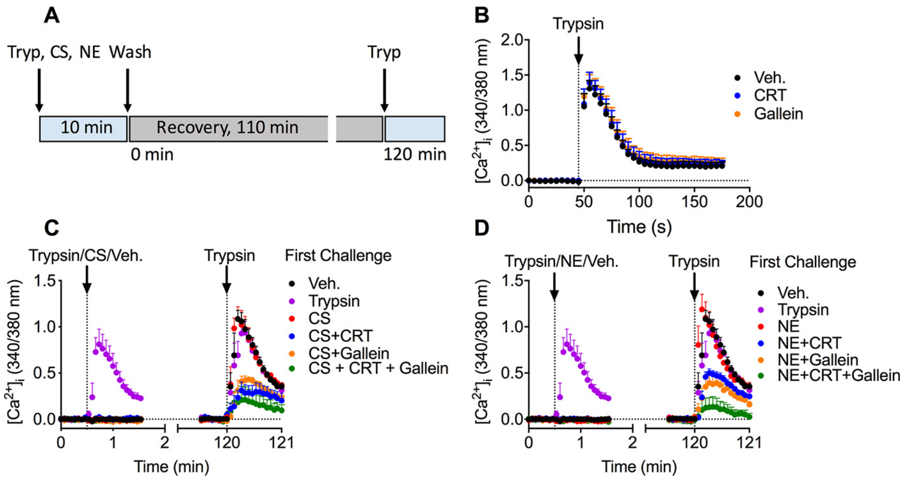

Figure 7. Recovery of PAR$_2$-mediated signaling. *A*, experimental design. HEK293 cells were first challenged with trypsin (10 nM), CS (100 nM), NE (100 nM), or vehicle for 10 min. Cells were then washed, recovered for 110 min, and then challenged with trypsin (10 nM) at 120 min after the first challenge with proteases. *B–D*, measurement of $[Ca^{2+}]_i$ in HEK293 cells. *B*, effects of PKD inhibitor (CRT0066101, CRT, 100 nM) or Gβγ inhibitor (gallein, 10 μM) on responses to a single challenge with trypsin. *C* and *D*, responses to a first challenge with trypsin, CS, or vehicle (*C*) or with trypsin, NE, or vehicle (*D*) and a second challenge with trypsin after 120 min. $n = 4$ (*B*) or 5 (*C* and *D*) experimental replicates from triplicate observations. *Error bars*, S.E.

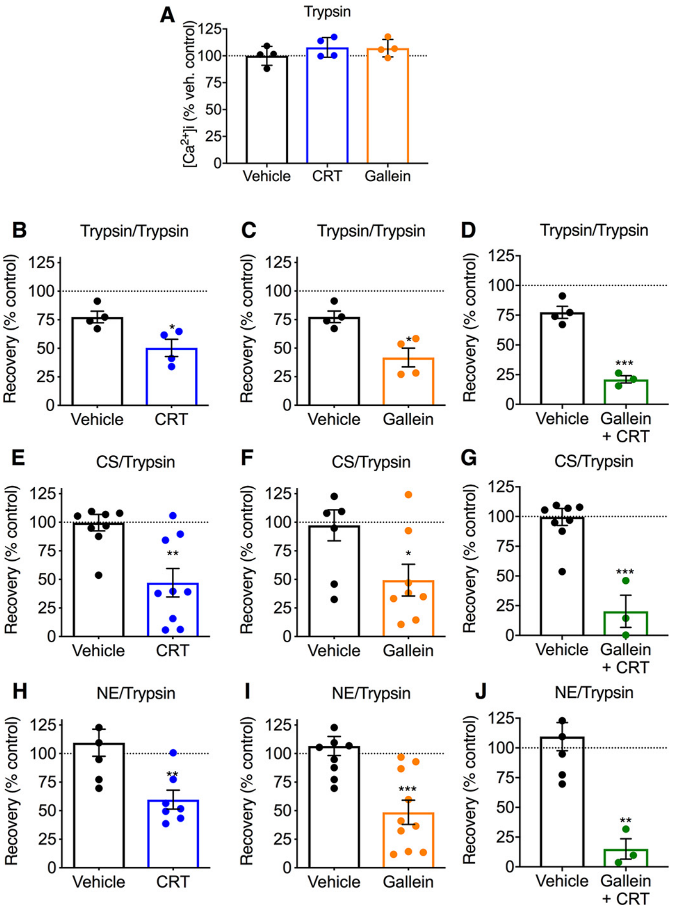

Figure 8. Recovery of PAR$_2$-mediated signaling. *A*, effects of PKD inhibitor (CRT0066101 (*CRT*), 100 nM) or Gβγ inhibitor (gallein, 10 μM) on responses of HEK293 cells to a single challenge with trypsin. *B–J*, recovery of Ca^{2+} signaling in HEK293 cells. Cells were first challenged with trypsin (10 nM) (*B–D*), CS (100 nM) (*E–G*) or NE (*H–J*). Cells were then washed, recovered for 120 min, and then challenged with trypsin (10 nM). In some experiments, cells were pre-incubated with PKD inhibitor (CRT0066101) (*B*, *E*, and *H*) or Gβγ inhibitor (gallein) (*C*, *F*, and *I*) or both PKD and Gβγ inhibitor (*D*, *G*, and *J*). $n = 3–10$ experimental replicates from triplicate observations. *, $p < 0.05$; **, $p < 0.01$; ***, $p < 0.001$ (Student's *t* test). *Error bars*, S.E.

results reveal a role for PKD and Gβγ in sustained protease-mediated mechanical allodynia in mice.

Discussion

We have recently investigated the mechanisms by which trypsin, CS, and NE initiate pain (18). After intraplantar injection in mice, trypsin, CS and NE cause mechanical allodynia by activating PAR$_2$ on Na$_V$1.8-positive nociceptors. These proteases also evoke hyperexcitability of nociceptors, a characteristic of chronic pain, but by distinct mechanisms (18). Trypsin induces an initial hyperexcitability of nociceptors by a mechanism that entails PAR$_2$ signaling at the plasma and activation of PKC. PAR$_2$ then internalizes and signals from endosomes by β-arrestin– and Gα$_q$–mediated mechanisms that activate extracellular signal–regulated kinase, which contributes to sustained hyperexcitability of nociceptors. In contrast, CS and NE evoke hyperexcitability by PAR$_2$ signaling at the plasma membrane, which activates PKA (14, 15, 18). Accordingly, whereas inhibitors of clathrin- and dynamin-mediated endocytosis block trypsin-evoked allodynia, they have no effect on nociceptive responses to CS and NE, which do not cause PAR$_2$ endocytosis (18). Regardless of the mechanism of PAR$_2$ activation and initial hyperexcitability, the maintenance of pain evoked by extracellular proteases requires mobilization of intracellular stores or *de novo* synthesis of PAR$_2$. These processes are necessary because trypsin-activated PAR$_2$ traffics to lysosomes and is degraded. Even though CS or NE do not cause endocytosis of PAR$_2$, once cleaved, this receptor cannot be reactivated by a protease (14, 15).

Our current results show that proteases that activate PAR$_2$ by biased mechanisms evoke Gβγ translocation to the Golgi apparatus of HEK293 cells. They also indicate that these proteases activate PKD within the Golgi apparatus. Gβγ and PKD promote mobilization of intact PAR$_2$ from the Golgi apparatus, which replenishes the plasma membrane with intact receptors that allow for a recovery of cellular responsiveness to extracellular proteases. These mechanisms also appear to operate in another cell line (KNRK) as well as in primary sensory neurons,

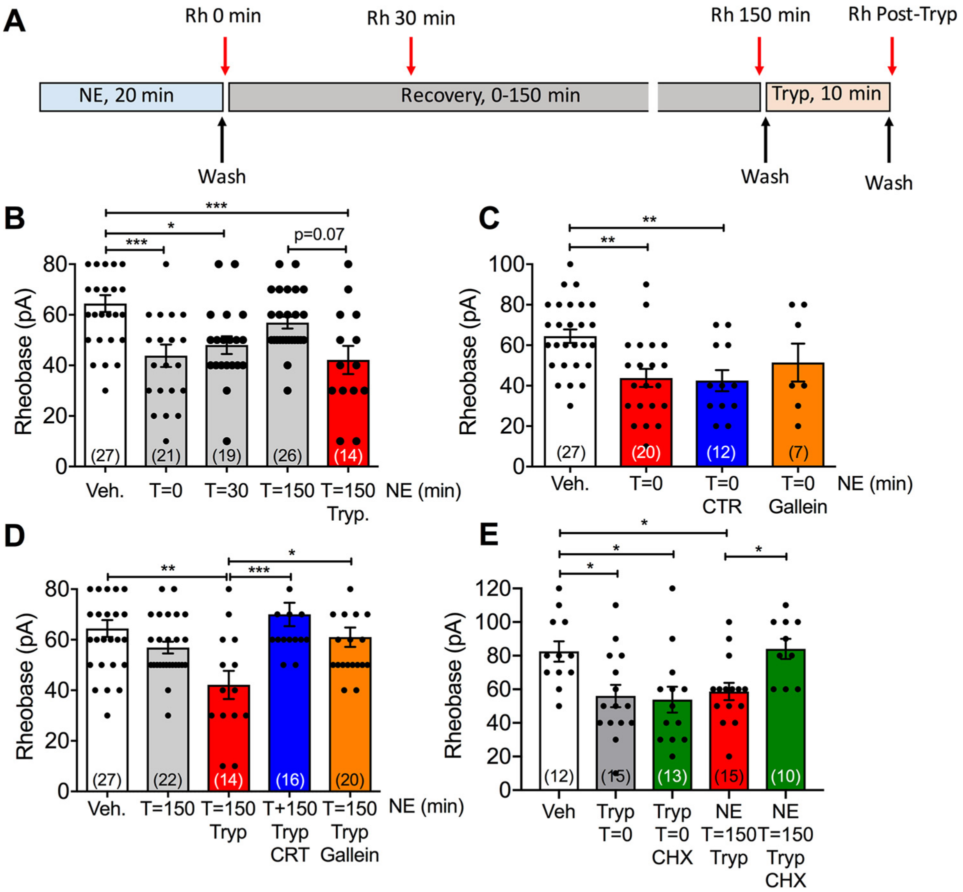

Figure 9. Recovery of PAR2-mediated hyperexcitability of nociceptors. *A*, experimental design. DRG neurons from mice were exposed to NE (7.8 nM, 0.2 units/ml) for 20 min, washed, and recovered for up to 150 min. Changes in neuronal excitability were assessed at 0, 30, or 150 min after washing by measurement of rheobase. To assess recovery of excitability, some neurons were challenged with trypsin (*Tryp*, 50 nM, 10 min). At 150 min after NE exposure, neurons were washed, and rheobase was immediately measured. To examine the mechanism of recovery, neurons were pre-incubated with PKD inhibitor (CRT0066101 (*CRT*), 10 nM), Gβγ inhibitor (gallein, 10 μM), protein synthesis inhibitor (cycloheximide (*CHX*), 10 μg/ml), or vehicle for 30 min before NE (inhibitors were included throughout). *B–E*, measurements of rheobase in protease-treated DRG neurons. *B*, time course of responses at time 0 min (*T* = 0), 30 min (*T* = 30), and 150 min (*T* = 150) after NE and recovery of trypsin response at 150 min after NE. *C*, NE responses at time 0 min after NE. *D*, effects of CRT and gallein on responses to trypsin at 150 min after NE. *E*, effects of cycloheximide on initial response to trypsin (0 min) and on responses to trypsin at 150 min after NE. *Numbers* in *parentheses* indicate numbers of neurons studied from 6–13 mice. *, $p < 0.05$; **, $p < 0.01$; ***, $p < 0.001$ (one-way ANOVA, Bonferroni multiple comparisons). *Error bars*, S.E.

where inhibitors of Gβγ and PKD prevented the recovery of trypsin-evoked hyperexcitability of NE-treated neurons. They may also function in intact mice, because Gβγ and PKD inhibitors blunted trypsin-, CS-, and NE-evoked mechanical allodynia. These results agree with our report that Gβγ and PKD mediate trypsin-evoked mobilization of PAR$_2$ from the Golgi apparatus (19). They also support the role for Gβγ in activating PKD within the Golgi apparatus (21), where PKD controls protein trafficking to secretory pathways (26, 27).

The use of FRET biosensors for PKD that are targeted to the cytosol or Golgi apparatus enabled analysis of PKD activity with high spatial and temporal fidelity and revealed that trypsin, CS, and NE can all activate PKD in the cytosol and Golgi apparatus. These responses are likely mediated by PAR$_2$ because the PAR$_2$-selective agonist 2-furoyl-LIGRLO-NH$_2$ also activated PKD in the Golgi apparatus, and I-343, a PAR$_2$ antagonist (18), abolished responses to trypsin, CS, and NE. Although I-343 can also inhibit PAR$_1$, which is expressed in HEK cells, I-343 had no effect on thrombin-activated PKD.

We observed that trypsin, CS, and NE all stimulated an increase in bystander BRET between Gγ-Venus and Giantin-RLuc8, which is consistent with translocation of Gγ to the Golgi apparatus. Whereas the overexpression of Gα_q was required for trypsin-evoked translocation of Gγ-Venus, overexpression of Gα_S was necessary for maximal CS- and NE-evoked translocation. These results are in accordance with the mechanisms by which these proteases activate PAR$_2$. Thus, the canonical agonist trypsin induces PAR$_2$ coupling to Gα_q, and the biased agonists CS and NE evoke PAR$_2$ coupling to Gα_s (14, 15).

Our studies of the contribution of PKD to mobilization of PAR$_2$ from the Golgi apparatus and sustained signaling by extracellular proteases were not always consistent between different cell types and experimental approaches. In HEK293 cells, we found that trypsin, CS, and NE all activated PKD in the Golgi apparatus, assessed using a Golgi-targeted FRET biosensor. Trypsin, CS, and NE caused a decrease in bystander BRET between PAR$_2$-RLuc8 and TGN38-Venus, which is consistent with mobilization of PAR$_2$ from the Golgi apparatus. By selective photoconversion of PAR$_2$-Kaede within the Golgi apparatus of KNRK cells, we were able to observe that CS and NE stimulated removal of PAR$_2$ from the Golgi apparatus and insertion into the plasma membrane. Inhibitors of PKD and

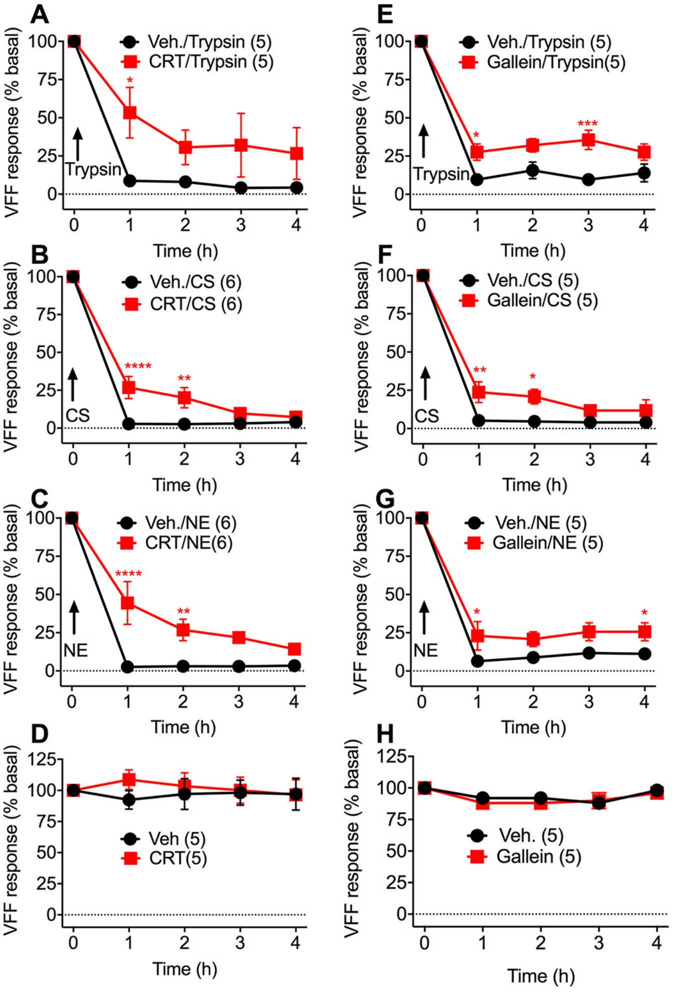

Figure 10. PKD and Gβγ-dependent mechanical hyperalgesia. Mice were pretreated with CRT0066101 (80 mg/kg, orally), gallein (100 mg/kg, intraperitoneally), or vehicle (orally or intraperitoneally) for 2 h (CRT0066101) or 30 min (gallein) before intraplantar injection of trypsin (140 nM) (*A*, *E*, *D*, and *H*), CS (2.5 μM) (*B* and *F*), or NE (1.18 μM) (*C* and *G*) (all 10 μl). *A–C* and *E–G*, VFF withdrawal responses of the ipsilateral protease-injected paws. *D* and *H*, VFF withdrawal responses of the contralateral noninjected paws. *Numbers* in *parentheses* indicate mouse numbers. *, $p < 0.05$; **, $p > 0.01$; ***, $p > 0.001$; ****, $p < 0.0001$ (two-way ANOVA, Bonferroni multiple comparisons). *Error bars*, S.E.

Gβγ attenuated the mobilization of PAR$_2$-Kaede from the Golgi apparatus of KNRK cells (confocal imaging). They also suppressed recovery of sustained PAR$_2$ signaling in HEK293 cells (Ca^{2+} assays) and neurons (rheobase assays). Although a PKD inhibitor suppressed removal of PAR$_2$-Kaede from the Golgi apparatus of KNRK cells, it did not affect the decrease in bystander BRET between PAR$_2$-RLuc8 and TGN38-Venus in HEK293 cells. We have no explanation for this discrepancy. One possibility is that PKD promotes mobilization of PAR$_2$ from the Golgi apparatus of KNRK cells but not HEK293 cells. This discrepancy could also be related to differences in assay sensitivity, where an effect of the PKD inhibitor could be assessed in assays of PAR$_2$-Kaede mobilization in individual KNRK cells but not in BRET assays of PAR$_2$-RLuc8 and TGN38-Venus proximity in populations of HEK293 cells. Another explanation could be that TGN38 is not confined to the Golgi apparatus. Although at steady state TGN38 is principally localized to the Golgi apparatus, it constitutively shuttles between the Golgi apparatus and plasma membrane by the exocytic and endocytic pathways (23). It is therefore possible that proximity between TGN38 and PAR$_2$ in these pathways may confound the results. It is also possible that multiple kinases, in addition to PKD, regulate PAR$_2$ trafficking from the Golgi apparatus or that PKD differentially controls trafficking of newly synthesized but not stored PAR$_2$. Further experiments are required to examine these possibilities. However, the observation that Gβγ and PKD inhibitors disrupt the recovery of PAR$_2$ Ca^{2+} signaling in HEK293 cells pretreated with trypsin, CS, or NE supports their role in maintaining the capacity of extracellular proteases to signal via PAR$_2$.

It is increasingly appreciated that GPCRs can generate signals in subcellular compartments. Compartmentalization of signaling can regulate specific physiological processes, including pain transmission (18, 35, 36). GPCRs can also activate PKD in distinct subcellular compartments, often by different mechanisms. Thus, PAR$_2$ agonists induce PKC-dependent activation of PKD at the plasma membrane, where PKD may regulate the activity of transient receptor potential ion channels (37). Vasopressin, bombesin, and neurokinin 3 receptors rapidly activate PKD by a PKC-dependent mechanism (38–40). Canonical and biased agonists of PAR$_2$ also cause Gβγ-dependent activation of PKD in the Golgi apparatus, where PKD can control PAR$_2$ mobilization (19). Gα_q subunits can also control PKD activity and regulate trafficking from the Golgi apparatus to the plasma membrane (29, 41).

Biased agonism describes the phenomenon whereby the binding of different ligands to the same receptor in an identical cellular background results in differential activation of signaling pathways (42). Proteases, which are activated during injury and inflammation, that cleave PAR$_2$ at different sites activate very distinct pathways of receptor signaling and trafficking (14, 15, 18). Our results reveal a common mechanism of recovery of PAR$_2$ signaling capacity at the plasma membrane, regardless of the mechanism of activation. Thus, after activation of PAR$_2$ by trypsin (PAR$_2$ coupling to Gα_q, Gα_s, β-arrestins, PAR$_2$ endocytosis), CS, or NE (PAR$_2$ coupling to Gα_s, retention at cell surface), Gβγ-mediated activation of PKD within the Golgi apparatus mediates the mobilization and plasma membrane trafficking of fresh PAR$_2$ that sustains signaling by extracellular proteases. Other GPCR family members that couple to different Gα subunits also evoke trafficking of Gβγ to the Golgi apparatus. For example, agonists of muscarinic M2 receptors (which couple to G$\alpha_{i/o}$) and M3 receptors (which couple to Gα_q) both evoke Golgi translocation of Gβγ (43). This may be a general mechanism by which activation of GPCRs at the plasma membrane repopulates the cell surface with nondesensitized receptors.

Our results also provide information about the maintenance of pain. We observed that brief exposure of nociceptors to NE induced an initial period of hyperexcitability that gradually recovered to baseline levels, when neurons recovered their capacity to respond to trypsin. Inhibitors of PKD and Gβγ both impeded this recovery. An inhibitor of protein synthesis also impeded the recovery of trypsin-evoked hyperexcitability of NE-treated neurons. The systemic administration of PKD and Gβγ inhibitors to intact mice also blunted nociception evoked by intraplantar administration of trypsin, CS, or NE. These results highlight the importance of GPCR trafficking for pain transmission. Endocytosis of GPCRs, including PAR$_2$, is important for the initiation and maintenance of pain transmission (18, 35, 36). However, in the case of nonrecycling GPCRs, notably PAR$_2$, synthesis of new receptors and mobilization and exocytosis of intact receptors is necessary for the maintenance of nociceptive signaling by extracellular ligands. These findings have implications for therapy. Inhibitors of clathrin- and dynamin-mediated endocytosis and lipid-conjugated antagonists that target GPCRs in endosomes can provide effective pain relief (18, 35, 36). Inhibitors of exocytosis, including G$\beta\gamma$ and PKD inhibitors, may also provide pain relief.

Limitations to the current study include the use of model HEK293 and KNRK cells, which may not replicate findings in nociceptive neurons and intact animals, possible confounding effects of tagging PAR$_2$ with luciferase or Kaede, and the use of pharmacological inhibitors that can lack selectivity (32, 33). However, we observed that inhibitors of different mediators of Golgi-to-plasma membrane trafficking (PKD and G$\beta\gamma$) gave consistent results in experiments with model cell lines, primary sensory neurons in short-term culture, and intact mice. Moreover, fusion to Kaede does not affect the function of PAR$_2$ (19).

In summary, this study provides evidence that proteases that activate PAR$_2$ by canonical and biased mechanisms stimulate PKD in the Golgi; PAR$_2$ mobilization and *de novo* synthesis repopulate the cell surface with intact receptors and sustain nociceptive signaling by extracellular proteases. Antagonism of these pathways may offer another approach to treat chronic pain.

Experimental procedures

Animals

Animal Ethics Committees of Monash University and Queen's University approved the procedures using mice. C57BL/6 mice (8–12 weeks, male) were studied. Mice were maintained in a light-controlled (12-h light/dark cycle) temperature-controlled (22 ± 4 °C) environment with free access to food and water.

Cell culture

HEK293 cells and KNRK cells were cultured in Dulbecco's modified Eagle's medium supplemented with 10% fetal bovine serum and containing 1% penicillin and streptomycin (5% CO$_2$, 37 °C). HEK293 and KNRK cells expressing human PAR$_2$ with N-terminal FLAG and C-terminal HA11 epitopes (FLAG-PAR$_2$-HA) have been described previously (19).

FRET PKD and PKC activation assays

HEK293 cells were plated at a density of 4×10^6 cells/10-cm dish. Cells were transiently transfected with the hPAR$_2$ (1 μg) plus FRET PKD biosensors Cyto-DKAR, Golgi-DKAR, or DKAR-T/A (2.5 or 5 μg) or PKC sensor Cyto-CKAR (5 μg) using polyethyleneimine (20). At 24 h after transfection, cells were seeded on poly-D-lysine–coated OptiPlate-96 96-well plates (PerkinElmer Life Sciences). FRET was assessed 72 h post-transfection, following overnight serum restriction. Cells were equilibrated with HBSS, 10 mM HEPES, pH 7.4, for 30 min. Cyan fluorescent protein/yellow fluorescent protein FRET was measured using a PHERAstar plate reader (BMG LabTech) with excitation wavelength 425 ± 5 nm, and emission wavelength 550 ± 25 nm/490 ± 10 nm (18, 35, 36). Cells were challenged with trypsin (10 nM), CS (100 nM), or NE (100 nM), and measurements continued for 20 min at 1-min intervals. In some experiments, cells were pre-incubated with the PAR$_2$-antagonist I-343 (10 μM) for 30 min, and antagonist was present throughout the experiments. For kinetic measurements, data were corrected to baseline and vehicle controls. The area under the curve (AUC, 20 min) was determined to quantify the effects of inhibitors.

BRET Gγ translocation assays

HEK293 cells were plated at a density of 4×10^6 cells/10-cm dish. Cells were transiently transfected with hPAR$_2$ (0.9 μg), Gα_q (1.33 μg) or Gα_s (1.33 μg), Gβ1 (1.33 μg), Gγ2-Venus (2 μg), and Giantin-RLuc8 (0.5 μg) using polyethyleneimine. At 24 h after transfection, cells were seeded on poly-D-lysine–coated OptiPlate-96 96-well plates (PerkinElmer Life Sciences), and cultured overnight. Cells were equilibrated with HBSS, 10 mM HEPES, pH 7.4, for 30 min before the assay. Coelenterazine h (5 μM, Nanolight Technologies) was added to the cells for 5 min before measurements. RLuc8 luminescence (480 nm) and Venus fluorescence (530 nm) were measured using a LumiSTAR Omega Luminometer (BMG LabTech) before and after exposure to proteases: trypsin, 10^{-13} to 10^{-7} M; NE, 10^{-12} to 10^{-7} M; CS, 10^{-12} to 10^{-7} M; or vehicle (control) (18, 35, 36). Data were corrected to baseline and vehicle-treated conditions to generate the ligand-induced signal, which was normalized to the maximum trypsin response.

BRET PAR$_2$ Golgi trafficking assays

HEK293 cells were transiently transfected with hPAR$_2$-RLuc8 (1 μg) and TGN38-Venus (4 μg). BRET was measured as described above.

[Ca^{2+}]$_i$ assays

HEK293 cells were plated (30,000 cells/well) in poly-D-lysine–coated ViewPlate-96 96-well plates (PerkinElmer Life Sciences). Cells were loaded with Fura-2/AM (1 μM; Invitrogen) for 1 h at 37 °C in assay buffer (150 mM NaCl, 2.6 mM KCl, 0.1 mM CaCl$_2$, 1.18 mM MgCl$_2$, 10 mM D-glucose, 10 mM HEPES, pH 7.4) containing 4 mM probenecid and 0.5% BSA. Fluorescence was measured at 340- and 380-nm excitation and 530-nm emission using a FlexStation III Microplate Reader (Molecular Devices) (19). The 340- and 380-nm ratio was measured as an indication of [Ca^{2+}]$_i$. To measure loss and recovery of PAR$_2$-mediated changes in [Ca^{2+}]$_i$, cells were first incubated with trypsin (10 nM), CS (100 nM), NE (100 nM), or vehicle for 10 min, washed three times with assay buffer, recovered at 37 °C for 110 min, and then rechallenged with trypsin (10 nM) at 120 min after the first challenge. For quantification of the recovery of Ca^{2+} signaling, the maximal responses to the second trypsin challenge were normalized to the vehicle-pretreated control.

Localization of FRET and BRET biosensors

HEK293 cells were transfected as stated with PAR_2-HA-RLuc8, Cyto-DKAR, Golgi-DKAR, Giantin-Venus, TGN38-Venus, or Gγ-Venus (2.5 μg). Cells were plated on 12-mm glass coverslips, and 48 h after transfection, cells were fixed in 4% paraformaldehyde (20 min, 4 °C). Cells were washed with PBS and incubated with blocking buffer (PBS + 0.3% saponin + 3% horse serum) (1 h, room temperature). PAR_2-HA-RLuc8 was detected using immunofluorescence with HA antibody; other sensors were detected with fluorescent tags. Cells were incubated with rat anti-HA (1:1000; Roche Applied Science, clone 3F10), and mouse anti-TGN58K (1:200; Abcam) in PBS + 0.2% saponin + 1% horse serum (1 h, room temperature). Cells were washed three times in PBS and incubated with goat anti-rat Alexa 488 and donkey anti-mouse Alexa 568 IgG (1:1000; Invitrogen) (1 h, room temperature). Slides were washed three times in PBS, counterstained with 4′,6-diamidino-2-phenylindole (1 μg/ml), and mounted with ProLong Glass antifade mounting medium (Invitrogen). Cells were imaged on a Leica SP8 confocal microscope with a ×63 (numerical aperture 1.4) objective with a digital zoom of 2.5. Images were processed with ImageJ (National Institutes of Health).

Live-cell imaging and quantification of PAR_2-Kaede trafficking

KNRK-PAR_2-Kaede cells were plated onto glass 8-well chamber slides at a density of 100,000 cells/well and cultured overnight. Cells were equilibrated in HBSS, 10 mM HEPES, pH 7.4, at 37 °C for 30 min before the assay. Live-cell images were collected using a Leica TCS SP8 laser-scanning confocal microscope with a Leica HCX PL APO ×63 oil immersion objective.

The Leica FRAP wizard was used to green/red photoconvert PAR_2-Kaede within the perinuclear region of interest with the laser settings of pre-photoconversion image at 400 Hz, UV laser at 10% power, and two passes at 400 Hz, as we have described previously (19). Images were collected for 5 min, cells were challenged with CS (100 nM) or NE (100 nM), and images were collected at 5-min intervals for another 30 min. FIJI software (National Institutes of Health) was used to determine the intensity of PAR_2-Kaede signal at the plasma membrane, in the perinuclear region, and throughout the cell. To quantify the depletion of PAR_2 from the plasma membrane, the intensities of Kaede green at the plasma membrane and throughout the entire cell were determined and expressed as a ratio. To quantify the depletion of PAR_2 from the Golgi apparatus and repletion of the plasma membrane with mobilized PAR_2, the intensities of Kaede red were determined at the plasma membrane, in the perinuclear region of the cell, and throughout the cell and were expressed as ratios.

Inhibitors

Cells were pre-incubated with CRT0066101 (100 nM; Tocris Bioscience), gallein (10 μM; Tocris Bioscience), Gö6983 (1 μM; Sigma-Aldrich), H-89 (1 μM; Sigma-Aldrich), GRK2i (100 μM; Tocris), or vehicle (control) for 30 min, and the inhibitors were present throughout the experiments.

Patch-clamp studies of nociceptors

To obtain dispersed neurons, mouse DRG (T9–T13) were incubated in collagenase (1 mg/ml; Worthington) and dispase (4 mg/ml; Roche Applied Science) (10 min, 37 °C) and triturated with a fire-polished Pasteur pipette. Dispersed cells were seeded onto laminin-coated (0.017 mg/ml) and poly-D-lysine–coated (2 mg/ml) glass coverslips in 24-well plates. Neurons were maintained in F12 medium (Sigma-Aldrich) supplemented with 10% fetal calf serum and containing penicillin and streptomycin (5% CO_2, 37 °C) for 16 h. Neurons were pre-incubated for 20 min with NE (7.8 nM, 0.2 units/ml) or vehicle (control) and washed three times with F12 medium. Changes in neuronal excitability were assayed immediately (0 min) or at 30 and 150 min after NE application. After 150 min, some cells were challenged with trypsin (50 nM, 10 min) and washed. To evaluate the role of PKD, Gβγ, and new protein synthesis on NE-evoked neural excitability, some cells were pre-incubated with CRT0066101 (10 nM), gallein (10 μM), cycloheximide (10 μg/ml), or vehicle (control) 30 min before NE application, and inhibitors were included throughout the study. The excitability of small-diameter neurons (<30-picofarad capacitance) was assessed using perforated patch-clamp with amphotericin B (240 μg/ml) in current clamp mode at room temperature, as we have described (18, 19). Only those neurons with resting membrane potentials more negative than −40 mV were analyzed. Changes in excitability were quantified by measuring the rheobase. Recordings were made using Axopatch 200B amplifiers, digitized by Digidata 1322A, and stored and processed using pClamp 10.1 software (Molecular Devices). The recording chamber was continuously perfused (2 ml/min) with external solution comprising 140 mM NaCl, 5 mM KCl, 10 mM HEPES, 10 mM D-glucose, 1 mM $MgCl_2$, 2 mM $CaCl_2$, pH to 7.4 with 3 M NaOH. The pipette solution was as follows: 110 mM potassium gluconate, 30 mM KCl, 10 mM HEPES, 1 mM $MgCl_2$, 2 mM $CaCl_2$, pH 7.25, with 1 M KOH.

Mechanical hyperalgesia

Mechanical hyperalgesia was assessed by measuring paw withdrawal responses to stimulation of the plantar surface of the mouse paw with calibrated VFF (14, 15, 18). CRT0066101 (Tocris Bioscience; 80 mg/kg) or vehicle (control, 0.9% NaCl) was administered by gavage (200 μl) 2 h before intraplantar injections of proteases. Gallein (100 mg/kg) or vehicle (control, 0.5% DMSO in 0.9% NaCl) was administered intraperitoneally (200 μl) 30 min before intraplantar injection of proteases. For intraplantar injections, mice were sedated with 5% isoflurane. Trypsin (140 nM, 0.04 units/μl), CS (2.5 μM, 0.06 units/μl), NE (1.18 μM, 0.03 units/μl), or vehicle was injected subcutaneously into the plantar surface of the left hind paw (10 μl). Withdrawal responses to stimulation of the plantar surface of the ipsilateral (injected) and contralateral (noninjected) hind paws with calibrated VFF were measured hourly for 4 h. Investigators were blinded to the experimental treatments, and mice were randomly assigned to treatment groups.

Statistics

Data are presented as mean ± S.E. For studies of cells, triplicate observations from $n > 3$ experiments were made for each treatment group. For experiments with isolated neurons, $n = 7–27$ DRG neurons from 6–13 mice were studied per treatment. For studies of nociceptive behavior, $n = 5–6$ mice were studied per treatment. Student's *t* tests were used to assess differences between two groups. Differences between multiple groups were assessed by one-way (FRET, BRET, electrophysiology) or two-way (mouse behavior) ANOVAs followed by Bonferroni's correction for multiple comparisons. $p < 0.05$ was considered significant at the 95% confidence level.

Author contributions—P. Z., D. P. P., S. J. V., B. L. S., and N. W. B. conceptualization; P. Z., L. A. P., D. D. J., N. N. J.-V., R. L., T. L., J. O. J., and C. L.-L. data curation; P. Z., L. A. P., D. D. J., N. N. J.-V., R. L., and T. L. formal analysis; P. Z., D. P. P., S. J. V., B. L. S., and N. W. B. supervision; P. Z., L. A. P., D. D. J., N. N. J.-V., R. L., T. L., S. J. V., B. L. S., and N. W. B. investigation; P. Z., D. D. J., N. N. J.-V., and R. L. visualization; P. Z., L. A. P., D. D. J., N. N. J.-V., R. L., T. L., and N. W. B. methodology; P. Z., L. A. P., D. D. J., R. L., and N. W. B. writing-original draft; D. D. J., N. N. J.-V., R. L., and T. L. validation; D. D. J., D. P. P., S. J. V., B. L. S., and N. W. B. project administration; D. P. P., S. J. V., B. L. S., and N. W. B. funding acquisition; D. P. P., S. J. V., B. L. S., and N. W. B. writing-review and editing; S. J. V., B. L. S., and N. W. B. resources.

References

1. Dong, C., Filipeanu, C. M., Duvernay, M. T., and Wu, G. (2007) Regulation of G protein-coupled receptor export trafficking. *Biochim. Biophys. Acta* **1768,** 853–870 CrossRef Medline
2. Smith, J. S., and Rajagopal, S. (2016) The β-arrestins: multifunctional regulators of G protein-coupled receptors. *J. Biol. Chem.* **291,** 8969–8977 CrossRef Medline
3. Hauser, A. S., Attwood, M. M., Rask-Andersen, M., Schiöth, H. B., and Gloriam, D. E. (2017) Trends in GPCR drug discovery: new agents, targets and indications. *Nat. Rev. Drug Discov.* **16,** 829–842 CrossRef Medline
4. Kang, D. S., Tian, X., and Benovic, J. L. (2014) Role of β-arrestins and arrestin domain-containing proteins in G protein-coupled receptor trafficking. *Curr. Opin. Cell Biol.* **27,** 63–71 CrossRef Medline
5. Grady, E. F., Garland, A. M., Gamp, P. D., Lovett, M., Payan, D. G., and Bunnett, N. W. (1995) Delineation of the endocytic pathway of substance P and its seven-transmembrane domain NK1 receptor. *Mol. Biol. Cell* **6,** 509–524 CrossRef Medline
6. von Zastrow, M., Svingos, A., Haberstock-Debic, H., and Evans, C. (2003) Regulated endocytosis of opioid receptors: cellular mechanisms and proposed roles in physiological adaptation to opiate drugs. *Curr. Opin. Neurobiol.* **13,** 348–353 CrossRef Medline
7. Marchese, A., and Benovic, J. L. (2001) Agonist-promoted ubiquitination of the G protein-coupled receptor CXCR4 mediates lysosomal sorting. *J. Biol. Chem.* **276,** 45509–45512 CrossRef Medline
8. Ossovskaya, V. S., and Bunnett, N. W. (2004) Protease-activated receptors: contribution to physiology and disease. *Physiol. Rev.* **84,** 579–621 CrossRef Medline
9. Bohm, S. K., Kong, W., Bromme, D., Smeekens, S. P., Anderson, D. C., Connolly, A., Kahn, M., Nelken, N. A., Coughlin, S. R., Payan, D. G., and Bunnett, N. W. (1996) Molecular cloning, expression and potential functions of the human proteinase-activated receptor-2. *Biochem. J.* **314,** 1009–1016 CrossRef Medline
10. Cottrell, G. S., Amadesi, S., Grady, E. F., and Bunnett, N. W. (2004) Trypsin IV, a novel agonist of protease-activated receptors 2 and 4. *J. Biol. Chem.* **279,** 13532–13539 CrossRef Medline
11. Corvera, C. U., Déry, O., McConalogue, K., Böhm, S. K., Khitin, L. M., Caughey, G. H., Payan, D. G., and Bunnett, N. W. (1997) Mast cell tryptase regulates rat colonic myocytes through proteinase-activated receptor 2. *J. Clin. Invest.* **100,** 1383–1393 CrossRef Medline
12. Oikonomopoulou, K., Hansen, K. K., Saifeddine, M., Tea, I., Blaber, M., Blaber, S. I., Scarisbrick, I., Andrade-Gordon, P., Cottrell, G. S., Bunnett, N. W., Diamandis, E. P., and Hollenberg, M. D. (2006) Proteinase-activated receptors, targets for kallikrein signaling. *J. Biol. Chem.* **281,** 32095–32112 CrossRef Medline
13. Ramachandran, R., Mihara, K., Chung, H., Renaux, B., Lau, C. S., Muruve, D. A., DeFea, K. A., Bouvier, M., and Hollenberg, M. D. (2011) Neutrophil elastase acts as a biased agonist for proteinase-activated receptor-2 (PAR2). *J. Biol. Chem.* **286,** 24638–24648 CrossRef Medline
14. Zhao, P., Lieu, T., Barlow, N., Sostegni, S., Haerteis, S., Korbmacher, C., Liedtke, W., Jimenez-Vargas, N. N., Vanner, S. J., and Bunnett, N. W. (2015) Neutrophil elastase activates protease-activated receptor-2 (PAR2) and transient receptor potential vanilloid 4 (TRPV4) to cause inflammation and pain. *J. Biol. Chem.* **290,** 13875–13887 CrossRef Medline
15. Zhao, P., Lieu, T., Barlow, N., Metcalf, M., Veldhuis, N. A., Jensen, D. D., Kocan, M., Sostegni, S., Haerteis, S., Baraznenok, V., Henderson, I., Lindström, E., Guerrero-Alba, R., Valdez-Morales, E. E., Liedtke, W., *et al.* (2014) Cathepsin S causes inflammatory pain via biased agonism of PAR2 and TRPV4. *J. Biol. Chem.* **289,** 27215–27234 CrossRef Medline
16. Böhm, S. K., Khitin, L. M., Grady, E. F., Aponte, G., Payan, D. G., and Bunnett, N. W. (1996) Mechanisms of desensitization and resensitization of proteinase-activated receptor-2. *J. Biol. Chem.* **271,** 22003–22016 CrossRef Medline
17. Déry, O., Thoma, M. S., Wong, H., Grady, E. F., and Bunnett, N. W. (1999) Trafficking of proteinase-activated receptor-2 and β-arrestin-1 tagged with green fluorescent protein: β-arrestin-dependent endocytosis of a proteinase receptor. *J. Biol. Chem.* **274,** 18524–18535 CrossRef Medline
18. Jimenez-Vargas, N. N., Pattison, L. A., Zhao, P., Lieu, T., Latorre, R., Jensen, D. D., Castro, J., Aurelio, L., Le, G. T., Flynn, B., Herenbrink, C. K., Yeatman, H. R., Edgington-Mitchell, L., Porter, C. J. H., Halls, M. L., *et al.* (2018) Protease-activated receptor-2 in endosomes signals persistent pain of irritable bowel syndrome. *Proc. Natl. Acad. Sci. U.S.A.* **115,** E7438–E7447 CrossRef Medline
19. Jensen, D. D., Zhao, P., Jimenez-Vargas, N. N., Lieu, T., Gerges, M., Yeatman, H. R., Canals, M., Vanner, S. J., Poole, D. P., and Bunnett, N. W. (2016) Protein kinase D and Gβγ subunits mediate agonist-evoked translocation of protease-activated receptor-2 from the Golgi apparatus to the plasma membrane. *J. Biol. Chem.* **291,** 11285–11299 CrossRef Medline
20. Kunkel, M. T., Toker, A., Tsien, R. Y., and Newton, A. C. (2007) Calcium-dependent regulation of protein kinase D revealed by a genetically encoded kinase activity reporter. *J. Biol. Chem.* **282,** 6733–6742 CrossRef Medline
21. Jamora, C., Yamanouye, N., Van Lint, J., Laudenslager, J., Vandenheede, J. R., Faulkner, D. J., and Malhotra, V. (1999) Gβγ-mediated regulation of Golgi organization is through the direct activation of protein kinase D. *Cell* **98,** 59–68 CrossRef Medline
22. Linstedt, A. D., and Hauri, H. P. (1993) Giantin, a novel conserved Golgi membrane protein containing a cytoplasmic domain of at least 350 kDa. *Mol. Biol. Cell* **4,** 679–693 CrossRef Medline
23. Banting, G., and Ponnambalam, S. (1997) TGN38 and its orthologues: roles in post-TGN vesicle formation and maintenance of TGN morphology. *Biochim. Biophys. Acta* **1355,** 209–217 CrossRef Medline
24. Bonacci, T. M., Mathews, J. L., Yuan, C., Lehmann, D. M., Malik, S., Wu, D., Font, J. L., Bidlack, J. M., and Smrcka, A. V. (2006) Differential targeting of Gβγ-subunit signaling with small molecules. *Science* **312,** 443–446 CrossRef Medline
25. Koch, W. J., Hawes, B. E., Inglese, J., Luttrell, L. M., and Lefkowitz, R. J. (1994) Cellular expression of the carboxyl terminus of a G protein-coupled receptor kinase attenuates Gβγ-mediated signaling. *J. Biol. Chem.* **269,** 6193–6197 Medline
26. Liljedahl, M., Maeda, Y., Colanzi, A., Ayala, I., Van Lint, J., and Malhotra, V. (2001) Protein kinase D regulates the fission of cell surface destined transport carriers from the trans-Golgi network. *Cell* **104,** 409–420 CrossRef Medline
27. Yeaman, C., Ayala, M. I., Wright, J. R., Bard, F., Bossard, C., Ang, A., Maeda, Y., Seufferlein, T., Mellman, I., Nelson, W. J., and Malhotra, V. (2004) Protein kinase D regulates basolateral membrane protein exit from trans-Golgi network. *Nat. Cell Biol.* **6,** 106–112 CrossRef Medline

28. Harikumar, K. B., Kunnumakkara, A. B., Ochi, N., Tong, Z., Deorukhkar, A., Sung, B., Kelland, L., Jamieson, S., Sutherland, R., Raynham, T., Charles, M., Bagherazadeh, A., Foxton, C., Boakes, A., Farooq, M., *et al.* (2010) A novel small-molecule inhibitor of protein kinase D blocks pancreatic cancer growth *in vitro* and *in vivo*. *Mol. Cancer Ther.* **9,** 1136–1146 CrossRef Medline
29. Coria, A. S., Masseroni, M. L., and Díaz Añel, A. M. (2014) Regulation of PKD1-mediated Golgi to cell surface trafficking by Gα_q subunits. *Biol. Cell* **106,** 30–43 CrossRef Medline
30. Gschwendt, M., Dieterich, S., Rennecke, J., Kittstein, W., Mueller, H.-J., and Johannes, F.-J. (1996) Inhibition of protein kinase C μ by various inhibitors. Inhibition from protein kinase C isoenzymes. *FEBS Lett.* **392,** 77–80 CrossRef Medline
31. Muñiz, M., Martín, M. E., Hidalgo, J., and Velasco, A. (1997) Protein kinase A activity is required for the budding of constitutive transport vesicles from the trans-Golgi network. *Proc. Natl. Acad. Sci. U.S.A.* **94,** 14461–14466 CrossRef Medline
32. Bain, J., Plater, L., Elliott, M., Shpiro, N., Hastie, C. J., McLauchlan, H., Klevernic, I., Arthur, J. S., Alessi, D. R., and Cohen, P. (2007) The selectivity of protein kinase inhibitors: a further update. *Biochem. J.* **408,** 297–315 CrossRef Medline
33. Davies, S. P., Reddy, H., Caivano, M., and Cohen, P. (2000) Specificity and mechanism of action of some commonly used protein kinase inhibitors. *Biochem. J.* **351,** 95–105 CrossRef Medline
34. DeFea, K. A., Zalevsky, J., Thoma, M. S., Déry, O., Mullins, R. D., and Bunnett, N. W. (2000) β-Arrestin-dependent endocytosis of proteinase-activated receptor 2 is required for intracellular targeting of activated ERK1/2. *J. Cell Biol.* **148,** 1267–1281 CrossRef Medline
35. Jensen, D. D., Lieu, T., Halls, M. L., Veldhuis, N. A., Imlach, W. L., Mai, Q. N., Poole, D. P., Quach, T., Aurelio, L., Conner, J., Herenbrink, C. K., Barlow, N., Simpson, J. S., Scanlon, M. J., Graham, B., *et al.* (2017) Neurokinin 1 receptor signaling in endosomes mediates sustained nociception and is a viable therapeutic target for prolonged pain relief. *Sci. Transl. Med.* **9,** eaal3447 CrossRef Medline
36. Yarwood, R. E., Imlach, W. L., Lieu, T., Veldhuis, N. A., Jensen, D. D., Klein Herenbrink, C., Aurelio, L., Cai, Z., Christie, M. J., Poole, D. P., Porter, C. J. H., McLean, P., Hicks, G. A., Geppetti, P., Halls, M. L., *et al.* (2017) Endosomal signaling of the receptor for calcitonin gene-related peptide mediates pain transmission. *Proc. Natl. Acad. Sci. U.S.A.* **114,** 12309–12314 CrossRef Medline
37. Amadesi, S., Grant, A. D., Cottrell, G. S., Vaksman, N., Poole, D. P., Rozengurt, E., and Bunnett, N. W. (2009) Protein kinase D isoforms are expressed in rat and mouse primary sensory neurons and are activated by agonists of protease-activated receptor 2. *J. Comp. Neurol.* **516,** 141–156 CrossRef Medline
38. Jacamo, R., Sinnett-Smith, J., Rey, O., Waldron, R. T., and Rozengurt, E. (2008) Sequential protein kinase C (PKC)-dependent and PKC-independent protein kinase D catalytic activation via G$_q$-coupled receptors: differential regulation of activation loop Ser^{744} and Ser^{748} phosphorylation. *J. Biol. Chem.* **283,** 12877–12887 CrossRef Medline
39. Poole, D. P., Amadesi, S., Rozengurt, E., Thacker, M., Bunnett, N. W., and Furness, J. B. (2008) Stimulation of the neurokinin 3 receptor activates protein kinase C epsilon and protein kinase D in enteric neurons. *Am. J. Physiol. Gastrointest. Liver Physiol.* **294,** G1245–G1256 CrossRef Medline
40. Sinnett-Smith, J., Jacamo, R., Kui, R., Wang, Y. M., Young, S. H., Rey, O., Waldron, R. T., and Rozengurt, E. (2009) Protein kinase D mediates mitogenic signaling by G$_q$-coupled receptors through protein kinase C-independent regulation of activation loop Ser^{744} and Ser^{748} phosphorylation. *J. Biol. Chem.* **284,** 13434–13445 CrossRef Medline
41. Waldron, R. T., Innamorati, G., Torres-Marquez, M. E., Sinnett-Smith, J., and Rozengurt, E. (2012) Differential PKC-dependent and -independent PKD activation by G protein α subunits of the G$_q$ family: selective stimulation of PKD Ser^{748} autophosphorylation by Gα_q. *Cell. Signal.* **24,** 914–921 CrossRef Medline
42. Kenakin, T. (2011) Functional selectivity and biased receptor signaling. *J. Pharmacol. Exp. Ther.* **336,** 296–302 CrossRef Medline
43. Akgoz, M., Kalyanaraman, V., and Gautam, N. (2004) Receptor-mediated reversible translocation of the G protein $\beta\gamma$ complex from the plasma membrane to the Golgi complex. *J. Biol. Chem.* **279,** 51541–51544 CrossRef Medline

Protein kinase D and Gβγ mediate sustained nociceptive signaling by biased agonists of protease-activated receptor-2

Peishen Zhao, Luke A. Pattison, Dane D. Jensen, Nestor N. Jimenez-Vargas, Rocco Latorre, TinaMarie Lieu, Josue O. Jaramillo, Cintya Lopez-Lopez, Daniel P. Poole, Stephen J. Vanner, Brian L. Schmidt and Nigel W. Bunnett

J. Biol. Chem. 2019, 294:10649-10662.
doi: 10.1074/jbc.RA118.006935 originally published online May 29, 2019
